frontiers | Research Topics

Probing brain-behavior relationship with multimodal imaging: Methods and clinical applications

Edited by
Bin Jing, Yingying Tang, Yoonmi Hong and Ye Wu

Published in
Frontiers in Neuroscience

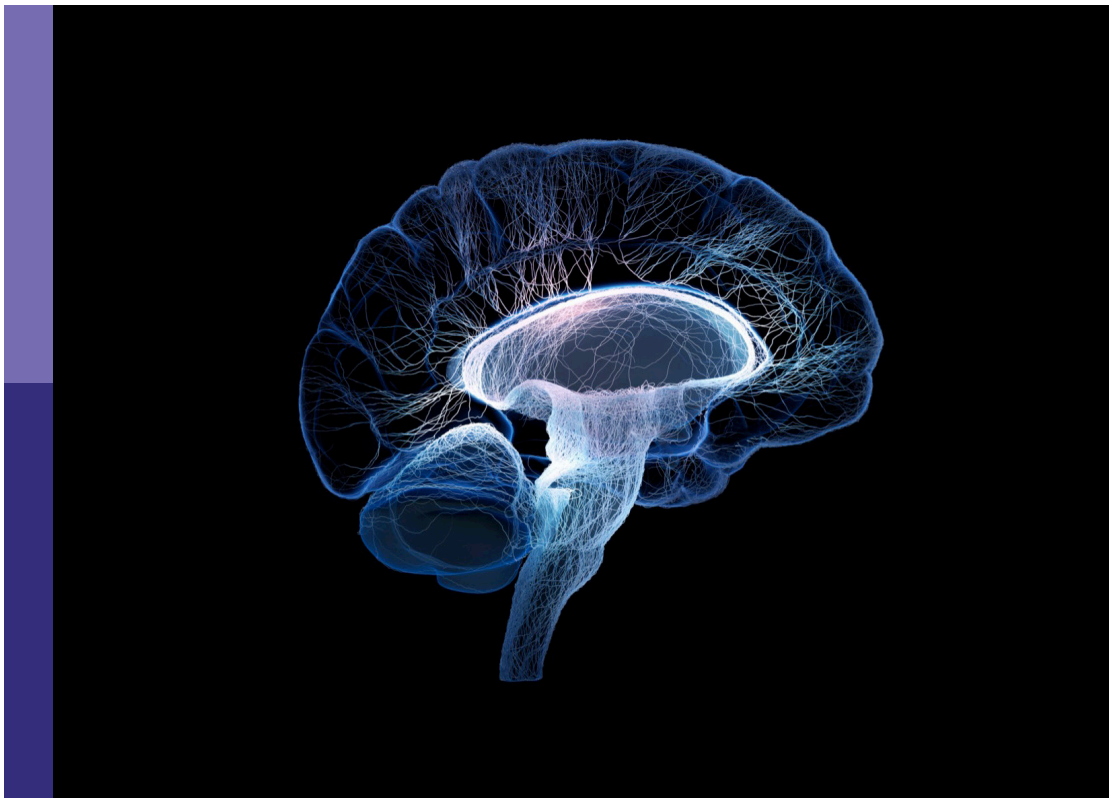

ISSN 1664-8714
ISBN 978-2-8325-4759-5
DOI 10.3389/978-2-8325-4759-5

About Frontiers

Frontiers is more than just an open access publisher of scholarly articles: it is a pioneering approach to the world of academia, radically improving the way scholarly research is managed. The grand vision of Frontiers is a world where all people have an equal opportunity to seek, share and generate knowledge. Frontiers provides immediate and permanent online open access to all its publications, but this alone is not enough to realize our grand goals.

Frontiers journal series

The Frontiers journal series is a multi-tier and interdisciplinary set of open-access, online journals, promising a paradigm shift from the current review, selection and dissemination processes in academic publishing. All Frontiers journals are driven by researchers for researchers; therefore, they constitute a service to the scholarly community. At the same time, the *Frontiers journal series* operates on a revolutionary invention, the tiered publishing system, initially addressing specific communities of scholars, and gradually climbing up to broader public understanding, thus serving the interests of the lay society, too.

Dedication to quality

Each Frontiers article is a landmark of the highest quality, thanks to genuinely collaborative interactions between authors and review editors, who include some of the world's best academicians. Research must be certified by peers before entering a stream of knowledge that may eventually reach the public - and shape society; therefore, Frontiers only applies the most rigorous and unbiased reviews. Frontiers revolutionizes research publishing by freely delivering the most outstanding research, evaluated with no bias from both the academic and social point of view. By applying the most advanced information technologies, Frontiers is catapulting scholarly publishing into a new generation.

What are Frontiers Research Topics?

Frontiers Research Topics are very popular trademarks of the *Frontiers journals series*: they are collections of at least ten articles, all centered on a particular subject. With their unique mix of varied contributions from Original Research to Review Articles, Frontiers Research Topics unify the most influential researchers, the latest key findings and historical advances in a hot research area.

Find out more on how to host your own Frontiers Research Topic or contribute to one as an author by contacting the Frontiers editorial office: frontiersin.org/about/contact

Probing brain-behavior relationship with multimodal imaging: Methods and clinical applications

Topic editors

Bin Jing — Capital Medical University, China

Yingying Tang — Shanghai Jiao Tong University, China

Yoonmi Hong — University of North Carolina at Chapel Hill, United States

Ye Wu — Nanjing University of Science and Technology, China

Citation

Jing, B., Tang, Y., Hong, Y., Wu, Y., eds. (2024). *Probing brain-behavior relationship with multimodal imaging: Methods and clinical applications*.

Lausanne: Frontiers Media SA. doi: 10.3389/978-2-8325-4759-5

Table of contents

frontiers | Frontiers in Neuroscience

TYPE Original Research
PUBLISHED 16 November 2022
DOI 10.3389/fnins.2022.1037244

OPEN ACCESS

EDITED BY
Yingying Tang,
Shanghai Jiao Tong University, China

REVIEWED BY
Weining Ma,
Shengjing Hospital of China Medical University, China
Cuiping Xu,
Beijing Institute of Functional Neurosurgery, China

*CORRESPONDENCE
Guoming Luan
luangm@ccmu.edu.cn

SPECIALTY SECTION
This article was submitted to Brain Imaging Methods, a section of the journal Frontiers in Neuroscience

RECEIVED 05 September 2022
ACCEPTED 01 November 2022
PUBLISHED 16 November 2022

CITATION
Xu K, Wang X, Zhou J, Guan Y, Li T and Luan G (2022) The differential role of magnetic resonance imaging in predicting surgical outcomes between children versus adults with temporal lobe epilepsy. *Front. Neurosci.* 16:1037244. doi: 10.3389/fnins.2022.1037244

The differential role of magnetic resonance imaging in predicting surgical outcomes between children versus adults with temporal lobe epilepsy

Ke Xu [1], Xiongfei Wang[1], Jian Zhou[1], Yuguang Guan[1], Tianfu Li[2,3] and Guoming Luan [1,3]*

[1]Department of Neurosurgery, Sanbo Brain Hospital, Capital Medical University, Beijing, China, [2]Department of Neurology, Sanbo Brain Hospital, Capital Medical University, Beijing, China, [3]Department of Brain Institute, Center of Epilepsy, Beijing Institute for Brain Disorders, Beijing Key Laboratory of Epilepsy Research, Sanbo Brain Hospital, Capital Medical University, Beijing, China

Objective: This study aims to investigate the clinical discrepancies and the different predictors of anterior temporal lobectomy (ATL) in children (<18 years at surgery) and adults (>18 years at surgery) with temporal lobe epilepsy (TLE).

Materials and methods: A total of 262 patients (56 children and 206 adults) with TLE who underwent ATL were included in this study. The clinical variables, including patients' characteristics, preoperative evaluations, pathology, surgical prognosis, and surgical predictors were assessed the discrepancies between TLE children versus adults using univariate and multivariate analyses. Kaplan-Meier survival analysis was used to calculate the probability of seizure freedom and AEDs withdrawal after ATL, and the difference between TLE children and adults was analyzed using the Log-Rank test.

Results: There were significant differences including semiology, magnetic resonance imaging (MRI) examinations, numbers of preoperative AEDs, and pathologies between TLE children and adults ($P < 0.05$, $Q < 0.05$). The MRI-detected epileptic focus was the only independent predictor of seizure freedom ($P = 0.002$, $Q = 0.036$) in TLE children, and the concordance of MRI-detected focus with video-electroencephalography (video-EEG)-detected epileptic zone was the only variable associated with seizure freedom in TLE adults ($OR = 2.686$, 95% $CI = 1.014–7.115$, $P = 0.047$). The TLE children experienced a higher probability of AEDs withdrawal than adults after surgery ($P = 0.005$).

Significance: There were remarkable differences in clinical manifestations, MRI examinations, number of preoperative AEDs, and pathologies between

TLE children versus adults. TLE children had a higher possibility of AEDs withdrawal than adults after surgery. The favorable seizure outcome of ATL depended on the early complete resection of MRI-detected epileptogenic focus in TLE children, while the concordance of MRI-detected focus with EEG-detected epileptogenic zone was the only predictor of favorable seizure outcomes in TLE adults.

KEYWORDS

temporal lobe epilepsy, neurosurgery, neuropathology, magnetic resonance imaging, seizure outcome

Introduction

Temporal lobe epilepsy (TLE) is considered as the most common type of epilepsy that is refractory to antiepileptic drugs (AEDs) (Engel et al., 2003). Anterior temporal lobectomy (ATL) is a widely used surgical procedure with a seizure freedom rate from 62 to 83% (Mathon et al., 2015). Various studies have shown magnetic resonance imaging (MRI) – detected epileptogenic focus, particularly the presence of mesial temporal sclerosis, is a predictor of favorable outcomes in patients undergoing surgical treatment for TLE (Antel et al., 2002; McIntosh et al., 2004; Clusmann, 2008; Sun et al., 2015). However, significant discrepancies in presurgical, surgical, and postsurgical features between children and adults with TLE (Spencer and Huh, 2008; Ryvlin et al., 2014; Baud et al., 2018; Barba et al., 2021), and differences in the predictive role of MRI in TLE children versus adults remain poorly reported before (Barba et al., 2021). Furthermore, a large variation in the proportion of patients within the different pathological categories between children and adults has been reported before (Blumcke et al., 2017). Therefore, the predictors of seizure outcomes after ATL in children may not be appropriate for adults, due to these differences in clinical manifestations and pathology of TLE (Goldstein et al., 1996).

Few studies have described differences in clinical manifestations and predictors for ATL between TLE children and adults in single center (Lee et al., 2010; Baud et al., 2018; Cloppenborg et al., 2019; Barba et al., 2021). Accordingly, this study will answer the following questions: (1) What are the discrepancies in etiologies and clinical manifestations between TLE children and adults? (2) What are the differences in surgical effects on TLE children and adults with prognosis and AEDs withdrawal? (3) Does MRI have a different predictive role for surgical outcomes in children and adults with TLE? This study will highlight the differences in clinical manifestations, surgical prognosis, and surgical predictors between TLE children versus adults, and provide suitable surgical candidates for different TLE populations.

Materials and methods

Patients selection

Data of patients with TLE who had undergone surgery at Sanbo Brain Hospital, Capital Medical University from January 2009 to December 2019 were retrospectively recorded. Detailed data including demographic characteristics, clinical examinations, and post-surgical pathologies that can influence surgical outcomes were collected. This study was approved by the Ethics Committee of Sanbo Brain Hospital, Capital Medical University (SBNK-2017-15-01).

The exclusion criteria were as follows: (1) patients with drug-resistant extratemporal epilepsy; (2) patients who underwent extended ATL other than standard ATL (Spencer et al., 1984); (3) patients who underwent lesionectomy for the temporal lobe tumors; (4) patients who had a history of epilepsy surgery; (5) patients who had incomplete pathological tissue; (6) patients with the surgical pathology of encephalomalacia; (7) patients who had a follow-up for less than 24 months after surgery.

Preoperative evaluation

The preoperative variables were collected from the medical records, which included sex, age at seizure onset, seizure duration, semiology, age at surgery, age at surgery, AEDs, history of febrile seizure (FS) (Menzler et al., 2011), MRI examinations, video-EEG, magnetoencephalography (MEG), [^{18}F]-fluorodeoxyglucose positron emission tomography (^{18}FDG-PET), stereoelectroencephalography (SEEG), and the side of surgery. Brain MRI of TLE patients was scanned with a 1.5 or 3.0-T scanner for T1, T2, and T2 fluid-attenuated inversion recovery (FLAIR) sequences. The standard 64-channel long-term video EEG monitoring was used in patients for at least 24 h. The video EEG was sampled at the rate of 1,024 samples and recorded in a double banana montage. The epileptogenic

zone was defined according to the scalp or invasive EEG results, and the MRI results classified as normal, hippocampal sclerosis (HS), temporal lobe (TL) abnormalities (temporal blurring, dysplasia, or atrophy), both HS and TL abnormalities, and tumor. Accordingly, those patients with concordance or discordance of MRI and video-EEG results were distinguished, respectively. To accurately locate the epileptogenic zone, the MEG [102 patients (26 children; 76 adults)] can help to delineate the epileptogenic zone by localizing interictal epileptic spikes, PET [144 patients (26 children; 118 adults)] that can locate the hypometabolic regions, and SEEG [52 patients (6 children; 46 adults)] were also performed. After completion of the presurgical evaluation by neurosurgeons, neurologists, neuropsychologists, electrophysiologists, and neuroradiologists, the surgical decision was made.

Surgical procedure

The purpose of ATL was to remove the epileptogenic zone and epileptogenic focus, and there is no difference in the surgical procedure between TLE children and adults. The standard ATL procedure included the resection of 3.0–3.5 cm from the anterolateral temporal lobe in the dominant hemisphere or the 4.0–4.5 cm of the temporal lobe in the non-dominant hemisphere. The resection of the mesial structure included the resection of the amygdala and the anterior 3.0 cm of the hippocampus. There was no difference in the resection of mesial structure between the dominant and non-dominant hemispheres (Spencer et al., 1984). For the patients with temporal lobe tumors, the ATL plus lesionectomy was performed.

Surgical outcomes and complications

Patients were evaluated at 3 months postoperatively and yearly thereafter. The 16-h scalp-EEG and MRI were performed routinely. The surgical complications including intracranial hemorrhage, intracranial infection, and neurological dysfunction were recorded after surgery. The timing of the first postoperative seizure onset (beyond the first postoperative week for patients with acute postoperative seizures) was considered the time of seizure recurrence. Seizure outcomes were categorized according to the Engel classification system (Engel Jr, 1993). Favorable seizure outcomes were defined as Engel class I during the last 2 years of follow-up, and unfavorable seizure outcomes were defined as Engel class II–IV. For patients with seizure freedom of more than 2 years (Braun and Schmidt, 2014), the protocol for AEDs reduction was determined by the neurologist. The AEDs gradually tapered one by one. Thereafter, if patients had auras, seizures, or epileptiform abnormalities on scalp EEG results (Tang and Xiao, 2017), the AEDs were continued at the minimum doses without further tapering.

Statistical analysis

Continuous variables were described using means ± standard deviations, and the categorical variables were described using frequencies and percentages. The difference between the adult and children's subgroups was based on a cut-off age of 18 years at the surgery (Blumcke et al., 2017). Accordingly, the clinical variables, including patients' characteristics, preoperative evaluations, pathology, and surgical prognosis were assessed the discrepancies between TLE children and adults using Pearson's chi-square or Student *t-test*.

The cut-off variables were determined according to Youden's index in a receiver operating characteristic curve analysis, and then variables were performed using Pearson's chi-square or Fisher's exact test to evaluate the predictors of a favorable outcome in TLE subgroups. The Benjamini-Hochberg false discovery rate (FDR) control to correct the final models for multiple comparisons. By default, this study used the first value in the list of variables as a reference category, after verifying that there were not too few cases in the chosen category. *P*-value and the FDR *Q*-value thresholds were set for significance. Finally, the variables showing a Q value < 0.05 in the univariate analysis were then into a multivariable logistic regression model in a backward manner for TLE adults and children, respectively. The odd ratios (ORs) and 95% confidence intervals (CIs) were calculated from the regression model.

Kaplan-Meier (KM) survival analysis was used to calculate the probability of seizure freedom and AEDs withdrawal after ATL, and the difference between TLE children and adults was analyzed using the Log-Rank test. The relationship between probable predictors and seizure freedom was also calculated by KM survival analysis in TLE adults and children, respectively. All analyses were performed using SPSS software (version 24.0, IBM, NY, USA), and a P value < 0.05 was considered statistically significant.

Results

Differences in patients' characteristics between temporal lobe epilepsy subgroups

Two hundred and sixty-two patients fulfilled the criteria and were analyzed in this study (56 children, 206 adults, **Figure 1**). The mean age at surgery was 11.39 ± 3.90 years in children and 28.16 ± 7.85 years in adults ($P < 0.001$; $Q < 0.001$); the mean age at seizure onset was 5.54 ± 4.37 years in children

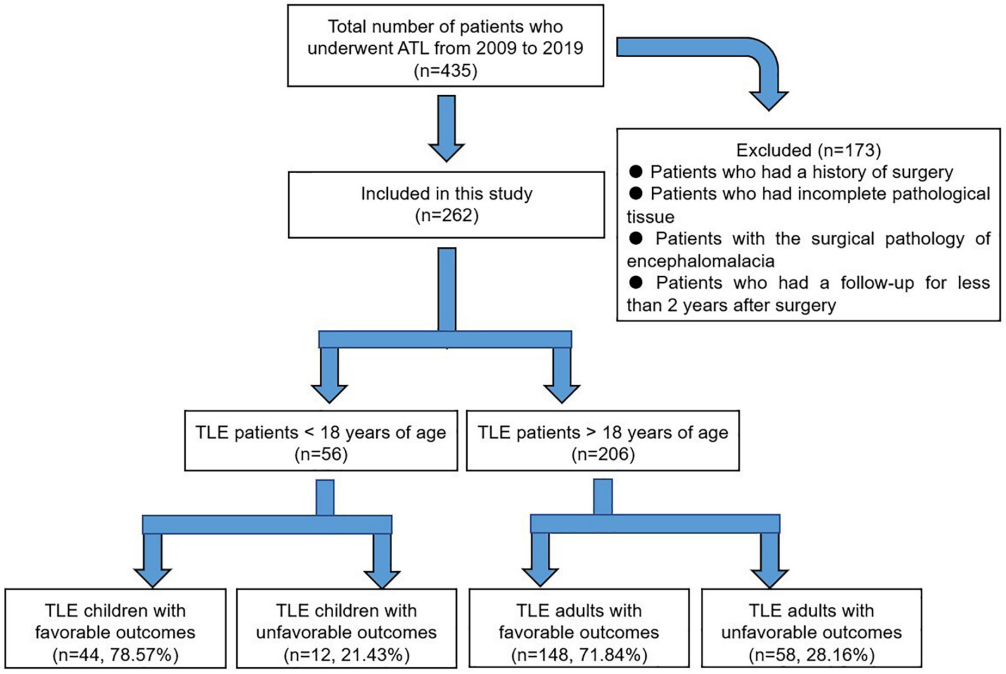

FIGURE 1
Outline of the study design and summary of outcomes. Favorable outcomes: patients with Engel class I during the last 2 years of follow-up; unfavorable outcomes: patients with Engel class II–IV during the last 2 years of follow-up.

and 13.13 ± 9.78 years in adults ($P < 0.001$; $Q < 0.001$); the mean duration of epilepsy was 6.04 ± 3.77 years in children and 14.86 ± 9.39 years in adults ($P < 0.001$; $Q < 0.001$). In addition, the detailed comparison of semiology (Fisher et al., 2017), types of AEDs, and history of FS between TLE children and adults were described in **Table 1**.

Differences in preoperative evaluation between temporal lobe epilepsy subgroups

Magnetic resonance imaging examinations were obtained in 56 children (2 were normal, 13 were HS, 13 were TL abnormalities, 3 were both HS and TL abnormalities, and 25 were temporal tumors) and 206 adults (7 were normal, 130 were HS, 37 were TL abnormalities, 16 were both HS and TL abnormalities, and 16 were temporal tumors; $P < 0.001$, $Q < 0.001$). During the video-EEG monitoring, interictal epileptic discharges (IEDs) were recorded in all patients with 31 (55.4%) children and 127 (61.7%) adults arising at unilateral temporal lobe ($P = 0.442$). The ictal onset rhythms (IORs) were detected in unilateral temporal lobe in 17 (30.4%) children and 80 (38.9%) adults ($P = 0.470$). The MEG spikes sources locating at unilateral temporal lobe were observed in 9 (34.6%) children and 44 (57.9%) adults ($P = 0.045$; $Q = 0.100$). The hypometabolic regions of PET locating in the unilateral temporal lobe were found in 19 (73.1%) children and 61 (51.7%) adults ($P = 0.047$; $Q = 0.095$). SEEG implantation was performed in 6 (10.7%) children and 46 (22.3%) adults ($P = 0.085$, **Table 1**).

Differences in surgical prognosis between temporal lobe epilepsy subgroups

The surgery on the left side was performed in 29 (51.8%) children and 109 (52.9%) adults ($P = 0.881$). There were no operative or perioperative deaths. Surgical complications occurred in 7 (12.5%) children; 1 (1.8%) had intracranial hemorrhage, 3 (5.4%) had intracranial infection, 1 (1.8%) had transient hemiplegia, and 2 (3.6%) had transient aphasia. Surgical complications were observed in 18 (8.7%) adults; 2 (0.9%) had intracranial heamorrhage, 1 (0.5%) had a subarachnoid hemorrhage, 2 (0.9%) had an intracranial infection, 4 (1.9%) had transient hemiplegia, and 9 (4.4%) had transient aphasia. Quadrantanopia was not considered a surgical complication in this study. There was no significant difference of surgical complications between TLE children and adults ($P = 0.395$, **Table 1**).

After a follow-up period of 2–5 years (mean 3.47 ± 1.91 years), 44 (78.6%) children achieved seizure freedom, and 148 (71.8%) adults achieved seizure freedom after ATL ($P = 0.395$, **Table 1**). For these seizure freedom patients,

TABLE 1 The difference in demographic characteristics between temporal lobe epilepsy (TLE) children and adults.

Demographic characteristics	Children	Adults	*P*-value	*Q*-value
Sex (male)	33 (58.93%)	108 (52.43%)	0.451	0.501
Age at seizure onset	5.54 ± 4.37	13.13 ± 9.78	**0.000***	**0.000***
Duration of epilepsy	6.04 ± 3.77	14.86 ± 9.39	**0.000***	**0.000***
Auras	16 (28.57%)	110 (53.39%)	**0.001***	**0.003***
Impaired awareness	43 (76.79%)	142 (68.93%)	0.321	0.458
Automatisms	33 (58.93%)	145 (70.39%)	0.109	0.182
Secondary-GTCS	23 (41.07%)	129 (62.62%)	**0.006***	**0.017***
FS	7 (12.50%)	43 (20.87%)	0.183	0.282
Numbers of preop AEDs				
Two types	39 (69.64%)	189 (91.75%)	**0.001***	**0.003***
Three types	17 (30.36%)	17 (8.25%)		
MRI results				
Normal	2 (3.57%)	7 (3.39%)	**0.000***	**0.000***
HS	13 (23.21%)	130 (63.11%)		
Additional TL abnormalities	13 (23.21%)	37 (17.96%)		
Both HS and additional TL abnormalities	3 (5.36%)	16 (7.77%)		
Tumor	25 (44.64%)	16 (7.77%)		
IEDs on unilateral temporal lobe	31 (55.36%)	127 (61.65%)	0.442	0.521
Ictal onset on unilateral temporal lobe	17 (30.36%)	80 (38.83%)	0.47	0.495
MEG on unilateral temporal lobe	9 (N = 26, 34.62%)	44 (N = 76, 57.89%)	**0.045***	0.1
PET on unilateral temporal lobe	19 (N = 26, 73.08%)	61 (N = 118, 51.69%)	**0.047***	0.095
SEEG implantation	6 (10.71%)	46 (22.33%)	0.085	0.155
Age at surgery	11.39 ± 3.90	28.16 ± 7.85	**0.000***	**0.000***
Surgery on the left side	29 (51.79%)	109 (52.91%)	0.881	0.881
Neuropathology				
FCD type I	12 (21.42%)	48 (23.30%)	**0.000***	**0.000***
HS	4 (7.14%)	106 (51.46%)		
FCD type IIIa	25 (44.64%)	32 (15.53%)		
Tumors	15 (26.78%)	16 (7.77%)		
Others	0 (0.00%)	4 (1.94%)		
Surgical complications	7 (12.50%)	18 (8.70%)	0.395	0.504
Favorable outcomes	44 (78.57%)	148 (71.84%)	0.395	0.493

HS, hippocampal sclerosis; GTCS, generalized tonic–clonic seizure; FS, febrile seizure; ATL, anterior temporal lobectomy; MRI, magnetic resonance imaging; TL, temporal lobe; IEDs, interictal epileptic discharges; AEDs, antiepileptic drugs; MEG, magnetoencephalography; PET, positron emission tomography; SEEG, stereo-electroencephalography; FCD, focal cortical dysplasia.

*$P < 0.05$. Bold: TLE children experienced earlier age at seizure onset, shorter duration of epilepsy, fewer auras, and fewer secondary-GTCS than those in TLE adults. The TLE children took more AEDs than those in TLE adults. More MRI-detected HS was observed in TLE adults, while more MRI-detected tumors were observed in TLE children. The TLE adults experienced elder age at surgery than those in TLE children. More neuropathology of HS was observed in TLE adults, while more neuropathology of tumors was observed in TLE children.

AEDs had completely discontinued in 32 (72.7%) children and 73 (35.4%) adults. Two (6.3%) children and 8 (10.9%) adults experienced seizure recurrence after AEDs withdrawal.

Differences in neuropathology between temporal lobe epilepsy subgroups

Surgical specimens were processed for histological analysis. The HS was diagnosed in 4 (7.1%) children and 106 (51.5%) adults. Focal cortical dysplasia (FCD) type I was diagnosed in 12 (21.4%) children (6 FCD type Ia, 6 FCD type Ib) and 48 (23.3%) adults (21 FCD type Ia, 27 FCD type Ib). Fifteen (26.8%) children were diagnosed with temporal tumors (14 gangliogliomas WHO grade I, 1 dysembryoplastic neuroepithelial tumor WHO grade I), and 16 (7.8%) adults were diagnosed with tumors (9 gangliogliomas WHO grade I, 5 dysembryoplastic neuroepithelial tumors WHO grade I, and 2 astrocytomas WHO grade II). Besides, 25 children (44.6%) and 32 adults (15.5%) were

diagnosed with FCD type IIIa ($P < 0.001$; $Q < 0.001$, Table 1).

Prognostic factors of seizure outcomes

In the univariate analysis of postoperative seizure outcomes, the duration of epilepsy (≤7.5 years), secondary-GTCS, MRI examinations, and neuropathology showed a significant difference in TLE children ($P < 0.05$, Table 2). However, the MRI examinations were the only independent predictor of favorable seizure outcomes after the FDR correction ($Q = 0.036$, Table 2). The TLE children with MRI-detected tumor had a better prognosis after ATL, while those with MRI-detected TL abnormalities were suggested to experience a worse seizure outcome (Figure 2).

After the FDR correction of univariate analysis in the TLE adults, the following factors were associated with favorable seizure outcomes: IEDs on the unilateral temporal lobe and concordance of MRI with IEDs ($Q < 0.05$, Table 3). Therefore, these two variables were recruited into the logistic regression model. The regression analysis revealed that the concordance of MRI with IEDs results was the only predictor of favorable

TABLE 2 Children's demographic characteristics and their relationship with seizure outcomes.

Demographic characteristics	Favorable outcome ($N = 44$)	Unfavorable Outcome ($N = 12$)	*P*-value	*Q*-value
	Number (%)	Number (%)		
Sex (male)	25 (56.82%)	8 (66.67%)	0.539	1.033
Age at seizure onset (≤7.5 years)	27 (61.36%)	9 (75.00%)	0.382	0.879
Duration of epilepsy (≤7.5 years)	33 (75.00%)	5 (41.67%)	**0.028***	0.215
Age at ATL (≤14.5 years)	40 (90.91%)	9 (75.00%)	0.14	0.403
Monthly seizure frequency (ł10 times)	27 (61.36%)	7 (58.33)	0.849	0.849
Automatisms	11 (25.00%)	5 (41.67%)	0.257	0.657
Impaired awareness	36 (81.82%)	7 (58.33%)	0.088	0.337
Autism	29 (65.91%)	4 (33.33%)	0.054	0.248
Secondary-GTCS	15 (34.09%)	8 (66.67%)	**0.042***	0.241
FS	6 (13.64%)	1 (8.33%)	0.622	0.953
Numbers of preop AEDs				
Two types	31 (70.45%)	8 (66.67%)	0.801	0.921
Three types	13 (29.54%)	4 (33.33%)		
MRI results				
Normal	2 (4.54%)	0 (0.00%)	**0.002***	**0.046***
HS	9 (20.45%)	4 (33.33%)		
Additional TL abnormalities	6 (13.63%)	7 (58.33%)		
Both HS and additional TL abnormalities	3 (6.81%)	0 (0.00%)		
Tumor	24 (54.54%)	1 (8.33%)		
IEDs on unilateral temporal lobe	25 (56.82%)	6 (50.00%)	0.674	0.912
Ictal onset on unilateral temporal lobe	14 (31.82%)	3 (25.00%)	0.649	0.933
Concordance of MRI with IEDs	19 (43.18%)	4 (33.33%)	0.539	1.033
Concordance of MRI with ictal onset	11 (25.00%)	2 (16.67%)	0.544	0.962
MEG on unilateral temporal lobe	6 ($N = 18$, 33.33%)	3 ($N = 8$, 37.50%)	0.837	0.875
PET on unilateral temporal lobe	15 ($N = 20$, 75.00%)	4 ($N = 6$, 66.67%)	0.686	0.877
SEEG implantation	3 (6.82%)	3 (25.00%)	0.105	0.345
Surgery on the left side	22 (50.00%)	7 (58.33%)	0.609	1.005
Neuropathology				
FCD type I	7 (15.91%)	5 (41.67%)	**0.022***	0.253
HS	2 (4.54%)	2 (16.67%)		
FCD type IIIa	11 (25%)	4 (33.33%)		
Tumors	24 (54.54%)	1 (8.33%)		

HS, hippocampal sclerosis; GTCS, generalized tonic–clonic seizure; FS, febrile seizure; ATL, anterior temporal lobectomy; MRI, magnetic resonance imaging; TL, temporal lobe; IEDs, interictal epileptic discharges; AEDs, antiepileptic drugs; MEG, magnetoencephalography; PET, positron emission tomography; SEEG, stereo-electroencephalography; FCD, focal cortical dysplasia.

*$P < 0.05$. Bold: The TLE children with MRI-detected tumors had a better prognosis after surgery than those with other MRI results.

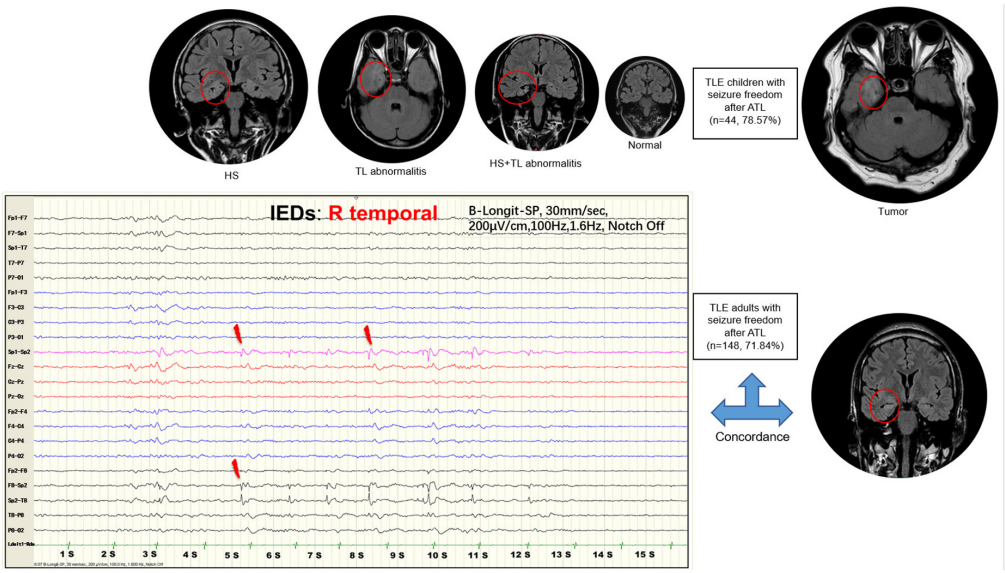

FIGURE 2
The differential role of magnetic resonance imaging (MRI) in predicting surgical outcomes between temporal lobe epilepsy (TLE) children versus adults. The favorable seizure outcome of anterior temporal lobectomy (ATL) depended on the early complete resection of MRI-detected epileptogenic focus in TLE children. The size of the image represented the contribution to the favorable outcomes after surgery. The concordance of MRI with interictal epileptic discharges (IEDs) results was the only predictor of favorable seizure outcomes in TLE adults. The scalp EEG were sampled at the rate of 1,024 samples, and the typically bandpass filtered for viewing between 1.6 and 100 Hz. The data was recorded in a double banana montage, and the sensitivity was 200 μV/cm.

seizure outcomes in TLE adults (OR = 0.2.686, 95% CI = 1.014–7.115, $P = 0.047$, Table 4).

Kaplan-Meier analysis of seizure-free survival

The KM survival curves were made to evaluate the seizure-free survival and AEDs withdrawal between children and adults. The results revealed that there was no significant difference in seizure-free survival between children and adults ($P = 0.353$, Figure 3A). However, TLE adults experienced a lower probability of AEDs withdrawal than children ($P = 0.005$, Figure 3B). The KM estimates of the probability of cumulative seizure-free survival in months were no significant difference in those with or without prognostic factors in TLE subgroups ($P > 0.05$, Figure 4).

Discussion

This study analyzed the significant differences in clinical manifestations, pathologies, and prognoses of TLE children versus adults, which promoted the understanding of the discrepancies between TLE children and adults. In addition, the predictive factor of MRI which affect the short and long-term prognosis after ATL was important for the appropriate selection and counselling in different TLE populations.

Differences in clinical manifestations and pathologies between temporal lobe epilepsy children and adults

As the results showed in this study, the TLE adults experienced more presence of auras, automatisms, and secondary-GTCS than those TLE children. In addition, the types of lesions in MR and pathology were significant differences in the TLE subgroups. This study revealed that HS was the most common pathology in the brain tissue of epileptic adults, and the FCD was the most common pathology among children, which was consistent with a previous study (Blumcke et al., 2017). The distinct pathology and long-term seizure duration promote the more complex epileptic network in TLE adults, which could induce comprehensive semiology. Therefore, TLE children and adults should be studied separately to reduce the bias in the prognostic analysis (Barba et al., 2021). A previous study found very similar clinical manifestations and responses to surgical treatment in TLE children and adults (Asadi-Pooya and Sperling, 2015). Conversely, the other multicentre analysis demonstrated significant differences in several presurgical, surgical, and postsurgical features between adults and children (Barba et al., 2021). These

TABLE 3 Adults' demographic characteristics and their relationship with seizure outcomes.

Demographic characteristics	Favorable outcome ($N = 148$)	Unfavorable outcome ($N = 58$)	*P*-value	*Q*-value
	Number (%)	Number (%)		
Sex (male)	75 (50.68%)	33 (56.89%)	0.421	0.509
Age at seizure onset (≤11.5 years)	72 (48.65%)	24 (41.38%)	0.347	0.532
Duration of epilepsy (≤25 years)	130 (87.84%)	47 (81.03%)	0.207	0.476
Age at ATL (≤22.5 years)	35 (23.65%)	12 (20.69%)	0.649	0.711
Monthly seizure frequency (≥10 times)	58 (39.19%)	26 (44.82%)	0.459	0.528
Auras	83 (56.08%)	27 (46.55%)	0.218	0.455
Secondary-GTCS	105 (70.96%)	37 (63.79%)	0.318	0.522
Automatisms	108 (72.97%)	37 (63.79%)	0.235	0.45
Secondary-GTCS	90 (60.81%)	39 (67.24%)	0.391	0.529
FS	35 (23.65%)	8 (13.79%)	0.117	0.336
Numbers of preop AEDs				
Two types	136 (91.89%)	53 (91.38%)	0.904	0.945
Three types	12 (8.11%)	5 (8.62%)		
MRI results				
Normal	4 (2.70%)	3 (5.17%)	0.058	0.222
HS	102 (68.92%)	28 (48.28%)		
Additional TL abnormalities	23 (15.54%)	14 (24.14%)		
Both HS and additional TL abnormalities	8 (5.41%)	8 (13.79%)		
Tumor	11 (7.43%)	5 (8.62%)		
IEDs on unilateral temporal lobe	101 (68.24%)	26 (44.83%)	**0.002***	**0.023***
Ictal onset rhythms on unilateral temporal lobe	64 (43.24%)	16 (27.59%)	**0.038***	0.291
Concordance of MRI with IEDs	87 (58.78%)	18 (31.03%)	**0.001***	**0.023***
Concordance of MRI with ictal onset	55 (37.16%)	11 (18.97%)	**0.042***	0.242
MEG on unilateral temporal lobe	29 ($N = 47$, 61.70%)	15 ($N = 29$, 51.72%)	0.392	0.501
PET on unilateral temporal lobe	48 ($N = 87$, 55.17%)	13 ($N = 31$, 41.94%)	0.205	0.524
SEEG implantation	33 (22.29%)	13 (22.41%)	0.986	0.986
Surgery on the left side	75 (50.68%)	34 (58.62%)	0.304	0.537
Neuropathology				
FCD type I	32 (21.62%)	16 (27.59%)	0.387	0.556
HS	76 (51.35%)	30 (51.72%)		
FCD type IIIa	27 (18.24%)	5 (8.62%)		
Tumors	11 (7.43%)	5 (8.62%)		
Others	2 (1.35%)	2 (3.45%)		

HS, hippocampal sclerosis; GTCS, generalized tonic–clonic seizure; FS, febrile seizure; ATL, anterior temporal lobectomy; MRI, magnetic resonance imaging; TL, temporal lobe; IEDs, interictal epileptic discharges; AEDs, antiepileptic drugs; MEG, magnetoencephalography; PET, positron emission tomography; SEEG, stereo-electroencephalography; FCD, focal cortical dysplasia.

*$P < 0.05$. Bold: The TLE adults with IEDs on the unilateral temporal lobe or concordance of MRI with IEDs experienced better surgical outcomes.

discrepancies might be explained by differences in inclusion criteria.

Predictive role of magnetic resonance imaging in the temporal lobe epilepsy children

Anterior temporal lobectomy was the choice to provide better access to the tumor or if the epileptogenic area was much larger than the tumor itself in children (Cataltepe et al., 2005). The completeness of tumor resection determined seizure outcomes in children (Khajavi et al., 1999; Lopez-Gonzalez et al., 2012), and several investigators had reported

TABLE 4 Predictors of seizure outcome in adults on multivariate analysis.

Variables	OR	95% CI	*P*-value
IEDs on unilateral temporal lobe	1.241	0.481–3.2	0.655
Concordance of MRI with IEDs results	2.686	1.014–7.115	**0.047***

IEDs, interictal epileptic discharges; MRI, magnetic resonance imaging; OR, odds ratio; CI, confidence interval.

*$P < 0.05$. Bold: The regression analysis revealed that the concordance of MRI with IED results was the only predictor of favorable seizure outcomes in TLE adults.

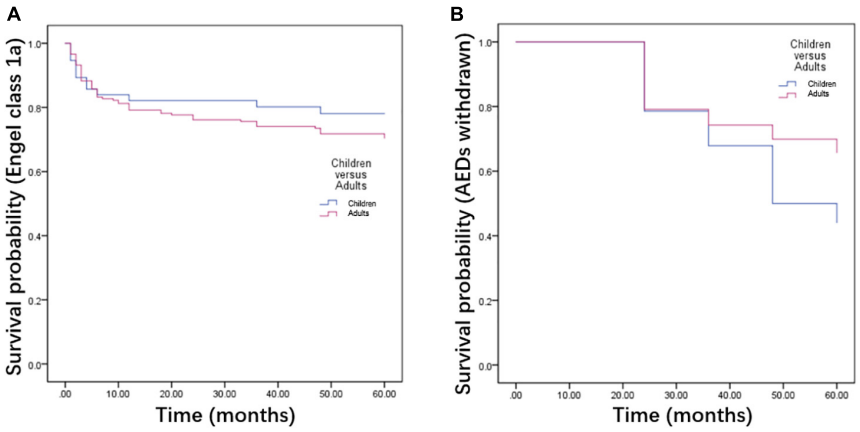

FIGURE 3
Kaplan-Meier survival curves of children and adults with temporal lobe epilepsy (TLE). There was no significant difference in seizure recurrence between TLE children and adults **(A)**. The TLE adults experienced a lower probability of antiepileptic drugs (AEDs) withdrawal than TLE children after surgery **(B)**.

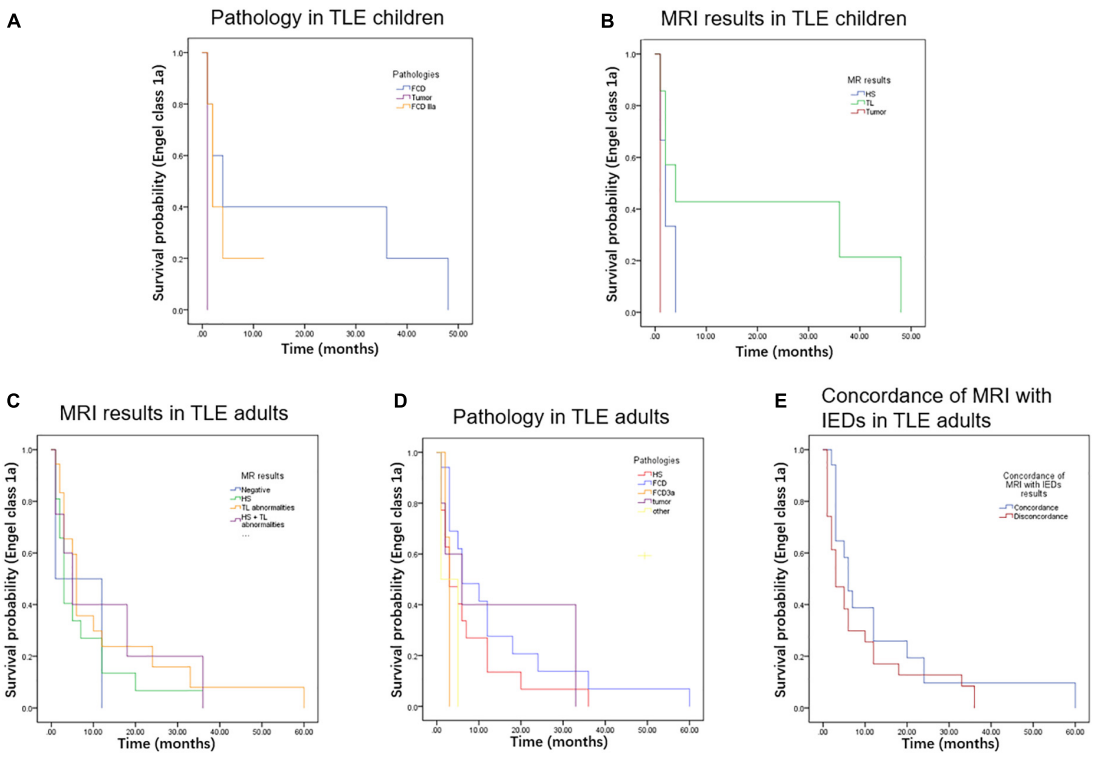

FIGURE 4
The Kaplan-Meier estimates of the probability of cumulative seizure-free survival in months were not a significant difference in those TLE children with different pathologies **(A)**, different MRI results **(B)**, in those TLE adults with different MRI results **(C)**, different pathologies **(D)**, and concordance of MRI with IEDs **(E)**.

that seizure freedom was more than 80% of patients after the completeness resection of the tumor (Boon et al., 1991; Britton et al., 1994; Cataltepe et al., 2005). The relationship between tumors and epileptogenic focus was still unclear (Zhang et al., 2020). Furthermore, it was found that HS in 56% of pediatric patients with temporal lobe tumors (Drake et al., 1987), and it would be speculated that the hippocampus was often epileptogenic because of abnormal synaptic reorganization of the hippocampus induced by seizures secondary to temporal tumors (Cataltepe et al., 2005).

In this study, 96% of children with temporal tumor-related epilepsy achieved a seizure-free outcome after ATL, which was proposed that ATL could completely remove the suspicious HS and potential FCD surrounding tumors in TLE children. Conversely, the children with TL abnormalities on MRI experienced worse seizure outcomes than those with tumors on MRI. Therefore, the early complete resection was prompted to improve surgical outcomes for children with temporal tumor-related epilepsy. In contrast, the TLE children with TL abnormalities on MRI should be considerable for ATL. Other predictive factors in TLE children including age at seizure onset, duration of epilepsy, and the presence of secondary-GTCS (Cohen-Gadol et al., 2006; Elliott et al., 2013; He et al., 2020; Barba et al., 2021) were not statistically significant after FDR correction in this study. The unified surgery and statistical methods would influence the results.

Predictive role of concordance of magnetic resonance with interictal epileptic discharges in temporal lobe epilepsy adult

The relationship between the predictive role of video-EEG and MRI on seizure outcome was still debated. Several studies detected a significant predictive contribution of video-EEG, particularly in patients with HS or with negative MRI examinations (Holmes et al., 2000; Schulz et al., 2000; Sun et al., 2015). In contrast, other studies demonstrated that the discrepancies between video-EEG and MRI examinations indicated a poor surgical outcome (Vinton et al., 2007; Bote et al., 2008). In the present study, we highlighted the concordance of MRI-detected focus with IEDs-detected epileptic zone, which played a predictive role in the favorable seizure outcome. However, this predictive role was neither in MRI nor video-EEG findings alone in TLE adults, and this concordance was also insignificant for the surgical outcome in TLE children. Therefore, there was a more extensive epileptogenic zone in TLE adults than in children. TLE children should undergo the early complete resection of epileptogenic focus, while TLE adults should undergo the resection of an area where the epileptogenic focus was concordant with the epileptogenic zone.

Differences in surgical prognosis between temporal lobe epilepsy children and adults

The results of this study revealed that the percentage of achieving seizure freedom was higher in children than in adults after ATL (78.57 vs. 71.84%), but the possibility of seizure recurrence in patients was not significantly different between children and adults at both 2-year and last follow-up in Log-rank test. Besides, there was only a slight drop in seizure freedom in TLE children overtimes (from 78.57 to 73.21%). Several studies revealed that the percentage of children with seizure freedom remained unchanged at the last follow-up (Miserocchi et al., 2013; Ormond et al., 2019). Besides, the probability of AEDs withdrawal in TLE children (72.72%) was higher than that in TLE adults (35.44%), which was consistent with the previous study (Barba et al., 2021). Previous studies supported a minimum seizure freedom period of 2 years before considering AEDs withdrawal (Beghi et al., 2013; Braun and Schmidt, 2014). Moreover, apart from age $>$ 30 years and longer disease duration, other factors associated with a higher risk of seizure recurrence after AEDs withdrawal were persistent auras, seizure relapse before withdrawal, and postoperative EEG abnormalities (Shih and Ochoa, 2009). Therefore, this study indicated the short duration of epilepsy, complete resection of the epileptic lesion, and non-epileptiform discharge on postoperative EEG in TLE children could achieve a higher possibility of AEDs withdrawal and a lower rate of seizure recurrence after AEDs than that in TLE adults.

Limitations

There were some limitations to this study. First, the consequences of this study were limited by its retrospective nature and relatively short follow-up after surgery of TLE patients. Second, the sample size of TLE children was relatively small which could influence the results. Finally, the neuropsychological analysis was unavailable in the study because of incomplete postoperative information.

Conclusion

There were remarkable differences in clinical manifestations, MRI examinations, and pathologies between TLE children versus adults. TLE children had a higher possibility of AEDs withdrawal than adults after surgery. The favorable seizure outcome of ATL depended on the early complete resection of MRI-detected epileptogenic focus in TLE children, while the concordance of MRI-detected focus with IEDs-detected epileptogenic zone was the predictor of favorable seizure outcomes in TLE adults.

Data availability statement

The original contributions presented in this study are included in the article/supplementary material, further inquiries can be directed to the corresponding author.

Ethics statement

The studies involving human participants were reviewed and approved by Sanbo Brain Hospital, Capital Medical University (SBNK-2017-15-01). Written informed consent from the participants' legal guardian/next of kin was not required to participate in this study in accordance with the national legislation and the institutional requirements.

Author contributions

KX: formal analysis, investigation, and writing the original draft. XW: validation. YG: methodology. JZ: investigation. TL: validation. GL: conceptualization, supervision, and writing – review and editing. All authors contributed to the article and approved the submitted version.

Funding

This work was supported by the National Natural Science Foundation of China (81790654 and 81790650) and Capital's Funds for Health Improvement and Research (2020-4-8012 and 2022-1-8011).

Conflict of interest

The authors declare that the research was conducted in the absence of any commercial or financial relationships that could be construed as a potential conflict of interest.

Publisher's note

All claims expressed in this article are solely those of the authors and do not necessarily represent those of their affiliated organizations, or those of the publisher, the editors and the reviewers. Any product that may be evaluated in this article, or claim that may be made by its manufacturer, is not guaranteed or endorsed by the publisher.

References

Antel, S. B., Li, L. M., Cendes, F., Collins, D. L., Kearney, R. E., Shinghal, R., et al. (2002). Predicting surgical outcome in temporal lobe epilepsy patients using MRI and MRSI. *Neurology* 58, 1505–1512.

Asadi-Pooya, A. A., and Sperling, M. R. (2015). Age at onset in patients with medically refractory temporal lobe epilepsy and mesial temporal sclerosis: Impact on clinical manifestations and postsurgical outcome. *Seizure* 30, 42–45. doi: 10.1016/j.seizure.2015.05.015

Barba, C., Cossu, M., Guerrini, R., Gennaro, G Di, Villani, F., Palma, L De, et al. (2021). Temporal lobe epilepsy surgery in children and adults: A multicenter study. *Epilepsia* 62, 128–142.

Baud, M. O., Perneger, T., Rácz, A., Pensel, M. C., Elger, C., Rydenhag, B., et al. (2018). European trends in epilepsy surgery. *Neurology* 91, e96–e106.

Beghi, E., Giussani, G., Grosso, S., Iudice, A., Neve, A La, Pisani, F., et al. (2013). Withdrawal of antiepileptic drugs: Guidelines of the Italian League Against Epilepsy. *Epilepsia* 54(Suppl. 7), 2–12.

Blumcke, I., Spreafico, R., Haaker, G., Coras, R., Kobow, K., Bien, C. G., et al. (2017). Histopathological findings in brain tissue obtained during epilepsy surgery. *Epilepsy Curr.* 377, 1648–1656.

Boon, P. A., Williamson, P. D., Fried, I., Spencer, D. D., Novelly, R. A., Spencer, S. S., et al. (1991). Intracranial, intraaxial, space-occupying lesions in patients with intractable partial seizures: An anatomoclinical, neuropsychological, and surgical correlation. *Epilepsia* 32, 467–476. doi: 10.1111/j.1528-1157.1991.tb04679.x

Bote, R. P., Blázquez-Llorca, L., Fernández-Gil, M. A., Alonso-Nanclares, L., Muñoz, A., and Felipe, J De (2008). Hippocampal sclerosis: Histopathology substrate and magnetic resonance imaging. *Semin. Ultrasound CT MR* 29, 2–14.

Braun, K. P., and Schmidt, D. (2014). Stopping antiepileptic drugs in seizure-free patients. *Curr. Opin. Neurol.* 27, 219–226.

Britton, J. W., Cascino, G. D., Sharbrough, F. W., and Kelly, P. J. (1994). Low-grade glial neoplasms and intractable partial epilepsy: Efficacy of surgical treatment. *Epilepsia* 35, 1130–1135. doi: 10.1111/j.1528-1157.1994.tb01778.x

Cataltepe, O., Turanli, G., Yalnizoglu, D., Topçu, M., and Akalan, N. (2005). Surgical management of temporal lobe tumor-related epilepsy in children. *J. Neurosurg.* 102, 280–287.

Cloppenborg, T., May, T. W., Blümcke, I., Fauser, S., Grewe, P., Hopf, J. L., et al. (2019). Differences in pediatric and adult epilepsy surgery: A comparison at one center from 1990 to 2014. *Epilepsia* 60, 233–245. doi: 10.1111/epi.14627

Clusmann, H. (2008). Predictors, procedures, and perspective for temporal lobe epilepsy surgery. *Semin. Ultrasound CT MR* 29, 60–70.

Cohen-Gadol, A. A., Wilhelmi, B. G., Collignon, F., White, J. B., Britton, J. W., Cambier, D. M., et al. (2006). Long-term outcome of epilepsy surgery among 399 patients with nonlesional seizure foci including mesial temporal lobe sclerosis. *J. Neurosurg.* 104, 513–524. doi: 10.3171/jns.2006.104.4.513

Drake, J., Hoffman, H. J., Kobayashi, J., Hwang, P., and Becker, L. E. (1987). Surgical management of children with temporal lobe epilepsy and mass lesions. *Neurosurgery* 21, 792–797.

Elliott, R. E., Bollo, R. J., Berliner, J. L., Silverberg, A., Carlson, C., Geller, E. B., et al. (2013). Anterior temporal lobectomy with amygdalohippocampectomy for mesial temporal sclerosis: Predictors of long-term seizure control. *J. Neurosurg.* 119, 261–272. doi: 10.3171/2013.4.JNS121829

Engel, J. Jr. (1993). Update on surgical treatment of the epilepsies. *Neurology* 43, 1612–1617.

Engel, J. Jr., Wiebe, S., French, J., Sperling, M., Williamson, P., Spencer, D., et al. (2003). Practice parameter: Temporal lobe and localized neocortical resections for epilepsy. *Epilepsia* 44, 741–751.

Fisher, R. S., Cross, J. H., D'Souza, C., French, J. A., Haut, S. R., Higurashi, N., et al. (2017). Instruction manual for the ILAE 2017 operational classification of seizure types. *Epilepsia* 58, 531–542. doi: 10.1111/epi.13671

Goldstein, R., Harvey, A. S., Duchowny, M., Jayakar, P., Altman, N., Resnick, T., et al. (1996). Preoperative clinical, EEG, and imaging findings do not predict seizure outcome following temporal lobectomy in childhood. *J. Child Neurol.* 11, 445–450.

He, X., Zhou, J., Guan, Y., Zhai, F., Li, T., and Luan, G. (2020). Prognostic factors of postoperative seizure outcomes in older patients with temporal lobe epilepsy. *Neurosurg. Focus* 48, E7.

Holmes, M. D., Born, D. E., Kutsy, R. L., Wilensky, A. J., Ojemann, G. A., and Ojemann, L. M. (2000). Outcome after surgery in patients with refractory temporal lobe epilepsy and normal MRI. *Seizure* 9, 407–411.

Khajavi, K., Comair, Y. G., Wyllie, E., Palmer, J., Morris, H. H., and Hahn, J. F. (1999). Surgical management of pediatric tumor-associated epilepsy. *J. Child Neurol.* 14, 15–25.

Lee, Y. J., Kang, H. C., Bae, S. J., Kim, H. D., Kim, J. T., Lee, B. I., et al. (2010). Comparison of temporal lobectomies of children and adults with intractable temporal lobe epilepsy. *Childs Nerv. Syst.* 26, 177–183.

Lopez-Gonzalez, M. A., Gonzalez-Martinez, J. A., Jehi, L., Kotagal, P., Warbel, A., and Bingaman, W. (2012). Epilepsy surgery of the temporal lobe in pediatric population: A retrospective analysis. *Neurosurgery* 70, 684–692.

Mathon, B., Ulvin, L Bédos, Adam, C., Baulac, M., Dupont, S., Navarro, V., et al. (2015). Surgical treatment for mesial temporal lobe epilepsy associated with hippocampal sclerosis. *Rev. Neurol. (Paris)* 171, 315–325.

McIntosh, A. M., Kalnins, R. M., Mitchell, L. A., Fabinyi, G. C., Briellmann, R. S., and Berkovic, S. F. (2004). Temporal lobectomy: Long-term seizure outcome, late recurrence and risks for seizure recurrence. *Brain* 127, 2018–2030.

Menzler, K., Thiel, P., Hermsen, A., Chen, X., Benes, L., Miller, D., et al. (2011). The role of underlying structural cause for epilepsy classification: Clinical features and prognosis in mesial temporal lobe epilepsy caused by hippocampal sclerosis versus cavernoma. *Epilepsia* 52, 707–711. doi: 10.1111/j.1528-1167.2011.02984.x

Miserocchi, A., Cascardo, B., Piroddi, C., Fuschillo, D., Cardinale, F., Nobili, L., et al. (2013). Surgery for temporal lobe epilepsy in children: Relevance of presurgical evaluation and analysis of outcome. *J. Neurosurg. Pediatr.* 11, 256–267.

Ormond, D. R., Clusmann, H., Sassen, R., Hoppe, C., Helmstaedter, C., Schramm, J., et al. (2019). Pediatric temporal lobe epilepsy surgery in bonn and review of the literature. *Neurosurgery* 84, 844–856. doi: 10.1093/neuros/nyy125

Ryvlin, P., Cross, J. H., and Rheims, S. (2014). Epilepsy surgery in children and adults. *Lancet Neurol.* 13, 1114–1126.

Schulz, R., Lüders, H. O., Hoppe, M., Tuxhorn, I., May, T., and Ebner, A. (2000). Interictal EEG and ictal scalp EEG propagation are highly predictive of surgical outcome in mesial temporal lobe epilepsy. *Epilepsia* 41, 564–570. doi: 10.1111/j.1528-1157.2000.tb00210.x

Shih, J. J., and Ochoa, J. G. (2009). A systematic review of antiepileptic drug initiation and withdrawal. *Neurologist* 15, 122–131.

Spencer, D. D., Spencer, S. S., Mattson, R. H., Williamson, P. D., and Novelly, R. A. (1984). Access to the posterior medial temporal lobe structures in the surgical treatment of temporal lobe epilepsy. *Neurosurgery* 15, 667–671. doi: 10.1227/00006123-198411000-00005

Spencer, S., and Huh, L. (2008). Outcomes of epilepsy surgery in adults and children. *Lancet Neurol.* 7, 525–537.

Sun, Z., Zuo, H., Yuan, D., Sun, Y., Zhang, K., Cui, Z., et al. (2015). Predictors of prognosis in patients with temporal lobe epilepsy after anterior temporal lobectomy. *Exp. Ther. Med.* 10, 1896–1902.

Tang, L., and Xiao, Z. (2017). Can electroencephalograms provide guidance for the withdrawal of antiepileptic drugs: A meta-analysis. *Clin. Neurophysiol.* 128, 297–302. doi: 10.1016/j.clinph.2016.11.024

Vinton, A. B., Carne, R., Hicks, R. J., Desmond, P. M., Kilpatrick, C., Kaye, A. H., et al. (2007). The extent of resection of FDG-PET hypometabolism relates to outcome of temporal lobectomy. *Brain* 130, 548–560.

Zhang, W., Chen, J., Hua, G., Zhu, D., Tan, Q., Zhang, L., et al. (2020). Surgical treatment of low-grade brain tumors associated with epilepsy. *Int. Rev. Neurobiol.* 151, 171–183.

frontiers | Frontiers in Neuroscience

TYPE Original Research
PUBLISHED 17 November 2022
DOI 10.3389/fnins.2022.1059320

OPEN ACCESS

EDITED BY
Ye Wu,
Nanjing University of Science and Technology, China

REVIEWED BY
Hongzhuo Wang,
The First Affiliated Hospital of Guangzhou University of Chinese Medicine, China
Gang Yin,
Sichuan Cancer Hospital, China

*CORRESPONDENCE
Yadi Yang
Yangyd@sysucc.org.cn
Yanqiu Feng
foree@smu.edu.cn

†These authors have contributed equally to this work and share first authorship

SPECIALTY SECTION
This article was submitted to Brain Imaging Methods, a section of the journal Frontiers in Neuroscience

RECEIVED 01 October 2022
ACCEPTED 31 October 2022
PUBLISHED 17 November 2022

CITATION
Zhang X, Pan J, Lin Y, Fu G, Xu P, Liang J, Ye C, Peng J, Lv X, Yang Y and Feng Y (2022) Structural network alterations in patients with nasopharyngeal carcinoma after radiotherapy: A 1-year longitudinal study.
Front. Neurosci. 16:1059320.
doi: 10.3389/fnins.2022.1059320

Structural network alterations in patients with nasopharyngeal carcinoma after radiotherapy: A 1-year longitudinal study

Xinyuan Zhang[1†], Jie Pan[2†], Yuhao Lin[1], Gui Fu[2], Pu Xu[1], Jiahui Liang[2], Chenfei Ye[3], Jie Peng[1], Xiaofei Lv[2], Yadi Yang[2*] and Yanqiu Feng[1,4*]

[1]School of Biomedical Engineering, Guangdong Provincial Key Laboratory of Medical Image Processing, Guangdong Province Engineering Laboratory for Medical Imaging and Diagnostic Technology, Southern Medical University, Guangzhou, China, [2]Department of Medical Imaging, Sun Yat-sen University Cancer Center, State Key Laboratory of Oncology in South China, Collaborative Innovation Center for Cancer Medicine, Guangdong Key Laboratory of Nasopharyngeal Carcinoma Diagnosis and Therapy, Guangzhou, China, [3]International Research Institute for Artificial Intelligence, Harbin Institute of Technology, Shenzhen, China, [4]Guangdong-Hong Kong-Macao Greater Bay Area Center for Brain Science and Brain-Inspired Intelligence, Key Laboratory of Mental Health of the Ministry of Education, Southern Medical University, Guangzhou, China

This longitudinal study explored the changed patterns of structural brain network after radiotherapy (RT) in patients with nasopharyngeal carcinoma (NPC). Diffusion tensor imaging (DTI) data were gathered from 35 patients with NPC at four time points: before RT (baseline), 0∼3 (acute), 6 (early delayed), and 12 months (late-delayed) after RT. The graph theory was used to characterize the dynamic topological properties after RT and the significant changes were detected over time at the global, regional and modular levels. Significantly altered regional metrics (nodal efficiency and degree centrality) were distributed in the prefrontal, temporal, parietal, frontal, and subcortical regions. The module, that exhibited a significantly altered within-module connectivity, had a high overlap with the default mode network (DMN). In addition, the global, regional and modular metrics showed a tendency of progressive decrease at the acute and early delayed stages, and a partial/full recovery at the late-delayed stage. This changed pattern illustrated that the radiation-induced brain damage began at the acute reaction stage and were aggravated at the early-delayed stage, and then partially recovered at the late-delayed stage. Furthermore, the spearman's correlations between the abnormal nodal metrics and temporal dose were calculated and high correlations were found at the temporal (MTG.R and HES.L), subcortical (INS.R), prefrontal (ORBinf.L and ACG.L), and parietal (IPL.R) indicating that these regions were more sensitive to dose and should be mainly considered in radiotherapy treatment plan.

KEYWORDS

nasopharyngeal carcinoma, radiotherapy, radiation-induced brain injury, structural network, diffusion tensor imaging

Introduction

Nasopharyngeal carcinoma (NPC) is a malignant tumor, and it is mostly found in Southern China and Southeast Asia (Chan, 2010; Tabuchi et al., 2011). Radiotherapy (RT) with or without adjuvant chemotherapy is the primary treatment for patients with NPC. However, the normal brain tissues surrounding the tumor are inevitably irradiated during cranial irradiation, causing brain abnormalities and cognitive decline. These abnormalities may compromise the quality of life of patients with NPC. Based on the pathophysiology of the side effects of RT, the time following RT can be classified into acute reaction period (days–weeks) (post-RT-AC), early-delayed period (1–6 months) (post-RT-ED), and late-delayed period (> 6 months) (post-RT-LD) (Lell, 2015). The RT-related brain changes are different during different periods but how the RT-related brain damage evolves over time is still unclear. Therefore, it is essential to further explore the temporal brain changes after completing RT which may facilitate clinical diagnosis and early intervention.

Recently, few cross-sectional or longitudinal studies have demonstrated that normal-appearing brain tissues underwent different changes at different post-RT periods in patients with NPC using various magnetic resonance imaging (MRI) analysis techniques (Lin et al., 2017, 2021; Guo et al., 2018; Lv et al., 2019; Wu et al., 2020; Qiu et al., 2021). Specifically, our previous longitudinal studies found that the volumes of the gray matter (Guo et al., 2018) and white matter (WM) in bilateral temporal subfields (Lin et al., 2021) and bilateral hippocampal subfields (Lv et al., 2019) decreased over time after RT. In addition, the cross-sectional or longitudinal studies on cortical brain morphology revealed progressive RT-induced reduction in cortical volume, cortical thickness, and cortical surface area, mainly in the temporal, basal occipital, and basal frontal lobes (Lin et al., 2017; Zhang et al., 2018). Aside brain morphological alteration, the WM microstructure changed after RT in patients with NPC (Wang et al., 2012; Xiong et al., 2013; Chen et al., 2015, 2020; Duan et al., 2016; Leng et al., 2017, 2019; Ding et al., 2018). Diffusion tensor imaging (DTI) is the only non-invasive MRI technique to assess brain white matter microstructure *in vivo* (Le Bihan et al., 2001). Most DTI studies adopted the regions of interest (ROI)-based analysis strategy to detect the microstructural changes in the temporal lobe of patients with NPC (Wang et al., 2012; Xiong et al., 2013; Chen et al., 2015). They found that diffusion metrics, such as FA and ADC in the temporal lobe, exhibited dose-related dynamic alterations over time after RT. Nevertheless, the ROI-based analysis is limited to specific regions and cannot reflect whole-brain changes. Recently, some studies investigated the changes in whole-brain WM at different post-RT periods by voxel-based analysis (Duan et al., 2016; Leng et al., 2017, 2019; Ding et al., 2018). They found that RT-induced brain alterations were dynamic and extensive, and were not limited to the temporal lobe.

However, the voxel-based analysis cannot reflect the dynamic interaction of distinct brain regions. The graph theory analysis models brain connectivity as a network to assess the structural and functional brain organization (Sporns, 2011), offering an opportunity to better understand how the brain changes from a network perspective. The structural connectivity (SC) network is usually considered to be the physical substrate of the functional connectivity (FC) network. In patients with NPC, functional and structural brain network topology change after RT (Ma et al., 2016; Tian and Zhao, 2017; Qiu et al., 2018; Leng et al., 2019; Chen et al., 2020). For structural brain networks, a longitudinal DTI study reported that both global and local efficiencies, as well as the nodal topology, were altered in post-RT patients (Tian and Zhao, 2017). This study only investigated the difference between pre-RT and post-RT, but did not consider the different patterns of brain changes at different post-RT periods. Subsequently, a cross-sectional DTI study on three points (baseline, post-RT-ED, and post-RT-LD) found that structural topological properties were altered in the post-RT-ED but began recovering in the post-RT-LD (Chen et al., 2020). Nevertheless, in this cross-sectional study, the data with different post-RT durations were not from the same group of patients with NPC; the cohort effect could compromise the ability to detect the RT-induced brain alteration; the study did not investigate the acute reaction period which exhibits different side effect of RT when compared to the post-RT-ED and post-RT-LD periods. Inclusion of three post-RT periods will facilitate better understand the RT-related brain changed patterns over time.

Therefore, this work will adopt a longitudinal study with four time points (baseline, post-RT-AC, post-RT-ED, and post-RT-LD) to investigate the dynamic changes in structural brain network. Our cohort group included 35 patients with NPC, and each patient was followed up with four repeated scans: prior to RT, 0∼3, 6, and 12 months follow-up after the completion of RT. The topological properties of the structural network at the global, regional, and modular levels were calculated. Based on the analysis of these topological properties, the dynamic brain changes after RT and the relationship between these brain alterations and radiation dose were assessed.

Materials and methods

Patients

Forty-three newly diagnosed treatment-naïve patients with NPC (aged 18–60) were initially enrolled. The inclusion criteria were as follows: right-handedness, no alcoholism or substance dependence, no high blood pressure, no diabetes, no brain tumors, no visible brain lesions, no history of cranial trauma, no history of any psychiatric or neurological disease, no current medications that may affect cognitive function, and

no contraindications for MRI scanning. Among 43 enrolled patients, eight patients with NPC were excluded because their DTI images suffered severe geometric distortions and/or motion artifacts, which could not be corrected by the post-processing technique. Finally, 35 patients with NPC (21 males; aged 23–60 years; averaging 40.11 ± 8.88 years) were selected and analyzed in this study. This study was approved by the Institutional Review Board of the Sun Yat-sen University Cancer Center. All participants provided written informed consent.

Treatment

All patients were treated with intensity-modulated radiotherapy (IMRT) (n = 32) or tomotherapy (TOMO) (n = 3), the details of which have been reported by previous studies (Sun et al., 2013; Tang et al., 2015). The prescribed regimen included a total dose of 68–70 Gy in 30–33 fractions at 2.12–2.33 Gy/fraction to the planning target volume (PTV) of the primary gross tumor volume (GTVnx), 60–70 Gy to the PTV of GTV of involved lymph nodes (GTVnd), 60–64 Gy to the PTV of the high-risk clinical target volume (CTV1), and 54–58 Gy to the PTV of the low-risk clinical target volume (CTV2). All patients received one fraction daily over a period of about 45 days, five consecutive days per week. Based on the guidelines defined by the 7th edition of the AJCC staging system for NPC, the patients with stage I to IIa disease received no chemotherapy, those with stage IIb received concurrent chemotherapy, and those with stages III to IVa–b received concurrent chemotherapy with/without neoadjuvant/adjuvant chemotherapy (Edge et al., 2010).

Follow-up procedure

To assess the dynamic alterations in structural brain network topology after RT, we repeatedly performed MRI scanning at the following stages for each patient: before initiation of RT (baseline), 0∼3 months (post-RT-AC), 6 months (post-RT-ED), and 12 months (post-RT-LD) after RT. Since the MRI data at each stage were acquired from the same group (35 patients), a longitudinal comparison strategy was performed to avoid potential bias due to cohort effect.

MRI acquisition

The MRI images were acquired on a GE Discovery MR 750 3.0T scanner (GE Medical Systems, WI, USA) at the Department of Medical Imaging, Sun Yat-sen University Cancer Center. The high-resolution T1-weighted volume data were acquired using three-dimensional spoiled gradient-recalled sequence with the following parameters: TR/TE = 8.2/3.2 ms, TI = 800 ms, flip angle = 8°, field of view = 256 × 256 × 180 mm^3, acquisition matrix = 256 × 256 × 180, voxel size = 1 × 1 × 1 mm^3. The DTI data were acquired using a twice-refocused spin-echo diffusion-weighted (DW) echo-planar imaging sequence with the following parameters: TR/TE = 10,000/63.8 ms, acquisition matrix = 128 × 128, field of view = 256 × 256 mm^2, in-plane resolution = 2 × 2 mm^2, slice thickness = 2 mm without inter-slice gap, 75 axial slices covering the whole brain, one volume with b = 0 s/mm^2, 30 volumes with b = 1,000 s/mm^2.

Data preprocessing and tractography

The data preprocessing included the following steps: (1) denoising the DW images using Marchenko-Pastur PCA (Veraart et al., 2016); (2) correcting the eddy current and head motion-induced distortion with an affine transformation; (3) skull stripping for the T1-weighted images and non-DW images (b = 0 s/mm^2) with FSL-Brain Extraction Tool (BET).

Whole-brain fiber reconstruction was performed for each diffusion data in native space using probabilistic tracking. Anatomically constrained tractography (Smith et al., 2012), seeding from the interface between grey matter and white matter, was used to achieve an anatomically plausible trajectory. A total of 10 million (M) seeding streamlines were initially generated and tracked. Finally, Spherical-deconvolution Informed Filtering of Tractograms (SIFT) (Smith et al., 2013) was performed to filter the streamlines from 10 to 1 M for improving the quantitative nature of whole-brain streamline reconstruction.

All these preprocessing steps and fiber tracking were accomplished within MRtrix3,[1] which is an open-source software package and includes scripts that interface with external packages, such as FSL[2] (Jenkinson et al., 2012).

Structural network construction

Figure 1 shows the flow chart of structural network construction, which is also accomplished within MRtrix3. First, 90 brain regions (nodes) were created for each participant with the automated anatomical labeling (AAL) atlas (Tzourio-Mazoyer et al., 2002). Particularly, for each participant, the non-diffusion images (b = 0 s/mm^2) were co-registered to the corresponding T1-weighted images with an affine transformation. Meanwhile, the T1-weighted images were non-linearly transformed to the Montreal Neurological Institute (MNI) space using the ICBM-152 brain template. Thereafter, these two transformations were inversed and combined into one transformation, which was applied to wrap the AAL from

1 https://www.mrtrix.org

2 https://fsl.fmrib.ox.ac.uk

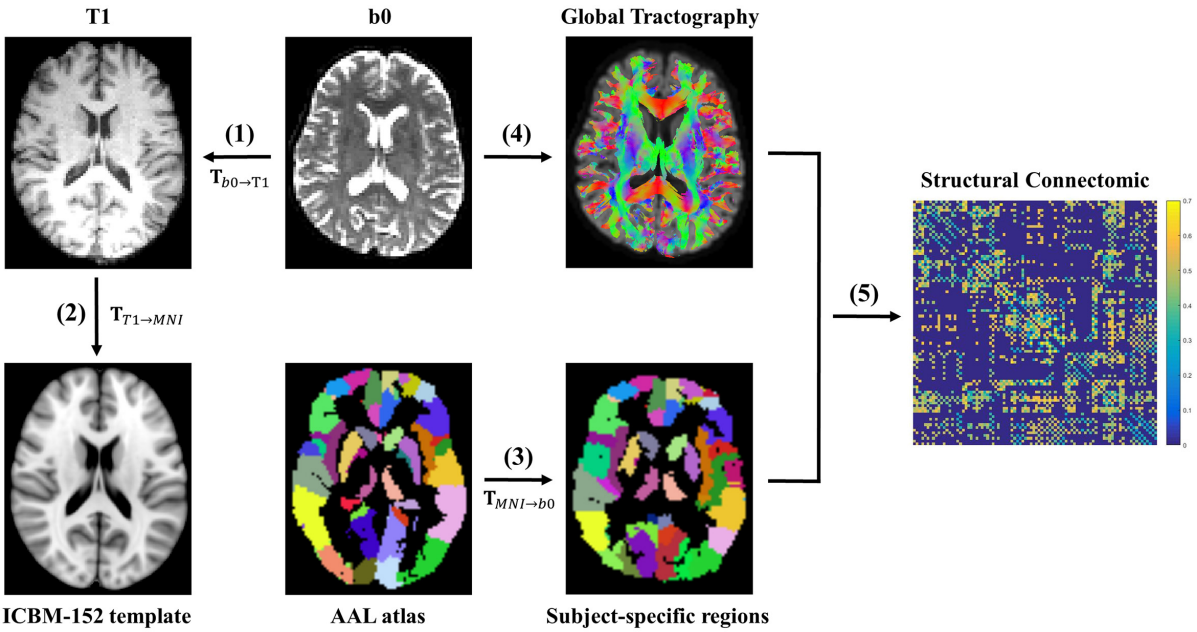

FIGURE 1
The flowchart of white matter structural network construction. **(1)** The non-diffusion image b0 was co-registered to the corresponding T1-weighted image with an affine transformation $T_{b0\rightarrow T1}$ for each participant. **(2)** The T1-weighted image was non-linearly transformed to the Montreal Neurological Institute (MNI) space using the ICBM-152 brain template, resulting in a non-linear transformation $T_{T1\rightarrow MNI}$. **(3)** These two transformations ($T_{b0\rightarrow T1}$ and $T_{T1\rightarrow MNI}$) were inversed and combined into one transformation ($T_{MNI\rightarrow b0}$), which was applied to wrap the AAL from the MNI space to the native diffusion space of each participant. Thereafter, 90 participant-specific brain regions were created. **(4)** A whole-brain fiber reconstruction was performed for each subject in native space using the probabilistic tracking in conjunction with DTI. **(5)** Finally, the 90 × 90 symmetric connectivity matrix for each participant was constructed by calculating the mean FA values of streamlines that connect each region pair.

MNI space to the native diffusion space of each participant. Finally, the 90 × 90 symmetric connectivity matrix for each participant was constructed by calculating the mean FA values of streamlines that connect each node pair.

Structural network analyses

The global and regional network metrics, as well as the modular metrics, were calculated to characterize the topological properties of altered structural networks. All the following network metrics were calculated using GRETNA.[3]

The global and regional network metrics

The global metrics calculated in our study consisted of global efficiency (E_{glob}), local efficiency (E_{loc}), cluster coefficient (Cp), shortest path length (Lp), normalized cluster coefficient (γ), normalized characteristic path length (λ), and small-worldness (σ). For regional properties, the following two nodal metrics were considered: nodal efficiency (NE) and degree centrality (DC). The definition and interpretation of these network metrics can be referred to Rubinov and Sporns (2010).

To avoid both spurious connections and bias of a single sparse threshold, the area under the curve (AUC) under sparsity, ranging from 27 to 40% with an interval of 0.5% for each global and regional measures, was calculated for the following statistical analysis.

The modular metrics

With regards to the modularity analysis, the total number of modules and the associated module membership of nodes were optimized by maximizing modularity Q, the detailed definition and interpretation of which can be referred to Newman, 2006. Particularly, the Louvain algorithm in the Brain Connectivity toolbox[4] was used to optimize the *Q*-value under varying sparsity, ranging from 0.05 to 0.3. Generally, a *Q*-value > 0.3 indicated a strong modular structure (Fortunato and Barthelemy, 2007; Hilger et al., 2017). Given that the

3 http://www.nitrc.org/projects/gretna/

4 http://www.brain-connectivity-toolbox.net/

number of modules and their membership varied across different sparsity, sparsity was fixed at 0.1 ($Q = 0.39$) to obtain a quite reasonable and consensus modularity partition, as shown in Figure 2. Thereafter, to assess the modular segregation, the within-module connectivity and between-module connectivity, which are defined as the strengths of edges within a single module and between a pair of modules, respectively, were calculated.

Statistical analysis

The one-way repeated measures analysis of variance (ANOVA) was used to compare four groups at the baseline, and three follow-up stages (post-RT-AC, post-RT-ED, and post-RT-LD) after RT for all of these metrics. All the measured data satisfied the assumptions of normality and homogeneous variance. The assumption of sphericity was violated for the regional network metrics in several brain regions, where the Greenhouse–Geisser method was used to correct the sphericity. Thereafter, a *post-hoc* analysis (multiple comparisons) was performed by using paired *t*-test to compare each pair within the four groups. When the differences between the paired observations did not follow a normal probability distribution, Wilcoxon Signed-Rank test, which is a non-parametric equivalent of the paired *t*-test, was used instead. Finally, false discovery rate (FDR) correction was used for multiple comparisons.

In addition, dose-response analysis was performed by calculating the Spearman's rank correlation coefficient (*r*-value) of the association between the abnormal nodal metrics and the radiation dose of ipsilateral temporal lobe.

Results

The global analysis

Figure 3 shows the global network measures of a cohort of 35 patients at four stages, including the baseline, post-RT-AC, post-RT-ED, and post-RT-LD. All four groups exhibited small-world characteristics with $\lambda \approx 1$, $\gamma > 1$, and $\sigma > 1$. For the global metrics, only E_{loc} exhibited a significant difference among four groups after FDR correction. Specifically, E_{loc} significantly decreased at post-RT-ED and post-RT-LD, compared to baseline. In addition, E_{loc} showed a recovering tendency at post-RT-LD, although no significant difference existed between post-RT-ED and post-RT-LD. Moreover, E_{glob}

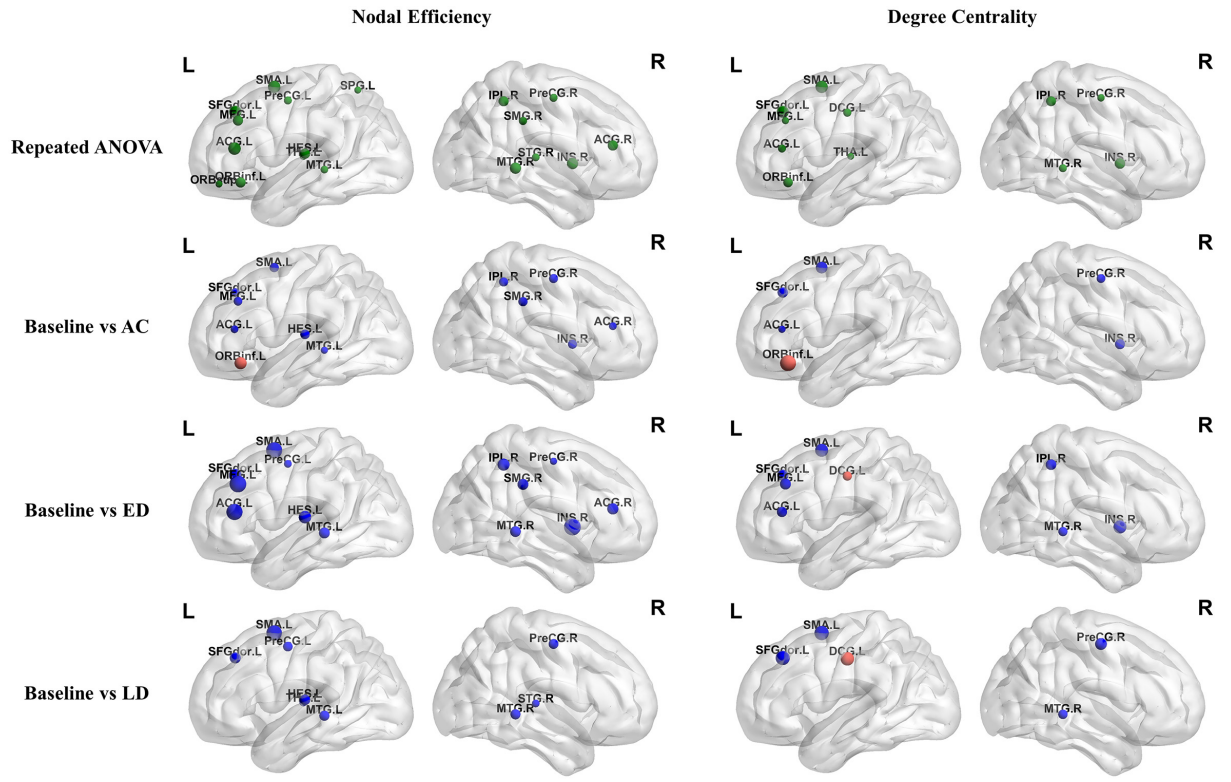

FIGURE 2
The within-module and between-module connectivity strengths analysis of the four modules used. L, left hemisphere; R, right hemisphere; AC, post-RT-AC; ED, post-RT-ED; LD, post-RT-LD; $^{**}p < 0.01$.

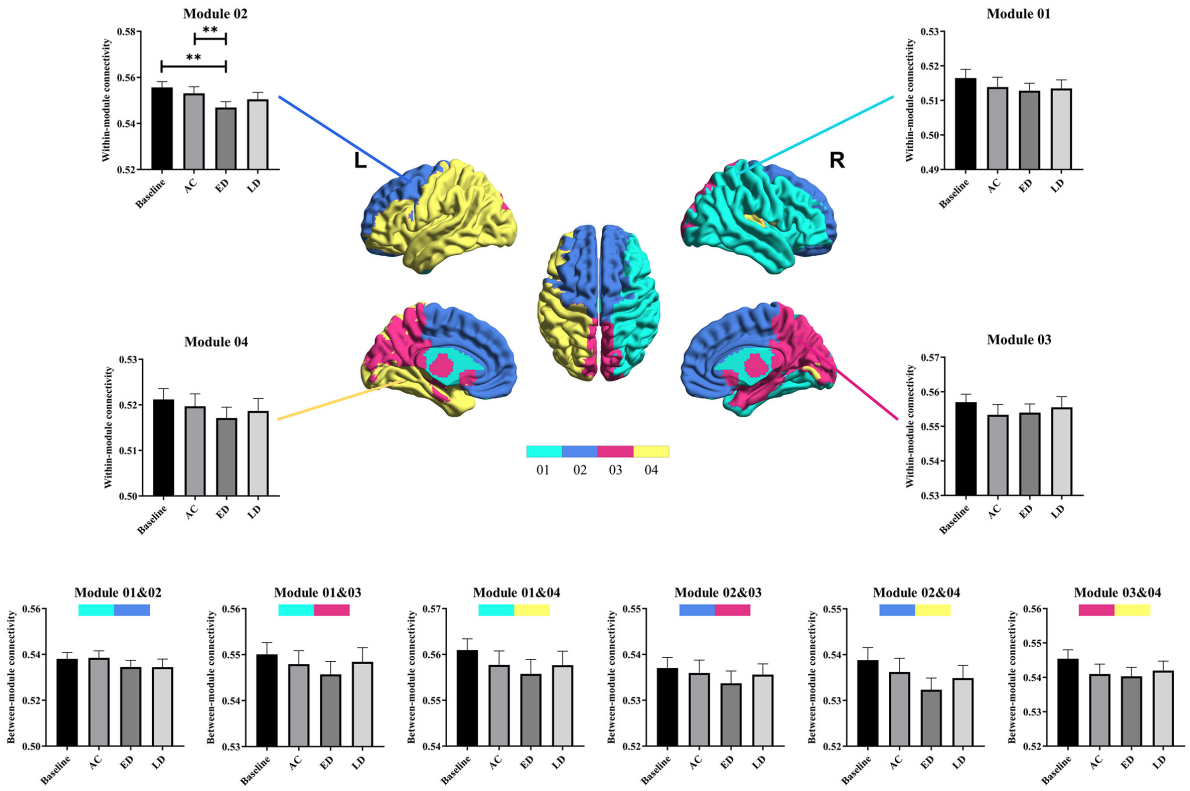

FIGURE 3
The *post-hoc* pairwise comparison results of the global network measures for four time stages (the baseline, post-RT-AC, post-RT-ED, and post-RT-LD) after false discovery rate (FDR) correction. AC, post-RT-AC; ED, post-RT-ED; LD, post-RT-LD; $^{**}p < 0.01$.

showed a tendency of progressive decrease at post-RT-AC and post-RT-ED and a partial recovery at post-RT-LD. Similarly, the small-world coefficient, sigma (σ), showed a tendency of increase at post-RT-ED and a partial recovery at post-RT-LD. The statistical results are shown in Table 1.

The regional analysis

Figure 4 shows the significantly altered regions for nodal efficiency and degree centrality by repeated measures ANOVA among four groups and by *post-hoc* pairwise comparison between the baseline and three post-RT stages (post-RT-AC, post-RT-ED, and post-RT-LD). The statistical results are shown in Table 2, and the relevant information of 90 regions from the AAL atlas together with corresponding abbreviations are listed in Supplementary Table 1.

For nodal efficiency, 18 regions had significant differences among the four groups. They were found in the prefrontal (ORBinf.L, ORBsup.L, SFGdor.L, MFG.L, ACG.L&R), temporal (HES.L, MTG.L&R, STG.R), parietal (IPL.R, SMG.R, SPG.L), frontal (SMA.L, PreCG.L&R), and subcortical (INS.R, THA.L) lobes. In these significantly altered nodes, only ORBinf.L increased at post-RT-AC, when compared to the baseline. Except for ORBinf.L, the nodal efficiency decreased at the follow-up stages after RT. In most regions with significantly decreased nodal efficiency after RT, the significant difference between baseline and post-RT-ED was larger than that between baseline and post-RT-AC and between baseline and post-RT-LD. This finding implied that the efficiency of parallel information transfer of the node first decreased and then recovered to a certain extent over time after RT.

The degree centrality exhibited significant difference among the four stages in the prefrontal (ORBinf.L, SFGdor.L, MFG.L, ACG.L), frontal (SMA.L, PreCG.R, DCG.L), temporal (MTG.R), parietal (IPL.R), and subcortical (INS.R, THA.L) lobes. For the ACG.L and INS.R, the degree centrality showed a significant and sustained decrease at post-RT-AC and post-RT-ED, and exhibited a full recovery at post-RT-LD, when compared to baseline. For the MFG.L and IPL.R, the degree centrality began to decrease at post-RT-ED and exhibited a full recovery at post-RT-LD. The PreCG.R, MTG.R, SMA.L, and SFGdor.L showed a significant and sustained decrease within 1 year after RT without recovering trend. In addition, the degree centrality showed

TABLE 1 The statistical results of the global network measures for four time stages.

Global network measures		Baseline vs. AC	Baseline vs. ED	Baseline vs. LD	AC vs. ED	AC vs. LD	ED vs. LD	Rep_ANOVA
E_{glob}	uncorr_p	0.1255	0.0094**	0.1170	0.2801	0.9243	0.3180	0.0608
	corr_p	0.2510	0.0564	0.3510	0.4202	0.9243	0.3815	
E_{loc}	uncorr_p	0.1165	0.0033**	0.0069**	0.0331*	0.3845	0.2379	0.0049**
	corr_p	0.1748	0.0197*	0.0206*	0.0661	0.3845	0.2855	
Cp	uncorr_p	1	0.0918	0.2136	0.3200	0.2538	0.7941	0.3659
	corr_p	1	0.5506	0.6408	0.4800	0.5077	0.9530	
Lp	uncorr_p	0.1083	0.0089**	0.1189	0.3641	0.9980	0.3383	0.0624
	corr_p	0.3249	0.0532	0.2379	0.4369	0.9980	0.5074	
γ	uncorr_p	0.9922	0.0512	0.4978	0.0506	0.5376	0.3965	0.3075
	corr_p	0.9922	0.1535	0.7467	0.3034	0.6451	0.7931	
λ	uncorr_p	0.2689	0.8708	0.4245	0.3451	0.5554	0.3566	0.6038
	corr_p	1	0.8708	0.6367	1	0.6665	0.7131	
σ	uncorr_p	0.8880	0.0427*	0.5219	0.0291**	0.4935	0.3397	0.2363
	corr_p	0.8880	0.1280	0.6263	0.1748	0.7402	0.6793	

The statistical results with *p*-values of the global network measures of 35 patients for four groups (the baseline, post-RT-AC, post-RT-ED, and post-RT-LD). E_{glob}, global efficiency; E_{loc}, local efficiency; Cp, cluster coefficient; Lp, shortest path length; γ, normalized cluster coefficient; λ, normalized characteristic path length; σ, small-worldness; uncorr_p, uncorrected *p*-value; corr_ p, corrected *p*-value with the false discovery rate (FDR) correction; Rep_ANOVA, one-way repeated measures analysis of variance; AC, post-RT-AC; ED, post-RT-ED; LD, post-RT-LD; $^{*}p < 0.05$; $^{**}p < 0.01$.

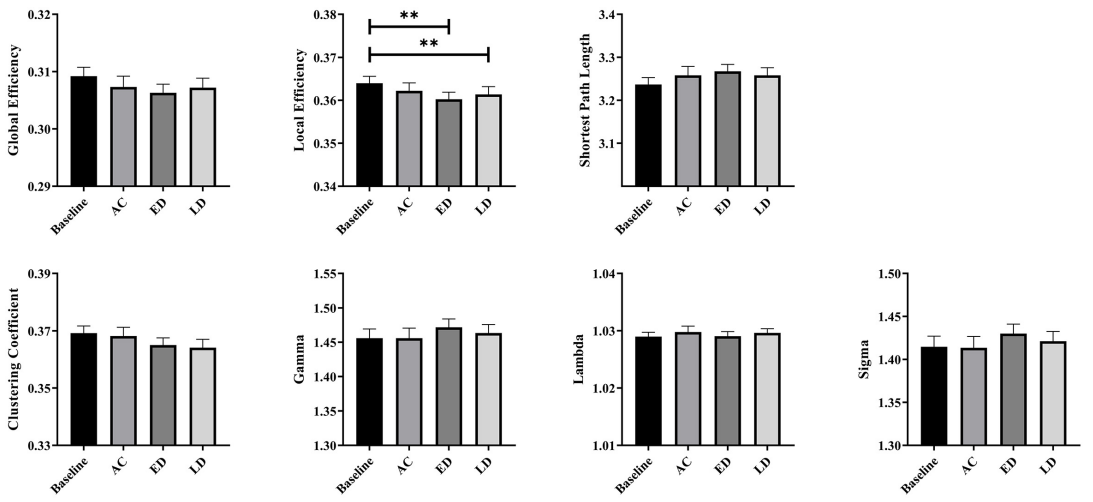

FIGURE 4
The regions with significantly different nodal efficiency and degree centrality across four stages by repeated measures ANOVA and for post-hoc pairwise comparisons between the baseline and three following post-RT stages (post-RT-AC, post-RT-ED, and post-RT-LD). The full names of the AAL atlas regions with corresponding abbreviations are listed in **Supplementary Table 1**. L, left hemisphere; R, right hemisphere; AC, post-RT-AC; ED, post-RT-ED; LD, post-RT-LD; Repeated ANOVA, one-way repeated measures analysis of variance.

a significant increase at post-RT-AC in the ORBinf.L and a significant and sustained increase at post-RT-ED and post-RT-LD in the DCG.L.

The modularity analysis

Four modules were identified according to the mean network matrix of whole patients at baseline. The detailed information of four modular networks are summarized in Table 3. The modularity analysis results are shown in Figure 2.

For the within-module connectivity strengths, only module 2 showed a statistically significant difference among the four stages. The module 2 comprises 21 regions, including the prefrontal lobe, frontal lobe, and parts of the parietal lobe. It has a high overlap with the default mode network (DMN), and is related to the normal cognitive and emotional functions. Specifically, the connectivity strength within module 2 at the

TABLE 2 The statistical results of regional analysis for nodal efficiency and degree centrality.

Regions	NE				DC			
	Rep_ANOVA	Baseline vs. AC	Baseline vs. ED	Baseline vs. LD	Rep_ANOVA	Baseline vs. AC	Baseline vs. ED	Baseline vs. LD
ORBinf.L	0.0106*	0.0043**	0.2303	0.1277	0.0140*	0.0008**	0.2102	0.0788
SFGdor.L	0.0041**	0.0220*	0.0034**	0.0076**	0.0048**	0.0099**	0.0074**	0.0018**
MFG.L	0.0111*	0.0208*	0.0006**	0.1581	0.0416*	0.0827	0.0076**	0.6431
ACG.L	0.0040**	0.0323*	0.0008**	0.1971	0.0294*	0.0399*	0.0107*	0.5435
SMA.L	0.0041**	0.0160*	0.0008**	0.0010**	0.0043**	0.0056**	0.0031**	0.0017**
THA.L	0.0427*	0.5560	0.6878	0.0317*	0.0479*	0.0967	0.7270	0.1639
PreCG.R	0.0289*	0.0189*	0.0430*	0.0128*	0.0386*	0.0212*	0.0575	0.0055**
INS.R	0.0068**	0.0177*	0.0006**	0.0745	0.0093**	0.0120*	0.0031**	0.0924
MTG.R	0.0073**	0.1240	0.0088**	0.0114*	0.0299*	0.2303	0.0173*	0.0155*
IPL.R	0.0116*	0.0182*	0.0051**	0.8055	0.0129*	0.1522	0.0090**	0.2650
ORBsup.L	0.0450*	0.3321	0.0619	0.7183	–	–	–	–
HES.L	0.0109*	0.0148*	0.0039**	0.0094**	–	–	–	–
MTG.L	0.0338*	0.0427*	0.0080**	0.0109*	–	–	–	–
SPG.L	0.0437*	0.0898	0.0637	0.6225	–	–	–	–
PreCG.L	0.0289*	0.0579	0.0322*	0.0139*	–	–	–	–
ACG.R	0.0111*	0.0319*	0.0071**	0.0542	–	–	–	–
STG.R	0.0326*	0.4946	0.1718	0.0333*	–	–	–	–
SMG.R	0.0279*	0.0172*	0.0082**	0.0692	–	–	–	–
DCG.L	–	–	–	–	0.0265*	0.2945	0.0168*	0.0024**

The *post-hoc* comparison statistical results between the baseline and three post-RT time points (post-RT-AC, post-RT-ED, and post-RT-LD) for regions with significantly different nodal efficiency and degree centrality across four time points. Eighteen regions with significant difference among four groups for the nodal efficiency and 11 regions for the degree centrality were present. The values in the table are the corrected *p*-values with the false discovery rate (FDR) correction. The full names of the AAL atlas regions with corresponding abbreviations are listed in Supplementary Table 1. NE, nodal efficiency; DC, degree centrality; Rep_ANOVA, one-way repeated measures analysis of variance; AC, post-RT-AC; ED, post-RT-ED; LD, post-RT-LD; *$p < 0.05$; **$p < 0.01$.

post-RT-ED was significantly lower than those at baseline and post-RT-AC. In addition, the within-module connectivity strengths for each module showed a tendency of progressive decrease at post-RT-AC and post-RT-ED and then exhibited a recovering trend at the post-RT-LD, when compared to baseline, but no significant difference was found.

For between-module connectivity strengths, no significant differences were found for each pair of modules. However, all the between-module connection strengths, except for that between modules 1 and 3, showed a tendency of sustained and progressive decrease at post-RT-AC and post-RT-ED and then exhibited a recovering trend at post-RT-LD, when compared to baseline.

Dose-correlation analysis

Figure 5 shows the correlations between the abnormal nodal parameter metrics (NE and DC) and the radiation dose of ipsilateral temporal lobe. The mean and/or maximum doses of ipsilateral temporal lobe were correlated with the changed NE and DC in several regions which were distributed in temporal, subcortical, prefrontal and parietal. In brief, the changed NE and DC were positively correlated with mean and/or maximum dose at ACG.L, INS.R, HES.L, and IPL.R, and negatively correlated at ORBinf.L and MTG.R. In addition, more brain regions exhibited a significant dose correlation with NE and DC at late-delayed period; more brain regions were correlated to the mean dose than the maximum dose. The spearman's correlations (*r*-values) with significant differences (*p*-values) for the mean dose and the maximum dose were shown in Supplementary Tables 2, 3, respectively.

Discussion

To our knowledge, this study is the first longitudinal cohort study to monitor the RT-induced alterations of brain structural network in patients with NPC after RT. The DTI probabilistic tractography and graph theoretical approach were used to assess RT-related brain changes at the global, local, and modular levels; the following findings were obtained: (1) E_{loc} shows a significant difference among four stages. Both E_{glob} and E_{loc} show a tendency of progressive decrease at post-RT-AC and post-RT-ED and a partial recovery at post-RT-LD. (2) Except for the ORRinf.L and DCG.L, all other regions exhibited significant

TABLE 3 The detailed information on four modular networks.

Modules	AAL atlas regions		
Module 01	PreCG.R	LING.R	SMG.R
	MFG.R	SOG.R	ANG.R
	ORBmid.R	MOG.R	PUT.R
	IFGoperc.R	IOG.R	STG.R
	IFGtriang.R	FFG.R	TPOsup.R
	ORBinf.R	PoCG.R	MTG.R
	ROL.R	SPG.R	TPOmid.R
	INS.R	IPL.R	ITG.R
Module 02	SFGdor.L	OLF.L	REC.R
	SFGdor.R	OLF.R	ACG.L
	ORBsup.R	SFGmed.L	ACG.R
	MFG.L	SFGmed.R	DCG.L
	IFGoperc.L	ORBsupmed.L	DCG.R
	SMA.L	ORBsupmed.R	PCL.L
	SMA.R	REC.L	PCL.R
Module 03	PCG.L	CAL.L	CAU.L
	PCG.R	CAL.R	CAU.R
	HIP.L	CUN.L	PAL.R
	HIP.R	CUN.R	THA.L
	PHG.L	SOG.L	THA.R
	PHG.R	PCUN.L	PCUN.R
	AMYG.R	HES.L	HES.R
Module 04	PreCG.L	LING.L	ANG.L
	ORBsup.L	MOG.L	PUT.L
	ORBmid.L	IOG.L	PAL.L
	IFGtriang.L	FFG.L	STG.L
	ORBinf.L	PoCG.L	TPOsup.L
	ROL.L	SPG.L	MTG.L
	INS.L	IPL.L	TPOmid.L
	AMYG.L	SMG.L	ITG.L

The AAL atlas regions included in the four modular networks. The full names of the AAL atlas regions with corresponding abbreviations are listed in **Supplementary Table 1**.

reductions in the nodal efficiency and degree centrality at post-RT-AC and post-RT-ED, and most of these regions showed a partial or full recovery at post-RT-LD. (3) The within-module connectivity strength of modular 2 exhibited significant and progressive decrease at post-RT-AC and post-RT-ED, compared to baseline, and showed a partially recovering trend at post-RT-LD. All the within- and between- module connectivity strengths, except for that between modules 1 and 3, showed a tendency of sustained and progressive decrease at post-RT-AC and post-RT-ED. Thereafter, a recovering trend at post-RT-LD was exhibited. All these findings imply that the brain injures begin at post-RT-AC, are aggravated at post-RT-ED, and undergo brain reorganization at the post-RT-LD. (4) The temporal irradiation dose was significantly correlated to the altered nodal parameters at the temporal (MTG.R and HES.L), subcortical (INS.R), prefrontal (ORBinf.L and ACG.L) and parietal (IPL.R), which suggests that these regions were more sensitive to dose and should be paid more attention during RT treatment plans.

The global network analysis revealed that the structural brain network possessed small-world properties ($\lambda \approx 1$, $\gamma > 1$, and $\sigma > 1$), at baseline and all three follow-up stages (post-RT-AC, post-RT-ED, and post-RT-LD). These results illustrate that the small-world networks are relatively robust to the changes of brain white matter (He et al., 2009; Colombo, 2013; Xu et al., 2017). For the presented global measures, only E_{loc} had statistically significant difference among the four groups. E_{loc} represents the efficiency of information exchange within a local subnetwork or among adjacent regions (Jiang et al., 2020). Reduced E_{loc} in a structural brain network may arise from the RT-associated injures of the fiber tracks (e.g., demyelination and axonal damage) (Nazem-Zadeh et al., 2012; Qiu et al., 2021). The results of significant decrease in E_{loc} at post-RT-ED and post-RT-LD were compatible with findings of prior fMRI studies reporting lower efficiency of information transfer after RT (Ding et al., 2018; Leng et al., 2021). Notably a significant decrease in E_{loc} firstly occurred 6 months after RT in our structural network study, later than the significant abnormalities in global properties of functional networks (<6 months) (Leng et al., 2021). These findings were plausible because brain function might be more vulnerable or sensitive to attack (Karim et al., 2017). In addition, both E_{glob} and E_{loc} showed a tendency of progressive decrease at post-RT-AC and post-RT-ED and partial recovery at post-RT-LD, although this trend was not statistically significant. These inconspicuous changes in trend of E_{glob} and E_{loc} may explain the inconsistent and unstable results from previous studies. Some DTI studies found a gradual and irreversible white matter damage (Nagesh et al., 2008; Welzel et al., 2008; Ding et al., 2018), whereas other groups found that the DTI metrics decreased in the early stage but partially recovered later (Wang et al., 2012; Xiong et al., 2013; Chen et al., 2015).

The significant alteration of the nodal parameters (nodal efficiency and degree centrality) among the four stages was mainly located in the temporal, frontal, prefrontal, parietal, and subcortical regions. Most of these regions showed a progressive decrease during 0–6 months post-RT and a partial or full recovery 12 months post-RT. This result may indicate that the structural brain reorganization mainly occurred in the late-delay stage, which is generally consistent with findings of previous studies (Wang et al., 2012; Xiong et al., 2013; Duan et al., 2016; Chen et al., 2020). However, some regions, including MTG.L&R, HES.L, PreCG.L&R, SFGdor.L, and SMA.L, exhibited a sustained decrease without recovering tendency within 1 year after RT, which may be due to two reasons: vulnerability of these regions to radiation causing an irreversible damage and the need of these regions for a longer recovery time (>12 months), which cloud not be observed in this 1-year longitudinal study after RT. The bilateral temporal lobes, including MTG.L&R and HES.L, exhibited decreased

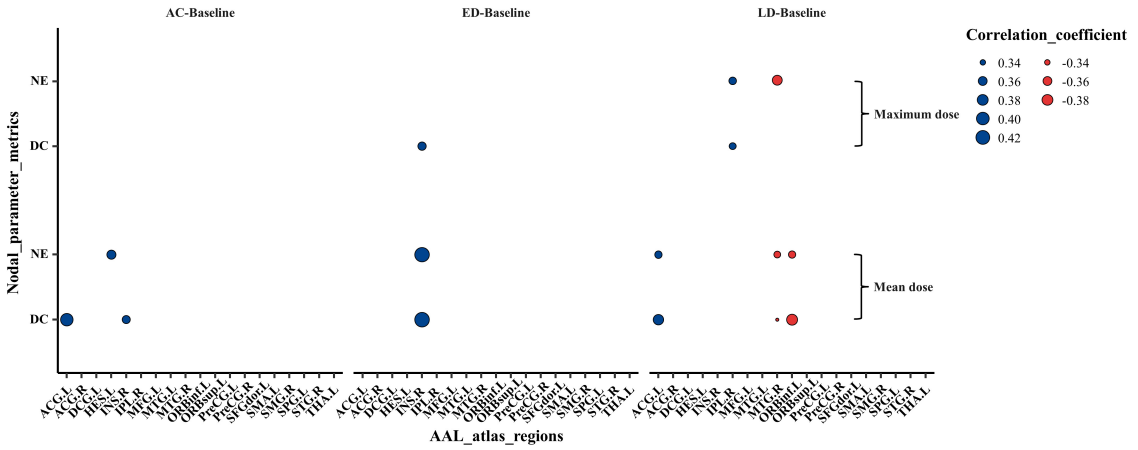

FIGURE 5
The Spearman's correlations between the abnormal nodal metrics (NE and DC) and the mean as well as maximum irradiation dose of ipsilateral temporal lobe. The Spearman's rank correlation coefficients (*r*-value) at the significance level of $p < 0.05$ were shown. The size of dots indicated the strength of the correlations and the color of dots indicated the orientation of the correlations (Blue: positive correlation, Red: negative correlation). NE, nodal efficiency; DC, degree centrality; AC, post-RT-AC; ED, post-RT-ED; LD, post-RT-LD.

nodal parameters without recovering tendency over the time after RT. This observation was not surprising because the temporal lobe is often inside the target volume and inevitably receives high-dose radiation and may suffer from severe injury. Late-delayed temporal injuries have been well documented as irreversible, and sometimes presented as necrosis of temporal lobes on routine medical imaging examinations (Mao et al., 2014; Lv et al., 2019). Additionally, the nodal parameters showed significant changes in the prefrontal, frontal, and parietal regions, which were outside the irradiation field. Previous TBSS analysis (Duan et al., 2016) revealed that the fractional anisotropy values were significantly lower in the frontal, parietal, and occipital WM after RT. A previous VBM study found a reduced GM volume in the frontal and parietal cortices (Lv et al., 2014). Altogether, the changes in nodal parameters in the prefrontal, frontal, and parietal regions may arise from the degeneration of associated white matter fibers or radiation-induced disruption of the blood brain barrier (BBB) (van Vulpen et al., 2002). Notably, the increased nodal parameters in the ORBinf.L and DCG.L might act as a compensatory mechanism that maintains normal cognitive function. The subcortical regions, including the THA.L and INS.R, exhibited a different changing pattern, when compared with baseline. Specifically, the INS.R shows a "decrease-decrease-recover" pattern after RT for both nodal efficiency and degree centrality, whereas THA.L begins to decrease 12 months post-RT (post-RT-LD) for nodal efficiency. The alteration of structural brain network in the insular and thalamus is probable, given that both regions are parts of the paralimbic system that are sensitive to irradiation. In addition, these findings are consistent with those of previous studies (Ding et al., 2018; Qiu et al., 2018; Yang et al., 2019; Zhang et al., 2020; Nan et al., 2022), which reported functional and/or morphological changes in the thalamus and insula.

The dose-correlation analysis shows the nodal parameters (NE and DC) had a positive correlation with temporal dose at ACG.L, INS.R, HES.L, and IPL.R, which may be due to the compensatory change in structural brain network that interconnects these regions. Whereas the nodal parameters had a negative correlation with temporal dose at ORBinf.L and MTG.R, indicating that a higher dose reduces the information transfer efficiency to these regions. In addition, through acute reaction stage to late-delayed stage, the number of significant dose-correlation brain regions increased. This finding suggests that the dose effect on brain change is more notable at the late-delayed stage. Furthermore, some brain regions were correlated to the mean dose and/or maximum dose which illustrates that both the mean dose and the maximum dose should be considered for the protection of normal organs.

This study explored the changed patterns of structural modularity over time after RT in patients with NPC. We found that the connectivity strength within module 2 at the post-RT-ED were significantly weaker than those at baseline and post-RT-AC, indicating radiation-induced disruption of topological organization of module 2. The module 2 mainly includes the prefrontal lobe, frontal lobe, and parts of the parietal lobe. The areas of module 2 and the DMN have a large overlap, and the DMN is associated with normal cognition and emotion (Alves et al., 2019). Moreover, the module 2 includes the medial prefrontal lobe, whereas module 4 includes the left side of the temporal lobe and parietal lobe. Several fiber bundles run between the medial prefrontal lobe and temporal lobe, which is highly related to memory processing (Vertes et al., 2007). The decreased connectivity strengths within module 2

and between modules 2 and 4 at the acute- and early delayed stages may be due to the damage of axonal fiber tracts between the medial prefrontal lobe and temporal lobe. These findings support the psychological disorders, cognitive dysfunction, and mood disorders commonly found in patients with NPC after RT (Tang et al., 2012; Mo et al., 2014; Wu et al., 2014). In addition, a "decrease-decrease-partially recovery" pattern was observed for the connectivity strengths within each module and between each pair of modules, although no significant alterations were found except for connectivity strengths within module 2. These observed results were roughly consistent with the findings on nodal parameters, further implying that the brain undergoes recovery and reorganization of structure to a certain extent at the late-delayed stage.

Despite the merits of this longitudinal study, several limitations were identified. First, the 1-year follow-up was insufficient to monitor all the dynamic changes in structural network properties after RT over time. A longer period, ranging over several years, should be considered to understand whether the injured structural network topology will eventually recover to "baseline" with time. Second, this study included 35 patients with NPC; this sample size was not large enough. A larger cohort size of patients with NPC is needed to provide more reliable statistical results and to accurately reveal the dynamic changing pattern of structural brain network after RT. Third, the relationship between the alterations in structural brain network and cognitive decline were not explored because of incomplete neurocognitive outcomes.

Conclusion

The follow-up data were used to track the dynamic changes in structural brain network after RT in patients with NPC. Our study found that the radiation-induced alterations in topological properties mainly began at the acute reaction stage, were aggravated at the early delayed stage, and then partially recovered at the late-delayed stage. The dynamic change patterns of topological properties facilitate to better understand how the radiation-induced brain injuries evolves over time and the early detection of radiation-induced changes in normal-appearing brain tissue to improve patient survival. In addition, a dose-correlation alteration was found in the temporal (MTG.R and HES.L), subcortical (INS.R), prefrontal (ORBinf.L and ACG.L), and parietal (IPL.R), indicating that these regions were more sensitive to dose and should be mainly considered in radiotherapy treatment plan.

Data availability statement

The raw data supporting the conclusions of this article will be made available by the authors, without undue reservation.

Ethics statement

The studies involving human participants were reviewed and approved by the Sun Yat-sen University Cancer Center. The patients/participants provided their written informed consent to participate in this study.

Author contributions

YY, YF, GF, and JL contributed to design of the study and data collection. XZ, JPa, PX, and YL were responsible for experimental implementation. YL, PX, CY, JPe, and XL performed the data analysis. XZ, JPa, GF, YY, and YF contributed to the manuscript writing. All authors read and approved the published version of the manuscript.

Funding

This work was funded by grants from the National Natural Science Foundation of China (61971214 and U21A6005), the Natural Science Foundation of Guangdong Province (2019A1515011513), and the Key-Area Research and Development Program of Guangdong Province (2018B030340001).

Conflict of interest

The authors declare that the research was conducted in the absence of any commercial or financial relationships that could be construed as a potential conflict of interest.

Publisher's note

Supplementary material

The Supplementary Material for this article can be found online at: https://www.frontiersin.org/articles/10.3389/fnins.2022.1059320/full#supplementary-material

References

Alves, P. N., Foulon, C., Karolis, V., Bzdok, D., Margulies, D. S., Volle, E., et al. (2019). An improved neuroanatomical model of the default-mode network reconciles previous neuroimaging and neuropathological findings. *Commun. Biol.* 2:370. doi: 10.1038/s42003-019-0611-3

Chan, A. T. (2010). Nasopharyngeal carcinoma. *Ann. Oncol.* 21 Suppl 7, vii308–vii312. doi: 10.1093/annonc/mdq277

Chen, Q., Lv, X., Zhang, S., Lin, J., Song, J., Cao, B., et al. (2020). Altered properties of brain white matter structural networks in patients with nasopharyngeal carcinoma after radiotherapy. *Brain Imaging Behav.* 14, 2745–2761. doi: 10.1007/s11682-019-00224-2

Chen, W., Qiu, S., Li, J., Hong, L., Wang, F., Xing, Z., et al. (2015). Diffusion tensor imaging study on radiation-induced brain injury in nasopharyngeal carcinoma during and after radiotherapy. *Tumori* 101, 487–490. doi: 10.5301/tj.5000348

Colombo, M. (2013). Olaf Sporns: Networks of the brain. *Minds Machines* 23, 259–262. doi: 10.1007/s11023-012-9294-y

Ding, Z., Zhang, H., Lv, X. F., Xie, F., Liu, L., Qiu, S., et al. (2018). Radiation-induced brain structural and functional abnormalities in presymptomatic phase and outcome prediction. *Hum. Brain Mapp.* 39, 407–427. doi: 10.1002/hbm.23852

Duan, F., Cheng, J., Jiang, J., Chang, J., Zhang, Y., and Qiu, S. (2016). Whole-brain changes in white matter microstructure after radiotherapy for nasopharyngeal carcinoma: A diffusion tensor imaging study. *Eur. Arch. Otorhinolaryngol.* 273, 4453–4459. doi: 10.1007/s00405-016-4127-x

Edge, S. B., Byrd, D. R., Carducci, M. A., Compton, C. C., Fritz, A., and Greene, F. (2010). *AJCC cancer staging manual*. New York, NY: Springer.

Fortunato, S., and Barthelemy, M. (2007). Resolution limit in community detection. *Proc. Natl. Acad. Sci. U.S.A.* 104, 36–41. doi: 10.1073/pnas.0605965104

Guo, Z., Han, L., Yang, Y., He, H., Li, J., Chen, H., et al. (2018). Longitudinal brain structural alterations in patients with nasopharyngeal carcinoma early after radiotherapy. *Neuroimage Clin.* 19, 252–259. doi: 10.1016/j.nicl.2018.04.019

He, Y., Dagher, A., Chen, Z., Charil, A., Zijdenbos, A., Worsley, K., et al. (2009). Impaired small-world efficiency in structural cortical networks in multiple sclerosis associated with white matter lesion load. *Brain* 132(Pt 12), 3366–3379. doi: 10.1093/brain/awp089

Hilger, K., Ekman, M., Fiebach, C. J., and Basten, U. (2017). Intelligence is associated with the modular structure of intrinsic brain networks. *Sci. Rep.* 7:16088. doi: 10.1038/s41598-017-15795-7

Jenkinson, M., Beckmann, C. F., Behrens, T. E., Woolrich, M. W., and Smith, S. M. (2012). Fsl. *Neuroimage* 62, 782–790. doi: 10.1016/j.neuroimage.2011.09.015

Jiang, Y., Yao, D., Zhou, J., Tan, Y., Huang, H., Wang, M., et al. (2020). Characteristics of disrupted topological organization in white matter functional connectome in schizophrenia. *Psychol. Med.* 52, 1333–1343. doi: 10.1017/S0033291720003141

Karim, H. T., Andreescu, C., Tudorascu, D., Smagula, S. F., Butters, M. A., Karp, J. F., et al. (2017). Intrinsic functional connectivity in late-life depression: Trajectories over the course of pharmacotherapy in remitters and non-remitters. *Mol. Psychiatry* 22, 450–457. doi: 10.1038/mp.2016.55

Le Bihan, D., Mangin, J. F., Poupon, C., Clark, C. A., Pappata, S., Molko, N., et al. (2001). Diffusion tensor imaging: Concepts and applications. *J. Magn. Reson. Imaging* 13, 534–546. doi: 10.1002/jmri.1076

Lell, M. M. (2015). "Therapy-induced changes in head and neck," in *Imaging of complications and toxicity following tumor therapy*, eds H.-U. Kauczor and T. Bäuerle (Cham: Springer International Publishing), 95–111.

Leng, X., Fang, P., Lin, H., An, J., Tan, X., Zhang, C., et al. (2017). Structural MRI research in patients with nasopharyngeal carcinoma following radiotherapy: A DTI and VBM study. *Oncol. Lett.* 14, 6091–6096. doi: 10.3892/ol.2017.6968

Leng, X., Fang, P., Lin, H., Qin, C., Tan, X., Liang, Y., et al. (2019). Application of a machine learning method to whole brain white matter injury after radiotherapy for nasopharyngeal carcinoma. *Cancer Imaging* 19:19. doi: 10.1186/s40644-019-0203-y

Leng, X., Qin, C., Lin, H., Li, M., Zhao, K., Wang, H., et al. (2021). Altered topological properties of static/dynamic functional networks and cognitive function after radiotherapy for nasopharyngeal carcinoma using resting-state fMRI. *Front. Neurosci.* 15:690743. doi: 10.3389/fnins.2021.690743

Lin, J., Lv, X., Niu, M., Liu, L., Chen, J., Xie, F., et al. (2017). Radiation-induced abnormal cortical thickness in patients with nasopharyngeal carcinoma after radiotherapy. *Neuroimage Clin.* 14, 610–621. doi: 10.1016/j.nicl.2017.02.025

Lin, X., Tang, L., Li, M., Wang, M., Guo, Z., Lv, X., et al. (2021). Irradiation-related longitudinal white matter atrophy underlies cognitive impairment in patients with nasopharyngeal carcinoma. *Brain Imaging Behav.* 15, 2426–2435. doi: 10.1007/s11682-020-00441-0

Lv, X. F., Zheng, X. L., Zhang, W. D., Liu, L. Z., Zhang, Y. M., Chen, M. Y., et al. (2014). Radiation-induced changes in normal-appearing gray matter in patients with nasopharyngeal carcinoma: A magnetic resonance imaging voxel-based morphometry study. *Neuroradiology* 56, 423–430. doi: 10.1007/s00234-014-1338-y

Lv, X., He, H., Yang, Y., Han, L., Guo, Z., Chen, H., et al. (2019). Radiation-induced hippocampal atrophy in patients with nasopharyngeal carcinoma early after radiotherapy: A longitudinal MR-based hippocampal subfield analysis. *Brain Imaging Behav.* 13, 1160–1171. doi: 10.1007/s11682-018-9931-z

Ma, Q., Wu, D., Zeng, L. L., Shen, H., Hu, D., and Qiu, S. (2016). Radiation-induced functional connectivity alterations in nasopharyngeal carcinoma patients with radiotherapy. *Medicine (Baltimore)* 95:e4275. doi: 10.1097/MD.0000000000004275

Mao, Y. P., Zhou, G. Q., Liu, L. Z., Guo, R., Sun, Y., Li, L., et al. (2014). Comparison of radiological and clinical features of temporal lobe necrosis in nasopharyngeal carcinoma patients treated with 2D radiotherapy or intensity-modulated radiotherapy. *Br. J. Cancer* 110, 2633–2639. doi: 10.1038/bjc.2014.243

Mo, Y. L., Li, L., Qin, L., Zhu, X. D., Qu, S., Liang, X., et al. (2014). Cognitive function, mood, and sleep quality in patients treated with intensity-modulated radiation therapy for nasopharyngeal cancer: A prospective study. *Psychooncology* 23, 1185–1191. doi: 10.1002/pon.3542

Nagesh, V., Tsien, C. I., Chenevert, T. L., Ross, B. D., Lawrence, T. S., Junick, L., et al. (2008). Radiation-induced changes in normal-appearing white matter in patients with cerebral tumors: A diffusion tensor imaging study. *Int. J. Radiat. Oncol. Biol. Phys.* 70, 1002–1010. doi: 10.1016/j.ijrobp.2007.08.020

Nan, F., Gao, J. M., Li, L., Zhang, Y. M., and Zhang, Y. (2022). Interaction of chemotherapy and radiotherapy in altering the shape of subcortical structures in patients with nasopharyngeal carcinoma. *Front. Oncol.* 12:952983. doi: 10.3389/fonc.2022.952983

Nazem-Zadeh, M. R., Chapman, C. H., Lawrence, T. L., Tsien, C. I., and Cao, Y. (2012). Radiation therapy effects on white matter fiber tracts of the limbic circuit. *Med. Phys.* 39, 5603–5613. doi: 10.1118/1.4745560

Newman, M. E. (2006). Modularity and community structure in networks. *Proc. Natl. Acad. Sci. U.S.A.* 103, 8577–8582. doi: 10.1073/pnas.0601602103

Qiu, Y., Guo, Z., Han, L., Yang, Y., Li, J., Liu, S., et al. (2018). Network-level dysconnectivity in patients with nasopharyngeal carcinoma (NPC) early post-radiotherapy: Longitudinal resting state fMRI study. *Brain Imaging Behav.* 12, 1279–1289. doi: 10.1007/s11682-017-9801-0

Qiu, Y., Guo, Z., Lin, X., Li, J., Li, Z., Han, L., et al. (2021). Standard radiotherapy for patients with nasopharyngeal carcinoma results in progressive tract-specific brain white matter alterations: A one-year follow-up via diffusion tensor imaging. *Radiother. Oncol.* 159, 255–264. doi: 10.1016/j.radonc.2021.03.039

Rubinov, M., and Sporns, O. (2010). Complex network measures of brain connectivity: Uses and interpretations. *Neuroimage* 52, 1059–1069. doi: 10.1016/j.neuroimage.2009.10.003

Smith, R. E., Tournier, J. D., Calamante, F., and Connelly, A. (2013). SIFT: Spherical-deconvolution informed filtering of tractograms. *Neuroimage* 67, 298–312. doi: 10.1016/j.neuroimage.2012.11.049

Smith, R. E., Tournier, J.-D., Calamante, F., and Connelly, A. (2012). Anatomically-constrained tractography: Improved diffusion MRI streamlines tractography through effective use of anatomical information. *NeuroImage* 62, 1924–1938.

Sporns, O. (2011). The human connectome: A complex network. *Ann. N Y Acad. Sci.* 1224, 109–125. doi: 10.1111/j.1749-6632.2010.05888.x

Sun, Y., Zhou, G. Q., Qi, Z. Y., Zhang, L., Huang, S. M., Liu, L. Z., et al. (2013). Radiation-induced temporal lobe injury after intensity modulated radiotherapy in nasopharyngeal carcinoma patients: A dose-volume-outcome analysis. *BMC Cancer* 13:397. doi: 10.1186/1471-2407-13-397

Tabuchi, K., Nakayama, M., Nishimura, B., Hayashi, K., and Hara, A. (2011). Early detection of nasopharyngeal carcinoma. *Int. J. Otolaryngol.* 2011:638058. doi: 10.1155/2011/638058

Tang, L. L., Chen, L., Mao, Y. P., Li, W. F., Sun, Y., Liu, L. Z., et al. (2015). Comparison of the treatment outcomes of intensity-modulated radiotherapy and two-dimensional conventional radiotherapy in nasopharyngeal carcinoma

patients with parapharyngeal space extension. *Radiother. Oncol.* 116, 167–173. doi: 10.1016/j.radonc.2015.07.038

Tang, Y., Luo, D., Rong, X., Shi, X., and Peng, Y. (2012). Psychological disorders, cognitive dysfunction and quality of life in nasopharyngeal carcinoma patients with radiation-induced brain injury. *PLoS One* 7:e36529. doi: 10.1371/journal.pone.0036529

Tian, Y., and Zhao, Y. (2017). Radiation-induced changes in structural network in patients with nasopharyngeal carcinoma. *Am. J. Clin. Exp. Med.* 5, 224–233. doi: 10.11648/j.ajcem.20170506.17

Tzourio-Mazoyer, N., Landeau, B., Papathanassiou, D., Crivello, F., Etard, O., Delcroix, N., et al. (2002). Automated anatomical labeling of activations in SPM using a macroscopic anatomical parcellation of the MNI MRI single-subject brain. *Neuroimage* 15, 273–289. doi: 10.1006/nimg.2001.0978

van Vulpen, M., Kal, H. B., Taphoorn, M. J., and El-Sharouni, S. Y. (2002). Changes in blood-brain barrier permeability induced by radiotherapy: Implications for timing of chemotherapy? (Review). *Oncol. Rep.* 9, 683–688.

Veraart, J., Novikov, D. S., Christiaens, D., Ades-Aron, B., Sijbers, J., and Fieremans, E. (2016). Denoising of diffusion MRI using random matrix theory. *Neuroimage* 142, 394–406. doi: 10.1016/j.neuroimage.2016.08.016

Vertes, R. P., Hoover, W. B., Szigeti-Buck, K., and Leranth, C. (2007). Nucleus reuniens of the midline thalamus: Link between the medial prefrontal cortex and the hippocampus. *Brain Res. Bull.* 71, 601–609. doi: 10.1016/j.brainresbull.2006.12.002

Wang, H. Z., Qiu, S. J., Lv, X. F., Wang, Y. Y., Liang, Y., Xiong, W. F., et al. (2012). Diffusion tensor imaging and 1H-MRS study on radiation-induced brain injury after nasopharyngeal carcinoma radiotherapy. *Clin. Radiol.* 67, 340–345. doi: 10.1016/j.crad.2011.09.008

Welzel, T., Niethammer, A., Mende, U., Heiland, S., Wenz, F., Debus, J., et al. (2008). Diffusion tensor imaging screening of radiation-induced changes in the white matter after prophylactic cranial irradiation of patients with small cell lung cancer: First results of a prospective study. *AJNR Am. J. Neuroradiol.* 29, 379–383. doi: 10.3174/ajnr.A0797

Wu, V. W. C., Ying, M. T., Kwong, D. L., Khong, P. L., Wong, G. K., and Tam, S. Y. (2020). A longitudinal study on parotid and submandibular gland changes assessed by magnetic resonance imaging and ultrasonography in post-radiotherapy nasopharyngeal cancer patients. *BJR Open* 2:20200003. doi: 10.1259/bjro.20200003

Wu, X., Gu, M., Zhou, G., Xu, X., Wu, M., and Huang, H. (2014). Cognitive and neuropsychiatric impairment in cerebral radionecrosis patients after radiotherapy of nasopharyngeal carcinoma. *BMC Neurol.* 14:10. doi: 10.1186/1471-2377-14-10

Xiong, W. F., Qiu, S. J., Wang, H. Z., and Lv, X. F. (2013). 1H-MR spectroscopy and diffusion tensor imaging of normal-appearing temporal white matter in patients with nasopharyngeal carcinoma after irradiation: Initial experience. *J. Magn. Reson. Imaging* 37, 101–108. doi: 10.1002/jmri.23788

Xu, M., Tan, X., Zhang, X., Guo, Y., Mei, Y., Feng, Q., et al. (2017). Alterations of white matter structural networks in patients with non-neuropsychiatric systemic lupus erythematosus identified by probabilistic tractography and connectivity-based analyses. *Neuroimage Clin.* 13, 349–360. doi: 10.1016/j.nicl.2016.12.021

Yang, Y. D., Lin, X. S., Li, J., Han, L. J., Li, Z. P., Liu, S. L., et al. (2019). Aberrant brain activity at early delay stage post-radiotherapy as a biomarker for predicting neurocognitive dysfunction late-delayed in patients with nasopharyngeal carcinoma. *Front. Neurol.* 10:752. doi: 10.3389/fneur.2019.00752

Zhang, Y. M., Gao, J. M., Zhou, H., Li, L., Liu, L. Z., Han, Z. D., et al. (2020). Pre-symptomatic local brain activity and functional connectivity alterations in nasopharyngeal carcinoma patients who developed radiation encephalopathy following radiotherapy. *Brain Imaging Behav.* 14, 1964–1978. doi: 10.1007/s11682-019-00145-0

Zhang, Y.-m, Chen, M.-n, Yi, X.-p, Li, L., Gao, J.-m, Zhang, J.-l, et al. (2018). Cortical surface area rather than cortical thickness potentially differentiates radiation encephalopathy at early stage in patients with nasopharyngeal carcinoma. *Front. Neurosci.* 12:599. doi: 10.3389/fnins.2018.00599

frontiers | Frontiers in Neuroscience

TYPE Original Research
PUBLISHED 30 November 2022
DOI 10.3389/fnins.2022.1036487

OPEN ACCESS

EDITED BY
Yoonmi Hong,
University of North Carolina at Chapel Hill, United States

REVIEWED BY
Shana Black,
The University of Utah, United States
Yanlu Wang,
Karolinska Institutet (KI), Sweden
Dong-Youl Kim,
Virginia Tech Carilion, United States
Yuncong Ma,
University of Pennsylvania, United States
Zhen Qiu,
Michigan State University, United States

*CORRESPONDENCE
Xu Wang
wangx@bucm.edu.cn
Guangxia Shi
shiguangxia2008@126.com

SPECIALTY SECTION
This article was submitted to Brain Imaging Methods, a section of the journal Frontiers in Neuroscience

RECEIVED 04 September 2022
ACCEPTED 14 November 2022
PUBLISHED 30 November 2022

CITATION
Wei X, Wang L, Yu F, Lee C, Liu N, Ren M, Tu J, Zhou H, Shi G, Wang X and Liu C-Z (2022) Identifying the neural marker of chronic sciatica using multimodal neuroimaging and machine learning analyses. *Front. Neurosci.* 16:1036487. doi: 10.3389/fnins.2022.1036487

Identifying the neural marker of chronic sciatica using multimodal neuroimaging and machine learning analyses

Xiaoya Wei[1], Liqiong Wang[1], Fangting Yu[1], Chihkai Lee[1], Ni Liu[2], Mengmeng Ren[2], Jianfeng Tu[1], Hang Zhou[1], Guangxia Shi[1]*, Xu Wang[3]* and Cun-Zhi Liu[1]

[1]International Acupuncture and Moxibustion Innovation Institute, School of Acupuncture-Moxibustion and Tuina, Beijing University of Chinese Medicine, Beijing, China, [2]Department of Radiology, Beijing Hospital of Traditional Chinese Medicine Affiliated to Capital Medical University, Beijing, China, [3]School of Life Sciences, Beijing University of Chinese Medicine, Beijing, China

Introduction: Sciatica is a pain disorder often caused by the herniated disk compressing the lumbosacral nerve roots. Neuroimaging studies have identified functional abnormalities in patients with chronic sciatica (CS). However, few studies have investigated the neural marker of CS using brain structure and the classification value of multidimensional neuroimaging features in CS patients is unclear.

Methods: Here, structural and resting-state functional magnetic resonance imaging (fMRI) was acquired for 34 CS patients and 36 matched healthy controls (HCs). We analyzed cortical surface area, cortical thickness, amplitude of low-frequency fluctuation (ALFF), regional homogeneity (REHO), between-regions functional connectivity (FC), and assessed the correlation between neuroimaging measures and clinical scores. Finally, the multimodal neuroimaging features were used to differentiate the CS patients and HC individuals by support vector machine (SVM) algorithm.

Results: Compared to HC, CS patients had a larger cortical surface area in the right banks of the superior temporal sulcus and rostral anterior cingulate; higher ALFF value in the left inferior frontal gyrus; enhanced FCs between somatomotor and ventral attention network. Three FCs values were associated with clinical pain scores. Furthermore, the three multimodal neuroimaging features with significant differences between groups and the SVM algorithm could classify CS patients and HC with an accuracy of 90.00%.

Discussion: Together, our findings revealed extensive reorganization of local functional properties, surface area, and network metrics in CS patients. The success of patient identification highlights the potential of using artificial intelligence and multimodal neuroimaging markers in chronic pain research.

KEYWORDS

brain networks, chronic pain, fMRI, chronic sciatica, support vector machines, ALFF, cortical surface area

Introduction

Sciatica is a pain disorder often caused by the herniated disk compressing the lumbosacral nerve roots, usually presenting as pain radiating from the low back down to the leg below the knee (Porchet et al., 2002; Deyo and Mirza, 2016). About a quarter of adults in the USA have experienced low back pain in the past 3 months, and 30% of those accompanied sciatica (Jensen et al., 2019). The global prevalence of sciatica varies from 1.2 to 43% (Konstantinou and Dunn, 2008; Finley et al., 2018), reflecting its ununified diagnostic criteria and diverse clinical manifestations. Pain caused by sciatica can easily progress to a chronic stage which may be either continuous or recurrent, and severely affects the quality of life and mental health (Foster and Reddington, 2021). However, the pathophysiologic mechanisms of chronic sciatica (CS) are not clear, which restricts the development of therapeutic protocols.

Previous neuroimaging studies have shown greater regional homogeneity (REHO) of the posterior cingulate (Liu et al., 2020) and lower functional connectivity (FC) between the dorsolateral prefrontal cortex (DLPFC) and anterior cingulate cortex (ACC) (Li et al., 2012) in patients with CS compared with healthy controls (HCs). However, these functional abnormalities may not fully account for the pathophysiology of CS, because a large number of studies have found both functional and structural (e.g., cortical surface area) changes associated with chronic pain (Seminowicz et al., 2011; Luchtmann et al., 2014; De Pauw et al., 2019; Niddam et al., 2019). Besides, multiple studies have suggested that communication between brain networks is changed in chronic pain patients, and connections across networks may reflect the presence of chronic pain (Kim et al., 2013; Hemington et al., 2016).

Given these neuroimaging findings on chronic pain, we speculated that patients with CS may also have abnormal changes in structural properties or between-regions FC. In addition, previous studies have applied machine learning techniques to distinguish patients with post-herpetic neuralgia (PHN) and HC using the amplitude of low-frequency fluctuation (ALFF) values (Huang et al., 2020). However, few studies have classified neuropathic pain patients from HC by multimodal neuroimaging features. The multidimensional neuroimaging features may serve as a bridge between clinical observations and neural mechanisms that can increase the understanding of CS as a complex and multifaceted pain-related disease.

Therefore, this study aimed to investigate the underlying neurobiological mechanisms of CS using surface-based morphometry, local functional metric, and network FC analyses in patients with CS using structural and functional magnetic resonance imaging (fMRI) data. Besides, the relationships between neuroimaging measures and clinical symptom scale scores were examined. Furthermore, the diagnosability of the neuroimaging properties was evaluated utilizing a support vector machine (SVM) of machine learning techniques and neuroimaging features with significant differences between CS patients and HC.

Materials and methods

Participants

This study included 34 CS patients who meet the diagnostic criteria of sciatica (Jensen et al., 2019) and 38 HC participants. Patients were recruited in the Dongzhimen Hospital Affiliated to Beijing University of Chinese Medicine from December 2020 to May 2021. The study recruited participants through hospital outpatient, the WeChat official account (one of China's popular social media platforms) of Dongzhimen Hospital, and brochures.

The key inclusion criteria of CS people were: (1) 35–65 years old; (2) having unilateral radiating leg pain below the knee for more than 3 months, accompanied by a positive straight-leg raise test or corresponding neurological deficit (paresthesia, muscle weakness, or reflex abnormalities) with magnetic resonance imaging (MRI) or computed tomography (CT) confirmed disk herniation, (3) leg pain intensity on the visual analog scale (VAS) (0–100 mm) of 40 mm or higher (Collins et al., 1997), (4) right-handed. The exclusion criteria were: (1) sciatica induced by other diseases than lumbar disk herniation, (2) having the severe spinal disease or severe progressive neurological symptoms, (3) having cardiovascular, liver, kidney, or hematopoietic system diseases, mental health disorders, or other severe coexisting diseases, (4) pregnant or lactating women or those planning to conceive during the trial. Additionally, 38 pain-free age- and sex-matched HCs were recruited from the same geographic area by public advertisement. All HCs also met the above exclusion criteria. In addition, HCs were asked whether had personal or family histories of pain disorders or had experienced any significant pain condition as the exclusion criteria.

This study has been approved by the Ethics Committee of Dongzhimen Hospital Affiliated to Beijing University of Chinese Medicine (No. 2020BZYLL0803), and it was part of a study registered in Chinese Clinical Trial Registry (ChiCTR2100044585). All participants provided written informed consent according to the Declaration of Helsinki after study procedures were explained to them thoroughly. We collected MRI data from all participants.

Clinical parameters

After recruitment, the following clinical measurements were evaluated by CS patients within the day before the MRI scanning. VAS was performed to rate the extent of pain in the leg

and low back. Oswestry Disability Index (ODI) (Fairbank and Pynsent, 2000) was conducted to identify self-reported function levels through examining perceived disability in 10 activities of daily living. Sciatica Frequency and Bothersomeness Index (SFBI) (Atlas et al., 1996) was used to assess the frequency and bothersomeness of sciatica with scores ranging from 0 to 24, respectively. The 36-item Short-Form Health Survey (SF-36) (Lam et al., 2005) was administered to assess the quality of life in eight aspects, and the scores on the physical and mental components of the SF-36 will be summarized.

Magnetic resonance imaging acquisition

Magnetic resonance imaging images were obtained at a Siemens 3.0 T MRI scanner (Skyra, Siemens, Erlangen, Germany) using a standard head coil at the Department of Radiology for Beijing Hospital of Traditional Chinese Medicine Affiliated to Capital Medical University. The high-resolution T1 structural MRI (sMRI) was acquired using a gradient echo sequence with the following parameters: repetition time (TR) = 2,530 ms, echo time (TE) = 2.98 ms, flip angle (FA) = 7°, inversion time = 1,100 ms, field of view (FOV) = 240 mm × 240 mm, number of slices = 192, voxel size = 1 mm × 1 mm × 1 mm, and in-plane resolution = 256 × 256. And resting-state functional MRI (rs-fMRI) was scanned using echo-planar imaging (EPI) sequence with the following parameters: whole brain, TR = 2,000 ms, TE = 30 ms, FOV = 224 mm × 224 mm, FA = 90°, slice thickness/gap = 3.5/0.6 mm, voxel size = 3.5 mm × 3.5 mm × 3.5 mm, axial slices = 32, in-plane resolution = 64 × 64, and 240 volumes. The scan duration was 5 min for the T1-weighted image and 8 min for EPI scans for blood oxygen-level dependent (BOLD)-based functional neuroimaging. We used comfortable foam pads to minimize head motion and earplugs to reduce noise interference. Before starting scanning, we instructed participants to keep their eyes closed, stay awake, avoid engaging in any specific thoughts and keep still.

Quality control of magnetic resonance imaging data

Visually checking image quality by a neuroradiologist (QR) to make sure there were no apparent structural abnormalities or artifacts present, and the images with head movement greater than 2 mm in any direction or head rotation greater than 1° were excluded. Two HCs were excluded from the study on account of excessive head motion (>2 mm in translation or >2.0° in rotation) during the rs-fMRI scanning. The two excluded participants were female, their ages were 48 and 54 years. As a result, 34 patients with CS and 36 HCs were included in further statistical analyses. Furthermore, we also extracted the mean framewise displacement (FD) (Van Dijk et al., 2012) for each participant to measure the extent of head motion and compared them between the two groups. The Mann–Whitney U of non-parametric test result showed that there is no significant difference in head motion among the three groups ($z = 1.575$, $p = 0.115$).

Structural magnetic resonance imaging data processing

First, the "recon-all" command with –all –qcache options implemented in FreeSurfer (V6.0)[1] was used to pre-process T1-weighted images, the key steps including motion correction, non-uniform intensity normalization, talairach transform computation, skull removal, volumetric segmentation, cortical surface reconstruction and so on. Mean cortical thickness and surface area were calculated for each of the 68 cortical regions of the Desikan-Killiany Atlas (34 per hemisphere). Cortical thickness was estimated for each participant using the distance from the white matter boundary to the corresponding pial surface (Fischl and Dale, 2000). The cerebral surface area was calculated by mesh generation and surface triangulation. Then mean cortical thickness and surface area were extracted for each cortical region.

Functional magnetic resonance imaging data processing and network analyses

The fMRI data were pre-processed using the software MATLAB 2017 and the toolbox for Data Processing and Analysis for Brain Imaging (DPABI) (version 6.1)[2] (Yan et al., 2016). For each participant's image data, we discarded the first 10 volumes because of signal equilibrium, a total of 230 volumes for each subject were processed with the slice timing, motion correction, spatial smoothing (8-mm FWHM), and spatial normalization to the Montreal Neurological Institute (MNI) space. Then we re-sampled the data into 3 mm × 3 mm × 3 mm. Finally, after removing the linear trend, we applied a 0.01–0.08 Hz bandpass filter.

It should be noted that ALFF was calculated without filtering during the pre-processing process, and REHO was not smoothed during the pre-processing but smoothed after it was calculated, to allow the data to be normalized, which would be conducive to statistical analysis and indicator standardization.

1 http://surfer.nmr.mgh.harvard.edu/

2 http://rfmri.org/dpabi

ALFF and REHO values were calculated using the DPBAI toolbox. ALFF is used to detect the regional intensity of spontaneous fluctuations in the BOLD signal, REHO calculates the temporal homogeneity of the BOLD signal between a given voxel with neighboring voxels. These measures were selected to pinpoint the spontaneous neural activity of specific regions and physiological states of the brain. The ALFF measures the gross power of oscillations within a certain frequency range, using the DPBAI software and regions of interest (ROIs) defined by the Anatomical Automatic Labeling (AAL) ROI library. The calculation procedure: (1) Fast Fourier Transform (FFT) was used to convert all voxels from the time domain to the frequency domain; (2) the ALFF of every voxel was calculated by averaging the square root of the power spectrum across 0. REHO was computed based on Kendall's coefficient of concordance (KCC) of the time series of the voxel with its nearest 26 neighboring voxels. The REHO was computed for all brain voxels.

We used the software MATLAB 2017 and the DPABI (version 6.1) to extract time courses of 160 ROIs in the Dosenbach 160 atlas (Dosenbach et al., 2010). Each ROI (i.e., node) was a 5 mm radius sphere centered on the atlas coordinates, including 19 voxels in each. To derive the connectivity matrix of the brain, we computed Pearson correlation coefficients of BOLD signals between each pair of 142 ROIs (Glasser et al., 2016) (Dosenbach 160 atlas exclude 18 ROIs of the cerebellum), which were then Fisher transformed to z-values. We grouped significant nodes according to a well-defined seven-network atlas derived from 1,000 healthy participants by Yeo et al. (2011): sensory-motor network (SMN), ventral attention network (VAN), visual network (VN), dorsal attention network (DAN), default mode network (DMN), frontoparietal network (FPN), and subcortical network (SC). Because the limbic network nodes from the Yeo atlas were not covered by the Dosenbach 160 atlas, we defined subcortical ROIs as the SC (Yang et al., 2021).

Statistical analyses

Demographic and clinical characteristics analyses

Demographic data collected from either group includes age, gender, educational level, and occupation. Participants were asked to indicate the physical activity level of the work they do most of the time, the nature of occupation was defined as manual work and mental work. We used Statistical Package for Social Sciences (SPSS) V21 software to conduct statistical analyses. Before statistical analyses, we checked the normality of each metric. Education in each group and age of the HC group were non-normally distributed, we used Kolmogorov–Smirnov non-parametric tests. As for categorical variables (i.e., gender and occupation), we used the Chi-Square test to evaluate the differences between groups. The significance level was set at $p < 0.05$.

Surface area and thickness analyses

The cortical surface area and cortical thickness of CS patients and HC were extracted. Then, we used SPSS V21 software to conduct statistical analyses. Two-sample independent t-tests were used to compare the regional-wise differences between the two groups if the measurements were normally distributed [False discovery rate (FDR) correction, $p < 0.05$], and if the data distribution is not normal, we used non-parametric tests of Mann–Whitney U. Effect sizes are depicted as Cohen's d. The effect size was computed at https://www.psychometrica.de/effect_size.html.

Amplitude of low-frequency fluctuation and regional homogeneity analyses

For ALFF and REHO maps, voxel-wise two-sample independent t-tests were performed to compare the results between the two groups, Gaussian Random Field theory (GRF) correction, voxel-level $p < 0.001$, and cluster-level $p < 0.05$. We extracted the values of ALFF and REHO results and calculated effect sizes using Cohen's d.

Network functional connectivity analyses

For FC analyses, we also used two-sample independent t-tests with FDR corrected ($p < 0.05$) in DPABINet (See text footnote 2, version 1.1). The figures were distributed in DPABINet and BrainNet Viewer.[3] Finally, we extracted the values and showed them in the tables. Cohen' s d was used as the effect size measure.

Brain metrics and clinical variables correlation analyses

We extracted metrics (ALFF, REHO, surface-based morphometry, and FC) with significant group differences and investigated their relationships with clinical variables. VAS score for leg pain, VAS score for back pain, ODI score, SF-36 for physical, SF-36 for mental, SFBI for frequency, and SFBI for bothersomeness were investigated. For non-normally distributed variables (VAS score for leg pain and SF-36 for mental score), we used Spearman's correlation analyses. For the other normally distributed variables, Pearson correlation was used to analyze the correlation. The above statistical analyses were implemented using SPSS V21 (significance level is $p < 0.05$).

Group classification with support vector machine

After revealing the significant ALFF values, surface area, and FCs in the CS group, we used these three kinds of features to accurately differentiate the 34 CS individuals from the 36 HCs. Features with different scales across different modalities were normalized to a value between 0 and 1

3 http://www.nitrc.org/projects/bnv

according to their maximum and minimum values. Then, the discriminant analysis was performed by using the SVM with a nested leave-one-out cross-validation (LOOCV) framework. First, the C regularization parameter and the linear kernel function were optimized by performing 5-fold cross-validation on the n-1 (i.e., 69) training data. Once the optimal SVM model was obtained, it was applied to classify the left-out individual as CS or HC.

The performances of a classifier were quantified using accuracy, sensitivity, specificity, and the area under the receiver operating characteristic (ROC) curve (AUC). Note that the specificity represented the proportion of the HC individuals correctly predicted, while the sensitivity represented the proportion of the CS individuals correctly predicted. Specifically, accuracy is calculated as (TP + TN)/(TP + TN + FN + FP), sensitivity is defined as TP/(TP + FN) and specificity is defined as TN/(FP + TN), where TN is the number of true negatives (HC individuals correctly classified), TP is the number of true positives (CS individuals correctly classified), FN is the number of false negatives (CS individuals classified as HC individuals), and FP is the number of false positives (HC individuals classified as CS individuals). In addition, the AUC is an evaluation measure based on the ROC curve, which illustrates the performance of the classifier. The ROC curve is delineated by plotting 1-specificity and sensitivity at different thresholds, and the thresholds of each ROC curve underwent stepwise variation from 0 to 1 in each 0.1 interval. Last, the model's performance was evaluated by computation of the Matthews Correlation Coefficient (MCC). The calculation formula (Ali et al., 2021) is as follows:

$$MCC = \frac{TP \times TN - FP \times FN}{\sqrt{(TP + FP)(TP + FN)(TN + FP)(TN + FN)}}$$

TABLE 1 Demographic and clinical characteristics of two groups.

Parameter	CS (n = 34)	HC (n = 36)	Statistics	P-value
Age (years)	54.29 (8.80)	58.50 (51, 62.75)	Z = 0.861	0.449[a]
Gender (M/F)	14/20	12/24	X^2 = 0.461	0.497[b]
Education (years)	12.97 (3.49)	11.50 (2.77)	Z = 0.909	0.381[a]
Occupation (Men/Man)	11/23	19/17	X^2 = 1.611	0.204[b]
Pain duration (years)	8.00 (3.38, 17.75)	N/A	N/A	N/A
VAS score for leg pain	55 (50, 70)	N/A	N/A	N/A
VAS score for back pain	57.50 (14.72)	N/A	N/A	N/A
ODI score	26.27 (11.33)	N/A	N/A	N/A
SF-36 for physical	35.32 (10.34)	N/A	N/A	N/A
SF-36 for mental	57.31 (47.42, 62.71)	N/A	N/A	N/A
SFBI for frequency	12.85 (4.84)	N/A	N/A	N/A
SFBI for bothersomeness	11.88 (4.27)	N/A	N/A	N/A

We used mean (standard deviation) if the measurements were normally distributed, and median (Q1, Q3) if the measurements were not normally distributed. [a]Non-parametric test, Kolmogorov–Smirnov. [b]Chi-square test. CS, chronic sciatica; HC, healthy controls; M/F, male/female; Men/Man, Mental work/Manual work; N/A, not applicable; VAS, visual analog scale, 0–100 mm; ODI, Oswestry Disability Index; SF-36, the 36-item Short-Form Health Survey; SFBI, Sciatica Frequency and Bothersomeness Index.

Results

Demographic and clinical characteristics

Thirty-four CS patients and 36 matched HCs completed the entire study. Age and years of education were not normally distributed, so the Kolmogorov–Smirnov test was used to test for group differences. No significant group differences were found in age (p = 0.449), gender (Chi-square test: p = 0.497), years of education (p = 0.381), and occupation (Chi-square test: p = 0.204) between the CS and HC groups (**Table 1**). And the median pain duration of CS was 8 months, the median pain score for the leg on the VAS was 55, and the mean VAS score for back pain was 57.50 (14.72) in patients. Otherwise, the mean SF-36 score for the physical duration of CS was 35.32 (10.34), and the median SF-36 score for mental was 57.31 in CS patients.

Amplitude of low-frequency fluctuation abnormality in chronic sciatica patients

Compared with the HC group, patients with CS had higher ALFF in the left inferior frontal gyrus (IFG) (t = 4.132, ES = −1.238, CI [−1.750 to −0.727]; **Figure 1A** and **Table 2**). However, the REHO analysis did not yield any significant results at the whole brain level.

Abnormal surface area in chronic sciatica patients

Compared with the HC group, patients with CS had the larger surface area in the right banks of the superior temporal sulcus (bankssts) (t = 3.666, ES = −0.877, CI [−1.367 to 0.386], FDR corrected p = 0.016) and right rostral anterior cingulate (rACC) (t = 3.417, ES = −0.817, CI [−1.305 to 0.329], FDR corrected p = 0.018; **Table 3** and **Figure 1B**). However, we did not find a significant difference in cortical thickness between the two groups.

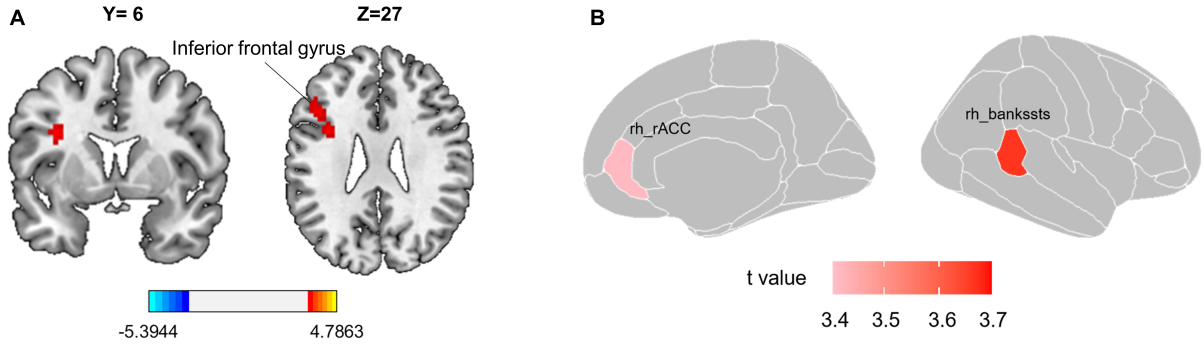

FIGURE 1
Group differences in local functional metric and surface morphology. **(A)** Patients with CS have significantly higher ALFF value in the left inferior frontal gyrus. The red color reflects ALFF values greater in CS patients than in the HC group. Gaussian Random Field theory (GRF) correction with voxel-level $p < 0.001$ and cluster-level $p < 0.05$. **(B)** Cortical surface area differences between CS patients and HC. *T*-values of two altered brain regions in the surface area of the right hemisphere. Positive (red) values reflect cortical area larger in CS patients than in the HC group, FDR corrected $p < 0.05$. CS, chronic sciatica; CS, chronic sciatica; HC, healthy controls; rh, right hemisphere; rACC, rostral anterior cingulate cortex; bankssts, banks of superior temporal sulcus.

TABLE 2 Significant differences in ALFF between two groups.

	Regions	Peak MNI coordinates			Voxels size	*t*-value	ES (95%CI)
		X	*Y*	*Z*			
ALFF							
CS > HC	Inferior frontal gyrus, L	−36	6	27	85	4.132	−1.238 (−1.750, −0.727)

Regions were identified in Figure 1A. Peak coordinates (*X*, *Y*, *Z*) are displayed according to MNI standard space, and labels according to the AAL atlas. GRF corrected, voxel-level $p < 0.001$, cluster-level $p < 0.05$. MNI, Montreal Neurological Institute; CS, chronic sciatica; HC, healthy controls; ALFF, the amplitude of low-frequency fluctuation; L, left; ES, effect sizes, Cohen's d; CI, confidence interval; the effect size was computed for groups with different sample size.

TABLE 3 Differences in surface area index between the two groups.

	Region	CS ($n = 34$)	HC ($n = 36$)	*t*-value	ES (95%CI)	*P*-value
CS > HC	rh_bankssts	941.24 (150.03)	834.78 (86.14)	3.666	−0.877 (−1.367, 0.386)	0.016*
	rh_rACC	662.29 (170.19)	542.17 (121.17)	3.417	−0.817 (−1.305, 0.329)	0.018*

We used mean (standard deviation) if the measurements were normally distributed. Two-sample *t*-test. *Survives false discovery rate (FDR) correction, $p < 0.05$. CS, chronic sciatica; HC, healthy controls; rh, right hemisphere; rACC, rostral anterior cingulate cortex; bankssts, banks of superior temporal sulcus; ES, effect sizes, Cohen's d; CI, confidence interval; the effect size was computed for groups with different sample size.

Functional connectivity alterations in chronic sciatica and its relationship with clinical symptoms

For FC analysis, there were 15 connections between SMN and VAN that exhibited higher connection strength in the CS group than in the HC group, with a few connections among other networks. In addition, there were 10 lower connections among six networks ($p < 0.05$, FDR corrected, Table 4 and Figures 2A,B). In addition, the FC between right vPFC and left precentral gyrus had a negative correlation with the VAS for leg pain score (Spearman *rho* = −0.349, $p = 0.043$, CI [−0.621 to −0.002]), the FC between left basal ganglia and left precentral gyrus had a negative correlation with the VAS for leg pain score (Spearman *rho* = −0.393, $p = 0.022$, CI [−0.651 to −0.052]), and the FC between mFC and left precentral gyrus had a negative correlation with the VAS for leg pain score (Spearman *rho* = −0.344, $p = 0.047$, CI [−0.617 to 0.004]). The correlation results were shown in Figure 2C.

Multimodal brain metrics discriminate between chronic sciatica patients and healthy control

In this study, ALFF, surface area, and FCs were utilized to classify whether a sample belonged to the CS group (Table 5 and Figure 3). For single-measurement analyses, the FCs exhibited a higher accuracy rate (accuracy = 85.71%) and MCC of

TABLE 4 The comparison of FCs between two groups.

Comparisons	Significant FC		Group		*t*-value	ES (95%CI)	*P*-value
	Region A	Region B	CS (n = 34)	HC (n = 36)			
Sciatica > HC	vPFC	Precentral	0.08 (0.18)	0.09 (0.06)	4.171	0.106 (−0.363, 0.575)	<0.05*
	Ant insula	Precentral	0.13 (0.14)	−0.11 (0.18)	4.047	−1.409 (−1.932, −0.885)	<0.05*
	Ant insula	Precentral	0.07 (0.18)	−0.05 (0.20)	4.356	−0.599 (−1.079, −0.120)	<0.05*
	Ant insula	Precentral	0.08 (0.19)	−0.12 (0.19)	4.848	−1.079 (−1.580, −0.577)	<0.05*
	dACC	Precentral	0.12 (0.25)	−0.13 (0.17)	5.062	−1.145 (−1.650, −0.639)	<0.05*
	dACC	Parietal	0.08 (0.25)	−0.17 (0.23)	4.530	−1.064 (−1.564, −0.563)	<0.05*
	Ant insula	Precentral	0.16 (0.19)	−0.18 (0.23)	4.258	−1.618 (−2.158, −1.078)	<0.05*
	Ant insula	Precentral	0.13 (0.17)	−0.04 (0.21)	5.014	−0.920 (−1.413, −0.427)	<0.05*
	Basal ganglia	Precentral	0.17 (0.21)	−0.08 (0.19)	3.913	−1.294 (−1.810, −0.779)	<0.05*
	Basal ganglia	Precentral	0.16 (0.24)	−0.04 (0.25)	4.869	−0.827 (−1.316, −0.339)	<0.05*
	Basal ganglia	Parietal	0.12 (0.23)	−0.11 (0.22)	4.538	−1.006 (−1.504, −0.509)	<0.05*
	mFC	Precentral	0.12 (0.25)	−0.13 (0.23)	5.142	−1.040 (−1.540, −0.541)	<0.05*
	mFC	Precentral	0.18 (0.23)	−0.15 (0.19)	3.981	−1.599 (−2.137, −1.061)	<0.05*
	vFC	Precentral	0.17 (0.21)	−0.03 (0.21)	4.094	−0.958 (−1.453, −0.463)	<0.05*
	vFC	Precentral	0.26 (0.20)	0.0001 (0.14)	4.324	−1.511 (−2.042, −0.980)	<0.05*

We used mean (standard deviation) if the measurements were normally distributed. CS, chronic sciatica; HC, health control; vPFC, ventral prefrontal cortex; ant insula, anterior insula; dACC, dorsal anterior cingulate cortex; mFC, medial frontal cortex; vFC, ventral frontal cortex. *Survives false discovery rate (FDR) correction, $p < 0.05$. ES, effect sizes, Cohen's d; CI, confidence interval; the effect size was computed for groups with different sample size.

0.715 than the ALFF (accuracy = 70.00%, and MCC = 0.424) and surface area (accuracy = 68.57%, MCC = 0.398). Surface morphology achieved the lowest accuracy rate. The classification accuracy improved after combining the significant measurements of the three features, achieving an accuracy of 90.00%, an AUC of 0.96, and an MCC of 0.800.

Discussion

Combining a variety of analysis methods, we demonstrated that CS patients had abnormal local neural activity, which was also reflected in the greater ALFF values of the left IFG. At a finer cortical scale, we could identify the significantly greater cortical surface area in the regions cingulate and temporal. At the resting-state functional network level, we found that CS patients showed greater FCs mainly between the SMN and VAN, especially the precentral gyrus and anterior insula. Finally, we found that multimodal combined neuroimaging features were more dominant in this disease classification performance.

Greater surface area of rostral anterior cingulate and banks of the superior temporal sulcus in right hemisphere

The ACC plays a vital role in the neuropathic pain effect in animals (Gao et al., 2020). For instance, increased GABAergic inhibitory control in the rACC could reduce ongoing pain and pain aversiveness caused by sciatic nerve injury (Juarez-Salinas et al., 2019). Using fMRI and electrophysiological recording, a previous study observed plasticity changes in the cingulate cortex in rats with neuropathic pain (Chao et al., 2018). However, the underlying role of the ACC in CS patients is much unclear. Our study showed a larger surface area in the rACC in CS patients compared to HC, suggesting that the rACC may be related to pain-induced negative emotion in CS patients. In another neuropathic pain disease, trigeminal neuralgia patients exhibited reduced ACC surface area compared with HC (Mo et al., 2021). The controversy may stem from different neuropathological processes. In the future, we will further explore whether the enlarged surface area of ACC can be the biomarker to distinguish CS patients from other neuropathic pain disorders.

Furthermore, the superior temporal gyrus might be involved in pain due to mismatches between pain expectation and perception (Smallwood et al., 2013). Patients with chronic traumatic neck pain showed a smaller cortical volume in the right superior temporal gyrus compared to HC (De Pauw et al., 2019). However, our study showed that CS patients have a greater cortical surface area in the right superior temporal gyrus, which may be due to the different etiologies and neuropathological processes of diseases. A study reported that patients with bipolar disorder showed a larger surface area of left bankssts, which could help distinguish them from patients with major depression, the overall accuracy was 74.3% (Fung et al., 2015). The surface area of the right bankssts and rACC in this study were also effective in distinguishing CS patients

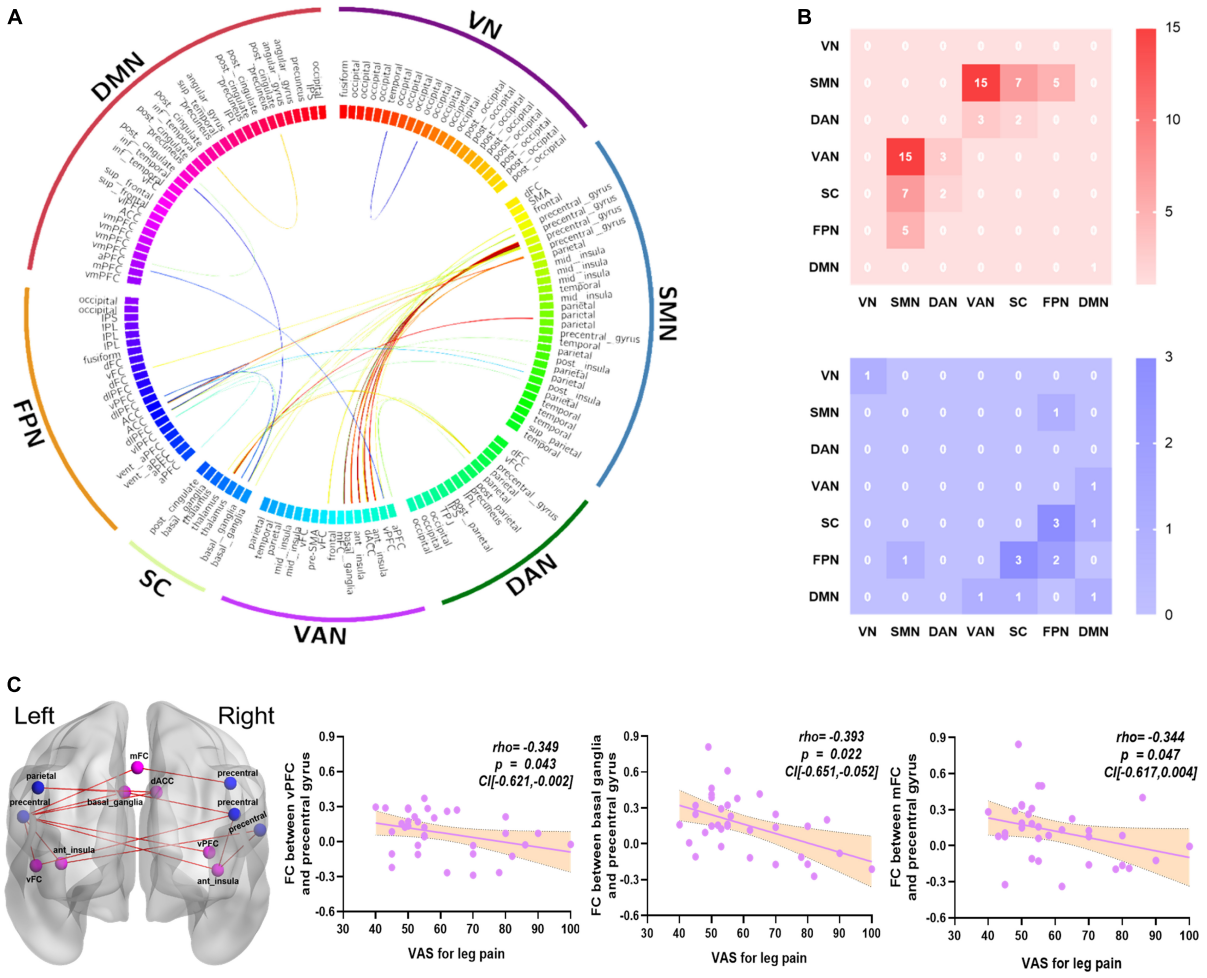

FIGURE 2
The altered FCs between networks and relationships with clinical symptoms. **(A)** The FCs significantly altered in the CS group compared with the HC group, which were mainly focused on SMN and VAN ($p < 0.05$, FDR corrected). **(B)** 15 greater FCs were involved in the SMN and VAN. The red color represents greater FCs; the blue color represents lower FCs. **(C)** The VAS for leg pain score had a negative correlation with the FC of right vPFC and left precentral gyrus (Spearman, $r = -0.349$, $p = 0.043$, CI [−0.621 to −0.002]); the FC of left basal ganglia and left precentral gyrus (Spearman, $r = -0.393$, $p = 0.022$, CI [−0.651 to −0.052]); and the FC of mFC and left precentral gyrus (Spearman, $r = -0.344$, $p = 0.047$, CI [−0.617 to 0.004]). The blue color nodes belong to SMN, the light purple nodes belong to VAN, the red color represents greater FCs. CS, chronic sciatica; HC, health control; vPFC, ventral prefrontal cortex; mFC, medial frontal cortex; SMN, somatomotor network; VAN, ventral attention network; VN, visual network; DAN, dorsal attention network; DMN, default mode network; FPN, frontoparietal network; SC, subcortical network; VAS, visual analog scale.

from HC, the accuracy was 66.99%. These results suggested that disease-specific neuroanatomical features (e.g., cortical surface area) may help establish reliable distinctions between different populations (e.g., between different types of disease, between patients with HC).

Frontal cortex showed greater spontaneous neuronal activity and functional connectivity's

In our study, we found significantly greater ALFF in the IFG in CS patients compared to HC. Consistent with previous studies involving aspects of chronic pain (Buckalew et al., 2010; Hashmi et al., 2013), we found the neural activity of the frontal lobe was significantly greater in CS patients. IFG is the important part of the prefrontal cortex (PFC), the brain region commonly associated with cognitive and emotional processing (Petrides, 2005; He et al., 2007). In CS patients, the abnormal functional activity of the two brain regions may influence pain perception through heightening emotional responses to pain (Gracely et al., 2004).

Consistent with a previous study, medial PFC/rACC had abnormally increased FCs with brain regions with the SMN (postcentral gyrus) in cLBP patients, and the FCs could discriminate cLBP patients from HCs with 91% accuracy

TABLE 5 Results of the discrimination analyses derived from the SVM between HC and CS.

Feature	Accuracy (%)	Sensitivity (%)	Specificity (%)	AUC (%)	MCC
ALFF	70.00	67.65	83.33	79.66	0.424
Surface area	68.57	55.88	77.78	66.99	0.398
FCs	85.71	85.29	86.11	90.85	0.715
Combining features	90.00	94.12	86.11	96.41	0.800

For single-measurement analyses, the FCs exhibited a higher accuracy rate (85.71%) than the other two features. The surface morphology (surface area) achieved the lowest accuracy rate of 68.57%. The classification accuracy improved after combining the features of the three measurements, achieving an accuracy of up to 90.00%. CS, chronic sciatica; HC, health control; ALFF, the amplitude of low-frequency fluctuation; FC, functional connectivity, AUC, the area under the curve; MCC, Matthews Correlation Coefficient; FC, functional connectivity; SVM, support vector machine.

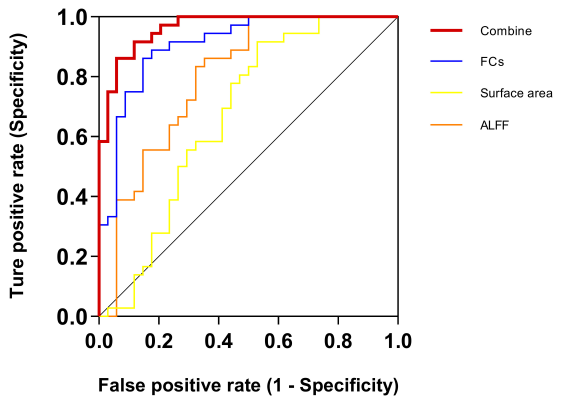

FIGURE 3
Receiver operating characteristic (ROC) for CS and HC SVM classification analyses. For single-measurement analyses, the functional connectivity (FC) exhibited a higher AUC of 90.85% than the other two measurements. The surface area achieved the lowest AUC of 66.99%. Critically, the AUC improved after combining all features of the three measurements, achieving an AUC up to 96.41%. ALFF, the amplitude of low-frequency fluctuation; FC, functional connectivity.

(Tu et al., 2020a). Our study found the greater FCs between the vPFC, mFC, and the precentral gyrus (SMN), indicating that communication between the frontal cortex and sensory-related regions was altered in CS patients. In addition, the two FCs were negatively correlated with the pain intensity of the leg, suggesting that the feeling of pain caused by CS is the main symptom and significantly reduces the patient's quality of life. However, DMN connectivities in the patients with cLBP and/or pain in a lower vs. the HC showed reductions of this network in the dorsolateral PFC, medial PFC, and ACC (Li et al., 2014). It may be due to its small sample size (20 patients and 10 HCs) and only focus on FCs within the DMN. Based on these results, we speculated that the persistent chronic pain and associated symptoms of CS were caused by abnormalities in frontal cortex.

The important functional connectivity's were mainly between sensory-motor network and ventral attention network regions

The SMN including the primary and secondary sensorimotor cortex, which receives and processes sensory information from the periphery, is thought to be the main brain network responsible for pain perception (Mayer et al., 2015). Abnormalities in the VAN were also widely seen in chronic pain patients with persistent diminished attention or inattention (Moriarty et al., 2011; Wen et al., 2012). The pathological changes of basal ganglia (Borsook et al., 2010; Starr et al., 2011) and neurological dysfunction of the anterior insular cortex (Ferraro et al., 2022) in the VAN have also been reported to be involved in pain processing leading to altered pain perception. Patients with failed back surgery syndrome with chronic low back pain have greater FC in the precentral gyrus and putamen (extending to the insula) in the SMN compared to HC (Kolesar et al., 2017). Consistent with previous studies, the FC between SMN and VAN was higher in CS patients, especially between the precentral gyrus and anterior insula, compared with HC. In addition, patients with CLBP had greater gray matter volume in the SMN regions and greater FC between the bilateral sensorimotor cortex and sensory association cortex during pain (Li et al., 2018). These studies may imply that enhanced cortical activity in the SMN and VAN regions also underlies the clinical pain status of CS patients. Furthermore, the precentral gyrus is a sensorimotor area that receives information projected from the basal ganglia, both of which play an important role in pain processing (Liu et al., 2012). Compared to HC, complex regional pain syndrome patients displayed greater resting connectivity from the caudate to the primary motor cortex (Lee et al., 2022). Our study found a greater FC between the basal ganglia and the precentral gyrus in CS patients, indicating that pain may increase the attention of CS patients to their pain sensation, and the FC was negatively correlated with the VAS score of leg pain, we speculate that engaging the conscious attention (Aminabadi et al., 2022) of CS patients can reduce pain perception.

Our study also showed the abnormal FCs within FPN and with the other networks, and previous studies have shown positively associated with pain rating changes (Kong et al., 2013). The frontoparietal region may play a dominant role in the formation and transmission of sensations (Lobanov et al., 2013), and RFPN is recognized as an important network that associates with perception and pain (Smith et al., 2009). Neural function activity in encephalic regions of FPN showed abnormal changes (Cui et al., 2022), and a significantly lower FC of RFPN was observed in MWoA patients (Li et al., 2015). In our study, we found increased FCs between FPN and SMN, and decreased FCs within FPN and with the other networks in CS patients, suggesting that FPN also plays an important role in the processing and regulation of CS pain.

Multimodal metrics successfully distinguish chronic sciatica patients from healthy control

In recent years, SVM techniques combined with neuroimaging metrics have been applied to differentiate pain patients from HCs and to predict the outcome of certain interventions (Bagarinao et al., 2014; Zeng et al., 2019; Huang et al., 2020; Tu et al., 2020b; Gui et al., 2021; Wei et al., 2022). The patients with neuropathic pain and the HC were classified by the mean ALFF values of the frontal gyrus and the precuneus using the linear SVM classifier, and the classification accuracy was 86.36% between the PHN patients and HC (Huang et al., 2020). A study identified a neural marker with abnormal FC within the SMN and FPN that could discriminate MwoA patients from HC with a 91.4% accuracy rate (Tu et al., 2020b). Patients with trigeminal neuralgia exhibited reductions in cortical indices in the cingulate cortex, and these abnormal whole brain-level morphological alterations successfully enable automated trigeminal neuralgia diagnosis with high specificity (trigeminal neuralgia: 95.35%; disease controls: 46.51%) (Mo et al., 2021). Interestingly, these studies reported that the classification performance of FCs between networks was higher than the ALFF values and cortical indices (structural features). Despite coming from various studies about different chronic and neuropathic pain diseases, these studies showed that ALFF values, inter-network FCs, and structural measurements (e.g., cortical indices) can be used as neurological features to distinguish chronic pain patients from healthy people, respectively.

However, chronic pain could affect multiple brain systems and cause extensive reorganization of brain structure and function, and the results of these studies were often derived from a few modalities, ignoring the combination of multiple modalities, which may affect the performance of the machine learning classifiers. In our study, SVM was applied to combined MRI imaging features (ALFF, cortical surface area, FCs), which distinguished CS patients from HC with higher accuracy of 90.00%. The finding implies that multimodal data analysis gives better results and exhibits the best model's performance (MCC = 0.800) than unimodal analysis. The multimodal analysis could combine the advantages of multiple imaging techniques to improve both spatial and temporal resolution and target disease neurobiomarkers with high specificity and sensitivity and provide many new opportunities to improve brain research. The identification of distinguishable or predictive neuroimaging biomarkers is needed as it can aid in diagnosis and prognosis, as well as be helpful in clinical decision-making. To date, one of the few factors that independently predict poor outcomes in sciatica is the duration of leg pain (Konstantinou et al., 2018), the application of multimodal neuroimaging biomarkers may help to assess the disease severity of patients and progression, especially during non-painful periods, assisting clinicians in early decision making, and tailor treatment plans for patients. For instance, they could be a useful diagnostic tool when patients are unable to communicate or self-reports are otherwise unreliable. Moreover, our findings may invite future studies with larger datasets to investigate the relationship between multimodal neuroimaging biomarkers and clinical measurements and develop therapeutic biomarkers to evaluate or predict the response of potential new treatments.

Study limitations

We acknowledge that our research has several limitations. First, the present study was based on 34 CS patients and 36 HCs, it is necessary to expand the sample size to confirm the results. Brain metrics and clinical variables correlation analysis were conducted with two-sided significance levels (alpha = 0.05) without corrections for multiple comparisons due to the small sample size and the exploratory nature of the study. Second, the study covered a range of ages from 35 to 65 years, restricting the generalization of the present results to other populations. Future studies with the younger or older age range are needed to increase external validity. Third, it might be a lack of a dataset of patients with other chronic pain disorders, we could not verify the specificity of the multimodal markers. Future studies with more datasets of pain-related disease will help clarify which specific chronic pain diseases (e.g., knee osteoarthritis, low back pain) are associated with functional impairment in different brain domains. Fourth, perhaps even more importantly, clinical measurements were evaluated at a single time point (1 day before MRI scanning) which does not necessarily reflect the long-term status of an individual, other time-dependent variables on multiple time points may provide more information on the chronic pain status. Fifth, the results of the brain's functional network are affected by different parcelation strategies. Other brain atlases are needed to further assess the reliability of the differentiation of CS individuals. Last, we acknowledged that we only recruited sciatica patients with diagnosed disk herniated disks, and it cannot distinguish if the results are due to pain, or due to the specific nature of the origins of the pain in the patient group, so our results should not be exaggerated.

Conclusion

Our findings provide new insights into the pathophysiologic mechanisms of CS and highlight the potential of multimodal features as markers in the research of neural mechanisms of chronic pain.

Data availability statement

The raw data supporting the conclusions of this article will be made available by the authors, without undue reservation.

Ethics statement

The studies involving human participants were reviewed and approved by Ethics Committee of Dongzhimen Hospital Affiliated to Beijing University of Chinese Medicine (No. 2020BZYLL0803). The patients/participants provided their written informed consent to participate in this study.

Author contributions

XYW: formal analysis, visualization, and writing – original draft and review and editing. XW: conceptualization, methodology, supervision, visualization, and writing – review and editing. GS: supervision, writing – review and editing, and investigation. LW and JT: supervision and funding acquisition. FY: data curation. CL, MR, and HZ: data curation and investigation. NL: supervision, data curation, and investigation. C-ZL: conceptualization, funding acquisition, and supervision. All authors contributed to the article and approved the submitted version.

Funding

This study was financially supported by the National Key R&D Program of China (No.2019YFC1712101).

Conflict of interest

The authors declare that the research was conducted in the absence of any commercial or financial relationships that could be construed as a potential conflict of interest.

Publisher's note

All claims expressed in this article are solely those of the authors and do not necessarily represent those of their affiliated organizations, or those of the publisher, the editors and the reviewers. Any product that may be evaluated in this article, or claim that may be made by its manufacturer, is not guaranteed or endorsed by the publisher.

References

Ali, L., He, Z., Cao, W., Rauf, H. T., Imrana, Y., and Bin Heyat, M. B. (2021). MMDD-ensemble: A multimodal data-driven ensemble approach for Parkinson's disease detection. *Front. Neurosci.* 15:754058. doi: 10.3389/fnins.2021.754058

Aminabadi, N. A., Golsanamlou, O., Halimi, Z., and Jamali, Z. (2022). Assessing the different levels of virtual reality that influence anxiety, behavior, and oral health status in preschool children: Randomized controlled clinical trial. *JMIR Perioper. Med.* 5:e35415. doi: 10.2196/35415

Atlas, S. J., Deyo, R. A., Patrick, D. L., Convery, K., Keller, R. B., and Singer, D. E. (1996). The quebec task force classification for spinal disorders and the severity, treatment, and outcomes of sciatica and lumbar spinal stenosis. *Spine* 21, 2885–2892. doi: 10.1097/00007632-199612150-00020

Bagarinao, E., Johnson, K. A., Martucci, K. T., Ichesco, E., Farmer, M. A., Labus, J., et al. (2014). Preliminary structural MRI based brain classification of chronic pelvic pain: A MAPP network study. *Pain* 155, 2502–2509. doi: 10.1016/j.pain.2014.09.002

Borsook, D., Upadhyay, J., Chudler, E. H., and Becerra, L. (2010). A key role of the basal ganglia in pain and analgesia–insights gained through human functional imaging. *Mol. Pain* 6:27. doi: 10.1186/1744-8069-6-27

Buckalew, N., Haut, M. W., Aizenstein, H., Morrow, L., Perera, S., Kuwabara, H., et al. (2010). Differences in brain structure and function in older adults with self-reported disabling and nondisabling chronic low back pain. *Pain Med.* 11, 1183–1197. doi: 10.1111/j.1526-4637.2010.00899.x

Chao, T. H., Chen, J. H., and Yen, C. T. (2018). Plasticity changes in forebrain activity and functional connectivity during neuropathic pain development in rats with sciatic spared nerve injury. *Mol. Brain* 11:55. doi: 10.1186/s13041-018-0398-z

Collins, S. L., Moore, R. A., and McQuay, H. J. (1997). The visual analogue pain intensity scale: What is moderate pain in millimetres? *Pain* 72, 95–97. doi: 10.1016/s0304-3959(97)00005-5

Cui, W. Q., Zhang, S. S., Xu, F., Brickell, A., Zhou, Q., Yang, B., et al. (2022). A resting-state functional magnetic resonance imaging study of abnormal frontoparietal network function in migraine without aura. *Med. Sci. Monit.* 28:e934975. doi: 10.12659/MSM.934975

De Pauw, R., Coppieters, I., Caeyenberghs, K., Kregel, J., Aerts, H., Lenoir, D., et al. (2019). Associations between brain morphology and motor performance in chronic neck pain: A whole-brain surface-based morphometry approach. *Hum. Brain Mapp.* 40, 4266–4278. doi: 10.1002/hbm.24700

Deyo, R. A., and Mirza, S. K. (2016). CLINICAL PRACTICE. Herniated lumbar intervertebral disk. *N. Engl. J. Med.* 374, 1763–1772. doi: 10.1056/NEJMcp1512658

Dosenbach, N. U., Nardos, B., Cohen, A. L., Fair, D. A., Power, J. D., Church, J. A., et al. (2010). Prediction of individual brain maturity using fMRI. *Science* 329, 1358–1361. doi: 10.1126/science.1194144

Fairbank, J. C., and Pynsent, P. B. (2000). The oswestry disability index. *Spine* 25, 2940–2952. doi: 10.1097/00007632-200011150-00017

Ferraro, S., Klugah-Brown, B., Tench, C. R., Yao, S., Nigri, A., Demichelis, G., et al. (2022). Dysregulated anterior insula reactivity as robust functional biomarker for chronic pain-Meta-analytic evidence from neuroimaging studies. *Hum. Brain Mapp.* 43, 998–1010. doi: 10.1002/hbm.25702

Finley, C. R., Chan, D. S., Garrison, S., Korownyk, C., Kolber, M. R., Campbell, S., et al. (2018). What are the most common conditions in primary care? Systematic review. *Can. Fam. Physician* 64, 832–840.

Fischl, B., and Dale, A. M. (2000). Measuring the thickness of the human cerebral cortex from magnetic resonance images. *Proc. Natl. Acad. Sci. U.S.A.* 97, 11050–11055. doi: 10.1073/pnas.200033797

Foster, N. E., and Reddington, M. (2021). Early referral to physical therapy: A reasonable choice for primary care patients with sciatica. *Ann. Intern. Med.* 174, 107–108. doi: 10.7326/M20-6545

Fung, G., Deng, Y., Zhao, Q., Li, Z., Qu, M., Li, K., et al. (2015). Distinguishing bipolar and major depressive disorders by brain structural morphometry: A pilot study. *BMC Psychiatry* 15:298. doi: 10.1186/s12888-015-0685-5

Gao, S. H., Shen, L. L., Wen, H. Z., Zhao, Y. D., Chen, P. H., and Ruan, H. Z. (2020). The projections from the anterior cingulate cortex to the nucleus accumbens and ventral tegmental area contribute to neuropathic pain-evoked aversion in rats. *Neurobiol. Dis.* 140:104862. doi: 10.1016/j.nbd.2020.104862

Glasser, M. F., Coalson, T. S., Robinson, E. C., Hacker, C. D., Harwell, J., Yacoub, E., et al. (2016). A multi-modal parcellation of human cerebral cortex. *Nature* 536, 171–178. doi: 10.1038/nature18933

Gracely, R. H., Geisser, M. E., Giesecke, T., Grant, M. A., Petzke, F., Williams, D. A., et al. (2004). Pain catastrophizing and neural responses to pain among persons with fibromyalgia. *Brain* 127(Pt 4), 835–843. doi: 10.1093/brain/awh098

Gui, S. G., Chen, R. B., Zhong, Y. L., and Huang, X. (2021). Machine learning analysis reveals abnormal static and dynamic low-frequency oscillations indicative of long-term menstrual pain in primary dysmenorrhea patients. *J. Pain Res.* 14, 3377–3386. doi: 10.2147/JPR.S332224

Hashmi, J. A., Baliki, M. N., Huang, L., Baria, A. T., Torbey, S., Hermann, K. M., et al. (2013). Shape shifting pain: Chronification of back pain shifts brain representation from nociceptive to emotional circuits. *Brain* 136(Pt 9), 2751–2768. doi: 10.1093/brain/awt211

He, B. J., Snyder, A. Z., Vincent, J. L., Epstein, A., Shulman, G. L., and Corbetta, M. (2007). Breakdown of functional connectivity in frontoparietal networks underlies behavioral deficits in spatial neglect. *Neuron* 53, 905–918. doi: 10.1016/j.neuron.2007.02.013

Hemington, K. S., Wu, Q., Kucyi, A., Inman, R. D., and Davis, K. D. (2016). Abnormal cross-network functional connectivity in chronic pain and its association with clinical symptoms. *Brain Struct. Funct.* 221, 4203–4219. doi: 10.1007/s00429-015-1161-1

Huang, J., Li, Y., Xie, H., Yang, S., Jiang, C., Sun, W., et al. (2020). Abnormal intrinsic brain activity and neuroimaging-based fMRI classification in patients with herpes zoster and postherpetic neuralgia. *Front. Neurol.* 11:532110. doi: 10.3389/fneur.2020.532110

Jensen, R. K., Kongsted, A., Kjaer, P., and Koes, B. (2019). Diagnosis and treatment of sciatica. *BMJ* 367:L6273. doi: 10.1136/bmj.l6273

Juarez-Salinas, D. L., Braz, J. M., Etlin, A., Gee, S., Sohal, V., and Basbaum, A. I. (2019). GABAergic cell transplants in the anterior cingulate cortex reduce neuropathic pain aversiveness. *Brain* 142, 2655–2669. doi: 10.1093/brain/awz203

Kim, J., Loggia, M. L., Edwards, R. R., Wasan, A. D., Gollub, R. L., and Napadow, V. (2013). Sustained deep-tissue pain alters functional brain connectivity. *Pain* 154, 1343–1351. doi: 10.1016/j.pain.2013.04.016

Kolesar, T. A., Bilevicius, E., and Kornelsen, J. (2017). Salience, central executive, and sensorimotor network functional connectivity alterations in failed back surgery syndrome. *Scand. J. Pain* 16, 10–14. doi: 10.1016/j.sjpain.2017.01.008

Kong, J., Jensen, K., Loiotile, R., Cheetham, A., Wey, H. Y., Tan, Y., et al. (2013). Functional connectivity of the frontoparietal network predicts cognitive modulation of pain. *Pain* 154, 459–467. doi: 10.1016/j.pain.2012.12.004

Konstantinou, K., and Dunn, K. M. (2008). Sciatica: Review of epidemiological studies and prevalence estimates. *Spine* 33, 2464–2472. doi: 10.1097/BRS.0b013e318183a4a2

Konstantinou, K., Dunn, K. M., Ogollah, R., Lewis, M., van der Windt, D., Hay, E. M., et al. (2018). Prognosis of sciatica and back-related leg pain in primary care: The ATLAS cohort. *Spine J.* 18, 1030–1040. doi: 10.1016/j.spinee.2017.10.071

Lam, C. L., Tse, E. Y., Gandek, B., and Fong, D. Y. (2005). The SF-36 summary scales were valid, reliable, and equivalent in a Chinese population. *J. Clin. Epidemiol.* 58, 815–822. doi: 10.1016/j.jclinepi.2004.12.008

Lee, B., Di Pietro, F., Henderson, L. A., and Austin, P. J. (2022). Altered basal ganglia infraslow oscillation and resting functional connectivity in complex regional pain syndrome. *J. Neurosci. Res.* 100, 1487–1505. doi: 10.1002/jnr.25057

Li, J., Dong, J. C., and Yue, J. J. (2012). [Effects of acupuncture on default mode network images of chronic sciatica patients in the resting network state]. *Zhongguo Zhong Xi Yi Jie He Za Zhi* 32, 1624–1627.

Li, J., Zhang, J. H., Yi, T., Tang, W. J., Wang, S. W., and Dong, J. C. (2014). Acupuncture treatment of chronic low back pain reverses an abnormal brain default mode network in correlation with clinical pain relief. *Acupunct. Med.* 32, 102–108. doi: 10.1136/acupmed-2013-010423

Li, K., Zhang, Y., Ning, Y., Zhang, H., Liu, H., Fu, C., et al. (2015). The effects of acupuncture treatment on the right frontoparietal network in migraine without aura patients. *J. Headache Pain* 16:518. doi: 10.1186/s10194-015-0518-4

Li, T., Zhang, S., and Kurata, J. (2018). Suppressed descending pain modulatory and enhanced sensorimotor networks in patients with chronic low back pain. *J. Anesth.* 32, 831–843. doi: 10.1007/s00540-018-2561-1

Liu, C. H., Yeh, T. C., Kung, Y. Y., Tseng, H. P., Yang, C. J., Hong, T. Y., et al. (2020). Changes in resting-state functional connectivity in nonacute sciatica with acupuncture modulation: A preliminary study. *Brain Behav.* 10:e01494. doi: 10.1002/brb3.1494

Liu, J., Zhao, L., Li, G., Xiong, S., Nan, J., Li, J., et al. (2012). Hierarchical alteration of brain structural and functional networks in female migraine sufferers. *PLoS One* 7:e51250. doi: 10.1371/journal.pone.0051250

Lobanov, O. V., Quevedo, A. S., Hadsel, M. S., Kraft, R. A., and Coghill, R. C. (2013). Frontoparietal mechanisms supporting attention to location and intensity of painful stimuli. *Pain* 154, 1758–1768. doi: 10.1016/j.pain.2013.05.030

Luchtmann, M., Steinecke, Y., Baecke, S., Lützkendorf, R., Bernarding, J., Kohl, J., et al. (2014). Structural brain alterations in patients with lumbar disc herniation: A preliminary study. *PLoS One* 9:e90816. doi: 10.1371/journal.pone.0090816

Mayer, E. A., Gupta, A., Kilpatrick, L. A., and Hong, J. Y. (2015). Imaging brain mechanisms in chronic visceral pain. *Pain* 156(Suppl. 1), S50–S63. doi: 10.1097/j.pain.0000000000000106

Mo, J., Zhang, J., Hu, W., Luo, F., and Zhang, K. (2021). Whole-brain morphological alterations associated with trigeminal neuralgia. *J. Headache Pain* 22:95. doi: 10.1186/s10194-021-01308-5

Moriarty, O., McGuire, B. E., and Finn, D. P. (2011). The effect of pain on cognitive function: A review of clinical and preclinical research. *Prog. Neurobiol.* 93, 385–404. doi: 10.1016/j.pneurobio.2011.01.002

Niddam, D. M., Lee, S. H., Su, Y. T., and Chan, R. C. (2019). Altered cortical morphology in patients with chronic shoulder pain. *Neurosci. Lett.* 712:134515. doi: 10.1016/j.neulet.2019.134515

Petrides, M. (2005). Lateral prefrontal cortex: Architectonic and functional organization. *Philos. Trans. R. Soc. Lond. B Biol. Sci.* 360, 781–795. doi: 10.1098/rstb.2005.1631

Porchet, F., Wietlisbach, V., Burnand, B., Daeppen, K., Villemure, J. G., and Vader, J. P. (2002). Relationship between severity of lumbar disc disease and disability scores in sciatica patients. *Neurosurgery* 50, 1253–1260. doi: 10.1097/00006123-200206000-00014

Seminowicz, D. A., Wideman, T. H., Naso, L., Hatami-Khoroushahi, Z., Fallatah, S., Ware, M. A., et al. (2011). Effective treatment of chronic low back pain in humans reverses abnormal brain anatomy and function. *J. Neurosci.* 31, 7540–7550. doi: 10.1523/JNEUROSCI.5280-10.2011

Smallwood, R. F., Laird, A. R., Ramage, A. E., Parkinson, A. L., Lewis, J., Clauw, D. J., et al. (2013). Structural brain anomalies and chronic pain: A quantitative meta-analysis of gray matter volume. *J. Pain* 14, 663–675. doi: 10.1016/j.jpain.2013.03.001

Smith, S. M., Fox, P. T., Miller, K. L., Glahn, D. C., Fox, P. M., Mackay, C. E., et al. (2009). Correspondence of the brain's functional architecture during activation and rest. *Proc. Natl. Acad. Sci. U.S.A.* 106, 13040–13045. doi: 10.1073/pnas.0905267106

Starr, C. J., Sawaki, L., Wittenberg, G. F., Burdette, J. H., Oshiro, Y., Quevedo, A. S., et al. (2011). The contribution of the putamen to sensory aspects of pain: Insights from structural connectivity and brain lesions. *Brain* 134(Pt 7), 1987–2004. doi: 10.1093/brain/awr117

Tu, Y., Jung, M., Gollub, R. L., Napadow, V., Gerber, J., Ortiz, A., et al. (2020a). Abnormal medial prefrontal cortex functional connectivity and its association with clinical symptoms in chronic low back pain. *Pain* 161, 230–231. doi: 10.1097/j.pain.0000000000001507

Tu, Y., Zeng, F., Lan, L., Li, Z., Maleki, N., Liu, B., et al. (2020b). An fMRI-based neural marker for migraine without aura. *Neurology* 94, e741–e751. doi: 10.1212/WNL.0000000000008962

Van Dijk, K. R., Sabuncu, M. R., and Buckner, R. L. (2012). The influence of head motion on intrinsic functional connectivity MRI. *Neuroimage* 59, 431–438. doi: 10.1016/j.neuroimage.2011.07.044

Wei, H. L., Xu, C. H., Wang, J. J., Feng, Q. Q., Xu, X. L., and Li, K. Y. (2022). Disrupted functional connectivity of the amygdala predicts the efficacy of non-steroidal anti-inflammatory drugs in migraineurs

without aura. *Front. Mol. Neurosci.* 15:819507. doi: 10.3389/fnmol.2022.819507

Wen, X., Yao, L., Liu, Y., and Ding, M. (2012). Causal interactions in attention networks predict behavioral performance. *J. Neurosci.* 32, 1284–1292. doi: 10.1523/JNEUROSCI.2817-11.2012

Yan, C. G., Wang, X. D., Zuo, X. N., and Zang, Y. F. (2016). DPABI: Data processing & analysis for (resting-state) brain imaging. *Neuroinformatics* 14, 339–351. doi: 10.1007/s12021-016-9299-4

Yang, H., Chen, X., Chen, Z. B., Li, L., Li, X. Y., Castellanos, F. X., et al. (2021). Disrupted intrinsic functional brain topology in patients with major depressive disorder. *Mol. Psychiatry* 26, 7363–7371. doi: 10.1038/s41380-021-01247-2

Yeo, B. T., Krienen, F. M., Sepulcre, J., Sabuncu, M. R., Lashkari, D., Hollinshead, M., et al. (2011). The organization of the human cerebral cortex estimated by intrinsic functional connectivity. *J. Neurophysiol.* 106, 1125–1165. doi: 10.1152/jn.00338.2011

Zeng, P., Huang, J., Wu, S., Qian, C., Chen, F., Sun, W., et al. (2019). Characterizing the structural pattern predicting medication response in herpes zoster patients using multivoxel pattern analysis. *Front. Neurosci.* 13:534. doi: 10.3389/fnins.2019.00534

frontiers | Frontiers in Neuroscience

TYPE Original Research
PUBLISHED 30 January 2023
DOI 10.3389/fnins.2022.1090224

OPEN ACCESS

EDITED BY
Ardalan Aarabi,
University of Picardie Jules Verne, France

REVIEWED BY
Minchul Kim,
Hallym University Kangnam Sacred Heart Hospital, Republic of Korea
Shile Qi,
Nanjing University of Aeronautics and Astronautics, China

*CORRESPONDENCE
Lin Tian
✉ tianz@njmu.edu.cn

†These authors have contributed equally to this work

SPECIALTY SECTION
This article was submitted to Brain Imaging Methods, a section of the journal Frontiers in Neuroscience

RECEIVED 05 November 2022
ACCEPTED 29 December 2022
PUBLISHED 30 January 2023

CITATION
Qin J, Wang S, Ni H, Wu Y, Chen L, Guo S, Zhang F, Zhou Z and Tian L (2023) Graph analysis of diffusion tensor imaging-based connectome in young men with internet gaming disorder.
Front. Neurosci. 16:1090224.
doi: 10.3389/fnins.2022.1090224

Graph analysis of diffusion tensor imaging-based connectome in young men with internet gaming disorder

Jiaolong Qin[1,2†], Shuai Wang[3,4†], Huangjing Ni[5], Ye Wu[1,2], Limin Chen[3], Shuaiyi Guo[4], Fuquan Zhang[6], Zhenhe Zhou[3,4] and Lin Tian[3,4*]

[1]PCA Lab, Key Lab of Intelligent Perception and Systems for High-Dimensional Information of Ministry of Education, School of Computer Science and Engineering, Nanjing University of Science and Technology, Nanjing, China, [2]Jiangsu Key Lab of Image and Video Understanding for Social Security, School of Computer Science and Engineering, Nanjing University of Science and Technology, Nanjing, China, [3]The Affiliated Mental Health Center of Jiangnan University, Wuxi Central Rehabilitation Hospital, Wuxi, China, [4]School of Wuxi Medicine, Nanjing Medical University, Wuxi, China, [5]School of Geographic and Biologic Information, Nanjing University of Posts and Telecommunications, Nanjing, China, [6]The Affiliated Brain Hospital of Nanjing Medical University, Nanjing, China

Although recent evidence suggests that dysfunctional brain organization is associated with internet gaming disorder (IGD), the neuroanatomical alterations related to IGD remain unclear. In this diffusion tensor imaging (DTI) study, we aimed to examine alterations in white matter (WM) structural connectomes and their association with IGD characteristics in 47 young men with IGD and in 34 well-matched healthy controls. Two approaches [namely, network-based statistics (NBS) and graph theoretical measures] were applied to assess differences in the specific topological features of the networks and to identify the potential changes in the topological properties, respectively. Furthermore, we explored the association between the alterations and the severity of internet addiction. An NBS analysis revealed widespread alterations of the cortico-limbic-striatal structural connectivity networks in young people with IGD: (1) an increased subnet1 comprising the insula and the regions responsible for visual, auditory, and sensorimotor functions and (2) two decreased subnet2 and subnet3 comprising the insula, striatum, and limbic regions. Additional correlation analysis showed a significant positive association between the mean fractional anisotropy- (FA-) weighted connectivity strength of subnet1 and internet addiction test (IAT) scores in the IGD group. The present study extends our knowledge of the neuroanatomical correlates in IGD and highlights the role of the cortico-limbic-striatal network in understanding the neurobiological mechanisms underlying this disorder.

KEYWORDS

internet gaming disorder, cortico-limbic-striatal network, structural connectivity, DTI, connectome

Introduction

In China, internet-based behavioral impairments have been considered a serious social problem, and the so-called treatment programs have been the subject of debate for the last decade (Bax, 2015). In 2013, the American Psychiatric Association introduced Internet gaming disorder (IGD) in the third part of the Diagnostic and Statistical Manual of Mental Disorders, Fifth Edition (DSM-5) as a candidate diagnosis with requirements for further study (American Psychiatric Association [APA], 2013). Consequently, with the collection of more research evidence (Yao et al., 2017), "gaming disorder" was classified by the World Health Organization (WHO) as a new condition and was officially included in the 11th edition of the International Classification of Diseases (ICD-11) as an addictive behavior disorder (Gaebel et al., 2020). ICD-11 characterized this disorder as a persistent or recurring pattern of online or offline gaming behavior. However, considering that online gaming users in China have grown to approximately 540 million, or 57.4% of total internet users, in the first half of 2020,[1] enormous attention has been paid to the phenomenon of clinical impairments or distress caused by maladaptive internet gaming (Yao et al., 2021).

The so-called IGD means excessive or poorly controlled preoccupations, urges, or behaviors regarding internet game playing that result in personal, familial, social, or occupational impairment for more than 12 months (American Psychiatric Association [APA], 2013). Moreover, IGD is often accompanied by depression and anxiety. Related research showed similarities in the neuropsychological processes between IGD and addictive substances (Grant et al., 2010). However, the pathological mechanisms underlying IGD remained elusive. Neuroimaging approaches were used to examine the underlying neurobiological mechanisms of IGD, and previous studies reported that IGD was associated with system-level alterations between the brain regions rather than functional impairment of isolated regions (Song et al., 2020). With the advent of connectomics, it is currently feasible to shift the view from an isolated regional perspective toward a system-level perspective (i.e., a network perspective) based on the integration of various forms of anatomical/functional data to assess the connectivity of networks in brain diseases including IGD (Bullmore and Sporns, 2009; Weinstein et al., 2017). A wide range of measures can be computed to assess the topological properties of the underlying brain networks (Rubinov and Sporns, 2010). To date, most studies addressing network alterations in IGD focused on functional networks derived from resting-state functional magnetic resonance imaging (rs-fMRI) (Lee et al., 2020; Song et al., 2020; Weinstein and Lejoyeux, 2020; Yan et al., 2021). These accumulated rs-fMRI studies on IGD demonstrated impaired interactions of functional brain networks involving the cortical-limbic-striatal circuitry that underlies reward processing, executive function, cognitive control, motor and sensory functions, and attention. Meanwhile, these studies provided novel evidence of aberrant core networks involving the central executive network, salience network, and default mode network (DMN) in this disorder (Weinstein et al., 2017; Chun et al., 2020; Weinstein and Lejoyeux, 2020).

An important question is whether the functional alterations observed across studies have a structural correlation. A study that focused on the covariance gray matter (GM) structural networks found higher GM volumes in DMN-related regions, which were associated with visuospatial attention and reward craving processing with increased severity of addiction to IGD (Chen et al., 2021). Using diffusion tensor imaging (DTI) data, previous studies reported increased fractional anisotropy (FA) values in the fasciculus linking reward circuitry, sensory, and motor control systems, which were related to the severity of internet addiction (Dong et al., 2012, 2018). Three studies established a white matter (WM) structural network to analyze its network metrics (namely, network controllability, and small-world topology) and reported that people with IGD had greater modular brain controllability and the shortest path length, as well as structural networks that shifted in the direction of random topology (Zhai et al., 2017; Park et al., 2018; Lei et al., 2020). However, very few studies examined alterations in the structural network in IGD using the connectomics method. To the best of our knowledge, no study has focused on WM structural network alterations in IGD using a network-based statistics (NBS) approach. In addition, this method can detect disrupted subnet patterns in whole brain networks.

The present study aime to identify differences in the WM structural connectome. To achieve our purpose, we included a fairly large sample of 47 young men with IGD and 34 well-matched male head circumferences (HCs) and applied the two approaches (namely, NBS and graph theoretical measures) to assess differences in the specific topological features of the networks and to identify potential changes in their topological properties. We hypothesized that the alterations in young people with IGD were mainly involved in the cortico-limbic-striatal network, which would likely be related to the severity of internet addiction.

Materials and methods

Participants

Given the higher prevalence of internet addiction in men vs. women in China (Li et al., 2013; Lau et al., 2017), only young men from local universities and the surrounding community were recruited *via* advertisements and word of mouth. Participants were preselected through an online questionnaire and telephone screening. In total, 47 young men who reported internet gaming as their primary online activity and met at least five of the nine DSM-5 criteria for IGD (American Psychiatric Association [APA], 2013) were screened. Subjects' internet addictive behavior was assessed with the Chinese version of Internet Addiction Test (IAT) (Young, 1998). All young people with IGD were satisfied when their IAT score was more than the proposed cutoff score (i.e., $\geq$ 50) (Dong et al., 2015, 2018). Participants who met less than three of the nine criteria for IGD proposed by DSM-5 were preselected as having HC. Of these, 34 young people were determined to be HCs based on their IAT scores of less than 30. Additionally, participants' current levels of depression and anxiety were assessed using the 24-item Hamilton Depression Scale (HAMD) and the 14-item Hamilton Anxiety Scale (HAMA) (Hamilton, 1959, 1967). All participants were right-handed as assessed with the Edinburgh Handedness Inventory (Oldfield, 1971). A brief, structured clinical interview tool, the Mini International Neuropsychiatric Interview, was used to screen for other psychiatric disorders. The exclusion criteria for selecting subjects were as follows: intracranial pathology, brain injury, neurological disorders, psychiatric disorders (except IGD), substance abuse, contraindications to MRI examinations, and excessive head

1 http://www.cnnic.net.cn/

TABLE 1 Demographic characteristics and clinical information of young people with internet gaming disorder (IGD) and healthy controls (HC).

Items	IGD (N = 47)	HC (N = 34)	P-value
Age (years)	20.60 ± 0.97	20.85 ± 1.79	0.41
14-HAMA	7.60 ± 5.10	3.81 ± 4.76▲	0.01*
24-HAMD	8.98 ± 6.40	4.50 ± 6.51▼	0.02*
Average gaming hours per week	23.26 ± 3.61	7.09 ± 3.33	< 0.01*
IAT score	69.15 ± 8.11	21.62 ± 3.90	< 0.01*
DMS-5 score	5.98 ± 1.01	1.76 ± 0.74	< 0.01*

*Statistically significant.
▲Only 21 subjects measured HAMA.
▼Only 21 subjects measured HAMD.
Values are expressed as mean ± standard deviation.
IAT, internet addiction test; HAMA, Hamilton Anxiety Scale; HAMD, Hamilton Depression Scale; IGD, internet gaming disorder; HCs, healthy controls.

motion. The demographic characteristics of young people with IGD and HC are summarized in **Table 1**.

This study was approved by the Medical Ethics Committee of the Wuxi Mental Health Center, Nanjing Medical University, China. All subjects gave written informed consent before participating in the study.

Imaging acquisitions and pre-processing

Magnetic resonance imaging scans were acquired with a 3.0-T Magnetom Trio Tim (Siemens Medical System, Erlangen, Germany) at the Department of Medical Imaging, The Affiliated Wuxi People's Hospital of Nanjing Medical University. All participants obtained DTI data and high-resolution three-dimensional T1-weighted images. Foam pads were used to reduce head motion and noise from the scanner. T1-weighted images were acquired using a 3D-MPRAGE sequence with the following parameters: repetition time/echo time (TR/TE) = 2,300/2.98 ms, 160 sagittal slices, thickness = 1.2 mm, flip angle = 9°, matrix = 256 × 256, field of view (FOV) = 256 mm × 256 mm, and acquisition voxel size = 1 mm × 1 mm × 1.2 mm. DTI images were obtained with the following parameters: diffusion was measured along 64 non-collinear directions (b-value = 1,000 s/mm^2), and one additional image without diffusion weighting (i.e., b = 0 s/mm^2), TR/TE = 7,000 ms/92 ms, flip angle = 90°, FOV = 256 mm × 256 mm, matrix = 128 × 128, slice thickness/gap = 3/0 mm, and acquisition voxel size = 2 mm × 2 mm × 3 mm.

Image preprocessing was performed using the diffusion toolbox of the functional magnetic resonance imaging of the brain (FMRIB) software library (FSL).[2] Visual and quantitative quality control of the DTI data was performed using a quality control tool in the FSL software.[3] Moreover, from the analyses, individuals with diffusion images with apparent signal drops were checked, and images without this type of diffusion were found. Finally, images from all gradient directions were retained based on visual inspection of several patient data sets with an in-house tool, indicating that gradients should not be removed. Thus, all gradient directions were retained for the analysis. Pre-processing steps included eddy current and motion artifact correction, diffusion tensor estimation, and tractography. Corrections for eddy current distortions and head motion were performed by applying a rigid body transformation of each diffusion-weighted image to the b0 image. The b-matrix of each sample was then reoriented to provide a more accurate estimate of the tensor orientations. The diffusion tensor matrix was calculated according to the Stejskal and Tanner equation. Three eigenvalues and eigenvectors were obtained by diagonalizing the tensor matrix and then FA maps were computed. Each b0 image was registered in the Montreal Neurological Institute (MNI) space *via* the corresponding T1 image using Diffusionkit[4] (Xie et al., 2016). The image registration of Diffusionkit is implemented by NiftyReg, which is open-source software for efficient registration of medical images and developed primarily by the Centre for Medical Image Computing at University College London. This transformation information was saved for later use. The diffusion images remained in native space.

Three-dimensional tract reconstruction was implemented using a diffusion toolkit.[5] Whole brain tractography was obtained using the Fiber Assignment by Continuous Tracking algorithm (Mori et al., 1999), and propagation was terminated if a minimum angle threshold of 50° was violated or a voxel with FA below 0.2 was encountered.

Construction of a structural network

Figure 1 depicts the construction pipeline of a structural brain network. Specifically, the automated anatomical labeling (AAL) atlas[6] (Tzourio-Mazoyer et al., 2002) with 90 regions (**Supplementary Table 1**) was employed as a node. Using the inverse of the transform information, the AAL atlas in the MNI space was registered into each subject's native space. Edges were defined as interregional fibers between each pair of nodes and met the conditions: (1) at least two double-ended fibers passed through pairwise nodes and (2) the length of the passing fibers was greater than 10 mm. Here, the FA value was treated as the weight of a network connection. Specifically, the FA weight of each edge was calculated by averaging the FA values of all the fibers that made up this edge, and the FA value of each fiber was the mean of the FA values of all the voxels in this fiber track. A group threshold was applied to balance the influence of false-positive and false-negative reconstructions of fibers (de Reus and van den Heuvel, 2013). Edges that were present in at least 60% of all subjects were retained while others were zeroed. All subsequent analyses were conducted on this group threshold network.

NBS analysis

Zalesky et al. (2010) proposed NBS, a non-parametric method, to eliminate the multiple-comparison problems encountered when conducting mass univariate significance tests. Statistical significance was detected to find the subnetwork, which consisted of specific subsets of nodes connected in the topological space. It is important to emphasize that no individual disconnection can be declared significant alone; only the disconnected subnetwork as a whole can be declared significant. We first used NBS to conduct an

2 http://fsl.fmrib.ox.ac.uk/fsl/fslwiki/

3 https://fsl.fmrib.ox.ac.uk/fsl/fslwiki/eddyqc/UsersGuide

4 https://www.nitrc.org/projects/diffusionkit

5 http://www.trackvis.org

6 http://www.gin.cnrs.fr/en/tools/aal-aal2/

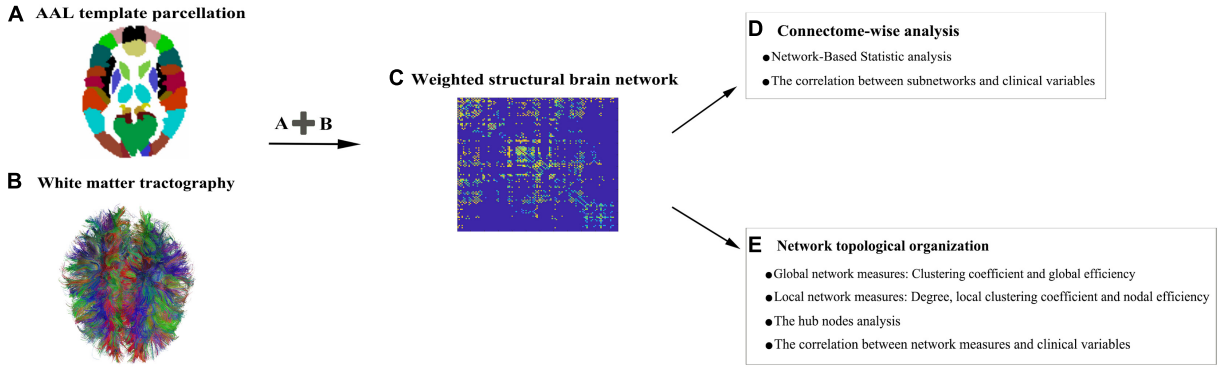

FIGURE 1
A flowchart for the construction of structural brain networks. **(A)** The 90 nodes of the brain network obtained from the automated anatomical labeling (AAL) atlas. **(B)** White matter (WM) fiber information prepared to check which pairs of nodes remain connected. **(C)** Region-based information extracted from the abovementioned image data. All pairwise connections between the nodes are calculated to generate a connection matrix. **(D,E)** A list of network analysis entries that are applied.

independent *t*-test analysis with age as a covariate. The general calculation procedures were as follows: (1) a primary threshold (*t*-value = 2.9, which was equal to setting $p < 0.005$ for the two-tailed test) was applied to a *t*-test, which was calculated for each edge to construct a set of suprathreshold connections. This identified all possible components (or subnetworks) mutually connected in a WM network at the primary threshold level. (2) The size of the actual remaining subnetwork *s* was determined. To estimate the significance of each subnetwork, the null distribution of the subnetwork size was empirically derived using a non-parametric permutation approach (5,000 permutations). For each permutation, all of the samples were shuffled randomly among the groups, and the *t*-test statistic was calculated independently for each edge. Afterward, the same threshold was applied to retain edges above this threshold, and the maximal subnetwork size was restored. (3) The corrected *p*-value was determined by calculating the proportion of the 5,000 permutations for which the maximum shuffled subnetwork was greater than *s*. A *p*-value of < 0.05 (corrected) was considered significant.

Network measure analysis

For global network characteristics, we used the clustering coefficient and global efficiency. For local network measures, we computed three popular network metrics, namely, nodal degree, local clustering coefficient, and nodal efficiency. Additionally, betweenness centrality was used to define a hub node. Their formal mathematical definitions and meanings have been described in detail elsewhere (Rubinov and Sporns, 2010), and we also presented these descriptions in the **Supplementary material**. These measures were calculated on the WM network of each subject using the Brain Connectivity Toolbox.[7] Before making between-group comparisons, the interaction between age and network metrics was regressed. Between-group significances of network metrics were determined using an independent two-sample *t*-test (two-tailed) with the Bonferroni's correction ($p < 0.05/90$).

7 http://www.nitrc.org/projects/bct/

Pearson's correlation analysis

Pearson's correlation analysis was used to examine the relationship between network measures and clinical variables (namely, IAT, average gaming hours per week, and DSM-5 score). In addition, we also investigated the association between the mean FA-weighted structural connectivity strength of each subnetwork and the clinical variables.

Results

Differences in structural connectivity patterns

Network-based statistical analysis identified three disconnected structural subnetworks in the IGD group (**Table 2** and **Figure 2**). Compared with HCs, young people with IGD showed a significant increase in connectivity strength in subnet1 with 16 edges and involving the bilateral orbitofrontal regions and visual regions (namely, the bilateral cuneus and fusiform gyrus, and the right superior occipital gyrus), auditory regions (i.e., the right temporal pole), and sensorimotor regions (namely, the bilateral post-central gyrus and the right inferior temporal gyrus) (corrected $p < 0.0012$). Furthermore, in young people with IGD, network disconnections comprising two subnetworks had significantly fewer connections. Subnet2 comprised 18 edges and was mainly within and between the limbic (namely, the bilateral amygdala, and the median cingulate) and the striatum (namely, the bilateral caudate, the putamen, and the left pallidum), the bilateral insula, and several areas responsible for visual/auditory and sensorimotor functions (namely, the bilateral precentral gyrus, the left post-central gyrus, the right superior parietal gyrus, the right paracentral lobule, and the right inferior temporal gyrus) (corrected $p < 0.0006$). Subnet3 included five edges, was centered with the right parahippocampal gyrus and the pallidum, and connected the regions of the right hemisphere including the post-central gyrus, the angular gyrus, the lingual gyrus, and the middle temporal gyrus (corrected $p < 0.018$).

TABLE 2 Subnetwork with a significant between-group difference based on the network-based statistics (NBS) analysis.

Network edges	*T*- value (*P*-value)	Network edges	*T*-value (*P*-value)
IGD increase, subnet1		IGD decrease, subnet2 (continue)	
Cuneus_L – Occipital_Sup_R	3.04 ($p < 0.005$)	Cingulum_Mid_R – Postcentral_R	3.00 ($p < 0.005$)
Cuneus_L – Fusiform_L	2.94 ($p < 0.005$)	Cingulum_Mid_R – Parietal_Sup_R	2.97 ($p < 0.005$)
Occipital_Sup_R – Fusiform_R	3.35 ($p < 0.005$)	Parietal_Sup_R – Paracentral_Lobule_R	3.11 ($p < 0.005$)
Frontal_Sup_Orb_L – Postcentral_L	3.51 ($p < 0.005$)	Cingulum_Mid_L – Caudate_L	3.33 ($p < 0.005$)
Fusiform_L – Postcentral_L	3.37 ($p < 0.005$)	Amygdala_L – Caudate_L	3.02 ($p < 0.005$)
Frontal_Inf_Orb_R – Postcentral_R	3.43 ($p < 0.005$)	Insula_R – Caudate_R	2.94 ($p < 0.005$)
Fusiform_R – Putamen_R	2.98 ($p < 0.005$)	Cingulum_Mid_R – Caudate_R	3.34 ($p < 0.005$)
Postcentral_L – Thalamus_L	3.54 ($p < 0.005$)	Cingulum_Ant_L – Putamen_L	2.99 ($p < 0.005$)
Postcentral_R –Temporal_Sup_R	3.13 ($p < 0.005$)	Cingulum_Ant_R – Putamen_R	3.00 ($p < 0.005$)
Putamen_R – TPOsup.R	3.03 ($p < 0.005$)	Caudate_L – Putamen_R	2.99 ($p < 0.005$)
Rolandic_Oper_R – Temporal_Inf_R	3.30 ($p < 0.005$)	Cingulum_Ant_L – Pallidum_L	2.99 ($p < 0.005$)
Insula_R – Temporal_Inf_R	3.62 ($p < 0.005$)	Caudate_L – Pallidum_L	3.12 ($p < 0.005$)
Cuneus_R – Temporal_Inf_R	3.19 ($p < 0.005$)	Caudate_R – Pallidum_L	3.51 ($p < 0.005$)
Occipital_Sup_R – Temporal_Inf_R	3.37 ($p < 0.005$)	Caudate_R – Temporal_Inf_R	4.55 ($p < 0.005$)
Postcentral_R – Temporal_Inf_R	3.38 ($p < 0.005$)	IGD decrease, subnet3	
Temporal_Pole_Sup_R – Temporal_Inf_R	2.91 ($p < 0.005$)	ParaHippocampal_R – Postcentral_L	2.98 ($p < 0.005$)
IGD decrease, subnet2		ParaHippocampal_R – Angular_R	2.92 ($p < 0.005$)
Precentral_R – Cingulum_Mid_R	3.61 ($p < 0.005$)	Lingual_R – Pallidum_R	3.05 ($p < 0.005$)
Insula_L – Amygdala_L	3.62 ($p < 0.005$)	Postcentral_L – Pallidum_R	3.37 ($p < 0.005$)
Insula_R – Amygdala_R	3.35 ($p < 0.005$)	ParaHippocampal_R – Temporal_Mid_R	3.17 ($p < 0.005$)
Precentral_L – Postcentral_R	3.24 ($p < 0.005$)		

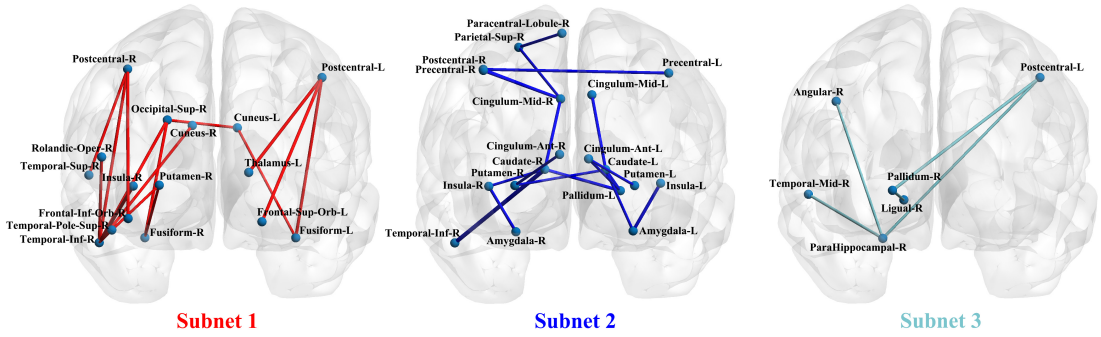

FIGURE 2
The three subnetwork results from the network-based statistics (NBS) analysis in a coronal view.

Network measures

Significant group effects on network clustering (t-value = 2.79, p = 0.0007) and global efficiency (t-value = 3.70, p = 0.0004) were observed in the analyses between young people with IGD and HC. The bilateral orbital frontal parts include two regions both left and right orbital frontal regions. Analogously, the bilateral supplementary motor areas are as the same, the left dorsolateral frontal part, and the right medial frontal part), one temporal region (the right superior temporal gyrus), one parietal region (the right paracentral lobule), three cingulum regions (namely, the bilateral median, and the right anterior cingulate), the right insula and subcortical nuclei (namely, the right parahippocampal gyrus, and the left putamen) (Tables 3–5). Specifically, compared with HC, young people with IGD displayed a significantly higher nodal efficiency and nodal degree in the right orbital part of the inferior frontal gyrus and left supplementary motor area. Moreover, young people with IGD also showed a significant increase in the local clustering coefficient in the right insula and a higher nodal degree in the right superior temporal gyrus.

The hub detection result revealed the similarities in the hub distribution of young people with IGD and HC (Figure 3). In hub distribution, 8 nodes (namely, the bilateral precuneus, the bilateral amygdala, the bilateral pallidum, and the bilateral Heschl gyrus) were working as hubs with 100% probability in both groups.

TABLE 3 Differences in local clustering coefficient between young people with IGD and HC.

Metric	Region	IGD (mean ± std)	NC (mean ± std)	*T*-value (*P*-value)
C_i	Insula_R	0.012 ± 0.020	−0.017 ± 0.045	3.92 (1.89e-04)
C_i	Cingulum_Ant_R	0.040 ± 0.080	−0.056 ± 0.134	4.03 (1.29 e-04)
C_i	Paracentral_Lobule_R	0.025 ± 0.044	−0.034 ± 0.088	3.94 (1.73 e-04)

C_i, local clustering coefficiency.

TABLE 4 Differences in the nodal degree between young people with IGD and HC.

Metric	Region	IGD (mean ± std)	NC (mean ± std)	*T*-value (*P*-value)
D_i	Frontal_Inf_Orb_L	0.609 ± 1.067	−0.843 ± 2.457	3.61 (5.30e-04)
D_i	Frontal_Inf_Orb_R	0.633 ± 1.187	−0.875 ± 2.351	3.79 (2.97e-04)
D_i	Supp_Motor_Area_L	0.377 ± 0.731	−0.521 ± 1.223	4.12 (9.24e-05)
D_i	Cingulum_Mid_L	0.507 ± 1.153	−0.701 ± 1.769	3.72 (3.74e-04)
D_i	Cingulum_Mid_R	0.394 ± 0.886	−0.544 ± 1.295	3.87 (2.20e-04)
D_i	Temporal_Sup_R	0.301 ± 0.621	−0.416 ± 0.990	4.00 (1.40e-04)

D_i, nodal degree.

TABLE 5 Differences in nodal efficiency between young people with IGD and HC.

Metric	Region	IGD (mean ± std)	NC (mean ± std)	*T*-value (*P*-value)
E_i	Frontal_Sup_L	0.022 ± 0.047	−0.031 ± 0.075	3.88 (2.12e-04)
E_i	Frontal_Inf_Orb_R	0.031 ± 0.054	−0.043 ± 0.124	3.68 (4.24e-04)
E_i	Supp_Motor_Area_L	0.020 ± 0.047	−0.028 ± 0.063	4.00 (1.41e-04)
E_i	Supp_Motor_Area_R	0.023 ± 0.056	−0.031 ± 0.072	3.78 (3.01e-04)
E_i	Frontal_Sup_Medial_R	0.018 ± 0.041	−0.024 ± 0.061	3.72 (3.74e-04)
E_i	Cingulum_Mid_L	0.028 ± 0.052	−0.039 ± 0.109	3.71 (3.90e-04)
E_i	ParaHippocampal_R	0.026 ± 0.049	−0.037 ± 0.094	3.90 (2.01e-04)
E_i	Paracentral_Lobule_L	0.032 ± 0.051	−0.045 ± 0.108	4.28 (5.22e-05)
E_i	Putamen_L	0.018 ± 0.041	−0.025 ± 0.068	3.61 (5.32e-04)

E_i, nodal efficiency.

The correlation results

We also compared the mean FA values of the edges of each subnetwork between the IGD and HC groups, and their comparison results showed the existence of significant between-group differences (**Figure 4A**). Because most of the patients with non-existing edges were in the decreasing subnet2 and subnet3, we only did the correlation analysis in the increasing subnet1. The mean FA-weighted connectivity strength of subnet1 was positively related to IAT scores ($r = 0.39$, $p = 0.031$) (**Figure 4B**). In addition, a positive correlation was found between the DSM-5 scores and the degree of the right superior temporal gyrus ($r = 0.37$, $p = 0.033$).

Discussion

Our findings indicated the following: (1) There were three abnormal subnets between young people with IGD and HC. Subnet1 showed an increase in the mean FA-weighted connectivity strength among the orbitofrontal area, the insula, and the visual, auditory, and sensorimotor regions, while the other two subnets (namely, subnet2, and subnet3) presented a decrease in the mean FA-weighted structural connectivity strength within and between the limbus, the striatum, and the insula. (2) Relative to HCs, young people with IGD showed an increase in network clustering and global efficiency. In addition, young people with IGD displayed significantly higher local clustering coefficient, nodal degree, and nodal efficiency in the orbital, dorsolateral, and medial frontal areas; the right parahippocampal gyrus; the left putamen; the right insula; the right superior temporal gyrus; the right paracentral lobule; and the cingulum. (3) The correlation results indicated an enhancement in the mean FA-weighted structural connectivity strength of subnet1 was positively related to the severity of IAT. Moreover, the right superior temporal gyrus, one of the nodes in subnet1, showed that its highest degree value was positively correlated with DSM-5 scores. **Figure 5** summarizes all these abovementioned results. Our results suggest that abnormal connections occur in the cortico-striatal-limbic circuitry that may be the result of excessive internet gaming.

Disorder-related distinctions of subnetworks in WM networks

As the NBS results showed an increase in the mean FA-weighted structural connectivity strength of subnet1, which included three brain regions (namely, the right orbital part of the inferior frontal gyrus, the right putamen, and the right insula) responsible for reward activity through the sensorimotor (namely, the right post-central gyrus, and the right inferior temporal gyrus) and visual (namely, the right superior occipital gyrus, and the right fusiform gyrus) areas to link together. The insula plays an important role in maintaining homeostasis through the integration of internal and external stimuli to guide behavior toward or away from the same stimuli (Gogolla, 2017). Specifically, the insula is associated with an increased tendency to engage in disgusting behaviors and an impaired ability to recognize disgust in others (Woolley et al., 2015). Accumulated evidence demonstrated the role of the insula in addictive behavior and suggested its promise as a target for the treatment of addiction (Ibrahim et al., 2019). The orbitofrontal area is the key brain area in the representation of reward or non-reward value, and is capable of controlling and correcting reward-related and punishment-related behaviors (Ibrahim et al., 2019). The putamen is involved in the processing of primary rewards and visual events in a complex task, which may play an important role in reinforcement learning through stimulus-reward association (Vicente et al., 2012). A growing body of evidence suggested that IGD was associated with alterations in brain regions responsible for reward processing and sensorimotor function (Weinstein et al., 2017; Dong et al., 2018; Weinstein and Lejoyeux, 2020). Our findings are in line with these previous studies. Furthermore, in the IGD group, the right insula showed an enhanced local clustering coefficient and was linked to the right inferior temporal gyrus, which was a key component of subnet1. An enhanced local clustering coefficient of the right insula suggested that its short-distance connections were increased. In subnet1, the right inferior temporal gyrus was a central node with a higher degree, and its majority edges were linked to areas responsible for visual and sensorimotor functions (namely, the right cuneus, the right superior occipital gyrus, the right post-central gyrus, and the right

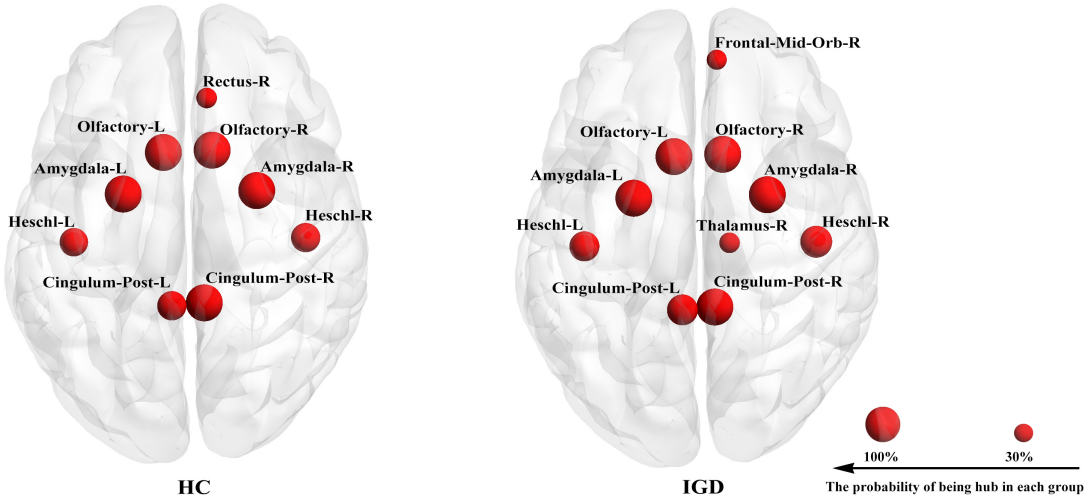

FIGURE 3
Each group has its own hub distribution. It showed the hub with a probability of being a hub greater than 30%.

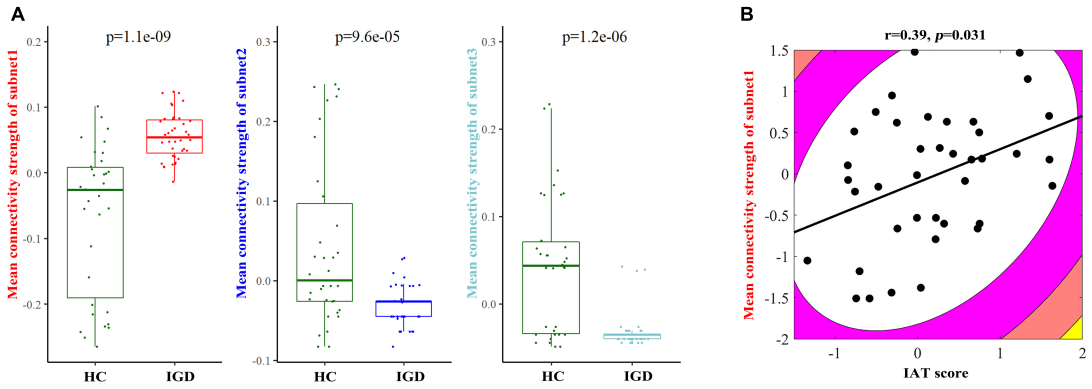

FIGURE 4
(A) Between-group comparison results of the mean fractional anisotropy- (FA–) weighted structural connectivity strength in each subnetwork between young people with internet gaming disorder (IGD) and healthy controls (HC). **(B)** An illustration of the correlation result between the mean FA-weighted structural connectivity strength of subnet1 and the IAT score in the IGD group.

temporal pole of the superior temporal gyrus). These results may indicate that increased short connections of the right insula come mainly from those regions associated with visual and sensorimotor functions, which may cause the insula to enhance its response to external stimuli. Thus, we speculate that the excessive use of the internet for gaming strengthens the connections among those regions responsible for visual, sensorimotor, and reward functions, which may increase individuals' feelings of game experience (i.e., subjective pleasure) and may aggravate their addictive behaviors.

In addition, a decrease in the mean FA-weighted structural connectivity strength of subnet2 and subnet3 was shown, and most of these altered connections were located mainly within the limbic areas (namely, the amygdala, the parahippocampal gyrus, the anterior cingulate gyrus, and the median cingulate gyrus), the striatum areas (namely, the caudate, the putamen, and the pallidum), and the bilateral insula. The striatum is thought to play an important role in the pathophysiology of IGD, and prior studies identified a dopamine-driven striatal function as a core candidate for promoting addictive behavior (Weinstein, 2010; Kuss and Griffiths, 2012; Tian et al., 2014; Weinstein et al., 2017). Recently, related brain imaging studies implicated the important role of the dysfunctional limbic system (especially the amygdala, the parahippocampal gyrus, and the cingulate gyrus) in the neuropathological mechanism of IGD (Weinstein, 2010; Kuss and Griffiths, 2012; Tian et al., 2014; Weinstein et al., 2017). The connections between the bilateral amygdala and the insula constituted an important part of subnet2. Berret et al. (2019) applied optogenetic approaches in the animal model and corroborated that the insula routed aversive somatosensory information to the amygdala and contributed to elaborate its negative valence, thus suppressing an essential drive to learn about such harmful information. The insula along with the amygdala is necessary for the retrieval of threat memories. Furthermore, Baur et al. (2013) analyzed resting-state functional and structural connectivity within the amygdala-insula in healthy subjects and demonstrated that this connectivity represented the index state and trait anxiety. Ko et al. (2015) examined the amygdala-centered network in IGD on the basis of rs-fMRI and found altered connectivity of the bilateral amygdala and the insula in adults with IGD than in controls. Hence, these decreased structural subnets, to a certain extent, may affect reward

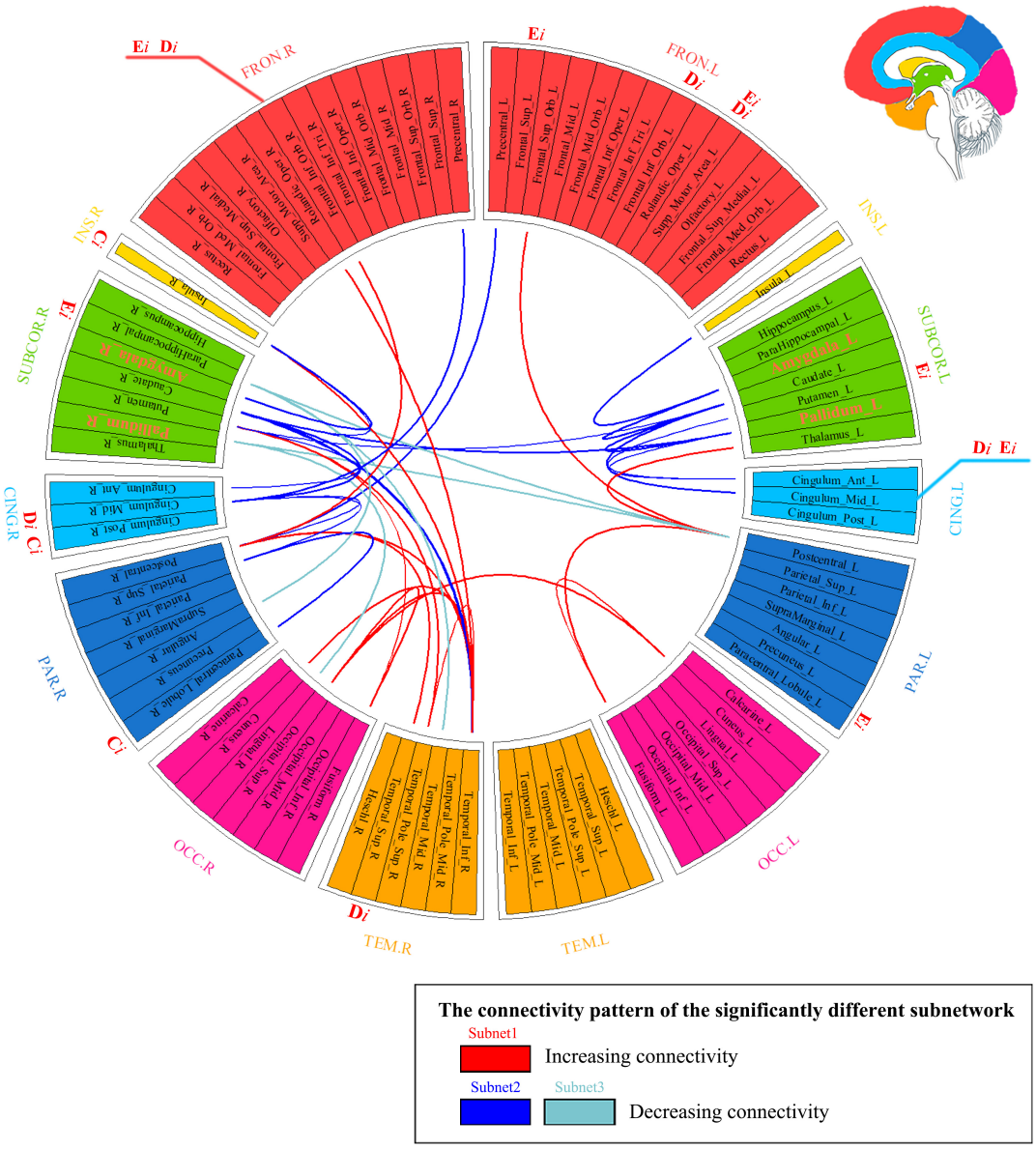

FIGURE 5
Summarizing the results of network analysis. It represented three subnetwork results (i.e., subnetworks 1–3) whose connections are marked with different colors in the connectogram. If a nodal measure showed the existence of a significant between-group difference, the location of the outer ring of the circle corresponding to this node was labeled as the nodal measure's name (namely D_i, E_i, and C_i). If the nodal measure's name was colored with red, it meant that the corresponding value increased. Hubs' name was marked with orange color and with a larger font size in the ring. FRON, frontal cortex; INS, insula; SUBCOR, subcortical region; CING, cingulum; PAR, parietal cortex; OCC, occipital cortex; TEM, temporal cortex; L, left hemisphere; R, right hemisphere.

processing, emotion processing and regulation, and cognitive control. Moreover, the involvement of the connectivity between the bilateral amygdala and the insula in these subnets may give a potential cue that young people with IGD underestimate the negative valence of excessive play and neglect the harmfulness from such behavior.

Taken together, these findings provide tentative evidence for enhanced structural connectivity among the insula, the sensorimotor, visual, and reward-related regions, and decreased structural connectivity in the insula, limbic, and striatal regions. Among these, the insula holds quite an important position in these findings, which suggest that, on the one hand, excessive play of internet games intensifies sensory stimuli and improves subjective pleasure and, on the other hand, individuals with IGD weaken their awareness of the risk of indulging in internet games. All these results may provide a potential explanation for why young people indulge in playing internet games and highlight the role of the insula in the pathological mechanism of IGD.

An increase in the mean FA-weighted structural connectivity strength of subnet1 was related to the severity of internet addiction

The result showed that the mean FA-weighted structural connectivity strength of subnet1 was significantly positively related

to the IAT score in young people with IGD. The IAT score can reflect the severity of the gaming addiction. This result implies that the higher the connectivity strength of subnet1, the more severe the impairment in IGD. As mentioned above, subnet1 exhibited an enhancement in the mean FA-weighted structural connectivity strength in young people with IGD and was involved in the insula and the frontal, visual, auditory, and sensorimotor regions. These areas are responsible for receiving external sensory stimuli and processing reward-related functions. Previous cross-sectional and longitudinal studies demonstrated that training can induce changes in WM structure. Bengtsson et al. (2005) found that the amount of piano practice in childhood enhanced FA values within related motor tracts. Scholz et al. (2009) designed a longitudinal study of individuals learning a new visuomotor skill, juggling, and reported an increase in the FA value of the intraparietal sulcus in the juggling group. An individual with excessive gaming use over a long period of time can induce experience-dependent changes in WM within regions responsible for visual, auditory, and sensorimotor processing. For example, Jeong et al. (2016) reported that men with IGD increased FA values within several fasciculi such as the forceps minor, the right corticospinal tract, the right inferior longitudinal fasciculus, and the right inferior fronto-occipital fasciculus, and also found a positive correlation of the FA values of these fasciculi with the duration of illness in IGD. These fasciculi play an important role in visual, auditory, motor, and working memory functions. Although WM in men with IGD was measured using different analysis methods, our findings showed three similarities (such as predominance in the right hemisphere, an increased FA value, and an impact on the WM bundles responsible for visual/auditory/sensorimotor function) with these of Jeong et al. (2016). For example, (1) the subnet1 result predominated within the right hemisphere; (2) subnet1 increased the mean FA-weighted structural connectivity value; and (3) most nodes in subnet1 were responsible for receiving the external stimuli. We speculate that enhanced WM structural connectivity within subnet1 may arise secondary to long-term internet gaming addiction and may affect the processing of visual/auditory/sensorimotor and reward functions.

Limitations and conclusion

Several limitations of the present study should be noted. First, the current study only recruited young men. Some previous neuroimaging studies revealed gender-related differences in IGD (Jeong et al., 2016), and men were more vulnerable to IGD than women (Borgonovi, 2016). Some scholars urged considering the importance of gender in understanding IGD (King and Potenza, 2020). Our study excluded the effect of gender on the findings. However, these findings should be considered specific to young men with IGD. Future studies need to verify these results in women and in those with other occupations. In addition, we have not obtained the HAMA and HAMD scores of all HC subjects, because of the lack of willingness to tests by some of them. However, in the preliminary HAMA/HAMD data, patients with IGD showed a significantly higher score than those with HCs. Considering psychological variables, depression and anxiety are more strongly associated with the development of IGD. Higher depression and anxiety might be representative indicators of the problems of individuals with IGD. If all HC subjects without HAMA/HAMD scores were removed and additional analyses were performed with HAMA/HAMD as a covariate, it still would not be possible to explain which factors (namely, HAMA/HAMD and a change in the number of HC subjects) affect the results and how much influence these factors have on the results, respectively. Due to this objective consideration, we had not included both variables as covariates in our primary data analyses. Further studies that explicitly recruit individuals with IGD and also low levels of anxiety and depression are needed to disentangle the effects of both variables on the structural connectivity networks. Finally, a cross-sectional study can never confirm a causal role for experience on the WM structure in brains, due to the possibility that common genetic factors influence both the WM structure and the propensity to train. A longitudinal study is needed to further corroborate whether altered subnets are a consequence of excessive use of internet games.

In conclusion, the present study is the first to assess WM structural network alterations in IGD using an NBS approach from a perspective of connectomics. We observed a widespread alteration of cortico-limbic-striatal structural connectivity networks, including an increased subnet1 (mainly involving the insula and regions responsible for visual, auditory, and sensorimotor functions) and decreased two subnet2 and subnet3 (mainly in the insula, striatum, and limbic regions). Moreover, the mean FA-weighted structural connectivity of subnet1 showed a significant positive relationship with the severity of internet addiction. In particular, the insula appeared in both increased and decreased subnets, playing an important position in these findings, highlighting its role in understanding the neurobiological mechanisms underlying IGD and in developing effective treatment strategies for this disorder.

Data availability statement

The raw data supporting the conclusions of this article will be made available by the authors, without undue reservation.

Ethics statement

This study was approved by the Medical Ethics Committee of Wuxi Mental Health Center, Nanjing Medical University, China. The patients/participants provided their written informed consent to participate in this study.

Author contributions

JQ was responsible for analyzing data and writing the manuscript. SW was responsible for data collection and writing the manuscript. LT was responsible for the study design and revising the manuscript. HN and YW were responsible for analyzing data and revising the manuscript. LC, FZ, and ZZ were responsible for data collection and recruiting for patients. All authors have critically reviewed the content and approved the final version submitted for publication.

Funding

This work was supported by the Chinese National Science Foundation (Nos. 81871081, 81701346, 81471354, and 62201265),

the Natural Science Foundation of Jiangsu Province (Grant No. BK20190736), and the Talent Support Programs of Wuxi Health Commission (Grant Nos. BJ2020083, FZXK2021012, and M202167).

Acknowledgments

Sincere appreciation is extended to young people with IGD and controls for their valuable participation.

Conflict of interest

The authors declare that the research was conducted in the absence of any commercial or financial relationships that could be construed as a potential conflict of interest.

Publisher's note

Supplementary material

The Supplementary Material for this article can be found online at: https://www.frontiersin.org/articles/10.3389/fnins.2022.1090224/full#supplementary-material

References

American Psychiatric Association [APA]. (2013). *Diagnostic and Statistical Manual of Mental Disorders: DSM-5*™, 5th Edn. Arlington, VA: American Psychiatric Publishing, Inc.

Baur, V., Hänggi, J., Langer, N., and Jäncke, L. (2013). Resting-state functional and structural connectivity within an insula–amygdala route specifically index state and trait anxiety. *Biol. Psychiat.* 73, 85–92. doi: 10.1016/j.biopsych.2012.06.003

Bax, T. (2015). "Internet gaming disorder" in China: biomedical sickness or sociological badness? *Games Cult.* 11, 233–255. doi: 10.1177/1555412014568188

Bengtsson, S., Nagy, Z., Skare, S., Forsman, L., Forssberg, H., and Ullén, F. (2005). Extensive piano practicing has regionally specific effects on white matter development. *Nat. Neurosci.* 8, 1148–1150. doi: 10.1038/nn1516

Berret, E., Kintscher, M., Palchaudhuri, S., Tang, W., Osypenko, D., Kochubey, O., et al. (2019). Insular cortex processes aversive somatosensory information and is crucial for threat learning. *Science* 364:w474. doi: 10.1126/science.aaw0474

Borgonovi, F. (2016). Video gaming and gender differences in digital and printed reading performance among 15-year-olds students in 26 countries. *J Adolesc.* 48, 45–61. doi: 10.1016/j.adolescence.2016.01.004

Bullmore, E., and Sporns, O. (2009). Complex brain networks: graph theoretical analysis of structural and functional systems. *Nat. Rev. Neurosci.* 10, 186–198. doi: 10.1038/nrn2575

Chen, S., Wang, M., Dong, H., Wang, L., Jiang, Y., Hou, X., et al. (2021). Internet gaming disorder impacts gray matter structural covariance organization in the default mode network. *J. Affect. Disorder.* 288, 23–30. doi: 10.1016/j.jad.2021.03.077

Chun, J., Park, C., Kim, J., Choi, J., Cho, H., Jung, D., et al. (2020). Altered core networks of brain connectivity and personality traits in internet gaming disorder. *J. Behav. Addict.* 9, 298–311. doi: 10.1556/2006.2020.00014

de Reus, M. A., and van den Heuvel, M. P. (2013). Estimating false positives and negatives in brain networks. *Neuroimage* 70, 402–409. doi: 10.1016/j.neuroimage.2012.12.066

Dong, G., DeVito, E., Huang, J., and Du, X. (2012). Diffusion tensor imaging reveals thalamus and posterior cingulate cortex abnormalities in internet gaming addicts. *J. Psychiatr. Res.* 46, 1212–1216. doi: 10.1016/j.jpsychires.2012.05.015

Dong, G., Lin, X., and Potenza, M. (2015). Decreased functional connectivity in an executive control network is related to impaired executive function in internet gaming disorder. *Prog. Neuropsychopharmacol. Biol. Psychiatry* 57, 76–85. doi: 10.1016/j.pnpbp.2014.10.012

Dong, G., Wu, L., Wang, Z., Wang, Y., Du, X., and Potenza, M. (2018). Diffusion-weighted mri measures suggest increased white-matter integrity in internet gaming disorder: evidence from the comparison with recreational internet game users. *Addict. Behav.* 81, 32–38. doi: 10.1016/j.addbeh.2018.01.030

Gaebel, W., Stricker, J., and Kerst, A. (2020). Changes from icd-10 to icd-11 and future directions in psychiatric classification. *Dial. Clin. Neurosci.* 22, 7–15. doi: 10.31887/DCNS.2020.22.1/wgaebel

Gogolla, N. (2017). The insular cortex. *Curr. Biol.* 27, R580–R586. doi: 10.1016/j.cub.2017.05.010

Grant, J., Potenza, M., Weinstein, A., and Gorelick, D. (2010). Introduction to behavioral addictions. *Am. J. Drug Alcohol Abuse* 36, 233–241. doi: 10.3109/00952990.2010.491884

Hamilton, M. (1959). The assessment of anxiety states by rating. *Br. J. Med. Psychol.* 32, 50–55. doi: 10.1111/j.2044-8341.1959.tb00467.x

Hamilton, M. (1967). Development of a rating scale for primary depressive illness. *Br. J. Soc. Clin. Psychol.* 6, 278–296. doi: 10.1111/j.2044-8260.1967.tb00530.x

Ibrahim, C., Rubin-Kahana, D., Pushparaj, A., Musiol, M., Blumberger, D., Daskalakis, Z., et al. (2019). The insula: a brain stimulation target for the treatment of addiction. *Front. Pharmacol.* 10:720. doi: 10.3389/fphar.2019.00720

Jeong, B., Han, D., Kim, S., Lee, S., and Renshaw, P. (2016). White matter connectivity and internet gaming disorder. *Addict. Biol.* 21, 732–742. doi: 10.1111/adb.12246

King, D. L., and Potenza, M. N. (2020). Gaming disorder among female adolescents: a hidden problem? *J. Adolesc. Health* 66, 650–652. doi: 10.1016/j.jadohealth.2020.03.011

Ko, C., Hsieh, T., Wang, P., Lin, W., Yen, C., Chen, C., et al. (2015). Altered gray matter density and disrupted functional connectivity of the amygdala in adults with internet gaming disorder. *Prog. Neuropsychopharmacol. Biol. Psychiatry* 57, 185–192. doi: 10.1016/j.pnpbp.2014.11.003

Kuss, D. J., and Griffiths, M. D. (2012). Internet and gaming addiction: a systematic literature review of neuroimaging studies. *Brain Sci.* 2, 347–374. doi: 10.3390/brainsci2030347

Lau, J., Gross, D., Wu, A., Cheng, K., and Lau, M. (2017). Incidence and predictive factors of internet addiction among Chinese secondary school students in Hong Kong: a longitudinal study. *Soc. Psychiatry Psychiatr. Epidemiol.* 52, 657–667. doi: 10.1007/s00127-017-1356-2

Lee, J., Lee, D., Namkoong, K., and Jung, Y. (2020). Aberrant posterior superior temporal sulcus functional connectivity and executive dysfunction in adolescents with internet gaming disorder. *J. Behav. Addict.* 9, 589–597. doi: 10.1556/2006.2020.00060

Lei, W., Xu, H., Xuchen, Y., and Yawen, S. (2020). Brain controllability and morphometry similarity of internet gaming addiction. *Methods* 192, 93–102. doi: 10.1016/j.ymeth.2020.08.005

Li, Y., Zhang, X., Lu, F., Zhang, Q., and Wang, Y. (2013). Internet addiction among elementary and middle school students in china: a nationally representative sample study. *Cyberpsychol. Behav. Soc. Netw.* 17, 111–116. doi: 10.1089/cyber.2012.0482

Mori, S., Crain, B., Chacko, V., and van Zijl, P. (1999). Three-dimensional tracking of axonal projections in the brain by magnetic resonance imaging. *Ann. Neurol.* 45, 265–269.

Oldfield, R. C. (1971). The assessment and analysis of handedness: the edinburgh inventory. *Neuropsychologia* 9, 97–113. doi: 10.1016/0028-3932(71)90067-4

Park, C., Chun, J., Cho, H., and Kim, D. (2018). Alterations in the connection topology of brain structural networks in internet gaming addiction. *Sci. Rep.* 8:15117. doi: 10.1038/s41598-018-33324-y

Rubinov, M., and Sporns, O. (2010). Complex network measures of brain connectivity: uses and interpretations. *Neuroimage* 52, 1059–1069. doi: 10.1016/j.neuroimage.2009.10.003

Scholz, J., Klein, M., Behrens, T., and Johansen-Berg, H. (2009). Training induces changes in white-matter architecture. *Nat. Neurosci.* 12, 1370–1371. doi: 10.1038/nn.2412

Song, K., Potenza, M., Fang, X., Gong, G., Yao, Y., Wang, Z., et al. (2020). Resting-state connectome-based support-vector-machine predictive modeling of internet gaming disorder. *Addict. Biol.* 26:e12969. doi: 10.1111/adb.12969

Tian, M., Chen, Q., Zhang, Y., Du, F., Hou, H., Chao, F., et al. (2014). Pet imaging reveals brain functional changes in internet gaming disorder. *Eur. J. Nucl. Med. Mol. Imaging* 41, 1388–1397. doi: 10.1007/s00259-014-2708-8

Tzourio-Mazoyer, N., Landeau, B., Papathanassiou, D., Crivello, F., Etard, O., Delcroix, N., et al. (2002). Automated anatomical labeling of activations in spm using a macroscopic anatomical parcellation of the mni mri single-subject brain. *Neuroimage* 15, 273–289. doi: 10.1006/nimg.2001.0978

Vicente, A., Bermudez, M., Romero, M., Perez, R., and Gonzalez, F. (2012). Putamen neurons process both sensory and motor information during a complex task. *Brain Res.* 1466, 70–81. doi: 10.1016/j.brainres.2012.05.037

Weinstein, A., and Lejoyeux, M. (2020). Neurobiological mechanisms underlying internet and gaming disorder. *Dial. Clin. Neurosci.* 22, 113–126. doi: 10.31887/DCNS.2020.22.2/aweinstein

Weinstein, A., Livny, A., and Weizman, A. (2017). New developments in brain research of internet and gaming disorder. *Neurosci. Biobehav. Rev.* 75, 314–330. doi: 10.1016/j.neubiorev.2017.01.040

Weinstein, A. M. (2010). Computer and video game addiction—a comparison between game users and non-game users. *Am. J. Drug. Alcohol Abuse* 36, 268–276. doi: 10.3109/00952990.2010.491879

Woolley, J., Strobl, E., Sturm, V., Shany-Ur, T., Poorzand, P., Grossman, S., et al. (2015). Impaired recognition and regulation of disgust is associated with distinct but partially overlapping patterns of decreased gray matter volume in the ventroanterior insula. *Biol. Psychiat.* 78, 505–514. doi: 10.1016/j.biopsych.2014.12.031

Xie, S., Chen, L., Zuo, N., and Jiang, T. (2016). Diffusionkit: a light one-stop solution for diffusion mri data analysis. *J. Neurosci. Methods* 273, 107–119. doi: 10.1016/j.jneumeth.2016.08.011

Yan, H., Li, Q., Yu, K., and Zhao, G. (2021). Large-scale network dysfunction in youths with internet gaming disorder: a meta-analysis of resting-state functional connectivity studies. *Prog. Neuropsychopharmacol. Biol. Psychiatry* 109:110242. doi: 10.1016/j.pnpbp.2021.110242

Yao, Y., Liu, L., Ma, S., Shi, X., Zhou, N., Zhang, J., et al. (2017). Functional and structural neural alterations in internet gaming disorder: a systematic review and meta-analysis. *Neurosci. Biobehav. Rev.* 83, 313–324. doi: 10.1016/j.neubiorev.2017.10.029

Yao, Y., Zhang, J., Fang, X., Liu, L., and Potenza, M. (2021). Reward-related decision-making deficits in internet gaming disorder: a systematic review and meta-analysis. *Addiction* 117, 19–32. doi: 10.1111/add.15518

Young, K. S. (1998). *Caught in the Net: How to Recognize the Signs of Internet Addiction–and a Winning Strategy for Recovery*. New York, NY: Wiley.

Zalesky, A., Fornito, A., and Bullmore, E. (2010). Network-based statistic: identifying differences in brain networks. *Neuroimage* 53, 1197–1207. doi: 10.1016/j.neuroimage.2010.06.041

Zhai, J., Luo, L., Qiu, L., Kang, Y., Liu, B., Yu, D., et al. (2017). The topological organization of white matter network in internet gaming disorder individuals. *Brain Imaging Behav.* 11, 1769–1778. doi: 10.1007/s11682-016-9652-0

frontiers | Frontiers in Neuroscience

TYPE Original Research
PUBLISHED 16 March 2023
DOI 10.3389/fnins.2023.1126865

OPEN ACCESS

EDITED BY
Ye Wu,
Nanjing University of Science and Technology, China

REVIEWED BY
Yunzhi Huang,
Nanjing University of Information Science and Technology, China
Jianzhong He,
Zhejiang University of Technology, China

*CORRESPONDENCE
Fangyin Li
✉ lify@zjcc.org.cn

†These authors have contributed equally to this work and share first authorship

SPECIALTY SECTION
This article was submitted to Brain Imaging Methods, a section of the journal Frontiers in Neuroscience

RECEIVED 18 December 2022
ACCEPTED 27 February 2023
PUBLISHED 16 March 2023

CITATION
Long D, Zhang M, Yu J, Zhu Q, Chen F and Li F (2023) Intelligent diagnosis of major depression disease based on multi-layer brain network.
Front. Neurosci. 17:1126865.
doi: 10.3389/fnins.2023.1126865

Intelligent diagnosis of major depression disease based on multi-layer brain network

Dan Long[1†], Mengda Zhang[2†], Jing Yu[3], Qi Zhu[3], Fengnong Chen[2] and Fangyin Li[1*]

[1]Zhejiang Cancer Hospital, Institute of Basic Medicine and Cancer (IBMC), Chinese Academy of Sciences, Hangzhou, Zhejiang, China, [2]School of Automation, Hangzhou Dianzi University, Hangzhou, China, [3]The College of Computer Science and Technology, Nanjing University of Aeronautics and Astronautics, Nanjing, China

Introduction: Resting-state brain network with physiological and pathological basis has always been the ideal data for intelligent diagnosis of major depression disease (MDD). Brain networks are divided into low-order networks and high-order networks. Most of the studies only use a single-level network to classify while ignoring that the brain works cooperatively with different levels of networks. This study hopes to find out whether varying levels of networks will provide complementary information in the process of intelligent diagnosis and what impact will be made on the final classification results by combining the characteristics of different networks.

Methods: Our data are from the REST-meta-MDD project. After the screening, 1,160 subjects from ten sites were included in this study (597 MDD and 563 normal controls). For each subject, we constructed three different levels of networks according to the brain atlas: the traditional low-order network based on Pearson's correlation (low-order functional connectivity, LOFC), the high-order network based on topographical profile similarity (topographical information-based high-order functional connectivity, tHOFC) and the associated network between them (aHOFC). Two sample *t*-test is used for feature selection, and then features from different sources are fused. Finally, the classifier is trained by a multi-layer perceptron or support vector machine. The performance of the classifier was evaluated using the leave-one-site cross-validation method.

Results: The classification ability of LOFC is the highest among the three networks. The classification accuracy of the three networks combined is similar to the LOFC network. These are seven features chosen in all networks. In the aHOFC classification, six features were selected in each round but not seen in other classifications. In the tHOFC classification, five features were selected in each round but were unique. These new features have crucial pathological significance and are essential supplements to LOFC.

Conclusion: A high-order network can provide auxiliary information for low-order networks but cannot improve classification accuracy.

KEYWORDS

multi-layer brain function network, major depression disease (MDD), intelligent diagnosis, the pathological basis, deep learning

1. Introduction

In recent years, because neuroimaging can directly provide *in vivo* brain function and structure information, more and more people have begun to use machine learning technology to extract imaging markers for intelligent diagnosis of major depression disease (MDD) (Gao et al., 2018). However, most of the studies are data-driven, and neither the data selection nor the interpretation of the results pays attention to the histopathological basis of MDD. Despite years of efforts, the pathological and physiological mechanism of MDD itself is still unclear. Many autopsy studies have shown that the density of global glial cells in emotion-related brain regions is decreased in depressed patients (O'Leary and Mechawar, 2021) [as shown in **Figure 1**: (Cotter et al., 2001)]. The glial cells provide metabolic and regulatory support to neurons, in which astrocytes are responsible for increasing the number of mature and functional synapses (Pannasch et al., 2011). The neural circuit pathways of the brain depend not only on neurons but also on glial cells that significantly affect structural and functional connections (Fields et al., 2015). The latest findings showed a strong correlation between the brain's microscopic neural circuits and the macroscopic fMRI-based resting-state functional network (Kahali et al., 2021). Therefore, we have reason to believe that the resting-state functional network carrying pathological features is one of the ideal data for the intelligent diagnosis of MDD.

As we all know, the human brain network is composed of different subnets. The whole brain supports functional separation and integration, presenting the so-called small-world attribute (Bassett and Bullmore, 2006), and different hierarchical subnets complete information collection and processing. The medium and low-level systems are responsible for collecting information, and the high-level systems are accountable for integrating and abstracting information. The human brain can change the collection and synthesis of information by adjusting the mental state. For example, the level of attention can change perception, information collection, and synthesis (Keller et al., 2019). Based on this neuropsychological mechanism, someone has developed a high-order functional connectivity (HOFC) network specially used to provide high-level information in the brain network (Zhang et al., 2016). A study showed that HOFC could improve the differences between groups, better capture individual differences, improve the modularity of the brain network, and provide supplementary information for the traditional low-order functional connectivity (LOFC) network. The results showed that multi-layer features extracted from different levels of networks could more accurately identify mild cognitive impairment (Zhang et al., 2016), even early mild cognitive impairment (Zhang et al., 2017). Therefore, we would like to know whether combining the characteristics of different brain networks can provide more abundant information and higher accuracy for the intelligent diagnosis of MDD.

We use a multicenter, extensive sample data to test our hypothesis in this study. First, we constructed three types of networks: 1. LOFC; 2. topographical information-based high-order functional connectivity [tHOFC (Zhang et al., 2016)] 3. associated HOFC [aHOFC (Zhang et al., 2017)]. Then two samples *t*-test is used to extract the features, and the multi-layer features are fused. Finally, MDD is classified by using a multi-layer perceptron (MLP) or support vector machine (SVM) training classifier. The whole experimental flow is shown in **Figure 2**.

2. Materials and methods

2.1. Subjects

All data in this study are from the REST-meta-MDD project. The brain imaging data of 1,300 depressed patients and 1,128 healthy controls through 25 research groups in 17 hospitals in China were collected in this project (Yan et al., 2019). We further screened the data to meet the needs of this study. For detailed methods, please refer to our previous paper (Long et al., 2022). In simple terms, it is to remove data whose repetition time is not 2.0; Delete the data of subjects with time series of 0; Finally, each site's data is tested for gender and age matching, and the unmatched sites are deleted. This means that the data of all sites in this study have passed the age and gender matching test. In the end, data from 10 sites (1,160 subjects) were included in this study. **Table 1** shows the subject information. For more details, please refer to Yan et al. (2019).

Three types of networks are constructed in this study: 1. LOFC, 2. tHOFC, 3. aHOFC. To make the results more universal, we chose the most widely used anatomical automatic labeling (AAL) (Tzourio-Mazoyer et al., 2002) as a brain atlas.

2.2. Data pre-processing

The data preprocessing was performed by DPARSF. Global signal regression was performed on all data. The time series were extracted according to the AAL brain atlas, and then the average time series of each brain region was calculated. Please refer to the literature for the detailed data preprocess (Yan et al., 2019).

2.3. Definition of brain network

All networks in this study were generated by the BrainNetClass Toolkit (Zhou et al., 2020). To distinguish HOFC, we call Pearson-based functional connectivity (FC) as LOFC, defined as follows: the brain is divided into n regions of interest (ROI) according to the brain atlas. The ith ROI can be expressed as a vector $x_i = [x_{1i}, x_{2i}, \ldots, x_{Ti}]' \in R^T$ ('indicates transposition), the whole brain signal can be expressed by matrix $X = [x_1, x_2, \ldots, x_N] \in R^{T\times N}$. The network was expressed as a weighted graph $W \in R^{N\times N}$. Each element in the matrix is a Pearson correlation (PC) between two brain regions. The PC-derived function network is usually used as a benchmark for comparison with other advanced methods. The formula is as follows:

$$FC_{ij} = \frac{\sum_{t=1}^{T}(x_i(t)-\overline{x_i})(x_j(t)-\overline{x_j})}{\sqrt{\sum_{t=1}^{T}(x_i(t)-\overline{x_i})^2}\sqrt{\sum_{t=1}^{T}(x_j(t)-\overline{x_j})^2}} \quad (1)$$

tHOFC takes the FC between each ROI and all other ROIs as the first-order feature and then calculates the PC between them based on the first-order feature. The obtained coefficient is the

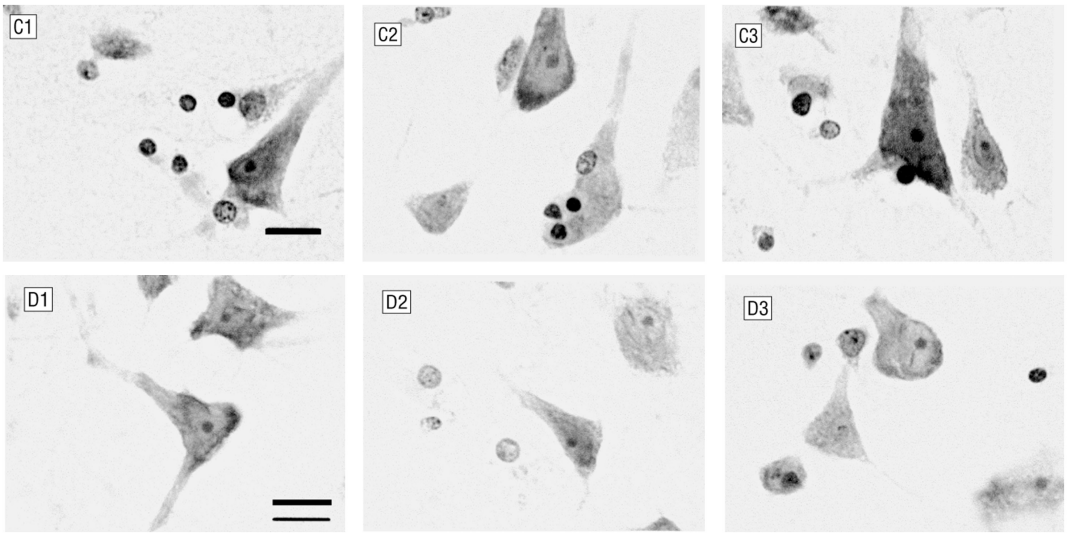

FIGURE 1
Glial cells and neurons in layer 6 of the anterior cingulate cortex. C1–C3 were control subjects (male, 44 years old), and D1–D3 were patients with major depression (female, 52 years old). Patients with major depression had fewer glial cells and smaller neurons (Nissl staining; bar, 12 μm).

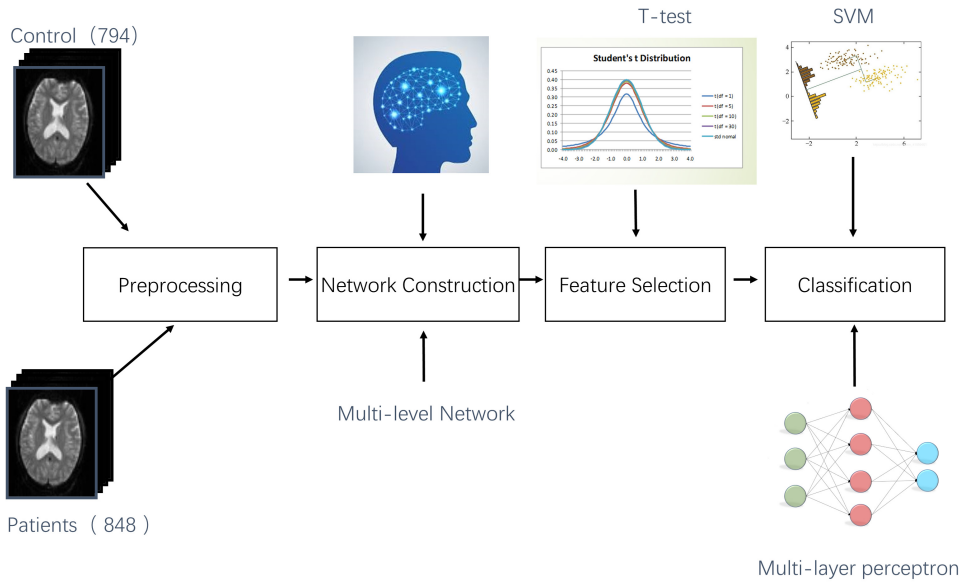

FIGURE 2
Flow chart of the study.

HOFC based on the connection topology attribute. The formula is as follows:

$$tHOFC_{ij} = \frac{\sum_k (w_{ik} - \overline{w_{i.}})(w_{jk} - \overline{w_{j.}})}{\sqrt{\sum_k (w_{ik} - \overline{w_{i.}})^2}\sqrt{\sum_k (w_{jk} - \overline{w_{j.}})^2}} \quad (2)$$

Among $w_{i.} = \{w_{ik} | k \in N, k \neq i\}, i, j, k = 1, 2, \ldots, N, k \neq i, j$. Since LOFC is used as the first-order feature instead of the bold time-series signal in the tHOFC calculation, the result is essentially different from that of LOFC. Studies have shown that tHOFC can provide supplementary information for conventional LOFC and help reveal the differences between subjects with mild cognitive impairment (MCI) and normal controls (Zhang et al., 2016, 2019).

Associated high-order functional connectivity is defined based on the mutual relationship between the topological attributes of tHOFC and LOFC, and the calculation method is similar to FC and tHOFC (Eq. 3). It measures the functional correlation between layers (the lower layer and the higher layer). It is a supplement to the information contained in LOFC and tHOFC. Some studies showed that combining these three networks can further improve the diagnostic accuracy of MCI (Zhang et al., 2017). Theoretically, unlike LOFC and tHOFC, the aHOFC matrix is not symmetric, and the self-connection is not 1. However, we find that the upper and lower triangles are highly related. Therefore, to simplify the calculation, we change the aHOFC into a symmetric matrix by

W ← (W + W^') / 2 (Zhou et al., 2020).

$$aHOFC_{ij} = \frac{\sum_k (tHOFC_{ik} - \overline{tHOFC_{i.}})(w_{jk} - \overline{w_{j.}})}{\sqrt{\sum_k (tHOFC_{ik} - \overline{tHOFC_{i.}})^2}\sqrt{\sum_k (w_{jk} - \overline{w_{j.}})^2}} \quad (3)$$

2.4. Feature selection

As shown in the upper left corner of Figure 3, the brain network constructed based on fMRI is a symmetric matrix (size:116 × 116). The upper triangle part is compressed into a one-dimensional vector to form initial features (1 × 6670). Too many indistinguishable features will adversely affect the classification results and reduce the robustness of the model. This study used a two-sample *t*-test to choose the features with discrimination. For learning, the reduced dimension features are sent to the classifier. For the multi-network joint classification, different features produced from three networks are connected to form a vector, the multi-layer feature (Long et al., 2012), and then put into the classifier for training. To ensure the model's generalization performance, we adopt leave-one-site cross-validation (LOSCV).

2.5. Classifier

This study uses two types of mathematical models to construct classifiers: deep learning and support vector machine. The first is the linear support vector machine (SVM). SVM is the most commonly used classification method and has achieved good results on small data sets (Gao et al., 2018). The second is deep learning models. As the classification tasks become more and more complex and the amount of data increases, more complex deep learning models are used for the intelligent diagnosis of MDD. MLP is a typical deep learning model.

The MLP classifier is based on domain-adversarial training of neural networks (DANN). The selected features are sent to the MLP for learning. Changing the size of the convolution weight matrix can achieve the implicit dimensionality reduction of the data in the upper layer, and the generated data is used as the input of the next layer.

The DANN model is implemented based on Pytorch and uses the adam optimizer to train the network model. The learning rate is 0.001. The network is divided into three parts: feature extractor (the first part), label predictor (the second part), and domain classifier (the third part). The details are shown in Figure 3. They use the adversarial relationship between the feature extractor and the domain classifier to mix source and target domain samples in a specific space. After the feature extractor, domain classifier, and label predictor are all trained, the source domain and target domain can be mixed and classified.

The second and third sub-networks are feedforward networks with the same structure. They contain two fully connected convolutional layers and transfer or update feature information through batch normalization (BN), rectification linear unit (ReLU), and Dropout (BN-ReLU-Dropout = 0.5). In parameter information transmission, the number of hidden layer nodes in each layer is 0.5 times the number of hidden layer nodes in the previous layer. Finally, the classification result is obtained through the sigmoid function. The lower part has a particular process called a gradient reversal layer (GRL) which multiplies the error transmitted to this layer by a negative number -λ so that the training objectives of the network before and after GRL will be opposite to achieve the effect of confrontation. The error of the whole network is generated by supervised source domain learning error (L_y) and unsupervised target domain learning error (L_d), both of which are calculated by binary cross entropy loss (BCE_{Loss}). Weighted BCE_{loss} solves the class imbalance problem with the super parameter W_c, where c is the class index, defined as (Eqs 4–6):

$$L = \frac{1}{N_{all}} \sum_{n=1}^{N_{all}} \left(\sum_{c=1}^{c} W_c E(y_{n,c}, y'_{n,c}) \right) \quad (4)$$

$$W_c = \frac{e^{1/Nc}}{\sum_{c=1}^{C} e^{1/Nc}} \quad (5)$$

$$E\left(y_{n,c}, \hat{y}_{n,c}\right) = -\left(y_{n,c} log \hat{y}_{n,c}\right) + \left(1 - y_{n,c}\right) \log\left(1 - \hat{y}_{n,c}\right) \quad (6)$$

where L is the weighted BCE_{Loss}, N_c is the sample numbers of class c, N_{sall}, and C are the total numbers of samples and classes, and $E(Y_{nc}, \hat{Y}nc)$ represents the BCE_{Loss} for the label truth Y_{nc} and the predicted probability $\hat{Y}nc$.

The random gradient descent optimizer uses the loss gradient calculated by backpropagation to update the network parameters. After many experiments, the GRL is placed between the feature extraction network and the domain classification network. The error transmitted to this layer is multiplied by a negative number-λ. The network training objectives before and after GRL are opposite to achieve the effect of confrontation.

TABLE 1 Subject information.

Number	1,160	Number of sites	10
Male	434	Female	726
MDD	597	Normal controls	563

3. Results

Although the three networks represent different meanings, a single feature in each network is the FC between two brain regions (HOFC or LOFC). There are seven features selected in each round of the three networks ($p < 0.01$). In the aHOFC classification, 26 features were selected in each round, six of which were not seen in other networks and were all related to the cerebellum. In the tHOFC classification, 36 features were selected in each round, five unique, with the highest number of FC between the cerebellum and the temporal lobe. In general, the cerebellum appears most frequently, which indicates that the cerebellum plays a crucial role in the pathological changes of MDD. The changes in the cerebellum and default mode network (DMN), occipital lobe, and frontal lobe can also distinguish MDD from ordinary people. See Figure 4 and Table 2 for more details.

In this experiment, two *p*-values were selected for feature selection ($p < 0.01$ and $p < 0.05$). When $p < 0.05$, using SVM as a classifier can achieve a classification accuracy of 60.25. The classification ability of different levels of networks

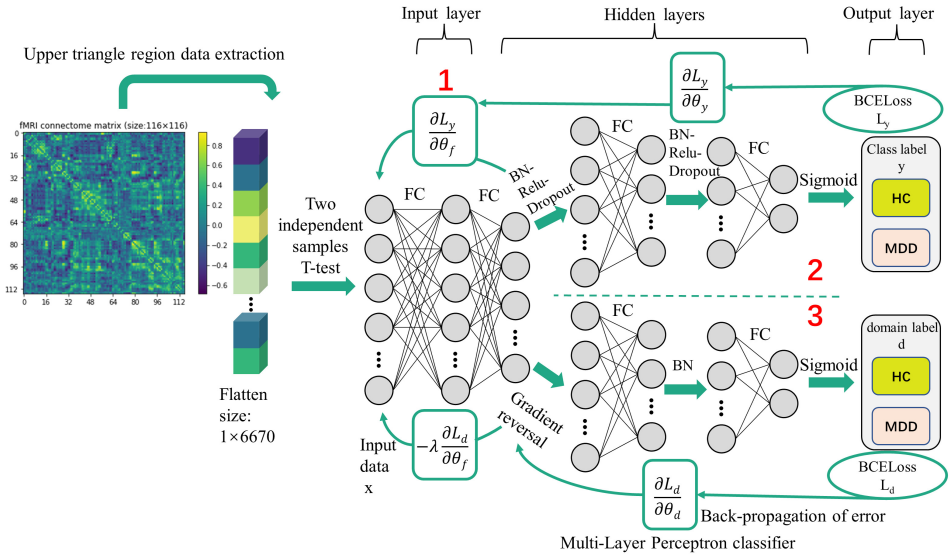

FIGURE 3
The domain-adversarial training of neural networks.

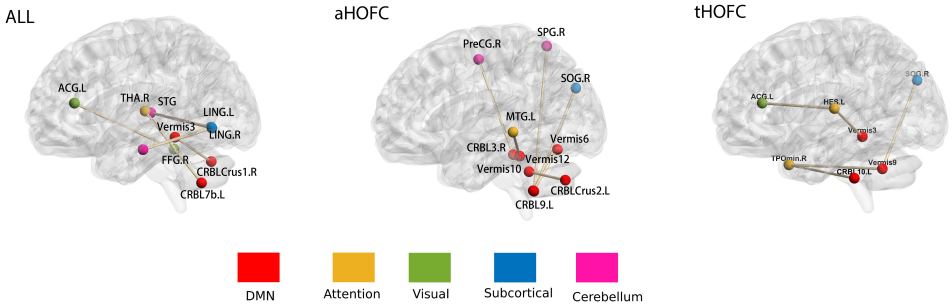

FIGURE 4
Features selected for networks. The whole brain was divided into six subnets marked with different colors: (1) DMN; (2) attention network; (3) visual network; (4) subcortical network; (5) cerebellum. The brain networks were visualized with the BrainNet Viewer (Xia et al., 2013); see **Table 2** for abbreviations of brain regions on the map.

TABLE 2 Features selected for networks.

Network	Functional connectivity
ALL	(ACG.L, FFG.R) (LING.L, STG.L)(LING.R, STG.L) (LING.L, STG.R) (THA.R, CRBL7b.L) (CRBLCrus1.R, Vermis3)
aHOFC	(PreCG.R, CRBL3.R) (SPG.R, CRBL9.R) (SOG.R, CRBL9.R) (MTG.L, Vermis12) (CRBL9.L, Vermis6) (CRBLCrus2.L, Vermis10)
tHOFC	(ACG.L, HES.L) (TPOmin.R, CRBL10.L) (HES.L, Vermis3) (SOG.R, Vermis9) (TPOmin.R, Vermis9)

R, right; L, left; ACG, anterior cingulate and paracingulate gyrus; FFG, fusiform gyrus; LING, lingual gyrus; STG, superior temporal gyrus; THA, thalamus; CRBLCrus1, cerebellum crus 1; PreCG, precentral gyrus; CRBL3, cerebellum superior 3; SPG, superior parietal gyrus; CRBL9, cerebellum inferior 9; SOG, superior occipital gyrus; MTG.L, middle temporal gyrus; CRBLCrus2, cerebellum crus 2;HES, Heschl gyrus; TPOmin, temporal pole, middle temporal gyrus; CRBL10, cerebellum inferior 10. ALL shows the features selected in each round of the three networks; aHOFC showed the unique features chosen in each round of the aHOFC; tHOFC showed the unique features selected in each round of the tHOFC.

is LOFC > HOFC ($P < 0.05$). The test results in Figure 5 show no statistical difference between the classification efficiency of LOFC and the combined networks ($P > 0.05$), indicating that the other two networks do not increase the classification ability. The classification results are similar based on aHOFC and tHOFC networks, but both are worse than multi-layer network classification. The choice of classifier (SVM or DANN) does no effect accuracy. During feature selection, p-value selection (0.01 or 0.05) has no effect on classification results. When the classifier is SVM, and feature selection is $p < 0.05$, the classification effect is better than that of DANN ($p < 0.01$). Epoch's best results are generally higher than the best test results, which suggests that we still need to find the best time to stop searching for the optimal solution during training. See Figure 5 and Table 3 for detailed results.

4. Discussion

To the best of our knowledge, this is the first time to use deep learning technology to realize MDD automatic classification in combination with a multi-layer network (Rahaman et al., 2020;

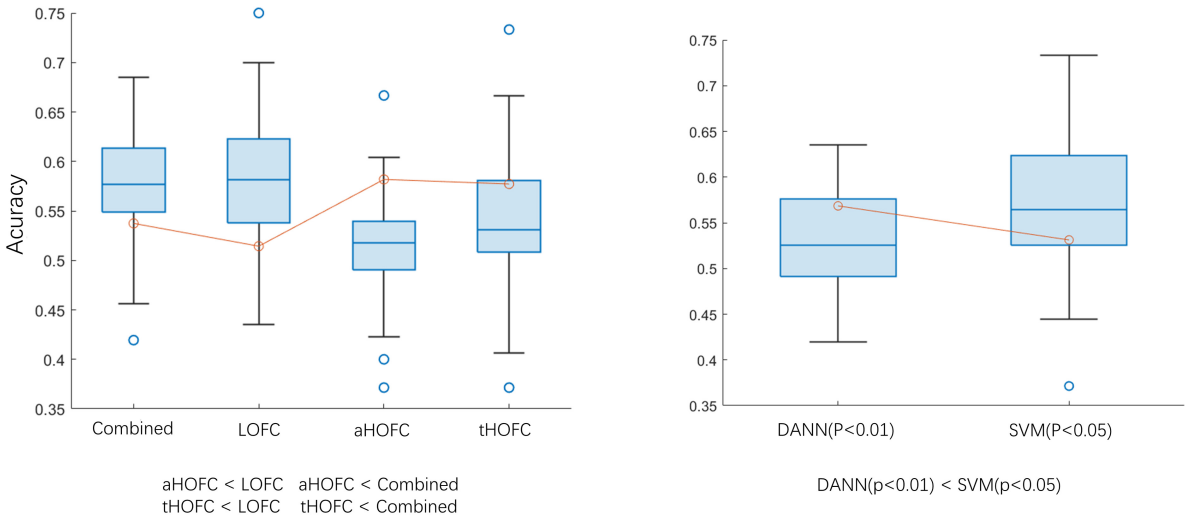

FIGURE 5
Classification accuracy comparison. aHOFC: all classification results based on aHOFC; tHOFC: all classification results based on tHOFC; LOFC: all classification results based on LOFC; Combined: classification result of three network features fusion. DANN ($p < 0.01$): using DANN as a classifier, the p-value of feature selection is 0.01; SVM ($p < 0.05$): using SVM as the classifier, the p-value of feature selection is 0.05. The inequalities represent statistical differences between the two groups of data.

TABLE 3 Average Classification accuracy.

	DANN (test)		SVM		DANN (best_test)	
	$p < 0.01$	$p < 0.05$	$p < 0.01$	$p < 0.05$	$p < 0.01$	$p < 0.05$
tHOFC	52.22 ± 3.77	53.64 ± 8.59	53.64 ± 4.47	55.44 ± 9.49	60.49 ± 6.91	60.12 ± 6.79
aHOFC	50.59 ± 4.68	52.89 ± 6.75	49.94 ± 5.09	52.33 ± 6.82	57.91 ± 5.77	60.53 ± 5.24
LOFC	55.66 ± 5.89	57.83 ± 5.28	59.00 ± 7.26	60.25 ± 5.86	63.86 ± 6.84	62.49 ± 7.74
Combined	54.02 ± 7.29	58.36 ± 3.27	59.14 ± 3.07	59.38 ± 5.28	60.62 ± 7.50	61.93 ± 7.95

DANN (test): classification result of domain-adversarial training of neural networks when the training accuracy is the highest. SVM, support vector machine; DANN (best_test), the highest accuracy with each epoch using domain-adversarial training of neural networks; combined, connect the features selected by the three networks and then classify; Unit is the percentage (%).

Zhang et al., 2021; Chen et al., 2022). The results show that the classification performance of low-order networks is higher than that of high-order networks. The aHOFC and tHOFC can provide new information for LOFC, but integration cannot improve classification performance.

Studies have shown that tHOFC (Zhang et al., 2016) and aHOFC (Zhang et al., 2017) are beneficial supplements to LOFC. This study proves this again. For example, we found that the cerebellar-cingulate gyrus is the most discriminative feature in the aHOFC network, which may reflect the disorder of the cerebellar-cortical-limbic circuit in MDD patients, leading to emotional and cognitive impairment. This result is consistent with previous studies (Lai and Wu, 2014). However, this FC does not appear in the LOFC network, which indicates that HOFC can provide other important information for LOFC.

We combine multiple networks at different levels for classification, but the classification ability of integrated features is similar to that of individual parts. It is possible that the simplicity of the feature fusion method is the cause of this issue. Future research needs to design more sophisticated ways to fuse features, stimulating the advantages of multi-level network features and improving classification performance. Previous studies have found that the classification efficiency of HOFC is higher than that of LOFC (Yan et al., 2019). However, these results did not appear in this study. The following reasons may cause this: (1) The sample size is different. This experiment is based on multicenter large data samples and is tested separately on an independent test set. Previous studies were based on small samples; and (2) Different disease types. This study is to classify MDD, and prior studies have classified Alzheimer's disease (AD). Although they are both mental diseases and may have some common pathological features, the two conditions differ. The results of AD may not be generalized to MDD. It also suggests that future research should develop more robust and generalized network models to classify neuropsychiatric diseases.

The classification accuracy of this study is low, and most of the classification accuracy is below 60%. There are two main reasons for this situation: (1) To ensure our conclusions' robustness and the classifier's generalization, we use big data from 10 sites. Different machine models, scanning parameters, and equipment status will reduce the accuracy of multi-site data classification. Therefore, the low accuracy is also reasonable. (2) Our cross-validation method adopts LOSCV. We train the model by extracting data from other research groups and classifying brand-new data. Although this can ensure the classifier 's generalization, it reduces the accuracy of the results.

Another significant contribution of this study was selecting FCs that genuinely represent the pathological changes of MDD. Our results indicated that the FC changes between the cerebellum and occipital lobe were the most distinguishing features. Studies have shown that the MDD group demonstrated decreased cerebellar–cerebral FC with the prefrontal lobe and DMN and increased FC with visual recognition network (lingual gyrus, middle occipital gyrus, and fusiform) (Guo et al., 2013). This enhancement has been typically viewed as either a compensatory reallocation (Cabeza et al., 2002; Grady et al., 2005) or dedifferentiation (Logan et al., 2002) which the increased FC between the cerebellum and the visual recognition network may compensate for the decrease in the cerebellar–cerebral FC (Liu et al., 2012). Our results indicated that the FC alteration was likely to be used to identify MDD.

This study has many limitations. First, we chose MLP as the classifier. Since we use network data, the recently emerged graph neural network is suitable for processing such data. Future research should use more robust models for MDD classification. Secondly, we only used fMRI data in this study. Clinical features and gene information are also crucial for the classification of MDD. Future research should integrate these data into the classification framework to improve accuracy. Thirdly, there is no difference between the classification results of SVM and MLP. This may be because our sample size is not large compared with the database like ImageNet. As the sample size gradually increases, DP will become more and more competent for this classification in the future.

5. Conclusion

This study wants to know whether the integration of three different levels of networks can improve the performance of MDD intelligent diagnosis. Experimental results show that combining different layers of networks cannot improve classification accuracy, but higher-order networks can provide new features for classification.

Data availability statement

The datasets presented in this study can be found in online repositories. The names of the repository/repositories and accession number(s) can be found below: http://rfmri.org/REST-meta-MDD.

Ethics statement

The studies involving human participants were reviewed and approved by http://rfmri.org/REST-meta-MDD. The patients/participants provided their written informed consent to participate in this study.

Author contributions

FL completed the theoretical research, technical method design, and manuscript revision. DL and MZ completed the technical method design, experiment and analysis, and the writing and revision of the manuscript. FC, JY, and QZ conducted research guidance, technical method demonstration, and manuscript review. All authors contributed to the article and approved the submitted version.

Funding

This work was funded by the general research program of the Health Commission of Zhejiang Province (2023KY596) and the Zhejiang Natural Science Foundation (LSY19A010001).

Acknowledgments

We would like to thank everyone who participated in the studies.

Conflict of interest

The authors declare that the research was conducted in the absence of any commercial or financial relationships that could be construed as a potential conflict of interest.

Publisher's note

References

Bassett, D., and Bullmore, E. (2006). Small-world brain networks. *Neuroscientist* 12, 512–523. doi: 10.1177/1073858406293182

Cabeza, R., Anderson, N., Locantore, J., and McIntosh, A. (2002). Aging gracefully: compensatory brain activity in high-performing older adults. *Neuroimage* 17, 1394–1402. doi: 10.1006/nimg.2002.1280

Chen, H., Li, C., Wang, G., Li, X., Rahaman, M., Sun, H., et al. (2022). GasHis-transformer: a multi-scale visual transformer approach for gastric histopathological image detection. *Pattern Recognit.* 130:108827. doi: 10.1016/j.patcog.2022.108827

Cotter, D., Mackay, D., Landau, S., Kerwin, R., and Everall, I. (2001). Reduced glial cell density and neuronal size in the anterior cingulate cortex in major

depressive disorder. *Arch. Gen. Psychiatry.* 58, 545–553. doi: 10.1001/archpsyc.58.6.545

Fields, R., Woo, D., and Basser, P. (2015). Glial regulation of the neuronal connectome through local and long-distant communication. *Neuron* 86, 374–386. doi: 10.1016/j.neuron.2015.01.014

Gao, S., Calhoun, V., and Sui, J. (2018). Machine learning in major depression: from classification to treatment outcome prediction. *CNS Neurosci. Ther.* 24, 1037–1052. doi: 10.1111/cns.13048

Grady, C., McIntosh, A., and Craik, F. (2005). Task-related activity in prefrontal cortex and its relation to recognition memory performance in young and old adults. *Neuropsychologia* 43, 1466–1481. doi: 10.1016/j.neuropsychologia.2004.12.016

Guo, W., Liu, F., Xue, Z., Gao, K., Liu, Z., Xiao, C., et al. (2013). Abnormal resting-state cerebellar-cerebral functional connectivity in treatment-resistant depression and treatment sensitive depression. *Prog. Neuropsychopharmacol. Biol. Psychiatry* 44, 51–57. doi: 10.1016/j.pnpbp.2013.01.010

Kahali, S., Raichle, M., and Yablonskiy, D. (2021). The role of the human brain neuron-glia-synapse composition in forming resting-state functional connectivity networks. *Brain Sci.* 11:1565. doi: 10.3390/brainsci11121565

Keller, A., Leikauf, J., Holt-Gosselin, B., Staveland, B., and Williams, L. (2019). Paying attention to attention in depression. *Transl. Psychiatry* 9:279. doi: 10.1038/s41398-019-0616-1

Lai, C., and Wu, Y. (2014). Decreased inter-hemispheric connectivity in anterior sub-network of default mode network and cerebellum: significant findings in major depressive disorder. *Int. J. Neuropsychopharmacol.* 17, 1935–1942. doi: 10.1017/S1461145714000947

Liu, L., Zeng, L., Li, Y., Ma, Q., Li, B., Shen, H., et al. (2012). Altered cerebellar functional connectivity with intrinsic connectivity networks in adults with major depressive disorder. *PLoS One* 7:e39516. doi: 10.1371/journal.pone.0039516

Logan, J., Sanders, A., Snyder, A., Morris, J., and Buckner, R. (2002). Under-recruitment and nonselective recruitment: dissociable neural mechanisms associated with aging. *Neuron* 33, 827–840. doi: 10.1016/S0896-6273(02)00612-8

Long, D., Liu, Y., Chen, Z., Xie, J., Shi, L., and Luo, C. (2022). The effect analysis of atlas and global signal regression in classification based on brain network for major depression disorders. *J. Imaging Sci. Technol.ogy* 66, 1–9. doi: 10.2352/J.ImagingSci.Technol.2022.66.4.040413

Long, D., Wang, J., Xuan, M., Gu, Q., Xu, X., Kong, D., et al. (2012). Automatic classification of early Parkinson's disease with multi-modal MR imaging. *PLoS One* 7:e47714. doi: 10.1371/journal.pone.0047714

O'Leary, L., and Mechawar, N. (2021). Implication of cerebral astrocytes in major depression: a review of fine neuroanatomical evidence in humans. *Glia* 69, 2077–2099. doi: 10.1002/glia.23994

Pannasch, U., Vargov, L., Reingruber, J., Ezan, P., Holcman, D., Giaume, C., et al. (2011). Astroglial networks scale synaptic activity and plasticity. *Proc. Natl. Acad. Sci. U.S.A.* 108, 8467–8472. doi: 10.1073/pnas.1016650108

Rahaman, M., Li, C., Yao, Y., Kulwa, F., Rahman, M., Wang, Q., et al. (2020). Identification of COVID-19 samples from chest X-Ray images using deep learning: a comparison of transfer learning approaches. *J. Xray Sci. Technol.* 28, 821–839. doi: 10.3233/XST-200715

Tzourio-Mazoyer, N., Landeau, B., Papathanassiou, D., Crivello, F., Etard, O., Delcroix, N., et al. (2002). Automated anatomical labeling of activations in SPM using a macroscopic anatomical parcellation of the MNI MRI single-subject brain. *Neuroimage* 15, 273–289. doi: 10.1006/nimg.2001.0978

Xia, M., Wang, J., and He, Y. (2013). BrainNet Viewer: a network visualization tool for human brain connectomics. *PLoS One* 8:e68910. doi: 10.1371/journal.pone.0068910

Yan, C., Chen, X., Li, L., Castellanos, F., Bai, T., Bo, Q., et al. (2019). Reduced default mode network functional connectivity in patients with recurrent major depressive disorder. *Proc. Natl. Acad. Sci. U.S.A.* 116, 9078–9083. doi: 10.1073/pnas.1900390116

Zhang, H., Chen, X., Shi, F., Li, G., Kim, M., Giannakopoulos, P., et al. (2016). Topographical information-based high-order functional connectivity and its application in abnormality detection for mild cognitive impairment. *J. Alzheimers Dis.* 54, 1095–1112. doi: 10.3233/JAD-160092

Zhang, H., Giannakopoulos, P., Haller, S., Lee, S., Qiu, S., and Shen, D. (2019). Inter-network high-order functional connectivity (IN-HOFC) and its alteration in patients with mild cognitive impairment. *Neuroinformatics* 17, 547–561. doi: 10.1007/s12021-018-9413-x

Zhang, J., Li, C., Kosov, S., Grzegorzek, M., Shirahama, K., Jiang, T., et al. (2021). LCU-net: a novel low-cost u-net for environmental microorganism image segmentation. *Pattern Recognit.* 115:107885. doi: 10.1016/j.patcog.2021.107885

Zhang, Y., Zhang, H., Chen, X., Lee, S., and Shen, D. (2017). Hybrid high-order functional connectivity networks using resting-state functional MRI for mild cognitive impairment diagnosis. *Sci. Rep.* 7:6530. doi: 10.1038/s41598-017-06509-0

Zhou, Z., Chen, X., Zhang, Y., Hu, D., Qiao, L., Yu, R., et al. (2020). A toolbox for brain network construction and classification (BrainNetClass). *Hum. Brain Mapp.* 41, 2808–2826. doi: 10.1002/hbm.24979

frontiers | Frontiers in Neuroscience

TYPE Original Research
PUBLISHED 16 March 2023
DOI 10.3389/fnins.2023.1116111

OPEN ACCESS

EDITED BY
Ye Wu,
Nanjing University of Science and Technology, China

REVIEWED BY
Hua-Jun Chen,
Fujian Medical University, China
Xiaoming Liu,
Huazhong University of Science and Technology, China
Qingrun Zeng,
Zhejiang University of Technology, China

*CORRESPONDENCE
Shanhong Mao
✉ maosh@ccmu.edu.cn
Chunlin Li
✉ lichunlin1981@163.com

SPECIALTY SECTION
This article was submitted to Brain Imaging Methods, a section of the journal Frontiers in Neuroscience

RECEIVED 05 December 2022
ACCEPTED 28 February 2023
PUBLISHED 16 March 2023

CITATION
Cao Y, Si Q, Tong R, Zhang X, Li C and Mao S (2023) Abnormal dynamic functional connectivity changes correlated with non-motor symptoms of Parkinson's disease. *Front. Neurosci.* 17:1116111. doi: 10.3389/fnins.2023.1116111

Abnormal dynamic functional connectivity changes correlated with non-motor symptoms of Parkinson's disease

Yuanyan Cao[1,2,3], Qian Si[4], Renjie Tong[1,2,3], Xu Zhang[1,2,3], Chunlin Li[1,2,3]* and Shanhong Mao[1,2,3]*

[1]School of Biomedical Engineering, Capital Medical University, Beijing, China, [2]Beijing Advanced Innovation Center for Big Data-Based Precision Medicine, Beijing, China, [3]Beijing Key Laboratory of Fundamental Research on Biomechanics in Clinical Application, Capital Medical University, Beijing, China, [4]School of Cyber Science and Technology, Beihang University, Beijing, China

Background: Non-motor symptoms are common in Parkinson's disease (PD) patients, decreasing quality of life and having no specific treatments. This research investigates dynamic functional connectivity (FC) changes during PD duration and its correlations with non-motor symptoms.

Methods: Twenty PD patients and 19 healthy controls (HC) from PPMI dataset were collected and used in this study. Independent component analysis (ICA) was performed to select significant components from the entire brain. Components were grouped into seven resting-state intrinsic networks. Static and dynamic FC changes during resting-state functional magnetic resonance imaging (fMRI) were calculated based on selected components and resting state networks (RSN).

Results: Static FC analysis results showed that there was no difference between PD-baseline (PD-BL) and HC group. Network averaged connection between frontoparietal network and sensorimotor network (SMN) of PD-follow up (PD-FU) was lower than PD-BL. Dynamic FC analysis results suggested four distinct states, and each state's temporal characteristics, such as fractional windows and mean dwell time, were calculated. The state 2 of our study showed positive coupling within and between SMN and visual network, while the state 3 showed hypo-coupling through all RSN. The fractional windows and mean dwell time of PD-FU state 2 (positive coupling state) were statistically lower than PD-BL. Fractional windows and mean dwell time of PD-FU state 3 (hypo-coupling state) were statistically higher than PD-BL. Outcome scales in Parkinson's disease–autonomic dysfunction scores of PD-FU positively correlated with mean dwell time of state 3 of PD-FU.

Conclusion: Overall, our finding indicated that PD-FU patients spent more time in hypo-coupling state than PD-BL. The increase of hypo-coupling state and decrease of positive coupling state might correlate with the worsening of non-motor symptoms in PD patients. Dynamic FC analysis of resting-state fMRI can be used as monitoring tool for PD progression.

KEYWORDS

Parkinson's disease, dynamic functional connectivity, independent component analysis (ICA), static functional connectivity, non-motor symptoms

1. Introduction

There were 6.1 million Parkinson's disease (PD) patients worldwide in 2016 (GBD 2016 Neurology Collaborators, 2018). PD progresses continuously over time, mainly affecting older people (Poewe et al., 2017). Motor symptoms, such as tremors, akinesia, and rigidity, are the main symptoms of PD, impacting a patient's ability to perform routine tasks and increasing the health care burden (GBD 2016 Neurology Collaborators, 2018). The occurrence of non-motor symptoms, such as cognitive impairment, depression, autonomic dysfunction and sleep disorders, progresses over time, resulting in deteriorating quality of life (Khoo et al., 2013; Diederich et al., 2020; Bloem et al., 2021). Occurrence of non-motor symptoms may earlier than motor symptoms, even in prodromal stage. Non-motor symptoms of PD may be used as early diagnosing biomarkers. Dopamine supplements and dopamine transporter agonists are commonly used treatments for PD that relieve motor symptoms. Treatments for PD non-motor symptoms were similar to those used for the general population (Armstrong and Okun, 2020; Vijiaratnam et al., 2021).

There are many ways to explore PD mechanisms. Functional magnetic resonance imaging (fMRI) is a non-invasive method to reveal brain activity by detecting blood oxygen level-dependent (BOLD) signals (Wu and Hallett, 2005; Smith et al., 2013a,b; Barkhof et al., 2014). The functional connectivity (FC) method measures correlations between time courses of regions of interest (ROIs) using Pearson correlation analysis (Shahhosseini and Miranda, 2022). FC analysis revealed that intrinsic networks existed in the brain (Allen et al., 2014) and was also used to explore the PD mechanism (Schindlbeck and Eidelberg, 2018; Ryman and Poston, 2020). FC within the motor network was correlated with the severity of PD motor symptoms (Chung et al., 2020). FC between the left amygdala and thalamus was increased in PD patients with depression compared to PD patients without depression (Hu et al., 2015). Anxiety severity of PD was positively correlated with their FC between the amygdala and superior parietal lobule (Zhang et al., 2019).

Unlike static FC analysis, dynamic FC analysis focuses on FC variability over time (Calhoun et al., 2014). Dynamic FC analysis was more sensitive and revealed more detailed information than static FC analysis (Du et al., 2017). The sliding window method is the most commonly used method for dynamic FC analysis, and a 30–60 s window size is appropriate, according to Allen et al. (2014). The FC matrix of each window can be grouped into different clusters, also known as states. Changes in temporal characteristics revealed PD mechanisms (Kim et al., 2017), and PD subjects with rapid eye movement (REM) sleep behavior disorder (RBD) spent more time in the state characterized by weaker positive coupling between the visual and default networks, and default and basal ganglia networks (Gan et al., 2021). PD patients with dementia spend increased time in a state with positive coupling within networks (Fiorenzato et al., 2019), while PD patients with mild cognitive impairment showed decreased connectivity between networks, especially between the sensorimotor and cognitive control networks (Díez-Cirarda et al., 2018). Compared with seed-based analysis, independent component analysis (ICA) reduces noise signals (Calhoun et al., 2001). Voxels in independent components were characterized by similar time courses and spatial distributions (Esposito et al., 2002).

Progressive dynamic FC changes during PD duration have rarely been studied. Non-motor symptoms of PD may occur before motor symptoms, and have potential to be early diagnosing biomarker. Non-motor symptoms exist through whole disease duration and become severer, which lead the potential to be progression biomarker of PD (Tolosa et al., 2021). So, it is important to explore the mechanisms of non-motor symptoms. fMRI method focused on fluctuations in the blood oxygen level dependent (BOLD) signal of different brain areas (Lee et al., 2013). fMRI was widely used in neuroscience studies (Smith et al., 2013a,b; Raimondo et al., 2021) and provided insight into the mechanism and diagnosis of PD (Tessitore et al., 2019; Wolters et al., 2019; De Micco et al., 2021).

Static FC and dynamic functional signal changes reflected brain activities. Correlations between functional changes in the brain and non-motor dysfunctions remain unclear. We hypothesize that the progression of non-motor symptoms may be associated with static FC changes and temporal characteristic dynamic FC changes. We utilized long term data of patients from PPMI dataset to address above questions. Static and dynamic FC between and within intrinsic networks were analyzed to determine static and dynamic FC changes during disease duration and correlations between FC changes and non-motor dysfunctions.

2. Materials and methods

2.1. Participants

Data used in the preparation of this article were obtained from the Parkinson's Progression Markers Initiative (PPMI) database,[1] which is a multicenter international study. For currently updated information on this study visit.[2] All data used in our study were downloaded before January 2021. For detailed inclusion criteria of the PPMI dataset, please visit (see text footnote 2).

A total of 101 PD patients scanned fMRI were recruited in PPMI dataset. We selected patients with below inclusion criteria to our study: (1) visited for at least 4 years; (2) scanned fMRI at baseline (PD-BL) and followed-up (PD-FU); (3) older than 50 years old, as pathogenesis of late-onset PD and early onset PD is different (Schrag and Schott, 2006; Fereshtehnejad and Posteuma, 2017) and this study focused on late-onset PD. We focused on the late-onset PD, because late-onset PD population was larger than early onset PD patients. Late- and early onset PD were separated in many studies (Rango et al., 2021; Sigirli et al., 2021). The patients with low image quality or diagnosed with other diseases, such as Alzheimer's disease, multiple system

1 https://www.ppmi-info.org/access-data-specimens/download-data

2 www.ppmi-info.org

atrophy, dementia with Lewy bodies, during visiting period were excluded from this study. Imaging data and information of Healthy control (HC) subjects were also downloaded from PPMI dataset, who were scanned fMRI. In total, data of 20 PD patients and 19 healthy control subjects were utilized in our study.

2.2. Neuropsychological and clinical assessments

The disease severity of PD patients was assessed using the Movement Disorder Society Unified Parkinson Disease Rating Scale (MDS-UPDRS) (Goetz et al., 2008), Part I of the UPDRS was used to evaluate non-motor symptoms of PD, and parts II and III evaluated motor symptoms. Total UPDRS was sum of part I-IV. Hoehn and Yahr (H and Y) staging (Hoehn and Yahr, 2001) were used to assess severity of PD. The UPDRS-III and H and Y staging scores used in this study were assessed at "ON" state, which was defined as the last dose of levodopa or dopamine agonist were taken <6 h before assessment. The "OFF" state meant the last dose of levodopa or dopamine agonist were taken ≥6 h before assessment. The drug treatment dosage was calculated as the levodopa-equivalent daily dose (LEDD) (Tomlinson et al., 2010). Patients' cognitive states were assessed using the Montreal Cognitive Assessment (MoCA) scale, Benton Judgment of Line Orientation Score (BJLOT), Letter Number Sequencing Score (LNS), Semantic Fluency Total Score (SFT), Symbol Digit Modalities Score (SDM), and Hopkins Verbal Learning Test–Revised (HVLT) scales. The total SFT score and subtest such as animal, fruit and vegetable scores were calculated in this study. HVLT contains several aspects, such as discrimination scores, immediate/recall scores, retention score, false alarms, delayed recall and delayed recognition. The ability of daily living (ADL) scale was used to evaluate life quality. Depression and anxiety were assessed by the Geriatric Depression Scale (GDS) score and State-Trait Anxiety Inventory (STAI). The University of Pennsylvania Smell Identification Test (UPSIT) was used to evaluate olfactory nerve dysfunction. Sleepiness quality and rapid eye movement (REM) sleep were assessed by the Epworth Sleepiness Scale (ESS) score and REM Sleep Behavior Disorder Questionnaire score. Autonomic function was assessed by the Scales for Outcomes in Parkinson's Disease-Autonomic dysfunction (SCOPA-AUT).

2.3. MRI acquisition

T1 MRI and rs-fMRI data were collected on Prisma fit 3-tesla Siemens MR scanner (Siemens, Erlangen, Germany). All participants were requested to remain calm and not think during scanning. T1 MRI data were acquired with the following parameters: repetition time (TR) = 2,300 ms, echo time = 3.0 ms, flip angle = 9°, matrix size = 176 × 240 × 170, and voxel size = 1 mm × 1 mm × 1 mm. The rs-fMRI data, consisting of 210 volumes per patient, were acquired with TR = 2.4 s, echo time = 25 ms, flip angle = 80°, matrix size = 68 × 66 × 40, and voxel size = 3.3 mm × 3.3 mm × 3 mm.

2.4. MRI data processing

The preprocessing of the fMRI data was conducted using the functional connectivity (CONN) toolbox (Whitfield-Gabrieli and Nieto-Castanon, 2012),[3] based on MATLAB (R2018a, MathWorks, Inc., Natick, MA, USA). The first ten scans were removed to maintain the stability of fMRI data. Thus, each participant provided 200 volumes for further analysis.

A slice-timing correction step was performed to correct the image acquisition time between slices. The fMRI data were realigned to the first volume to correct for head movement and then co-registered to the T1 MRI data using an affine transformation. The T1 MRI data were normalized to standard Montreal Neurological Institute (MNI) space and segmented into gray matter, white matter, and cerebrospinal fluid using the tissue probability maps. A non-linear transformation was applied to the functional data with the same parameters as the T1 MRI data. The functional data were smoothed with a Gaussian kernel of 6 mm full width half maximum, to reduce the noise signal.

2.5. ICA analysis

Independent component analysis (ICA) grouping was performed to obtain specific data components using Group ICA of the functional MRI Toolbox (GIFT v4.0 c).[4] Voxel-level variance normalization was performed on all data. The number of independent components was estimated using a minimum description length approach. Functional data were decomposed using two data reduction steps (subject-specific and group-level PCA). The Infomax method was used to calculate independent components, and the ICASSO method implemented in GIFT was used to maintain reliability.

ICASSO was run 100 times, and 80% similarity was selected. Significant components from all independent components were chosen according to the location of the peak coordinate and time course characteristics (Allen et al., 2014; Kim et al., 2017). The selected components were identified as seven resting state networks (RSN): the default modal network (DMN), attention network (ATT), basal ganglia network (BG), visual network (VIS), sensorimotor network (SMN), auditory network (AUD), and frontoparietal network (FP) (Yeo et al., 2011).

2.6. Static functional connectivity analysis

The time courses of the selected components were extracted. Correlations between every pair of selected components formed the subject-specific static FC matrix. Static FC group comparisons were calculated among HC, PD-BL, and PD-FU using the multivariate analysis of covariance (MANCOVA) toolbox contained in GIFT with a corrected false discovery rate (FDR). *Post hoc* analyses were performed between HC and PD-BL and between PD-BL and PD-FU.

3 https://web.conn-toolbox.org/

4 https://trendscenter.org/software/gift

2.7. Dynamic functional connectivity analysis

Dynamic FC analysis was conducted using the dynamic functional network connectivity toolbox (dFNC) contained in the GIFT toolbox. The time courses of selected components were linear detrended and 3D-despiked. The time courses were also filtered using a low-pass filter with a cutoff of 0.15 Hz, as recommended in the GIFT manual.

A sliding window approach was used to analyze dynamic functional connectivity changes. The sliding window method is the most commonly used method for dynamic FC analysis, and a 30-60 s window size is appropriate, according to previous studies (Allen et al., 2014; Kim et al., 2017). The sliding window size was set to 22 TR (52.8 s) and the step was set to 1 TR (2.4 s), based on previous research (Allen et al., 2014; Kim et al., 2017). As a result, each participant had 178 windows across the entire scan. Correlations between the time course of each selected component pair in each window formed dynamic FC matrices. The K-means clustering method was performed to sort all dynamic FC matrices into different clusters, also known as states. A penalty on the L1 norm was imposed with 100 repetitions, and the elbow method was used to decide the clustering number.

Temporal properties of the dynamic FC analysis, such as fractional windows, mean dwell times, and numbers of transitions, were calculated for further statistical analysis. The fractional window is the proportion of time spent in each state, and the mean dwell time is the average time spent by each participant in each state. The number of transitions is calculated as the number of times switching between states.

2.8. Statistical analysis

Group differences in general information between the HC and PD groups, such as age, gender, years of education, and clinical assessments, were calculated using the two-sample *t*-test and the chi-square test. Differences in temporal properties among HC and PD subgroups were calculated using two sample *t*-test or rank sum test. Statistical differences of clinical assessments and temporal properties between PD-BL and PD-FU were tested using paired *t*-test or Wilcoxon signed rank test. Selecting *t*-test or non-parametric test was depended on the result of normality test. Correlations between temporal properties and clinical assessment scores were analyzed using partial correlation analysis, which controlled effect of age, sex, and education years. Above statistical analysis was performed in SPSS Statistics 22.0 (IBM Corporation, Armonk, NY, USA), and the threshold for statistical significance was $p < 0.05$. Multiple comparisons of *p*-values were corrected with FDR correction.

3. Results

3.1. Demographics

Twenty PD patients (13 male and 7 female) and 19 healthy subjects (15 male and 4 female) met the inclusion and exclusion criteria described in (Section "2.1. Participants"). There were no significant differences in age and gender between the PD and HC groups. The years of education of the PD group were statistically shorter than those of the HC group. After years of follow-up, the H and Y stage (ON state) of the PD group increased. The LEDD of PD-FU was significantly higher than PD-BL. These results indicated that the severity of PD increased after years of follow-up. The UPDRS-I scores of PD-FU increased compared to PD-BL. The HVLT-False alarms and SDM scores of PD-FU were smaller than HC group. The SCOPA-AUT scores of PD-FU were bigger than HC group. The UPSIT scores of PD-BL were smaller than HC group. Above results indicated that the non-motor symptoms of PD patients were worsen after years of follow-up. Other clinical assessments, such as UPDRS-III (ON state), total UPDRS, MoCA, BJLOT, ESS, GDS, SFT, and STAI scores, did not significantly change between PD-BL and PD-FU. Details of these results are shown in **Table 1**.

3.2. ICA components and RSN

The minimum description length approach estimated an average of 47 components. Sixty independent components were selected for greater accuracy. Twenty-nine components were identified as meaningful according to the selection criteria described in (Section "2.5. ICA analysis"), and the selected components were grouped into seven resting-state intrinsic networks. The selected components and networks are shown in **Figure 1**.

3.3. Static FC analysis results

We performed two steps analysis to reveal static FC changes of PD in different stages. Static FC differences between the HC and PD-BL group were calculated with age, sex and education years as covariates, using two sample *t*-test. The difference between HC and PD-BL did not survive the FDR correction, which was used for multiple *p*-value correction. Differences between PD-BL and PD-FU were calculated using paired *t*-test, with FDR correction method to correct *p*-values. Results showed that network averaged connections between FP and SMN of PD-FU were lower than PD-BL ($p < 0.05$, $t = -3.64$) (**Figure 2**).

3.4. Dynamic FC analysis

All dynamic FC matrices are clustered into four states according to the elbow method. 19% of the matrices clustered into state 1, characterizing positive coupling within the VIS network. State 2 contained 22% of the matrices, which characterized positive coupling within SMN, within VIS, between SMN and VIS, between DMN and SMN, and between DMN and VIS. State 3 had 56% of the matrices, showing hypo-coupling within and between all networks. State 4 was the smallest, with only 3% of matrices (**Figure 3**).

Temporal characteristics such as fractional windows, mean dwell time and transition number of HC group and PD

TABLE 1 Demographic information for the HC and PD subgroups.

				BL-HC		FU-BL		FU-HC	
	PD-BL (n = 20)	PD-Y3 (n = 20)	HC (n = 19)	P-value	T/Z value	P-value	T value	P-value	T value
Age (years)	64.35 ± 7.96	67.35 ± 8.0	62.84 ± 10.5	0.62	0.51	–	–	–	–
Gender (M: F)	13: 7	–	15: 4	0.33	0.94	–	–	–	–
Education years	13.4 ± 3.2	–	16.84 ± 2.54	**0.002**	−3.16	–	–	–	–
Disease duration (months)	4.99 ± 4.82	–	–	–	–	–	–	–	–
LEDD	215.65 ± 164.61	590.36 ± 229.67	–	–	–	<**0.001**	5.98	–	–
H and Y stage (ON)	1.37 ± 0.48	1.7 ± 0.47	–	–	–	**0.03**	2.18	–	–
ADL	90 ± 6.88	89.25 ± 5.68	–	–	–	0.51	−0.66	–	–
UPDRS-I	6.7 ± 5.17	8.15 ± 5.03	–	–	–	**0.03**	2.42	–	–
UPDRS-II (ON)	6.4 ± 4.59	7.65 ± 4.73	–	–	–	0.46	0.74	–	–
UPDRS-III (ON)	15.9 ± 9.83	18.1 ± 9.22	–	–	–	0.35	0.94	–	–
Total UPDRS (ON)	29.26 ± 15.38	33.9 ± 15.15	–	–	–	0.23	1.25	–	–
HVLT-immediate recall	26.05 ± 6.12	25.8 ± 5.91	25.89 ± 5.08	0.70	0.38	0.83	0.21	0.87	0.17
HVLT-delayed recall	9.1 ± 2.94	8.4 ± 3.42	8.21 ± 3.12	0.38	0.88	0.26	−1.13	0.91	0.11
HVLT-recognition	10.8 ± 2.73	11.2 ± 1.11	11.21 ± 1.03	0.68	0.42	0.85	−0.21	0.84	0.20
HVLT-false alarms	0.8 ± 0.95	0.6 ± 0.75	2.16 ± 2.17	0.06	−1.91	0.34	−1.10	**0.02**	−2.33
HVLT-discrimination	10 ± 2.92	10.6 ± 1.6	7.16 ± 5.52	0.11	1.58	0.76	−0.36	0.05	1.92
HVLT-retention	0.84 ± 0.2	0.8 ± 0.24	0.79 ± 0.23	0.55	0.60	0.38	−0.88	0.89	0.14
BJLOT	12.6 ± 1.93	13.3 ± 1.56	13.37 ± 1.8	0.14	−1.49	0.21	−1.27	0.73	−0.35
ESS	6.3 ± 4.35	6.95 ± 5.25	5.58 ± 3.31	0.84	0.2	0.36	0.92	0.59	0.54
GDS	1.9 ± 2.22	1.85 ± 2	0.95 ± 1.58	0.13	1.5	0.81	0.25	0.86	0.18
LNS	10.75 ± 1.97	10.15 ± 2.74	11.37 ± 2.29	0.47	−0.73	0.23	−1.2	0.14	−1.46
REM	3.45 ± 1.99	3.6 ± 2.21	2.76 ± 1.66	0.35	0.95	0.89	0.14	0.3	1.04
SCOPA-AUT	9.65 ± 6.77	10.5 ± 5.72	6.28 ± 3.84	0.09	1.7	0.34	0.95	**0.012**	2.51
SFT	50.35 ± 11.52	50.55 ± 10.77	48.16 ± 9.48	0.52	0.65	0.91	0.12	0.52	0.65
SFT-animal	23.25 ± 4.98	22.95 ± 6.03	20.89 ± 4.65	0.14	1.52	0.82	−0.23	0.39	1.06
SFT-fruit	13.8 ± 4.10	13.45 ± 3.86	14.11 ± 3.77	0.81	−0.24	0.67	−0.43	0.58	−0.55
SFT-vegetable	13.3 ± 4.66	14.15 ± 3.84	13.16 ± 3.88	0.92	0.1	0.3	1.07	0.38	0.88
STAI-state sub score	32.8 ± 8.76	31.75 ± 8.24	30.05 ± 8.19	0.34	0.96	0.65	−0.46	0.50	0.68
STAI-trait sub score	31.8 ± 8.48	31.3 ± 7.48	29.74 ± 8.93	0.38	0.89	0.92	−0.10	0.43	0.79
STAI total	64.6 ± 16.67	63.05 ± 14.7	59.79 ± 15.48	0.36	0.93	0.58	0.57	0.4	0.84
SDM	41.25 ± 9.44	38.2 ± 9.40	48.16 ± 10.12	**0.03**	−2.21	0.11	1.7	**0.003**	−3.19
MoCA	27.25 ± 2.34	27.4 ± 2.56	28.21 ± 1.13	0.3	−1.04	0.69	−0.4	0.61	−0.52
UPSIT	20.9 ± 8.79	–	33.58 ± 4.57	<**0.001**	−5.61	–	–	–	–

LEDD, levodopa-equivalent daily dose; H and Y, hoehn and yahr staging; ADL, ability of daily living; UPDRS, Movement Disorder Society Unified Parkinson Disease Rating Scale; BJLOT, Benton Judgment of Line Orientation Score; LNS, Letter Number Sequencing Score; REM, Rapid Eye Movement; SCOPA-AUT, Scales for Outcomes in Parkinson's Disease-Autonomic dysfunction; VLT, verbal learning test; SFT, Semantic Fluency Total Score; SDM, Symbol Digit Modalities Score; MoCA, Montreal Cognitive Assessment; GDS, geriatric depression scale score; STAI, State-Trait Anxiety Inventory; ESS, epworth sleepiness scale score; UPSIT, University of Pennsylvania Smell Identification Test. P-values of multiple comparison were correction with Bonferroni correction. The p-values which were smaller than 0.05 were written with bold.

subgroups were calculated. Age, sex, and education years may affect cognitive function. The effect of age, sex and education years were controlled when calculating difference between HC and PD-BL group. Results showed that there was no statistical difference between HC and PD-BL group of above temporal characteristics. Changes between PD-BL and PD-FU were performed sign rank test, because data wasn't normality distributed. The temporal properties analysis showed that the fractional windows and mean dwell time of PD-FU at state 2 were statistically lower than PD-BL. Fractional windows and mean dwell time of PD-FU at state 3 were statistically higher than PD-BL (Figure 4).

3.5. Correlation analysis

Correlations between clinical scale scores and measurements of rs-fMRI were computed. Clinical scales included UPDRS-I,

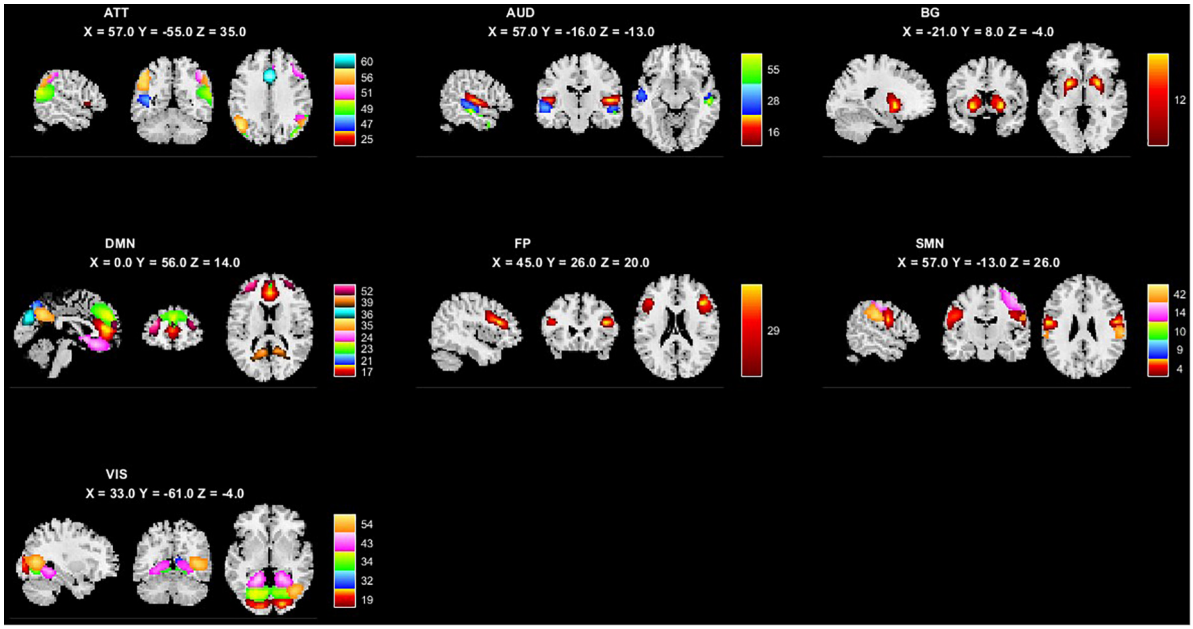

FIGURE 1
The 29 independent components and 7 networks identified by group ICA. Seven functional networks and 29 selected independent components are shown: ATT, attention network; AUD, auditory network; BG, basal ganglia network; DMN, default modal network; FP, frontoparietal network; SMN, sensorimotor network.

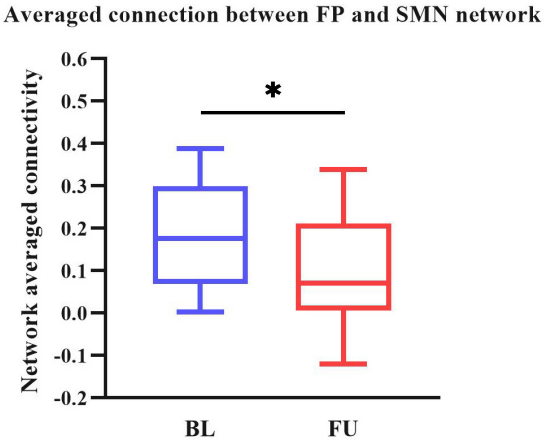

FIGURE 2
Averaged connection between FP and SMN network of PD-FU was lower than PD-BL. The *p*-value of comparison corrected using FDR correction (*: $p < 0.05$; $t = -3.64$). PD, Parkinson's disease; BL, baseline; FU, follow-up; FP, frontal parietal network; SMN, sensorimotor network.

UPDRS-II(ON), UPDRS-III(ON), SCOPA-AUT, and ADL. Rs-fMRI measures included static FC of brain areas, fractional window, mean dwell time and transition number. Age, sex and education years may affect correlation result of abovementioned score. The effect of age, sex, and education years were controlled as variances, using partial correlation method. Results showed that SCOPA-AUT scores positively correlated with the mean dwell time of state 3 of PD-FU (Figure 5). There was no correlation between clinical scores and temporal characteristics of PD-BL.

4. Discussion

The H and Y stages of the PD group increased after 3 years of follow-up in this study, while UPDRS-III scores (ON) did not change significantly after 3 years. As PD patients collected from PPMI dataset in this study accepted treatment, motor symptom changes were assessed by the UPDRS-III (ON). UPDRS-I and SCOPA-AUT scores of the PD group increased, and the SDM and ADL scores decreased after 3 years in our study. These results indicated that PD severity increased over time. The dopamine supplement treatment was collected as LEDD, which significantly increased after follow-up. Non-motor symptoms, such as autonomic dysfunction, progressed over time, even after long-term treatment in the present study. The UPDRS-III scores which were used to assess motor symptoms of PD, didn't significantly change. Our results indicate that dopamine supplement treatment was not effective enough to relieve all non-motor symptoms in this study.

Our result showed that network averaged connection between FP and SMN of PD-FU was lower than PD-BL. FP is associated with execution function. The decreased connection between FP to SMN in PD-FU may be associated with worsen of motor symptoms. While we didn't find statistical correlation between decrease of network connection and clinical assessment scores.

Results showed that PD-FU spent more time at state 3, which characterized as hypo-coupling between networks. PD-FU spent less time at state 2, which was characterized as positive coupling between networks. These results indicated that coupling between networks of PD-FU decreased and may converted to hypo-coupling state. The loss of coupling may associate with the worsen of PD. These results are consistent with those of Li et al. (2021), which showed that the fractional windows and mean dwell time of

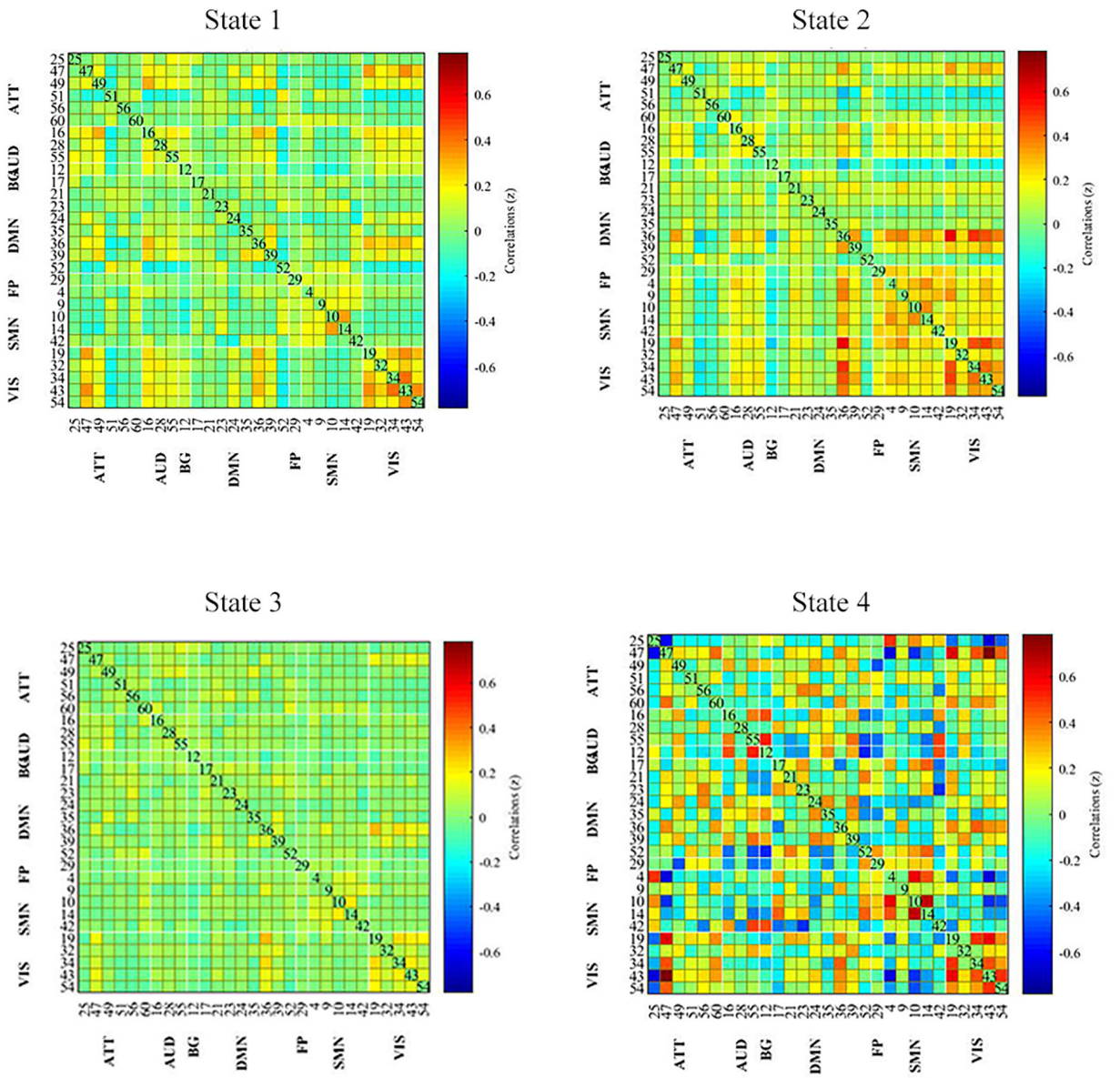

FIGURE 3
Dynamic functional connectivity state results. The dynamic FC matrices were clustered into 4 states. Averaged across subjects-specific median cluster of all participants were showed. Total occurrences for State 1-4 were 19, 22, 56, and 3%, respectively. ATT, attention network; AUD, auditory network; BG, basal ganglia network; DMN, default modal network; FP, frontoparietal network; SMN, sensorimotor network.

states that characterized positive correlations between FP and SMN decreased in PD compared to HC (Chen et al., 2021). In Li et al.'s (2021) study, the mean dwell time of the above ON state increased compared with the OFF state, indicating that dopamine depletion affects functional connectivity stability between FP and SMN (Chen et al., 2021).

Autonomic dysfunction was widespread in PD and occurred at an earlier stage. Autonomic dysfunction, such as gastrointestinal dysfunction in PD patients, was a risk factor for falling, with severe consequences (Kwon et al., 2021). The SCOPA-AUT scale was used in this study to assess autonomic dysfunctions. The autonomic functions of PD patients at FU were impaired in our study. The correlation results showed that the SCOPA-AUT scores of PD-FU positively correlated with the mean dwell time of state 3. Above results indicated that the increase of hypo-coupling state correlated with autonomic dysfunction. Our results in line with precious studies, which showed the correlation between functional connectivity of RSN and autonomic dysfunctions (Ashraf-Ganjouei et al., 2018; Dayan et al., 2018; Li et al., 2021; Nakano et al., 2021).

5. Limitations

There are some limitations to this work. Only 20 PD and 19 HC patients were collected from PPMI in this study. PD patients were only followed up for 3 years, which was much less than the entire length of PD duration. A larger scale and longer visiting period for the longitudinal study is needed in future studies. Most of the PD

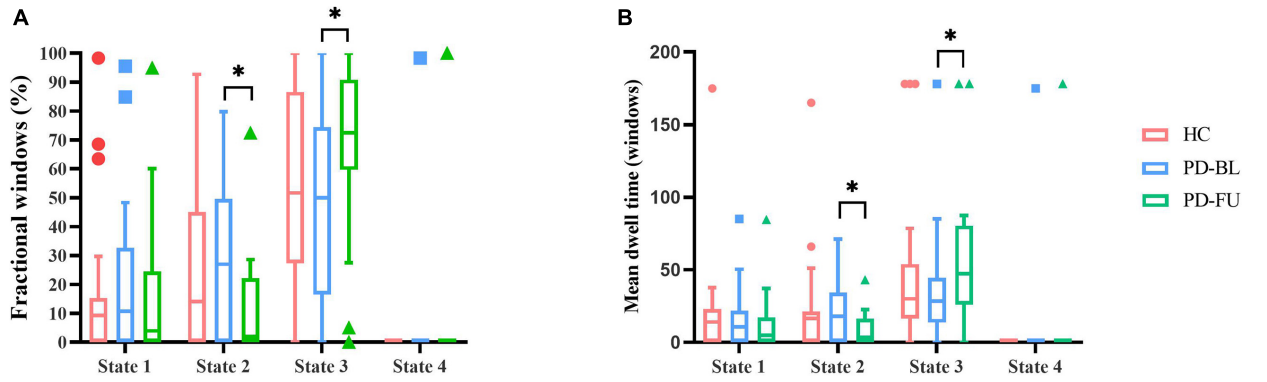

FIGURE 4
Results of temporal properties of dynamic functional state analysis. The median of fractional windows **(A)** and mean dwell time **(B)** of all subjects in each state are shown using a Tukey box plot. *: $p < 0.05$. PD, Parkinson's disease; BL, baseline; FU, follow-up; HC, healthy control.

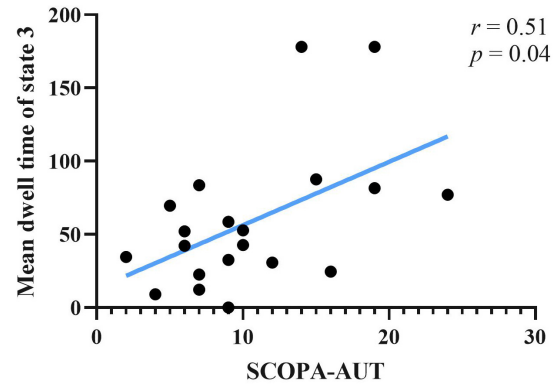

FIGURE 5
Correlation between SCOPA-AUT scores of PD-FU and mean dwell time of state 3. PD, Parkinson's disease; SCOPA-AUT, Scales for Outcomes in Parkinson's Disease-Autonomic dysfunction.

patients in the recent study received treatment, and the UPDRS-III scores of the OFF states were missing. PD patients did not undergo MRI scans before accepting any treatment. We cannot entirely remove the treatment effect. Although some studies revealed that dopamine treatment rarely affected non-motor symptoms, randomized controlled trials are needed in the future.

6. Conclusion

We found four distinct dynamic FC states in PD patients according to dynamic functional correlations within and between RSN. The state 2 of our study showed positive coupling within and between SMN and visual network, while the state 3 showed hypo-coupling through all RSN networks. Our finding indicated that PD-FU patients spent more time in hypo-coupling state (state 3) than PD-BL. The increase of hypo-coupling state and decrease of positive coupling state might correlate with the worsening of non-motor symptoms in PD patients. The dynamic FC analysis may be used as monitoring tool for non-motor symptoms and disease progression.

Data availability statement

The original contributions presented in this study are included in the article/supplementary material, further inquiries can be directed to the corresponding authors.

Ethics statement

The studies involving human participants were reviewed and approved by the all data used in this study were downloaded from PPMI dataset. The patients/participants provided their written informed consent to participate in this study.

Author contributions

YC: methodology, investigation, formal analysis, and writing–original draft. QS and RT: methodology. SM, CL and XZ: review and editing. All authors contributed to the article and approved the submitted version.

Funding

The research reported in this article was funded by the National Natural Science Foundation of China, 62171300.

Acknowledgments

We thank the patients and healthy volunteers participating in the PPMI study, the investigators who contributed, and the Michael J. Fox Foundation. PPMI–a public-private partnership–is

funded by the Michael J. Fox Foundation for Parkinson's Research and funding partners, including 4D Pharma, AbbVie Inc., AcureX Therapeutics, Allergan, Amathus Therapeutics, Aligning Science Across Parkinson's (ASAP), Avid Radiopharmaceuticals, Bial Biotech, Biogen, BioLegend, Bristol Myers Squibb, Calico Life Sciences LLC, Celgene Corporation, DaCapo Brainscience, Denali Therapeutics, The Edmond J. Safra Foundation, Eli Lilly and Company, GE Healthcare, GlaxoSmithKline, Golub Capital, Handl Therapeutics, Insitro, Janssen Pharmaceuticals, Lundbeck, Merck & Co., Inc., Meso Scale Diagnostics, LLC, Neurocrine Biosciences, Pfizer Inc., Piramal Imaging, Prevail Therapeutics, F. Hoffmann-La Roche Ltd., and its affiliated company Genentech Inc., Sanofi Genzyme, Servier, Takeda Pharmaceutical Company, Teva Neuroscience, Inc., UCB, Vanqua Bio, Verily Life Sciences, Voyager Therapeutics, Inc., and Yumanity Therapeutics, Inc.

Conflict of interest

The authors declare that the research was conducted in the absence of any commercial or financial relationships that could be construed as a potential conflict of interest.

Publisher's note

References

Allen, E. A., Damaraju, E., Plis, S. M., Erhardt, E. B., Eichele, T., and Calhoun, V. D. (2014). Tracking whole-brain connectivity dynamics in the resting state. *Cereb Cortex* 24, 663–676. doi: 10.1093/cercor/bhs352

Armstrong, M. J., and Okun, M. S. (2020). Diagnosis and treatment of parkinson disease: a review. *JAMA* 323, 548–560. doi: 10.1001/jama.2019.22360

Ashraf-Ganjouei, A., Majd, A., Javinani, A., and Aarabi, M. H. (2018). Autonomic dysfunction and white matter microstructural changes in drug-naïve patients with Parkinson's disease. *PeerJ* 6:e5539. doi: 10.7717/peerj.5539

Barkhof, F., Haller, S., and Rombouts, S. A. (2014). Resting-state functional MR imaging: a new window to the brain. *Radiology* 272, 29–49. doi: 10.1148/radiol.14132388

Bloem, B., Okun, M., and Klein, C. (2021). Parkinson's disease. *Lancet* 397, 2284–2303. doi: 10.1016/s0140-6736(21)00218-x

Calhoun, V. D., Adali, T., Pearlson, G. D., and Pekar, J. J. (2001). A method for making group inferences from functional MRI data using independent component analysis. *Hum. Brain Mapp.* 14, 140–151. doi: 10.1002/hbm.1048

Calhoun, V. D., Miller, R., Pearlson, G., and Adalı, T. (2014). The chronnectome: time-varying connectivity networks as the next frontier in fMRI data discovery. *Neuron* 84, 262–274. doi: 10.1016/j.neuron.2014.10.015

Chen, L., Bedard, P., Hallett, M., and Horovitz, S. G. (2021). Dynamics of top-down control and motor networks in Parkinson's disease. *Mov. Dis.* 36, 916–926. doi: 10.1002/mds.28461

Chung, S. J., Kim, H. R., Jung, J. H., Lee, P. H., Jeong, Y., and Sohn, Y. H. (2020). Identifying the functional brain network of motor reserve in early Parkinson's disease. *Mov. Dis.* 35, 577–586. doi: 10.1002/mds.28012

Dayan, E., Sklerov, M., and Browner, N. (2018). Disrupted hypothalamic functional connectivity in patients with PD and autonomic dysfunction. *Neurology* 90, e2051–e2058. doi: 10.1212/wnl.0000000000005641

De Micco, R., Agosta, F., Basaia, S., Siciliano, M., Cividini, C., Tedeschi, G., et al. (2021). Functional connectomics and disease progression in drug-naïve Parkinson's disease patients. *Mov. Dis.* 36, 1603–1616. doi: 10.1002/mds.28541

Diederich, N. J., Sauvageot, N., Pieri, V., Hipp, G., and Vaillant, M. (2020). The clinical non-motor connectome in early Parkinson's disease. *J Parkinson's Dis.* 10, 1797–1806. doi: 10.3233/JPD-202102

Díez-Cirarda, M., Strafella, A. P., Kim, J., Peña, J., Ojeda, N., Cabrera-Zubizarreta, A., et al. (2018). Dynamic functional connectivity in Parkinson's disease patients with mild cognitive impairment and normal cognition. *Neuro. Clin.* 17, 847–855. doi: 10.1016/j.nicl.2017.12.013

Du, Y., Pearlson, G. D., Lin, D., Sui, J., Chen, J., Salman, M., et al. (2017). Identifying dynamic functional connectivity biomarkers using GIG-ICA: application to schizophrenia, schizoaffective disorder, and psychotic bipolar disorder. *Hum. Brain Mapp.* 38, 2683–2708. doi: 10.1002/hbm.23553

Esposito, F., Formisano, E., Seifritz, E., Goebel, R., Morrone, R., Tedeschi, G., et al. (2002). Spatial independent component analysis of functional MRI time-series: to what extent do results depend on the algorithm used? *Hum. Brain Mapp.* 16, 146–157. doi: 10.1002/hbm.10034

Fereshtehnejad, S., and Posteuma, R. (2017). Subtypes of Parkinson's disease: What do they tell us about disease progression? *Curr. Neurol. Neurosci. Rep.* 17:34. doi: 10.1007/s11910-017-0738-x

Fiorenzato, E., Strafella, A. P., Kim, J., Schifano, R., Weis, L., Antonini, A., et al. (2019). Dynamic functional connectivity changes associated with dementia in Parkinson's disease. *Brain* 142, 2860–2872. doi: 10.1093/brain/awz192

Gan, C., Ma, K., Wang, L., Si, Q., Wang, M., Yuan, Y., et al. (2021). Dynamic functional connectivity changes in Parkinson's disease patients with REM sleep behavior disorder. *Brain Res.* 1764:147477. doi: 10.1016/j.brainres.2021.147477

GBD 2016 Neurology Collaborators (2018). Global, regional, and national burden of Parkinson's disease, 1990-2016: a systematic analysis for the global burden of disease study 2016. *Lancet Neurol.* 17, 939–953. doi: 10.1016/s1474-4422(18)30295-3

Goetz, C. G., Tilley, B. C., Shaftman, S. R., Stebbins, G. T., Fahn, S., Martinez-Martin, P., et al. (2008). Movement disorder society-sponsored revision of the unified Parkinson's disease rating scale (MDS-UPDRS): scale presentation and clinimetric testing results. *Mov. Dis.* 23, 2129–2170. doi: 10.1002/mds.22340

Hoehn, M. M., and Yahr, M. D. (2001). Parkinsonism: onset, progression and mortality. *Neurology* 57, S11–S26.

Hu, X., Song, X., Yuan, Y., Li, E., Liu, J., Liu, W., et al. (2015). Abnormal functional connectivity of the amygdala is associated with depression in Parkinson's disease. *Mov. Dis.* 30, 238–244. doi: 10.1002/mds.26087

Khoo, T. K., Yarnall, A. J., Duncan, G. W., Coleman, S., O'Brien, J. T., Brooks, D. J., et al. (2013). The spectrum of nonmotor symptoms in early parkinson disease. *Neurology* 80, 276–281. doi: 10.1212/WNL.0b013e31827deb74

Kim, J., Criaud, M., Cho, S. S., Díez-Cirarda, M., Mihaescu, A., Coakeley, S., et al. (2017). Abnormal intrinsic brain functional network dynamics in Parkinson's disease. *Brain* 140, 2955–2967. doi: 10.1093/brain/awx233

Kwon, K.-Y., Park, S., Lee, E. J., Lee, M., and Ju, H. (2021). Association of fall risk factors and non-motor symptoms in patients with early Parkinson's disease. *Sci. rep.* 11:5171. doi: 10.1038/s41598-021-84720-w

Lee, M. H., Smyser, C. D., and Shimony, J. S. (2013). Resting-state fMRI: a review of methods and clinical applications. *Am. J. Neuroradiol.* 34, 1866–1872. doi: 10.3174/ajnr.A3263

Li, G., Chen, Z., Zhou, L., Zhao, A., Niu, M., Li, Y., et al. (2021). Altered structure and functional connectivity of the central autonomic network in idiopathic rapid eye movement sleep behaviour disorder. *J. Sleep Res.* 30:e13136. doi: 10.1111/jsr.13136

Nakano, T., Kajiyama, Y., Revankar, G. S., Hashimoto, R., Watanabe, Y., Kishima, H., et al. (2021). Neural networks associated with quality of life in patients with Parkinson's disease. *Parkins. Related Dis.* 89, 6–12. doi: 10.1016/j.parkreldis.2021.06.007

Poewe, W., Seppi, K., Tanner, C. M., Halliday, G. M., Brundin, P., Volkmann, J., et al. (2017). Parkinson disease. *Nat. Rev. Dis. Primers* 3:17013. doi: 10.1038/nrdp.2017.13

Raimondo, L., Oliveira, ĹA. F., Heij, J., Priovoulos, N., Kundu, P., Leoni, R. F., et al. (2021). Advances in resting state fMRI acquisitions for functional connectomics. *NeuroImage* 243:118503. doi: 10.1016/j.neuroimage.2021.118503

Rango, M., Dossi, G., Squarcina, L., and Bonifati, C. (2021). Brain mitochondrial impairment in early-onset Parkinson's disease with or without PINK1 mutation. *Mov. Dis.* 35, 504–507. doi: 10.1002/mds.27946

Ryman, S. G., and Poston, K. L. (2020). MRI biomarkers of motor and non-motor symptoms in Parkinson's disease. *Parkins. Related Dis.* 73, 85–93. doi: 10.1016/j.parkreldis.2019.10.002

Schindlbeck, K. A., and Eidelberg, D. (2018). Network imaging biomarkers: insights and clinical applications in Parkinson's disease. *Lancet Neurol.* 17, 629–640. doi: 10.1016/s1474-4422(18)30169-8

Schrag, A., and Schott, J. M. (2006). Epidemiological, clinical, and genetic characteristics of early-onset parkinsonism. *Lancet Neurol.* 5, 355–363. doi: 10.1016/S1474-4422(06)70411-2

Shahhosseini, Y., and Miranda, M. F. (2022). Functional connectivity methods and their applications in fMRI data. *Entropy* 24:390. doi: 10.3390/e24030390

Sigirli, D., Ozdemir, S., Erer, S., Sahin, I., Ercan, I., Ozpar, R., et al. (2021). Statistical shape analysis of putamen in early-onset Parkinson's disease. *Clin Neurol. Neurosurg.* 209:106936. doi: 10.1016/j.clineuro.2021.106936

Smith, S. M., Beckmann, C. F., Andersson, J., Auerbach, E. J., Bijsterbosch, J., Douaud, G., et al. (2013a). Resting-state fMRI in the human connectome project. *NeuroImage* 80, 144–168. doi: 10.1016/j.neuroimage.2013.05.039

Smith, S. M., Vidaurre, D., Beckmann, C. F., Glasser, M. F., Jenkinson, M., Miller, K. L., et al. (2013b). Functional connectomics from resting-state fMRI. *Trends Cogn. Sci.* 17, 666–682. doi: 10.1016/j.tics.2013.09.016

Tessitore, A., Cirillo, M., and De Micco, R. (2019). Functional connectivity signatures of parkinson's disease. *J. Parkinson's Dis.* 9, 637–652. doi: 10.3233/JPD-191592

Tolosa, E., Garrido, A., Scholz, S. W., and Poewe, W. (2021). Challenges in the diagnosis of Parkinson's disease. *Lancet Neurol.* 20, 385–397. doi: 10.1016/s1474-4422(21)00030-2

Tomlinson, C. L., Stowe, R., Patel, S., Rick, C., Gray, R., and Clarke, C. E. (2010). Systematic review of levodopa dose equivalency reporting in Parkinson's disease. *Mov. Dis.* 25, 2649–2653. doi: 10.1002/mds.23429

Vijiaratnam, N., Simuni, T., Bandmann, O., Morris, H. R., and Foltynie, T. (2021). Progress towards therapies for disease modification in Parkinson's disease. *Lancet Neurol.* 20, 559–572. doi: 10.1016/s1474-4422(21)00061-2

Whitfield-Gabrieli, S., and Nieto-Castanon, A. (2012). Conn: a functional connectivity toolbox for correlated and anticorrelated brain networks. *Brain Connect.* 2, 125–141. doi: 10.1089/brain.2012.0073

Wolters, A. F., van de Weijer, S. C. F., Leentjens, A. F. G., Duits, A. A., Jacobs, H. I. L., and Kuijf, M. L. (2019). Resting-state fMRI in Parkinson's disease patients with cognitive impairment: a meta-analysis. *Parkins. Related Dis.* 62, 16–27. doi: 10.1016/j.parkreldis.2018.12.016

Wu, T., and Hallett, M. (2005). A functional MRI study of automatic movements in patients with Parkinson's disease. *Brain* 128, 2250–2259. doi: 10.1093/brain/awh569

Yeo, B. T., Krienen, F. M., Sepulcre, J., Sabuncu, M. R., Lashkari, D., Hollinshead, M., et al. (2011). The organization of the human cerebral cortex estimated by intrinsic functional connectivity. *J. Neurophysiol.* 106, 1125–1165. doi: 10.1152/jn.00338.2011

Zhang, H., Qiu, Y., Luo, Y., Xu, P., Li, Z., Zhu, W., et al. (2019). The relationship of anxious and depressive symptoms in Parkinson's disease with voxel-based neuroanatomical and functional connectivity measures. *J. Affect. Dis.* 245, 580–588. doi: 10.1016/j.jad.2018.10.364

frontiers | Frontiers in Neuroscience

TYPE Original Research
PUBLISHED 23 March 2023
DOI 10.3389/fnins.2023.1144802

OPEN ACCESS

EDITED BY
Bilge Karacali,
İzmir Institute of Technology, Türkiye

REVIEWED BY
Kuangshi Li,
Dongzhimen Hospital, Beijing University of Chinese Medicine, China
Sisi Zheng,
Beijing Anding Hospital, Capital Medical University, China

*CORRESPONDENCE
Hua-Jun Chen
✉ chj0075@126.com
Nao-Xin Huang
✉ nxhuang@foxmail.com

†These authors have contributed equally to this work

SPECIALTY SECTION
This article was submitted to Brain Imaging Methods, a section of the journal Frontiers in Neuroscience

RECEIVED 15 January 2023
ACCEPTED 06 March 2023
PUBLISHED 23 March 2023

CITATION
Lin J-H, Chen X-H, Wu Y, Cao Y-B, Chen H-J and Huang N-X (2023) Altered isotropic volume fraction in gray matter after sleep deprivation and its association with visuospatial memory: A neurite orientation dispersion and density imaging study. *Front. Neurosci.* 17:1144802. doi: 10.3389/fnins.2023.1144802

Altered isotropic volume fraction in gray matter after sleep deprivation and its association with visuospatial memory: A neurite orientation dispersion and density imaging study

Jia-Hui Lin[1†], Xu-Hui Chen[1†], Ye Wu[2†], Yun-Bin Cao[1†], Hua-Jun Chen[1*] and Nao-Xin Huang[1*]

[1]Department of Radiology, Fujian Medical University Union Hospital, Fuzhou, China, [2]School of Computer Science and Engineering, Nanjing University of Science and Technology, Nanjing, China

Background and aims: Diffusion magnetic resonance imaging (dMRI) studies have revealed microstructural abnormalities in white matter resulting from sleep deprivation (SD). This study aimed to adopt neurite orientation dispersion and density imaging (NODDI) to investigate the effect of SD on gray matter (GM) microstructural properties and its association to visuospatial memory (VSM).

Methods: Twenty-four healthy women underwent two sessions of dMRI scanning and visuospatial ability assessment by Complex Figure Test (CFT), once during rested wakefulness (RW) and once after 24 h of SD. We calculated NODDI metrics, including intracellular volume fraction (ICVF), orientation dispersion index (ODI), and isotropic volume fraction (ISO). Differences in NODDI-related metrics between RW and SD were determined using a voxel-wise paired *t*-test. We identified an association between NODDI metrics and CFT results using Spearman's correlation coefficient.

Results: Sleep deprivation worsened subjects' performance in the delayed-CFT trial. We observed no significant difference in ICVF and ODI between RW and SD. After SD, subjects showed decreases in ISO, primarily in the prefrontal cortex and temporal lobe, while exhibiting ISO increases in the anterior and posterior cerebellar lobe and cerebellar vermis. Furthermore, ISO change in the left superior, middle and inferior frontal gyrus was significantly correlated with completion time change in delayed-CFT trial performance.

Conclusion: Our results suggested that SD hardly affected the density and spatial organization of neurites in GM, but the extra-neurite water molecule diffusion process was affected (perhaps resulting from neuroinflammation), which contributed to VSM dysfunction.

KEYWORDS

sleep deprivation, neurite orientation dispersion and density imaging, gray matter, isotropic volume fraction, visuospatial memory

Introduction

Sleep is a complex physiological process that is essential in humans for maintaining cognition (Colrain, 2011). Visuospatial memory (VSM) is one of the crucial domains in cognition that plays a basic role in daily life, which is required for orientation, spatial localization, and using a navigation map (Perrochon et al., 2014). Sleep deprivation (SD), even a single night thereof, can have detrimental effects on VSM (Gosselin et al., 2017; Pasula et al., 2018). Meanwhile, animal experiments have found that SD is associated with alterations in brain structure. For example, one study revealed that SD increases the breakdown of neuronal-membrane phospholipids (Hinard et al., 2012). Another study found that SD induces spine density changes in the hippocampus and prefrontal cortex in rats (Acosta-Pena et al., 2015). However, the neural mechanisms underlying VSM deficit after SD are not well understood. Elucidating the neurobiological effects of SD on the brain might help us grasp the significance of sleep in neuroscience.

Diffusion magnetic resonance imaging (dMRI) is a non-invasive approach that measures the diffusion of water molecules in tissue, providing information about the underlying brain microstructure (Pierpaoli et al., 1996). In recent years, many studies have used dMRI to investigate the effect of SD on brain microstructure (Rocklage et al., 2009; Cui et al., 2015; Elvsashagen et al., 2015; Zhu et al., 2017; Voldsbekk et al., 2021; Wang et al., 2022). For instance, one diffusion tensor imaging (DTI) study found that SD was associated with impaired white matter (WM) integrity [as reflected by reduced fractional anisotropy (FA)] of the bilateral frontotemporal and parieto-occipital tracts, corpus callosum, thalamus, and brain stem (Elvsashagen et al., 2015). In addition, several DTI studies have reported that WM microstructural properties enable the prediction of cognitive vulnerability to SD (Rocklage et al., 2009; Wang et al., 2022). Moreover, the individual's cognitive stability/resistance to SD is associated with the integrity of the WM tract, which connects the frontoparietal attention networks (Cui et al., 2015; Zhu et al., 2017). Notably, several inherent drawbacks of DTI limit its utility in SD-related studies. For example, DTI assumes that water diffusion is Gaussian distribution, so it is not able to completely characterize tissue microstructure (Steven et al., 2014). In addition, DTI extracts information from dMRI data *via* "signal representations" approach, which lacks specificity and remains an indirect characterization of microstructure (Huang S. et al., 2022). Furthermore, due to its assumption of a single tissue compartment, DTI cannot distinguish microstructural properties between intra-cellular and extra-cellular spaces (Beaulieu, 2002).

In recent years, several advanced multi-compartment diffusion models have been proposed to overcome the limitations of DTI. For instance, a recent dMRI study using spherical mean technique (SMT), a multi-compartment model that estimates brain tissue microstructure in the intra- and extra-axonal spaces, revealed that the effect of SD on WM microstructure mainly involves the extra-axonal water molecule diffusion process (Voldsbekk et al., 2021). Neurite orientation dispersion and density imaging (NODDI) is another multi-compartment diffusion model that parametrizes the dMRI signal as a function of biophysically meaningful parameters [e.g., dendrite and axon density in gray matter (GM) and WM, respectively] (Zhang et al., 2012; Kamiya et al., 2020), which has been validated in the histology of animal and human brain (Sepehrband et al., 2015). NODDI-derived metrics provide detailed information on the brain's tissue microstructure. Specifically, intracellular volume fraction (ICVF) quantifies the packing density of neurites (including dendrites and axons); the orientation dispersion index (ODI) indicates the spatial organization or geometric complexity of neurites; and isotropic volume fraction (ISO) reflects extra-cellular isotropic diffusion (Kraguljac et al., 2022). The primary advantage of NODDI is that its metrics are more directly related to the brain's microstructure because it models the biophysical properties of the tissue (Kamiya et al., 2020). NODDI has been used to explore brain microstructural alterations in several physiological and pathological conditions, such as brain development (Zhao et al., 2021), aging (Merluzzi et al., 2016), Parkinsonism (Mitchell et al., 2019), and Wilson disease (Song et al., 2018). Nevertheless, previous DTI and SMT studies have focused solely on WM microstructural changes after SD (Rocklage et al., 2009; Cui et al., 2015; Elvsashagen et al., 2015; Zhu et al., 2017; Voldsbekk et al., 2021; Wang et al., 2022), and the effect of SD on GM microstructure remains unclear.

In light of the above, in this study, we exploratorily adopted NODDI to: (1) investigate whether GM microstructural alteration occurred after 24 h of SD and (2) determine the association between changes in GM diffusion metrics and VSM alterations after SD.

Materials and methods

Subjects

Twenty-four healthy women participated in this study, who were all right-handed; the participants had an average age of 20 ± 0.81 years as well as an average of 13 ± 0.93 years of education. Participants who met any one of the following criteria were excluded: (1) a history of sleep disorder or any other neuropsychiatric conditions; (2) the taking of psychotropic medications; (3) chronic and severe medical illness such as heart failure, malignancies, or chronic renal failure; (4) contraindications to MRI scanning. The Ethical Committee of Fujian Medical University Union Hospital (Fuzhou, China) approved this study, and all subjects provided their informed written consent.

Experimental procedure

We followed the same experimental procedure as that described in our previous study (Huang N. X. et al., 2022). The flowchart of experimental procedure is shown in **Figure 1**. Each participant made three visits to the laboratory: briefing, rested wakefulness (RW), and SD sessions. The first visit was the briefing session, in which we briefed subjects on the procedure and obtained their signed informed consent. RW and SD sessions started after at least

Abbreviations: CFT, complex figure test; DTI, diffusion tensor imaging; GM, gray matter; ICVF, intracellular volume fraction; ISO, isotropic volume fraction; MRI, magnetic resonance imaging; NODDI, neurite orientation dispersion and density imaging; ODI, orientation dispersion index; RW, rested wakefulness; SD, sleep deprivation; SMT, spherical mean technique; WM, white matter.

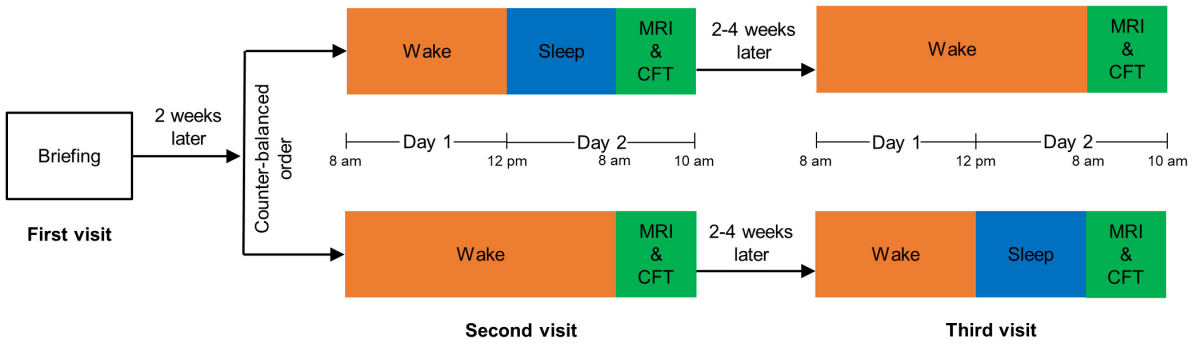

FIGURE 1
The flowchart of experimental procedure. MRI, magnetic resonance imaging; CFT, complex figure test.

2 weeks of habitual sleep. To minimize the possible residual effects of SD on cognition (Van Dongen et al., 2003), the RW session and the SD session were set 2–4 weeks apart, and their order was counterbalanced across all participants.

For the RW session, we asked participants to stay awake from 8:00 a.m. to 12:00 p.m. (day 1) and to sleep from 0:00 a.m. to 8:00 a.m. (day 2). For the SD session, participants were asked to stay awake from 8:00 a.m. (day 1) to 8:00 a.m. (day 2). Subjects stayed in our laboratory for both these sessions, accompanied by two research assistants to prevent them from falling back to sleep during the awakening state. Participants were permitted to engage in non-strenuous activities such as reading, talking, or internet surfing, but strenuous activities and the intake of stimulating substances were not allowed.

Visuospatial ability assessment

A trained staff member assessed subjects' visuospatial ability using the Complex Figure Test (CFT) (Shin et al., 2006). CFT is a popular neuropsychological assessment tool for visuospatial ability, including three subtests: CFT-copy, immediate-CFT, and delayed-CFT trials. In the CFT-copy trial, subjects were presented the complex figure and were asked to copy the entire figure onto a blank sheet of paper; Following the CFT-copy trial, the immediate-CFT trial was performed, in which subjects were asked to reproduce the complex figure from memory; In the delayed-CFT trial that was performed 25 min after the immediate-CFT trial, subjects reproduced the complex figure once again (Shin et al., 2006). The CFT-copy trial was used to evaluate visuospatial constructional ability, while immediate-CFT and delayed-CFT trials were used to evaluate VSM (Shin et al., 2006). The assessment was scheduled for 8:00–10:00 a.m. on day 2 for each of the RW and SD sessions.

MRI data acquisition

We acquired MRI data using a 3.0 Tesla Siemens Prisma MRI scanner (Siemens, Erlangen, Germany). Diffusion-weighted images were obtained using a multi-shell echo-planar imaging sequence, which consisted of four *b*-values (0, 1,000, 2,000, and 3,000 s/mm^2) along 6, 30, 30, and 30 gradient directions, respectively. Other image acquisition parameters were as follows: repetition time (T_R) = 4,200 ms; time to echo (T_E) = 72 ms; number of averages = 1; flip angle = 90°; slice thickness = 2 mm; field of view (FOV) = 216 mm × 216 mm; matrix = 108 × 108; voxel size = 2 × 2 × 2 mm^3; slice number = 72 (axial slices without gaps); multiband factor = 2. T1-weighted (T1W) structural images were acquired using a magnetization-prepared rapid gradient-echo (MPRAGE) sequence with the following parameters: T_R = 1,610 ms; T_E = 2.25 ms; flip angle = 8°; slice thickness = 1.0 mm; FOV = 224 mm × 224 mm; matrix = 224 × 224; voxel size = 1 × 1 × 1 mm^3; slice number = 176 (sagittal slices without gaps). MRI scanning was scheduled for 8:00–10:00 a.m. on day 2 for each of the RW and SD sessions.

MRI data pre-processing

We visually inspected the T1W and dMRI images of all subjects to detect any signal dropouts or artifacts. Next, we pre-processed the images *via* the well-established pipeline, described as follows. For both T1W and dMRI data, the procedure began with axial alignment, centering, Gibbs ringing removal based on Local Subvoxel-Shifts (Kellner et al., 2016), and intensity inhomogeneity correction *via* N4ITK (Tustison et al., 2010). For dMRI data, we also included the following steps: (1) Marchenko–Pastur principal-component analysis (MP-PCA) denoising (Veraart et al., 2016a,b) to improve the signal-to-noise ratio (SNR) without reducing spatial resolution; (2) FSL's eddy_correct tool was used for eddy current correction (Jenkinson et al., 2012); (3) brain mask generation using a brain extraction tool (BET) (Jenkinson et al., 2012); and (4) distortion correction *via* registration of individual T1W and dMRI data (Wu et al., 2018). Then, the transformation was applied to each diffusion-weighted volume, and the gradient vectors were rotated using the rotation matrix estimated from the affine transformation.

NODDI-based microstructural modeling

To investigate advanced brain microstructural properties, we fit our NODDI model (Zhang et al., 2012) to the multi-shell (i.e., *b* = 1,000, 2,000, and 3,000 s/mm^2) dMRI data using the Accelerated Microstructure Imaging *via* Convex Optimization

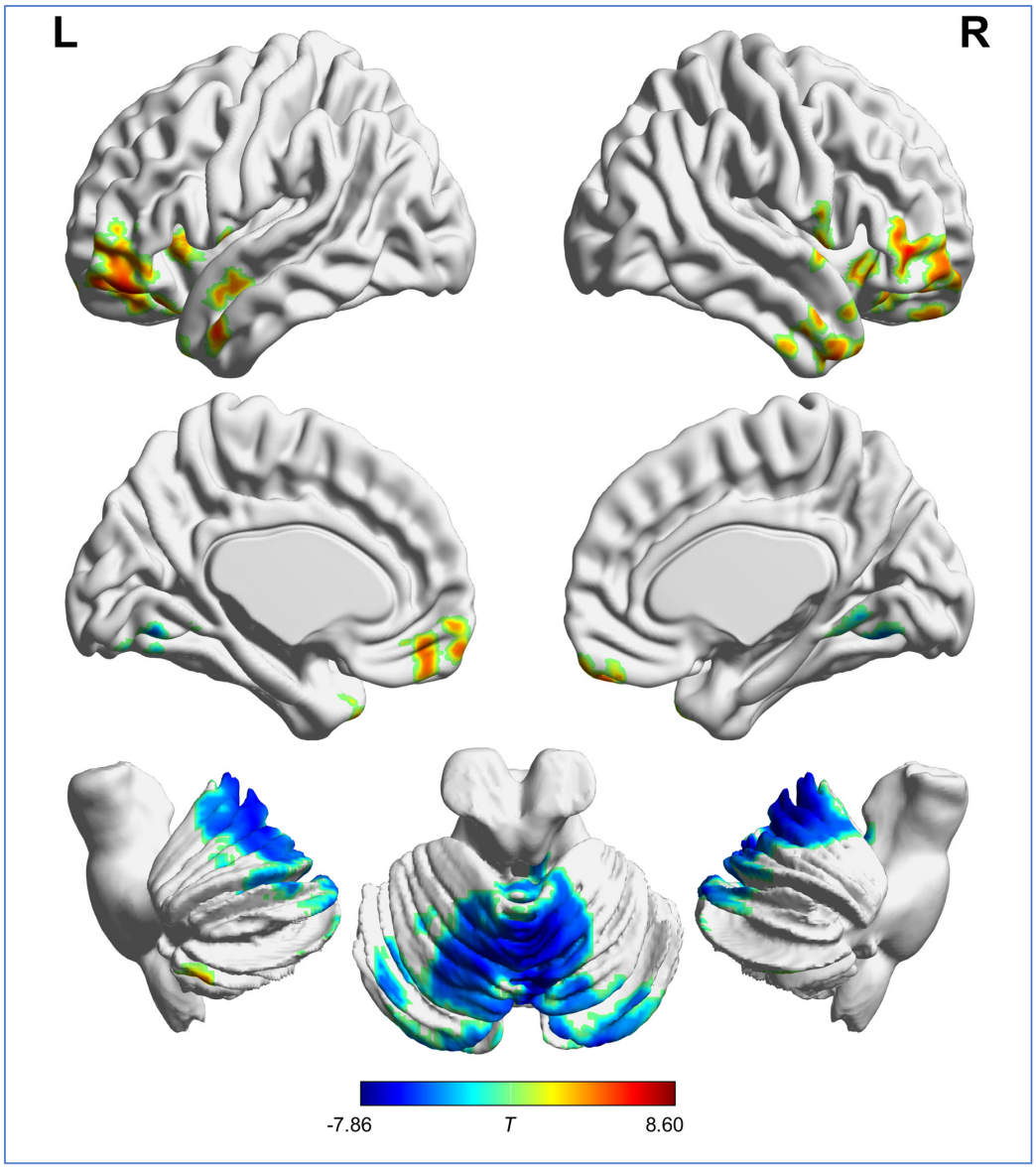

FIGURE 2
Brain regions with significant difference in ISO between RW and SD. "L" and "R" represent the left and right side of the brain, respectively. Red indicates ISO reduction and blue indicates ISO increment after SD. ISO, isotropic volume fraction; RW, rested wakefulness; SD, sleep deprivation.

(AMICO) toolbox (Daducci et al., 2015). We also used the AMICO toolbox to significantly speed up the time needed to fit the NODDI model by reformulating the NODDI model as a linear system without sacrificing accuracy. Using NODDI, we calculated ICVF, ODI, and ISO.

Each individual's T1W images were transformed from anatomically corrected space to diffusion-corrected space *via* two-step linear registration using the Functional Magnetic Resonance Imaging of the Brain (FMRIB) Linear Image Registration Tool (FLIRT) (Jenkinson et al., 2012). Advanced Normalization Tools (ANTs)[1] was used to linearly register each subject's T1W images to MNI atlas [International Consortium for Brain Mapping (ICBM) 2009b Nonlinear Asymmetric], and the transformation matrix that resulted was applied to warp each subject's microstructural map to the MNI space. To reduce the effect of fine-grained local variations in anatomy between individuals, voxels within the mask region were then convolved with the specified full-width half maximum (FWHM, equaling voxel size × 2.3548 mm) Gaussian smoothing kernel.

Statistical analysis

We determined differences in NODDI metrics between RW and SD using a voxel-wise paired *t*-test, with statistical significance set at corrected $P < 0.05$. The false discovery rate (FDR) was used for multiple-comparison corrections. We identified the association between NODDI metrics and VSM performance by calculating

1 https://stnava.github.io/ANTs

TABLE 1 Differences in isotropic volume fraction between the rested wakefulness and sleep deprivation.

Regions	Voxels	Brodmann area	MNI coordinates			Peak *T*-value
			x	*y*	*z*	
Left superior, middle, and inferior frontal gyrus	1,262	10/11/47	−43	43	−17	8.60
Right middle and inferior temporal gyrus and temporal pole	566	21/20/38	47	11	−41	6.07
Left medial frontal gyrus and rectus gyrus	475	11	7	53	−25	5.44
Right middle and inferior frontal gyrus	1,359	11/47	55	39	3	7.71
Left superior and middle temporal gyrus, temporal pole, and anterior insula	613	22/21/38/13	−59	7	−33	6.82
Left superior temporal gyrus and temporal pole	119	38	−33	19	−45	6.49
Right temporal pole	116	22	51	5	1	5.07
Right posterior cerebellar lobe	187		45	−61	−53	7.39
Left posterior cerebellar lobe	199		−37	−41	−55	5.92
Bilateral anterior and posterior cerebellar lobe and cerebellar vermis, and lingual gyrus	4,133	18	5	−71	−19	−7.86

MNI, Montreal Neurological Institute.

the Spearman correlation coefficient using Statistical Product and Service Solutions (SPSS) software version 22.0 (IBM Corp., Armonk, NY, USA).

Results

Subjects took longer to complete the delayed-CFT trial after SD than after RW (84.6 ± 37.2 *vs.* 67.4 ± 28.2 s; $P = 0.022$). In addition, their scores in the delayed-CFT trial were lower after SD than after RW (22.1 ± 6.9 *vs.* 24.3 ± 7.9; $P = 0.034$). RW and SD states did not differ significantly in their CFT-copy (times: 136.6 ± 43.5 *vs.* 133.3 ± 45.1 s; $P = 0.788$; score: 35.2 ± 1.1 *vs.* 34.9 ± 1.8; $P = 0.421$) or immediate-CFT (times: 108.4 ± 41.2 *vs.* 122.5 ± 48.8 s; $P = 0.272$; score: 24.5 ± 8.6 *vs.* 22.9 ± 7.3; $P = 0.170$) trial results.

Voxel-wise analysis showed no significant difference in ICVF and ODI between RW and SD. The distribution of brain regions with altered ISO is shown in Figure 2 and Table 1. Compared with after RW, after SD, subjects exhibited decreased ISO in the left superior, middle and inferior frontal gyrus, left medial frontal and rectus gyrus, left superior and middle temporal gyrus, temporal pole, and anterior insula, right middle and inferior frontal gyrus, right middle and inferior temporal gyrus and temporal pole, and bilateral posterior cerebellar lobe; and increased ISO in the bilateral anterior and posterior cerebellar lobe and cerebellar vermis, and lingual gyrus.

The result of the correlation analysis is shown in Figure 3. Between the RW and SD states, changes in mean ISO in the left superior, middle and inferior frontal gyrus was negatively correlated with changes in completion time in the delayed-CFT trial ($r = -0.518$, $P = 0.010$).

Discussion

This study aimed to adopt NODDI to explore whether microstructural alterations occurred in GM after SD and determine whether NODDI measurements were associated with VSM. The main findings were as follows. First, we observed no significant changes in ICVF or ODI after SD, indicating that SD hardly affected the density and spatial organization of neurites in GM. Second, ISO decreases were observed in a series of cognition-related brain regions (including the left superior, middle and inferior frontal gyrus, left medial frontal and rectus gyrus, left superior and middle temporal gyrus, temporal pole, and anterior insula, right middle and inferior frontal gyrus, right middle and inferior temporal gyrus and temporal pole) and bilateral posterior cerebellar lobe; while we saw ISO increases in the bilateral anterior and posterior cerebellar lobe and cerebellar vermis, and lingual gyrus. Third, CFT results indicated that SD primarily induced VSM dysfunction, which was in agreement with a previous study (Gosselin et al., 2017). Fourth, after SD, ISO changes in the left superior, middle and inferior frontal gyrus was associated with VSM dysfunction.

Consistent with prior SMT research, which found that SD showed no significant effect on myelin and axonal integrity in WM (as reflected by a lack of differences in intra-neurite volume fraction) (Voldsbekk et al., 2021), our current study revealed that SD hardly affected the density and spatial organization of neurites in GM. Meanwhile, a previous DTI study found that SD alters the content of water molecules in WM, as reflected by decreased mean diffusivity (Ding et al., 2012). A previous SMT study also demonstrated that SD affects the extra-axonal water molecule diffusion process, as shown by a decrease in extra-neurite mean/radial diffusivity (Voldsbekk et al., 2021). In line with these previous studies (Ding et al., 2012; Voldsbekk et al., 2021), the effect of SD on ISO observed in the current study indicated that SD affected the extra-neurite water molecule diffusion process in GM. Given that ISO is suggested to be a biomarker of neuroinflammation (Kraguljac et al., 2022) and that SD leads to neuroinflammation (inducing astrocytic phagocytosis and microglial activation) (Bellesi et al., 2017), the changes in ISO observed in the current study could be attributed to SD-related neuroinflammation processes.

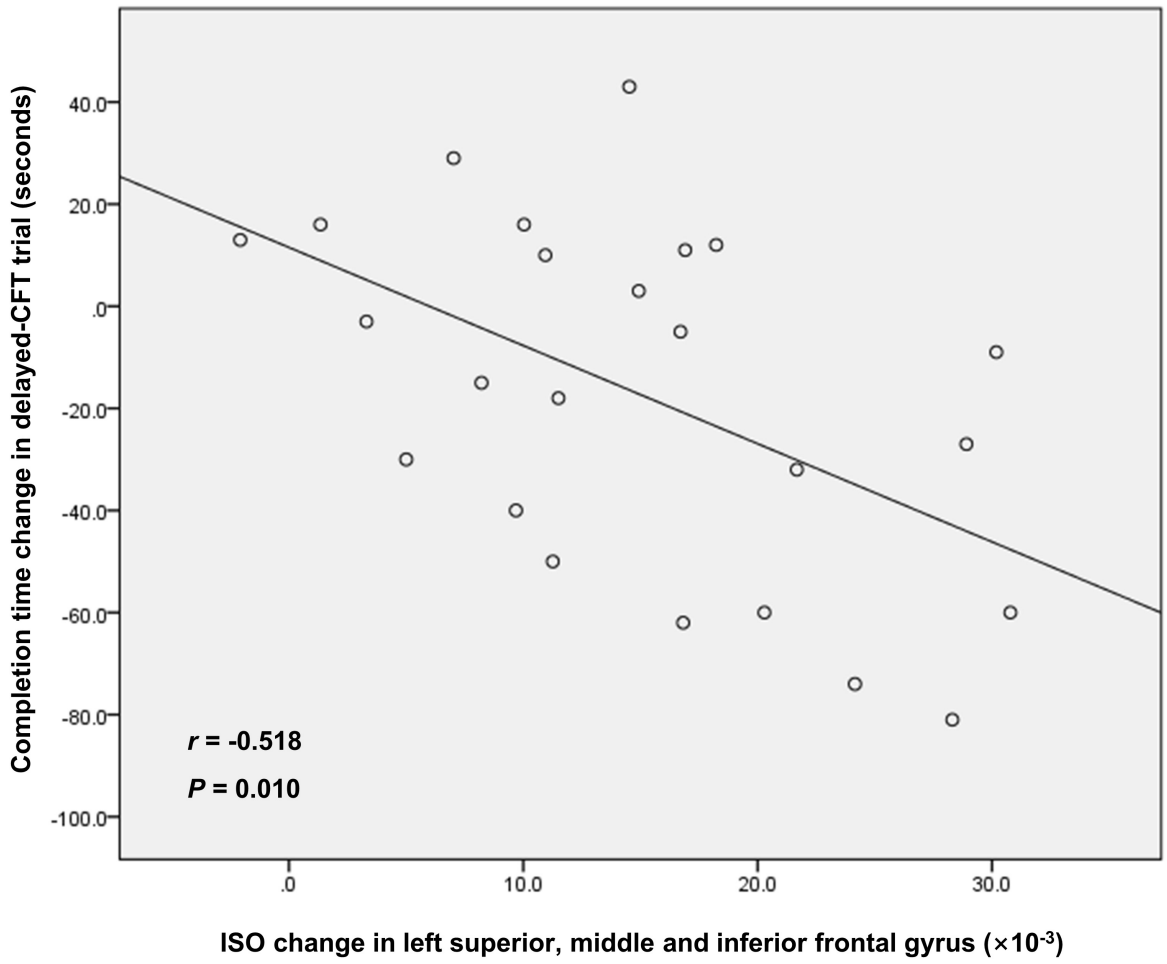

FIGURE 3
The correlation between ISO change in left superior, middle, and inferior frontal gyrus and completion time change in delayed-CFT trial. ISO, isotropic volume fraction; CFT, complex figure test.

After SD, subjects showed ISO reductions in the prefrontal cortex (including the superior, middle, and inferior frontal gyrus; medial frontal gyrus; and rectus gyrus) and the temporal lobe (including the superior, middle, and inferior temporal gyrus; and temporal pole) and anterior insula. Consistently, as reported in prior studies, SD also causes metabolic activity reduction and functional-communication abnormalities in these brain regions (Thomas et al., 2000; Li et al., 2021). The prefrontal cortex is important for cognitive control, working memory, and behavioral flexibility (Buchta et al., 2017); the temporal lobe is involved in auditory cognition, visual processes, and memory (Jackson et al., 2018). The anterior insula has reciprocal connections to limbic regions (such as the anterior cingulate cortex, ventromedial prefrontal cortex, amygdala, and the ventral striatum), which is involved in the integration of autonomic and visceral information into emotional, cognitive, and motivational functions (Namkung et al., 2017). The decreases in ISO observed in the above-mentioned areas might be one of the neural substrates responsible for SD-related cognitive dysfunctions, such as cognitive control and working memory (Killgore, 2010).

In addition, changes in NODDI metrics after SD in the cerebellum were primarily dominated by ISO increases in the bilateral anterior and posterior cerebellar lobe and cerebellar vermis; and ISO increases were also observed in the bilateral lingual gyrus. In agreement with our findings, a previous study found that SD affects metabolic activity in these regions (Thomas et al., 2000). The anterior cerebellar lobe forms functional circuits with sensorimotor regions to support motor execution, and the posterior cerebellar lobe forms functional circuits with association cortices to support various functions from motor planning to working memory (Stoodley and Schmahmann, 2018). Functionally, the cerebellar vermis is concerned with axial motor control and the modulation of affective behavior (Klein et al., 2016; Fujita et al., 2020). The lingual gyrus is associated with basic visual processing (Palejwala et al., 2020). It has been confirmed that several domains including mood, working memory, motor performance, and visual perception are particularly vulnerable to SD (Durmer and Dinges, 2005; Killgore, 2010), which might be explained by the ISO changes in the cerebellum and lingual gyrus.

Several limitations of the current study should be noted. First is the relatively small sample size; subsequent studies should be performed with larger sample sizes to strengthen statistical significance. Second, we enrolled only female participants to avoid the effect of gender as a confounding factor (Dai et al., 2012) on

the results. Third, in this study, we evaluated the effect of SD on visuospatial ability only. SD has been verified to cause detrimental effects across multiple cognitive domains, such as attention, vigilance, perception, memory, and executive functions (Killgore, 2010). The association between NODDI metric alterations and changes in multiple cognitive domains need to be examined in future studies.

In conclusion, our results suggested that SD hardly affected the density and spatial organization of neurites in GM, but it did affect the extra-neurite water molecule diffusion process (perhaps resulting from neuroinflammation), which contributed to VSM dysfunction.

Data availability statement

The original contributions presented in this study are included in the article/supplementary material, further inquiries can be directed to the corresponding authors.

Ethics statement

The studies involving human participants were reviewed and approved by the Ethics Committee of Fujian Medical University Union Hospital. The patients/participants provided their written informed consent to participate in this study.

Author contributions

J-HL: data curation, formal analysis, investigation, and writing – review and editing. X-HC and Y-BC: data curation, formal analysis, investigation, and writing – original draft. YW: methodology. H-JC: conceptualization, data curation, formal analysis, funding acquisition, investigation, project administration, supervision, visualization, and writing – review and editing. N-XH: data curation, formal analysis, funding acquisition, investigation, visualization, and writing – review and editing. All authors contributed to the article and approved the submitted version.

Conflict of interest

The authors declare that the research was conducted in the absence of any commercial or financial relationships that could be construed as a potential conflict of interest.

Publisher's note

All claims expressed in this article are solely those of the authors and do not necessarily represent those of their affiliated organizations, or those of the publisher, the editors and the reviewers. Any product that may be evaluated in this article, or claim that may be made by its manufacturer, is not guaranteed or endorsed by the publisher.

References

Acosta-Pena, E., Camacho-Abrego, I., Melgarejo-Gutierrez, M., Flores, G., Drucker-Colin, R., and Garcia-Garcia, F. (2015). Sleep deprivation induces differential morphological changes in the hippocampus and prefrontal cortex in young and old rats. *Synapse* 69, 15–25. doi: 10.1002/syn.21779

Beaulieu, C. (2002). The basis of anisotropic water diffusion in the nervous system - a technical review. *NMR Biomed.* 15, 435–455. doi: 10.1002/nbm.782

Bellesi, M., de Vivo, L., Chini, M., Gilli, F., Tononi, G., and Cirelli, C. (2017). Sleep loss promotes astrocytic phagocytosis and microglial activation in mouse cerebral cortex. *J. Neurosci.* 37, 5263–5273. doi: 10.1523/JNEUROSCI.3981-16.2017

Buchta, W. C., Mahler, S. V., Harlan, B., Aston-Jones, G. S., and Riegel, A. C. (2017). Dopamine terminals from the ventral tegmental area gate intrinsic inhibition in the prefrontal cortex. *Physiol. Rep.* 5:e13198. doi: 10.14814/phy2.13198

Colrain, I. M. (2011). Sleep and the brain. *Neuropsychol. Rev.* 21, 1–4. doi: 10.1007/s11065-011-9156-z

Cui, J., Tkachenko, O., Gogel, H., Kipman, M., Preer, L. A., Weber, M., et al. (2015). Microstructure of frontoparietal connections predicts individual resistance to sleep deprivation. *Neuroimage* 106, 123–133. doi: 10.1016/j.neuroimage.2014.11.035

Daducci, A., Canales-Rodriguez, E. J., Zhang, H., Dyrby, T. B., Alexander, D. C., and Thiran, J. P. (2015). Accelerated microstructure imaging via convex optimization (AMICO). from diffusion MRI data. *Neuroimage* 105, 32–44. doi: 10.1016/j.neuroimage.2014.10.026

Dai, X. J., Gong, H. H., Wang, Y. X., Zhou, F. Q., Min, Y. J., Zhao, F., et al. (2012). Gender differences in brain regional homogeneity of healthy subjects after normal sleep and after sleep deprivation: a resting-state fMRI study. *Sleep Med.* 13, 720–727. doi: 10.1016/j.sleep.2011.09.019

Ding, A. Y., Zhou, I. Y., Lee, F. Y., and Wu, E. X. (2012). "DTI detection of microstructural changes induced by sleep deprivation," in *Proceedings of the 20th Annual Meeting of the International Society of Magnetic Resonance in Medicine, ISMRM 2012*, (Concord, CA: International Society of Magnetic Resonance in Medicine).

Durmer, J. S., and Dinges, D. F. (2005). Neurocognitive consequences of sleep deprivation. *Semin. Neurol.* 25, 117–129. doi: 10.1055/s-2005-867080

Elvsashagen, T., Norbom, L. B., Pedersen, P. O., Quraishi, S. H., Bjørnerud, A., Malt, U. F., et al. (2015). Widespread changes in white matter microstructure after a day of waking and sleep deprivation. *PLoS One* 10:e0127351. doi: 10.1371/journal.pone.0127351

Fujita, H., Kodama, T., and du Lac, S. (2020). Modular output circuits of the fastigial nucleus for diverse motor and nonmotor functions of the cerebellar vermis. *Elife* 9:e58613. doi: 10.7554/eLife.58613

Gosselin, D., De Koninck, J., and Campbell, K. (2017). Novel measures to assess the effects of partial sleep deprivation on sensory, working, and permanent memory. *Front. Psychol.* 8:1607. doi: 10.3389/fpsyg.2017.01607

Hinard, V., Mikhail, C., Pradervand, S., Curie, T., Houtkooper, R. H., Auwerx, J., et al. (2012). Key electrophysiological, molecular, and metabolic signatures of sleep and wakefulness revealed in primary cortical cultures. *J. Neurosci.* 32, 12506–12517. doi: 10.1523/JNEUROSCI.2306-12.2012

Huang, N. X., Gao, Z. L., Lin, J. H., Lin, Y. J., and Chen, H. J. (2022). Altered stability of brain functional architecture after sleep deprivation: a resting-state functional magnetic resonance imaging study. *Front. Neurosci.* 16:998541.

Huang, S., Huang, C., Li, M., Zhang, H., and Liu, J. (2022). White matter abnormalities and cognitive deficit after mild traumatic brain injury: comparing DTI, DKI, and NODDI. *Front. Neurol.* 13:803066. doi: 10.3389/fneur.2022.803066

Jackson, R. L., Bajada, C. J., Rice, G. E., Cloutman, L. L., and Lambon Ralph, M. A. (2018). An emergent functional parcellation of the temporal cortex. *Neuroimage* 170, 385–399. doi: 10.1016/j.neuroimage.2017.04.024

Jenkinson, M., Beckmann, C. F., Behrens, T. E., Woolrich, M. W., and Smith, S. M. (2012). Fsl. *Neuroimage* 62, 782–790. doi: 10.1016/j.neuroimage.2011.09.015

Kamiya, K., Hori, M., and Aoki, S. (2020). NODDI in clinical research. *J. Neurosci. Methods* 346:108908. doi: 10.1016/j.jneumeth.2020.108908

Kellner, E., Dhital, B., Kiselev, V. G., and Reisert, M. (2016). Gibbs-ringing artifact removal based on local subvoxel-shifts. *Magn. Reson. Med.* 76, 1574–1581. doi: 10.1002/mrm.26054

Killgore, W. D. (2010). Effects of sleep deprivation on cognition. *Prog. Brain Res.* 185, 105–129. doi: 10.1016/B978-0-444-53702-7.00007-5

Klein, A. P., Ulmer, J. L., Quinet, S. A., Mathews, V., and Mark, L. P. (2016). Nonmotor functions of the cerebellum: an introduction. *AJNR Am. J. Neuroradiol.* 37, 1005–1009. doi: 10.3174/ajnr.A4720

Kraguljac, N. V., Guerreri, M., Strickland, M. J., and Zhang, H. (2022). Neurite orientation dispersion and density imaging in psychiatric disorders: a systematic literature review and a technical note. *Biol. Psychiatry Glob. Open Sci.* 3, 10–21. doi: 10.1016/j.bpsgos.2021.12.012

Li, B. Z., Cao, Y., Zhang, Y., Chen, Y., Gao, Y. H., Peng, J. X., et al. (2021). Relation of decreased functional connectivity between left thalamus and left inferior frontal gyrus to emotion changes following acute sleep deprivation. *Front. Neurol.* 12:642411. doi: 10.3389/fneur.2021.642411

Merluzzi, A. P., Dean, D. C. III, Adluru, N., and Suryawanshi, G. (2016). Age-dependent differences in brain tissue microstructure assessed with neurite orientation dispersion and density imaging. *Neurobiol. Aging* 43, 79–88. doi: 10.1016/j.neurobiolaging.2016.03.026

Mitchell, T., Archer, D. B., Chu, W. T., Coombes, S. A., Lai, S., Wilkes, B. J., et al. (2019). Neurite orientation dispersion and density imaging (NODDI). and free-water imaging in Parkinsonism. *Hum. Brain Mapp.* 40, 5094–5107. doi: 10.1002/hbm.24760

Namkung, H., Kim, S. H., and Sawa, A. (2017). The insula: an underestimated brain area in clinical neuroscience, psychiatry, and neurology. *Trends Neurosci.* 40, 200–207. doi: 10.1016/j.tins.2017.02.002

Palejwala, A. H., O'Connor, K. P., Milton, C. K., Anderson, C., Pelargos, P., Briggs, R. G., et al. (2020). Anatomy and white matter connections of the fusiform gyrus. *Sci. Rep.* 10:13489.

Pasula, E. Y., Brown, G. G., McKenna, B. S., Mellor, A., Turner, T., Anderson, C., et al. (2018). Effects of sleep deprivation on component processes of working memory in younger and older adults. *Sleep* 41, 1–9. doi: 10.1093/sleep/zsx213

Perrochon, A., Kemoun, G., Dugue, B., and Berthoz, A. (2014). Cognitive impairment assessment through visuospatial memory can be performed with a modified walking corsi test using the 'Magic Carpet'. *Dement. Geriatr. Cogn. Dis. Extra* 4, 1–13. doi: 10.1159/000356727

Pierpaoli, C., Jezzard, P., Basser, P. J., Barnett, A., and Di Chiro, G. (1996). Diffusion tensor MR imaging of the human brain. *Radiology* 201, 37–648. doi: 10.1148/radiology.201.3.8939209

Rocklage, M., Williams, V., Pacheco, J., and Schnyer, D. M. (2009). White matter differences predict cognitive vulnerability to sleep deprivation. *Sleep* 32, 1100–1103. doi: 10.1093/sleep/32.8.1100

Sepehrband, F., Clark, K. A., Ullmann, J. F., Kurniawan, N. D., Leanage, G., Reutens, D. C., et al. (2015). Brain tissue compartment density estimated using diffusion-weighted MRI yields tissue parameters consistent with histology. *Hum. Brain Mapp.* 36, 3687–3702. doi: 10.1002/hbm.22872

Shin, M. S., Park, S. Y., Park, S. R., Seol, S. H., and Kwon, J. S. (2006). Clinical and empirical applications of the rey-osterrieth complex figure test. *Nat. Protoc.* 1, 892–899. doi: 10.1038/nprot.2006.115

Song, Y. K., Li, X. B., Huang, X. L., Zhao, J., Zhou, X. X., Wang, Y. L., et al. (2018). A study of neurite orientation dispersion and density imaging in wilson's disease. *J. Magn. Reson. Imaging* 48, 423–430.

Steven, A. J., Zhuo, J., and Melhem, E. R. (2014). Diffusion kurtosis imaging: an emerging technique for evaluating the microstructural environment of the brain. *AJR Am. J. Roentgenol.* 202, W26–W33.

Stoodley, C. J., and Schmahmann, J. D. (2018). Functional topography of the human cerebellum. *Handb. Clin. Neurol.* 154, 59–70.

Thomas, M., Sing, H., Belenky, G., Holcomb, H., Mayberg, H., Dannals, R., et al. (2000). Neural basis of alertness and cognitive performance impairments during sleepiness. i. effects of 24 h of sleep deprivation on waking human regional brain activity. *J. Sleep Res.* 9, 335–352.

Tustison, N. J., Avants, B. B., Cook, P. A., Zheng, Y., Egan, A., Yushkevich, P. A., et al. (2010). N4ITK: improved N3 bias correction. *IEEE Trans. Med. Imaging* 29, 1310–1320.

Van Dongen, H. P., Maislin, G., Mullington, J. M., and Dinges, D. F. (2003). The cumulative cost of additional wakefulness: dose-response effects on neurobehavioral functions and sleep physiology from chronic sleep restriction and total sleep deprivation. *Sleep* 26, 117–126.

Veraart, J., Fieremans, E., and Novikov, D. S. (2016a). Diffusion MRI noise mapping using random matrix theory. *Magn. Reson. Med.* 76, 1582–1593.

Veraart, J., Novikov, D. S., Christiaens, D., Ades-Aron, B., Sijbers, J., and Fieremans, E. (2016b). Denoising of diffusion MRI using random matrix theory. *Neuroimage* 142, 394–406.

Voldsbekk, I., Groote, I., Zak, N., Roelfsm, D., Geierm, O., Due-Tønnessenm, P., et al. (2021). Sleep and sleep deprivation differentially alter white matter microstructure: a mixed model design utilising advanced diffusion modelling. *Neuroimage* 226:117540.

Wang, C., Fang, P., Li, Y., Wu, L., Hu, T., Yang, Q., et al. (2022). Predicting attentional vulnerability to sleep deprivation: a multivariate pattern analysis of DTI data. *Nat. Sci. Sleep* 14, 791–803.

Wu, Y., Zhang, F., Makris, N., Ning, Y., Norton, I., She, S., et al. (2018). Investigation into local white matter abnormality in emotional processing and sensorimotor areas using an automatically annotated fiber clustering in major depressive disorder. *Neuroimage* 181, 16–29.

Zhang, H., Schneider, T., Wheeler-Kingshott, C. A., and Alexander, D. C. (2012). NODDI: practical in vivo neurite orientation dispersion and density imaging of the human brain. *Neuroimage* 61, 1000–1016.

Zhao, X., Shi, J., Dai, F., Wei, L., Zhang, B., Yu, X., et al. (2021). Brain development from newborn to adolescence: evaluation by neurite orientation dispersion and density imaging. *Front. Hum. Neurosci.* 15:616132.

Zhu, Y., Wang, L., Xi, Y., Dai, T., Fei, N., Liu, L., et al. (2017). White matter microstructural properties are related to inter-individual differences in cognitive instability after sleep deprivation. *Neuroscience* 365, 206–216.

frontiers | Frontiers in Neuroscience

TYPE Original Research
PUBLISHED 11 April 2023
DOI 10.3389/fnins.2023.1141261

OPEN ACCESS

EDITED BY
Jinglei Lv,
The University of Sydney, Australia

REVIEWED BY
Jianzhong He,
Zhejiang University of Technology, China
Shujun Liang,
Southern Medical University, China

*CORRESPONDENCE
Shijun Qiu
✉ qiu-sj@163.com
Ye Wu
✉ wuye@njust.edu.cn

SPECIALTY SECTION
This article was submitted to Brain Imaging Methods, a section of the journal Frontiers in Neuroscience

RECEIVED 10 January 2023
ACCEPTED 27 March 2023
PUBLISHED 11 April 2023

CITATION
Lyu W, Chen Y, Zhao K, Tan X, Wu Y and Qiu S (2023) Alterations of peripheral cytokines, BDNF, and surface-based morphometry indices in T2DM patients without cognitive impairment.
Front. Neurosci. 17:1141261.
doi: 10.3389/fnins.2023.1141261

Alterations of peripheral cytokines, BDNF, and surface-based morphometry indices in T2DM patients without cognitive impairment

Wenjiao Lyu[1], Yuna Chen[2], Kui Zhao[1], Xin Tan[1], Ye Wu[3]* and Shijun Qiu[1]*

[1]Department of Radiology, The First Affiliated Hospital of Guangzhou University of Chinese Medicine, Guangzhou, Guangdong, China, [2]Department of Endocrinology, The First Affiliated Hospital of Guangzhou University of Chinese Medicine, Guangzhou, Guangdong, China, [3]School of Computer Science and Engineering, Nanjing University of Science and Technology, Nanjing, Jiangsu, China

Purpose: This study aimed to investigate potential biological mechanisms underlying cognitive function alterations in Type 2 diabetes mellitus (T2DM) patients by integrating cortical morphology with peripheral cytokine levels and brain-derived neurotrophic factor (BDNF) levels, and to offer potential insights for the early detection of T2DM-related cognitive impairment.

Methods: This study included 16 T2DM patients with a Montreal Cognitive Assessment (MoCA) score of at least 26 points, as well as 16 healthy controls with normal cognitive function. The participants also completed the digit span test and digit symbol substitution test. Participants' serum levels of Interleukin 4 (IL-4), IL-6, IL-10, tumor necrosis factor-alpha (TNF-α), interferon-gamma (IFN-γ), and BDNF were also examined. Each subject underwent a high-resolution 3T structural brain MRI scan. Based on the aparc. a2009s atlas, we calculated the cortical thickness, sulcus depth, gyrification index, and fractal dimension for each participant using surface-based morphometry (SBM). Correlation analysis between cognitive measures, serum levels of cytokines and BDNF, and SBM indices were further performed.

Results: The levels of IL-4 and BDNF showed significant group differences. In the T2DM group, the sulcus depth exhibited a significant decrease in the left transverse frontopolar gyri and sulci, as well as in the right pole-occipital; the fractal dimension showed a significant increase in the right posterior-dorsal part of the cingulate gyrus; and the gyrification index significantly increased in the left inferior part of the precentral sulcus and right triangular part of the inferior frontal gyrus. Correlation analysis revealed a significant positive correlation between IL-10 levels and the sulcus depth of left transverse frontopolar gyri and sulci; a significant positive correlation between the sulcus depth of the right pole-occipital and the digit span test-forward scores, and a significant negative correlation between the gyrification index of the left inferior part of the precentral sulcus and the digit span test-backward scores among T2DM participants.

Conclusion: T2DM patients without cognitive impairment displayed reductions in IL 4 and BDNF levels, as well as significant alterations in their SBM indices,

indicating that prior to the emergence of cognitive impairment, the SBM indices, peripheral cytokines, and BDNF may have altered in T2DM patients. IL-10 may lessen inflammation-related brain edema and preserve sulcus depth in T2DM patients through its anti-inflammatory activity.

KEYWORDS

type 2 diabetes mellitus, magnetic resonance imaging, cytokines, brain-derived neurotrophic factor, cognitive impairment, surface-based morphometry

1. Introduction

Type 2 diabetes mellitus (T2DM) is a disease caused by insufficient or relatively insufficient insulin secretion, with elevated blood glucose as the main manifestation. Currently, there are nearly 500 million people with T2DM worldwide, and the global incidence of T2DM is increasing year by year, which makes T2DM one of the diseases that threaten human health worldwide (Chatterjee et al., 2017; Sun et al., 2022). Among the many complications of T2DM, cognitive impairment has attracted increasing attention in recent years. Notably, individuals with T2DM have a 1.5 times increased risk for Alzheimer's disease and other dementias (Biessels et al., 2006). Cognitive impairment can impair T2DM patients' self-management, resulting in poor glycemic control or recurrent bouts of hypoglycemia, which can lead to cardiovascular events or death (Feil et al., 2012; Punthakee et al., 2012). Therefore, early diagnosis and early intervention of cognitive impairment in T2DM are critical to improving patient prognosis.

The development and application of magnetic resonance imaging (MRI) technology enabled the detection of structural alterations in the brain without invasion or radiation. A growing number of studies have been carried out using MRI to investigate the relationship between cognitive impairment and structural alterations in the brain in T2DM. Surface-based morphometry (SBM) is a cortical analysis approach that has recently gained popularity among researchers due to its ability to calculate various cerebral cortex indices and hence yield more cortical information than voxel-based morphometry (VBM) (Ahn et al., 2011). SBM has been applied to investigate cerebral cortical abnormalities in neuropsychiatric disorders, such as Alzheimer's disease (Nho et al., 2012), schizophrenia (Palaniyappan and Liddle, 2012), autism (Nordahl et al., 2007), etc. Several studies have recently begun to explore alterations in SBM indices in T2DM patients (Kang et al., 2022; Shao et al., 2022). In addition, it has also been demonstrated that cytokines and brain-derived neurotrophic factor (BDNF) levels may be associated with the development of T2DM-related cognitive impairment (Zhen et al., 2013; Simo et al., 2017; Sun et al., 2018). Despite recent achievements in MRI analysis and molecular biology techniques, the underlying mechanisms of T2DM related cognitive impairment are far from well clarified. Moreover, to the best of our knowledge, there is still lacking the combination of SBM indices and cytokines levels to assess cognitive impairment in T2DM of the currently available studies. We speculate that combining these approaches to evaluate alterations in cortical structure as well as peripheral blood cytokines and BDNF in T2DM patients who have not yet exhibited cognitive impairment may give insights into the underlying mechanisms and early detection of T2DM-related cognitive impairment.

The purpose of this study was to investigate potential biological mechanisms underlying cognitive function alterations in T2DM patients by integrating cortical morphology with peripheral cytokine levels and BDNF levels, and to offer potential insights for the early detection of T2DM-related cognitive impairment.

2. Materials and methods

2.1. Participants

Patients with T2DM needed to meet the diagnostic criteria of the American Diabetes Association (ADA), have been diagnosed for more than 6 months, and had no previous diabetic crisis or diabetic complications. All subjects should be right-handed, have a MoCA score of at least 26, have at least 6 years of education, and have no history of cardiovascular disease, tumor, autoimmune system diseases, neurological diseases, psychiatric diseases, etc. In addition, none of the subjects have experienced trauma, surgery, infection, tobacco, alcohol, or drug use (except for regular use of blood glucose control drugs in T2DM patients) within 4 weeks before inclusion, and female subjects should not be pregnant or lactating. After strict inclusion and exclusion criteria, a total of 16 T2DM patients without cognitive impairment and 16 healthy controls were enrolled (ages between 29 and 65; recruitment period: June 2020 to June 2021). Detailed demographic information can be found in **Table 1**.

2.2. Cognitive tests

Prior to the acquisition of MRI images, each participant underwent a series of cognitive function tests. Chinese version of the Montréal Cognitive Assessment Scale-B (MoCA-B) (Nasreddine et al., 2005) test was primarily used to determine whether the subject with cognitive impairment, and only the subjects with MoCA scores $\geq$ 26 can be included in this study. Moreover, the digit span test (DST, including forward and backward versions) (Leung et al., 2011) and digit symbol substitution test (DSST) (Jaeger, 2018) were also used for a more comprehensive understanding of cognitive function.

TABLE 1 Demographics and clinical characteristics of the participants.

	T2DM (N = 16)	HC (N = 16)	Statistics (t/U)	P-value
Gender (F/M)	5/11	8/8		0.473
Age (years)	45.625 ± 9.344	42.125 ± 10.436	0.999	0.326
Education (years)	12.0 (9.0, 14.0)	12.0 (10.5, 16.0)	100.00	0.287
Systolic BP (mmHg)	131.19 ± 18.16	126.94 ± 16.69	0.689	0.496
Diastolic BP (mmHg)	83.86 ± 8.73	81.94 ± 8.31	0.643	0.525
BMI	24.32 ± 2.56	23.19 ± 2.77	1.196	0.241
MoCA	27.00 (26.00, 28.25)	29.00 (27.75, 30.00)	76.50	0.050
DST_F	8.50 (7.00, 9.00)	8.00 (8.00, 9.00)	117.50	0.697
DST_B	4.50 (4.00, 5.00)	5.00 (4.00, 6.00)	104.00	0.360
DSST	50.19 ± 10.60	51.56 ± 14.20	−0.310	0.758
IL-4 (pg/mL)	5.68 (5.01,5.68)	5.68 (5.68,10.34)	76.00	0.031*
IL-6 (pg/mL)	1.61 (1.42, 2.07)	1.42 (1.32, 1.67)	161.50	0.207
IL-10 (pg/mL)	1.29 ± 0.51	1.274 ± 0.87	0.072	0.943
TNF-α (pg/mL)	2.54 ± 0.48	2.49 ± 0.42	0.309	0.760
IFN-γ (pg/mL)	9.76 (9.76, 10.09)	9.76 (9.76,11.06)	110.00	0.473
BDNF (pg/mL)	3026.69 ± 2031.81	5012.69 ± 2180.96	−2.664	0.012*
HbA1c (%)	8.13 ± 1.56	NA	NA	NA
FBG (mmol/L)	8.26 (7.58, 9.07)	NA	NA	NA

Data are presented as N, median (Q1, Q3), and mean ± SD. T2DM, type 2 diabetes mellitus group; HC, healthy control group; F, female; M, male; Systolic BP, systolic blood pressure; Diastolic BP, diastolic blood pressure; BMI, body mass index; MoCA, Montreal cognitive assessment; DST_F, digit span test forward; DST_B, digit span test backward; DSST, digit symbol substitution test; IL-4, interleukin 4; IL-6, interleukin 6; IL-10, interleukin 10; TNF-α, tumor necrosis factor-alpha; IFN-γ, interferon-gamma; BDNF, brain-derived neurotrophic factor; HbA1c, Hemoglobin A1c; FBG, fasting blood glucose. Fisher's exact test was used for the statistical difference of gender. Two sample t-test was used for statistical group differences of age, systolic blood pressure, diastolic blood pressure, BMI, DSST, IL-10, TNF-α and BDNF. Non-parametric Mann–Whitney U test was performed for group comparison of the remaining variables. One asterisk (*) indicates the significant level with $P < 0.05$.

2.3. Clinical measurements and laboratory examinations

Each subject was measured for blood pressure, height, and weight in addition to the usual clinical physical examination. Blood pressure was used to exclude patients with moderate to severe hypertension, and height and weight were used to calculate body mass index (BMI) and to exclude obese patients. All subjects will also have venous blood collected to measure serum levels of BDNF, interleukin 4 (IL-4), interleukin 6 (IL-6), interleukin 10 (IL-10), tumor necrosis factor-alpha (TNF-α), interferon-gamma (IFN-γ) and, in addition, hemoglobin A1c (HbA1c) and fasting blood glucose (FBG) in patients with T2DM to rule out hyperglycemic crisis and to assess the diabetic condition. Clinical examination and blood collection should be done in the morning on the day of the MRI test on an empty stomach.

2.4. Imaging data acquisition

A 3.0 Tesla MAGNETOM Prisma MRI scanner (Siemens Healthcare, Erlangen, Germany) equipped with a 64-channel head-neck coil was used to collect the MRI data. The parameters of 3D T1WI sequence as following: Field of View (FOV) = 256 mm^2 × 256 mm^2, slice thickness = 1.0 mm, number of slices = 192, voxel size = 1.0 mm^3 × 1.0 mm^3 × 1.0 mm^3, Repetition time (TR) = 2530 ms, Echo time (TE) = 2.98 ms, integrated Parallel Acquisition Techniques (iPAT) = 2, flip angle = 7°, Echo spacing = 7.1 ms, Total acquisition time (TA) = 5 min 58 s.

2.5. Data preprocessing and SBM indices computation

Both T1-weighted imaging data preprocessing and SBM indices computation were carried out using SPM 12[1] and computational anatomy toolbox (CAT12) software[2] based on Matlab 2021b (The Mathworks Inc., Natick, MA, United States). Before data preprocessing, all the images were reviewed by two radiologists to confirm that there were no organic lesions in the brain, such as hemorrhages, infarcts, malformations, etc.

The image pre-processing steps were as follows: First, convert T1 imaging data from DICOM into NIfTI, then choose ICBM space template as Affine Regularisation and medium strength of SPM inhomogeneity correction for initial SPM 12 preprocessing, and then use the center of the mass algorithm to set origin, APRG approach for Skull- Stripping and optimized shooting method for spatial registration at CAT 12 preprocessing.

The SBM indices calculating steps were as follows: First, extract surface parameters, which contain sulcus depth, gyrification index, and fractal dimension in addition to cortical thickness. Then resample and smooth surface data with a 15 mm full-width half max (FWHM) Gaussian kernel for cortical thickness, and 20 mm FWHM Gaussian kernel for the other indices. Then extract surface values based on the aparc_2009 atlas (Destrieux et al., 2010).

2.6. Statistical analysis

Two-sample t-test, Mann-Whitney U-test and Fisher's exact test were employed to assess differences between groups for demographic information, clinical data, and laboratory data, depending on the type of data and whether it corresponded to a normal distribution. For the detection of inter-group differences

1 http://www.fil.ion.ucl.ac.uk/spm
2 http://www.neuro.uni-jena.de/cat/

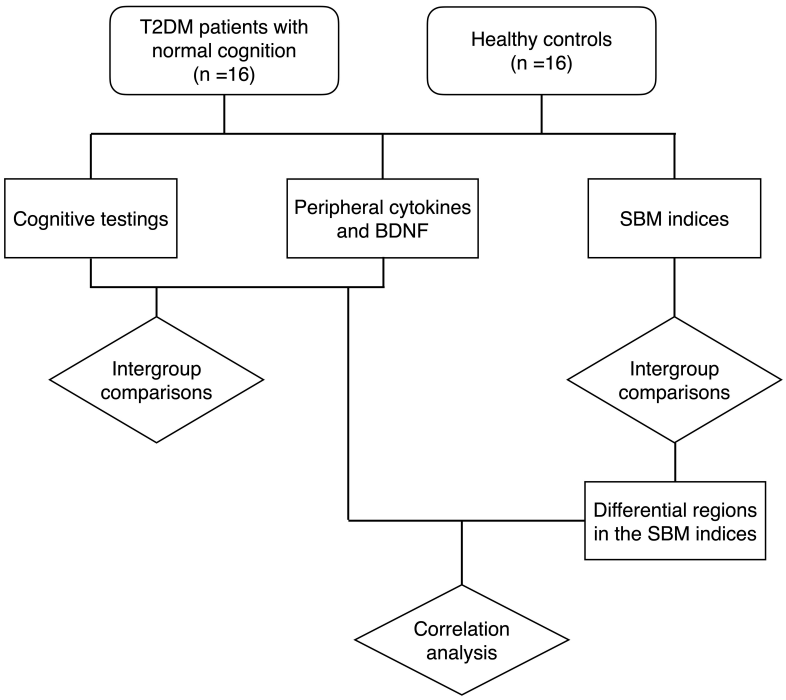

FIGURE 1
The flow chart of the study. T2DM, type 2 diabetes mellitus group; BDNF, brain-derived neurotrophic factor; SBM, surface-based morphometry.

in SBM indices, gender was added as a covariate, and SPM software was used to perform factorial design, followed by two-sample *t*-tests with Holm-Bonferroni correction. The relationships between cognitive function scores, cytokines and SBM indices were calculated using Spearman partial correlation analysis controlled with gender. $P < 0.05$ was regarded as statistically significant. Statistical analyses were carried out using JASP software[3] and R-Studio software.[4] The flow of the study is shown in Figure 1.

3. Results

3.1. Demographics, clinical characteristics, and laboratory results

There were no significant differences in terms of gender, age, years of education, blood pressure and BMI between the two groups. Regarding the cognitive function scores, we only recruited T2DM patients without cognitive impairment. However, their MoCA scores were lower than those of healthy controls, although the difference was not statistically significant ($P = 0.05$). There were no significant group differences in the scores of DST and DSST between the two groups. Laboratory results of peripheral blood showed a significant decrease in the levels of IL-4 and BDNF in the T2DM group ($P < 0.05$). Other cytokines revealed no statistically significant differences between groups. Detailed information for the T2DM and HC groups is presented in Table 1.

3 https://jasp-stats.org/

4 https://www.rstudio.com/

3.2. Differential brain regions in the SBM indices between groups

In the T2DM group, the sulcus depth exhibited a significant decrease in the left transverse frontopolar gyri and sulci, as well as in the right pole-occipital ($P = 0.040$ and 0.017, respectively, Holm-Bonferroni corrected); the fractal dimension showed a significant increase in the right posterior-dorsal part of the cingulate gyrus ($P = 0.007$, Holm-Bonferroni corrected); and the gyrification

TABLE 2 Information of the differential brain regions in the SBM indices between T2DM patients with normal cognitive function and healthy controls.

SBM index	Hemisphere	Atlas regions	*t*-value	*P*-value
Sulcus depth	Left	Transverse frontopolar gyri and sulci	−2.755	0.040*
Sulcus depth	Right	Pole occipital	−2.527	0.017*
Fractal dimension	Right	Posterior dorsal part of the cingulate gyrus	3.161	0.007**
Gyrification index	Left	Inferior part of the precentral sulcus	3.808	0.034*
Gyrification index	Right	Triangular part of the inferior frontal gyrus	2.353	0.038*

Two sample t-test, Holm-Bonferroni corrected. T2DM, type 2 diabetes mellitus group; SBM, surface-based morphometry. One asterisk (*) indicates the significant level with $P < 0.05$. Two asterisks (**) indicates the significant level with $P < 0.01$.

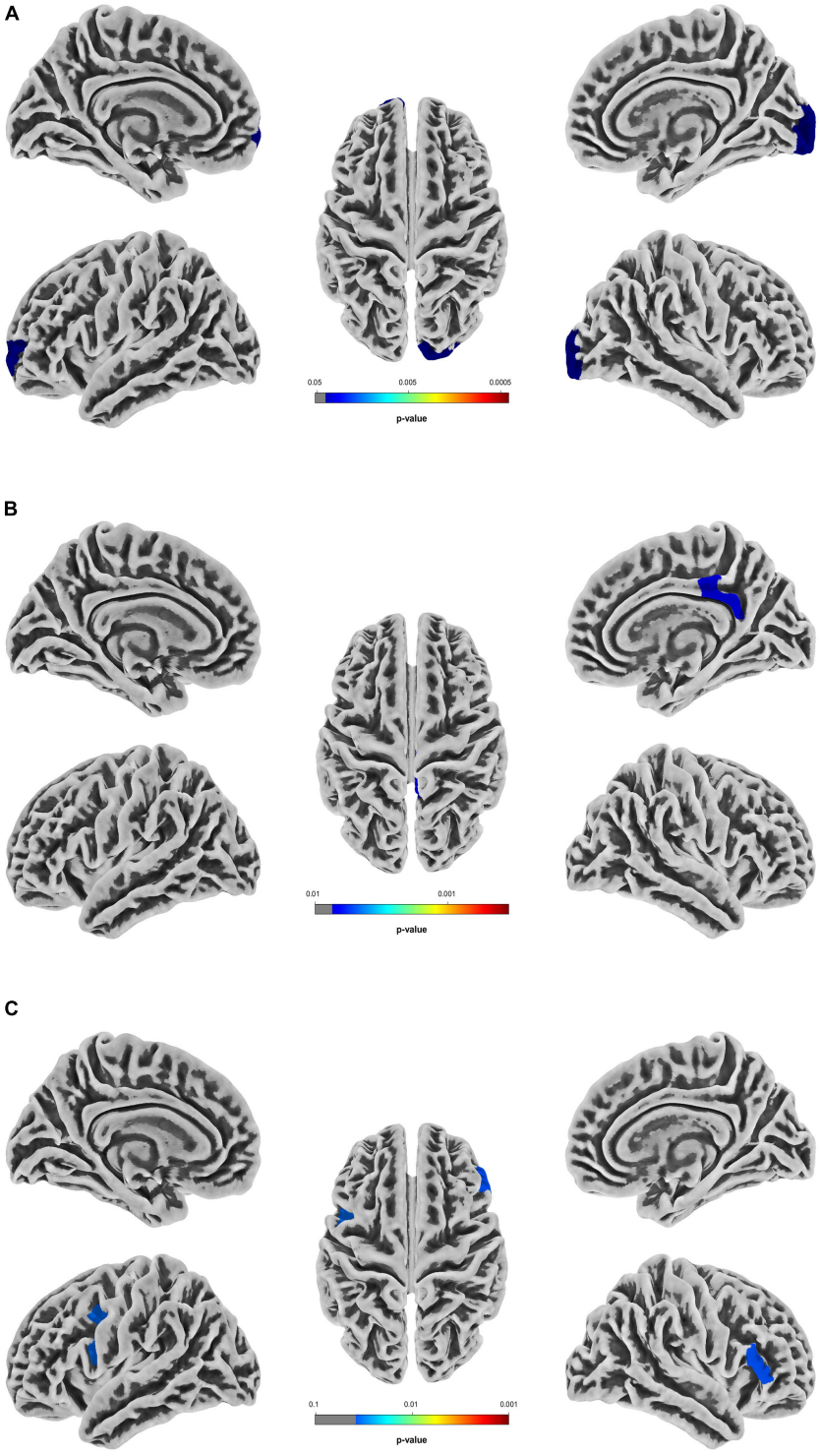

FIGURE 2
Differential brain regions in the SBM indices between T2DM patients with normal cognitive function and healthy controls. **(A)** Differential brain regions with intergroup differences in sulcus depth. **(B)** Differential brain regions with intergroup differences in fractal dimension. **(C)** Differential brain regions with intergroup differences in gyrification index. Two sample t-test, Holm-Bonferroni corrected. T2DM, type 2 diabetes mellitus group; SBM, surface-based morphometry.

index indicated a significant increase in the left inferior part of the precentral sulcus and right triangular part of the inferior frontal gyrus (P = 0.034 and 0.038, respectively, Holm-Bonferroni corrected). After adjustment for multiple comparisons, there was no significant difference in cortical thickness between groups. The information of the differential brain regions in the SBM indices is shown in Table 2, and the locations of the differential brain regions are shown in Figure 2.

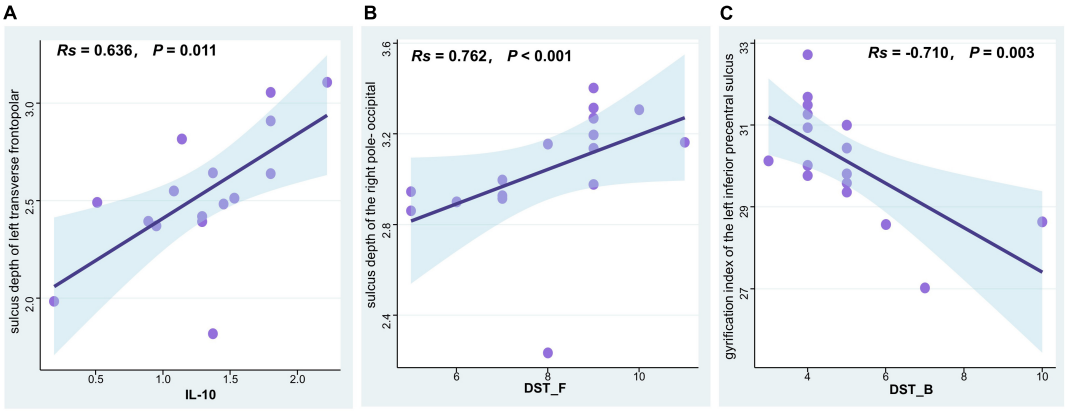

FIGURE 3
Correlation analysis of SBM indices, cytokine levels, and cognitive function scores in T2DM patients with normal cognitive function. **(A)** IL-10 levels were positively associated with the sulcus depth of left transverse frontopolar gyri and sulci (Spearman correlation, $R = 0.636$, $P = 0.011$). **(B)** The digit span test-forward scores were positively associated with the sulcus depth of the right pole-occipital (Spearman correlation, $R = 0.762$, $P < 0.001$). **(C)** The digit span test-backward scores were negatively associated with the gyrification index of the left inferior part of the precentral sulcus (Spearman correlation, $R = -0.710$, $P = 0.003$). T2DM, type 2 diabetes mellitus group; SBM, surface-based morphometry; IL-10, interleukin 10; DST_F, digit span test-forward; DST_B, digit span test-backward.

3.3. Correlations between cognitive function scores, cytokines and SBM indices in the T2DM group

Spearman's partial correlation analysis revealed a significant positive correlation between IL-10 levels and the sulcus depth of left transverse frontopolar gyri and sulci ($R = 0.636$, $P = 0.011$), a significant positive correlation between the sulcus depth of the right pole- occipital and the digit span test-forward ($R = 0.762$, $P < 0.001$), and a significant negative correlation between the gyrification index of the left inferior part of the precentral sulcus and the digit span test-backward ($R = -0.710$, $P = 0.003$) among T2DM participants (Figure 3).

4. Discussion

In this study, we examined the levels of peripheral blood cytokines and BDNF in T2DM patients without cognitive impairment, as well as healthy controls, and calculated indices such as sulcal gyrus depth, fractal dimension, gyrification index and thickness of the cerebral cortex utilizing the SBM approach. We noticed that T2DM patients had significant alterations in their cytokine levels, BDNF levels and SBM indices prior to the development of cognitive impairment. Further correlation analysis in T2DM patients revealed a non-negligible association between cytokine levels, SBM indices, and cognitive function scores. It is suggested that combining biological indices such as cytokines and BDNF with magnetic resonance imaging analysis technology can provide new insights into understanding the underlying mechanism of T2DM-related cognitive impairment and further explore biomarkers for its early diagnosis.

The cognitive decline induced by T2DM is an insidious process with complex causes, and the specific mechanism has not been clearly explained. Before mild cognitive impairment (MCI), T2DM patients may experience subtle cognitive changes in cognitive function, which is dubbed diabetes-associated cognitive decrements (Biessels and Despa, 2018). Despite the fact that we only recruited T2DM patients who were cognitively normal (none of them had a MoCA score below 26), it's possible that some of them were undergoing a decline in cognitive function. Hence this period is crucial for unraveling the pathological mechanisms of T2DM-related cognitive impairment and developing therapeutic strategies in advance of effective intervention.

Many neurodegenerative diseases, including Alzheimer's disease (AD), Parkinson's disease, and mild cognitive impairment (Nagatsu et al., 2000; Guerreiro et al., 2007; Brosseron et al., 2014), are thought to be related to chronic neuroinflammation. Therefore, cytokines, as small molecular proteins that play an important role in the regulation of inflammation and immune system, have been focused on research (Dinarello, 2007). Elevated levels of TNF-α and IFN-γ have been found both in pathological brain specimens of postmortem patients with AD and in relevant animal model studies, so these two cytokines are considered to be neurotoxic (Brosseron et al., 2014; Uddin et al., 2022). Although conflicting results as to its association with cognitive function, IL-6 is generally thought to be related to either acute or chronic inflammatory pathophysiology of cognitive impairment (Brosseron et al., 2014; Lyra e Silva et al., 2021). One research found that T2DM patients with cognitive impairment had considerably greater peripheral blood IL-6 levels than T2DM patients without cognitive impairment (Anita et al., 2022), whereas another reported that T2DM patients' IL-6 levels were significantly lower than those of healthy people (Yang et al., 2020). However, we did not observe any appreciable inter-group variations in TNF-α,IFN-γ, or IL-6. Our modest sample size, which will be enlarged for more analysis in the future, could be responsible for this. IL-4 and IL-10 are both anti-inflammatory cytokines that are commonly related to neuroprotection. It has been demonstrated that improved cognitive function is related to higher serum IL-4 and IL-10 concentrations in diabetic rats (Wang et al., 2020). IL-10 levels have been demonstrated to be considerably lower in T2DM patients than in healthy participants (Bashir et al., 2022), while elevated IL-10 levels

have also been identified in studies related to nerve fiber injury (Magrinelli et al., 2015). BDNF is assumed to facilitate learning and long-term memory for its supporting neuronal growth and survival, boosting dendritic branching, and regulating synapses (Gadani et al., 2012; Lu et al., 2014). Lower serum BDNF levels have been linked to the severity of cognitive impairment (Shimada et al., 2014; Siuda et al., 2017), and numerous investigations have revealed that individuals with T2DM have considerably lower BDNF levels than healthy subjects (Zhen et al., 2013, 2018; Sun et al., 2018; Anita et al., 2022). We also find the levels of BDNF in T2DM group were significantly decreased, which is consistent with the conclusions of previous studies (Krabbe et al., 2007; Zhen et al., 2013). Animal studies have shown that IL-4 is associated with learning ability, memory formation, and cognitive function (Derecki et al., 2010; Gadani et al., 2012; Kipnis et al., 2012). Moreover, one research concluded that IL-4 can stimulate microglia to generate BDNF (McCormick and Heller, 2015), implying that IL-4 may directly act as a cytoprotective cytokine of neurons. There are, however, limited clinical investigations on the relationship between IL-4 and alterations in cognitive function in T2DM patients. According to our research, serum IL-4 levels in T2DM patients are considerably lower than in healthy participants. In conjunction with the BDNF changes mentioned above, our findings indicate that IL-4 and BDNF may be involved in the process of cognitive function alterations in T2DM patients. Although there were no significant differences in IL-10 levels across the groups, we did observe that in T2DM patients, serum IL-10 levels were positively linked with the sulcus depth of left transverse frontopolar gyri and sulci. Additionally, there was a substantial positive correlation between DST and the sulcus depth of the right pole-occipital. Therefore, we hypothesize that IL-10 is engaged in the anti-inflammatory process of T2DM patients, alleviating edema induced by inflammation to maintain the depth of the sulcus depth. This might be relevant to the maintenance of normal cognitive function, but whether it involves compensatory mechanisms needs to be explored and proved further.

The gyrification index and fractal dimension are commonly utilized as key indices of cortical complexity, and aberrations in these parameters may serve as biological markers for neuropsychiatric disorders (King et al., 2010; Matsuda and Ohi, 2018), but the conclusions are controversial. Recently research showed individuals with T2DM had higher gyrification index than healthy participants (Crisóstomo et al., 2021), while another study revealed that the gyrification index is lower in T2DM patients with mild cognitive impairment (Shao et al., 2022). Some experts suggest that the relationship between gyrification index and cognitive function is changing dynamically during the progression of neurodegenerative diseases, and also that alterations in various brain areas are not synchronized (Lebed et al., 2012; Núñez et al., 2020). Fractal dimension is a morphological variability sensitive index used to evaluate brain structural complexity (Chen et al., 2022). Decreased fractal dimension has been found in mild cognitive impairment patients and AD patients (Ruiz de Miras et al., 2017; Nicastro et al., 2020). On the alterations in fractal dimension in T2DM patients, however, very few studies have been conducted. We speculate that the fractal dimension, like the gyrification index, undergoes dynamic changes during the progression of cognitive function alterations in T2DM patients.

Inevitably, there are some limitations to our study. First off, our sample size is somewhat limited because of the stringent inclusion and exclusion criteria. Based on this research, we would continue to increase the sample size in future investigations. Secondly, our study was a cross-sectional study, we intend to conduct long-term follow-up observations on the subjects in the future to capture the key nodes of cognitive impairment in T2DM patients. Thirdly, due to the complicated medication regimen for patients with T2DM, we could not take the patients' medication situation into consideration in this study. How to evaluate the influence of medicine use in future studies related to T2DM is a topic worth exploring.

5. Conclusion

T2DM patients without cognitive impairment displayed reductions in IL 4 and BDNF levels, as well as significant alterations in their SBM indices, indicating that prior to the emergence of cognitive impairment, the SBM indices, peripheral cytokines, and BDNF may have altered in T2DM patients. IL-10 may lessen inflammation-related brain edema and preserve sulcus depth in T2DM patients through its anti-inflammatory activity. The combination of inflammatory biomarkers and MRI may yield valuable perspectives on comprehending the mechanisms of cognitive impairment in T2DM individuals. Further study with expanded sample size and follow-up investigations should be carried out to establish if cytokines, BDNF, and the SBM indices are involved in the process of compensating for cognitive function ahead of the onset of T2DM-related cognitive impairment.

Data availability statement

The raw data supporting the conclusions of this article will be made available by the authors, without undue reservation.

Ethics statement

The studies involving human participants were reviewed and approved by Medical Research Ethics Committee of Guangzhou University of Chinese Medicine (No. K2019-143). The patients/participants provided their written informed consent to participate in this study. Written informed consent was obtained from the individual(s) for the publication of any potentially identifiable images or data included in this article.

Author contributions

WL: data curation, methodology, formal analysis, investigation, writing – original draft, and visualization. YC and KZ: data curation and investigation. XT: conceptualization and validation. YW: methodology, validation, visualization, and writing – review and editing. SQ: conceptualization, funding acquisition, project administration, resources, supervision, and writing – review and editing. All authors contributed to the article and approved the submitted version.

Funding

The funding from the National Natural Science Foundation of China (81920108019) covers the participants' transportation subsidies and publication fees.

Conflict of interest

The authors declare that the research was conducted in the absence of any commercial or financial relationships that could be construed as a potential conflict of interest.

Publisher's note

All claims expressed in this article are solely those of the authors and do not necessarily represent those of their affiliated organizations, or those of the publisher, the editors and the reviewers. Any product that may be evaluated in this article, or claim that may be made by its manufacturer, is not guaranteed or endorsed by the publisher.

References

Ahn, H.-J., Seo, S. W., Chin, J., Suh, M. K., Lee, B. H., Kim, S. T., et al. (2011). The cortical neuroanatomy of neuropsychological deficits in mild cognitive impairment and Alzheimer's disease: A surface-based morphometric analysis. *Neuropsychologia* 49, 3931–3945. doi: 10.1016/j.neuropsychologia.2011.10.010

Anita, N. Z., Zebarth, J., Chan, B., Wu, C.-Y., Syed, T., Shahrul, D., et al. (2022). Inflammatory markers in type 2 diabetes with vs. Without cognitive impairment; a systematic review and meta-analysis. *Brain Behav. Immunity* 100, 55–69. doi: 10.1016/j.bbi.2021.11.005

Bashir, H., Majid, S., Khan, M. S., Bhat, M. H., Hamid, R., Ashraf, R., et al. (2022). Inter-relationship of Pro-and anti-inflammatory biomarkers with the development of type 2 diabetes mellitus. *Heliyon* 8:e11329. doi: 10.1016/j.heliyon.2022.e11329

Biessels, G. J., and Despa, F. (2018). Cognitive decline and dementia in diabetes mellitus: Mechanisms and clinical implications. *Nat. Rev. Endocrinol.* 14, 591–604. doi: 10.1038/s41574-018-0048-7

Biessels, G. J., Staekenborg, S., Brunner, E., Brayne, C., and Scheltens, P. (2006). Risk of dementia in diabetes mellitus: A systematic review. *Lancet Neurol.* 5, 64–74. doi: 10.1016/S1474-4422(05)70284-2

Brosseron, F., Krauthausen, M., Kummer, M., and Heneka, M. T. (2014). Body fluid cytokine levels in mild cognitive impairment and Alzheimer's disease: A comparative overview. *Mol. Neurobiol.* 50, 534–544. doi: 10.1007/s12035-014-8657-1

Chatterjee, S., Khunti, K., and Davies, M. J. (2017). Type 2 diabetes. *Lancet* 389, 2239–2251.

Chen, Y., Zuo, Y., Kang, S., Pan, L., Jiang, S., Yan, A., et al. (2022). Using fractal dimension analysis to assess the effects of normal aging and sex on subregional cortex alterations across the lifespan from a Chinese dataset. *Cereb. Cortex* bhac417. doi: 10.1093/cercor/bhac417

Crisóstomo, J., Duarte, J. V., Moreno, C., Gomes, L., and Castelo-Branco, M. (2021). A novel morphometric signature of brain alterations in type 2 diabetes: Patterns of changed cortical gyrification. *Eur. J. Neurosci.* 54, 6322–6333. doi: 10.1111/ejn.15424

Derecki, N. C., Cardani, A. N., Yang, C. H., Quinnies, K. M., Crihfield, A., Lynch, K. R., et al. (2010). Regulation of learning and memory by meningeal immunity: A key role for IL-4. *J. Exp. Med.* 207, 1067–1080.

Destrieux, C., Fischl, B., Dale, A., and Halgren, E. (2010). Automatic parcellation of human cortical gyri and sulci using standard anatomical nomenclature. *Neuroimage* 53, 1–15. doi: 10.1016/j.neuroimage.2010.06.010

Dinarello, C. A. (2007). Historical insights into cytokines. *Eur. J. Immunol.* 37, S34–S45.

Feil, D. G., Zhu, C. W., and Sultzer, D. L. (2012). The relationship between cognitive impairment and diabetes self-management in a population-based community sample of older adults with Type 2 diabetes. *J. Behav. Med.* 35, 190–199. doi: 10.1007/s10865-011-9344-6

Gadani, S. P., Cronk, J. C., Norris, G. T., and Kipnis, J. (2012). IL-4 in the brain: A cytokine to remember. *J. Immunol.* 189, 4213–4219. doi: 10.4049/jimmunol.1202246

Guerreiro, R. J., Santana, I., Brás, J. M., Santiago, B., Paiva, A., and Oliveira, C. (2007). Peripheral inflammatory cytokines as biomarkers in Alzheimer's disease and mild cognitive impairment. *Neurodegener. Dis.* 4, 406–412.

Jaeger, J. (2018). Digit symbol substitution test: The case for sensitivity over specificity in neuropsychological testing. *J. Clin. Psychopharmacol.* 38:513. doi: 10.1097/JCP.0000000000000941

Kang, S., Chen, Y., Wu, J., Liang, Y., Rao, Y., Yue, X., et al. (2022). Altered cortical thickness, degree centrality, and functional connectivity in middle-age type 2 diabetes mellitus. *Front. Neurol.* 13:939318. doi: 10.3389/fneur.2022.939318

King, R. D., Brown, B., Hwang, M., Jeon, T., George, A. T., and Alzheimer's Disease Neuroimaging Initiative (2010). Fractal dimension analysis of the cortical ribbon in mild Alzheimer's disease. *Neuroimage* 53, 471–479.

Kipnis, J., Gadani, S., and Derecki, N. C. (2012). Pro-cognitive properties of T cells. *Nat. Rev. Immunol.* 12, 663–669. doi: 10.1038/nri3280

Krabbe, K., Nielsen, A., Krogh-Madsen, R., Plomgaard, P., Rasmussen, P., Erikstrup, C., et al. (2007). Brain-derived neurotrophic factor (BDNF) and type 2 diabetes. *Diabetologia* 50, 431–438.

Lebed, E., Jacova, C., Wang, L., and Beg, M. F. (2012). Novel surface-smoothing based local gyrification index. *IEEE Trans. Med. Imaging* 32, 660–669. doi: 10.1109/TMI.2012.2230640

Leung, J. L., Lee, G. T., Lam, Y., Chan, R. C., and Wu, J. Y. (2011). The use of the Digit Span Test in screening for cognitive impairment in acute medical inpatients. *Int. Psychogeriatr.* 23, 1569–1574.

Lu, B., Nagappan, G., and Lu, Y. (2014). BDNF and synaptic plasticity, cognitive function, and dysfunction. *Handb. Exp. Pharmacol.* 220, 223–250.

Lyra e Silva, N. M., Gonçalves, R. A., Pascoal, T. A., Lima-Filho, R. A., Resende, E. P. F., Vieira, E. L., et al. (2021). Pro-inflammatory interleukin-6 signaling links cognitive impairments and peripheral metabolic alterations in Alzheimer's disease. *Transl. Psychiatry* 11, 1–15. doi: 10.1038/s41398-021-01349-z

Magrinelli, F., Briani, C., Romano, M., Ruggero, S., Toffanin, E., Triolo, G., et al. (2015). The association between serum cytokines and damage to large and small nerve fibers in diabetic peripheral neuropathy. *J. Diabetes Res.* 2015:547834. doi: 10.1155/2015/547834

Matsuda, Y., and Ohi, K. (2018). Cortical gyrification in schizophrenia: Current perspectives. *Neuropsychiatr. Dis. Treat.* 14:1861.

McCormick, S. M., and Heller, N. M. (2015). Commentary: IL-4 and IL-13 receptors and signaling. *Cytokine* 75, 38–50.

Nagatsu, T., Mogi, M., Ichinose, H., and Togari, A. (2000). Changes in cytokines and neurotrophins in Parkinson's disease. *Adv. Res. Neurodegener.* 60, 277–290.

Nasreddine, Z. S., Phillips, N. A., Bedirian, V., Charbonneau, S., Whitehead, V., Collin, I., et al. (2005). The montreal cognitive assessment, MoCA: A brief screening tool for mild cognitive impairment. *J. Am. Geriatr. Soc.* 53, 695–699. doi: 10.1111/j.1532-5415.2005.53221.x

Nho, K., Risacher, S. L., Crane, P. K., DeCarli, C., Glymour, M. M., Habeck, C., et al. (2012). Voxel and surface-based topography of memory and executive deficits in mild cognitive impairment and Alzheimer's disease. *Brain Imaging Behav.* 6, 551–567. doi: 10.1007/s11682-012-9203-2

Nicastro, N., Malpetti, M., Cope, T. E., Bevan-Jones, W. R., Mak, E., Passamonti, L., et al. (2020). Cortical complexity analyses and their cognitive correlate in Alzheimer's disease and frontotemporal dementia. *J. Alzheimers Dis.* 76, 331–340.

Nordahl, C. W., Dierker, D., Mostafavi, I., Schumann, C. M., Rivera, S. M., Amaral, D. G., et al. (2007). Cortical folding abnormalities in autism revealed by surface-based morphometry. *J. Neurosci.* 27, 11725–11735. doi: 10.1523/JNEUROSCI.0777-07.2007

Núñez, C., Callén, A., Lombardini, F., Compta, Y., Stephan-Otto, C., and Alzheimer's Disease Neuroimaging Initiative (2020). Different cortical gyrification patterns in Alzheimer's disease and impact on memory performance. *Ann. Neurol.* 88, 67–80. doi: 10.1002/ana.25741

Palaniyappan, L., and Liddle, P. F. (2012). Aberrant cortical gyrification in schizophrenia: A surface-based morphometry study. *J. Psychiatry Neurosci.* 37, 399–406.

Punthakee, Z., Miller, M. E., Launer, L. J., Williamson, J. D., Lazar, R. M., Cukierman-Yaffee, T., et al. (2012). Poor cognitive function and risk of severe hypoglycemia in type 2 diabetes: Post hoc epidemiologic analysis of the ACCORD trial. *Diabetes Care* 35, 787–793. doi: 10.2337/dc11-1855

Ruiz de Miras, J., Costumero, V., Belloch, V., Escudero, J., Ávila, C., and Sepulcre, J. (2017). Complexity analysis of cortical surface detects changes in future Alzheimer's disease converters. *Hum. Brain Mapp.* 38, 5905–5918. doi: 10.1002/hbm.23773

Shao, P., Li, X., Qin, R., Xu, H., Sheng, X., Huang, L., et al. (2022). Altered local gyrification and functional connectivity in type 2 diabetes mellitus patients with mild cognitive impairment: A pilot cross-sectional small-scale single center stud. *Front. Aging Neurosci.* 14:934071. doi: 10.3389/fnagi.2022.934071

Shimada, H., Makizako, H., Doi, T., Yoshida, D., Tsutsumimoto, K., Anan, Y., et al. (2014). A large, cross-sectional observational study of serum BDNF, cognitive function, and mild cognitive impairment in the elderly. *Front. Aging Neurosci.* 6:69. doi: 10.3389/fnagi.2014.00069

Simo, R., Ciudin, A., Simo-Servat, O., and Hernandez, C. (2017). Cognitive impairment and dementia: A new emerging complication of type 2 diabetes-The diabetologist's perspective. *Acta Diabetol.* 54, 417–424. doi: 10.1007/s00592-017-0970-5

Siuda, J., Patalong-Ogiewa, M., Żmuda, W., Targosz-Gajniak, M., Niewiadomska, E., Matuszek, I., et al. (2017). Cognitive impairment and BDNF serum levels. *Neurol. Neurochir. Pol.* 51, 24–32.

Sun, H., Saeedi, P., Karuranga, S., Pinkepank, M., Ogurtsova, K., Duncan, B. B., et al. (2022). IDF Diabetes Atlas: Global, regional and country-level diabetes prevalence estimates for 2021 and projections for 2045. *Diabetes Res. Clin. Pract.* 183:109119. doi: 10.1016/j.diabres.2021.109119

Sun, Z. C., Yu, J., Liu, Y. L., Hong, Z. Z., Ling, L., Li, G. Q., et al. (2018). Reduced serum levels of brain-derived neurotrophic factor are related to mild cognitive impairment in chinese patients with type 2 diabetes mellitus. *Ann. Nutr. Metab.* 73, 271–281. doi: 10.1159/000493275

Uddin, M. S., Kabir, M. T., Jalouli, M., Rahman, M. A., Jeandet, P., Behl, T., et al. (2022). Neuroinflammatory signaling in the pathogenesis of Alzheimer's disease. *Curr. Neuropharmacol.* 20:126.

Wang, G., Zhang, X., Lu, X., Liu, J., Zhang, Z., Wei, Z., et al. (2020). Fish oil supplementation attenuates cognitive impairment by inhibiting neuroinflammation in STZ-induced diabetic rats. *Aging* 12:15281. doi: 10.18632/aging.103426

Yang, X., Chen, Y., Zhang, W., Zhang, Z., Yang, X., Wang, P., et al. (2020). Association between inflammatory biomarkers and cognitive dysfunction analyzed by MRI in diabetes patients. *Diabetes Metab. Syndr. Obes.* 13:4059.

Zhen, Y. F., Zhang, J., Liu, X. Y., Fang, H., Tian, L. B., Zhou, D. H., et al. (2013). Low BDNF is associated with cognitive deficits in patients with type 2 diabetes. *Psychopharmacology* 227, 93–100.

Zhen, Y.-F., Liu, X.-Y., Zhou, D.-H., Du, X., Yin, G., Zhang, Y., et al. (2018). Cognition, serum BDNF levels, and BDNF Val66Met polymorphism in type 2 diabetes patients and healthy controls. *Oncotarget* 9:3653. doi: 10.18632/oncotarget.23342

frontiers | Frontiers in Neuroscience

TYPE Original Research
PUBLISHED 20 April 2023
DOI 10.3389/fnins.2023.1163111

OPEN ACCESS

EDITED BY
Ye Wu,
Nanjing University of Science and Technology, China

REVIEWED BY
Elma M. Paredes-Aragon,
National Institute of Neurology and Neurosurgery, Mexico
Hanjiaerbieke Kukun,
First Affiliated Hospital of Xinjiang Medical University, China

*CORRESPONDENCE
Han Li
✉ leoincmu@gmail.com
Shouliang Qi
✉ qisl@bmie.neu.edu.cn

RECEIVED 10 February 2023
ACCEPTED 03 April 2023
PUBLISHED 20 April 2023

CITATION
Bacon EJ, Jin C, He D, Hu S, Wang L, Li H and Qi S (2023) Functional and effective connectivity analysis of drug-resistant epilepsy: a resting-state fMRI analysis. *Front. Neurosci.* 17:1163111. doi: 10.3389/fnins.2023.1163111

Functional and effective connectivity analysis of drug-resistant epilepsy: a resting-state fMRI analysis

Eric Jacob Bacon[1,2], Chaoyang Jin[1], Dianning He[1], Shuaishuai Hu[3], Lanbo Wang[4], Han Li[3]* and Shouliang Qi[1,2]*

[1]College of Medicine and Biological Information Engineering, Northeastern University, Shenyang, China, [2]Key Laboratory of Intelligent Computing in Medical Image, Ministry of Education, Northeastern University, Shenyang, China, [3]Department of Neurosurgery, Shengjing Hospital of China Medical University, Shenyang, China, [4]Department of Radiology, Shengjing Hospital of China Medical University, Shenyang, China

Objective: Epilepsy is considered as a neural network disorder. Seizure activity in epilepsy may disturb brain networks and damage brain functions. We propose using resting-state functional magnetic resonance imaging (rs-fMRI) data to characterize connectivity patterns in drug-resistant epilepsy.

Methods: This study enrolled 47 participants, including 28 with drug-resistant epilepsy and 19 healthy controls. Functional and effective connectivity was employed to assess drug-resistant epilepsy patients within resting state networks. The resting state functional connectivity (FC) analysis was performed to assess connectivity between each patient and healthy controls within the default mode network (DMN) and the dorsal attention network (DAN). In addition, dynamic causal modeling was used to compute effective connectivity (EC). Finally, a statistical analysis was performed to evaluate our findings.

Results: The FC analysis revealed significant connectivity changes in patients giving 64.3% (18/28) and 78.6% (22/28) for DMN and DAN, respectively. Statistical analysis of FC was significant between the medial prefrontal cortex, posterior cingulate cortex, and bilateral inferior parietal cortex for DMN. For DAN, it was significant between the left and the right intraparietal sulcus and the frontal eye field. For the DMN, the patient group showed significant EC connectivity in the right inferior parietal cortex and the medial prefrontal cortex for the DMN. There was also bilateral connectivity between the medial prefrontal cortex and the posterior cingulate cortex, as well as between the left and right inferior parietal cortex. For DAN, patients showed significant connectivity in the right frontal eye field and the right intraparietal sulcus. Bilateral connectivity was also found between the left frontal eye field and the left intraparietal sulcus, as well as between the right frontal eye field and the right intraparietal sulcus. The statistical analysis of the EC revealed a significant result in the medial prefrontal cortex and

the right intraparietal cortex for the DMN. The DAN was found significant in the left frontal eye field, as well as the left and right intraparietal sulcus.

Conclusion: Our results provide preliminary evidence to support that the combination of functional and effective connectivity analysis of rs-fMRI can aid in diagnosing epilepsy in the DMN and DAN networks.

KEYWORDS

default mode network, dorsal attention network, resting-state functional magnetic resonance, functional connectivity, effective connectivity, epilepsy

1. Introduction

Epilepsy is a common and serious neurological disorder that affects around 50 million people worldwide (World Health Organization [WHO], 2023). Drug-resistant epilepsy (DRE) also known as refractory epilepsy is one of the most complex types of epilepsy. DRE is a complicated and heterogeneous condition in which seizures persist despite adequate trials of two or more carefully chosen and used antiepileptic drugs (AEDs). The term "adequate trial" refers to the use of AEDs at therapeutic doses for a sufficient period of time. The International League Against Epilepsy (ILAE) defines adequate trial failure as the persistence of disabling seizures despite the use of two tolerated, appropriately chosen and used AED schedules, either alone or in combination (Scheffer et al., 2017). Around 20%–30% of the epileptic population remains refractory to treatment and is considered to have drug-resistant epilepsy (Dalic and Cook, 2016).

Diagnosis of DRE has remained challenging for neuroscientists and researchers. This difficulty can be explained by a variety of factors, including a lack of consensus definition, complex seizure semiology, limited diagnostic tools, comorbidities, and medication adherence issues (Jehi et al., 2022). For accurate diagnosis and management, a multidisciplinary approach and careful consideration of the patient's individual circumstances are required. Treatment options that can help mitigate these challenges include optimizing AED therapy, surgical intervention, non-surgical interventions, complementary and alternative medicine, multidisciplinary care, and education and support. Recent technological advancements have simplified the process by providing numerous credible methods for analyzing and diagnosing brain diseases.

The development of new technology in neuroimaging has brought new insights into how brain disease can be diagnosed and cured. Many technologies for observing brain function non-invasively were developed and used to acquire brain signals. Among them, functional magnetic resonance imaging (fMRI) is considered one of the most prominent in the field (Glover, 2011). This technology enabled the observation of regional brain activation by detecting the amount of oxygen in blood in each part of the brain. Here, we assume that the active region consumes more oxygen for energy. Resting state and task-based are two main kinds of fMRI utilized in the neuroimaging study. The main difference between the two lies in the acquisition procedure. Task-based fMRI is acquired when the subject performs specific tasks. In contrast, a resting state is acquired when the subject rests (Logothetis, 2008).

Understanding the properties of the brain network may help guide surgical intervention for better postoperative outcomes in drug-resistant epilepsy. A variety of resting state networks, each showing a definite spatial topography and putatively corresponding to a specific brain function (Yun et al., 2022). One of them, known as the default-mode network (DMN), is the most famous and essential network for the resting condition, as it consistently shows increased activity during rest than during active and passive cognitive tasks (Yun et al., 2022). The DMN areas typically comprise the posterior cingulate (PCC), medial prefrontal cortex (MPFC), and inferior parietal cortex (IPC) (Raichle et al., 2015). Same as DMN, the dorsal attention network (DAN) is another crucial resting-state fMRI network known to be active when performing specific tasks. However, DAN has also been proven to be associated with mesial temporal epilepsy in a resting state (Szczepanski et al., 2013). The DAN is centered on bilateral regions of the frontal and parietal cortex, including the frontal eye field (FEF) and the intraparietal sulcus (IPS).

Analyzing resting state fMRI (rs-fMRI) data remains challenging for neuroscientists. Brain connectivity modeling is a well-studied approach to illustrating brain function. One of the popular fMRI methods for studying brain networks is functional connectivity (rs-FC). Rs-FC measurements can detect coherent spontaneous neuronal activities within a brain network (van den Heuvel and Hulshoff Pol, 2010; Hlinka et al., 2011). This method has been explored by many researchers and is based on the temporal correlation between BOLD signals (Blood oxygenation level dependency) in distant brain regions. Lee et al. (2014) investigated changes in FC in brain networks for partial refractory epilepsy. The analysis was based on rs-fMRI using intrinsic connectivity contrast (ICC). Liu et al. (2021) also evaluated functional connectivity patterns in epilepsy associated with focal cortical dysplasia (FCD) to explore the underlying pathological mechanism of this disorder. Rs-FC is probably a good analytical approach to investigate rs-fMRI networks, but recent studies have highlighted some weaknesses and limitations of this approach (Buckner et al., 2013). These weaknesses could be covered by other analytical approaches, such as effective connectivity (EC) analysis. This method provides adequate details on directed causal influences between different regions of interest and covers some of the shortcomings observed during the FC analysis. Many studies have supported this using a similar technique to perform brain

network assessments and diagnose brain diseases. Using rs-fMRI, Wei et al. (2016) performed an effective connectivity analysis to examine idiopathic generalized epilepsy-related changes in major neurocognitive brain networks. Jiang et al. (2018) also assessed the functional and effective connectivity of the attention and default mode networks of rs-fMRI. Although, the EC method has many advantages and covers some limitations of FC analysis. However, several questions remain unanswered, so relatively few studies characterizing effective or directed connectivity analysis of epileptic disease exist. From all these observations, concrete actions must be taken to create a more efficient and precise method to eliminate these shortcomings.

We propose to analyze functional and effective connectivity based on rs-fMRI in this study. Our study aims to explore brain activities within the DMN and DAN of candidates with DRE. We hypothesize that studying functional and causal interactions within the brain network could help characterize and localize the epileptic zone. We also hypothesize that DRE candidates will have frequent seizures as a result of impaired brain communication caused by abnormal connectivity. Effective and functional connectivity analysis will be performed to achieve our goal. The idea behind such an approach is to effectively contribute to the diagnosis of the epileptogenic zone and facilitate surgical operations by making them more precise.

Our study is organized as follows. The functional connectivity analysis will first be performed using the CONN toolbox to analyze rs-fMRI candidates. It will consist of performing a seed-based correlation analysis to assess the connectivity patterns between each patient and the healthy controls for DMN and DAN separately. Next, the effective connectivity analysis will be performed using the DCM (Dynamic Causal Modeling) approach and the statistical Bayesian modeling inference, including Bayesian model selection and averaging. Finally, we evaluated our findings through statistical analysis. A two-sample *t*-test was conducted to differentiate connectivity within each network for the patients and healthy groups. This original study assesses the applicability of seed-based correlation and DCM analysis based on rs-fMRI data to diagnose epileptic networks.

2. Materials and methods

2.1. Participants

The dataset in this study initially consisted of 71 subjects (38 patients and 33 HCs). To increase the population size in this study, the data was collected from three different sources (2 samples of patients and a single sample of healthy controls). The first sample consisted of 12 patients who underwent presurgical evaluation from January 2018 to July 2019 at Shengjing Hospital of China Medical University. The evaluation involved a detailed clinical history and neurological examination, complete neuropsychological evaluation, psychiatric assessment, inter-ictal and ictal onset patterns in long-term scalp video-electroencephalogram (video-EEG), magnetic resonance imaging (MRI), and fMRI results. All 12 patients underwent surgical resection for medically refractory epilepsy with histopathological confirmation of FCD.

The others two samples were collected from an open-source website.[1] The second sample corresponding to the second group of patients is provided by Thompson et al. (2020). Participants were patients with medically drug-resistant who had elected to undergo neurosurgical treatment for their epilepsy.

The third sample is from the healthy control candidates collected by Gu et al. (2022). The subjects had no history of medical, neurological, or psychiatric disease. None of the subjects was taking medication at the time of testing.

The image quality of all subjects and datasets was checked and controlled in a concise manner. The procedure and selection criteria were given in **Figure 1**. Our current study included a total of 47 subjects, including 28 patients and 19 healthy controls. All patients were collected and evaluated in accordance with standard principles. The evaluation included a detailed clinical history, a neurological examination, a complete neuropsychological assessment, a psychiatric assessment, and inter-ictal and ictal onset patterns in a long-term scalp video-electroencephalogram (video-EEG), MRI, and fMRI. They were all diagnosed with focal epilepsy, and the presurgical evaluation test results for each patient are shown in **Table 1**.

This study was approved by the ethics committee of Shengjing Hospital of China Medical University and the informed consent was signed by the participant or a legal guardian/next of kin (for the participant under the age of 18).

2.2. Data acquisition

All rs-fMRI measurements were acquired and processed with a specific epilepsy protocol as used in the clinical routine. For sample 1, the MR images were acquired with a PET/MR scanner (SIGNA PET/MR; GE Healthcare, Waukesha, WI, USA) using a 16-channel head coil. The protocol included the following sequences: Sag 3D T1BRAVO (T1w; TR = 8.5 ms, TE = 3.3 ms, flip angle = 12°, voxel size = 0.469 × 0.469 × 1,000 mm^3, FOV = 512 × 512). Resting-state BOLD images were acquired using a SIGNA PET/MR (TR = 2,000 ms, TE = 35 ms, Flip angle = 90 degrees, 3.5 × 3.4 × 4.0 mm^3 voxel size).

Sample 2 images were acquired as follows: T1-W structural scans were obtained on a 3T GE Discovery 750w (BRAVO, 32 ch head coil, TE = 3.376 ms, TR = 8.588 ms, Flip angle = 12 deg., 1.0 × 1.0 × 0.8 mm voxel size). Resting-state BOLD-fMRI sessions were obtained in a subset of subjects before implantation (4.8 min per session, 32 ch head coil, TR = 2,260 ms, TE = 30 ms, Flip angle = 80 degrees, 3.4 × 3.4 × 4.0 mm^3 voxel size).

Sample 3 data were collected on a 3 Tesla Prisma Siemens Fit scanner using a Siemens 20-channel receive-array coil. Anatomical images were acquired using an MPRAGE sequence (TR: 2,300 milliseconds, TE: 2.28 milliseconds, 1 mm isotropic spatial resolution, FOV: 256 millimeters, flip angle: 8 degrees, matrix size: 256 × 256 × 192, acceleration factor: 2). Each scanning section consisted of an anatomical session, two 10-min resting-state sessions, and several 15-min sleep sessions. Blood oxygenation level-dependent (BOLD) fMRI data were acquired using an EPI sequence (TR: 2,100 milliseconds, TE: 25 milliseconds, slice

1 openneuro.org

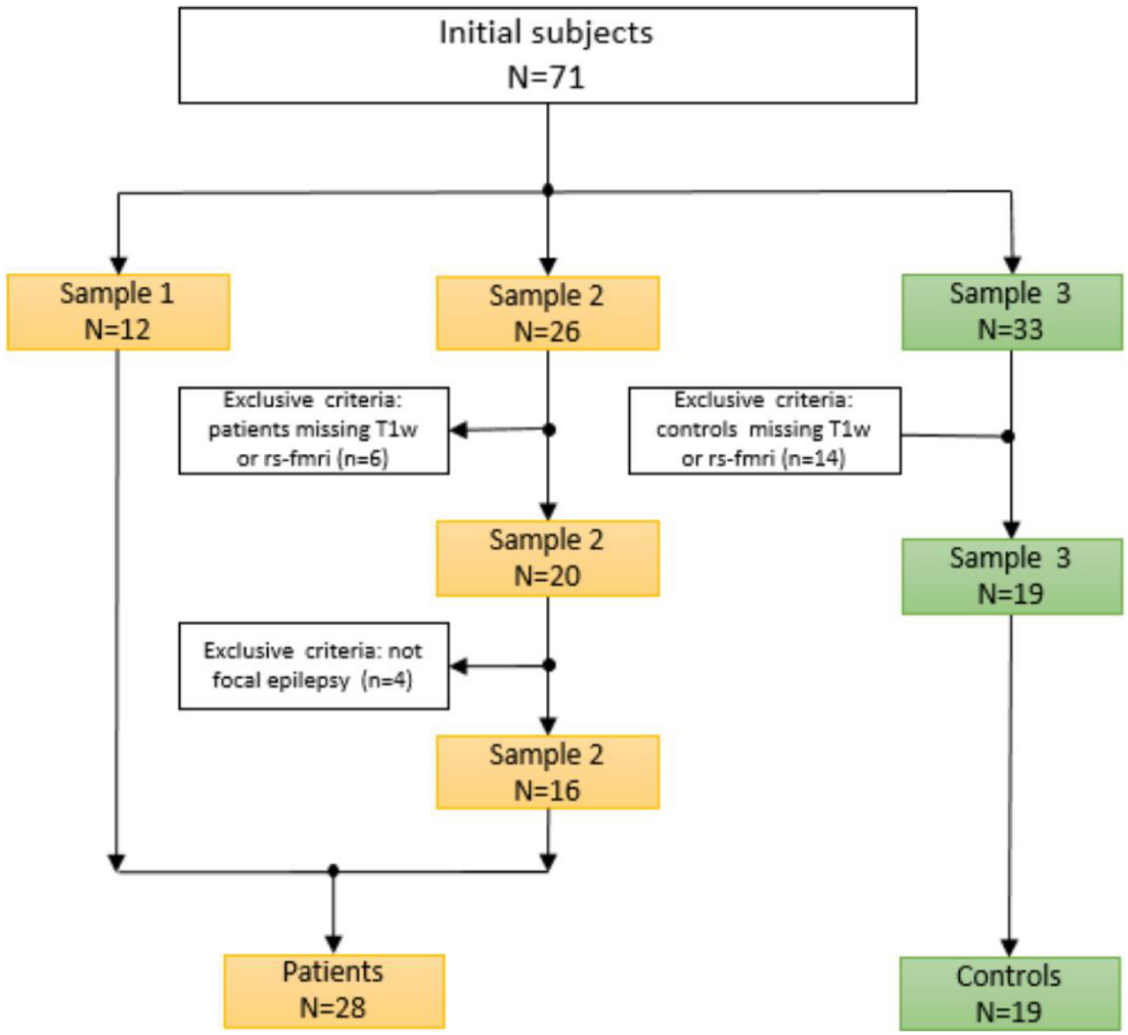

FIGURE 1
Criteria and the procedure for selecting subjects.

thickness: 4 mm, slices: 35, FOV: 240 mm, in-plane resolution: 3 mm × 3 mm).

2.3. Data processing

The functional connectivity analysis in this study uses the CONN toolbox.[2] CONN is a powerful and well-known neuroimaging toolbox that helps process task-related and rs-fMRI data (Whitfield-Gabrieli and Nieto-Castanon, 2012; Schurz et al., 2014). For this study, we subdivided our method into three main steps: data preprocessing, processing, and statistical analysis (Figure 2). The classical CONN pre-processing procedure was performed using the default configuration. It included the realignment and unwarping of the functional images, motion correction, slice-timing correction, and co-registration with the structural data (target resolution for functional images = 2 mm). Structural segmentation and normalization, functional normalization, ART-based (Artifact Detection Tools) functional outlier detection and scrubbing, and functional smoothing (full-width-at-half maximum [FWHM 8-mm Gaussian kernel) were carried out in MNI-space. After pre-processing data, the processing step will follow. The CONN default processing was set as it implements the component-based noise correction method (CompCor) strategy for physiological and other noise source reduction, additional removal of movement, and temporal covariates, temporal filtering, and windowing of the residual blood oxygen level-dependent (BOLD) contrast signal. During the processing step, resting-state signals will be extracted from the gray matter, and the cortex will be divided into different regions of interest (ROI). Additionally, the mean time series of each ROI will be extracted as regressors, where other internal processing conditions will be specified along with the regressors. After that, individual connectivity maps will be created for each participant. Eight nodes derived from the networks were selected as the atlases or regions of interest. One can refer to Table 2 for the details concerning the networks and coordinate information of their nodes.

2 www.nitrc:projects/conn

2.4. Functional connectivity

The functional connectivity analysis includes the first-level and second-level analyses (Figure 2). The whole analysis was based on the seed-based connectivity (SBC) procedures defined in CONN tool. In the first-level analysis, for each subject, every region in DMN and DAN is used as a seed to conduct a seed-to-voxel functional connectivity analysis, such as to compute the correlation maps between the seed and voxels in the rest of the brain. DMN has 4 regions, including the posterior cingulate cortex (PCC), medial prefrontal cortex (MPFC), and bilateral inferior parietal cortex (LIPC and RIPC). DAN has four regions, including the frontal eye field (FEF) and the intraparietal sulcus (IPS) at the left and right hemispheres. Finally, a z-transformed connectivity map is obtained for each region of each subject.

In the second-level analysis, we first set a contrast (a label of "1" is given to a drug-resistant patient, and "0" is given to a healthy control) and highlight the functional connectivity for the group-level analysis. For each region in DMN and DAN, a non-parametric test was used to compare the z-transformed connectivity maps of each drug-resistant patient and the healthy control group. This means that the comparison will be performed 224 (28 patients by 8 regions) times. The obtained results were considered significant at a threshold of voxel-wise $p < 0.001$ uncorrected and cluster-level $p < 0.05$, false discovery rate (FDR) corrected for between-group comparisons. If one or more significant clusters are found for each patient, we consider significant connectivity changes.

Moreover, ROI-to-ROI connectivity analysis was performed to estimate the functional connectivity values between each pair of regions in DMN and DAN. The mean connectivity values of each region within each network were extracted for the patient and healthy control groups.

TABLE 1 Seizure onset zones for patients determined through the presurgical evaluation.

Patient	Seizure onset zone
01	Left frontal
02	Left middle temporal
03	Left frontal
04	Left middle temporal
05	Left middle temporal
06	Left middle temporal
07	Left middle temporal
08	Left middle and lateral temporal
09	Right hippocampus and temporal lobe
10	Left temporal lobe
11	Left hippocampus and middle temporal
12	Right frontal
13	Left mesial temporal lobe
14	Right mesial temporal lobe
15	Right hippocampus
16	Left occipital lobe
17	Left frontal cystic mass
18	Left mesial temporal lobe
19	Left frontal encephalomalacia
20	Right mesial temporal lobe
21	Right anterior frontal lobe
22	Left mesial temporal lobe
23	Left mesial temporal lobe and frontal lobe
24	Left temporal pole
25	Right mesial temporal lobe
26	Right mesial temporal lobe and right frontal pole
27	Right mesial temporal lobe, Possible right frontal base
28	Left mesial temporal lobe

2.5. Effective connectivity

This study used the spectral dynamic causal modeling (DCM) approach to determine causal connectivity. All DCM analysis was performed with SPM12 according to the steps described in Sharaev et al. (2016). Spectral DCM analysis uses a neuronally plausible power-law model of the coupled dynamics of neuronal populations to generate complex cross spectra among the measured responses. Figure 1 shows the procedure included running general linear modeling followed by time series extraction, after which the DCM can be specified for each subject. The data used for the time series extraction includes data fully preprocessed during CONN analyses. After the GLM estimation, time series extraction was unsuccessful for 6 subjects, and we finally had 22 subjects for our further analysis.

The challenge of the effective connectivity analysis was to assess the activities between different brain regions for two rs-fMRI networks. To achieve this goal, neural modeling schemes must be specified, and this will help in making inferences as it provides details about the interactivities and the connectivity strength between different regions (nodes) within a specific network

TABLE 2 Network nodes and their coordinates.

Network	Node	Coordinate (*x*, *y*, *z*)
Default mode network	Medial prefrontal cortex (MPFC)	1, 55, −3
	Left lateral inferior parietal (LIPC)	−39, −77, 33
	Right lateral inferior parietal (RIPC)	47, −67, 29
	Posterior cingulate cortex (PCC)	1, −61, 38
Dorsal attention network	Left frontal eye field (L-FEF)	−27, −9, 64
	Right frontal eye field (R-FEF)	30, −6, 64
	Intraparietal sulcus (L-IPS)	−39, −43, 52
	Intraparietal sulcus (R-IPS)	39, −42, 54

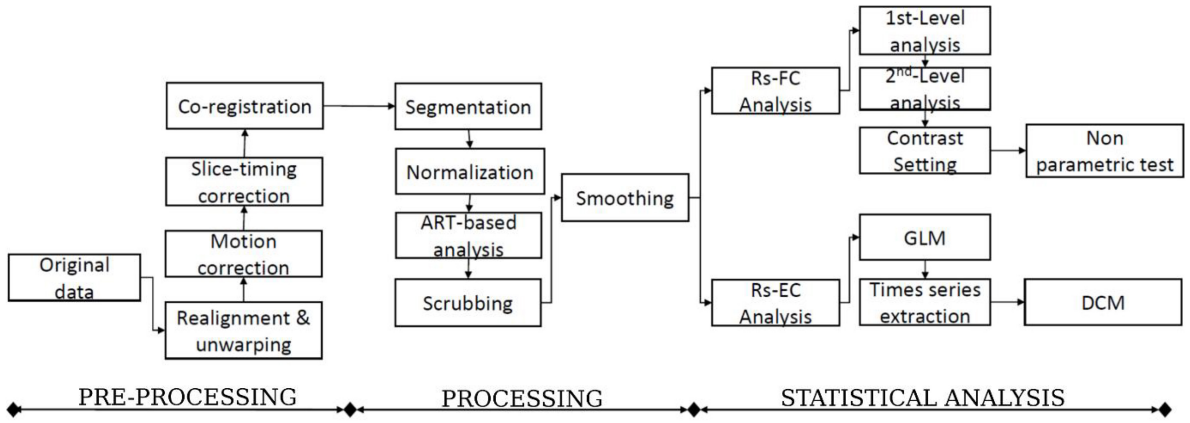

FIGURE 2
The flowchart of the functional and effective connectivity study (FC: Functional connectivity, EC: Effective connectivity, and DCM: Dynamic causal modeling).

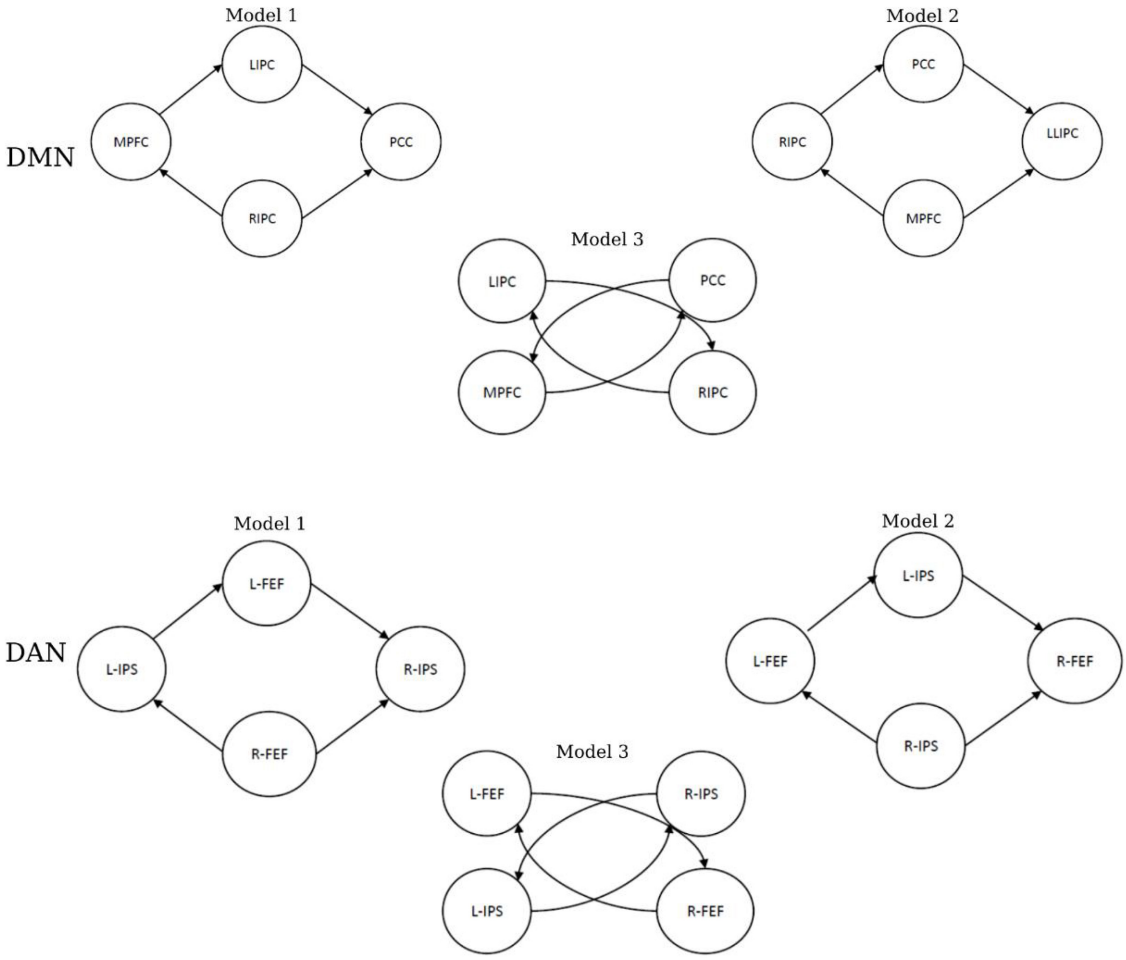

FIGURE 3
The specified models of effective connectivity in the default mode network (DMN) and dorsal attention network (DAN).

(Friston et al., 2014; Bidhan and Mukesh, 2015). Therefore, six models were constructed for each subject. **Figure 3** shows three models that were specified for the DMN and DAN. In addition, fixed effects (FFX) Bayesian Model Selection (BMS) was conducted to determine the best model that balances the data fitting and model convolution (Rosa et al., 2010). Moreover, for the best model, Bayesian Model Averaging (BMA) was conducted (Hinne et al., 2020). The probability-weighted values obtained from the BMA

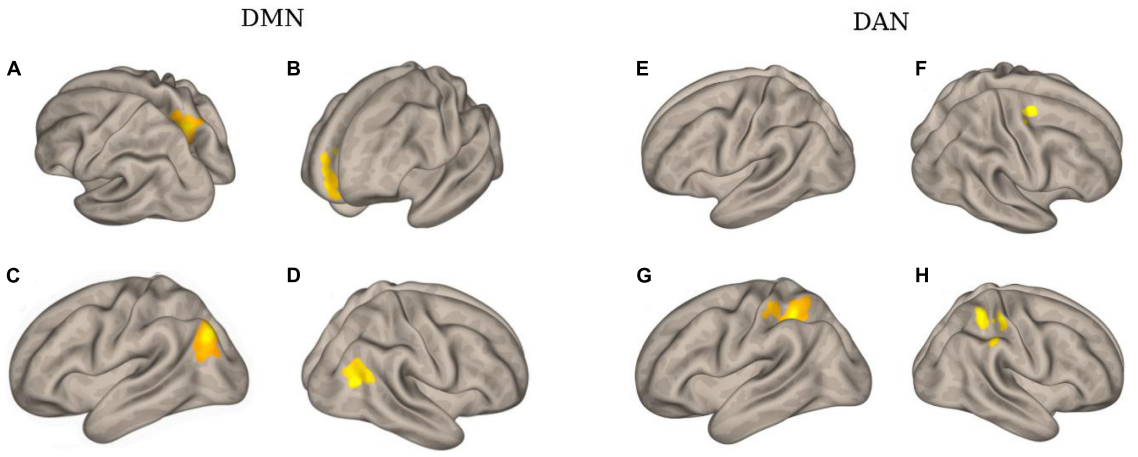

FIGURE 4
The clusters with different functional connectivity connected to the regions [as the seed) in the DMN and DAN network [here are the results of one patient (No. 02) as an example]. **(A)** Using PCC as the seed; **(B)** using MPFC as the seed; **(C)** using LIPC as the seed; **(D)** using RIPC as the seed; **(E)** using L-FEF as the seed; **(F)** using R-FEF as the seed; **(G)** using L-IPS as the seed; and **(H)** using R-IPS as the seed.

TABLE 3 An example of functional connectivity between one patient (No. 02) and healthy controls.

Network	Node (seed)	Region with clusters	Peak location (x, y, z)			*T*-value	The number of voxels
DMN	LIPC	L-LOC	−34	−78	36	7.96	681
	RIPC	R-LOC	48	−62	26	5.94	421
	MPFC	MedFC	0	58	−2	7.86	671
	PCC	Precu	6	−56	32	4.77	2,030
DAN	L-FEF	–	–	–	–	–	–
	R-FEF	R-PreCG	28	−6	34	5.04	54
	L-IPS	L-SPL	−34	−48	44	7.13	912
	R-IPS	R-SPL	34	−44	52	6.72	805

L, left; R, right; IPC, lateral parietal; MPFC, medial prefrontal cortex; IPC, inferior parietal cortex; PCC, posterior cingulate cortex; FEF, frontal eye field; IPS, intraparietal sulcus; LOC, lateral occipital; MedFC, frontal medial cortex; Precu, precuneous cortex; FP, frontal pole; SPL, superior parietal lobule; PreCG, precentral gyrus.

parameters models were quantitively analyzed using a classical one-sample *t*-test to examine the significance of the non-zero values.

2.6. Statistical analysis

After performing the functional and effective connectivity analysis, a statistical test was performed to evaluate our study's results. All the statistical tests were performed using SPSS.

Once the average connectivity values among the pairs of each region were estimated in DMN and the DAN, these values were subjected to a two-sample *t*-test to verify the difference in connectivity between the patient group and healthy controls.

3. Results

3.1. Resting-state functional connectivity

Selecting the DMN and DAN networks as regional seeds, the functional connectivity analysis revealed drug-resistant epilepsy showing abnormal clusters in patients. For DMN, significant connectivity changes were observed in 64.3% (18/28) of patients. In comparison, 78.6% (22/28) of connectivity changes were observed for DAN.

Figure 4 and Table 3 illustrate an example of the observed changes within the DMN and DAN for a single patient. The abnormal locations included the lateral occipital, middle, and superior temporal gyrus, medial frontal cortex, and superior parietal lobule for DMN. Whereas, for DAN, these changes were seen in the precentral gyrus, superior parietal lobule, inferior temporal gyrus, inferior frontal gyrus, and temporal fusiform cortex. Comparing the individual performance of each network, the left lateral parietal lobule and posterior cingulate cortex nodes had the highest number of patients with significant connectivity changes, with 42.4% (13/28) for DMN. The best connectivity performance for the DAN, on the other hand, was observed in the left intraparietal sulcus node, yielding 53.6% (15/28). Table 4 contains additional information about the findings of individual patient for both networks.

Furthermore, the statistical analysis between the connectivity of patient and healthy control groups is shown in Figure 5. For

TABLE 4 The region with different functional connectivity to the regional seeds in DMN and DAN networks (obtained by comparing the generated functional connectivity mapping between each individual patient and the healthy control group).

Sub.	DMN				DAN			
	LIPC	RIPC	MPFC	PCC	L-FEF	R-FEF	L-IPS	R-IPS
		–	–	–	–	–	–	–
02	L-LOC	R-LOC	MedFC	Precu	–	R-PreCG	L-SPL	R-SPL
03	L-Caudate	L- tri IFG	–	R-MTG	L-FP	R-ITG	PC	R-STG
04	L-LOC	R-LOC	MedFC	Precu	–	R-PreCG	L-SPL	R-SPL
05	L-LG	L-LG	–	L-LG	L-LG	L-LG	L-LG	L-LG
06	L-LOC	R-LOC	MedFC	Precu	–	R-PreCG	L-SPL	R-SPL
07	-	R-LOC	MedFC	Precu	–	R-PreCG	L-SPL	R-SPL
08	–	–	–	–	–	–	–	–
09	L-oper IFG	L-AG	R-SPL	L-oper IFG	–	–	L-ITG	R-SPL
10	R-LOC	L-LOC	R-LOC	L-LOC	–	MedFC	–	–
11	R-OP	L-ITG	R-OP	L-OP	L-TFusC	L-TFusC	L-MFG	L-FG oper
12	L-LOC	L-LOC	MedFC	Precu	–	R-PreCG	R-SPL	R-SPL
13	L-LOC	–	–	–	–	–	R-ITG	L-LOC
14	–	–	–	–	–	–	–	R-SPL
15	–	–	–	–	–	–	R-SPL	–
16	–	–	–	–	R-MTG	L-OP	L-PostCG	–
17	–	R-Cereb	–	–	L-FP	–	–	–
18	–	–	–	–	–	–	L-SPL	–
19	–	–	R-Cereb	–	R-Cereb	–	L-SPL	–
20	–	–	–	–	–	–	–	–
21	–	–	FP l	–	L-PreCG	–	–	–
22	R-Cereb	R-Cereb	R-Cereb	R-Cereb	R-Cereb	R-Cereb	R-Cereb	L-FP
23	–	–	R-Cereb	–	R-Cereb	–	–	–
24	–	–	R-Cereb	–	R-SPL	–	–	–
25	–	–	Brain-S	Brain-S	Brain-S	Brain-S	R-LOC	Brain-S
26	R-Cereb	R-Cereb	R-Cereb	R-Cereb	R-Cereb	R-Cereb	R-Cereb	R-Cereb
27	–	–	–	–	L-PreCG	–	–	–
28	R-SPL	–	R-PreCG	-	R-Cereb	L-MTG	L-MTG	L-MTG

(-), no findings; L, left; R, right; LP, lateral parietal; MPFC, medial prefrontal cortex; PCC, posterior cingulate cortex; FEF, frontal eye field; IPS, intraparietal sulcus; OP, occipital lobe; LOC, lateral occipital; IFG, inferior frontal gyrus; MedFC, frontal medial cortex; Precu, precuneous cortex; FP, frontal pole; SPL, superior parietal lobule; PreCG, precentral gyrus; PostCG, post cingulate gyrus; ITG, inferior temporal gyrus; MTG, middle frontal gyrus; Cereb, cerebellum; Brain-S, brain stem; LG, lingual gyrus; AG, angular gyrus; oper, operculum; TFusC, temporal fusiform cortex.

the DMN, the two-sample *t*-test was significant between the medial prefrontal cortex and posterior cingulate cortex ($p = 0.001$) and the bilateral inferior parietal cortex ($p = 0.0002$ and 0.003). Significant connectivity was also found between the posterior cingulate cortex and the right inferior parietal cortex ($p = 1.4e-07$). For DAN, the two-sample *t*-test was significant between the left and right frontal eye fields ($p = 1.2e-10$). Additionally, significance was found between the left and right intraparietal sulcus ($p = 0.004$).

3.2. Resting-state effective connectivity

Bayesian model selection (BMS) for the patient and healthy control groups is shown in Figure 6. During BMS analysis, for the DMN and DAN, the fully connected models were the best for 4 of the 6 models specified for the patient and healthy control groups. For both networks, models 1 and 2 were the best for patients and healthy controls. At the group level, models 1 and 2 were the best for both networks in 22 out of 22 patients (90.9%). A similar scenario was observed for the healthy control group. Models 1 and 2 were the best for both networks in 17 out of 19 (89.5%) patients. For both networks, model 3 was weaker for the patient and healthy control groups. For the patient group, model 3 was better, with 3/22 (13.6%) and 4/22 (18.2%) for DMN and DAN, respectively. For the healthy control group, model 3 was the best for 2 out of 19 subjects (10.5%) for DMN and DAN.

The results of BMA and the *t*-test are shown in Tables 5A, B. The one-sample *t*-test analysis found different significant

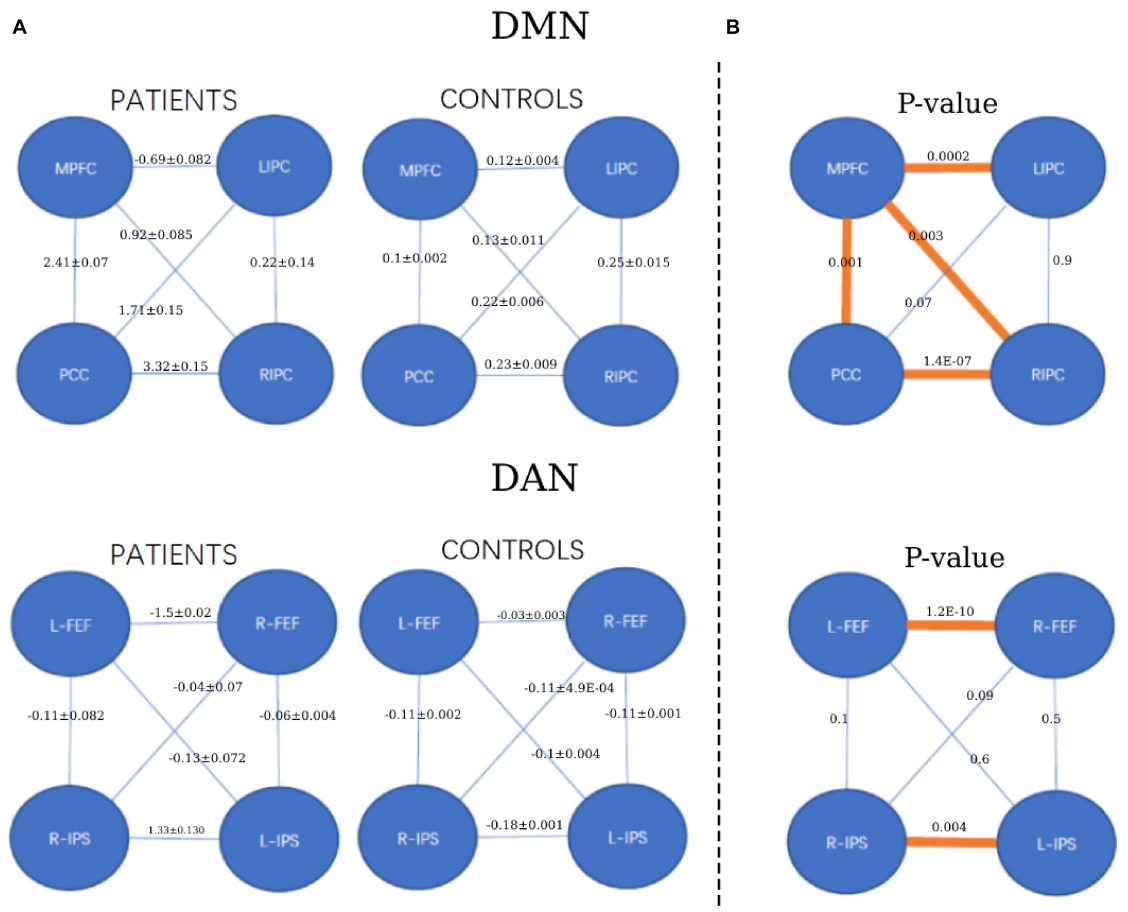

FIGURE 5
The strength of functional connectivity (mean and standard deviation) in the patient and healthy control groups and their comparisons. **(A)** The strength of FC for each group (patients and controls). **(B)** The *p*-value of FC comparisons between the patient and healthy control groups. *$p < 0.05$, orange colors.

connections for each network and group. For DMN, the patient group yielded significant connectivity from the right inferior parietal cortex to the medial prefrontal cortex (EC = 0.02), bilateral connectivity was found between the medial prefrontal cortex and the posterior cingulate cortex (EC = 0.02), and bilateral connectivity in the inferior parietal cortex (EC = 0.02). Healthy controls did not show significant connectivity.

For DAN, the patient group yielded significant connectivity from the right frontal eye field to the left intraparietal sulcus (EC = 0.2) and from the right intraparietal sulcus to the left frontal eye field (EC = 0.03). Bilateral connectivity was found between the left frontal eye field and the left intraparietal sulcus (EC = 0.04, EC = 0.2), as well as between the right frontal eye field and the right intraparietal sulcus (EC = 0.13, EC = 0.03).

For the healthy control group, significant connectivity was observed from the left frontal eye field to the left intraparietal sulcus (EC = 0.15), from the right frontal eye field to the left intraparietal sulcus (EC = 0.02), and from the left intraparietal sulcus to the right frontal eye field (EC = 0.04). Non-trivial connections have been considered, and self-connections in graphs have been ignored for simplicity. In addition, only significant connections with a connection strength greater than 0.1 Hz and a probability greater than 0.95 were reported. The winning model that summarizes the strength of interactions within the networks for each group is shown in Figure 7.

Finally, the statistical analysis results of the effective connectivity values between the patient and healthy control groups are shown in Tables 5C, D. For the DMN, the two-sample *t*-test was significant from the middle prefrontal cortex to the left inferior parietal (p = 5.5E-05), and from the right inferior parietal cortex (p = 7.93E-09).

For the DAN, the two-sample *t*-test was significant from the left frontal eye field to the intraparietal sulcus (p = 1.30E-10), the left intraparietal sulcus to the right frontal eye field (p = 3.50E-07), and the right intraparietal sulcus to the left and left frontal eye fields (p = 2.20E-14 and 7.70E-11, respectively).

4. Discussion

4.1. Significance and importance of this study

Drug-resistant epilepsy remains one of the most severe cerebral diseases, and its diagnosis remains very tedious. Resting-state

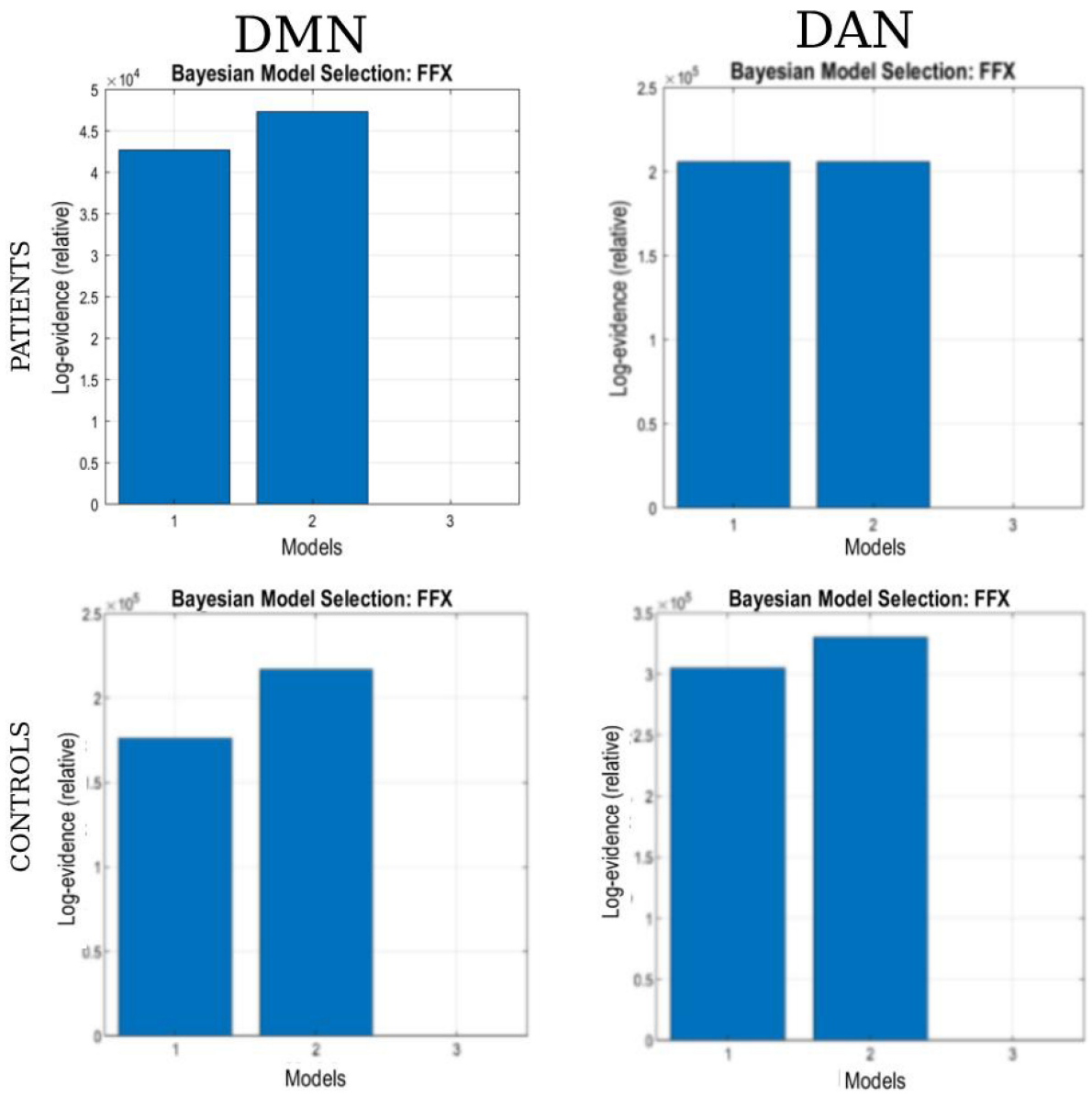

FIGURE 6
The Bayesian model selection (BMS) at the single-group level. The columns represent the network (DAN and DMN), and each row represents the study group (patients and healthy controls).

fMRI is an essential neuroimaging tool that has shown interesting results in diagnosing brain diseases. The purpose of this study is to investigate brain activities in rs-fMRI networks. The primary experiment of this study provides new information in the study of the connectivity of rs-fMRI networks of patients with drug-resistant epilepsy. Functional and effective connectivity analysis approaches were used to assess connectivity behaviors in the default mode and the dorsal attention networks. Overall, the study provides satisfactory results.

The FC analysis showed abnormal activities in 18 out of 28 patients for the DMN compared with the DAN, which showed slightly higher performance showing activities in 22 out of 28 patients. This result supports that DMN and DAN are two crucial rs-fMRI networks to be evaluated during the presurgical analysis of candidates for refractory epilepsy (Blumenfeld et al., 2004; Hinne et al., 2020). This assertion is confirmed by Widjaja et al. (2013), who reported a decreased FC within the DMN in children with medically refractory epilepsy. Zhou et al. (2020) also highlighted the crucial role of the DAN network by investigating right temporal lobe epilepsy candidates.

The DCM analysis performed well and showed connectivity for the DMN and DAN networks. The BMA values and the one-sample *t*-test analysis revealed significant connectivity within patient and healthy control group networks. For DMN, the EC was significant in the posterior cingulate cortex and medial prefrontal cortex for patients, while none was significant for healthy controls. This result suggests that the posterior cingulate and the middle prefrontal cortex represent two regions with high sensitivity for drug-resistant candidates. In their study, Cook et al. (2019) confirmed this observation in which the effective connectivity of the DMN in

patients with left temporal lobe epilepsy was assessed using the spectral DCM approach. Their study revealed connections between the posterior cingulate and medial prefrontal cortex (Cook et al., 2019).

In addition, the patient group showed significant connectivity from the right intraparietal sulcus and all other nodes for DAN. Left and right bilateral connectivity was also observed in the intraparietal sulcus. This result suggests that the right parietal lobule is a sensitive region in the DAN. Zhou et al. (2020) examined cognitive damage of the DAN in patients with right temporal lobe epilepsy (rTLE) and found a significant difference in the right superior parietal lobule (SPL) and right precuneus (PCU) in patients with rTLE compared with healthy controls.

Furthermore, comparing the results of the DCM analysis of the group of patients to that of healthy controls, a significant difference in connectivity was also observed for the two networks. More activities were observed in the patient group compared with the control group. This hyper-activity observed within the group of patients may result from the frequent appearance of seizures in drug-resistant candidates. This last hypothesis (that abnormal interactions may cause frequent seizures in candidates for drug-resistant epilepsy) answers the objective of this study. Thus, the study provides evidence that effective connectivity is a powerful presurgical and post-surgical analysis technique. This analytical approach was used by Jiang et al. (2018). In their study, the Granger causality effective connectivity analysis approach was used to study the attention networks and default mode network of refractory participants. The specific disrupted networks appear to be associated with the specific cognitive characteristics of drug-resistant.

Finally, for the DMN, the statistical analysis of the FC showed significant differences between the medial prefrontal cortex and the posterior cingulate cortex and also between the posterior cingulate cortex and the right inferior parietal cortex. It was significant for DAN between the left and right frontal eye field and the intraparietal sulcus.

Moreover, for the DMN, the statistical analysis of the EC showed a significant difference from the right inferior parietal cortex to the middle prefrontal and posterior cingulate cortex. Additionally, the difference was observed from the posterior cingulate cortex to the middle prefrontal cortex and the left inferior parietal cortex. This result suggests that the brain networks of the patient and control groups exhibit different characteristics. Xiao et al. (2020) evaluated functional connectivity and topological properties of brain networks and found that their alterations were associated with neuropsychological disease.

4.2. Importance of resting state in drug-resistant epilepsy analysis

Our study proposes to assess the functional and effective connectivity of the default mode and the dorsal attention networks, two networks known to present altered connectivity for epilepsy patients. The vital role of rs-fMRI in assessing altered brain connectivity for epilepsy patients has been investigated by several researchers.

These assessments have demonstrated noticeable progress. Boerwinkle et al. (2020) prospectively examined the influence of rs-fMRI on the organization of pediatric epilepsy surgery. Jiang et al. (2018) also assessed the functional and causal connectivity of the attention networks and default mode network using rs-fMRI and revealed that epileptic activity might disrupt network interactions and further influence information communication. Zhang et al. (2011) also investigated epilepsy networks using resting-state fMRI, emphasized the importance of local network topology when investigating mechanisms underlying tumor-related epilepsy, and provided motivation for further investigation of the epilepsy process at the network level.

4.3. Functional and effective connectivity performance comparison

Brain connectivity is defined as a pattern of interactions between the different areas of the brain. Functional connectivity focuses on the temporal correlation among the activity of different brain areas, while effective connectivity relies on the causal interactions among the activity of different brain areas. The fundamental difference between functional and effective connectivity is the temporal implication of the source of the effect, and this study has investigated the importance of functional and effectivity analysis for the presurgical analysis of drug-resistant. We also tried to compare the best approach to be used when trying to investigate rs-fMRI patients. However, our evaluation revealed that both connectivity methods could answer our needs at different levels. The descriptions above answer this study's goal, combining both methods to bring out meaningful answers and facilitate surgical operations for drug-resistant candidates.

Several researchers who used and compared both analyses approaches confirmed this study's assumption. Among them, Saetia et al. (2020) studied the interpretability of the effective connectivity model compared with the functional connectivity model. Park et al. (2018) also evaluated the ensuing dynamic effective connectivity in terms of the consistency of baseline connectivity within DMN using the rs-fMRI. They speculated that human brain networks at rest show dynamic functional connectivity induced by effective dynamic connectivity, which can be modeled efficiently using dynamic causal modeling and hierarchical Bayesian inference. Mao et al. (2020) investigated the functional connectivity and effective connectivity of the habenula in 34 subjects with irritable bowel syndrome (IBS) and 34 healthy controls and assessed the feasibility of differentiating IBS patients from healthy controls using a machine learning method.

4.4. Limitations and challenges

Despite the promising results obtained during our study, some challenges and limitations to this approach persist and must be overcome. First, a seed-based analysis is known as a relatively assumption-based approach. It requires the *a priori* selection of

TABLE 5 The strength of effective connectivity (mean and standard deviation, in Hz) in the patient and healthy control groups and their comparisons.

(A) Group	Connection	From MPFC	From PCC	From LIPC	From RIPC
Patient	To MPFC	0	**0.02 ± 0.001**	0	**0.2 ± 0.003**
	To PCC	**0.02 ± 0.001**	0	**0.07 ± 0.005**	0.13 ± 0.002
	To LIPC	0.19 ± 0.004	0	0	**0.02 ± 0.001**
	To RIPC	0	0	**0.02 ± 0.001**	0
Healthy control	To MPFC	0	0	0	0.11 ± 0.001
	To PCC	0	0	0.07 ± 0.001	0.11 ± 0.001
	To LIPC	0.22 ± 0.003	0	0	0
	To RIPC	0	0	0	0

(B) Group	Connection	From L-FEF	From R-FEF	From L-IPS	From R-IPS
Patient	To L-FEF	0	0	**0.2 ± 0.003**	**0.03 ± 0.001**
	To R-FEF	0	0	0.01 ± 0.002	**0.01 ± 0.001**
	To L-IPS	**0.04 ± 0.002**	**0.2 ± 0.004**	0	0
	To R-IPS	0.13 ± 0.006	**0.13 ± 0.003**	0	0
Healthy control	To L-FEF	0	0	0.017 ± 0.001	0.15 ± 0.001
	To R-FEF	0	0	**0.04 ± 0.003**	0.13 ± 0.002
	To L-IPS	**0.15 ± 0.002**	**0.02 ± 0.0**	–0	0
	To R-IPS	−0.002 ± 0.001	−0.003 ± 0.0	0	0

(C) Connection	From MPFC	From PCC	From LIPC	From RIPC
To MPFC	0	0.7	0	0.6
To PCC	0.7	0	0	0.07
To LIPC	**5.50E-05**	0	0	**0.05**
To RIPC	0	0	0.7	0

(D) Connection	From L-FEF	From R-FEF	From L-IPS	From R-IPS
To L-FEF	0	0	0.9	**2.20E-14**
To R-FEF	0	0	**3.50E-07**	**7.70E-11**
To L-IPS	**1.30E-10**	0.8	0	0
To R-IPS	0.7	0.8	0	0

(A) Default mode network; (B) dorsal attention network; (C) the *p*-value of comparison of EC between the patient and healthy control groups in DMN; (D) the *p*-value of comparison of EC between the patient and healthy control groups in DAN.
(A) The bold font represents the parameters with significant non-zero values by a one-sample *t*-test ($p < 0.05$).
(B) The bold font represents the parameters with significant non-zero values by a one-sample *t*-test ($p < 0.05$).
(C) The bold font represents significant differences in a two-sample *t*-test ($p < 0.05$).
(D) The bold font represents significant differences in a two-sample *t*-test ($p < 0.05$).

a specific voxel, atlas, or network. However, the choice of seed may biologically bias the connectivity findings toward specific, smaller, or overlapping sub-systems rather than larger, distinct networks (Cole et al., 2010). The combination of a data and hypothesis-driven approach may provide a suitable answer to this problem (McKeown, 2000; Caulo et al., 2011). Second, the data size is crucial during analysis because a small sample size limits the statistical power. The sample size in this study is relatively small, which may impact the results (Grady et al., 2021). This issue must be considered preliminary and needs to be replicated in future studies with larger sample sizes and more detailed scale tests. Third, the lack of post-operative outcomes information in both patient samples makes comparison with our findings impossible. Fourth, different acquisition procedures may have an adverse effect on the interpretability of the result. The rs-fMRI population used in this study was acquired using slightly differential procedures. For the patients, sample 1 was obtained with the eyes closed, while sample 2 was obtained with the eyes open. For the healthy control group, a mixed eyes open-closed acquisition was used. This obvious acquisition difference may have an effect on each candidate's brain activity in sensorimotor and occipital regions (Wei et al., 2018). This limitation, however,

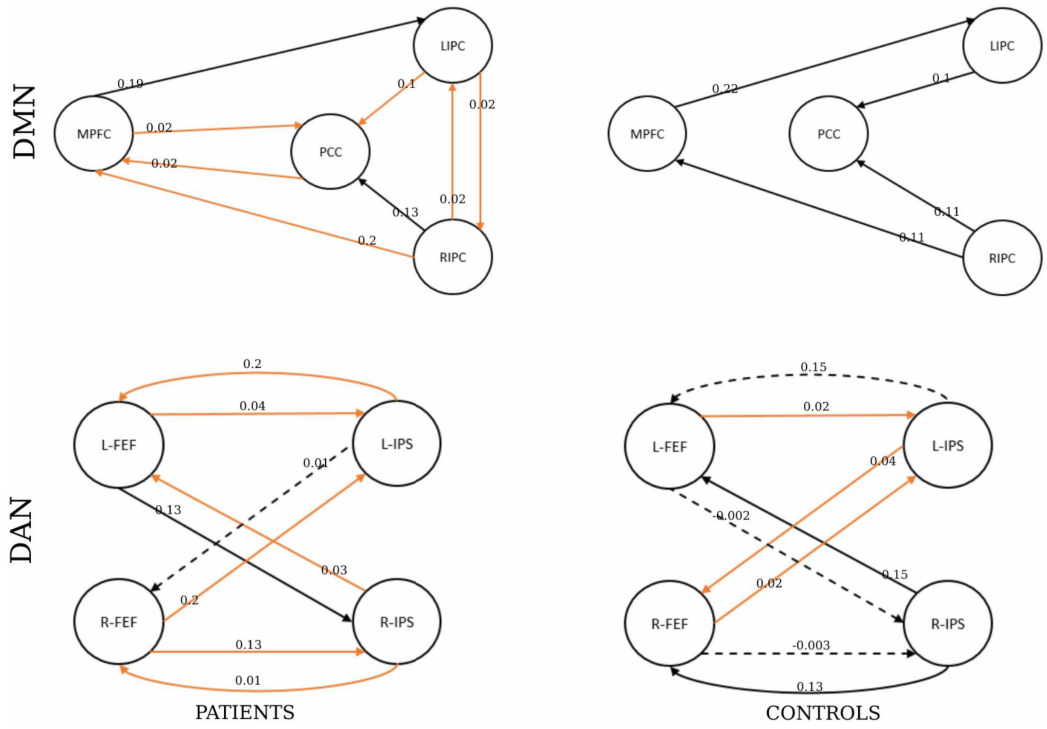

FIGURE 7
The winning model at the group level. The number shows the connectivity parameters (Hz) of the winning model in the patients and healthy control groups represented by the columns. The rows represent the network type. The solid lines represent connectivity values greater than 0.1 Hz, and their thickness shows the size of the value. The dotted lines represent the connectivity values below 0.1 Hz. The orange represents the parameters with significant non-zero values by a one-sample *t*-test ($p < 0.05$).

has not resulted in statistical evidence and only a small portion of brain activity is affected (Agcaoglu et al., 2019). This claim is supported by Patriat et al. (2013), who discovered that when the acquisition procedure was changed, only the visual network changed significantly.

Finally we also explored node-based connectivity analysis using the DCM method in this study. The expressiveness or complexity of the underlying neural model limits the interpretability of DCM. This complexity is constrained by the nature of the data at hand (Sadeghi et al., 2020). The strengths of the DCM approach lie in the hemodynamic model that links neuronal population firing to BOLD data, which creates potential mismatches. This mismatch may result in incorrect edge strength estimates within the DCM, potentially leading to the selection of wrong edge configurations. Another limitation concerns the large number of nodes used in the resting state analysis, leading to a considerable number of parameters in the DCM, making estimation difficult. Perhaps anatomical connectivity analysis can help reduce some of the challenges.

5. Conclusion

Brain connectivity analysis has always been challenging for researchers. This study characterized drug-resistant epilepsy by assessing functional and effective connectivity within resting state networks. The DMN and DAN networks were investigated at a subject and group level. Our analysis provided evidence of abnormal functional connectivity for the DMN and DAN. In addition, dynamic causal modeling analysis has shown significant effective connectivity within both networks. Finally, the statistical analysis has demonstrated the connectivity differences within the networks of both patients and healthy control groups. Our findings provide preliminary evidence to support that combining functional and effective connectivity analysis may highly contribute to diagnosing altered brain networks in drug-resistant candidates. The results of this research may offer new insight into the neuropathophysiological mechanisms of brain network dysfunction in drug-resistant epilepsy. In our subsequent studies, we will examine connectivity patterns between the DAN and DMN.

Data availability statement

The datasets presented in this article are not readily available because of the requirement of the Ethics Committee of Shengjing Hospital of China Medical University (Shenyang, China). Requests to access the datasets should be directed to HL, leoincmu@gmail.com.

Ethics statement

The studies involving human participants were reviewed and approved by the Ethics Committee of Shengjing Hospital of China

Medical University. Written informed consent to participate in this study was provided by the participants' legal guardian/next of kin.

Author contributions

EB performed experiments and analyzed the data along with SQ and CJ. SQ, DH, and HL conceived the study, presented the results, and wrote the manuscript along with EB. SH and LW collected and analyzed the data. SQ and LW supervised the algorithm development and analyzed the data. All authors read and approved the final manuscript.

Funding

This work was supported by the National Natural Science Foundation of China under Grant (82072008), the Natural Science Foundation of Liaoning Province (2020-BS-049 and 2021-YGJC-21), and the Fundamental Research Funds for the Central Universities (N2119010 and N2224001-10).

Conflict of interest

The authors declare that the research was conducted in the absence of any commercial or financial relationships that could be construed as a potential conflict of interest.

Publisher's note

All claims expressed in this article are solely those of the authors and do not necessarily represent those of their affiliated organizations, or those of the publisher, the editors and the reviewers. Any product that may be evaluated in this article, or claim that may be made by its manufacturer, is not guaranteed or endorsed by the publisher.

References

Agcaoglu, O., Wilson, T. W., Wang, Y. P., Stephen, J., and Calhoun, V. D. (2019). Resting state connectivity differences in eyes open versus eyes closed conditions. *Hum. Brain Mapp.* 40, 2488–2498. doi: 10.1002/hbm.24539

Bidhan, L., and Mukesh, D. (2015). Perceptual decision-making difficulty modulates feedforward effective connectivity to the dorsolateral prefrontal cortex. *Front. Hum. Neurosci.* 9:498. doi: 10.3389/fnhum.2015.00498

Blumenfeld, H., McNally, K. A., Vanderhill, S. D., Paige, A. L., Chung, R., Davis, K., et al. (2004). Positive and negative network correlations in temporal lobe epilepsy. *Cereb. Cortex* 14, 892–902. doi: 10.1093/cercor/bhh048

Boerwinkle, V. L., Mirea, L., Gaillard, W. D., Sussman, B. L., Larocque, D., Bonnell, A., et al. (2020). Resting-state fMRI connectivity impact on epilepsy surgery plan and surgical candidacy: Prospective clinical work. *J. Neurosurg. Pediatr.* 25, 574–581. doi: 10.3171/2020.1.PEDS19695

Buckner, R. L., Krienen, F. M., and Yeo, B. T. (2013). Opportunities and limitations of intrinsic functional connectivity MRI. *Nat. Neurosci.* 16, 832–837. doi: 10.1038/nn.3423

Caulo, M., Esposito, R., Mantini, D., Briganti, C., Sestieri, C., Mattei, P. A., et al. (2011). Comparison of hypothesis-and a novel hybrid data/hypothesis-driven method of functional MR imaging analysis in patients with brain gliomas. *Am. J. Neuroradiol.* 32, 1056–1064. doi: 10.3174/ajnr.A2428

Cole, D. M., Smith, S. M., and Beckmann, C. F. (2010). Advances and pitfalls in the analysis and interpretation of resting-state FMRI data. *Front. Syst. Neurosci.* 4:8. doi: 10.3389/fnsys.2010.00008

Cook, C. J., Hwang, G., Mathis, J., Nair, V. A., Conant, L. L., Allen, L., et al. (2019). Effective connectivity within the default mode network in left temporal lobe epilepsy: Findings from the epilepsy connectome project. *Brain Connect.* 9, 174–183. doi: 10.1089/brain.2018.0600

Dalic, L., and Cook, M. J. (2016). Managing refractory epilepsy: Challenges and solutions. *Neuropsychiatr. Dis. Treat.* 12, 2605–2616. doi: 10.2147/ndt.s84852

Friston, K. J., Kahan, J., Biswal, B., and Razi, A. (2014). A DCM for resting state fMRI. *Neuroimage* 94, 396–407. doi: 10.1016/j.neuroimage.2013.12.009

Glover, G. H. (2011). Overview of functional magnetic resonance imaging. *Neurosurg. Clin. N. Am.* 22, 133–139. doi: 10.1016/j.nec.2010.11.001

Grady, C. L., Rieck, J. R., Nichol, D., Rodrigue, K. M., and Kennedy, K. M. (2021). Influence of sample size and analytic approach on stability and interpretation of brain-behavior correlations in task-related fMRI data. *Hum. Brain Mapp.* 42, 204–219. doi: 10.1002/hbm.25217

Gu, Y., Han, F., Sainburg, L. E., Schade, M. M., Buxton, O. M., et al. (2022). An orderly sequence of autonomic and neural events at transient arousal changes. *Neuroimage* 264:119720. doi: 10.1016/j.neuroimage.2022.119720

Hinne, M., Gronau, Q. F., van den Bergh, D., and Wagenmakers, E. J. (2020). A conceptual introduction to bayesian model averaging. *Adv. Methods Pract. Psychol. Sci.* 3, 200–215. doi: 10.1177/2515245919898657

Hlinka, J., Palus, M., Vejmelka, M., Mantini, D., and Corbetta, M. (2011). Functional connectivity in resting-state fMRI: Is linear correlation sufficient? *Neuroimage* 54, 2218–2225. doi: 10.1016/j.neuroimage.2010.08.042

Jehi, L., Jette, N., Kwon, C. S., Josephson, C. B., Burneo, J. G., Cendes, F., et al. (2022). Timing of referral to evaluate for epilepsy surgery: Expert consensus recommendations from the surgical therapies commission of the international league against epilepsy. *Epilepsia* 63, 2491–2506. doi: 10.1111/epi.17350

Jiang, L., Qian, R., Fu, X., Zhang, D., Peng, N., Niu, C., et al. (2018). Altered attention networks and DMN in refractory: A resting-state functional and causal connectivity study. *Epilepsy Behav.* 88, 81–86. doi: 10.1016/j.yebeh.2018.06.045

Lee, H. W., Arora, J., Papademetris, X., Tokoglu, F., Negishi, M., Scheinost, D., et al. (2014). Altered functional connectivity in seizure onset zones revealed by fMRI intrinsic connectivity. *Neurology* 83, 2269–2277. doi: 10.1212/wnl.0000000000001068

Liu, W., Lin, M., Yue, Q., Gong, Q., Zhou, D., and Wu, X. (2021). Brain functional connectivity patterns in focal cortical dysplasia related epilepsy. *Seizure* 87, 1–6. doi: 10.1016/j.seizure.2021.02.009

Logothetis, N. K. (2008). What we can do and what we cannot do with fMRI. *Nature* 453, 869–878. doi: 10.1038/nature06976

Mao, C. P., Chen, F. R., Huo, J. H., Zhang, L., Zhang, G. R., Zhang, B., et al. (2020). Altered resting-state functional connectivity and effective connectivity of the habenula in irritable bowel syndrome: A cross-sectional and machine learning study. *Hum. Brain Mapp.* 41, 3655–3666. doi: 10.1002/hbm.25038

McKeown, M. J. (2000). Detection of consistently task-related activations in fMRI data with hybrid independent component analysis. *Neuroimage* 11, 24–35. doi: 10.1006/nimg.1999.0518

Park, H. J., Friston, K. J., Pae, C., Park, B., and Razi, A. (2018). Dynamic effective connectivity in resting state fMRI. *Neuroimage* 180, 594–608. doi: 10.1016/j.neuroimage.2017.11.033

Patriat, R., Molloy, E. K., Meier, T. B., Kirk, G. R., Nair, V. A., Meyerand, M. E., et al. (2013). The effect of resting condition on resting-state fMRI reliability and consistency: A comparison between resting with eyes open, closed, and fixated. *Neuroimage* 78, 463–473. doi: 10.1016/j.neuroimage.2013.04.013

Raichle, M. E., MacLeod, A. M., Snyder, A. Z., Powers, W. J., Gusnard, D. A., and Shulman, G. L. (2015). The brain's default mode network. *Annu. Rev. Neurosci.* 38, 433–447. doi: 10.1146/annurev-neuro-071013-014030

Rosa, M. J., Bestmann, S., Harrison, L., and Penny, W. (2010). Bayesian model selection maps for group studies. *Neuroimage* 49, 217–224. doi: 10.1016/j.neuroimage.2009.08.051

Sadeghi, S., Mier, D., Gerchen, M. F., Schmidt, S. N., and Hass, J. (2020). Dynamic causal modelling for fMRI with Wilson-Cowan-based neuronal equations. *Front. Neurosci.* 14:593867. doi: 10.3389/fnins.2020.593867

Saetia, S., Rosas, F., Ogata, Y., Yoshimura, N., and Koike, Y. (2020). Comparison of resting-state functional and effective connectivity between default mode network and memory encoding related areas. *J. Neurosci. Neurol. Disord.* 4, 029–037. doi: 10.29328/journal.jnnd.1001031

Scheffer, I. E., Berkovic, S., Capovilla, G., Connolly, M. B., French, J., Guilhoto, L., et al. (2017). ILAE classification of the epilepsies: Position paper of the ILAE commission for classification and terminology. *Epilepsia* 58, 512–521. doi: 10.1111/epi.13709

Schurz, M., Wimmer, H., Richlan, F., Ludersdorfer, P., Klackl, J., and Kronbichler, M. (2014). Resting-state and task-based functional brain connectivity in developmental dyslexia. *Cereb. Cortex* 25, 3502–3514. doi: 10.1093/cercor/bhu184

Sharaev, M. G., Zavyalova, V. V., Ushakov, V. L., Kartashov, S. I., and Velichkovsky, B. M. (2016). Effective connectivity within the default mode network: Dynamic causal modeling of resting-state fMRI data. *Front. Hum. Neurosci.* 10:14.

Szczepanski, S. M., Pinsk, M. A., Douglas, M. M., Kastner, S., and Saalmann, Y. B. (2013). Functional and structural architecture of the human dorsal frontoparietal attention network. *Proc. Natl. Acad. Sci. U.S.A.* 110, 15806–15811.

Thompson, W. H., Nair, R., Oya, H., Esteban, O., Shine, J. M., Petkov, C. I., et al. (2020). A data resource from concurrent intracranial stimulation and functional MRI of the human brain. *Sci. Data* 7:258. doi: 10.1038/s41597-020-00595-y

van den Heuvel, M. P., and Hulshoff Pol, H. H. (2010). Exploring the brain network: A review on resting-state fMRI functional connectivity. *Eur. Neuropsychopharmacol.* 20, 519–534. doi: 10.1016/j.euroneuro.2010.03.008

Wei, H., An, J., Shen, H., Zeng, L. L., Qiu, S., and Hu, D. (2016). Altered effective connectivity among core neurocognitive networks in idiopathic generalized epilepsy: An fMRI evidence. *Front. Hum. Neurosci.* 10:447. doi: 10.3389/fnhum.2016.00447

Wei, J., Chen, T., Li, C., Liu, G., Qiu, J., and Wei, D. (2018). Eyes-open and eyes-closed resting states with opposite brain activity in sensorimotor and occipital regions: Multidimensional evidences from machine learning perspective. *Front. Hum. Neurosci.* 12:422. doi: 10.3389/fnhum.2018.00422

Whitfield-Gabrieli, S., and Nieto-Castanon, A. (2012). Conn: A functional connectivity toolbox for correlated and anticorrelated brain networks. *Brain Connect.* 2, 125–141. doi: 10.1089/brain.2012.0073

Widjaja, E., Zamyadi, M., Raybaud, C., Snead, O. C., and Smith, M. L. (2013). Impaired default mode network on resting-state fMRI in children with medically refractory epilepsy. *AJNR Am. J. Neuroradiol.* 34, 552–557.

World Health Organization [WHO] (2023). *Epilepsy*. Available online at: www.who.int/news-room/fact-sheets/detail/epilepsy (accessed February 4, 2023).

Xiao, F., Spruyt, K., Lu, C., Zhao, D., Zhang, J., and Han, F. (2020). Resting-state brain network topological properties and the correlation with neuropsychological assessment in adolescent narcolepsy. *Sleep* 43:zsaa018. doi: 10.1093/sleep/zsaa018

Yun, S. D., Pais, R. P., Palomero, G. N., and Shah, N. J. (2022). Mapping of whole-cerebrum resting-state networks using ultra-high resolution acquisition protocols. *Hum. Brain Mapp.* 43, 3386–3403. doi: 10.1002/hbm.25855

Zhang, X., Tokoglu, F., Negishi, M., Arora, J., Winstanley, S., Spencer, D. D., et al. (2011). Social network theory applied to resting-state fMRI connectivity data in the identification of epilepsy networks with iterative feature selection. *J. Neurosci. Methods* 199, 129–139. doi: 10.1016/j.jneumeth.2011.04.020

Zhou, S., Xiong, P., Ren, H., Tan, W., Yan, Y., and Gao, Y. (2020). Aberrant dorsal attention network homogeneity in patients with right temporal lobe epilepsy. *Epilepsy Behav.* 111:107278. doi: 10.1016/j.yebeh.2020.107278

frontiers | Frontiers in Neuroscience

TYPE Original Research
PUBLISHED 25 May 2023
DOI 10.3389/fnins.2023.1199106

OPEN ACCESS

EDITED BY
Yingying Tang,
Shanghai Jiao Tong University, China

REVIEWED BY
Shouliang Qi,
Northeastern University, China
Anar Amgalan,
University of Southern California, United States

*CORRESPONDENCE
Hui Xu
✉ huixujx@gmail.com
Bo Yin
✉ 76yinbo@163.com

RECEIVED 02 April 2023
ACCEPTED 08 May 2023
PUBLISHED 25 May 2023

CITATION
Xu H, Xu C, Yang Z, Bai G and Yin B (2023) Two sides of the same coin: distinct neuroanatomical patterns predict crystallized and fluid intelligence in adults.
Front. Neurosci. 17:1199106.
doi: 10.3389/fnins.2023.1199106

Two sides of the same coin: distinct neuroanatomical patterns predict crystallized and fluid intelligence in adults

Hui Xu[1,2]*, Cheng Xu[3], Zhenliang Yang[4], Guanghui Bai[5] and Bo Yin[1]*

[1]Department of Neurosurgery, The Second Affiliated Hospital and Yuying Children's Hospital of Wenzhou Medical University, Wenzhou, Zhejiang, China, [2]Peter Boris Centre for Addictions Research, St. Joseph's Healthcare Hamilton, McMaster University, Hamilton, ON, Canada, [3]School of Psychology and Cognitive Science, East China Normal University, Shanghai, China, [4]Faculty of Psychology, Tianjin Normal University, Tianjin, China, [5]Department of Radiology, The Second Affiliated Hospital and Yuying Children's Hospital of Wenzhou Medical University, Wenzhou, Zhejiang, China

Background: Crystallized intelligence (Gc) and fluid intelligence (Gf) are regarded as distinct intelligence components that statistically correlate with each other. However, the distinct neuroanatomical signatures of Gc and Gf in adults remain contentious.

Methods: Machine learning cross-validated elastic net regression models were performed on the Human Connectome Project Young Adult dataset (N = 1089) to characterize the neuroanatomical patterns of structural magnetic resonance imaging variables that are associated with Gc and Gf. The observed relationships were further examined by linear mixed-effects models. Finally, intraclass correlations were computed to examine the similarity of the neuroanatomical correlates between Gc and Gf.

Results: The results revealed distinct multi-region neuroanatomical patterns predicted Gc and Gf, respectively, which were robust in a held-out test set (R^2 = 2.40, 1.97%, respectively). The relationship of these regions with Gc and Gf was further supported by the univariate linear mixed effects models. Besides that, Gc and Gf displayed poor neuroanatomical similarity.

Conclusion: These findings provided evidence that distinct machine learning-derived neuroanatomical patterns could predict Gc and Gf in healthy adults, highlighting differential neuroanatomical signatures of different aspects of intelligence.

KEYWORDS

crystallized intelligence, fluid intelligence, neuroanatomy, morphometry, machine learning, elastic net regression

1. Introduction

General intelligence is defined as a general capability to understand complex ideas, adapt flexibly to the changing environment, solve problems, and engage in critical reasoning (Neisser et al., 1996; Gottfredson, 1997). Markers of neural substrates in brain regions and genetic biomarkers have been closely linked to intelligence (Posthuma et al., 2002; Genç et al., 2018), prompting the use of neuroimaging techniques to uncover the neural signature of intelligence. Furthermore, general intelligence has been postulated to consist of two independent components, crystallized intelligence (Gc) and fluid intelligence (Gf) (Cattell, 1943). While Gc reflects our ability to acquire skills through knowledge and experience and is related to verbal ability and general knowledge (Deary et al., 2007; Yuan et al., 2018), Gf refers to the capacity for problem-solving and logical reasoning and is suggested as one of the most important features associated with various cognitive abilities (Varriale et al., 2018). Despite the evidence that Gc and Gf are regarded as distinct intelligence components that statistically correlate with each other (Cattell, 1943; Li et al., 2004), it remains contentious whether there are distinct neuroanatomical signatures of Gc and Gf in adults.

An increasing number of functional magnetic resonance imaging (MRI) studies have found that Gf is linked with multiple cortical regions, which is postulated by the Parieto-Frontal Integration Theory (P-FIT) (Gray et al., 2003; Jung and Haier, 2007; Cipolotti et al., 2022). Based on P-FIT, Gf is linked to the executive network, which includes the dorsolateral prefrontal cortex, inferior and superior parietal lobules, and anterior cingulate gyrus (Jung and Haier, 2007). This explains the goal-directed behavior that is expressed by individual differences in Gf (Barbey et al., 2013; Barbey, 2018). Additionally, substantial evidence from structural MRI (sMRI) studies found higher Gc expression, which remained stable over time. The Gc level was associated with greater gray matter volume (GMV) reduction, and thinning of the cortex thickness (CT) (Yuan et al., 2018). Moreover, individual differences in Gc may depend on declarative knowledge stored in the temporal lobe and inferior prefrontal cortex, leading to widespread cortical region differences across individuals (Martin and Chao, 2001; McClelland and Rogers, 2003; Gainotti, 2006). Furthermore, Gf and Gc exhibit distinct trajectories of development (McArdle et al., 2000). However, these studies investigated the neural substrates of Gc and Gf using different models of modalities. These studies had small sample sizes for brain-intelligence associations using MRI (Marek et al., 2022), which led to low sensitivity for true effects (i.e., type I error) and increased risk for false positives (i.e., type II error) (Button et al., 2013).

Recently, studies started adopting larger samples to characterize the neuroanatomical correlates of Gc and Gf. One study used a large cohort of adults from the Human Connectome Project (HCP) and reported higher performance in Gf, which was associated with cortical expansion in regions related to working memory, attention, and visuospatial processing. In contrast, Gc was associated with thinner CT and higher cortical surface area (CSA) in language-related networks (N = 740) (Tadayon et al., 2020). Another Adolescent Brain Cognitive Development study (N = 10,652) conducted a double generalized linear model to assess the independent association between the mean and dispersion of CT/CSA and intelligence. It was found that higher intelligence in preadolescents was associated with higher mean CT in orbitofrontal and primary sensory cortices but with lower CT in the dorsolateral and medial prefrontal cortex, particularly in the rostral anterior cingulate (Zhao et al., 2022). However, these two studies were conducted using mass univariate approaches without cross-validation (CV), which might increase the risks of overfitting. In contrast, machine learning approaches with CV can assess and prevent overfitting more effectively than univariate approaches, ultimately leading to more generalized findings. One example of a machine learning approach is elastic net regression (ENR), which is an ideal approach to analyzing a large number of inter-correlated variables or predictors (Zou and Hastie, 2005; Owens et al., 2022). One study tested numerous machine learning algorithms for their effectiveness in the context of neuroimaging data and found that ENR models with CV performed well over a range of sample sizes as compared to other approaches (Jollans et al., 2019).

Several recent machine learning studies with CV comprehensively investigated predictive intelligence. Two moderately large studies (N = 415 and 392, respectively) found that distinct functional and structural connections contributed to the prediction of individual Gc and Gf (Dhamala et al., 2021), and the findings revealed neurobiological features of the functional connectome of Gc and Gf across the sexes (Dhamala et al., 2022). Additionally, another study (N = 308) reported that absolute GMV enabled significant predictions of individual intelligence scores (Hilger et al., 2020). However, these studies had several limitations. Firstly, the samples were enrolled from datasets with a relatively small sample size (less than 500). Secondly, these studies only investigated functional and structural connections or one neuroanatomical measure, GMV, and their relationship with intelligence. However, cortical GMV comprises CT and cortical surface area (CSA), which are known to be distinct morphological features of the cortical architecture (Tadayon et al., 2020). Both CT and CSA have distinct developmental trajectories and uncorrelated genetic backgrounds (Storsve et al., 2014), suggesting that CSA and CT should be considered separate morphometric features in neurodevelopment (Panizzon et al., 2009; Xu et al., 2023b).

To address these limitations, the current study used a machine learning approach to predict Gc and Gf from CSA, CT, and GMV. Data were drawn from the HCP, which remains one of the largest studies to date with contemporaneously collected Gc, Gf, and sMRI data. This study conducted ENR models with the CV approach, which is well suited to assess the overfitting and generalization of findings (Xu et al., 2023a). This approach simultaneously investigates all brain morphological variables as predictors of a target. Hence, this approach elucidates the neuroanatomical structures that are uniquely important to Gc and Gf. As a secondary strategy, this study also used a traditional univariate approach (linear mixed effects modeling) to confirm the presence of a univariate relationship between Gc and Gf and the neuroanatomical features contributing to the ENR models. Furthermore, intraclass correlation analyses were performed to examine the neuroanatomical pattern similarity of Gc and Gf. This study aimed to investigate whether Gc and Gf could be effectively predicted in an independent sample using a machine learning

approach and uncover the distinct neuroanatomical patterns of Gc and Gf in adults.

2. Materials and methods

2.1. Participants

In this study, the HCP release S1200 dataset was used. Participants were recruited at Washington University in St. Louis over 2 days between August 2012 and October 2015 (Van Essen et al., 2012). The protocols were approved by each institution's research ethics board. All participants provided written informed consent in accordance with the Declaration of Helsinki. All participants were young adults between 22 and 35 years old. The exclusion criteria were as follows: history of psychiatric disorder, substance abuse, neurodevelopmental disorder or damage, cardiovascular disease, severe health conditions (such as diabetes, multiple sclerosis, cerebral palsy, premature birth), or MRI contraindications (large tattoos, non-removable piercings, metal devices in the body or claustrophobia, etc.). The complete details of the inclusion and exclusion criteria and the informed consent for participants can be found in references (Van Essen et al., 2012, 2013). Some participants were excluded from further analysis due to the following reasons: missing sMRI scans, missing demographic data, and missing behavioral data. A total of 1,089 participants (90.75% of the initial sample size) were included in the final analysis (**Table 1**).

2.2. Intelligence assessment

Cognitive ability was assessed by the NIH Toolbox Cognition Battery with extensively validated neuropsychological tasks (Mungas et al., 2014). Two composite scores (crystallized cognition composite and fluid cognition composite) were derived from the scores of participants when performing NIH Toolbox Cognitive Battery tasks (Mungas et al., 2014). Gc was measured by Picture Vocabulary and Oral Reading Recognition Tests, which assessed language and verbal skills. Likewise, Gf was measured using the Dimensional Change Card Sort, Flanker Inhibitory Control and Attention Test, Picture Sequence Memory, List Sorting Working Memory, and the Pattern Comparison Processing Speed Test, which broadly assessed processing speed, memory, and executive functioning (**Figure 1A**).

2.3. MRI data acquisition and pre-processing

In the HCP dataset, T1-weighted structural images were collected using a 32-channel head coin on a 3T Siemens Skyra scanner (Siemens AG, Erlanger, Germany) with the following scanning parameters: isotropic resolution = 0.7 mm^3, field of view = 224 mm × 240 mm, matrix size = 320 × 320, repetition time = 2,400 ms, echo time = 2.14 ms, inversion time = 1,000 ms, flip angle = 8°, and 256 sagittal slices. Data were reconstructed and pre-processed using a modified version of the FreeSurfer pipeline (Fischl et al., 2004) in FreeSurfer Image Analysis Suite version 5.3[1] (Fischl, 2012). For details of acquisition parameters, reconstruction, and pre-processing of the HCP sMRI data, see references (Van Essen et al., 2012; Glasser et al., 2013) and **supplementary materials**. All structural images were reviewed by a technician immediately after acquisition to ensure scans were without any significant problems (i.e., artifacts and substantial movement). For a detailed explanation of HCP quality control, check reference (Marcus et al., 2013). The quantitative measures of CT and CSA for cortical regions were defined by the Desikan atlas (Desikan et al., 2006), while the GMV for subcortical regions from the ASEG parcellation and intracranial volume (ICV) was derived in FreeSurfer (Fischl, 2012).

2.4. Data analyses

ENR model analyses (**Figure 1**) were conducted in Python using Scikit-Learn (Pedregosa et al., 2011) and the Brain Predictability toolbox (Hahn et al., 2021). LME model analyses were performed using R (Version 4.1.3[2]) and RStudio ("Ghost Orchid" Release; see text footnote 2), with the lme4 package (Version 1.1-28) (Bates et al., 2015).

1 http://surfer.nmr.mgh.harvard.edu

2 https://www.r-project.org/

TABLE 1 Demographic characteristics of sample (N = 1089).

Metric	M (SD) or percent
Age	28.83 (3.68)
Sex	
Female	54.27%
Male	45.73%
Total family income	
<$10,000	7.16%
10K–19,999	7.99%
20K–29,999	12.49%
30K–39,999	12.03%
40K–49,999	10.38%
50K–74,999	20.75%
75K–99,999	13.50%
≥ 1,00,000	15.70%
Education level	
≤ 11 years	3.49%
12 years	13.77%
13 years	6.34%
14 years	12.40%
15 years	6.06%
16 years	42.15%
≥ 17 years	15.79%

M, mean; SD, standard deviation. These demographic variables were used as covariates in the following model analyses.

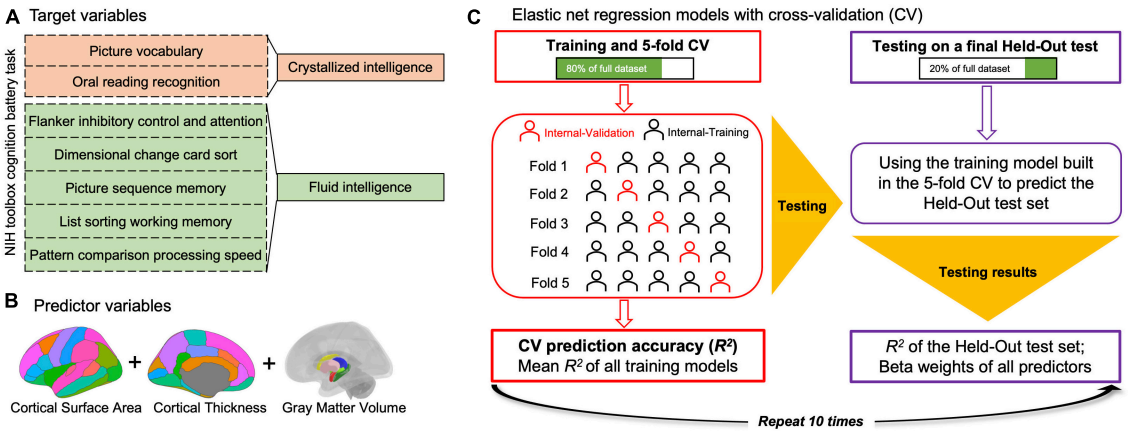

FIGURE 1
Schematic of elastic net regression (ENR) model analyses conducted. ENR models were built in which crystallized intelligence or fluid intelligence was the target, respectively, **(A)** and the predictors were regional sMRI variables (i.e., the cortical thickness and cortical surface area of each cortical region, gray matter volume of each subcortical region, and total intracranial volume) **(B)**. A modified coefficient of determination (R^2) was calculated as the measure of prediction accuracy for each model. All ENR analyses were repeated 10 times to ensure stability of findings across different train/test splits and results across repetitions were averaged **(C)**.

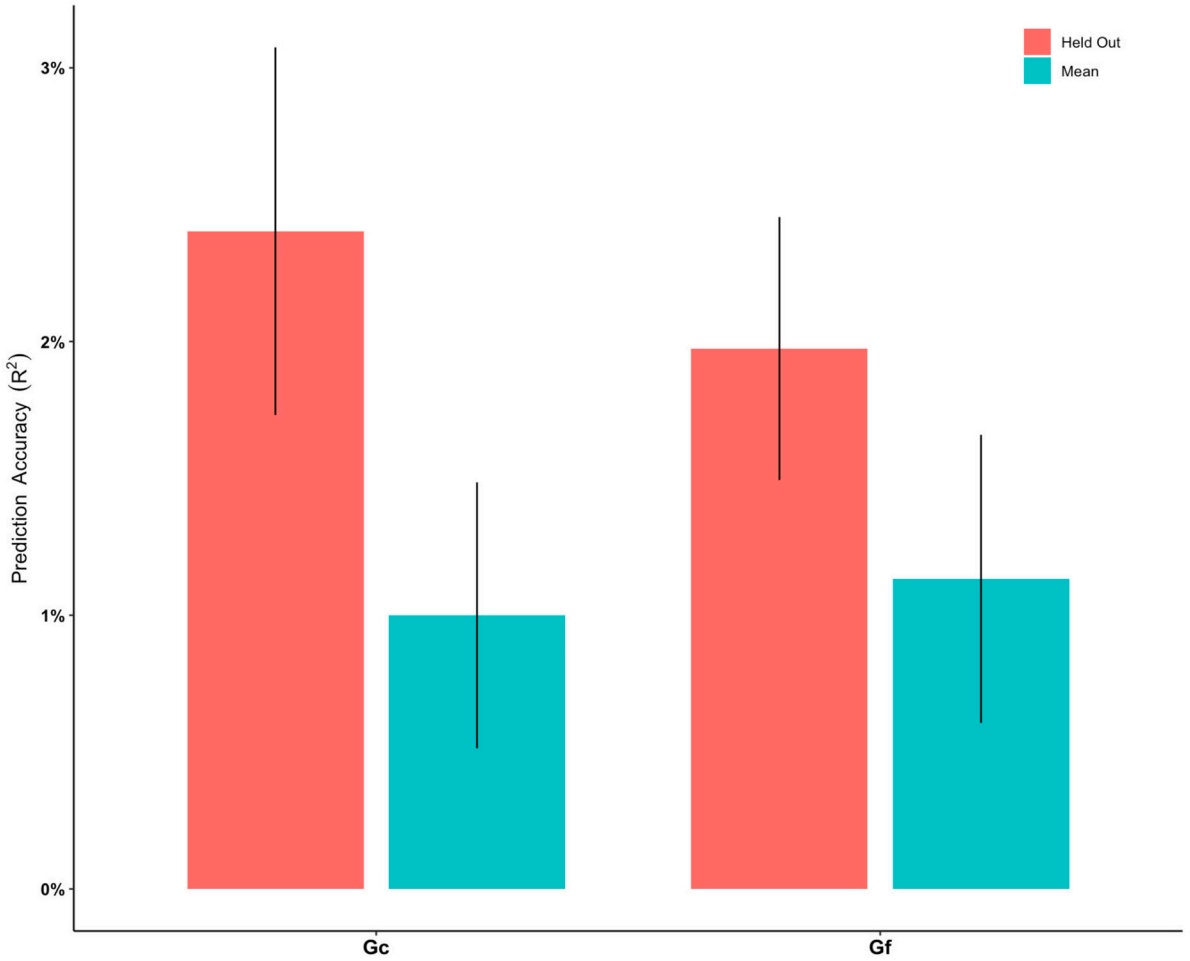

FIGURE 2
Prediction accuracy (R^2) for elastic net regression models to predict crystalized intelligence (Gc) and fluid intelligence (Gf), respectively. "Mean" indicate the mean R^2 of all models built in the training phase. "Held Out" indicates the all R^2 of all models from the training phase being tested on the held-out test set. Error bars stand for standard error of mean.

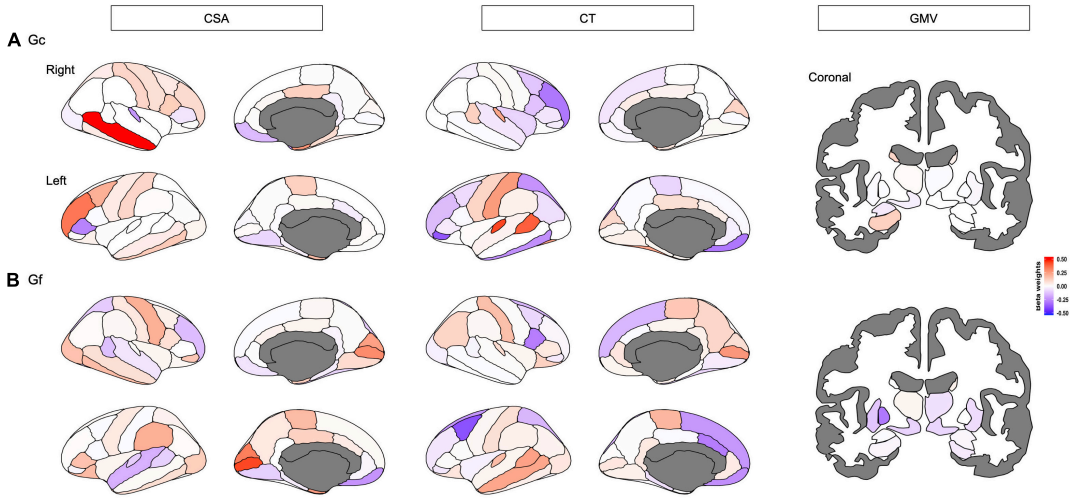

FIGURE 3
Distinct neuroanatomical patterns were indexed by beta weights of different features including cortical surface area (CSA), and cortical thickness (CT) of each cortical region, and gray matter volume (GMV) of each subcortical that predicted **(A)** crystalized intelligence (Gc) and **(B)** fluid intelligence (Gf), respectively. Red-shaded brain regions or bars indicate positive beta weights, while blue-shaded brain regions or bars indicate negative beta weights.

2.4.1. Elastic net regression model analyses

To remove the covariance (e.g., demographic variables, including age, sex, total family income, and education level), residual covariates were removed from a pool of variables, comprising Gc and Gf. The ENR models were built with Gc or Gf as the dependent variable. Hence, the predictors (i.e., independent variables) of the model-building algorithm were regional sMRI variables (i.e., the CT and CSA of each cortical region, the GMV of each subcortical region, and total ICV; **Figure 1B**). The model aimed to investigate neuroanatomical patterns that could predict Gc and Gf.

A modified coefficient of determination (R^2) was calculated as a measure of accuracy for each model. All elastic net analyses were repeated 10 times to validate findings across different train/test splits, and the results across multiple repetitions were averaged (**Figure 1C**).

Initially, 20% of the total participants were selected as the held-out test set. For the remaining participants, a 5-fold CV was used to build and test five separate elastic net regression models. In this approach, the training data were split into five equal groups (i.e., "folds"). A model was then built using four of the 5-folds (i.e., the training data) and tested on the 5-fold (i.e., the validation set) to determine its accuracy. After five repetitions, with each fold serving as the test set exactly once, the mean of the five models was used to predict the held-out test set.

Within this 5-fold CV, hyperparameter tuning was performed in the training set with a nested 3-fold CV. A random hyperparameter search algorithm was used on 200 randomly selected combinations of hyperparameters (Alibrahim and Ludwig, 2021). In the 3-fold CV, the training data were split into 3-folds in each of the five model-building phases. Within each of the 3-folds, 200 randomly selected combinations of parameters were tested, and the best combination was selected. The combination that yielded the best accuracy from all the folds was used to build a model for 5-fold iteration in the outer loop.

2.4.2. Linear mixed effects model analyses

To better interpret elastic net regression analyses, a secondary analysis was conducted to test the association of Gc and Gf with each sMRI variable from the final elastic net regression model. The linear mixed effects (LME) model analyzed each sMRI variable as a fixed effect. Demographic variables (sex, age, education level, and total family income) and ICV were fixed effects, and family ID was used as a random effect. The Gc or Gf was the dependent variable. The $P < 0.05$ after Bonferroni correction was used to indicate significance. Regions included in ERN models were only considered as neural correlates of Gc and Gf if they were also associated in the same direction in the univariate analyses.

2.4.3. Intraclass correlation analyses

To examine the neuroanatomical distinctiveness of Gc and Gf, absolute similarity coefficients (i.e., intraclass correlation (ICC)) were calculated across the entire set of sMRI features. The regression coefficients for each regional brain measure from LME models and beta weights from ENR models served as the elements of ICC analyses. The double-entry intraclass correlations (McCrae, 2008), which accounted for absolute similarities in magnitude and direction of the neuroanatomical profiles of Gc and Gf, were used to quantify the degree of absolute neuroanatomical similarity between Gc and Gf. These indices were computed separately across CSA features, CT features, and GMV features, and across all sMRI features again. The neuroanatomical similarity between Gc and Gf was interpreted using cut-offs based on "poor reliability/replicability" (ICC = 0.00−0.50), "moderate reliability/replicability" (ICC = 0.50−0.75), "good reliability/replicability" (ICC = 0.75−0.90), and "excellent reliability/replicability" (ICC = 0.90−1.00) (Koo and Li, 2016). Additionally, Pearson correlations were conducted in sMRI features between Gc and Gf accordingly.

3. Results

3.1. ENR models

The ENR model predicted Gc with R^2 of 1.00% after a 5-fold cross-validation. The R^2 was 2.40% when predicting the held-out test set across 10 repetitions of the ENR procedure (Figure 2 and Supplementary Table 1). The pattern of regions that contributed to the mode (beta weights ranging between −0.3744 and 0.5356) included CSA and CT of the widespread frontal, parietal, and temporal regions (e.g., rostral middle frontal gyrus, medial orbitofrontal cortex, caudal middle frontal, posterior cingulate cortex, and caudal anterior cingulate cortex), and GMV of the subcortical regions, including the bilateral hippocampus and left thalamus (Figure 3A). Brain regions with positive/negative beta weights in the ENR model are reported in Supplementary Table 2.

The ENR model predicted Gf with an R^2 of 1.13% after a 5-fold cross-validation. The R^2 was 1.97% when predicting the held-out test set across 10 repetitions of the ENR procedure (Figure 2 and Supplementary Table 1). The pattern of regions that contributed to the mode (beta weights ranging between −0.3866 and 0.4309) included CSA and CT of the widespread frontal, parietal, and temporal regions (e.g., rostral middle frontal gyrus, medial orbitofrontal cortex, caudal middle frontal, superior and inferior parietal lobule, posterior cingulate cortex, and caudal anterior cingulate cortex), and GMV of the subcortical regions, including the bilateral nucleus accumbens and left pallidum (Figure 3B). Brain regions with positive/negative beta weights in the ENR model are reported in Supplementary Table 3.

3.2. LME models

Linear mixed effects model analyses (Table 2) revealed the association between Gc and the CSA of widespread cortical regions (including bilateral rostral middle frontal gyrus, caudal middle frontal, superior frontal gyrus, and parahippocampal gyrus) and the GMV of subcortical regions (including the bilateral hippocampus and left thalamus). However, Gf was significantly associated with only CSA in limited cortical regions (including bilateral the pericalcarine fissure). According to the ENR model, the brain regions that were significant in the LME model for both Gc and Gf are displayed in Figure 4.

3.3. Neuroanatomical pattern similarity

intraclass correlation analyses of regression coefficients indicated that all sMRI features had poor similarity with all ICC below 0.50 between Gc and Gf (ICC = 0.1649−0.4761; Pearson's r = 0.2614−0.5184; Table 3). Similarly, beta weights of all sMRI features reported poor similarity with all ICC below 0.40 between Gc and Gf (ICC = 0.0817−0.3910; Pearson's r = 0.0812−0.4851; Table 3).

4. Discussion

This study aimed to provide a comprehensive examination of distinct neuroanatomical patterns to predict Gc and Gf in healthy adults using a cross-validated machine learning approach. Results of this approach indicted that distinct multi-region neuroanatomical patterns predicted Gc and Gf, respectively, with robust prediction accuracy in a held-out test set (R^2 = 2.40% for Gc and R^2 = 1.97% for Gf). Univariate LME model analyses supported the results, where the same brain regions identified in ENR models were significantly associated with Gc and Gf. Additionally, ICC findings exhibited poor neuroanatomical pattern similarity between Gc and Gf, indicating distinct neuroanatomical patterns to predict Gc and Gf. Taken together, these findings provided evidence that machine learning-derived distinct neuroanatomical patterns could predict Gc and Gf in healthy adults.

Interestingly, the ENR model indicated that Gc was more predictable than Gf from multi-region neuroanatomical patterns. Previous research proposed that Gc and Gf exhibited distinct developments and transformations across the lifespan (Cattell, 1967). While Gc is the ability to use previously learned knowledge and life experience, which are thought to be influenced by education and cultural factors, Gf is regarded as the ability to solve new problems using logical reasoning and adapt to unknown situations, which are thought to be more dependent on biological processes (Heaton et al., 2014). In this study, Gc reflected the scores of tasks such as vocabulary and decoding, while Gf reflected the scores of cognitive tasks including cognitive flexibility, working memory, and information processing speed (Mungas et al., 2014). The eloquent nature of the mapping between neuroanatomical morphometry profile and language, including vocabulary and reading as measured by Gc, may explain the higher variance of the scores when compared to Gc, which relies on brain functional networks for different cognitive functions. Another possible explanation for the higher predictability of Gc relative to Gf could be the impact of environment on neuroanatomical morphometry (Maggioni et al., 2020). Additionally, Gc is more stable throughout life and generally less susceptible to factors that affect cognitive function (e.g., mood and stress) (Riedel et al., 2002; O'Neill et al., 2020), resulting in the higher predictability of Gc over Gf. Additionally, a previous study found that cortical grey matter morphology provided little information about Gf and was probably incapable of predicting Gf (Oxtoby et al., 2019). This study validated this claim, whereby a low CSA led to low Gf predictivity. In this regard, Gf reflected higher cognitive functions, which were more dependent on large-scale brain networks (Gray et al., 2003; Barbey, 2018).

Moreover, the feature of neuroanatomical morphometry most linked to intelligence was CSA, which had more significant associations with Gc and Gf than CT or subcortical GMV. From the evolutionary perspective of the human cerebral cortex, the brain region is theorized to be enlarged mainly by the expansion of the surface area without a comparable increase in its thickness (Rakic et al., 2009). This suggests that the frontal

10.3389/fnins.2023.1199106

TABLE 2 Significant sMRI correlates of Gc and Gf in linear mixed effect models after Bonferroni correction.

Hemisphere	Region	*B*	SE	*t*	$P_{Bonferroni}$	R^2
Gc						
CSA						
Right	Middle temporal gyrus	0.0066	0.0011	6.2413	0.0000	0.0428
Left	Rostral middle frontal gyrus	0.0033	0.0006	5.3011	0.0000	0.0342
Right	Rostral middle frontal gyrus	0.0030	0.0006	5.0896	0.0001	0.0330
Left	Lateral orbitofrontal cortex	0.0076	0.0016	4.8867	0.0002	0.0330
Left	Middle temporal gyrus	0.0058	0.0011	5.0853	0.0001	0.0328
Right	Precentral gyrus	0.0041	0.0009	4.7772	0.0003	0.0316
Left	Inferior temporal gyrus	0.0046	0.0009	5.0032	0.0001	0.0310
Left	Postcentral gyrus	0.0045	0.0009	4.8172	0.0003	0.0308
Right	Superior temporal gyrus	0.0052	0.0011	4.6094	0.0007	0.0304
Right	Postcentral gyrus	0.0043	0.0009	4.5031	0.0012	0.0284
Left	Precentral gyrus	0.0038	0.0009	4.3840	0.0020	0.0283
Left	Caudal middle frontal	0.0046	0.0010	4.4200	0.0017	0.0281
Right	Insula	0.0070	0.0016	4.2863	0.0031	0.0278
Right	Pars opercularis	0.0074	0.0017	4.4289	0.0017	0.0273
Right	Superior frontal gyrus	0.0023	0.0006	4.0546	0.0084	0.0269
Left	Superior temporal gyrus	0.0042	0.0011	4.0035	0.0104	0.0266
Left	Precuneus	0.0039	0.0010	3.9497	0.0130	0.0261
Left	Insula	0.0066	0.0016	4.0335	0.0092	0.0258
Left	Superior frontal gyrus	0.0021	0.0005	3.8975	0.0161	0.0258
Right	Fusiform gyrus	0.0040	0.0010	3.9316	0.0140	0.0252
Left	Lateral occipital gyrus	0.0029	0.0008	3.8073	0.0232	0.0251
Left	Rostral anterior cingulate	0.0106	0.0026	3.9977	0.0107	0.0249
Right	Superior parietal lobule	0.0027	0.0007	3.7923	0.0246	0.0247
Left	Supramarginal gyrus	0.0030	0.0008	3.7491	0.0292	0.0240
Right	Posterior cingulate	0.0076	0.0020	3.8591	0.0189	0.0240
Right	Parahippocampal gyrus	0.0151	0.0041	3.6537	0.0424	0.0235
Right	Frontal pole	0.0332	0.0088	3.7840	0.0256	0.0233
Right	Inferior temporal gyrus	0.0035	0.0010	3.6820	0.0380	0.0229
GMV						
	ICV	0.0000	0.0000	5.4403	0.0000	0.0380
Right	Hippocampus	0.0044	0.0011	4.0211	0.0097	0.0265
Left	Thalamus	0.0020	0.0005	3.9643	0.0123	0.0258
Left	Hippocampus	0.0039	0.0010	4.0502	0.0086	0.0251
Gf						
CSA						
Left	Pericalcarine fissure	0.0097	0.0023	4.3083	0.0028	0.0198
Right	Precentral gyrus	0.0041	0.0011	3.8765	0.0175	0.0164
Right	Lateral occipital gyrus	0.0035	0.0009	3.9168	0.0149	0.0159
Left	Cuneus	0.0102	0.0027	3.8300	0.0212	0.0158
Right	Pericalcarine fissure	0.0077	0.0021	3.6214	0.0479	0.0144

Gc, crystalized intelligence; Gf, fluid intelligence; sMRI, structural magnetic resonance imaging; B, unstandardized regression coefficient; SE, standard error; CT, cortical thickness; CSA: cortical thickness; GMV, gray matter volume. FDR, false discovery rate; $P_{\text{Bonferroni}}$, *P*-value after Bonferroni correction; ICV, intracranial volume.

TABLE 3 Neuroanatomical similarity between Gc and Gf in different sMRI features.

Neuroanatomical similarity	Regression coefficients of LME models		Beta weights of ENR models	
	r	ICC	*r*	ICC
CSA features	0.4827	0.4761	0.0812	0.0817
CT features	0.5184	0.4579	0.3906	0.3910
GMV features	0.2614	0.1649	0.4851	0.2853
All sMRI features	0.4660	0.4388	0.2703	0.2712

Gc, crystalized intelligence; Gf, fluid intelligence; sMRI, structural magnetic resonance imaging. *r* represents Pearson's *r* for the 156 sMRI features [68 indices of regional cortical surface area (CSA) + 68 indices of regional cortical thickness (CT) + 20 indices of gray matter volume (GMV) separately] for Gc and Gf; *ICC* represent intraclass correlation (ICC) between these same regions for Gc and Gf.

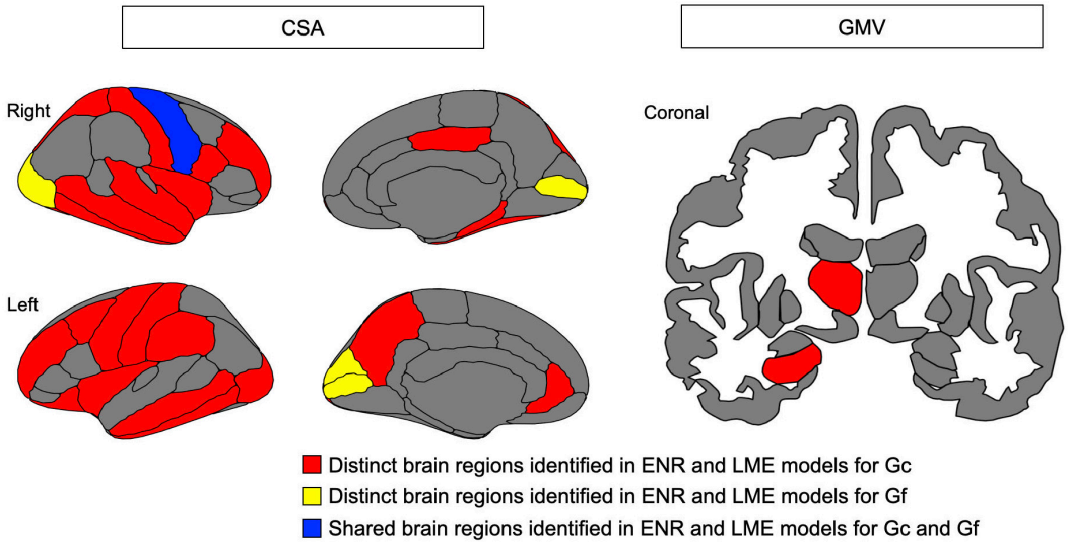

FIGURE 4
Brain map for cortical surface area (CSA) of cortical region and gray matter volume (GMV) of subcortical region identified as contributing to predict crystalized intelligence (Gc) and (B) fluid intelligence (Gf), respectively, in elastic net regression (ENR) models and found to be significantly associations in linear mixed effect (LME) models. Red indicates distinct brain regions identified in ENR and LME models for Gc; yellow indicates distinct brain regions identified in ENR and LME models for Gf; blue indicted shared brain regions identified in ENR and LME models for both Gc and Gf.

and parietal surface area are enlarged first, followed by increasing thickness for young adults with higher intelligence. Evidence has verified that CSA and CT possess distinct genetic bases and developmental trajectories (Panizzon et al., 2009). Furthermore, gene expression is inversely correlated with development (Vidal-Pineiro et al., 2020). CSA and CT contribute to different aspects of intelligence (Gc and Gf). This study revealed the poor similarity between the neural correlates of Gc and Gf, evidenced by the low ICC in both ENR and LME models. The poor similarity between the neuroanatomical correlates of Gc and Gf supports the concept of distinct neuroanatomical patterns, suggesting that Gc and Gf may be "two sides of the same coin" (i.e., different aspects of intelligence have differential neuroanatomical signatures).

This study had several noteworthy strengths. This is a study for a machine learning-based approach to predict Gc and Gf using multiple metrics of the brain (i.e., CT, CSA, and GMV). The brain regions analyzed via the machine learning approach were largely supported by a univariate LME model, which validated the distinct brain regions to predict Gc and Gf. Additionally, the findings of this study were largely consistent with previous univariate analyses on the sMRI correlates of intelligence, highlighting the significance of the neuroanatomical correlates of intelligence. Furthermore, Gc and Gf were predicted by distinct neuroanatomical patterns with poor pattern similarity, which exhibited different neural substrates of distinct intelligence components in adults.

In retrospect, this study had several limitations. Firstly, the study used a cross-sectional design, which would discredit claims regarding the causality of the observed relationships. Future longitudinal studies should be performed to address this issue (Xu et al., 2018, 2019). Secondly, the current results are limited only to sMRI data, which could be further validated by resting-state functional MRI data or functional MRI data for related tasks (e.g., executive function) (Niu et al., 2020; Yang et al., 2020). Another direction to be explored is to determine whether the predictive model accuracy can be improved by an alternative machine learning approach. There is work suggesting that convolutional neural network modeling can outperform standard machine learning algorithms (Abrol et al., 2021). While this approach would require substantially more computational resources than the current analysis, this may improve the accuracy of predictive models.

5. Conclusion

In summary, using a cross-validated elastic net regression approach, this study indicated distinct neuroanatomical patterns that predicted Gc and Gf with robust accuracy in healthy adults. These findings verified the results of prior works to understand the neuroanatomical foundations of intelligence and demonstrate the utility of machine learning in this field of research. In addition, the distinct structural neural correlates of Gc and Gf were comprehensively studied and recognized for their involvement in different individual cognitive functions.

Data availability statement

Publicly available datasets were analyzed in this study. This data can be found here: All data were provided by the Human Connectome Project, WU-Minn Consortium (Principal Investigators: David Van Essen and Kamil Ugurbil; 1U54MH091657) funded by the 16 NIH Institutes and Centers that support the NIH Blueprint for Neuroscience Research and the McDonnell Center for Systems Neuroscience at Washington University in St. Louis.

Ethics statement

The studies involving human participants were reviewed and approved by the Second Affiliated Hospital and Yuying Children's Hospital of Wenzhou Medical University. The patients/participants provided their written informed consent to participate in this study.

Author contributions

HX: conceptualization, methodology, data curation, formal analysis, software, visualization, investigation, supervision, writing – original draft, and writing – review and editing. CX, ZY, and GB: methodology, and writing – reviewing and editing. BY: funding acquisition, project administration, supervision, and writing – review and editing. All authors contributed to the article and approved the submitted version.

Funding

This study was funded by the Natural Science Foundation of Zhejiang Province (No. LY15H090016), Wenzhou Science and Technology Bureau in China (No. Y20140577), and Beijing New Health Industry Development Foundation (No. XM2020-02-002).

Conflict of interest

The authors declare that the research was conducted in the absence of any commercial or financial relationships that could be construed as a potential conflict of interest.

Publisher's note

All claims expressed in this article are solely those of the authors and do not necessarily represent those of their affiliated organizations, or those of the publisher, the editors and the reviewers. Any product that may be evaluated in this article, or claim that may be made by its manufacturer, is not guaranteed or endorsed by the publisher.

Supplementary material

The Supplementary Material for this article can be found online at: https://www.frontiersin.org/articles/10.3389/fnins.2023.1199106/full#supplementary-material

References

Abrol, A., Fu, Z., Salman, M., Silva, R., Du, Y., Plis, S., et al. (2021). Deep learning encodes robust discriminative neuroimaging representations to outperform standard machine learning. *Nat. Commun.* 12:353. doi: 10.1038/s41467-020-20655-6

Alibrahim, H., and Ludwig, S. A. (2021). "Hyperparameter optimization: comparing genetic algorithm against grid search and bayesian optimization," in *Paper Presented at the 2021 IEEE congress on evolutionary compssutation (CEC)*, (Kraków).

Barbey, A. K. (2018). Network neuroscience theory of human intelligence. *Trends Cogn. Sci.* 22, 8–20. doi: 10.1016/j.tics.2017.10.001

Barbey, A. K., Colom, R., and Grafman, J. (2013). Dorsolateral prefrontal contributions to human intelligence. *Neuropsychologia* 51, 1361–1369. doi: 10.1016/j.neuropsychologia.2012.05.017

Bates, D., Mächler, M., Bolker, B., and Walker, S. (2015). Fitting linear mixed-effects models using lme4. *J. Stat. Softw.* 67, 1–48. doi: 10.18637/jss.v067.i01

Button, K. S., Ioannidis, J. P., Mokrysz, C., Nosek, B. A., Flint, J., Robinson, E. S., et al. (2013). Power failure: why small sample size undermines the reliability of neuroscience. *Nat. Rev. Neurosci.* 14, 365–376. doi: 10.1038/nrn3475

Cattell, R. B. (1943). The measurement of adult intelligence. *Psychol. Bull.* 40, 153–193. doi: 10.1037/h0059973

Cattell, R. B. (1967). The theory of fluid and crystallized general intelligence checked at the 5–6 year-old level. *Br. J. Educ. Psychol.* 37, 209–224. doi: 10.1111/j.2044-8279.1967.tb01930.x

Cipolotti, L., Ruffle, J. K., Mole, J., Xu, T., Hyare, H., Shallice, T., et al. (2022). Graph lesion-deficit mapping of fluid intelligence. *Brain* 146, 167–181. doi: 10.1093/brain/awac304

Deary, I. J., Strand, S., Smith, P., and Fernandes, C. (2007). Intelligence and educational achievement. *Intelligence* 35, 13–21. doi: 10.1016/j.intell.2006.02.001

Desikan, R. S., Segonne, F., Fischl, B., Quinn, B. T., Dickerson, B. C., Blacker, D., et al. (2006). An automated labeling system for subdividing the human cerebral cortex on MRI scans into gyral based regions of interest. *Neuroimage* 31, 968–980. doi: 10.1016/j.neuroimage.2006.01.021

Dhamala, E., Jamison, K. W., Jaywant, A., and Kuceyeski, A. (2022). Shared functional connections within and between cortical networks predict cognitive abilities in adult males and females. *Hum. Brain Mapp.* 43, 1087–1102. doi: 10.1002/hbm.25709

Dhamala, E., Jamison, K. W., Jaywant, A., Dennis, S., and Kuceyeski, A. (2021). Distinct functional and structural connections predict crystallised and fluid cognition in healthy adults. *Hum. Brain Mapp.* 42, 3102–3118. doi: 10.1002/hbm.25420

Fischl, B. (2012). FreeSurfer. *Neuroimage* 62, 774–781. doi: 10.1016/j.neuroimage.2012.01.021

Fischl, B., van der Kouwe, A., Destrieux, C., Halgren, E., Segonne, F., Salat, D. H., et al. (2004). Automatically parcellating the human cerebral cortex. *Cereb. Cortex* 14, 11–22. doi: 10.1093/cercor/bhg087

Gainotti, G. (2006). Anatomical functional and cognitive determinants of semantic memory disorders. *Neurosci. Biobehav. Rev.* 30, 577–594. doi: 10.1016/j.neubiorev.2005.11.001

Genç, E., Fraenz, C., Schlüter, C., Friedrich, P., Hossiep, R., Voelkle, M. C., et al. (2018). Diffusion markers of dendritic density and arborization in gray matter predict differences in intelligence. *Nat. Commun.* 9:1905. doi: 10.1038/s41467-018-04268-8

Glasser, M. F., Sotiropoulos, S. N., Wilson, J. A., Coalson, T. S., Fischl, B., Andersson, J. L., et al. (2013). The minimal preprocessing pipelines for the human connectome project. *Neuroimage* 80, 105–124. doi: 10.1016/j.neuroimage.2013.04.127

Gottfredson, L. S. (1997). Why g matters: the complexity of everyday life. *Intelligence* 24, 79–132. doi: 10.1016/S0160-2896(97)90014-3

Gray, J. R., Chabris, C. F., and Braver, T. S. (2003). Neural mechanisms of general fluid intelligence. *Nat. Neurosci.* 6, 316–322. doi: 10.1038/nn1014

Hahn, S., Yuan, K., Thompson, W. K., Owens, M., Allgaier, N., and Garavan, H. (2021). Brain Predictability toolbox: a Python library for neuroimaging-based machine learning. *Bioinformatics* 37, 1637–1638. doi: 10.1093/bioinformatics/btaa974

Heaton, R. K., Akshoomoff, N., Tulsky, D., Mungas, D., Weintraub, S., Dikmen, S., et al. (2014). Reliability and validity of composite scores from the NIH toolbox cognition battery in adults. *J. Int. Neuropsychol. Soc.* 20, 588–598. doi: 10.1017/S1355617714000241

Hilger, K., Winter, N. R., Leenings, R., Sassenhagen, J., Hahn, T., Basten, U., et al. (2020). Predicting intelligence from brain gray matter volume. *Brain Struct. Funct.* 225, 2111–2129. doi: 10.1007/s00429-020-02113-7

Jollans, L., Boyle, R., Artiges, E., Banaschewski, T., Desrivieres, S., Grigis, A., et al. (2019). Quantifying performance of machine learning methods for neuroimaging data. *Neuroimage* 199, 351–365. doi: 10.1016/j.neuroimage.2019.05.082

Jung, R. E., and Haier, R. J. (2007). The parieto-frontal integration theory (P-FIT) of intelligence: converging neuroimaging evidence. *Behav. Brain Sci.* 30, 135–154; discussion154–187. doi: 10.1017/s0140525x07001185

Koo, T. K., and Li, M. Y. (2016). A guideline of selecting and reporting intraclass correlation coefficients for reliability research. *J. Chiropr. Med.* 15, 155–163. doi: 10.1016/j.jcm.2016.02.012

Li, S. C., Lindenberger, U., Hommel, B., Aschersleben, G., Prinz, W., and Baltes, P. B. (2004). Transformations in the couplings among intellectual abilities and constituent cognitive processes across the life span. *Psychol. Sci.* 15, 155–163. doi: 10.1111/j.0956-7976.2004.01503003.x

Maggioni, E., Squarcina, L., Dusi, N., Diwadkar, V. A., and Brambilla, P. (2020). Twin MRI studies on genetic and environmental determinants of brain morphology and function in the early lifespan. *Neurosci. Biobehav. Rev.* 109, 139–149. doi: 10.1016/j.neubiorev.2020.01.003

Marcus, D. S., Harms, M. P., Snyder, A. Z., Jenkinson, M., Wilson, J. A., Glasser, M. F., et al. (2013). Human connectome project informatics: quality control, database services, and data visualization. *Neuroimage* 80, 202–219. doi: 10.1016/j.neuroimage.2013.05.077

Marek, S., Tervo-Clemmens, B., Calabro, F. J., Montez, D. F., Kay, B. P., Hatoum, A. S., et al. (2022). Reproducible brain-wide association studies require thousands of individuals. *Nature* 603, 654–660. doi: 10.1038/s41586-022-04492-9

Martin, A., and Chao, L. L. (2001). Semantic memory and the brain: structure and processes. *Curr. Opin. Neurobiol.* 11, 194–201. doi: 10.1016/s0959-4388(00)00196-3

McArdle, J. J., Hamagami, F., Meredith, W., and Bradway, K. P. (2000). Modeling the dynamic hypotheses of Gf–Gc theory using longitudinal life-span data. *Learn. Individ. Differ.* 12, 53–79. doi: 10.1016/S1041-6080(00)00036-4

McClelland, J. L., and Rogers, T. T. (2003). The parallel distributed processing approach to semantic cognition. *Nat. Rev. Neurosci.* 4, 310–322. doi: 10.1038/nrn1076

McCrae, R. R. (2008). A note on some measures of profile agreement. *J. Pers. Assess.* 90, 105–109. doi: 10.1080/00223890701845104

Mungas, D., Heaton, R., Tulsky, D., Zelazo, P. D., Slotkin, J., Blitz, D., et al. (2014). Factor structure, convergent validity, and discriminant validity of the NIH toolbox cognitive health battery (NIHTB-CHB) in adults. *J. Int. Neuropsychol. Soc.* 20, 579–587. doi: 10.1017/S1355617714000307

Neisser, U., Boodoo, G., Bouchard, T. J. Jr., Boykin, A. W., Brody, N., Ceci, S. J., et al. (1996). Intelligence: knowns and unknowns. *Am. Psychol.* 51, 77–101. doi: 10.1037/0003-066X.51.2.77

Niu, X., Xu, H., Guo, C., Yang, T., Kress, D., Gao, L., et al. (2020). Strengthened thalamoparietal functional connectivity in patients with hemifacial spasm: a cross-sectional resting-state fMRI study. *Br. J. Radiol.* 93:20190887.

O'Neill, J., Kamper-DeMarco, K., Chen, X., and Orom, H. (2020). Too stressed to self-regulate? Associations between stress, self-reported executive function, disinhibited eating, and BMI in women. *Eat Behav.* 39:101417. doi: 10.1016/j.eatbeh.2020.101417

Owens, M. M., Hyatt, C., Xu, H., Thompson, M., Miller, J., Lynam, D., et al. (2022). Replicability of the neuroanatomical correlates of impulsive personality traits in the ABCD study. *PsyArXiv [Preprint]*. doi: 10.31234/osf.io/u3bxc

Oxtoby, N. P., Ferreira, F. S., Mihalik, A., Wu, T., Brudfors, M., Lin, H., et al. (2019). "ABCD neurocognitive prediction challenge 2019: predicting individual residual fluid intelligence scores from cortical grey matter morphology," in *Paper Presented at the adolescent brain cognitive development neurocognitive prediction*, (Cham).

Panizzon, M. S., Fennema-Notestine, C., Eyler, L. T., Jernigan, T. L., Prom-Wormley, E., Neale, M., et al. (2009). Distinct genetic influences on cortical surface area and cortical thickness. *Cereb. Cortex* 19, 2728–2735. doi: 10.1093/cercor/bhp026

Pedregosa, F., Varoquaux, G., Gramfort, A., Michel, V., Thirion, B., Grisel, O., et al. (2011). Scikit-learn: machine learning in Python. *J. Mach. Learn. Res.* 12, 2825–2830.

Posthuma, D., De Geus, E. J., Baaré, W. F., Hulshoff Pol, H. E., Kahn, R. S., and Boomsma, D. I. (2002). The association between brain volume and intelligence is of genetic origin. *Nat. Neurosci.* 5, 83–84. doi: 10.1038/nn0202-83

Rakic, P., Ayoub, A. E., Breunig, J. J., and Dominguez, M. H. (2009). Decision by division: making cortical maps. *Trends Neurosci.* 32, 291–301. doi: 10.1016/j.tins.2009.01.007

Riedel, W. J., Klaassen, T., and Schmitt, J. A. J. (2002). Tryptophan, mood, and cognitive function. *Brain Behav. Immun.* 16, 581–589. doi: 10.1016/S0889-1591(02)00013-2

Storsve, A. B., Fjell, A. M., Tamnes, C. K., Westlye, L. T., Overbye, K., Aasland, H. W., et al. (2014). Differential longitudinal changes in cortical thickness, surface area and volume across the adult life span: regions of accelerating and decelerating change. *J. Neurosci.* 34, 8488–8498. doi: 10.1523/JNEUROSCI.0391-14.2014

Tadayon, E., Pascual-Leone, A., and Santarnecchi, E. (2020). Differential contribution of cortical thickness, surface area, and gyrification to fluid and crystallized intelligence. *Cereb. Cortex* 30, 215–225. doi: 10.1093/cercor/bhz082

Van Essen, D. C., Smith, S. M., Barch, D. M., Behrens, T. E., Yacoub, E., Ugurbil, K., et al. (2013). The WU-minn human connectome project: an overview. *Neuroimage* 80, 62–79. doi: 10.1016/j.neuroimage.2013.05.041

Van Essen, D. C., Ugurbil, K., Auerbach, E., Barch, D., Behrens, T. E., Bucholz, R., et al. (2012). The human connectome project: a data acquisition perspective. *Neuroimage* 62, 2222–2231. doi: 10.1016/j.neuroimage.2012.02.018

Varriale, V., van der Molen, M. W., and De Pascalis, V. (2018). Mental rotation and fluid intelligence: a brain potential analysis. *Intelligence* 69, 146–157. doi: 10.1016/j.intell.2018.05.007

Vidal-Pineiro, D., Parker, N., Shin, J., French, L., Grydeland, H., Jackowski, A. P., et al. (2020). Cellular correlates of cortical thinning throughout the lifespan. *Sci. Rep.* 10:21803. doi: 10.1038/s41598-020-78471-3

Xu, H., MacKillop, J., and Owens, M. M. (2023a). A machine learning-derived neuroanatomical pattern predicts delayed reward discounting in the human connectome project young adult sample. *J. Neurosci. Res.* [Epub ahead of prit]. doi: 10.1002/jnr.25185

Xu, H., Wang, X., Chen, Z., Bai, G., Yin, B., Wang, S., et al. (2018). Longitudinal changes of caudate-based resting state functional connectivity in mild traumatic brain injury. *Front. Neurol.* 9:467. doi: 10.3389/fneur.2018.00467

Xu, H., Xu, C., Gu, P., Hu, Y., Guo, Y., and Bai, G. (2023b). Neuroanatomical restoration of salience network links reduced headache impact to cognitive function improvement in mild traumatic brain injury with posttraumatic headache. *J. Headache Pain* 24:43. doi: 10.1186/s10194-023-01579-0

Xu, H., Zhao, T., Luo, F., and Zheng, Y. (2019). Dissociative changes in gray matter volume following electroconvulsive therapy in major depressive disorder: a longitudinal structural magnetic resonance imaging study. *Neuroradiology* 61, 1297–1308. doi: 10.1007/s00234-019-02276-z

Yang, Q., Xu, H., Zhang, M., Wang, Y., and Li, D. (2020). Volumetric and functional connectivity alterations in patients with chronic cervical spondylotic pain. *Neuroradiology* 62, 995–1001. doi: 10.1007/s00234-020-02413-z

Yuan, P., Voelkle, M. C., and Raz, N. (2018). Fluid intelligence and gross structural properties of the cerebral cortex in middle-aged and older adults: a multi-occasion longitudinal study. *Neuroimage* 172, 21–30. doi: 10.1016/j.neuroimage.2018.01.032

Zhao, Q., Voon, V., Zhang, L., Shen, C., Zhang, J., and Feng, J. (2022). The ABCD study: brain heterogeneity in intelligence during a neurodevelopmental transition stage. *Cereb. Cortex* 32, 3098–3109. doi: 10.1093/cercor/bhab403

Zou, H., and Hastie, T. (2005). Regularization and variable selection via the elastic net. *J. R. Stat. Soc. Ser. B Methodol.* 67, 301–320. doi: 10.1111/j.1467-9868.2005.00503.x

frontiers | Frontiers in Neuroscience

TYPE Original Research
PUBLISHED 02 June 2023
DOI 10.3389/fnins.2023.1189420

OPEN ACCESS

EDITED BY
Yingying Tang,
Shanghai Jiao Tong University, China

REVIEWED BY
Abdul Hanif Khan Yusof Khan,
Putra Malaysia University, Malaysia
Mohamed Sherif Sirajudeen,
Majmaah University, Saudi Arabia

*CORRESPONDENCE
Jungsoo Lee
✉ jungsoo0319@gmail.com
Yun-Hee Kim
✉ yunkim@skku.edu;
✉ yun1225.kim@gmail.com

RECEIVED 19 March 2023
ACCEPTED 04 May 2023
PUBLISHED 02 June 2023

CITATION
Kim H, Lee G, Lee J and Kim Y-H (2023) Alterations in learning-related cortical activation and functional connectivity by high-definition transcranial direct current stimulation after stroke: an fNIRS study.
Front. Neurosci. 17:1189420.
doi: 10.3389/fnins.2023.1189420

Alterations in learning-related cortical activation and functional connectivity by high-definition transcranial direct current stimulation after stroke: an fNIRS study

Heegoo Kim[1,2,3], Gihyoun Lee[1,2,4], Jungsoo Lee[5]* and Yun-Hee Kim[1,2,4,6]*

[1]Department of Physical and Rehabilitation Medicine, Center for Prevention and Rehabilitation, Heart Vascular Stroke Institute, Samsung Medical Center, Seoul, Republic of Korea, [2]Department of Health Sciences and Technology, Samsung Advanced Institute for Health Science & Technology (SAIHST), Sungkyunkwan University, Seoul, Republic of Korea, [3]Department of Rehabilitation Medicine, CHA Bundang Medical Center, CHA University, Seongnam, Republic of Korea, [4]Department of Physical and Rehabilitation Medicine, Sungkyunkwan University School of Medicine, Suwon, Republic of Korea, [5]Department of Medical IT Convergence Engineering, Kumoh National Institute of Technology, Gumi, Republic of Korea, [6]Haeundae Sharing and Happiness Hospital, Pusan, Republic of Korea

Introduction: Motor learning is a key component of stroke neurorehabilitation. High-definition transcranial direct current stimulation (HD-tDCS) was recently developed as a tDCS technique that increases the accuracy of current delivery to the brain using arrays of small electrodes. The purpose of this study was to investigate whether HD-tDCS alters learning-related cortical activation and functional connectivity in stroke patients using functional near-infrared spectroscopy (fNIRS).

Methods: Using a sham-controlled crossover study design, 16 chronic stroke patients were randomly assigned to one of two intervention conditions. Both groups performed the sequential finger tapping task (SFTT) on five consecutive days, either with (a) real HD-tDCS or (b) with sham HD-tDCS. HD-tDCS (1 mA for 20 min, 4 × 1) was administered to C3 or C4 (according to lesion side). fNIRS signals were measured during the SFTT with the affected hand before (baseline) and after each intervention using fNIRS measurement system. Cortical activation and functional connectivity of NIRS signals were analyzed using a statistical parametric mapping open-source software package (NIRS-SPM), *OptoNet* II®.

Results: In the real HD-tDCS condition, oxyHb concentration increased significantly in the ipsilesional primary motor cortex (M1). Connectivity between the ipsilesional M1 and the premotor cortex (PM) was noticeably strengthened after real HD-tDCS compared with baseline. Motor performance also significantly improved, as shown in response time during the SFTT. In the sham HD-tDCS condition, functional connectivity between contralesional M1 and sensory cortex was enhanced compared with baseline. There was tendency toward improvement in SFTT response time, but without significance.

Discussion: The results of this study indicated that HD-tDCS could modulate learning-related cortical activity and functional connectivity within motor networks to enhance motor learning performance. HD-tDCS can be used as an additional tool for enhancing motor learning during hand rehabilitation for chronic stroke patients.

KEYWORDS

high-definition transcranial direct stimulation, functional near-infrared spectroscopy, stroke, motor learning, cortical activation, functional connectivity

1. Introduction

Stroke is a leading cause of disability, and many stroke patients live with lasting sensorimotor impairment (Anwer et al., 2022). Long-term disability in upper extremity motor function due to stroke can cause major challenges in performing activities of daily living (Langhorne et al., 2009), social participation (Sveen et al., 1999), and returning to work (Baldwin and Butler, 2006). Understanding the changes that occur in motor-related neurological mechanisms after stroke might facilitate the development of appropriate therapies that could enable better functional improvement.

Relearning specific motor skills required to complete daily tasks is a key component of stroke rehabilitation for upper extremity motor function. Learning a new motor skill requires the operation of several distinct motor learning processes that rely on different neuronal substrates (Spampinato and Celnik, 2021). On the cortical level, the prefrontal cortices and parietal lobes, which comprise the frontoparietal network, are engaged both in forming motor memory in the early learning phase and in delayed recall of learned motor skills (Doyon et al., 2003; Lewis and Miall, 2003). The motor cortex, including the primary motor cortex (M1), premotor cortex (PM), and supplementary motor area (SMA), is strongly interconnected with the frontoparietal network at the cortical level (Dahms et al., 2020). Also, for appropriate motor output of learned skills to the descending motor system, motor cortices must interact with the striatum and other parts of the basal ganglia (BG) (Dahms et al., 2020). After stroke, activity-dependent adaptations within the distributed neural networks can be induced by practicing skilled movements and changes in cortical representations (Kami et al., 1995; Karni et al., 1998), despite specific lesions. However, it is difficult to draw clear conclusions about the neural mechanisms used to recruit brain areas during motor learning because of the heterogeneity of stroke.

Transcranial direct current stimulation (tDCS) techniques have been used to alter neuronal activity and establish causal relationships between motor network components and behavioral outcomes to improve motor learning (Ammann et al., 2016) by controlling the polarity of induced electrical stimulation (Dissanayaka et al., 2017). Recently, high-definition tDCS (HD-tDCS) has been developed to increase the spatial precision of current delivery to a targeted cortical region using arrays of small electrodes (Villamar et al., 2013). A 4 × 1 ring configuration is one common arrangement of HD-tDCS electrodes to concentrate peak stimulation in a target region (Lefebvre et al., 2019). A previous brain modeling study that used high-resolution magnetic resonance imaging (MRI) demonstrated that the area of cortex undergoing modulation using a 4 × 1 ring configuration for HD-tDCS is more highly focused than that with the bipolar montage used in conventional tDCS (Datta et al., 2009). As measured by behavioral and neurophysiological parameters, HD-tDCS has been shown to improve motor learning capacity (Iannone et al., 2022) and have long-lasting effects in enhancing motor cortex excitability (Kuo et al., 2013). Taken together, the results of previous research indicate a need to clarify the neuronal mechanisms that underlie the modulatory effects of HD-tDCS.

Neuroimaging techniques are used to expand understanding of neuronal mechanisms (Esmaeilpour et al., 2020). Functional near-infrared spectroscopy (fNIRS) is a noninvasive optical imaging technique that can illustrate cortical activity by quantifying the concentrations of oxyhemoglobin (oxyHb) and deoxyhemoglobin (deoxyHb) using continuous-wave light (650–950 nm) emitted through the skull into the brain (Ferrari and Quaresima, 2012). Unlike conventional functional neuroimaging modalities, such as functional MRI (fMRI) and positron emission tomography (PET) (Leff et al., 2011; Ferrari and Quaresima, 2012), fNIRS has a relatively high tolerance to motion artifacts as it continuously detects hemodynamic responses, even during motor tasks. Therefore, the use of fNIRS in clinical trials is expanding (Delorme et al., 2019; Lee S.-H. et al., 2020; Huo et al., 2021). A recent fNIRS study suggested that the resting-state functional connectivity of the dorsolateral prefrontal cortex increased after HD-tDCS in healthy subjects (Yaqub et al., 2018). An fNIRS study in stroke patients demonstrated that HD-tDCS could rebalance interhemispheric cortical activity and reduce the hemodynamic burden in the affected hemisphere during simple finger tapping tasks (Kim et al., 2022). Furthermore, the usefulness of an fNIRS study on the effect of focal HD-tDCS stimulation on upper limb motor function in stroke patients was proposed (Muller et al., 2021). However, whether HD-tDCS modulates both cortical activation and functional connectivity during motor learning after stroke remains unclear.

The purpose of this study was to investigate the changes of cortical activation and functional connectivity during motor learning task with affected hand in stroke patients. We hypothesized the cortical activation and functional connectivity would show different patterns depending on application of HD-tDCS on ipsilesional M1 in stroke patients. In this study, we used fNIRS to investigate how HD-tDCS to ipsilesional motor areas of stroke patients affected cortical activation during motor learning with the affected hand compared with sham HD-tDCS. We also examined how HD-tDCS application induces changes in functional connectivity of ipsilesional and contralesional M1 during motor learning with the affected hand in stroke patients.

2. Methods

2.1. Participants

Potential participants were recruited from an outpatient stroke rehabilitation clinic at Samsung Medical Center in Seoul, Republic of Korea, from June 2021 to June 2022. Clinicians in rehabilitation medicine identified suitable participants who meet the inclusion and exclusion criteria for this study and obtained informed consent from those subjects. Twenty-one chronic stroke patients enrolled in this study. Among them, five patients withdrew consent before

TABLE 1 Demographic information of participants.

Subject number	Sex	Age (years)	Onset duration (months)	Side of lesion	Location of lesion	Type of stroke	Allocated condition order	Handedness
1	M	58	64.7	Rt.	BG, CR	Infarction	Condition 2—condition 1	Rt. handed
2	M	38	51.7	Lt.	BG, CR	Infarction	Condition 1—condition 2	Rt. handed
3	F	69	8.7	Lt.	BG, CR	Infarction	Condition 1—condition 2	Bi-handed
4	F	64	31.2	Lt.	BG, CR	Infarction	Condition 1—condition 2	Rt. handed
5	F	54	15.6	Rt.	BG, CR	Infarction	Condition 2—condition 1	Rt. handed
6	F	76	53.5	Rt.	BG, CR	Infarction	Condition 2—condition 1	Rt. handed
7	M	48	67.9	Lt.	BG	Hemorrhage	Condition 2—condition 1	Rt. handed
8	M	33	67.4	Lt.	BG, CR	Hemorrhage	Condition 1—condition 2	Rt. handed
9	F	55	122.0	Lt.	BG, CR	Infarction	Condition 2—condition 1	Rt. handed
10	F	71	175.5	Lt.	BG, CR	Hemorrhage	Condition 1—condition 2	Rt. handed
11	M	58	73.2	Rt.	BG, CR	Infarction	Condition 2—condition 1	Rt. handed
12	F	37	45.6	Lt.	BG, CR, TH	Hemorrhage	Condition 2—condition 1	Rt. handed
13	F	65	130.8	Lt.	BG, CR	Hemorrhage	Condition 2—condition 1	Rt. handed
14	F	62	197.0	Rt.	BG, CR	Infarction	Condition 1—condition 2	Rt. handed
15	M	71	68.0	Rt.	BG, CR	Infarction	Condition 1—condition 2	Rt. handed
16	M	50	38.4	Lt.	BG, CR	Hemorrhage	condition 1 – condition 2	Rt. handed

M, male; F, female; Rt., right; Lt. left; BG, basal ganglia; CR, corona radiata; TH, thalamus.

intervention for personal reasons, thus, 16 patients (7 males and 9 females, mean age 56.8 ± 13.0 years) completed the study protocol. The inclusion criteria were unilateral hemiparetic stroke (both ischemic and hemorrhagic), age between 19 and 80 years, chronic stroke symptoms for more than 6 months, lesions including BG, and the ability to move individual fingers. The exclusion criteria were a history of psychiatric disease, significant neurological disease other than stroke, metal implants, and contraindications to tDCS application (Russo et al., 2017). Written informed consent was provided by all patients before participation. The patient demographics are described in Table 1, and the lesion map is presented in Supplementary Figure 1. The lesions were manually drawn on T1-weighted structural MRI with lesion mapping software (MRIcro Software).[1] The lesions were normalized to the standard Montreal Neurological Institute (MNI) space and overlaid on a template of the MNI space. For patients with lesions on the right side, the lesions were flipped to the left side to better visualize the distribution. The experimental procedures were approved by the Ethics Committee of Samsung Medical Center. This study was registered at ClinicalTrials.gov (NCT04903457).

2.2. Study design

Using a sham-controlled, double-blind, crossover study design, all participants completed 10 days of HD-tDCS intervention. Before the intervention, all participants underwent MRI to examine lesion location and volume. At the same visit, fNIRS measurements were conducted during 15 min of the sequential finger tapping task (SFTT) to assess the initial motor learning capacity of each participant. Referring to the experimental protocols of previous tDCS cross-over studies (Gálvez et al., 2013; Hamoudi et al., 2018), each participant underwent treatment with 2 HD-tDCS conditions for 5 consecutive days (days 1 to 5), separated by a 4-week washout period, in random order of intervention: (a) condition 1: 20 min of real HD-tDCS stimulation (real HD-tDCS) over the affected motor area and (b) condition 2: sham stimulation that applied the current used in the actual stimulation only during the 30-s ramp-up and-down periods (sham HD-tDCS). If a patient was first allocated to condition 1, that patient underwent the condition 2 process after the 4-week washout window period. The order of these treatments was randomly allocated. To measure hemodynamic changes during a motor learning task, fNIRS was conducted during a 15-min of SFTT after HD-tDCS application on every intervention day. In addition, to examine motor performance, each participant's accuracy and response time during the SFTT were measured along with fNIRS measurements. The study design is illustrated in Figure 1A.

2.3. High-definition tDCS

A battery-driven Starstim 8 tDCS system (Neuroelectrics®, Barcelona, Spain) was used in a 4 × 1 ring configuration of HD electrodes (surface: 3.14 cm^2; current density, anode, 0.32 mA/cm^2; each cathode, ~0.08 mA/cm^2) to deliver a constant direct current to the affected hemisphere. The anode, which was the center electrode of the 4 × 1 ring montage of HD electrodes, was placed on the scalp overlying C3 or C4 (based on the 10–20 system) to cover the ipsilesional motor cortical area. The four cathodes surrounded the anode at a center-to-center distance of 3.5 cm. Thus, when a participant's lesion was on the right side, the anode was placed on C4,

1 http://www.cabiatl.com/mricro/mricro/index.html

and the cathodes were placed on C2, C6, FC4, and CP4. When a participant's lesion was on the left side, the anode was placed on C3, and the cathodes were placed on C1, C5, FC3, and CP3. A constant current of 1 mA was delivered for 20 min, with 30-s ramp-up and-down phases. In the sham procedure, stimulation was applied to the same area in the same electrode montage, but real stimulation was provided only during the ramp-up and-down periods to provide the same skin tingling sensation (Martïnez-Përez et al., 2020). First, a period of "ramping up" is administered, in which the stimulation reaches the maximum programmed current (e.g., 30 s to reach 1 mA). Ramping up is then followed by a short stimulatory period, in which the participant receives stimulation for a few seconds. Finally, "ramping down" involves the current gradually being switched off (Thair et al., 2017). HD-tDCS application is illustrated in Figure 1B.

2.4. Measurement of changes in hemodynamic response during the sequential finger tapping task

Changes in hemodynamic responses during the SFTT with the affected hand were measured in each patient on every intervention day. Using an fNIRS measurement system (NIRScout®; NIRx Medical Technologies, Berlin, Germany) on a multi-modal-compatible fNIRS platform, the hemodynamic response signals were obtained as optical changes collected in a continuous wave. The fNIRS system used two wavelengths, 760 and 850 nm, with a sampling rate of 10.25 Hz. With 20 sources and detectors, the fNIRS topomap consisted of 67 channels, with 3 cm between each source and detector. The fNIRS topomap was designed to cover nearly the whole brain area, including the frontal, motor, parietal, temporal, and occipital cortices (Figure 1C). During fNIRS measurements, all patients performed the SFTT with the affected hand. NIRStar 15.2 software (NIRx Medical Technologies) was used for signal acquisition, recording the raw fNIRS data, and obtaining signal quality indicators for measurement channels following hardware calibration. Channels with poor signal quality were identified using the following criteria and excluded from further analysis. First, channels with gain larger than 7, showing inadequate light detection, were rejected. The gain is calculated by the NIRx device during a calibration procedure performed prior to each experiment. In the NIRx system, gain values less than 7 are defined as optical signals within the range of 0.09–1.4 V and at noise levels less than 2.5% (Shoushtarian et al., 2020). If the acquired signal quality was poor during calibration, the contact between the scalp and analogous optodes was adjusted until the overall signal quality was acceptable.

An SFTT protocol programmed using SuperLabPro® 2.0 software (Cedrus, Co., Phoenix, AZ, United States) was used with all participants (Figure 1C). During the SFTT with fNIRS measurement, each patient

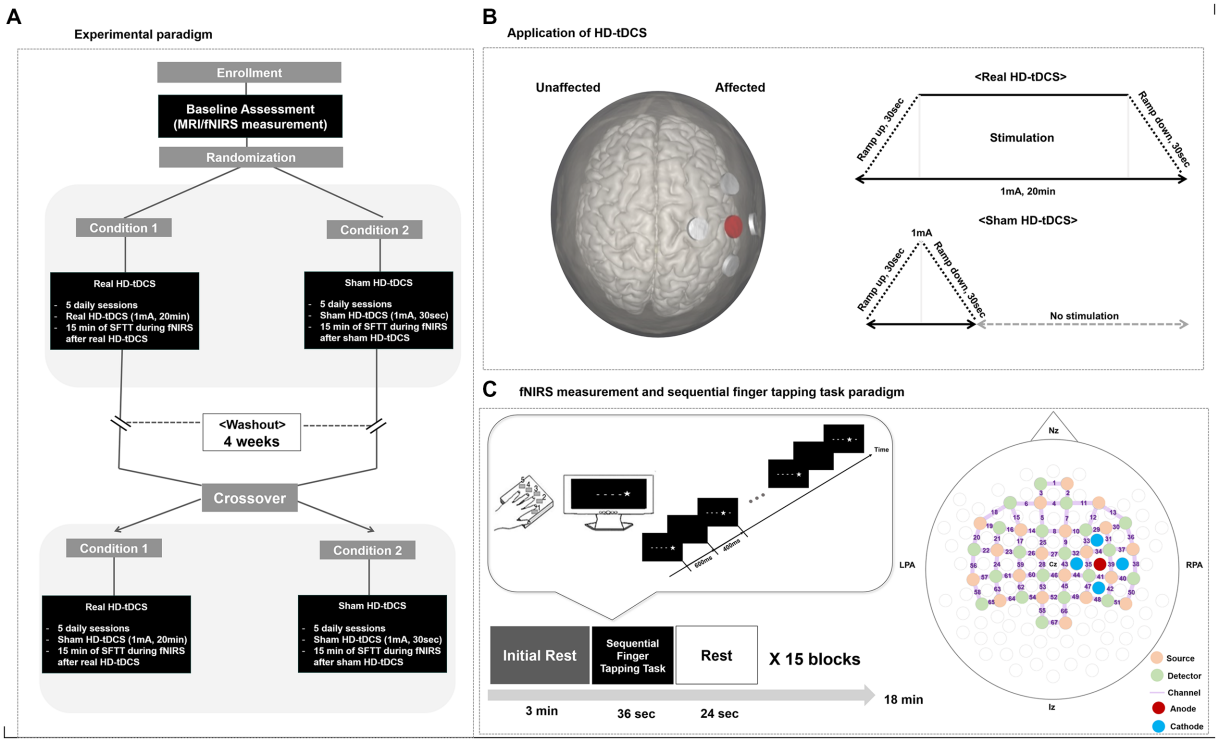

FIGURE 1
Study design. **(A)** Experimental paradigm. **(B)** Application of HD-tDCS. When a participant's lesion was on the right side, the anode was placed on C4, and the cathodes were placed on C2, C6, FC4, and CP3. When a participant's lesion was on the left side, the anode was placed on C3, and the cathodes were placed on C1, C5, FC3, and CP5. In the real HD-tDCS condition, a constant current was delivered at 1mA for 20min, with ramp-up and-down phases of 30s. In the sham HD-tDCS condition, current was ramped up from 0 to 1mA during the first 30s, then ramp-down to 0mA during the next 30s, and remain at 0mA for the next 20min. **(C)** fNIRS measurement during the SFTT and the fNIRS topomap. A star appeared on the black screen for 600ms, and then an empty black screen appeared for 400ms after the star disappeared. HD-tDCS, high-definition transcranial direct current stimulation; fNIRS, functional near-infrared spectroscopy; SFTT, sequential finger tapping task; Nz, nasion; Iz, inion; LPA, left pre-auricular; RPA, right pre-auricular.

was seated 50 cm from a computer monitor, and the affected hand performing the task was held in a supported position. As a visual cue on the monitor, a star appeared at any one of five positions arranged in a horizontal line on the computer screen in front of the participant. The participant was instructed to use their affected fingers to press the button on a customized keyboard that corresponded to the stimulus presented on the screen as quickly and accurately as possible (thumb = 1, index finger = 2, middle finger = 3, ring finger = 4, little finger = 5). The star appeared for 600 ms, after which the screen went blank for 400 ms. Each sequence was composed of 9 digits, and the task block included 15 repetitions of that sequence. Information about the sequence order was not provided to the participant for this implicit motor learning task. Three pre-determined sequences with the same difficulty were randomly assigned to the baseline, real HD-tDCS, and sham HD-tDCS conditions.

2.5. Measurement of motor performance during the sequential finger tapping task

Accuracy and response time during the SFTT were used to measure changes in motor performance of the affected hand at every intervention session. To measure SFTT performance, each patient's mean response time and number of correct responses (accuracy) (Kim et al., 2006) were calculated with SuperLabPro® software. The response time was defined as the mean time required for the patient to press the correct key after appearance of the stimulus on the screen. The accuracy and response time were measured for 36 stimuli within each trial, with 15 trial blocks for each task. Also, we calculated the skill index (SI). Usually, when speed increases, accuracy decreases, and vice versa. The SI is used to compensate for the trade-off between speed and accuracy (Cuypers et al., 2013). In other words, the SI considers both the accuracy and response time parameters during the task and was calculated using the following formula.

$$\mathrm{SI} = \frac{\text{Percentage of correct responses}\,(\%)}{\text{Mean response time per block}\,(\text{msec})}$$

2.6. fNIRS data analysis

The fNIRS data for patients with a left-side lesion were flipped to the fNIRS channels on the opposite side, so that the lesion location for all subjects could be analyzed on the same side. The cortical activation map produced during the SFTT with the affected hand was analyzed using statistical parametric mapping (SPM) analysis with the Near-Infrared Spectroscopy-Statistical Parametric Mapping open-source software package (NIRS-SPM)[2] (Tak et al., 2008) implemented in MATLAB® (MathWorks, Inc., Natick, MA, United States). To test for significant changes in oxyHb concentration during task blocks compared with rest blocks, a general linear model was used with a canonical hemodynamic response curve (Ye et al., 2009). Then, the statistical contrast in reference to the base signal was tested, and cortical activity was presented as the *t*-value during experiment. In group analysis of all subjects, statistical analysis was performed based on the individual-level beta values to determine the activated channels. Then, the *t*-statistic maps computed for group analysis were plotted onto a conventional brain template aligned to the affected hemisphere, and regions with significant differences in oxyHb concentration were identified ($p < 0.05$, uncorrected) (Benjamini and Hochberg, 1995). Individual-level *t*-values for all 67 channels were extracted to statistically analyze the *t*-value for each channel. Then, the *t*-values of each channel were presented as individual regions of interest (ROIs) that were selected by fNIRS optode location decider (fOLD) channels (Zimeo Morais et al., 2018) in MATLAB®.

The analysis of functional connectivity between the bilateral M1 and other cortical regions using fNIRS data was performed using *OptoNet* II® software (25 March 2021),[3] which is a MATLAB-based application for functional cortical connectivity analysis of fNIRS signals (Lee et al., 2019; Lee G. et al., 2020). The functional connectivity between the bilateral M1 and other cortical regions was estimated by analyzing the phase-locking value (PLV) in *OptoNet* II®. The PLV can indicate synchrony between two recording sites in a precise frequency range and uses responses to repeated stimuli to search for latencies at which the phase difference between signals varies minimally across trials (phase-locking) (Lachaux et al., 1999). The intertrial variability of this phase difference was measured using the PLV; if the phase difference varied minimally across trials, the PLV was close to 1; otherwise, it was close to zero (Lachaux et al., 1999). After extracting the PLV from each of the 15 task blocks in each SFTT trial for each individual, the PLVs for each block were averaged. Because fNIRS channels for analyzing functional connectivity for cortical regions were determined by the fOLD channels (Zimeo Morais et al., 2018), they included the channels used to analyze *t*-values in SPM analysis as follows: medial pre-frontal (MPF), Ch. 1, 2, 3, 4; ipsilesional frontal area ($\mathrm{Fr_{Ipsi}}$), Ch. 10, 11, 12, 13, 29, 30; contralesional frontal area ($\mathrm{Fr_{Contra}}$), Ch. 6, 14, 15, 16, 18, 19; ipsilesional M1 ($\mathrm{M1_{Ipsi}}$), Ch. 34, 35, 39; contralesional M1 ($\mathrm{M1_{Contra}}$), Ch. 23, 24, 59; SMA, Ch. 9, 25, 27; ipsilesional PM ($\mathrm{PM_{Ipsi}}$), Ch. 31, 32, 33; contralesional PM ($\mathrm{PM_{Contra}}$), Ch. 17, 21, 26; ipsilesional sensory cortex ($\mathrm{Sn_{Ipsi}}$), Ch. 40, 41, 44; contralesional sensory cortex ($\mathrm{Sn_{Contra}}$), Ch. 57, 60, 61; ipsilesional parietal lobe ($\mathrm{Pr_{Ipsi}}$), Ch. 48, 49; contralesional parietal lobe ($\mathrm{Pr_{Contra}}$), Ch. 54, 64; ipsilesional temporal lobe ($\mathrm{Tm_{Ipsi}}$), Ch. 36, 38; contralesional temporal lobe ($\mathrm{Tm_{Contra}}$), Ch. 20, 56; and occipital lobe (Occ), Ch. 55, 66. The fNIRS signals were processed with normalization for each epoch to prevent signal distortion caused by differences between functional region groups in the number of fNIRS channels. The PLVs between the bilateral M1 and other ROIs were extracted to compare changes in functional connectivity at every measurement.

2.7. Statistical analysis

The data were analyzed using SPSS version 20 (SPSS, Inc., Chicago, IL, United States). To evaluate the normality of the distribution, the data were examined using the Kolmogorov–Smirnov test. The statistical

2 http://bisp.kaist.ac.kr/NIRS-SPM

3 https://sites.google.com/site/dsucore/free/optonet

significance of changes in the *t*-values of channels 35 and 59 and the PLVs from the fNIRS measurements was determined through three stages of analysis. First, repeated measures analysis of variance (RM-ANOVA) was used to confirm the interaction between conditions (real HD-tDCS and sham HD-tDCS) and changes in the *t*-values and PLVs of the fNIRS measurement on the five intervention days. Second, the Friedman test was used to examine the effects of days within each condition at each measurement because the *t*-values and PLVs were found to have non-parametric distributions. Third, the *t*-values and PLVs obtained for each intervention were compared with the baseline values and evaluated using the Wilcoxon signed-rank test. For statistical analysis of the SFTT variables, three stages of analysis were performed. First, RM-ANOVA was used to test the interaction between conditions and blocks of the SFTT for each measurement. Second, the Friedman test or RM-ANOVA, depending on the normality distribution of data, was used to assess the effects of the blocks within each condition on each intervention day. Third, SFTT variables in each block were compared with the first block on every measurement day using the Wilcoxon signed rank test. For all analyses, the level of significance was set at $p = 0.05$.

3. Results

3.1. Cortical activity analysis during the sequential finger tapping task using NIRS-SPM

Figure 2A shows changes in the average cortical activation in terms of oxyHb during the SFTT with the affected hand from baseline to day 5 in each condition, as illustrated by the NIRS-SPM analysis. On day 5 in the real HD-tDCS condition, the oxyHb concentration during SFTT with the affected hand increased primarily around the ipsilesional motor cortices. The changes in *t*-values for channel 35 and 59, which represent the ipsilesional and contralesional M1, respectively, are illustrated in Figure 2B. The *t*-value changes for those channels show no day × condition interaction. As the intervention progressed, the *t*-value of channel 35 increased from baseline to day 5 with statistical significance (Friedman test, $X^2 = 16.828$, df = 5, $p = 0.005$) in the real HD-tDCS condition. In the sham HD-tDCS condition, the *t*-value of channel 35 tended to increase as the intervention progressed, but the difference was not statistically significant. On days 4 and 5 in the real HD-tDCS condition, the increase in the *t*-value of channel 35 attained statistical significance compared to baseline (Wilcoxon signed-rank test, day 4, $p = 0.034$; day 5, $p = 0.020$). The *t*-value of channel 59 tended to decrease from baseline to day 5 without statistical significance in both the real HD-tDCS and sham HD-tDCS conditions. A significant decrease in channel 59 occurred on day 5 and day 3 in the real HD-tDCS and sham HD-tDCS conditions, respectively (Wilcoxon signed rank test, real HD-tDCS, $p = 0.026$; sham HD-tDCS, $p = 0.008$). The changes in the *t*-values of the ROI channels are presented in Table 2.

3.2. Functional connectivity analysis during sequential finger tapping task

Figure 3 shows changes in mean PLV between $M1_{Ipsi}$ and the other ROIs during SFTT with the affected hand between baseline and the fifth day in each condition. The values above each ROI indicate the PLV between $M1_{Ipsi}$ and each ROI in Figure 3. The changes in PLV at each ROI showed no day × condition interaction for any ROI. At baseline, the PLV between $M1_{Ipsi}$ and Sn_{Ipsi} indicated a relatively strong connection compared with connections between $M1_{Ipsi}$ and the other ROIs. From days 1 to 5, as the intervention progressed, the PLV between $M1_{Ipsi}$ and PM_{Ipsi} showed a tendency to increase compared with baseline in the real HD-tDCS condition, but the difference was not statistically significant. The PLV between $M1_{Ipsi}$ and Sn_{Ipsi} tended to increase as the days progressed in the real HD-tDCS condition but without statistical significance. The PLV between $M1_{Ipsi}$ and PM_{Ipsi} increased from a baseline value of 0.70 ± 0.24 to 0.88 ± 0.08 (mean ± standard deviation) on day 3, which was a statistically significant change (Wilcoxon signed rank test, $p = 0.007$). On day 5, the PLV difference between $M1_{Ipsi}$ and PM_{Ipsi} increased with statistical significance from baseline to 0.88 ± 0.08 (Wilcoxon signed-rank test, $p = 0.017$). The PLV between $M1_{Ipsi}$ and Sn_{Ipsi} did not increase significantly in the real HD-tDCS condition compared with baseline on any day. In the sham HD-tDCS condition, the PLV between $M1_{Ipsi}$ and other ROIs maintained a level similar to that at baseline. On day 5, relatively strong connections were shown between $M1_{Ipsi}$ and Sn_{Contra} compared with baseline, but this was not statistically significant.

Changes in PLV at each ROI showed a day × condition interaction between $M1_{Contra}$ and Fr_{Ipsi} was statistically significant (RM-ANOVA, $F = 3.155$, $p = 0.015$). The PLV between $M1_{Contra}$ and Fr_{Contra} tended to decrease from baseline to day 5 in the real HD-tDCS condition. On the other hand, the PLV between $M1_{Contra}$ and Fr_{Contra} increased significantly from baseline to day 5 in the sham HD-tDCS condition (Wilcoxon signed rank test, $p = 0.039$). The PLV between $M1_{Contra}$ and Fr_{Ipsi} also tended to decrease without statistical significance from baseline to day 5 in the real HD-tDCS condition. However, the PLV between $M1_{Contra}$ and Fr_{Ipsi} showed a tendency to increase in the sham HD-tDCS condition. The PLV between $M1_{Contra}$ and Fr_{Ipsi} increased with significance on day 5 (Wilcoxon signed rank test, $p = 0.020$) in the sham HD-tDCS condition, and in the same condition, the PLV between $M1_{Contra}$ and Sn_{Contra} increased significantly compared with baseline on days 3, 4, and 5 (Wilcoxon signed rank test, day 3, $p = 0.011$; day 4, $p = 0.034$; day 5, $p = 0.023$). Changes in the mean PLV between $M1_{Contra}$ and the other ROIs during SFTT with the affected hand from baseline to the fifth day in each condition are presented in Supplementary Figure 2.

3.3. Statistical analysis during the sequential finger tapping task

Figure 4 shows changes in accuracy and response time during every block from baseline to day 5 in each condition. RM-ANOVA failed to demonstrate a block × condition interaction in the accuracy changes on each day. At baseline, the accuracy of the SFTT increased with statistical significance from blocks 1 to 15 (RM-ANOVA, $F = 2.507$, $p = 0.038$) (Figure 4A). In the real HD-tDCS condition, the accuracy improved significantly by block on day 2 (Friedman test, $X^2 = 29.766$, df = 14, $p = 0.008$) and day 5 (Friedman test, $X^2 = 29.239$, df = 14, $p = 0.010$) (Figure 4A). In the sham HD-tDCS condition, the accuracy tended to increase on all days; it changed significantly on block days 1, 2, and 4 (Friedman test, day 1: $X^2 = 29.143$, df = 14, $p = 0.010$; day 2: $X^2 = 24.789$, df = 14, $p = 0.037$; day 4: $\S^2 = 23.796$, df = 14, $p = 0.048$) (Figure 4A). No significant differences in response time were found to have a block × condition interaction on any day. The response time in

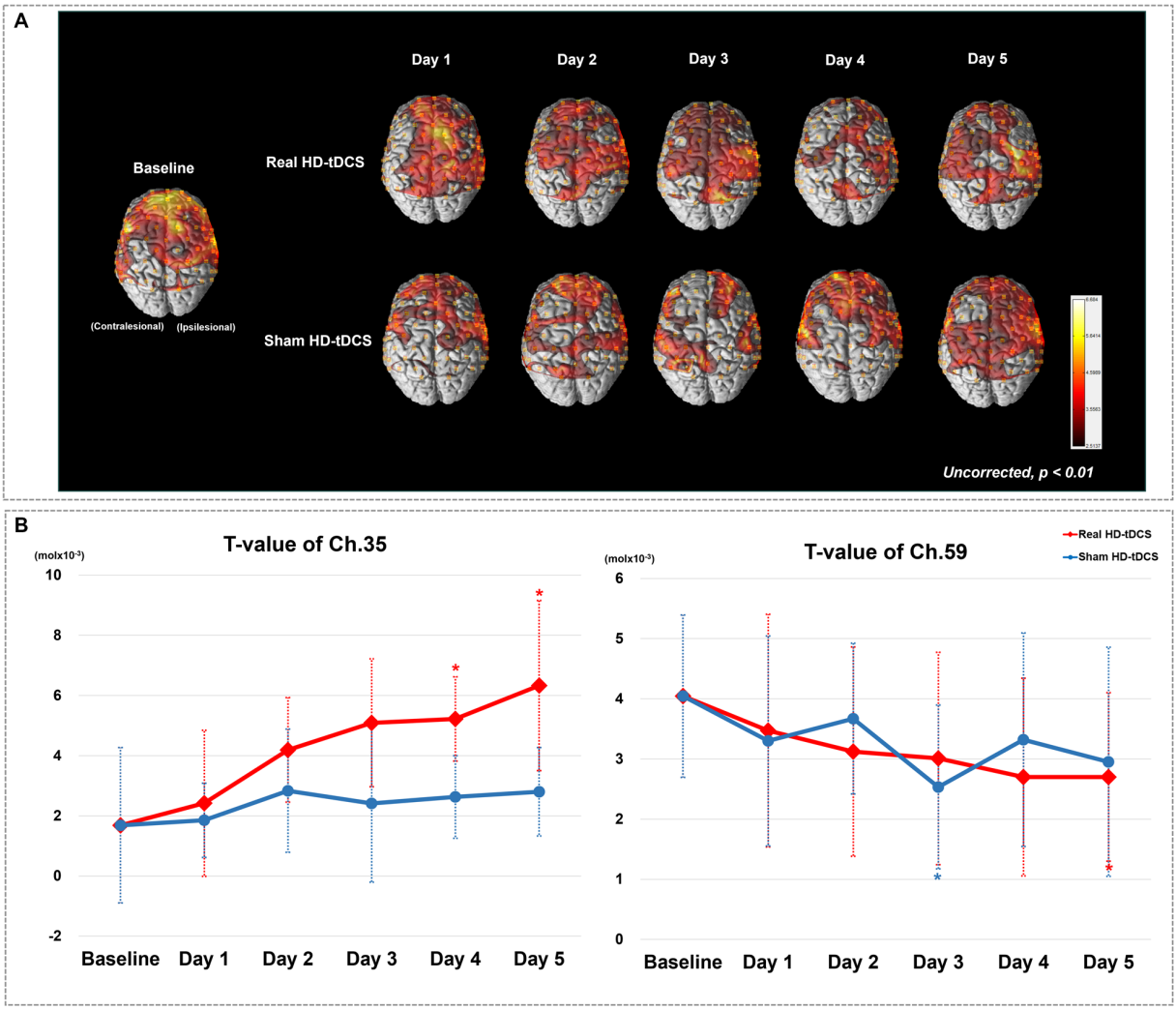

FIGURE 2
(A) Average cortical activation maps during the SFTT with the affected hand. SFTT, sequential finger tapping task. **(B)** *T*-value changes in the ipsilesional (channel 35) and contralesional (channel 59) M1 from baseline to day 5. Red and blue asterisks indicate statistical significance between baseline and each measurement day in the real HD-tDCS and sham HD-tDCS conditions, respectively (Wilcoxon signed rank test, $p<0.05$).

the SFTT tended to decrease from blocks 1 to 15 without statistical significance at baseline (Figure 4B). In the real HD-tDCS condition, the response time differed significantly by block on day 3 (Friedman test, $X^2 = 34.517$, df = 14, $p = 0.002$), day 4 (Friedman test, $X^2 = 43.270$, df = 14, $p < 0.001$), and day 5 (Friedman test, $X^2 = 27.757$, df = 14, $p = 0.015$). In the sham HD-tDCS condition, no statistically significant differences were observed between blocks on any day.

The SI did not show statistically significant block × condition interactions on any day. At baseline, the SI increased significantly by block (Friedman test, $X^2 = 31.033$, df = 14, $p = 0.005$). In the real HD-tDCS condition, the SI changed significantly by block on all days (Friedman test, day 1: $X^2 = 39.487$, df = 14, $p < 0.001$; day 2: $X^2 = 47.534$, df = 14, $p < 0.001$; day3: $X^2 = 45.585$, df = 14, $p < 0.001$; day 4: $X^2 = 33.365$, df = 14, $p = 0.003$; day 5: $X^2 = 40.163$, df = 14, $p < 0.001$). In the sham HD-tDCS condition, the SI changed significantly by block on day 1 (Friedman test, $X^2 = 35.677$, df = 14, $p = 0.001$) and day 3 (RM-ANOVA, $F = 3.009$, $p = 0.020$). The SI changes in every block from baseline to day 5 for each condition are described in Supplementary Figure 3.

4. Discussion

In this study, we investigated changes in cortical activation and functional connectivity during the SFTT after stroke treatment with HD-tDCS on the motor cortical area. We also examined changes in motor performance as reflected by the SFTT. Our main findings are that the HD-tDCS intervention could promote cortical activation of the ipsilesional motor area during SFTT with the affected hand. Furthermore, in the cortical network, the HD-tDCS intervention enhanced functional connectivity between $M1_{Ipsi}$ and PM_{Ipsi}. Without the application of HD-tDCS, functional connectivity between $M1_{Contra}$ and Sn_{Contra} was promoted during motor learning after stroke. Also, the hemodynamic changes caused by the real HD-tDCS intervention were accompanied by improvement in motor performance and upper extremity function in chronic stroke patients compared with the sham HD-tDCS.

In normal motor learning, increases in cortical activation of the contralateral motor area during the early stage of motor learning and

TABLE 2 Changes in *t*-values on cortical activation mapping through statistical parametric mapping at each intervention session.

			Real HD-tDCS					Sham HD-tDCS				
Region of interest	Channel	Baseline	Day 1	Day 2	Day 3	Day 4	Day 5	Day 1	Day 2	Day 3	Day 4	Day 5
MPF	Ch. 4	3.121 (3.959)	3.126 (5.304)	3.158 (4.484)	**2.699*(4.029)**	2.004 (4.195)	**1.672*(3.594)**	2.719 (2.601)	2.641 (3.831)	2.643 (3.646)	**2.145*(3.799)**	**2.546*(3.813)**
Fr_{Ipsi}	Ch. 12	2.581 (2.532)	**1.357*(2.326)**	1.945 (2.447)	2.148 (3.429)	**1.961*(2.553)**	1.704 (2.658)	2.233 (2.396)	2.234 (3.910)	3.073 (1.751)	1.634 (2.919)	3.165 (2.630)
Fr_{Contra}	Ch. 15	3.041 (3.517)	**1.671*(1.773)**	1.447 (2.532)	2.903 (4.609)	2.098 (2.945)	**0.672*(1.985)**	**1.876*(3.425)**	**2.499*(2.257)**	2.893 (3.827)	2.504 (1.419)	1.841 (2.849)
$M1_{Ipsi}$	Ch. 35	2.512 (3.915)	2.354 (4.407)	2.882 (4.678)	3.662 (2.990)	**4.841*(4.092)**	**7.223*(5.944)**	1.163 (2.191)	1.850 (6.350)	2.315 (1.629)	1.656 (2.489)	1.886 (4.358)
$M1_{Contra}$	Ch. 59	3.535 (3.527)	2.358 (5.889)	2.863 (2.279)	2.637 (4.802)	2.417 (3.296)	**1.692*(3.320)**	2.053 (3.534)	2.978 (4.052)	**2.004**(2.791)**	3.567 (4.156)	3.075 (5.753)
SMA	Ch. 27	2.321 (2.181)	**2.461*(3.226)**	1.697 (3.093)	3.248 (4.146)	0.530 (3.948)	1.493 (5.023)	0.975 (3.441)	1.647 (2.601)	−0.469 (4.862)	2.062 (4.559)	1.328 (4.650)
PM_{Ipsi}	Ch. 32	1.543 (3.345)	3.131 (3.172)	2.361 (3.465)	3.375 (4.067)	2.911 (2.586)	2.813 (2.352)	1.804 (2.167)	1.461 (4.142)	2.166 (2.633)	1.092 (3.440)	0.915 (5.183)
PM_{Contra}	Ch. 26	4.062 (3.566)	4.232 (4.801)	3.396 (3.223)	3.208 (5.522)	3.569 (4.354)	3.020 (3.563)	**2.021*(3.062)**	3.400 (4.046)	2.258 (2.796)	3.130 (3.479)	2.882 (6.079)
Sn_{Ipsi}	Ch. 44	3.166 (3.354)	2.602 (4.356)	2.273 (6.092)	2.877 (3.850)	0.713 (3.432)	1.785 (4.842)	0.597 (2.484)	1.470 (2.347)	1.190 (1.996)	1.196 (2.701)	1.354 (3.683)
Sn_{Contra}	Ch. 60	4.011 (3.488)	3.329 (5.164)	3.822 (3.172)	1.816 (5.338)	**1.601*(3.423)**	3.480 (3.407)	**1.794*(2.608)**	1.959 (4.117)	**2.510*(2.160)**	**2.587*(3.712)**	**3.083*(3.856)**
Pr_{Ipsi}	Ch. 49	2.204 (3.050)	1.902 (5.931)	3.084 (2.755)	0.842 (3.336)	1.485 (3.021)	3.485 (3.466)	1.714 (2.185)	1.522 (2.746)	3.091 (4.339)	0.525 (2.980)	2.262 (4.712)
Pr_{Contra}	Ch. 54	1.135 (2.386)	1.638 (4.267)	3.044 (4.554)	2.694 (4.367)	2.063 (4.323)	2.736 (2.608)	1.276 (2.930)	1.974 (4.650)	2.162 (3.349)	0.616 (6.269)	1.785 (4.218)
Tm_{Ipsi}	Ch. 36	2.430 (3.173)	0.589 (1.841)	1.724 (2.782)	0.427 (3.520)	1.650 (2.667)	2.405 (2.469)	0.719 (1.802)	1.475 (4.526)	1.479 (2.969)	1.667 (2.624)	1.824 (1.521)
Tm_{Contra}	Ch. 20	3.871 (3.695)	**2.461*(2.796)**	2.123 (4.231)	**1.183*(3.624)**	**0.976*(4.095)**	**1.053*(5.082)**	**1.608*(2.968)**	2.898 (3.806)	**1.473*(1.427)**	**0.814*(2.141)**	1.254 (2.935)
Occ	Ch. 66	1.975 (3.730)	2.590 (5.932)	2.424 (5.399)	1.699 (2.466)	1.995 (2.398)	2.951 (3.189)	1.592 (3.006)	2.068 (3.271)	2.732 (5.168)	1.580 (3.086)	1.646 (5.631)

All data are expressed as median (interquartile range). MPF, medial prefrontal cortex; Fr_{Ipsi}, ipsilesional frontal area; Fr_{Contra}, contralesional frontal area; $M1_{Ipsi}$, ipsilesional primary motor cortex; $M1_{Contra}$, contralesional primary motor cortex; SMA, supplementary motor area; PM_{Ipsi}, ipsilesional premotor cortex; PM_{Contra}, contralesional premotor cortex; Sn_{Ipsi}, ipsilesional sensory cortex; Sn_{Contra}, contralesional sensory cortex; Pr_{Ipsi}, ipsilesional parietal cortex; Pr_{Contra}, contralesional parietal cortex; Tm_{Ipsi}, ipsilesional temporal lobe; Tm_{Contra}, contralesional temporal lobe; Occ, occipital lobe. *Significant change compared with baseline (Wilcoxon-signed rank test, $p < 0.05$). Bold values mean significant change compared with baseline.

10.3389/fnins.2023.1189420

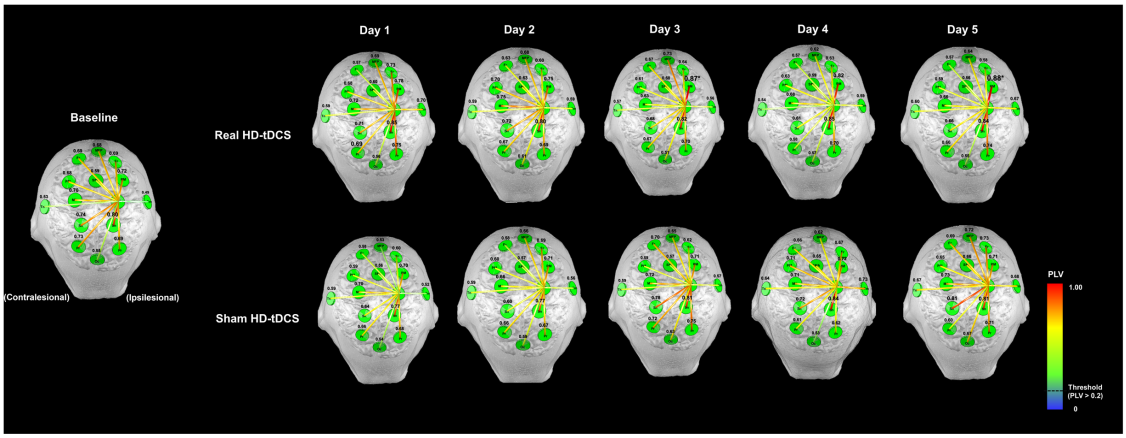

FIGURE 3
Changes in functional connectivity between the ipsilesional M1 and other ROIs during the SFTT with the affected hand. The letters in green circles indicate the names of the ROIs, and the colored lines represent functional connectivity between the ipsilesional M1 and each ROI. The numbers above each green circle are the mean PLV between the ipsilesional M1 and that ROI. The functional connectivity line is represented by a warmer color if the PLV was close to 1 and a cooler color if the PLV was close to 0, and only the high-value lines (threshold >0.2) are represented. The PLV between the ipsilesional M1 and PM increased on days 3 and 5 compared with baseline in the real HD-tDCS condition (Wilcoxon signed rank test, $p< 0.05$). MPF, medial prefrontal cortex; Fr, frontal area; M1, primary motor cortex; SMA, supplementary motor area; PM, premotor cortex; Sn, sensory cortex; Pr, parietal cortex; Tm, temporal lobe; Occ; occipital lobe.

improvements in response time, rather than in accuracy, are thought to indicate successful motor learning (Park et al., 2010; Krakauer et al., 2019). This study found increases in cortical activity in the ipsilesional motor area during SFTT with the affected hand after the real HD-tDCS intervention, which was accompanied by significant improvement in SFTT response time. The *t*-values for oxyHb in the channels representing the $M1_{Ipsi}$ during SFTT with the affected hand increased significantly by day in the real HD-tDCS condition. After the sham HD-tDCS intervention, SFTT performance did not reach the same level as with the real HD-tDCS intervention. In the normal process of motor learning, recruitment of M1 plays a key role through use-dependent mechanisms (Hardwick et al., 2013). Therefore, modulating M1 by enhancing cortical activation in stroke patients has been suggested as a strategy for improving motor learning after stroke (Lefebvre et al., 2013; Kang et al., 2016). With the focal montage provided by the 4×1 configuration, HD-tDCS was shown to effectively improve motor skill learning in healthy subjects (Iannone et al., 2022). Also, application of HD-tDCS to the motor area has been shown to increase task-related cortical activation of the motor area (Muthalib et al., 2014; Besson et al., 2019). Our results of enhanced cortical activation after HD-tDCS application to ipsilesional M1 with motor learning training differ from those of a previous study. Prior results showed decreased cortical activation with HD-tDCS and a simple motor task in chronic stroke patients (Kim et al., 2022). This difference could be due to the motor task paradigm. First, the duration of the motor task at 1 of our sessions was longer than that of Kim et al. (2022). Second, our motor task paradigm contains repetitions of a sequence, unlike the simple motor task of the previous study. Multiple sessions of a sequence-specific motor learning task enhance response to repetition of experience-driven changes of M1, unlike a simple motor task (Karni et al., 1998). It is conceivable that the motor task paradigm plays a critical role in the effectiveness of HD-tDCS on task-related cortical activation in chronic stroke patients. Our cortical activation results imply that HD-tDCS could augment motor performance, especially in terms of response time, by increasing cortical activation of the motor area after stroke. In other words, they suggest that HD-tDCS could alter cortical activation and motor learning patterns after stroke to better reflect the normal pattern of early-stage motor learning.

The motor cortical areas M1, PM, and SMA act as a hub for forming networks with other cortical or subcortical regions engaged in motor learning (Dahms et al., 2020). In the real HD-tDCS condition, the intensity of connection between $M1_{Ipsi}$ and PM_{Ipsi} increased and was accompanied by a decrease in connection with $M1_{Contra}$ and the frontal areas. With those hemodynamic changes, response time during the SFTT improved significantly. When reproducing motor sequences with precise timing, the PM plays a crucial role in temporal organization of movements by producing a rhythmic pattern of motor sequences and sending a projection to M1 to produce motor sequence outputs with optimal timing (Halsband et al., 1993). Previous findings demonstrated that performance of automatic sequential finger movements involved greater activity of the PM to compensate for reduced connections between the PM and M1 that result from degenerative changes in the brain (Wu and Hallett, 2005). After stroke, contributions of the PM that support the role of M1 represent a tract-specific structure–function relationship for improving motor performance (Schulz et al., 2012). Participants in our study had lesions including the BG, which indicate impairment in generating significant output from learned sequences to the descending motor system. Thus, strengthened functional connectivity between $M1_{Ipsi}$ and PM_{Ipsi} after HD-tDCS indicate that PM_{Ipsi} plays an important role in supporting $M1_{Ipsi}$ in projecting the motor output of skilled movements by inducing timing-effective motor performance of a learned skill. We also found that functional connectivity between $M1_{Contra}$ and Sn_{Contra} was strengthened when stroke patients repeated the motor learning task without the HD-tDCS intervention. It is widely recognized that implicit sensorimotor recalibration serves to minimize motor execution errors during performance of implicit motor learning (Krakauer et al., 2019; Kim et al., 2021). In our

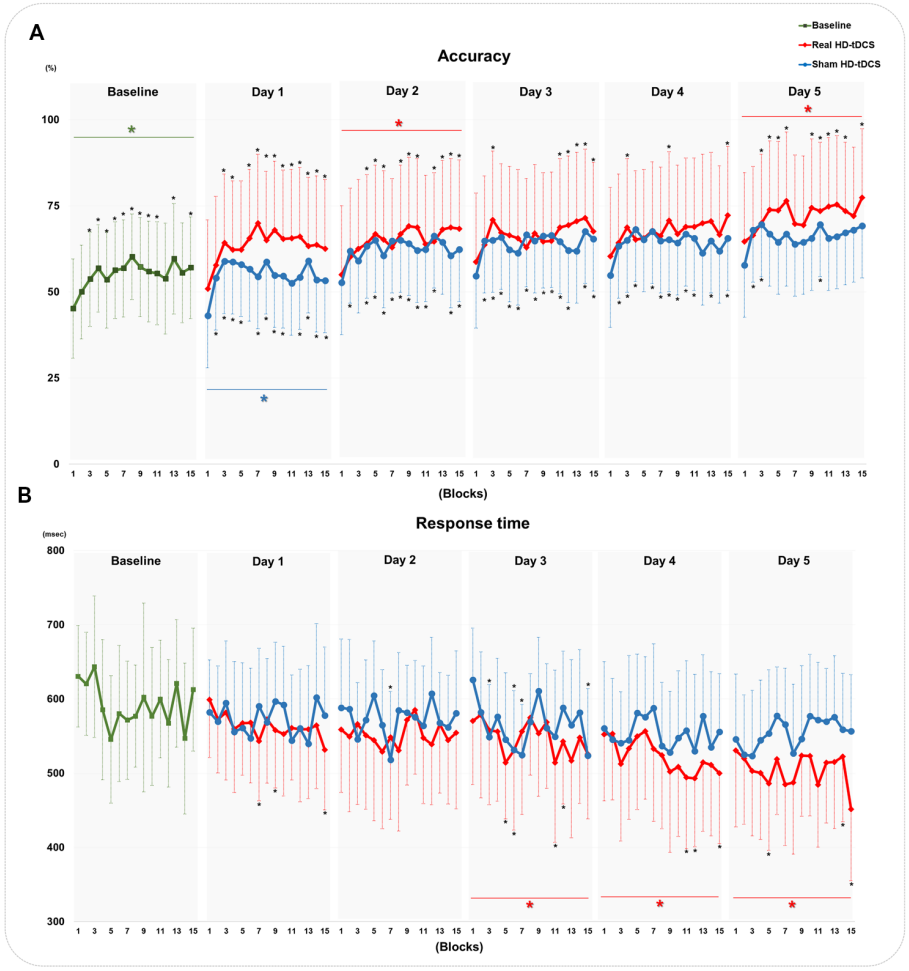

FIGURE 4
Changes in the accuracy and response time of the SFTT. **(A)** Changes in accuracy at baseline and in the real HD-tDCS and sham HD-tDCS conditions. **(B)** Changes in the response time at baseline and in the real HD-tDCS and sham HD-tDCS conditions. Green asterisks indicate statistical significance between block 1 and block 15 at baseline (Friedman test, $p<0.05$). Red asterisks indicate statistical significance between block 1 and block 15 in the real HD-tDCS condition on each day (Friedman test, $p<0.05$). Blue asterisks indicate statistical significance from block 1 to block 15 in the sham HD-tDCS condition on each day (Friedman test, $p<0.05$). Black asterisks indicate statistical significance between block 1 and each other block on each measurement day (Wilcoxon signed rank test, $*p<0.05$, $**p<0.01$). SFTT, sequential finger tapping task; HD-tDCS, high-definition transcranial direct current stimulation.

patients, we found an effort to recruit implicit sensorimotor adaptation and thereby reduce motor execution errors during an implicit motor learning task with the affected hand that took the form of a significant strong connection between $M1_{Contra}$ and Sn_{Contra}, but not between $M1_{Ipsi}$ and Sn_{Ipsi}. The enhanced functional connectivity between $M1_{Contra}$ and Sn_{Contra} might indicate that the sensory-motor network was strengthened in the contralesional hemisphere because of the interhemispheric imbalance after stroke (Berenguer-Rocha et al., 2020). These findings support imaging evidence from a previous study indicating that application of inhibitory brain stimulation over the contralesional sensory and motor cortex could enhance motor learning in post-stroke patients (Meehan et al., 2011). In previous findings (Mary et al., 2017), the lower resting-state connectivity between the sensorimotor cortex and other learning-related areas was related to a reduced need to perform error detection and correction in a healthy young subject. The results of the current study showed strengthened functional connectivity of $M1_{Ipsi}$ with PM_{Ipsi}, $M1_{Contra}$, and Sn_{Contra}, in chronic stroke patients with learning-related lesions. The differences in those findings imply that the strengthened functional connectivity in cortical levels induces motor learning by compensating for the role of learning-related lesions in chronic stroke patients, unlike the healthy population.

To the best of our knowledge, this is the first study to investigate the modulating effect of HD-tDCS on learning-related hemodynamic changes in chronic stroke patients with restricted subcortical lesions by analyzing changes in both cortical activation and functional connectivity at the whole brain level. Our findings provide evidence that HD-tDCS could improve motor performance during a motor learning task by increasing learning-related cortical activation in $M1_{Ipsi}$ and strengthening the learning-related connection between $M1_{Ipsi}$ and PM_{Ipsi}. Nonetheless, this study has several limitations. First, there is a potential lack of statistical power due to our small sample size; therefore, our results cannot be generalized to the entire stroke population. Second, lack of successive recordings during repeated

administrations over several weeks prevented analysis of HD-tDCS after-effects. Future research with a larger sample size in the stroke population and long-term sustainability are needed to identify the clinically relevant effects of HD-tDCS for motor learning in stroke patients. Third, we could not measure the hemodynamic changes that occurred during application of HD-tDCS. To investigate the direct mechanisms underlying HD-tDCS, future studies need to measure hemodynamic changes during HD-tDCS. Fourth, the stroke lesions of participants were diverse; most of patients had concomitant lesion of the corona radiata well as the BG. Therefore, it was not possible to interpret the results in relation only with BG lesion. To affirm the learning-related hemodynamic changes associated with specific lesions, future studies need to concentrate on stroke patients with homogenous lesions.

5. Conclusion

This study has demonstrated that HD-tDCS induced increases in cortical activation at $M1_{lpsi}$ and enhanced functional connectivity between $M1_{lpsi}$ and PM_{lpsi} in chronic stroke patients. Learning-related changes in cortical activation and functional connectivity caused by HD-tDCS correlated with improved motor performance, particularly motor learning task response time. The results of our study imply that HD-tDCS to $M1_{lpsi}$ could allow efficient hemodynamic changes in motor network areas that promote successful motor learning among stroke patients.

Data availability statement

The raw data supporting the conclusions of this article will be made available by the authors, without undue reservation.

Ethics statement

The studies involving human participants were reviewed and approved by the Samsung Medical Center. The patients/participants provided their written informed consent to participate in this study. Written informed consent was obtained from the individual(s) for the publication of any potentially identifiable images or data included in this article.

Author contributions

HK: conceptualization, methodology, formal analysis, investigation, writing—original draft, and visualization. GL: methodology and investigation. JL: conceptualization, methodology, investigation, interpretation, and writing—review and editing, supervision. Y-HK: conceptualization, resources, interpretation, writing—review and editing, supervision, project administration, and funding acquisition. All authors contributed to the article and approved the submitted version.

Funding

This study was supported by the Korea Medical Device Development Fund grant of the Korea Government (Ministry of Science and ICT; Ministry of Trade, Industry, and Energy; Ministry of Health and Welfare; Ministry of Food and Drug Safety) (KMDF-RS-2022-00140478) and the National Research Foundation of Korea (NRF) grant funded by the Korea Government (MSIT) (no. RS-2023-00208884).

Conflict of interest

The authors declare that the research was conducted in the absence of any commercial or financial relationships that could be construed as a potential conflict of interest.

Publisher's note

Supplementary material

The Supplementary material for this article can be found online at: https://www.frontiersin.org/articles/10.3389/fnins.2023.1189420/full#supplementary-material

References

Ammann, C., Spampinato, D., and Mārquez-Ruiz, J. (2016). Modulating motor learning through transcranial direct-current stimulation: an integrative view. *Front. Psychol.* 7:1981. doi: 10.3389/fpsyg.2016.01981

Anwer, S., Waris, A., Gilani, S. O., Iqbal, J., Shaikh, N., Pujari, A. N., et al. (2022). Rehabilitation of upper limb motor impairment in stroke: a narrative review on the prevalence, risk factors, and economic statistics of stroke and state of the art therapies. *Healthcare* 10:190. doi: 10.3390/healthcare10020190

Baldwin, M. L., and Butler, R. J. (2006). Upper extremity disorders in the workplace: costs and outcomes beyond the first return to work. *J. Occup. Rehabil.* 16, 296–316. doi: 10.1007/s10926-006-9043-2

Benjamini, Y., and Hochberg, Y. (1995). Controlling the false discovery rate: a practical and powerful approach to multiple testing. *J. R. Stat. Soc. B* 57, 289–300.

Berenguer-Rocha, M., Baltar, A., Rocha, S., Shirahige, L., Brito, R., and Monte-Silva, K. (2020). Interhemispheric asymmetry of the motor cortex excitability in stroke: relationship with sensory-motor impairment and injury chronicity. *Neurol. Sci.* 41, 2591–2598. doi: 10.1007/s10072-020-04350-4

Besson, P., Muthalib, M., Dray, G., Rothwell, J., and Perrey, S. (2019). Concurrent anodal transcranial direct-current stimulation and motor task to influence sensorimotor cortex activation. *Brain Res.* 1710, 181–187. doi: 10.1016/j.brainres.2019.01.003

Cuypers, K., Leenus, D. J., Van Den Berg, F. E., Nitsche, M. A., Thijs, H., Wenderoth, N., et al. (2013). Is motor learning mediated by tDCS intensity? *PLoS One* 8:e67344. doi: 10.1371/journal.pone.0067344

Dahms, C., Brodoehl, S., Witte, O. W., and Klingner, C. M. (2020). The importance of different learning stages for motor sequence learning after stroke. *Hum. Brain Mapp.* 41, 270–286. doi: 10.1002/hbm.24793

Datta, A., Bansal, V., Diaz, J., Patel, J., Reato, D., and Bikson, M. (2009). Gyri-precise head model of transcranial direct current stimulation: improved spatial focality using a

ring electrode versus conventional rectangular pad. *Brain Stimul.* 2, 201–207.e1. doi: 10.1016/j.brs.2009.03.005

Delorme, M., Vergotte, G., Perrey, S., Froger, J., and Laffont, I. (2019). Time course of sensorimotor cortex reorganization during upper extremity task accompanying motor recovery early after stroke: an fNIRS study. *Restor. Neurol. Neurosci.* 37, 207–218. doi: 10.3233/RNN-180877

Dissanayaka, T., Zoghi, M., Farrell, M., Egan, G. F., and Jaberzadeh, S. (2017). Does transcranial electrical stimulation enhance corticospinal excitability of the motor cortex in healthy individuals? A systematic review and meta-analysis. *Eur. J. Neurosci.* 46, 1968–1990. doi: 10.1111/ejn.13640

Doyon, J., Penhune, V., and Ungerleider, L. G. (2003). Distinct contribution of the cortico-striatal and cortico-cerebellar systems to motor skill learning. *Neuropsychologia* 41, 252–262. doi: 10.1016/S0028-3932(02)00158-6

Esmaeilpour, Z., Shereen, A. D., Ghobadi-Azbari, P., Datta, A., Woods, A. J., Ironside, M., et al. (2020). Methodology for tDCS integration with fMRI. *Hum. Brain Mapp.* 41, 1950–1967. doi: 10.1002/hbm.24908

Ferrari, M., and Quaresima, V. (2012). A brief review on the history of human functional near-infrared spectroscopy (fNIRS) development and fields of application. *Neuroimage* 63, 921–935. doi: 10.1016/j.neuroimage.2012.03.049

Gălvez, V., Alonzo, A., Martin, D., and Loo, C. K. (2013). Transcranial direct current stimulation treatment protocols: should stimulus intensity be constant or incremental over multiple sessions? *Int. J. Neuropsychopharmacol.* 16, 13–21. doi: 10.1017/S1461145712000041

Halsband, U., Ito, N., Tanji, J., and Freund, H.-J. (1993). The role of premotor cortex and the supplementary motor area in the temporal control of movement in man. *Brain* 116, 243–266. doi: 10.1093/brain/116.1.243

Hamoudi, M., Schambra, H. M., Fritsch, B., Schoechlin-Marx, A., Weiller, C., Cohen, L. G., et al. (2018). Transcranial direct current stimulation enhances motor skill learning but not generalization in chronic stroke. *Neurorehabil. Neural Repair* 32, 295–308. doi: 10.1177/1545968318769164

Hardwick, R. M., Rottschy, C., Miall, R. C., and Eickhoff, S. B. (2013). A quantitative meta-analysis and review of motor learning in the human brain. *Neuroimage* 67, 283–297. doi: 10.1016/j.neuroimage.2012.11.020

Huo, C., Xu, G., Li, W., Xie, H., Zhang, T., Liu, Y., et al. (2021). A review on functional near-infrared spectroscopy and application in stroke rehabilitation. *Med. Nov. Technol. Dev.* 11:100064. doi: 10.1016/j.medntd.2021.100064

Iannone, A., Santiago, I., Ajao, S. T., Brasil-Neto, J., Rothwell, J. C., and Spampinato, D. A. (2022). Comparing the effects of focal and conventional tDCS on motor skill learning: a proof of principle study. *Neurosci. Res.* 178, 83–86. doi: 10.1016/j.neures.2022.01.006

Kami, A., Meyer, G., Jezzard, P., Adams, M. M., Turner, R., and Ungerleider, L. G. (1995). Functional MRI evidence for adult motor cortex plasticity during motor skill learning. *Nature* 377, 155–158. doi: 10.1038/377155a0

Kang, N., Summers, J. J., and Cauraugh, J. H. (2016). Transcranial direct current stimulation facilitates motor learning post-stroke: a systematic review and meta-analysis. *J. Neurol. Neurosurg. Psychiatry* 87, 345–355. doi: 10.1136/jnnp-2015-311242

Karni, A., Meyer, G., Rey-Hipolito, C., Jezzard, P., Adams, M. M., Turner, R., et al. (1998). The acquisition of skilled motor performance: fast and slow experience-driven changes in primary motor cortex. *Proc. Natl. Acad. Sci. U. S. A.* 95, 861–868. doi: 10.1073/pnas.95.3.861

Kim, H. E., Avraham, G., and Ivry, R. B. (2021). The psychology of reaching: action selection, movement implementation, and sensorimotor learning. *Annu. Rev. Psychol.* 72, 61–95. doi: 10.1146/annurev-psych-010419-051053

Kim, H., Kim, J., Lee, G., Lee, J., and Kim, Y.-H. (2022). Task-related hemodynamic changes induced by high-definition Transcranial direct current stimulation in chronic stroke patients: an uncontrolled pilot fNIRS study. *Brain Sci.* 12:453. doi: 10.3390/brainsci12040453

Kim, Y.-H., You, S. H., Ko, M.-H., Park, J.-W., Lee, K. H., Jang, S. H., et al. (2006). Repetitive transcranial magnetic stimulation–induced corticomotor excitability and associated motor skill acquisition in chronic stroke. *Stroke* 37, 1471–1476. doi: 10.1161/01.STR.0000221233.55497.51

Krakauer, J. W., Hadjiosif, A. M., Xu, J., Wong, A. L., and Haith, A. M. (2019). Motor learning. *Compr. Physiol.* 9, 613–663. doi: 10.1002/cphy.c170043

Kuo, H.-I., Bikson, M., Datta, A., Minhas, P., Paulus, W., Kuo, M.-F., et al. (2013). Comparing cortical plasticity induced by conventional and high-definition 4× 1 ring tDCS: a neurophysiological study. *Brain Stimul.* 6, 644–648. doi: 10.1016/j.brs.2012.09.010

Lachaux, J. P., Rodriguez, E., Martinerie, J., and Varela, F. J. (1999). Measuring phase synchrony in brain signals. *Hum. Brain Mapp.* 8, 194–208. doi: 10.1002/(SICI)1097-0193(1999)8:4<194::AID-HBM4>3.0.CO;2-C

Langhorne, P., Coupar, F., and Pollock, A. (2009). Motor recovery after stroke: a systematic review. *Lancet Neurol.* 8, 741–754. doi: 10.1016/S1474-4422(09)70150-4

Lee, G., Park, J.-S., and Jung, Y.-J. (2019). OptoNet: a MATLAB-based toolbox for cortical network analyses using functional near-infrared spectroscopy. *Opt. Eng.* 59:061602. doi: 10.1117/1.OE.59.6.061602

Lee, G., Park, J.-S., Lee, J., Kim, J., Jung, Y.-J., and Kim, Y.-H. (2020). OptoNet II: an advanced MATLAB-based toolbox for functional cortical connectivity analysis with surrogate tests using fNIRS. *IEEE Access* 9, 15983–15991. doi: 10.1109/ACCESS.2020.3042808

Lee, S.-H., Lee, H.-J., Shim, Y., Chang, W. H., Choi, B.-O., Ryu, G.-H., et al. (2020). Wearable hip-assist robot modulates cortical activation during gait in stroke patients: a functional near-infrared spectroscopy study. *J. Neuroeng. Rehabil.* 17, 1–8. doi: 10.1186/s12984-020-00777-0

Lefebvre, S., Jann, K., Schmiesing, A., Ito, K., Jog, M., Schweighofer, N., et al. (2019). Differences in high-definition transcranial direct current stimulation over the motor hotspot versus the premotor cortex on motor network excitability. *Sci. Rep.* 9, 1–15. doi: 10.1038/s41598-019-53985-7

Lefebvre, S., Laloux, P., Peeters, A., Desfontaines, P., Jamart, J., and Vandermeeren, Y. (2013). Dual-tDCS enhances online motor skill learning and long-term retention in chronic stroke patients. *Front. Hum. Neurosci.* 6:343. doi: 10.3389/fnhum.2012.00343

Leff, D. R., Orihuela-Espina, F., Elwell, C. E., Athanasiou, T., Delpy, D. T., Darzi, A. W., et al. (2011). Assessment of the cerebral cortex during motor task behaviours in adults: a systematic review of functional near infrared spectroscopy (fNIRS) studies. *Neuroimage* 54, 2922–2936. doi: 10.1016/j.neuroimage.2010.10.058

Lewis, P. A., and Miall, R. C. (2003). Distinct systems for automatic and cognitively controlled time measurement: evidence from neuroimaging. *Curr. Opin. Neurobiol.* 13, 250–255. doi: 10.1016/S0959-4388(03)00036-9

Martïnez-Përez, V., Campoy, G., Palmero, L. B., and Fuentes, L. J. (2020). Examining the dorsolateral and ventromedial prefrontal cortex involvement in the self-attention network: a randomized, sham-controlled, parallel group, double-blind, and multichannel HD-tDCS study. *Front. Neurosci.* 14:683. doi: 10.3389/fnins.2020.00683

Mary, A., Wens, V., Op De Beeck, M., Leproult, R., De Tiège, X., and Peigneux, P. (2017). Resting-state functional connectivity is an age-dependent predictor of motor learning abilities. *Cereb. Cortex* 27, 4923–4932. doi: 10.1093/cercor/bhw286

Meehan, S. K., Dao, E., Linsdell, M. A., and Boyd, L. A. (2011). Continuous theta burst stimulation over the contralesional sensory and motor cortex enhances motor learning post-stroke. *Neurosci. Lett.* 500, 26–30. doi: 10.1016/j.neulet.2011.05.237

Muller, C. O., Muthalib, M., Mottet, D., Perrey, S., Dray, G., Delorme, M., et al. (2021). Recovering arm function in chronic stroke patients using combined anodal HD-tDCS and virtual reality therapy (ReArm): a study protocol for a randomized controlled trial. *Trials* 22, 1–18. doi: 10.1186/s13063-021-05689-5

Muthalib, M., Dutta, A., Besson, P., Rothwell, J., Ward, T., and Perrey, S. Comparison of online vs offline effects of HD-tDCS induced modulation of cortical sensorimotor networks using a combined fNIRS-EEG setup. Poster Presented at the International Society on Oxygen Transport to Tissues (ISOTT) Conference. London (2014).

Park, J.-W., Kim, Y.-H., Jang, S. H., Chang, W. H., Park, C.-H., and Kim, S. T. (2010). Dynamic changes in the cortico-subcortical network during early motor learning. *Neurorehabilitation* 26, 95–103. doi: 10.3233/NRE-2010-0540

Russo, C., Souza Carneiro, M. I., Bolognini, N., and Fregni, F. (2017). Safety review of transcranial direct current stimulation in stroke. *Neuromodulation* 20, 215–222. doi: 10.1111/ner.12574

Schulz, R., Park, C.-H., Boudrias, M.-H., Gerloff, C., Hummel, F. C., and Ward, N. S. (2012). Assessing the integrity of corticospinal pathways from primary and secondary cortical motor areas after stroke. *Stroke* 43, 2248–2251. doi: 10.1161/STROKEAHA.112.662619

Shoushtarian, M., Alizadehsani, R., Khosravi, A., Acevedo, N., Mckay, C. M., Nahavandi, S., et al. (2020). Objective measurement of tinnitus using functional near-infrared spectroscopy and machine learning. *PLoS One* 15:e0241695. doi: 10.1371/journal.pone.0241695

Spampinato, D., and Celnik, P. (2021). Multiple motor learning processes in humans: defining their neurophysiological bases. *Neuroscientist* 27, 246–267. doi: 10.1177/1073858420939552

Sveen, U., Bautz-Holter, E., Margrethe Sodring, K., Bruun Wyller, T., and Laake, K. (1999). Association between impairments, self-care ability and social activities 1 year after stroke. *Disabil. Rehabil.* 21, 372–377.

Tak, S., Jang, K. E., Jung, J., Jang, J., Jeong, Y., and Ye, J. C. NIRS-SPM: Statistical parametric mapping for near infrared spectroscopy. Multimodal Biomedical Imaging III. San Jose, California, United States: International Society for Optics and Photonics (2008).

Thair, H., Holloway, A. L., Newport, R., and Smith, A. D. (2017). Transcranial direct current stimulation (tDCS): a beginner's guide for design and implementation. *Front. Neurosci.* 11:641. doi: 10.3389/fnins.2017.00641

Villamar, M. F., Volz, M. S., Bikson, M., Datta, A., Dasilva, A. F., and Fregni, F. (2013). Technique and considerations in the use of 4x1 ring high-definition transcranial direct current stimulation (HD-tDCS). *J. Vis. Exp.* 77:e50309. doi: 10.3791/50309-v

Wu, T., and Hallett, M. (2005). The influence of normal human ageing on automatic movements. *J. Physiol.* 562, 605–615. doi: 10.1113/jphysiol.2004.076042

Yaqub, M. A., Woo, S.-W., and Hong, K.-S. (2018). Effects of HD-tDCS on resting-state functional connectivity in the prefrontal cortex: an fNIRS study. *Complexity* 2018, 1–13. doi: 10.1155/2018/1613402

Ye, J. C., Tak, S., Jang, K. E., Jung, J., and Jang, J. (2009). NIRS-SPM: statistical parametric mapping for near-infrared spectroscopy. *Neuroimage* 44, 428–447. doi: 10.1016/j.neuroimage.2008.08.036

Zimeo Morais, G. A., Balardin, J. B., and Sato, J. R. (2018). fNIRS Optodes' location decider (fOLD): a toolbox for probe arrangement guided by brain regions-of-interest. *Sci. Rep.* 8, 1–11. doi: 10.1038/s41598-018-21716-z

frontiers | Frontiers in Neuroscience

TYPE Methods
PUBLISHED 16 June 2023
DOI 10.3389/fnins.2023.1199150

OPEN ACCESS

EDITED BY
Bin Jing,
Capital Medical University, China

REVIEWED BY
Zhen Zhou,
University of Pennsylvania, United States
Xuan Li,
Helmholtz Association of German Research Centres (HZ), Germany

*CORRESPONDENCE
Yudan Ren
✉ yudan.ren@nwu.edu.cn

†These authors have contributed equally to this work and share first authorship

RECEIVED 03 April 2023
ACCEPTED 30 May 2023
PUBLISHED 16 June 2023

CITATION
Song L, Ren Y, Wang K, Hou Y, Nie J and He X (2023) Mapping the time-varying functional brain networks in response to naturalistic movie stimuli.
Front. Neurosci. 17:1199150.
doi: 10.3389/fnins.2023.1199150

Mapping the time-varying functional brain networks in response to naturalistic movie stimuli

Limei Song[1†], Yudan Ren[1*†], Kexin Wang[1], Yuqing Hou[1], Jingsi Nie[2] and Xiaowei He[1]

[1]School of Information Science and Technology, Northwest University, Xi'an, China, [2]School of Foreign Studies, Xi'an Jiaotong University, Xi'an, China

One of human brain's remarkable traits lies in its capacity to dynamically coordinate the activities of multiple brain regions or networks, adapting to an externally changing environment. Studying the dynamic functional brain networks (DFNs) and their role in perception, assessment, and action can significantly advance our comprehension of how the brain responds to patterns of sensory input. Movies provide a valuable tool for studying DFNs, as they offer a naturalistic paradigm that can evoke complex cognitive and emotional experiences through rich multimodal and dynamic stimuli. However, most previous research on DFNs have predominantly concentrated on the resting-state paradigm, investigating the topological structure of temporal dynamic brain networks generated *via* chosen templates. The dynamic spatial configurations of the functional networks elicited by naturalistic stimuli demand further exploration. In this study, we employed an unsupervised dictionary learning and sparse coding method combing with a sliding window strategy to map and quantify the dynamic spatial patterns of functional brain networks (FBNs) present in naturalistic functional magnetic resonance imaging (NfMRI) data, and further evaluated whether the temporal dynamics of distinct FBNs are aligned to the sensory, cognitive, and affective processes involved in the subjective perception of the movie. The results revealed that movie viewing can evoke complex FBNs, and these FBNs were time-varying with the movie storylines and were correlated with the movie annotations and the subjective ratings of viewing experience. The reliability of DFNs was also validated by assessing the Intra-class coefficient (ICC) among two scanning sessions under the same naturalistic paradigm with a three-month interval. Our findings offer novel insight into comprehending the dynamic properties of FBNs in response to naturalistic stimuli, which could potentially deepen our understanding of the neural mechanisms underlying the brain's dynamic changes during the processing of visual and auditory stimuli.

KEYWORDS

dynamic functional brain network, time-varying, dictionary learning and sparse coding, naturalistic stimuli, fMRI

1. Introduction

The study of functional brain networks (FBNs) can reveal the mechanisms and properties of brain functions, which is significant for elucidating the cognitive, sensory, and emotional functions of the brain (Rubinov and Sporns, 2010; Barrett and Satpute, 2013). The key characteristic of FBNs is their dynamic change across time for adapting to the continuously complex external environment (Hutchison et al., 2013; Calhoun et al., 2014; Ma et al., 2014; Lurie et al., 2020). Research on dynamic functional networks (DFNs) using functional magnetic resonance imaging (fMRI) have largely advanced our understanding of dynamic brain activity in responding to external sensory information (Tononi et al., 1996; Park and Friston, 2013; Calhoun et al., 2014).

Current studies on dynamic FBNs mainly rely on the resting-state paradigm (Hutchison et al., 2013; Allen et al., 2014; Liegeois et al., 2017; Savva et al., 2019). However, the resting-state is challenging to use when investigating specific cognitive processes due to its unrestrained nature and undesired behavioral disturbances, such as head movements and microsleep (Van Dijk et al., 2012; Buckner et al., 2013; Tagliazucchi and Laufs, 2014). In addition, electrophysiological and neuroimaging studies suggest that neural responses under the resting-state paradigm show general reliability and reproducibility (Belitski et al., 2008; Wang et al., 2017).

Naturalistic paradigms have been found to be more reliable and effective than the resting-state paradigm in exploring FBNs by providing cognitive constraints and high reliability (Sonkusare et al., 2019). These paradigms involve rich multimodal dynamic stimuli that reflect our everyday experience, resulting in more intricate patterns of functional brain activity and more diverse FBNs. Movies, as a typical representative of the passive viewing naturalistic paradigm, provide continuous audiovisual experiences that elicit stronger emotions than brief and isolated emotion-inducing events (Hasson et al., 2004; Meer et al., 2020; Saarimaki, 2021). Hence, using movies as stimuli in fMRI studies can better induce higher-order and complex FBNs related to cognition and emotion, thus leading to a more comprehensive understanding of DFNs and their relationship with cognition, sensation, and emotion.

However, most of the current research on DFNs focuses on the topology of time-varying connectivity, which limits the regions or nodes of the network to the selected template or the region of interest (ROI) (Hutchison et al., 2013; Calhoun et al., 2014). Less attention has been paid to the dynamic spatial patterns of the large-scale complex FBNs themselves induced by natural stimuli. To fully understand FBNs derived from fMRI data, it is necessary to investigate the spatio-temporal dynamics of these FBNs (Ge et al., 2020). In addition, while recent studies have analyzed the test–retest reliability of dynamic functional connectivity constrained by selected brain parcellation under the naturalistic paradigm (Tian et al., 2021; Zhang et al., 2021), the reliability of large-scale dynamic spatial patterns of FBNs remains unclear. Therefore, further research is required to explore the dynamic spatial patterns of FBNs and their relationship with cognition and perception, as well as their reliability during naturalistic conditions.

Inspired by the effectiveness of dictionary learning and sparse coding (DLSC) method in detecting static and dynamic FBNs (Lv, 2013; Ren et al., 2017a; Ge et al., 2020), we developed a data-driven method that combines group-wise DLSC approach with sliding window strategy, to identify and quantify the dynamic spatial patterns of time-varying FBNs from naturalistic fMRI data (NfMRI). Our method successfully identified several higher-order and complex FBNs, such as cerebellum-related networks, and revealed the significant correlations between movie annotations and detected DFNs. Additionally, we observed that specific individual DFNs were correlated with individuals' subjective emotional perceptions to the movie. Furthermore, we validated the reliability of DFNs derived from two scanning sessions with 3 months intervals by evaluating their ICCs. In general, our study provides novel insights into the dynamic characteristics of FBNs under naturalistic stimuli.

2. Results

2.1. Group-wise static FBNs

We first identified seven consistent and representative group-wise static FBNs for both session A and session B via the DLSC approach. Figure 1 shows the representative FBNs of session A. These networks include either typically activated simple networks or complex networks. The simple networks involve the visual network (Figure 1A) and the auditory network (Figure 1B). The complex networks consist of multiple co-activated brain networks/regions, including auditory and cerebellar network (AC) (Figure 1C), the audiovisual and sensorimotor network (VAS) (Figure 1D), the partial default mode network (DMN), the salience and cerebellar network (pDSC) (Figure 1E), the DMN and cerebellar network (DC) (Figure 1F), and the dorsal attention network (DAN) (Figure 1G). Specifically, the AC network is primarily composed of auditory, cerebellar posterior crus 1,2 and vermis (Figure 1C). The VAS network is composed of visual, auditory, and sensorimotor cortex (Figure 1D). The pDSC encompasses the posterior cingulate cortex, medial prefrontal cortex, angular gyrus, anterior insula, dorsal anterior cingulate cortex, cerebellar posterior crus1,2, cerebellums 9 and vermis. Notably, the pDSC network excludes the precuneus (Figure 1E). The DC network mainly consists posterior cingulate cortex, medial prefrontal cortex angular gyrus, precuneus, cerebellar posterior crus1, 2, cerebellums 9 and vermis (Figure 1F). The DAN network includes intraparietal sulcus and the frontal eye fields (Figure 1G). A comparison between these identified FBNs and well-established resting-state templates or networks from previous studies conducted under natural stimulation is presented in Supplementary Figure S8.

The FBNs derived from session B showed a high degree of spatial consistency with those observed in session A (Supplementary Figure S1), as demonstrated by the relatively high overlap rate and Pearson correlation coefficient (PCC) values between the two sets of FBNs (Table 1). Specifically, the mean overlapping rate and the mean PCC of the seven FBNs were 0.44 ± 0.11 [Mean ± standard deviation (SD)] and 0.82 ± 0.18 (Mean ± SD), respectively, suggesting the consistency and stability of the DLSC framework in detecting FBNs across two scanning sessions.

2.2. Dynamic spatial patterns of FBNs

We applied the sliding time window method with a window length of 60 repetition time (TR) units and step size of 1TR, resulting in 470 available windows. Correspondingly, 470 FBNs were obtained

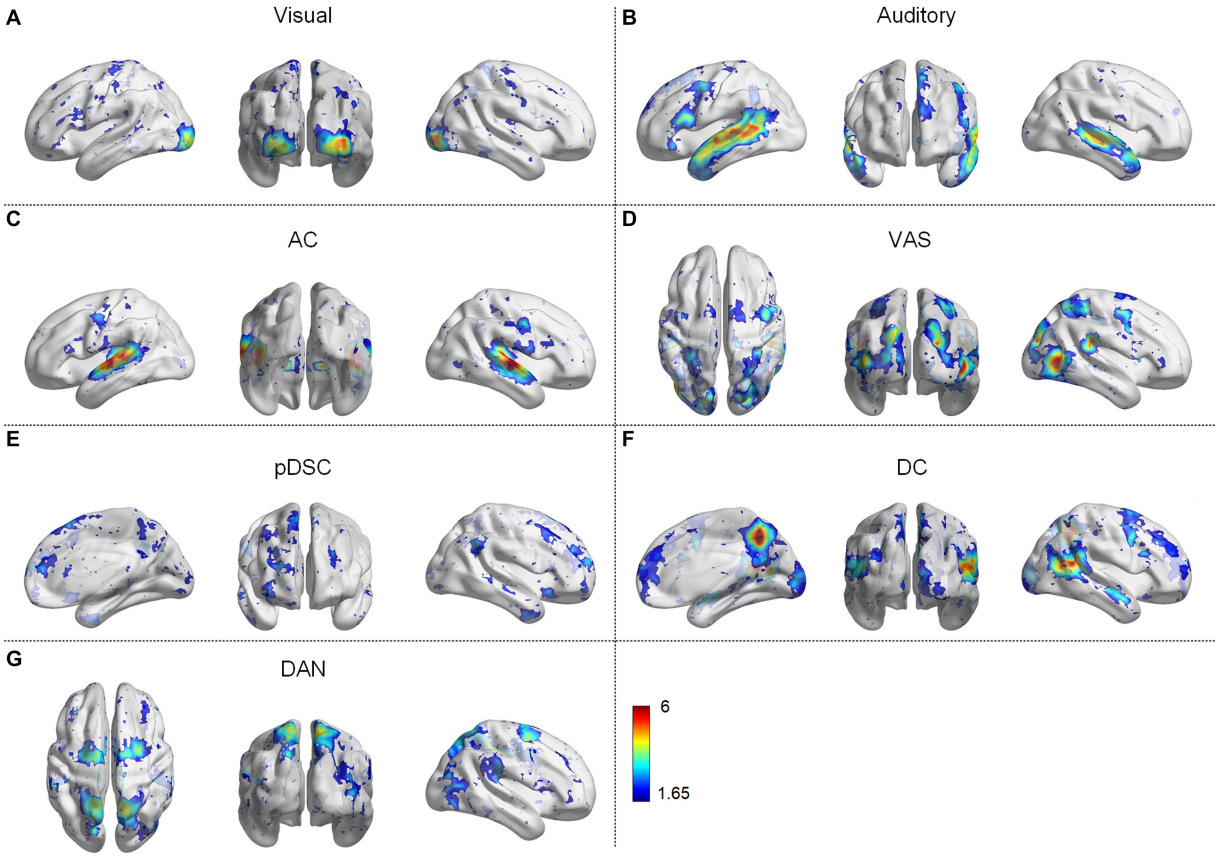

FIGURE 1
Group-wise static functional brain networks (FBNs) of session A, including **(A)** visual network, **(B)** auditory network, **(C)** auditory and cerebellar network (AC), **(D)** audiovisual and sensorimotor network (VAS), **(E)** partial default mode network (DMN), salience, and cerebellar network (pDSC), **(F)** DMN and cerebellar network (DC), **(G)** dorsal attention network (DAN).

TABLE 1 Overlapping rate and Pearson correlation coefficient (PCC) across two sessions for seven representative brain functional networks (FBNs).

	Visual	Auditory	AC	VAS	pDSC	DC	DAN	Mean±SD
Overlap	0.34	0.58	0.5	0.52	0.27	0.5	0.39	0.44 ± 0.11
PCC	0.9	0.95	0.97	0.93	0.47	0.87	0.68	0.82 ± 0.18

by applying the DLSC method, which could reflect the dynamics of time-varying large-scale networks. To provide representative visualization of these FBNs, we selected and displayed the FBNs from the first window among every 50 windows. For example, the first brain activation map in Figure 2 represents the visual network obtained during the first window (1TR to 60TR), corresponding to a time period of 1 s to 132 s.

To quantitatively explore the dynamic spatial patterns of FBNs, we assessed the dynamic temporal changes of the number of activated voxels (NAV) (Figure 2) and the intensity of activated voxels (IAV) (Figure 3) for the seven FBNs. Our results revealed that for each network, both NAV and IAV exhibited temporal variations, with relatively consistent trends between the two metrics. The IAV showed less variability compared to NAV due to the calculation method of averaging activation intensities of all voxels exceeding a predefined threshold, resulting in a relatively narrow range of variation in the overall activation strength of the whole network. The peaks of NAV and IAV curves corresponded to the FBNs that displayed more pronounced and widespread patterns of activation, whereas the troughs of these curves responded to FBNs with diminished or even absent activation patterns. These findings highlight that FBNs were dynamic and evolved temporally in response to the unfolding plot of the movie, which is also consistent with the underlying neural basis of complex perception and behavior (Calhoun et al., 2014). Additionally, the lower-order perceptual networks, including visual network, auditory network, and VAS network, exhibited relatively stable level of activation over time, whereas the higher-order networks, such as pDSC, DC, and DAN networks, showed greater fluctuations in activation curves. The AC network, specifically, comprising both lower-order network (i.e., auditory network) and higher-order networks (i.e., cerebellar network), also displayed substantial fluctuations in its activation curves (Figures 2, 3). These results suggest that different FBNs exhibit distinct temporal dynamics in response to external stimuli, which may reflect their respective roles in higher-level cognitive and attentional processes.

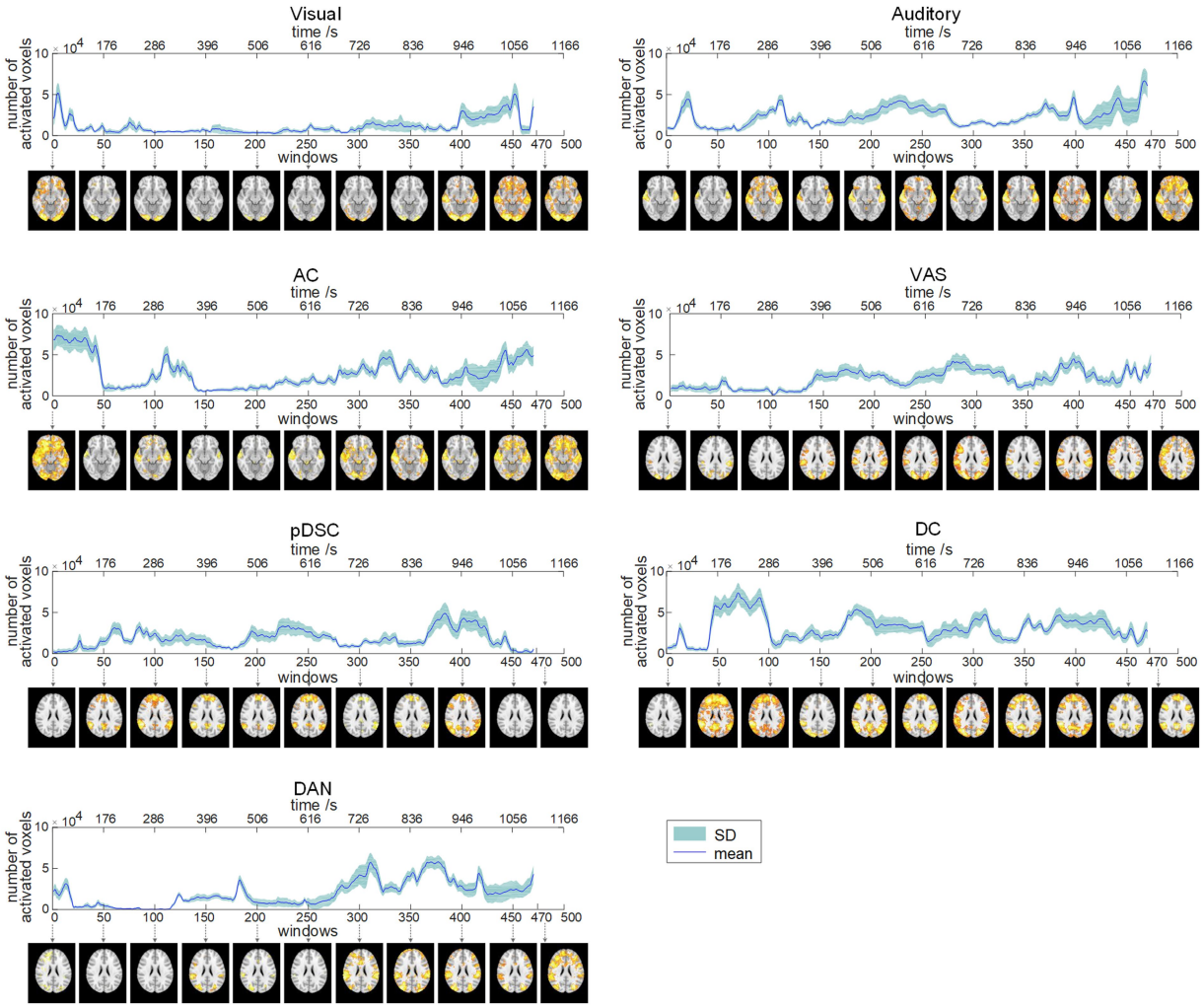

FIGURE 2
Dynamic evolution of the number of activated voxels (NAV) of seven brain function networks (FBNs) (session A). The corresponding FBNs of the first window among every 50 windows are displayed at the bottom.

The results of session B were generally consistent with those of session A, as evidenced by the visual comparison of the results depicted in Supplementary Figures S2, S3. Moreover, the PCC values for both NAV and IAV curves across session A and session B were relatively high for most FBNs (Supplementary Table S1), suggesting that the identified dynamic spatial patterns of FBNs induced by the movie viewing are reproducible and consistent across two scanning sessions.

2.3. Correlation between DFNs and movie annotations

To investigate the relationship between DFNs and the unfolding of the movie, we assessed the spearman correlation between dynamic changes of NAV/IAV and movie annotations, which include language use, changepoints, the presence of positive valence of scenes (scenes_p), the presence of negative valence of scenes (scenes_n), the presence of faces with positive (face_p), and presence of faces with negative (face_n). The results showed that two DMN-related networks, i.e., the DC and pDSC networks, were significantly correlated with movie annotations. Specifically, both NVA and IVA metrics of the DC network showed statistically significant correlations with the appearance of positive facial expressions based on permutation-based testing ($p < 0.05$) (see Methods) (Tables 2, 3). Notably, the value of p for the IAV metric was less than 0.01 (Table 3). Additionally, the changes in INV of the pDSC network were significantly and positively correlated with the appearance of the changepoint in the movie scenes (permutation 5,000 times, $p < 0.05$) (Table 3).

2.4. Dynamic inter-subject correlation analyses

The neural response evoked by the naturalistic stimuli exhibit not only high consistency across individuals, but also inter-subject variability and uniqueness reflecting personal experiences and intrinsically-driven processes under natural viewing condition, which varies across different brain regions/networks (Golland et al., 2007; Ren et al., 2017b). Hence, to quantify these group consistency and

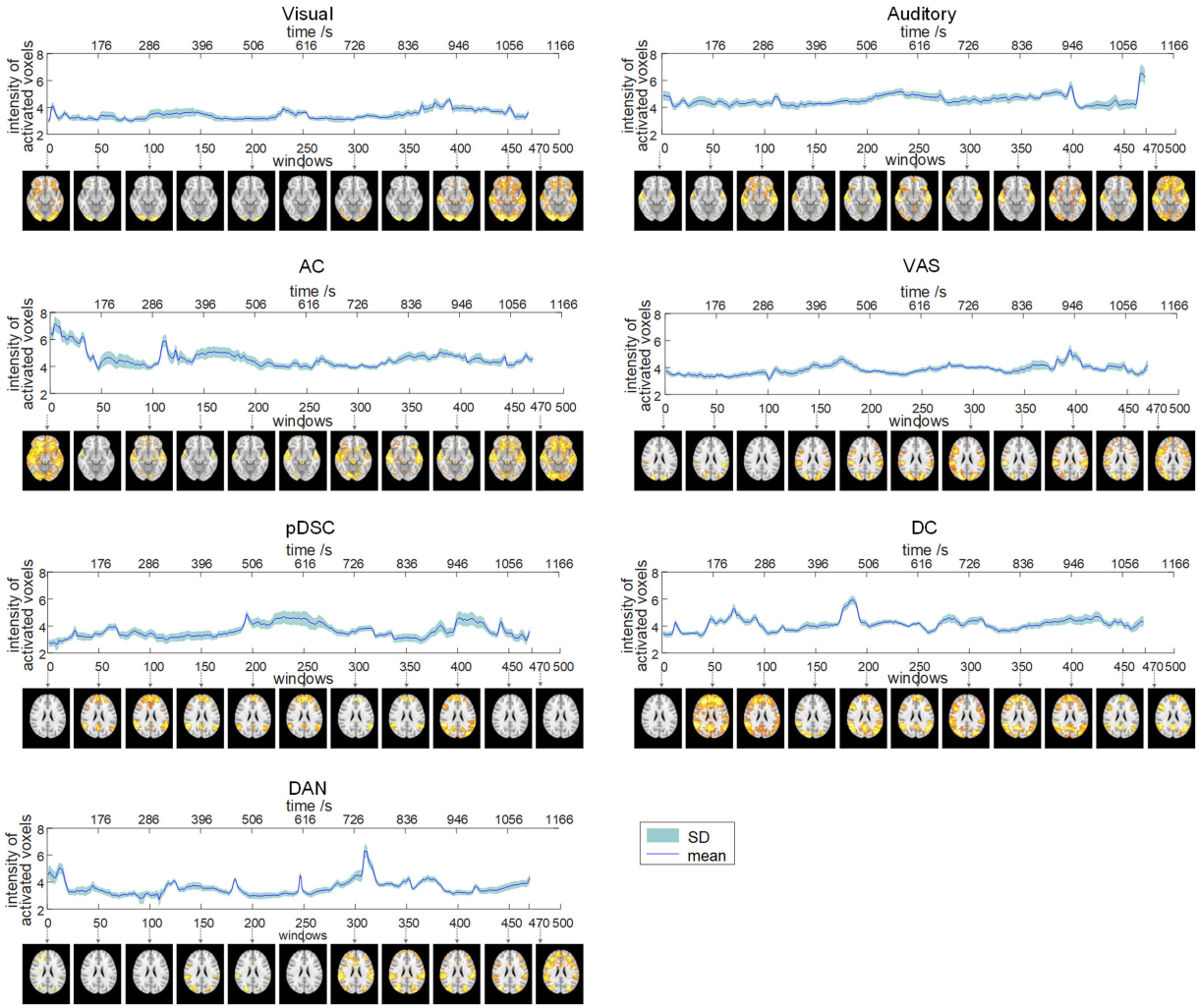

FIGURE 3
Dynamic evolution of the intensity of activated voxels (IAV) of seven FBNs (session A). The corresponding FBNs of the first window among every 50 windows are displayed at the bottom.

TABLE 2 The Spearman correlation between the changes in the number of active voxels (NAV) and movie annotations.

	Visual	Auditory	AC	VAS	pDSC	DC	DAN
language	−0.03	0.00	−0.09	−0.12	−0.17	−0.11	−0.14
changepoint	−0.15	−0.10	−0.04	0.11	0.02	0.14	0.06
scenes_p	0.00	−0.11	0.07	0.03	−0.05	0.08	−0.11
scenes_n	−0.10	0.01	−0.09	−0.19	−0.08	0.02	−0.12
face_p	−0.07	−0.11	0.08	0.00	−0.02	**0.16***	−0.09
face_n	−0.05	0.02	−0.08	−0.28	−0.07	−0.01	−0.20

Bold font indicates significant correlation (*$p < 0.05$). Permutation test with 5,000 iterations.

individual variations in defined DFNs, we adopted their corresponding group-wise static FBNs as templates to calculate the dynamic inter-subject correlation (ISC) (see Methods). Accordingly, the group-level dynamic ISC can represent the degree of temporal consistency across subjects in different FBNs (the thick blue line in Figure 4). The average values of group-level dynamic ISC during the entire period for seven FNBs (including visual, auditory, AC, VAS, pDSC, DC, and DAN networks) were 0.33 ± 0.12, 0.51 ± 0.13, 0.58 ± 0.12, 0.39 ± 0.12, 0.25 ± 0.10, 0.31 ± 0.08, and 0.34 ± 0.08 (Mean ± SD), respectively. While relatively high ISC values were observed in networks encompassing lower-level perceptual regions, especially those related to auditory processing, such as auditory and AC networks, the higher-order networks demonstrated lower ISC values that can indicate the occurrence of intrinsically-driven processes during individual movie viewing, including pDSC and DC networks, consistent with previous research (Ren et al., 2017b). Moreover, individual-level dynamic ISC

TABLE 3 The Spearman correlation between the changes in the intensity of active voxels (IAV) and movie annotations.

	Visual	Auditory	AC	VAS	pDSC	DC	DAN
language	−0.14	0.03	−0.12	0.00	−0.17	−0.08	−0.08
changepoint	−0.18	−0.14	0.02	0.01	**0.15***	0.12	−0.01
scenes_p	−0.18	−0.04	0.03	−0.10	0.04	0.13	−0.07
scenes_n	−0.01	0.07	−0.08	−0.06	−0.15	−0.01	−0.07
face_p	−0.06	−0.01	−0.02	−0.09	0.05	**0.19****	−0.07
face_n	−0.12	0.04	−0.07	−0.19	−0.19	−0.06	−0.11

Bold font indicates significant correlation (*$p < 0.05$, **$p < 0.01$). Permutation test with 5,000 iterations.

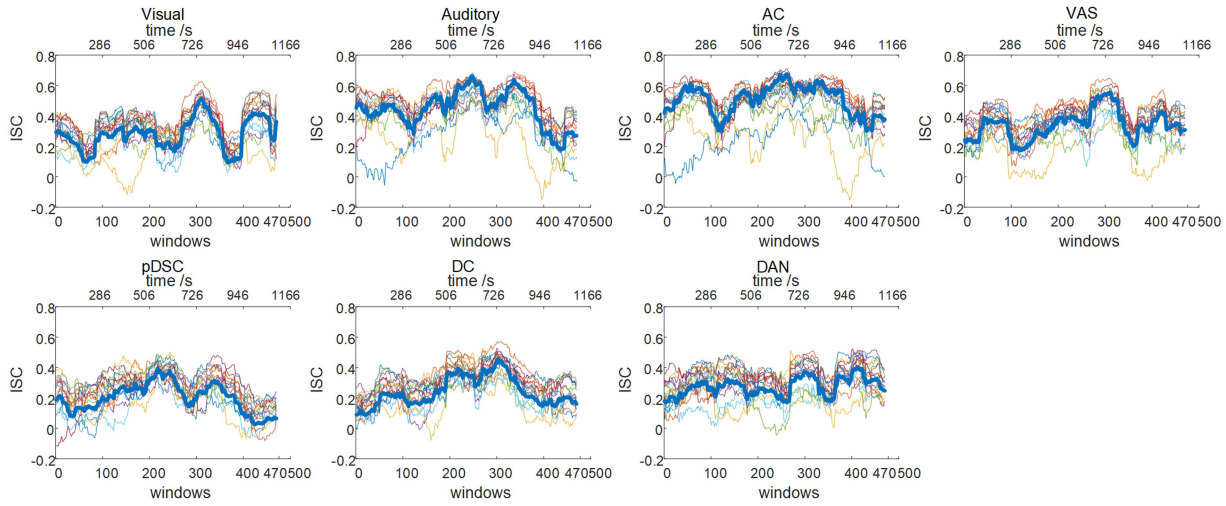

FIGURE 4
Dynamic inter-subject correlation (ISC) (session A): group-wise and individual dynamic ISC. The thick blue line represents the group-wise dynamic ISC, and the thin colorful lines depict the dynamic ISC of 16 different individuals.

also showed inter-subject variations especially in those higher-order networks under movie stimuli (colorful thin lines in Figure 4).

The dynamic ISC of session B were largely consistent with session A (Supplementary Figure S4). Quantitatively, the PCC values for seven FBNs across two sessions were relatively high (Table 4), with an average PCC value of 0.82 ± 0.18 (Mean ± SD), thereby reaffirming the consistency of DFNs identified by our DLSC framework across two sessions.

2.5. Correlations between movie ratings and individual differences in dynamic ISC of DFNs

In the preceding section, there was relatively lower consistency in individual neural responses observed in higher-order brain networks, such as the pDSC and DC networks. This variability may be indicative of individual differences and unique experiences during natural viewing conditions. To investigate this assumption further, that is, exploring the potential relationship between subjective movie viewing experiences and the dynamics of DFNs, we examined whether the individual dynamic ISCs were correlated with their personal ratings of the movie. We applied an inter-subject representational similarity analysis (IS-RSA) (see Methods) to explore whether participants with similar subjective ratings also exhibited similar dynamic neural response patterns. Specifically, we employed a multidimensional scaling approach (MDS) (Carroll and Arabie, 1998) to characterize the answers to the post-movie questionnaire. Our result revealed that participants had varying experiences while watching the movie, with some reporting high engagement characterized by low boredom, high enjoyment, high emotion, and high audio quality, while others had low engagement (Figure 5A). The distances between movie ratings were measured by the Euclidean distance matrix of questionnaire answers across all individuals (Figure 5B). We computed Pearson distance to represent the inter-subject distances of dynamic ISC values for seven representative FBNs, respectively (Supplementary Figure S5). By evaluating the correlation between the movie rating distances and the inter-subject distances of the dynamic ISC, we found significant positive correlations (permutation 5,000 times, $p < 0.05$) in three cerebellum-related networks, that is, AC, pDSC, and DC networks. The distance matrices of dynamic ISC for these three networks are presented in Figure 5C, and their simple linear regressions are shown in Figure 5D. However, the other DFNs did not show statistically significant associations ($p > 0.05$) (Table 5). We did not repeat this experiment in session B as it involved a repeated viewing of the same movie, and the post-viewing questionnaire was not conducted.

10.3389/fnins.2023.1199150

TABLE 4 The PCC of group-wise dynamic inter-subject correlation (ISC) across two sessions.

	Visual	Auditory	AC	VAS	pDSC	DC	DAN	Mean±SD
PCC	0.89	0.63	0.87	0.79	0.76	0.86	0.83	0.81 ± 0.09

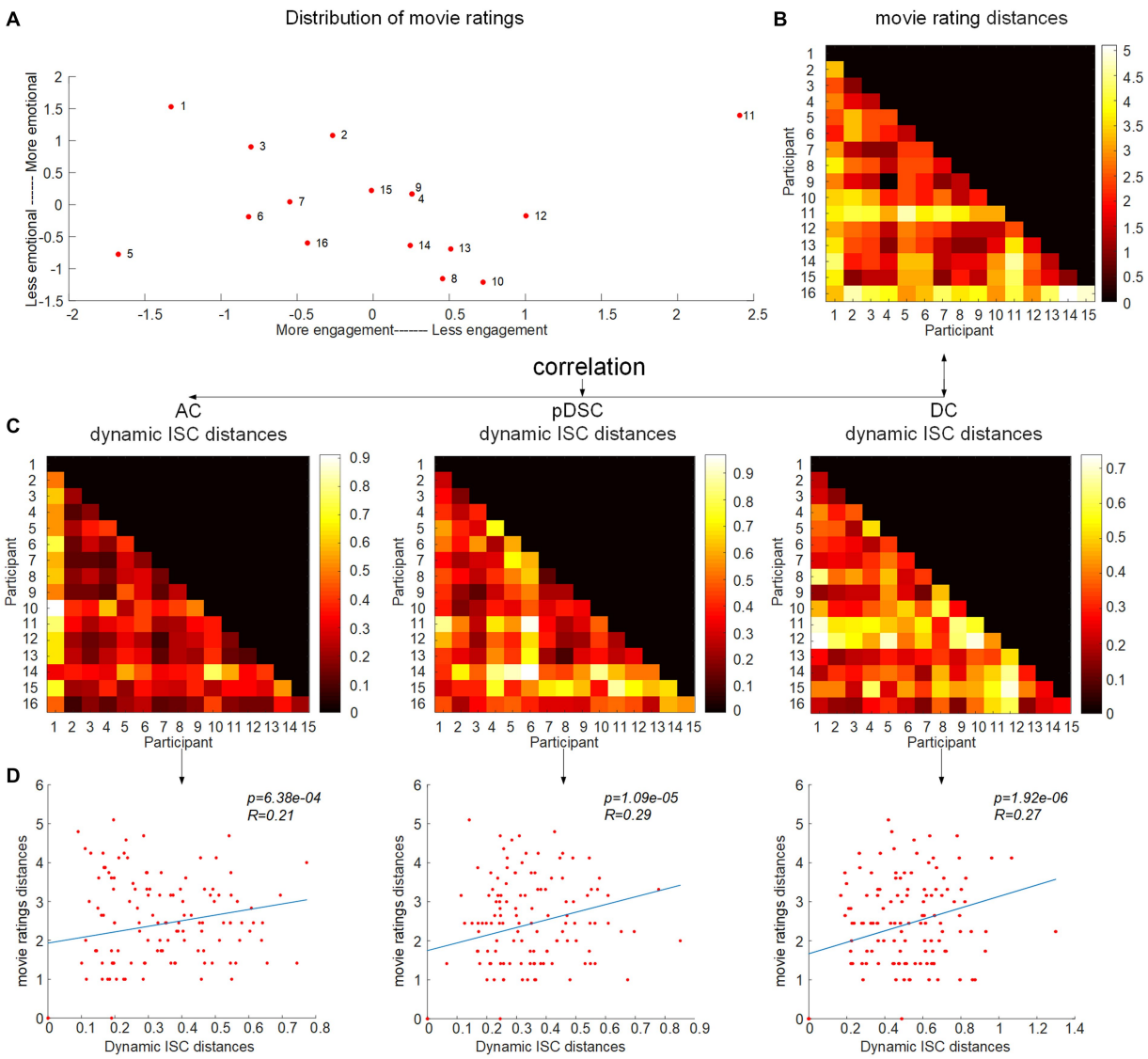

FIGURE 5
Correlation between the movie ratings and difference of individual dynamic ISC. **(A)** The inter-subject distances of the movie ratings were mapped onto a two-dimensional plane, with movie ratings shown in the inset and coded accordingly. The arrangement of movie ratings from left to right signifies participants' engagement with the movie, as those who were more engaged reported higher levels of enjoyment, emotion, and audio quality and lower levels of boredom. The top-to-bottom scale reflects the participants' ratings of evoked emotions. **(B)** Inter-subject distance matrix of the movie ratings. **(C)** Distance matrices of dynamic ISC for AC, pDSC, and DC networks. **(D)** The correlation between the movie rating distances and the inter-subject distances of dynamic ISC.

2.6. Test–retest reliability of DFNs

It was assumed that similar sensory experiences would lead to the emergence of DFNs in a consistent and reliable manner. Therefore, we assessed the level of reliability of the DFNs that develop in response to the movie storyline across two sessions. Specifically, we first calculated the scan-wise intra-group correlation coefficient (ICC) values for seven static FBNs. The results showed that the visual, AC, and VAS networks exhibited excellent reliability, the auditory and DAN networks possessed good reliability levels, and the pDSC and DC networks had moderate reliability, indicating that the networks associated with primary perceptual processes were relatively more reliable, while the higher-level networks showed less reliability, consistent with previous studies (Choe et al., 2017) (Figure 6B).

We further analyzed the reliability of the DFNs (see Methods). The reliability of the auditory, AC, VAS, and DC networks, triggered

TABLE 5 The Spearman correlation between movie rating distances and inter-subject distances of dynamic ISC for seven representative FBNs.

	Visual	Auditory	AC	VAS	pDSC	DC	DAN
Correlation	−0.02	0.07	**0.15***	0.13	**0.20***	**0.17***	0.05

Bold font indicates significant correlation (*$p < 0.05$). Permutation test with 5,000 iterations.

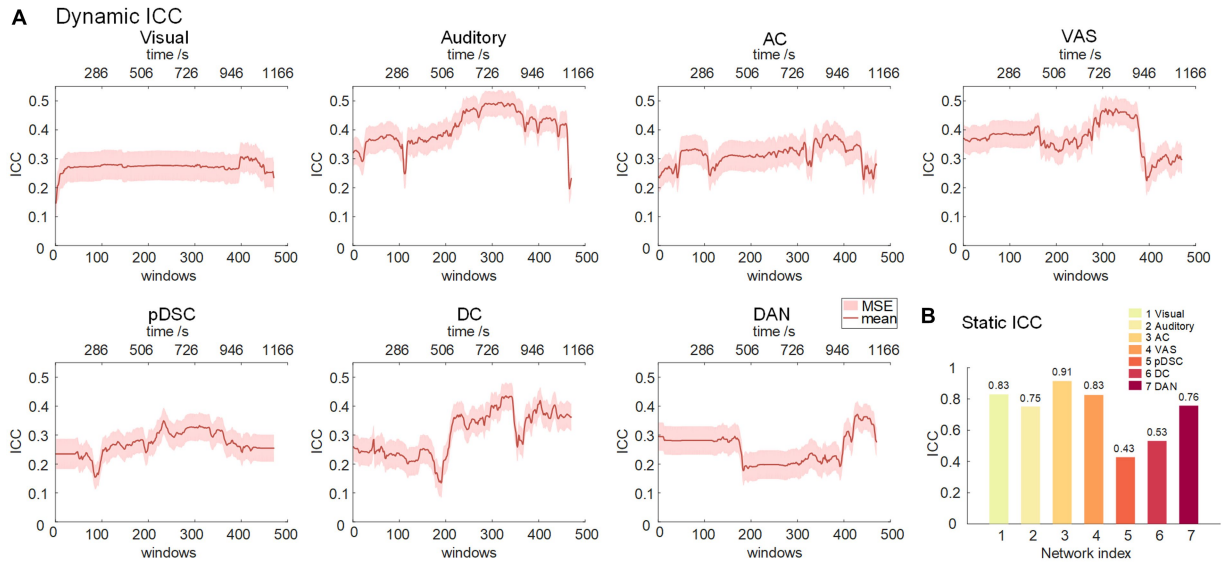

FIGURE 6
Intra-group correlation coefficient (ICC) for seven representative FBNs. **(A)** Dynamic ICC. The red line represents the group-wise dynamic ICC. **(B)** Static ICC.

by this touching movie, gradually increased during the mid to late period (about 300–390 window, corresponding to 600–1,000 s time period), and reached its peak in the near-end period. This is consistent with the narrative structure of the movie (Supplementary Table S2), wherein the plot also reaches its climax near the end (at around 17 min or 1,020 s) (Nguyen et al., 2017). The findings suggest that as the storyline develops, individuals may experience greater behavioral constraints and engagements, leading to an increase in the test–retest reliability of brain activities.

3. Discussion

Brain is a complex and dynamic system, composed of different brain regions forming functional brain networks that perform different cognitive functions (Raichle, 2006; Allen et al., 2014; Monti et al., 2014; Shine et al., 2016). This study explored the dynamic functional brain networks (DFNs) involved in higher-order cognitive processes, sensory perception, and emotional responses to naturalistic stimuli. Utilizing the proposed method, the study revealed rich and complex higher-order FBNs, including cerebellum-related networks, which are challenging to detect by conventional resting-state paradigm. The spatial patterns of these FBNs were time-varying with the movie storylines, and were correlated with the movie annotations and the subjective experience of the participants.

Specifically, our findings showed that two cerebellum-related networks, the DC network, and the pDSC network, were significantly connected to movie annotations. The DC network, which involves the cerebellum, posterior cingulate cortex, and precuneus region, was significantly and positively correlated with the appearance of positive facial expression during movie viewing. This finding is consistent with previous studies, which have shown that the cerebellum and posterior cingulate cortex are involved in facial emotion recognition, and that the precuneus is activated during the appearance of happy faces (Pelletier-Baldelli et al., 2015). The pDSC network, including partial DMN, salience network, and cerebellum, showed a significant positive correlation with the appearance of changepoints in movie scenes. This finding is also in line with previous studies, which have demonstrated that the changepoints in movie scenes are related to bottom-up attention, and that the salience network (SN) provides effective control of DMN activity when external event stimuli require an attentional response (Kelly et al., 2008; Menon and Uddin, 2010; Jilka et al., 2014). In addition, the cerebellum also plays a part in bottom-up attention (Gottwald et al., 2003; Kellermann et al., 2012). Overall, our results add weight to the notion that cerebellum-related DFNs are involved in higher-order cognitive and emotional processes.

Furthermore, the dynamic ISC analyses demonstrate relatively low consistency in the neural responses of higher-order brain networks across individuals. This variability suggests individual differences and unique experiences during natural viewing conditions, as evidenced by the strong correlations between the subjective ratings of the movie and dynamic ISC distances of DC and pDSC networks revealed by IS-RSA analyses. Exceptionally, the AC network exhibited relatively high temporal consistency across subjects but also existed a

significant correlation with individuals' subjective movie ratings, where the high ISC values were probably caused by the involvement of large auditory regions in the AC network. This could also explain the relatively weaker correlation between the AC network and movie ratings in comparison to that of the DC and pDSC networks (Figure 5 and Table 5). Intriguingly, all these three networks involve cerebellar posterior crus1,2 and vermis regions. Previous functional connectivity studies have confirmed that there are strong links between the posterior cerebellum and the temporal lobes, suggesting these regions share neural similarities and are involved in sensory integration and emotional processing (Yeo et al., 2011; Chan et al., 2019; Heleven et al., 2019; Van Overwalle et al., 2020b). In addition, several positron emission tomography (PET) studies suggest that the posterior cerebellum is involved in various emotional responses, such as fear, sadness, and happiness (Schwartz and Davidson, 1997; Turner et al., 2007; Verger et al., 2020). Additionally, Nguyen et al. (2017) have shown that the crus1,2 areas in the posterior cerebellum exhibit peak activities during important moments embedded in the movie, and Van Overwalle et al. (2020a) have shown that the cerebellar posterior crus 2 is specialized for mentalizing appraisal processes. Our study extends these previous findings by demonstrating that the dynamic nature of cerebellum-related FBNs is significantly correlated with individual-specific emotional responses.

Finally, our results also demonstrated that the DFNs elicited by ecologically valid sensory experiences were reproducible and reliable. Seven representative FBNs identified by our method were consistent across two scanning sessions with relatively-long interval (Figure 2, Supplementary Figure S1, and Table 1), and the changes in NVA and IVA for DFNs also showed high PCC values across two sessions, suggesting substantial consistency (Figures 2, 3, Supplementary Figures S2, S3, and Table 2). These results indicate that DFNs are reproducible during repeated movie viewing, further demonstrating that the naturalistic paradigm provides reliable experimental conditions for measuring DFNs. Furthermore, our results suggest that DFNs show good test–retest reliability, and the development of the movie plot enhances the test–retest reliability of the auditory, AC, VAS, and DC networks. This may reflect an increase in cognitive engagement as the storyline progresses, where the positive influences of cognitive participation on reliability appear to exceed the negative effect of familiarity from potential repeated viewings (Wang et al., 2017).

Overall, our study of time-varying spatial patterns of FBNs in the context of naturalistic paradigm improves our understanding of human perception, emotion, and subjective cognition. The results highlight the reliable correlations between cerebellum-related DFNs and sensory, cognitive, emotional, and subjective senses, which could motivate further research on the neural mechanisms underlying ecologically valid sensory experiences. Thus, our study provides valuable insights into the dynamic nature of brain networks and their role in higher-order cognitive and emotional processes, with potential applications in both basic and clinical neuroscience.

4. Limitations and future directions

Linking neural activity to higher cognitive and emotional functions in a dynamic and complex natural environment remains a challenge. In this work, we selected a relatively long time window of 60TRs to capture the accumulation of higher-order complex emotions and to improve the reproducibility of the FBNs (Savva et al., 2019). However, the relatively slow temporal resolution of fMRI with a large window size hinders the assessment of the responses of the brain to the perception of transient movie features. In the future, we expect to address this limitation by using electroencephalography (EEG) or magnetoencephalogram (MEG) with higher temporal resolution.

While the dataset used in this study is relatively small, all individuals watched a complete movie (20 min), which has been shown to strongly stimulate higher-order cognitions and emotions (Jaaskelainen et al., 2021). To increase the accuracy and reliability of our results, we performed a second acquisition after 3 months, despite the considerable expenses incurred for the acquisition of the complete movie. Nevertheless, we acknowledge that an abundance of subjects would further strengthen our findings, and we plan to apply our model to NfMRI datasets with a larger sample size in future studies.

5. Materials and methods

5.1. Experimental paradigm

The experiment consisted of two scanning sessions. Following a first session (session A) conducted 3 months earlier, participants underwent a second scanning session (session B) employing the same experimental paradigm. In each session, participants freely watched the 20-min short film "Butterfly Circus." In addition, all participants completed a questionnaire immediately after session A.

The short film, "Butterfly Circus," depicts a touching story of a limbless man who is encouraged by the showman of a renowned circus to discover his true potential. The narrative architecture of the film follows three distinctive drama acts that feature significant developments, complications, and turning points (Supplementary Table S2). Additionally, basic movie annotations were provided, including: the use of language, changepoints, the presence of positive valence of scenes, the presence of negative valence of scenes, the presence of faces with positive, and the presence of faces with negative (Supplementary Figure S6). Further details regarding the participants can be found in the Supplementary material (1.2).

5.2. Data acquisition and preprocessing

Sixteen right-handed (ages 27 ± 2.7) healthy participated in this study. FMRI images were acquired from a whole-body 3 T Siemens Trio MRI scanner with the following scanning parameters: repetition time (TR) 2,200 ms, echo time (TE) 30 ms, flip angle (FA) 79°, the field of view (FOV) 192×192 mm, pixel bandwidth 2,003 Hz, a 64×64 acquisition matrix, 44 axial slices, and $3 \times 3 \times 3$ mm 3 voxel resolution. Functional images were preprocessed using FMRI Expert Analysis Tool (FEAT) from FMRIB's Software Library (https://fsl.fmrib.ox.ac.uk/fsl/fslwiki), which involved motion correction, slice timing correction, spatial smoothing with 6-mm full width at half maximum Gaussian kernel, band pass filtering (0.0085 ± 0.15 Hz), linear registration to the standard Montreal Neurological Institute space (2 mm MNI152 standard template), and masking.

5.3. Dynamic sparse representation

To discover and characterize DFNs, we proposed a computational framework comprised of two stages: (A) using group-wise dictionary learning and sparse coding (DLSC) to represent static FBNs (Figure 7A), (B) sliding-window method applying for the representation of dynamic spatial patterns of FBNs (Figure 7B).

In stage A, first, the whole-brain fMRI signals of each subject were extracted and stacked into a 2D matrix $\boldsymbol{S}_i$ $\left(\boldsymbol{S}_i \in \mathbb{R}^{t\times n}\right)$, followed by spatial concatenation of the individual matrix $\boldsymbol{S}_i$ into a group-wise matrix $\boldsymbol{S}$ $(\boldsymbol{S}_i \in \mathbb{R}^{t\times(p\times n)})$ (top panel in Figure 7A), where t represents the time length of fMRI signals, n refers to the number of the individual brain voxels, p stands for the number of subjects. Second, we applied the dictionary learning algorithm to the group-wise matrix $\boldsymbol{S}$ to learn a meaningful group-wise dictionary $\boldsymbol{D}$ $(\boldsymbol{D} \in \mathbb{R}^{t\times K})$. This dictionary $\boldsymbol{D}$ consists of K atoms that can well represent the temporal features embedded in naturalistic fMRI data and are commonly shared by all the subjects (Ren et al., 2017a; Ge et al., 2020). Hence the group-wise dictionary $\boldsymbol{D}$ can be used to sparsely represent individual fMRI signals $\boldsymbol{S}_i$, resulting in the individual spatial patterns α_i $\left(\alpha_i \in \mathbb{R}^{K\times n}\right)$ (K<<n) that exhibit correspondences across subjects (middle panel in Figure 7A). Notably, we used the online dictionary learning and sparse coding algorithm, which is an effective method for extracting instinctive information from the original signal and is suitable for group-level data operations (Ponce and Sapiro, 2010; Lv, 2013). Third, to obtain the group-wise static FBNs, we performed one-sample t-test on each element of individual loading coefficient matrix α_i (middle panel of Figure 7A). Specifically, for all the subjects together, we hypothesized that each element in the loading coefficient matrix α_i is group-wisely null. To evaluate this assumption, we conducted one-sample t-test on the corresponding element in the loading coefficient matrix α_i for different subjects, in order to test whether this hypothesis was accepted or rejected (Ren et al., 2017a). The resulting t-value was then transformed into a z-score, forming a group-wise loading coefficient matrix **A** composed of z-scores (Friston et al., 1994). Since each individual coefficient matrix α_i is sparse, the t-test result of the group-wise loading coefficient matrix **A** is also sparse. Afterwards, each row of matrix **A** can be mapped back to brain volume with z-scores, referred to as z-score maps. Consequently, the z-score map obtained from this analysis can depict spatially consistent activation across all subjects, thus representing the static group-wise FBNs (bottom panel of Figure 1A).

In stage B, in order to obtain a series of dynamic spatial patterns that evolve over time for each subject, we slid the same time window on the individual signal matrix $\boldsymbol{S}_i$ and group-wise dictionary $\boldsymbol{D}$ simultaneously. This approach not only allows us to establish correspondence of individual-level FBNs among individuals, but also generates the corresponding dynamic FBNs. Consequently, we obtained individual signal matrices $\boldsymbol{S}_{i1}, \boldsymbol{S}_{i2}, \ldots, \boldsymbol{S}_{ij}, \ldots, \boldsymbol{S}_{iw}$, which represent the

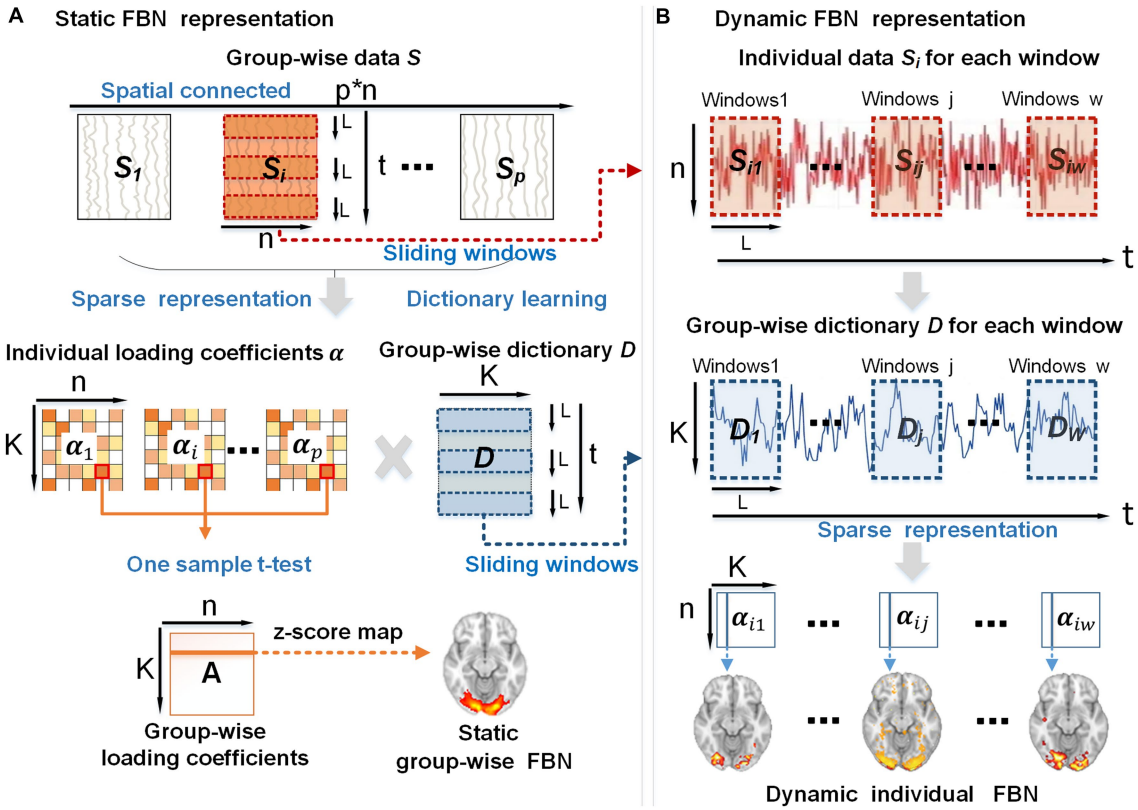

FIGURE 7
The overview of the proposed framework. **(A)** Using group-wise dictionary learning and sparse coding to represent static FBNs. **(B)** Sliding-window method applying for the representation of dynamic individual FBNs. *p*, the subject number; *n*, the number of voxels in the brain; *K*, the number of atoms in the dictionary; *t*, the time points; *L*, the length of each window; *w*, the total number of windows generated by the sliding-window method.

individual's signal for each window, as well as group-wise dictionaries $\boldsymbol{D}_1, \boldsymbol{D}_2, \ldots, \boldsymbol{D}_j, \ldots, \boldsymbol{D}_w$, which represent the group-wise dictionary for each window (top two panels in Figure 7B). The chosen window length, denoted as L (in our study, L = 60 TRs with a step size of 1 TR), resulted in a total of w = 470 windows. Consequently, the individual signal matrix $\boldsymbol{S}_i$ and group-wise dictionary $\boldsymbol{D}$ were divided into multistage signal matrices $\boldsymbol{S}_{ij}$ and dictionaries $\boldsymbol{D}_j$ (j∈1, 2, …, w) (top two panels in Figure 7B). Next, based on $\boldsymbol{S}_{ij}$ and $\boldsymbol{D}_j$ of each window, we leveraged sparse representation algorithms to extract a sequence of coefficient matrices $\pm_{ij}$ to represent individual dynamic spatial patterns of FBNs (bottom panel in Figure 7B). The above experiments were performed on each subject in session A and session B.

To identify the matching FBNs across two sessions, we manually selected representative FBNs from session A and match them with responding FBNs in session B based on their highest Pearson Correlation Coefficient (PCC) values and the maximum number of overlapping voxels (overlapping rate) (Benesty et al., 2009; Lv et al., 2015a). A detailed pipeline for selection of representative FBNs can be found in the Supplementary material (1.4). The PCC was defined as the correlation between the representative FBNs of session A and session B, and the overlapping rate of the FBNs in session A and session B was defined quantitatively as:

$$\mathbf{R}(\mathbf{X},\mathrm{Y}) = \frac{|X \cap Y|}{|\mathrm{Y}|} \tag{1}$$

where $\boldsymbol{X}$ is the representative FBN of session A, and Y refers to responding FBN of session B.

The DLSC algorithms rely on two key parameters: the number of dictionary atoms (K) and the sparsity penalty parameter (λ). However, there is no golden standard for determining the optimal values of these parameters. Based on previous studies that used DLSC algorithms for FBNs recognition, K was experimentally and empirically set to 400, and λ was set to a range of 0.1–0.5 (Lv et al., 2015b; Zhang et al., 2017; Ge et al., 2018). Therefore, in this study, we set $K = 400$, while systematically tested the setting of λ (0.1, 0.5). Through our experiments, we found that the largest number of networks could be identified with manual inspection when utilizing the parameters $K = 400$ and $\lambda = 0.5$. Consequently, we chose this set of parameters.

The window size is a crucial parameter that can determine the tradeoff between time resolution and estimation results. Previous related studies have empirically converged to window size values between 30 and 240 s (Hutchison et al., 2013; Preti et al., 2017). Additionally, Savva et al. (2019) suggested window size of at least 120 s to ensure the reproducibility of the result. Hence, we selected a window width of 60TRs (132 s).

5.4. Association between dynamic functional network and movie annotations

To quantify the dynamic changes of spatial patterns of FBNs, we employed two methods including calculating the number of activated voxels (NAV) and the intensity of activated voxels (IAV) of each FBN across all windows, respectively. Specifically, NAV was derived by counting the number of all voxels exceeding the threshold value ($z = 1.65$), while IAV was obtained by averaging the intensities of all voxels above this threshold. The group-wise NAV/IAV was derived by computing the average value of the NAV/IAV across all individuals.

The sliding window method produced 470 DFNs with a window length of 60 TRs and a step size of 1. Correspondingly, the duration of the scan was 530 TRs, with each TR corresponding to an annotation, resulting in 530 movie annotations in total. To establish correspondence between the DFNs and movie annotations, we selected the movie annotations occurring at the center point of each temporal window to correspond to each DFN based on previous studies (Simony et al., 2016; Tzachor and Hoshen, 2022). Specifically, we focused on a segment of movie annotations spanning from 31 to 500 TRs and examined their correlations with corresponding 470 dynamic FBNs.

The Spearman correlation coefficient between group-wise NAV/IAV and annotation vectors was computed to explore the association between group-wise dynamic changes in spatial patterns of FBNs and movie annotations, which were constructed for Language, Changepoint, Positive Scenes, Negative Scenes Positive Faces, and Negative Faces. Movie annotations were converted to vectors of 0 and 1 based on their onset and offset times (Supplementary Figure S6). To establish the statistical significance of the observed correlations, the correlation between the group-wise NAV/IAV and annotation vector was re-calculated 5,000 times by shuffling the vectors in each iteration. The observed correlation was compared with a null distribution of correlation generated by 5,000 permutations. If the observed correlation falls in the extreme tails of the distribution (i.e., the value of p is less than 0.05), we can conclude that there is a significant difference in group-wise NAV/IAV and movie annotation.

5.5. Dynamic inter-subject correlation

Inter-subject correlation (ISC) analysis measures the inter-subject consistency for temporal responses across participants (Hasson et al., 2004; Di and Biswal, 2020). To evaluate the ISC of dynamic FBNs, we first used the group-wise static FBNs as masks to extract the time-series signals of the corresponding FBN for each participant. Next, we averaged all the time-series signals within FBN, resulting in the FBN-level time-series signals for each FBN. Subsequently, we also applied the sliding window strategy and calculated the ISC of the FBN-level time-series signals in each time window for each subject, where the time window size was set to the same value as that in the "Dynamic sparse representation" section (i.e., 60TRs). Consequently, we derived the dynamic ISC metric for each subject for each representative FBN. To calculate the dynamic group-wise ISC metric, we performed Fisher z-transformation on the ISC values of all subjects for each window and subsequently averaged the ISC value across all individuals for each window.

5.6. Movie rating representation

The study employed a post-movie questionnaire to collect participants' subjective appraisals of the movie, which consisted of eight questions. However, the RSA analysis excluded four questions because there was insufficient variability among participants (Supplementary Data). The remaining four questions are more focused on evaluating the movie subjectively, that is, how participants rated their feeling during the first movie session, including boredom, enjoyment, feeling happy or sad, and audio quality. Regarding question 4, specifically, the audio quality does not vary while recording, and each participant said they all had a comparable understanding of the movie's plot. The participants' level of engagement may have influenced how they rated the

scale. All questions in the survey utilized a 1 to 5 rating scale. To represent participant differences in movie ratings, we employed a multidimensional scaling method to map responses to the questionnaire onto a two-dimensional representation.

5.7. The link between movie ratings and dynamic ISC

Inter-subject representational similarity analysis (IS-RSA) is a promising approach for examining the potential relationship between inter-subject variability in brain dynamics and individual differences in behavioral disposition (Kriegeskorte et al., 2008; Finn et al., 2020; Meer et al., 2020). Thus, we conducted the IS-RSA to assess the correlation between post-hoc behavioral movie ratings and dynamic ISC distances across all subjects.

We constructed inter-subject distance matrices to represent movie impressions and dynamic ISC. Specifically, inter-subject distances for movie impressions were calculated by measuring the Euclidean distance of questionnaire ratings between each possible pair of participants, resulting in 16 (number of participants) × 15 matrices. To examine the dynamics ISC distance, we calculated the Pearson distance between the dynamics ISC matrices for every possible pair of participants, producing a dynamic ISC distance matrix of size 16 × 15.

To assess the strength of associations between the movie ratings and dynamic ISC, we calculated the Spearman correlation between the lower triangular parts of the above two distance matrices. To assess the statistical significance of the results, we performed permutation testing 5,000 times. For each iteration, we squeezed the two matrices, dynamics ISC distance and movie rating distance, into row vectors, and randomly selected a new starting point for each row vector. This procedure allowed us to generate a null distribution of correlations and determine whether the observed correlation was significant.

5.8. Test–retest reliability of DFNs

To assess the level of reliability of dynamic FBNs during the natural viewing conditions, we calculated the test–retest reliability of the matching dynamic FBNs across two sessions. Specifically, we measured the intra-group correlation coefficient (ICC) for each window to determine the level of consistency in the FBNs across time (Shrout and Fleiss, 1979; McGraw and Wong, 1996). For comparison, we also calculated the static test–retest reliability of FBNs by calculating ICC over the entire period. ICC can be defined by the following equation:

$$\mathrm{ICC} = \frac{\mathrm{MS}_p - \mathrm{MS}_e}{\mathrm{MS}_p + (\mathrm{d}-1)\mathrm{MS}_e} \quad (2)$$

Here, d refers to the number of observations, which in our study was equal to 2. MS_p represents the mean square variation between subjects, while MS_e represents the mean square variation within subjects. The test–retest reliability was divided into five levels: excellent (ICC > 0.8), good (ICC 0.6–0.79), moderate (ICC 0.4–0.59), fair (ICC 0.2–0.39), and poor (ICC < 0.2). The test–retest reliability was assessed at the scan-wise level, and the methodology for this process was carried out in accordance with the previous study (Guo et al., 2012; Wang et al., 2017).

Data availability statement

The original contributions presented in the study are included in the article/Supplementary material, further inquiries can be directed to the corresponding author.

Ethics statement

Ethical review and approval was not required for the study on human participants in accordance with the local legislation and institutional requirements. The patients/participants provided their written informed consent to participate in this study.

Author contributions

LS and YR contributed to the conception and design of the study. LS, YR, and JN drafted the manuscript and performed the research. LS and KW contributed to analyzing the data. YH and XH contributed to supervision, writing review, and editing. All authors contributed to the article and approved the submitted version.

Funding

This work was supported by the National Natural Science Foundation of China (Grant Nos. 62006187, 61971350, and 12271434), the Youth Innovation Team Foundation of Education Department of Shaanxi Province Government (Grant No. 21JP119), the China Postdoctoral Science Foundation Funded Project (Grant No. 2021M702650), the Natural Science Basic Research Program of Shaanxi (Grant No. 2023-JC-JQ-57), and the Key Research and Development Program Project of Shaanxi Province (Grant No. 2020SF-036).

Conflict of interest

The authors declare that the research was conducted in the absence of any commercial or financial relationships that could be construed as a potential conflict of interest.

Publisher's note

Supplementary material

The Supplementary material for this article can be found online at: https://www.frontiersin.org/articles/10.3389/fnins.2023.1199150/full#supplementary-material

References

Allen, E. A., Damaraju, E., Plis, S. M., Erhardt, E. B., Eichele, T., and Calhoun, V. D. (2014). Tracking whole-brain connectivity dynamics in the resting state. *Cereb. Cortex* 24, 663–676. doi: 10.1093/cercor/bhs352

Barrett, L. F., and Satpute, A. B. (2013). Large-scale brain networks in affective and social neuroscience: towards an integrative functional architecture of the brain. *Curr. Opin. Neurobiol.* 23, 361–372. doi: 10.1016/j.conb.2012.12.012

Belitski, A., Gretton, A., Magri, C., Murayama, Y., Montemurro, M. A., Logothetis, N. K., et al. (2008). Low-frequency local field potentials and spikes in primary visual cortex convey independent visual information. *J. Neurosci.* 28, 5696–5709. doi: 10.1523/JNEUROSCI.0009-08.2008

Benesty, J., Chen, J., Huang, Y., and Cohen, I. (2009). "Pearson correlation coefficient" in *Noise reduction in speech processing*. eds. I. Cohen, Y. Huang, J. Chen, and J. Benesty (Berlin, Heidelberg: Springer), 1–4.

Buckner, R. L., Krienen, F. M., and Yeo, B. T. (2013). Opportunities and limitations of intrinsic functional connectivity MRI. *Nat. Neurosci.* 16, 832–837. doi: 10.1038/nn.3423

Calhoun, V. D., Miller, R., Pearlson, G., and Adali, T. (2014). The chronnectome: time-varying connectivity networks as the next frontier in fMRI data discovery. *Neuron* 84, 262–274. doi: 10.1016/j.neuron.2014.10.015

Carroll, J. D., and Arabie, P. (1998). "Multidimensional scaling" in *Measurement, judgment and decision making*. ed. M. H. Birnbaum (Cambridge, MA: Academic Press), 179–250.

Chan, H. Y., Smidts, A., Schoots, V. C., Dietvorst, R. C., and Boksem, M. A. S. (2019). Neural similarity at temporal lobe and cerebellum predicts out-of-sample preference and recall for video stimuli. *NeuroImage* 197, 391–401. doi: 10.1016/j.neuroimage.2019.04.076

Choe, A. S., Nebel, M. B., Barber, A. D., Cohen, J. R., Xu, Y., Pekar, J. J., et al. (2017). Comparing test-retest reliability of dynamic functional connectivity methods. *NeuroImage* 158, 155–175. doi: 10.1016/j.neuroimage.2017.07.005

Di, X., and Biswal, B. B. (2020). Intersubject consistent dynamic connectivity during natural vision revealed by functional MRI. *NeuroImage* 216:116698. doi: 10.1016/j.neuroimage.2020.116698

Finn, E. S., Glerean, E., Khojandi, A. Y., Nielson, D., Molfese, P. J., Handwerker, D. A., et al. (2020). Idiosynchrony: from shared responses to individual differences during naturalistic neuroimaging. *NeuroImage* 215:116828. doi: 10.1016/j.neuroimage.2020.116828

Friston, K. J., Holmes, A. P., Worsley, K. J., Poline, J. P., Frith, C. D., and Frackowiak, R. S. (1994). Statistical parametric maps in functional imaging: a general linear approach. *Hum. Brain Mapp.* 2, 189–210. doi: 10.1002/hbm.460020402

Ge, F., Lv, J, Hu, X., Guo, L., Han, J., Zhao, S., et al. (2018). Exploring intrinsic networks and their interactions using group wise temporal sparse coding. In International Symposium on Biomedical Imaging (ISBI 2018) (Washington, D.C., USA, IEEE Xplore).

Ge, B., Wang, H., Wang, P., Tian, Y., Zhang, X., and Liu, T. (2020). Discovering and characterizing dynamic functional brain networks in task FMRI. *Brain Imaging Behav.* 14, 1660–1673. doi: 10.1007/s11682-019-00096-6

Golland, Y., Bentin, S., Gelbard, H., Benjamini, Y., Heller, R., Nir, Y., et al. (2007). Extrinsic and intrinsic systems in the posterior cortex of the human brain revealed during natural sensory stimulation. *Cereb. cortex* 17, 766–777. doi: 10.1093/cercor/bhk030

Gottwald, B., Mihajlovic, Z., Wilde, B., and Mehdorn, H. M. (2003). Does the cerebellum contribute to specific aspects of attention? *Neuropsychologia* 41, 1452–1460. doi: 10.1016/S0028-3932(03)00090-3

Guo, C. C., Kurth, F., Zhou, J., Mayer, E. A., Eickhoff, S. B., Kramer, J. H., et al. (2012). One-year test-retest reliability of intrinsic connectivity network fMRI in older adults. *NeuroImage* 61, 1471–1483. doi: 10.1016/j.neuroimage.2012.03.027

Hasson, U., Nir, Y., Levy, I., Fuhrmann, G., and Malach, R. (2004). Intersubject synchronization of cortical activity during natural vision. *Science* 303, 1634–1640. doi: 10.1126/science.1089506

Heleven, E., van Dun, K., and Van Overwalle, F. (2019). The posterior cerebellum is involved in constructing social action sequences: an fMRI study. *Sci. Rep.* 9, 1–11. doi: 10.1038/s41598-019-46962-7

Hutchison, R. M., Womelsdorf, T., Allen, E. A., Bandettini, P. A., Calhoun, V. D., Corbetta, M., et al. (2013). Dynamic functional connectivity: promise, issues, and interpretations. *NeuroImage* 80, 360–378. doi: 10.1016/j.neuroimage.2013.05.079

Jaaskelainen, I. P., Sams, M., Glerean, E., and Ahveninen, J. (2021). Movies and narratives as naturalistic stimuli in neuroimaging. *NeuroImage* 224:117445. doi: 10.1016/j.neuroimage.2020.117445

Jilka, S. R., Scott, G., Ham, T., Pickering, A., Bonnelle, V., Braga, R. M., et al. (2014). Damage to the salience network and interactions with the default mode network. *J. Neurosci.* 34, 10798–10807. doi: 10.1523/JNEUROSCI.0518-14.2014

Kellermann, T., Regenbogen, C., De Vos, M., Mößnang, C., Finkelmeyer, A., and Habel, U. (2012). Effective connectivity of the human cerebellum during visual attention. *J. Neurosci.* 32, 11453–11460. doi: 10.1523/JNEUROSCI.0678-12.2012

Kelly, A. C., Uddin, L. Q., Biswal, B. B., Castellanos, F. X., and Milham, M. P. (2008). Competition between functional brain networks mediates behavioral variability. *NeuroImage* 39, 527–537. doi: 10.1016/j.neuroimage.2007.08.008

Kriegeskorte, N., Mur, M., and Bandettini, P. A. (2008). Representational similarity analysis-connecting the branches of systems neuroscience. *Front. Syst. Neurosci.* 2:4. doi: 10.3389/neuro.06.004.2008

Liegeois, R., Laumann, T. O., Snyder, A. Z., Zhou, J., and Yeo, B. T. T. (2017). Interpreting temporal fluctuations in resting-state functional connectivity MRI. *NeuroImage* 163, 437–455. doi: 10.1016/j.neuroimage.2017.09.012

Lurie, D. J., Kessler, D., Bassett, D. S., Betzel, R. F., Breakspear, M., Kheilholz, S., et al. (2020). Questions and controversies in the study of time-varying functional connectivity in resting fMRI. *Netw. Neurosci.* 4, 30–69. doi: 10.1162/netn_a_00116

Lv, J. (2013). Identifying functional networks via sparse coding of whole brain FMRI signals. In Annual International IEEE EMBS Conference on Neural Engineering (San Diego, California, IEEE), pp. 778–781.

Lv, J., Jiang, X., Li, X., Zhu, D., Chen, H., Zhang, T., et al. (2015a). Sparse representation of whole-brain fMRI signals for identification of functional networks. *Med. Image Anal.* 20, 112–134. doi: 10.1016/j.media.2014.10.011

Lv, J., Jiang, X., Li, X., Zhu, D., Zhang, S., Zhao, S., et al. (2015b). Holistic atlases of functional networks and interactions reveal reciprocal organizational architecture of cortical function. *IEEE Trans. Biomed. Eng.* 62, 1120–1131. doi: 10.1109/TBME.2014.2369495

Ma, S., Calhoun, V. D., Phlypo, R., and Adalı, T. (2014). Dynamic changes of spatial functional network connectivity in healthy individuals and schizophrenia patients using independent vector analysis. *NeuroImage* 90, 196–206. doi: 10.1016/j.neuroimage.2013.12.063

McGraw, K. O., and Wong, S. P. (1996). Forming inferences about some intraclass correlation coefficients. *Psychol. Methods* 1, 30–46. doi: 10.1037/1082-989X.1.1.30

Meer, J. N. V., Breakspear, M., Chang, L. J., Sonkusare, S., and Cocchi, L. (2020). Movie viewing elicits rich and reliable brain state dynamics. *Nat. Commun.* 11:5004. doi: 10.1038/s41467-020-18717-w

Menon, V., and Uddin, L. Q. (2010). Saliency, switching, attention and control: a network model of insula function. *Brain Struct. Funct.* 214, 655–667. doi: 10.1007/s00429-010-0262-0

Monti, R. P., Hellyer, P., Sharp, D., Leech, R., Anagnostopoulos, C., and Montana, G. (2014). Estimating time-varying brain connectivity networks from functional MRI time series. *NeuroImage* 103, 427–443. doi: 10.1016/j.neuroimage.2014.07.033

Nguyen, V. T., Sonkusare, S., Stadler, J., Hu, X., Breakspear, M., and Guo, C. C. (2017). Distinct cerebellar contributions to cognitive-perceptual dynamics during natural viewing. *Cereb. Cortex* 27, 5652–5662. doi: 10.1093/cercor/bhw334

Park, H. J., and Friston, K. (2013). Structural and functional brain networks: from connections to cognition. *Science* 342:1238411. doi: 10.1126/science.1238411

Pelletier-Baldelli, A., Bernard, J. A., and Mittal, V. A. (2015). Intrinsic functional connectivity in salience and default mode networks and aberrant social processes in youth at ultra-high risk for psychosis. *PLoS One* 10:e0134936. doi: 10.1371/journal.pone.0134936

Ponce, J. M. F. B. J., and Sapiro, G. (2010). Online learning for matrix factorization and sparse coding. *J. Mach. Learn. Res.* 11, 19–60. doi: 10.48550/arXiv.0908.0050

Preti, M. G., Bolton, T. A. W., and Van De Ville, D. (2017). The dynamic functional connectome: state-of-the-art and perspectives. *NeuroImage* 160, 41–54. doi: 10.1016/j.neuroimage.2016.12.061

Raichle, M. E. (2006). The brain's dark energy. *Science* 314, 1249–1250. doi: 10.1126/science.1134405

Ren, Y., Lv, J., Guo, L., Fang, J., and Guo, C. C. (2017a). Sparse coding reveals greater functional connectivity in female brains during naturalistic emotional experience. *PLoS One* 12:e0190097. doi: 10.1371/journal.pone.0190097

Ren, Y., Nguyen, V. T., Guo, L., and Guo, C. C. (2017b). Inter-subject functional correlation reveal a hierarchical organization of extrinsic and intrinsic systems in the brain. *Sci. Rep.* 7:10876. doi: 10.1038/s41598-017-11324-8

Rubinov, M., and Sporns, O. (2010). Complex network measures of brain connectivity: uses and interpretations. *NeuroImage* 52, 1059–1069. doi: 10.1016/j.neuroimage.2009.10.003

Saarimaki, H. (2021). Naturalistic stimuli in affective neuroimaging: a review. *Front. Hum. Neurosci.* 15:675068. doi: 10.3389/fnhum.2021.675068

Savva, A. D., Mitsis, G. D., and Matsopoulos, G. K. (2019). Assessment of dynamic functional connectivity in resting-state fMRI using the sliding window technique. *Brain Behav.* 9:e01255. doi: 10.1002/brb3.1255

Schwartz, G. E., and Davidson, R. J. (1997). Neuroanatomical correlates of happiness, sadness, and disgust. *Am. J. Psychiatry* 154, 926–933. doi: 10.1176/ajp.154.7.926

Shine, J. M., Bissett, P. G., Bell, P. T., Koyejo, O., Balsters, J. H., Gorgolewski, K. J., et al. (2016). The dynamics of functional brain networks: integrated network states during cognitive task performance. *Neuron* 92, 544–554. doi: 10.1016/j.neuron.2016.09.018

Shrout, P. E., and Fleiss, J. L. (1979). Intraclass correlations: uses in assessing rater reliability. *Psychol. Bull.* 86, 420–428. doi: 10.1037/0033-2909.86.2.420

Simony, E., Honey, C. J., Chen, J., Lositsky, O., Yeshurun, Y., Wiesel, A., et al. (2016). Dynamic reconfiguration of the default mode network during narrative comprehension. *Nat. Commun.* 7:12141. doi: 10.1038/ncomms12141

Sonkusare, S., Breakspear, M., and Guo, C. (2019). Naturalistic stimuli in neuroscience: critically acclaimed. *Trends Cogn. Sci.* 23, 699–714. doi: 10.1016/j.tics.2019.05.004

Tagliazucchi, E., and Laufs, H. (2014). Decoding wakefulness levels from typical fMRI resting-state data reveals reliable drifts between wakefulness and sleep. *Neuron* 82, 695–708. doi: 10.1016/j.neuron.2014.03.020

Tian, L., Ye, M., Chen, C., Cao, X., and Shen, T. (2021). Consistency of functional connectivity across different movies. *NeuroImage* 233:117926. doi: 10.1016/j.neuroimage.2021.117926

Tononi, G., Sporns, O., and Edelman, G. M. (1996). A complexity measure for selective matching of signals by the brain. *Proc. Natl. Acad. Sci.* 93, 3422–3427. doi: 10.1073/pnas.93.8.3422

Turner, B. M., Paradiso, S., Marvel, C. L., Pierson, R., Ponto, L. L. B., Hichwa, R. D., et al. (2007). The cerebellum and emotional experience. *Neuropsychologia* 45, 1331–1341. doi: 10.1016/j.neuropsychologia.2006.09.023

Tzachor, I., and Hoshen, Y. (2022). Window projection features are all you need for time series anomaly detection. In ICLR 2023 Conference Withdrawn Submission.

Van Dijk, K. R., Sabuncu, M. R., and Buckner, R. L. (2012). The influence of head motion on intrinsic functional connectivity MRI. *NeuroImage* 59, 431–438. doi: 10.1016/j.neuroimage.2011.07.044

Van Overwalle, F., Ma, Q., and Heleven, E. (2020a). The posterior crus II cerebellum is specialized for social mentalizing and emotional self-experiences: a meta-analysis. *Soc. Cogn. Affect. Neurosci.* 15, 905–928. doi: 10.1093/scan/nsaa124

Van Overwalle, F., Van de Steen, F., van Dun, K., and Heleven, E. (2020b). Connectivity between the cerebrum and cerebellum during social and non-social sequencing using dynamic causal modelling. *NeuroImage* 206:116326. doi: 10.1016/j.neuroimage.2019.116326

Verger, A., Rousseau, P. F., Malbos, E., Chawki, M. B., Nicolas, F., Lancon, C., et al. (2020). Involvement of the cerebellum in EMDR efficiency: a metabolic connectivity PET study in PTSD. *Eur. J. Psychotraumatol.* 11:1767986. doi: 10.1080/20008198.2020.1767986

Wang, J., Ren, Y., Hu, X., Nguyen, V. T., Guo, L., Han, J., et al. (2017). Test-retest reliability of functional connectivity networks during naturalistic fMRI paradigms. *Hum. Brain Mapp.* 38, 2226–2241. doi: 10.1002/hbm.23517

Yeo, B. T., Krienen, F. M., Sepulcre, J., Sabuncu, M. R., Lashkari, D., Hollinshead, M., et al. (2011). The organization of the human cerebral cortex estimated by intrinsic functional connectivity. *J. Neurophysiol.* 106, 1125–1165. doi: 10.1152/jn.00338.2011

Zhang, S., Li, X., Guo, L., and Liu, T. (2017). Exploring human brain activation via nested sparse coding and functional operators. In International Symposium on Biomedical Imaging (ISBI 2017) (Melbourne, VIC, Australia, IEEE).

Zhang, X., Liu, J., Yang, Y., Zhao, S., Guo, L., Han, J., et al. (2021). Test–retest reliability of dynamic functional connectivity in naturalistic paradigm functional magnetic resonance imaging. *Hum. Brain Mapp.* 43, 1463–1476. doi: 10.1002/hbm.25736

frontiers | Frontiers in Neuroscience

TYPE Original Research
PUBLISHED 28 July 2023
DOI 10.3389/fnins.2023.1206604

OPEN ACCESS

EDITED BY
Bin Jing,
Capital Medical University, China

REVIEWED BY
Cory Alcon,
High Point University, United States
Sharon Wang-Price,
Texas Woman's University, United States
Lijiang Wei,
Beijing Normal University, China

*CORRESPONDENCE
Min Fang
✉ fm-tn0510@shutcm.edu.cn

†These authors have contributed equally to this work and share first authorship

RECEIVED 16 April 2023
ACCEPTED 13 July 2023
PUBLISHED 28 July 2023

CITATION
Tang C, Guo G, Fang S, Yao C, Zhu B, Kong L, Pan X, Li X, He W, Wu Z and Fang M (2023) Abnormal brain activity in lumbar disc herniation patients with chronic pain is associated with their clinical symptoms. *Front. Neurosci.* 17:1206604. doi: 10.3389/fnins.2023.1206604

Abnormal brain activity in lumbar disc herniation patients with chronic pain is associated with their clinical symptoms

Cheng Tang[1†], Guangxin Guo[2,3†], Sitong Fang[1], Chongjie Yao[2], Bowen Zhu[1], Lingjun Kong[1], Xuanjin Pan[2], Xinrong Li[2], Weibin He[4], Zhiwei Wu[5,6] and Min Fang[1,5*]

[1]Shuguang Hospital, Shanghai University of Traditional Chinese Medicine, Shanghai, China, [2]School of Acupuncture-Moxibustion and Tuina, Shanghai University of Traditional Chinese Medicine, Shanghai, China, [3]Shanghai Municipal Hospital of Traditional Chinese Medicine, Shanghai University of Traditional Chinese Medicine, Shanghai, China, [4]Department of Neurosurgery, Renmin Hospital of Wuhan University, Wuhan, China, [5]Research Institute of Tuina, Shanghai Academy of Traditional Chinese Medicine, Shanghai, China, [6]Yueyang Hospital of Integrated Chinese and Western Medicine, Shanghai University of Traditional Chinese Medicine, Shanghai, China

Introduction: Lumbar disc herniation, a chronic degenerative disease, is one of the major contributors to chronic low back pain and disability. Although many studies have been conducted in the past on brain function in chronic low back pain, most of these studies did not classify chronic low back pain (cLBP) patients according to their etiology. The lack of etiologic classification may lead to inconsistencies between findings, and the correlation between differences in brain activation and clinical symptoms in patients with cLBP was less studied in the past.

Methods: In this study, 36 lumbar disc herniation patients with chronic low back pain (LDHCP) and 36 healthy controls (HCs) were included to study brain activity abnormalities in LDHCP. Visual analogue scale (VAS), oswestry disability index (ODI), self-rating anxiety scale (SAS), self-rating depression scale (SDS) were used to assess clinical symptoms.

Results: The results showed that LDHCP patients exhibited abnormally increased and diminished activation of brain regions compared to HCs. Correlation analysis showed that the amplitude of low frequency fluctuations (ALFF) in the left middle frontal gyrus is negatively correlated with SAS and VAS, while the right superior temporal gyrus is positively correlated with SAS and VAS, the dorsolateral left superior frontal gyrus and the right middle frontal gyrus are negatively correlated with VAS and SAS, respectively.

Conclusion: LDHCP patients have brain regions with abnormally increased and abnormally decreased activation compared to healthy controls. Furthermore, some of the abnormally activated brain regions were correlated with clinical pain or emotional symptoms.

KEYWORDS

lumbar disc herniation, chronic low back pain, resting-state functional magnetic resonance, amplitude of low-frequency fluctuations, anxiety, prefrontal lobe

Introduction

Chronic low back pain (cLBP), as a common clinical disease, is one of the leading causes of disability (Wang et al., 2022) and remains a major medical and social problem worldwide. The 2019 Global Burden of Disease Study pointed out that approximately 568.4 million people suffer from cLBP (Chen et al., 2022). One of the major factors causing chronic low back pain is lumbar disc herniation (LDH). As clinical neuropathic pain, LDH is mainly due to intervertebral disc injuries and degenerative changes with age. Rupture of the fibrous ring and protrusion of the nucleus pulposus tissue causes physical compression of the paravertebral nerve roots, which results in low back pain and dysfunction (Martin et al., 2002; Wang et al., 2021). On the other hand, the immune system will recognize the exposed nucleus pulposus and produce multiple proinflammatory factors, including interleukin-1, prostaglandin E2, 5-hydroxytryptamine, and tumor necrosis factor, to increase the sensitivity and extent of pain (Zhao et al., 2019). Studies have found that negative emotions, such as anxiety and depression, can exacerbate pain, with the increasing severity and duration of chronic pain (Sheng and Zhang, 2019; Li et al., 2021; Kao et al., 2022). A study on the chronic pain model of LDH also pointed out that LDH is often accompanied by depression, especially in females with severe pain and a longer course of the disease (Cai et al., 2019). As one of the main specificity factors of cLBP, LDH is frequently lack of compatibility between the severity of lumbar spine CT/MRI findings and clinical symptoms in clinical practice. For example, some patients have a large herniated nucleus pulposus but no significant clinical symptoms, while others have unbearable pain, weakness, and other clinical symptoms with only a bulging lumbar disc. We speculate that the emotional state of the patient regarding LDHCP may be an important factor in this phenomenon. Emotional experiences and psychological states can influence clinical pain symptoms through functional and structural changes in the central nervous system and should therefore also be taken into account in the diagnosis and treatment of LDH (Mu et al., 2019; Price and Duman, 2020).

As scientific exploration of the brain continues to extend, more and more imaging techniques are making it possible to accurately assess pain and emotional interactions. The amplitude of low frequency fluctuation (ALFF), regional homogeneity, and functional connectivity are commonly used to assess pathological changes in functional magnetic resonance imaging (fMRI) studies. These neuroimaging methods can quantify and visualize higher central changes in cLBP (Weizman et al., 2018; Huang et al., 2020; Li et al., 2020). However, previous fMRI studies have mostly failed to classify cLBP specifically or nonspecifically according to etiology, which may make the findings somewhat controversial. For example, Zhang et al. reported that cLBP patients' ALFF is increased in the post−/precentral gyrus, paracentral lobule (PCL)/supplementary motor area (SMA), and PCL/SMA ALFF reliably discriminated cLBP patients from HCs in an independent cohort (Zhang et al., 2019). Another team argued that cLBP patients had reduced ALFF in the right posterior cingulate cortex/precuneus cortex and left primary somatosensory cortex (S1), but elevated ALFF in the right medial prefrontal cortex, right middle temporal gyrus, bilateral inferior temporal gyrus, bilateral insula, and left cerebellum (Zhang et al., 2017). Thus, it is important to classify whether chronic low back pain is a specific etiology or not. It has been reported that cerebellar associated with injury perception and endogenous pain modulation, inhibitory cerebellar t-DCS would increase pain perception and reduced endogenous pain inhibition while excitatory cerebellar t-DCS increased endogenous pain inhibition (Stacheneder et al., 2022). Similarly, we can try to find the specific brain regions with altered brain function in LDHCP and conduct interventional longitudinal studies on the corresponding brain regions in subsequent studies. Studying its pain-causing brain function pathological features by fMRI analysis methods would help LDH clinical diagnosis and treatment, but regretfully there are few corresponding studies. Among fMRI analysis methods, ALFF can directly reflect the magnitude of baseline changes in the brain blood oxygen level-dependent effect (BOLD) signal and indirectly indicate the intensity of local neuronal spontaneous activity in the brain. ALFF is considered to be one of the most common methods for observing changes in brain function at rest and is widely used in brain function studies of pain-related diseases (Zang, 2016; Du et al., 2018; Pan et al., 2018; Ge et al., 2022). Therefore, we used a data-driven ALFF analysis to explore differences in brain activity between patients with lumbar disc herniation chronic low back pain (LDHCP) and healthy controls (HCs). The Visual Analog Scale (VAS), Oswestry Disability Index (ODI), Self-Rated Anxiety Scale (SAS), and Self-Rated Depression Scale (SDS) were used to assess clinical symptoms and explore their association with abnormal brain regions in LDHCP. We hypothesized that LDHCP will result in abnormal brain activity and the abnormal brain activity in LDHCP would be related to their clinical symptoms.

Materials and methods

Subjects

36 LDHCP patients were recruited at Yueyang Hospital of Integrated Traditonal Chinese and Western Medicine, Shanghai University of Traditonal Chinese Medicine (Shanghai, China) from December 2021 to December 2022. The clinical trial was registered on November 24, 2021 at the China Clinical Trials Registry with registration number ChiCTR2100053542. 36 age-and sex-matched HCs were recruited from communities. All subjects underwent Mini-mental State Examination (MMSE) test prior to enrollment to ensure the subjects were cognitively normal.

The inclusive criteria of LDHCP were as follows: (1) Age between 18 and 65 years, right-handed; (2) CT or MRI shows herniated disc in the lumbar spine and suffering from low back pain for at least 3 months or longer; (3) VAS score $\geq$ 30/100 points; (4) ODI score $\geq$ 20/100 points; and (5) not receiving pain therapy for at least 1 month before our enrollment. The inclusive criteria of HCs were as follows: (1) aged between 20 and 65 years; (2) right-handed; (3) no LDH history and related symptoms; and (4) without negative emotions.

The exclusive criteria were used for both HC and LDHCP groups: (1) subjects with organic brain lesions or history of brain surgery; (2) subjects with contraindications to MRI; (3) pregnant or lactating subjects; (4) subjects with alcohol or drug dependence; (5) subjects with other serious co-morbidities; and (6) subjects with an MMSE score less of than 27 points (Folstein et al., 1975).

Clinical assessment

This study used VAS, ODI, SAS, SDS to assess LDHCP's somatic pain, functional activity and related anxiety and depression status. VAS is reliable in assessing the severity of low back pain and in

predicting disability (Thong et al., 2018; Shafshak and Elnemr, 2021). VAS divides the pain level evenly on a straight line with 10 scales into two endpoints: no pain and extreme pain, corresponding to scores of 0 and 10, respectively. ODI is a effective and validated scale for measuring disability in patients with low back pain and has high-quality psychometric properties in terms of construct validity, test–retest reliability and internal consistency (Chapman et al., 2011; Sheahan et al., 2015; Arpinar et al., 2020). It consists of 10 scoring items, namely back pain and leg pain, personal care, lifting heavy objects, walking, sitting, standing, sleeping, sexual life, social life, and traveling. The patient's performance in each item is scored on a scale of 6 degrees from mild to severe, corresponding to grades 0 to 5 points. The SAS is very similar to the SDS and is a fairly simple clinical tool for analyzing patients' subjective symptoms (Thurber et al., 2002; Dunstan and Scott, 2020). It is suitable for adults with symptoms of anxiety or depression and has a wide range of applications. SAS has high reliability estimates while SDS has good sensitivity and specificity (Knight et al., 1983; Turner and Romano, 1984). It is important to emphasize that SAS and SDS tests are performed within 1 h prior to each MRI to quantify the subject's state of mind as much as possible.

Magnetic resonance imaging data acquisition

Magnetic resonance imaging was performed by a 3.0T SIEMENS MAGNETOM (Germany) with a 32 channel head coil at Yueyang Hospital of Integrated Traditional Chinese and Western Medicine Affiliated to Shanghai University of Traditional Chinese Medicine, China. All subjects wore cotton earplugs to reduce noise interference and their heads were fixed with a soft foam pad to reduce head movement bias. During the MRI scan, all subjects were asked to remain awake and relaxed, with no excessive head movements or mental activity allowed, otherwise the data collected would not be included in the study. The scanning parameters were set as follows: (1) functional MRI: 33 interleaved axial slices, matrix size = 64 × 64, field of view (FOV) = 220 mm × 220 mm, repetition time (TR) = 2,000 ms, echo time (TE) = 30 ms, flip angle = 90 degrees, slice thickness = 4 mm, gap = 0 (voxel size3.4 × 3.4 × 4.0), number of volumes = 240. (2) structural MRI: Sequence = SPGR, sagittal slices, slice number = 160, matrix size = 256 × 256, FOV = 256 × 256 mm, TR/TE = 1900/2.93 ms, flip angle = 9 degrees, slice thickness = 1, gap = 0 (voxel size = 1 × 1 × 1). After the scan, the subject was asked if he/she had fallen asleep during the scan and if he/she gave an accurate or vague answer, the subject's MRI data was also excluded. All scans were performed by the same MRI physician who had been formally trained by Siemens.

Data preprocessing

RESTplus (Resting-state fMRI data analysis Toolkit),[1] a brain imaging data processing and analysis software based on statistical parametric mapping (SPM12),[2] was used for rs-fMRI data preprocessing. The procedure was as follows: (1) convert the original Dicom files to NIFTI format; (2) remove the first 10 time points to stabilize the longitudinal magnetization; (3) slice timing to eliminate differences in acquisition times between adjacent scan levels; (4) realign to calibrate the subject's head position at different time points in the scan and remove data from patients with head motion >3 mm and rotation >3° in any direction; (5) normalizing to Montreal Neurological Institute (MNI) space by Diffeomorphic Anatomical Registration Through Exponentiated Lie Algebra (DARTEL) using T1 image new segment; (6) smoothing of the functional image aligned to the MNI standard space using a 6-mm full width at half maximum (FWHM) kernel; (7) detrending to reduce thermal interference from the MR coil and noise generated by the subject's personal factors (e.g., breathing, heartbeat, etc.); and (8) low-frequency filtering (Filter): 0.01–0.08 Hz signal is selected to filter the image for calculation to eliminate interference from other high-frequency signals.

Amplitude of low-frequency fluctuations calculation

ALFF values were calculated using RESTplus (Resting-state fMRI data analysis Toolkit, see text footnote 1). The procedure for calculating the ALFF for each voxel in the brain is as follows: (1) pass the time series of each voxel through a 0.01–0.08 Hz band-pass filter after removing the linear drift; (2) obtain the power spectrum by performing a fast Fourier change on the filter results; (3) square the power spectrum; (4) calculate the average of the power spectrum within 0.01–0.08 Hz as the ALFF; and (5) divide the ALFF divided by the average ALFF of all voxels in the whole brain to obtain the normalized ALFF (mALFF).

Statistical analysis

SPSS 24 (IBM, United States) was used for the statistical analysis of demographic and clinical data in this study. For the count data, frequency distributions were described and statistical differences between groups were analyzed using the chi-square test; for the measurement data, the *t*-test was used if the data conformed to a normal distribution, and if not, the Mann–Whitney *U* test for independent samples was used. Statistical tests were all performed using a two-tailed test, $\alpha = 0.05$, and differences were considered statistically significant if $p < 0.05$. Imaging data statistics were analyzed using SPM software. Voxel-by-voxel statistics were performed using a general linear model (GLM) with two-sample *t*-tests for subjects in both groups, with gender and age as covariates. Family-wise error (FWE) was used to correct the results for multiple comparisons, with a voxel-level significance threshold of $p < 0.001$ and a cluster-level significance threshold of $p < 0.05$. If the continuous variables conform to normality, Pearson correlation coefficient will be used to assess whether there is a correlation between signal values of brain region activity and clinical symptom scores. If the continuous variables do not conform to normality, correlations between indicators are calculated using the Spearman correlation method. $P < 0.05$ is the threshold of statistical difference for correlation analysis.

1 http://www.restfmri.net

2 http://www.fil.ion.ucl.ac.uk/spm

Results

Demographic and clinical data

A total of 72 participants were selected for this study, including 36 (12 male/24 female) LDHCP patients and 36 (14 male/22 female) HCs. Table 1 shows the demographic and clinical characteristics of the participants. As shown in Table 1, there were no significant differences in gender ($p = 0.624$), age ($p = 0.456$), weight ($p = 0.061$), occupation ($p = 0.551$), MMSE ($p = 0.11$) between LDHCP and HCs. Subjects in both groups were comparable.

TABLE 1 Demographic characteristics of the LDH and HC groups.

	LDHCP	HCs	*p*
Gender	12/24	14/22	0.624[a]
Age	38.58 ± 1.93	38.17 ± 2.48	0.456[b]
Weight (KG)	61 (55, 70)	69 (59, 74)	0.061[c]
Occupation	8/28	6/30	0.551[a]
(Physically / Non-physically)			
MMSE	27.02 ± 1.20	27.47 ± 0.99	0.11[b]
VAS	6 (5, 7)	/	NA
ODI	19 (14, 27)	/	NA
SAS	41.30 ± 0.92	/	NA
SDS	41.19 ± 1.39	/	NA

[a]χ^2-test; [b]Two sample t-test; [c]Non-parametric-tests.
LDHCP, Lumbar disc herniation patients with chronic pain; HCs, health controls; MMSE, Mini-mental State Examination; VAS, Visual Analog Scale; ODI, Oswestry Disability Index Questionnaire; SAS, self-rating anxiety scale; SDS, Self-rating depression scale.

Amplitude of low-frequency fluctuations analysis

In this study, there were differential brain areas with increased and decreased ALFF values in the LDHCP patients compared to the HC group (Figure 1A). Brain areas with increased ALFF were mainly located in Right inferior frontal gyrus, orbital part (Frontal_Inf_Orb_R); Right superior temporal gyrus (Temporal_Sup_R); Right lenticular nucleus, putamen (Putamen_R); Right rolandic operculum (Rolandic_Oper_R); Right Inferior frontal gyrus, opercular part (Frontal_Inf_Oper_R); (Table 2 and Figure 1B The brain area pointed by the green arrow); brain areas with decreased ALFF were mainly located in Left Superior frontal gyrus (Frontal_Sup_L), Left middle frontal gyrus (Frontal_Mid_L), Right middle frontal gyrus (Frontal_Mid_R), Left Precuneus (Precuneus_L), Right Supplementary motor area (Supp_Motor_Area_R) (Table 2 and Figure 1B The brain area pointed by the yellow arrow).

Clinical symptoms correlation

In LDHCP patients' clinical symptom scores, the VAS scores showed a significant Pearson correlation with the ODI scores and the SAS scores, respectively. The correlation coefficient between VAS and ODI is 0.47, $p = 0.034$ (Figure 2A) and between VAS and SAS scores is 0.40, $p = 0.014$ (Figure 2B).

Clinical-magnetic resonance imaging correlations

In LDHCP patients, Right superior temporal gyrus (Temporal_Sup_R) is positively correlated with VAS scores ($R = 0.42$, $p = 0.009$)

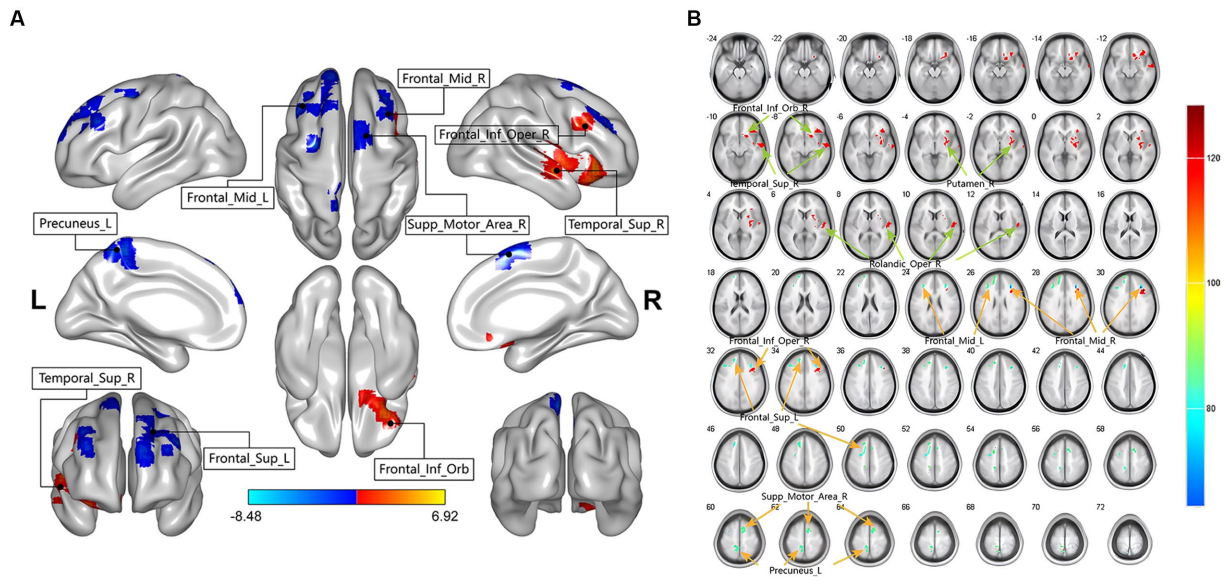

FIGURE 1
The two-sample t-test showing significant differences in mean-standardized amplitude of low-frequency fluctuations (mALFF) between LDHCP patients and HCs. The color bar indicates T-values. **(A)** Spatial location map of abnormally activated brain regions in LDHCP patients; **(B)** Layers section of abnormally activated brain regions in LDHCP patients.

TABLE 2 Brain region with a significant difference in mALFF between two groups.

Brain regions	Cluster size	Peak MNI coordinates			*t*-values	*P*
AAL	(voxels)	*x*	*y*	*z*		
LDHCP > HC						
Frontal_Inf_Orb_R	124	36	30	−9	5.9883	<0.001
Temporal_Sup_R	53	66	−9	−9	5.2409	0.017
Putamen_R	86	27	−9	0	4.9789	0.001
Rolandic_Oper_R	41	51	−15	9	5.2708	0.049
Frontal_Inf_Oper_R	44	36	21	30	6.9224	0.038
LDHCP < HC						
Frontal_Sup_L	114	−15	27	45	−5.3203	<0.001
Frontal_Mid_L	45	−36	27	30	−5.3483	0.034
Frontal_Mid_R	51	30	30	27	−8.4784	0.02
Precuneus_L	70	−9	−39	63	−4.8403	0.004
Supp_Motor_Area_R	56	9	3	63	−5.0943	0.013

Results were corrected for multiple comparisons using the Family Wise Error (FWE) with a cluster level significance threshold of $P < 0.05$. Frontal_Inf_Orb_R, Right inferior frontal gyrus, orbital part; Temporal_Sup_R, Right superior temporal gyrus; Putamen_R, Right lenticular nucleus; Rolandic_Oper_R, Right rolandic operculum; Frontal_Inf_Oper_R, Right Inferior frontal gyrus, opercular part; Frontal_Sup_L, Left Superior frontal gyrus; Frontal_Mid_L, Left middle frontal gyrus; Frontal_Mid_R, Right middle frontal gyrus; Precuneus_L, Left Precuneus; Supp_Motor_Area_R, Right Supplementary motor area.

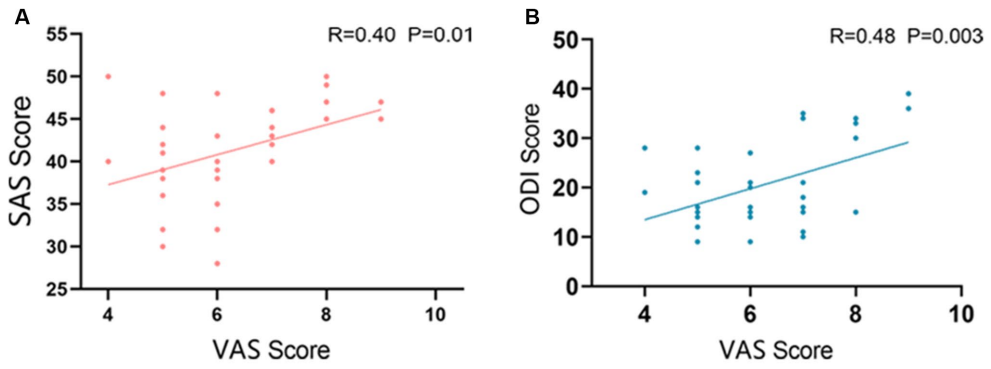

FIGURE 2
Correlation between clinical symptoms. **(A)** The correlation between VAS and ODI (R=0.47 *P*=0.034); **(B)** The correlation between VAS and SAS (R=0.40 *P*=0.014).

(Figure 3A); Right superior temporal gyrus (Temporal_Sup_R) is positively correlated with SAS ($R = 0.41$, $p = 0.012$) (Figure 3B); Left Superior frontal gyrus (Frontal_Sup_L) is negatively correlated with VAS scores ($R = -0.46$, $p = 0.004$) (Figure 3C); Left middle frontal gyrus (Frontal_Mid_L) is negatively correlated with VAS scores ($R = -0.35$, $p = 0.031$) (Figure 3D); Left middle frontal gyrus (Frontal_Mid_L) is negatively correlated with SAS scores ($R = -0.41$, $p = 0.01$) (Figure 3E); Right middle frontal gyrus (Frontal_Mid_R) is negatively correlated with SDS ($R = -0.32$, $p = 0.05$) (Figure 3F).

Discussion

This study is based on the 0.01–0.08 Hz classic frequency band in ALFF analysis to explore the brain regions where local neural activity changes in LDHCP patients compared with HC group and the possible links between these changes and clinical symptoms. In our study, we found that LDHCP patients have functional abnormalities in several brain regions in the resting state. Among them, the right superior temporal gyrus, the left dorsolateral superior frontal gyrus, and the left and right middle frontal gyrus were correlated with clinical pain or mood-related scores, respectively. Correlation analysis also found a significant correlation between VAS and ODI, but no correlation was found between brain regions and ODI. The absolute value of the correlation coefficient R ranged from 0.32 to 0.46, which was considered a low correlation in a mathematical sense. Several studies have pointed out that patients with chronic pain tend to have negative emotions. In turn, negative emotions such as anxiety, depression, fear and catastrophic beliefs contribute to the pain perception and disability of patients with chronic low back pain, affecting their life quality and functional status (Bletzer et al., 2017; Le Borgne et al., 2017; Serbic and Pincus, 2017; Koechlin et al., 2018). It is in accordance with our results of correlation between clinical symptoms.

In our study, the right superior temporal gyrus, left dorsolateral superior frontal gyrus, and left middle frontal gyrus of LDHCP patients are associated with VAS, while the right superior temporal gyrus and middle frontal gyrus are associated with anxiety or

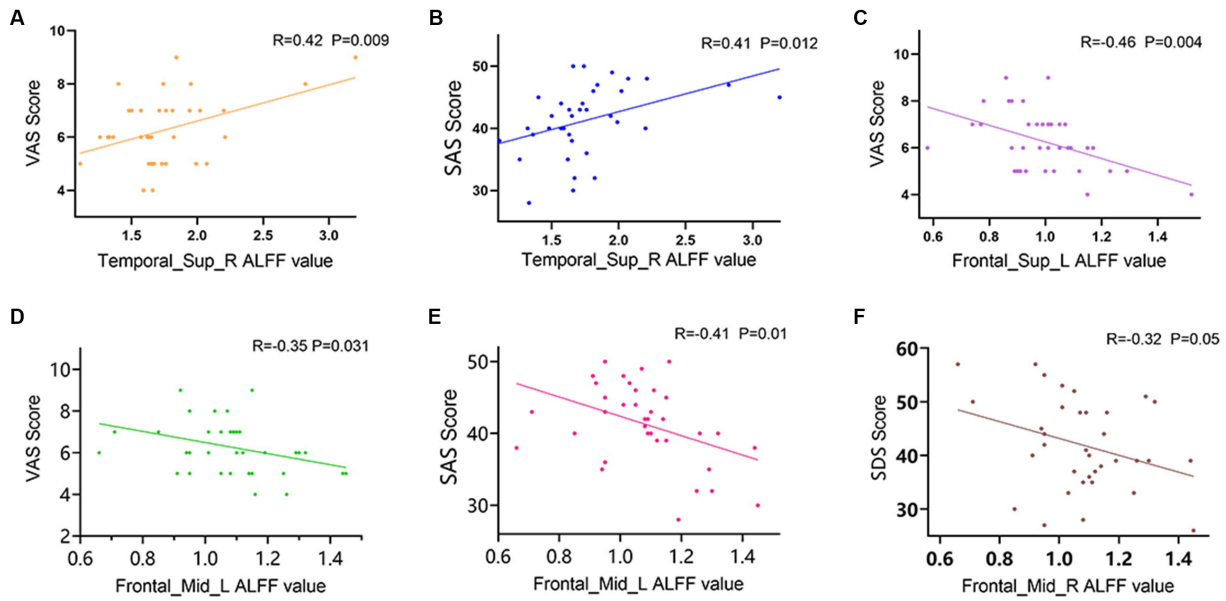

FIGURE 3
Correlation between mALFF values of abnormally activated brain regions and clinical symptoms in LDHCP patients. **(A)** Positive correlation between the mALFF values in the Temporal_Sup_R and the VAS scores; **(B)** Positive correlation between the mALFF values in the Temporal_Sup_R and the SAS scores; **(C)** Negative correlation between the mALFF values in the Frontal_Sup_L and the VAS scores; **(D)** Negative correlation between the mALFF values in the Frontal_Mid_L and the VAS scores; **(E)** Negative correlation between the mALFF values in the Frontal_Mid_L and the SAS scores; **(F)** Negative correlation between the mALFF values in the Frontal_Mid_R and the SDS scores.

depression. The frontal lobe, as an emotion regulation center, is related to attention, working memory and verbal behavior, and can receive rich emotional information, which is closely related to anxiety. Peng et al. (2019) stated that patients with anxiety depression have significantly reduced gray matter volumes in the right inferior frontal gyrus and orbitofrontal gyrus compared to non-anxious depressed and healthy controls. Patients with generalized anxiety disorder have been reported a reduced network connectivity in the prefrontal lobes (Wang W. et al., 2016), while major depressive disorder with somatic symptoms also shows lower ReHo values in the right middle frontal gyrus compared to HC (Geng et al., 2019). A meta-analysis of magnetic resonance spectra also proved that anxiety is associated with metabolic dysfunction in several brain regions, including the dorsolateral prefrontal and hippocampus (Delvecchio et al., 2017). These previous studies have explored the possibility that abnormal activation of frontal subregions may be a potential target for the development of anxiety and depression from a variety of perspectives, including structural, local functional activity, whole brain network connectivity and alterations in metabolic transmitters. In addition to the frontal regions of the brain, the temporal lobe has also been linked to anxiety. The temporal lobe serves as an important node involved in the top-down process of anxiety emotion regulation in the frontal-amygdala loop (Montag et al., 2013). A graph theory study based on the topological properties of brain networks also found that the clustering coefficients of the inferior temporal gyrus were significantly higher in patients with anxiety disorders than in non-anxiety disorders, suggesting that abnormalities in temporal lobe function are associated with the neural network mechanisms by which anxiety disorders occur (Fang et al., 2017).

It is well known that the various parts of our brain do not function independently of each other. Spatially distributed brain areas interact with each other through local information and connections within and between networks to perform different functions. The prefrontal cortex (PFC) abnormalities not only affect negative emotions, but also exhibit a complex association with pain. The PFC, as the higher center of nociceptive encoding, is able to integrate nociceptive sensory and emotional information to produce memory, cognition and evaluation of pain, relying on its connections with brain regions such as the hippocampus, periaqueductal gray matter of the midbrain, thalamus and amygdala (Wang et al., 2020). When dealing with stimuli from acute and chronic pain, the PFC undergoes changes in neurotransmitters, gene expression, glial cells and neuroinflammation, which cause changes in its structure, activity and connectivity (Davey et al., 2019). The gray matter volume of the mPFC extending to the ACC region was found to be significantly reduced in patients with CLBP (Yuan et al., 2017), and the functional connectivity of the mPFC/ACC with other regions in the DMN was reduced (James et al., 2001; Tu et al., 2019). The middle frontal gyrus, as a central region in the prefrontal cortex for processes related to cognitive control and emotion regulation, is more sensitive to pain perception and sensation. Wang J. J. et al. (2016) reported reduced ALFF values in the orbitofrontal cortex and right middle frontal gyrus bilaterally in migraine patients compared to HCs and were associated with depressive co-morbidity. In addition, dorsolateral prefrontal cortex (DLPFC), one of the main components of the central control network ECN, are not only involved in higher cognitive functions but also have important responsibilities in the nociceptive downstream inhibitory pathway, playing a facilitative or inhibitory role in pain (Beltran Serrano et al., 2019). Several studies have pointed out that cLBP patients have significantly reduced gray matter volume in the frontal middle gyrus or DLPFC, as well as reduced functional connectivity of the left lateral prefrontal lobes in

the disabled subgroup of cLBP patients compared to the non-disabled subgroup, suggesting that our pain chronicity may be related to abnormalities in the downstream inhibitory function of the DLPFC. Pain not only is a physical phenomenon, but also an emotional experience. There are relatively few studies relating the temporal lobe to pain, but the temporal lobe is implicated in emotion regulation and memory processing and may be involved in pain-related emotional processing and memory formation (Houde et al., 2020). Peng suggested that somatic pain VAS scores in the Parkinson's with pain group were associated with activation of the left middle temporal gyrus, a brain region associated with nociception, by a mechanism that may be due to a dopamine deficiency associated with mood disorders that enhances the propagation of injury signals and pain sensitivity (Peng, 2020).

Interestingly, in the correlation results of this study, we found a positive correlation between pain and anxiety, while the right superior temporal gyrus and the left middle frontal gyrus correlated with both clinical pain and anxiety scores. This suggests to us that abnormalities in the right superior temporal gyrus and left middle frontal gyrus may be the main and mediating factor for the occurrence of pain and emotion interaction in LDHCP patients. Future analysis and validation of large sample brain imaging cohort studies could focus on these 2 brain regions as areas of interest. After a large sample or multicenter validation, an attempt could also be made to use changes in these two brain regions as an evaluation indicator for clinical interventions. By observing the changes in brain region activities before and after different interventions, the efficacy of different treatments for LDHCP may thus be evaluated. Other brain areas differing in LDHCP patients compared to the HC group in this study, which did not show a correlation with clinical scale scores, also have an important influence in pain and emotional processing. Studies have shown that the DMN is one of the main networks affected by chronic pain (Jones et al., 2020), being modulated and reorganized by chronic pain. The precuneus, a functional center of the default mode network which modulates pain sensitivity and pain thresholds, is structurally and functionally altered in chronic pain (Zhang et al., 2014; Wang et al., 2019). The right inferior orbital frontal gyrus is anatomically connected to the limbic system and other prefrontal brain regions and is a superior integration center for emotional processing. Patients with depression showed reduced clustering coefficients in the inferior orbital frontal gyrus and reduced hemodynamic activation (Zhang et al., 2020; Feng et al., 2021).

However, some LDHCP studies have shown results different from our findings. Wen et al. found a completely different finding from ours, they point out that the LDHCP patients exhibited increased fALFF in right lingual gyri in the conventional band, and showed increased fALFF in left Cerebelum_Crus1 in the slow-4 band (Wen et al., 2022). In addition to finding similar results to our study in the prefrontal cortex or temporal lobe, Zhou et al. (2018) also noted that LDHCP patients had abnormal activation in brain regions such as the insula, cingulate gyrus, posterior cerebellum, inferior parietal lobule, middle occipital gyrus, and postcentral gyrus. It is worth noting that patients recruited by Zhou et al. (2018) had pain in their legs in addition to cLBP. We consider these controversial findings mainly for the following three reasons. First, different pain locations and differences in the distribution of subjects in terms of age, gender, and disease duration may be the main reasons for the different study results (von Leupoldt et al., 2011; Zhao et al., 2013; Wink, 2019; Tsvetanov et al., 2021). Second, different brain imaging data acquisition machines, processing software, and preprocessing steps used by different study groups may make differences in the study results (Murphy et al., 2007; Ashburner, 2009; Goto et al., 2013; Qing et al., 2015; Shirer et al., 2015; Hartwig et al., 2017; Gargouri et al., 2018). Third, the correction methods and thresholds set by different teams during the statistical analysis may make differences in the study results (Durnez et al., 2014; Fasiello et al., 2022; Noble et al., 2022). In the future, the academic community should endeavor to establish a uniform standard for the above mentioned points as soon as possible in order to eliminate these controversial conclusions. Overall, in this experiment, our findings point to a negative correlation between the left middle frontal gyrus ALFF and SAS and VAS in LDHCP patients, while the right superior temporal gyrus was positively correlated with SAS and VAS, and the left dorsolateral superior frontal gyrus and right middle frontal gyrus were negatively correlated with VAS and SAS, respectively, which is in accordance with the results of previous relevant studies. There are also limitations to our study. First, we did not differentiate further subgroups of lumbar disc herniation in terms of the degree and direction of herniation. Secondly, many patients were unable to provide the specific time of the first episode of LDHCP, so we did not collect LDHCP duration as a factor in this study. Third, the pain-focused position was not specifically limited in this study. These factors should be progressively modified in future studies, taking into account the actual clinical situation.

Conclusion

This study describes the regions of altered spontaneous neural activity in LDHCP patients compared to HCs. The right superior temporal gyrus, dorsolateral superior frontal gyrus and middle frontal gyrus may have important roles in regulating negative emotions and pain, providing new evidence to support the exploration of pathological mechanisms in LDHCP.

Data availability statement

The raw data supporting the conclusions of this article will be made available by the authors, without undue reservation.

Ethics statement

The studies involving human participants were reviewed and approved by the Medical Research Ethics Committee of Yueyang Hospital of Integrated Traditonal Chinese and Western Medicine (approval number: 2021-67), Shanghai University of Traditonal Chinese Medicine, Shanghai, China. The patients/participants provided their written informed consent to participate in this study.

Author contributions

MF and LK: designing research studies. CY, BZ, ZW, and SF: conduction of the study and data acquisition. CT, WH, and GG:

analyzing data. XP and XL: collecting and organizing research literature. CT and GG: writing the manuscript. All authors discussed the results, commented on the manuscript, and carefully reviewed and approved the submitted version.

Funding

This work was supported by the National Natural Science Foundation of China (grant numbers: 82030121, 82004493, 82105042, and 82205304); and Innovation Team and Talents Cultivation Program of National Administration of Traditional Chinese Medicine (ZYYCXTD-C-202008).

Acknowledgments

We thank all patients, volunteers, and research assistants for their contribution to this project. We also give special thanks to Zhiyang Yin, Tianding Tang and Yuxin Wen for their help with the photographic presentation of the study results.

Conflict of interest

The authors declare that the research was conducted in the absence of any commercial or financial relationships that could be construed as a potential conflict of interest.

Publisher's note

References

Arpinar, V. E., Gliedt, J. A., King, J. A., Maiman, D. J., and Muftuler, L. T. (2020). Oswestry disability index scores correlate with MRI measurements in degenerating intervertebral discs and endplates. *Eur. J. Pain* 24, 346–353. doi: 10.1002/ejp.1490

Ashburner, J. (2009). Computational anatomy with the SPM software. *Magn. Reson. Imaging* 27, 1163–1174. doi: 10.1016/j.mri.2009.01.006

Beltran Serrano, G., Rodrigues, L. P., Schein, B., Souza, A., Torres, I. L. S., da Conceição Antunes, L., et al. (2019). Comparison of hypnotic suggestion and transcranial direct-current stimulation effects on pain perception and the descending pain modulating system: a crossover randomized clinical trial. *Front. Neurosci.* 13:662. doi: 10.3389/fnins.2019.00662

Bletzer, J., Gantz, S., Voigt, T., Neubauer, E., and Schiltenwolf, M. (2017). Chronic low back pain and psychological comorbidity: a review. *Schmerz* 31, 93–101. doi: 10.1007/s00482-016-0143-4

Cai, L., He, Q., Lu, Y., Hu, Y., Chen, W., Wei, L., et al. (2019). Comorbidity of pain and depression in a lumbar disc herniation model: biochemical alterations and the effects of fluoxetine. *Front. Neurol.* 10:1022. doi: 10.3389/fneur.2019.01022

Chapman, J. R., Norvell, D. C., Hermsmeyer, J. T., Bransford, R. J., DeVine, J., McGirt, M. J., et al. (2011). Evaluating common outcomes for measuring treatment success for chronic low back pain. *Spine* 36, S54–S68. doi: 10.1097/BRS.0b013e31822ef74d

Chen, S., Chen, M., Wu, X., Lin, S., Tao, C., Cao, H., et al. (2022). Global, regional and national burden of low back pain 1990-2019: a systematic analysis of the global burden of disease study 2019. *J. Orthop. Trans.* 32, 49–58. doi: 10.1016/j.jot.2021.07.005

Davey, C. G., Chanen, A. M., Hetrick, S. E., Cotton, S. M., Ratheesh, A., Amminger, G. P., et al. (2019). The addition of fluoxetine to cognitive behavioural therapy for youth depression (YoDA-C): a randomised, double-blind, placebo-controlled, multicentre clinical trial. *Lancet Psychiatry* 6, 735–744. doi: 10.1016/s2215-0366(19)30215-9

Delvecchio, G., Stanley, J. A., Altamura, A. C., and Brambilla, P. (2017). Metabolic alterations in generalised anxiety disorder: a review of proton magnetic resonance spectroscopic studies. *Epidemiol. Psychiatr. Sci.* 26, 587–595. doi: 10.1017/s2045796017000361

Du, J. G., Xiao, H., and Zuo, Y. X. (2018). Amplitude of Low Frequency Fluctuation (ALFF) study of the spontaneous brain activities of patients with phantom limb pain. *Eur. Rev. Med. Pharmacol. Sci.* 22, 7164–7171. doi: 10.26355/eurrev_201811_16248

Dunstan, D. A., and Scott, N. (2020). Norms for Zung's self-rating anxiety scale. *BMC Psychiatry* 20:90. doi: 10.1186/s12888-019-2427-6

Durnez, J., Roels, S. P., and Moerkerke, B. (2014). Multiple testing in fMRI: an empirical case study on the balance between sensitivity, specificity, and stability. *Biom. J.* 56, 649–661. doi: 10.1002/bimj.201200056

Fang, J. P., Cehng, H. M., Cao, Z. Y., and Liu, D. L. (2017). Brain network topographic properties of drug naive Parkinson's disease patients with anxiety Chinese. *J. Geriatr. Heart Brain Vessel Dis.* 19, 797–801. doi: 10.3969/j.issn.1009-0126.2017.08.004

Fasiello, E., Gorgoni, M., Scarpelli, S., Alfonsi, V., Ferini Strambi, L., and De Gennaro, L. (2022). Functional connectivity changes in insomnia disorder: a systematic review. *Sleep Med. Rev.* 61:101569. doi: 10.1016/j.smrv.2021.101569

Feng, K., Law, S., Ravindran, N., Chen, G. F., Ma, X. Y., Bo, X., et al. (2021). Differentiating between bipolar and unipolar depression using prefrontal activation patterns: promising results from functional near infrared spectroscopy (fNIRS) findings. *J. Affect. Disord.* 281, 476–484. doi: 10.1016/j.jad.2020.12.048

Folstein, M. F., Folstein, S. E., and McHugh, P. R. (1975). "Mini-mental state". A practical method for grading the cognitive state of patients for the clinician. *J. Psychiatr. Res.* 12, 189–198. doi: 10.1016/0022-3956(75)90026-6

Gargouri, F., Kallel, F., Delphine, S., Ben Hamida, A., Lehéricy, S., and Valabregue, R. (2018). The influence of preprocessing steps on graph theory measures derived from resting state fMRI. *Front. Comput. Neurosci.* 12:8. doi: 10.3389/fncom.2018.00008

Ge, S., Hu, Q., Xia, G., Tan, Y., Guo, Y., and Sun, C. (2022). The ALFF Alterations of Spontaneous Pelvic Pain in the Patients of Chronic Prostatitis/Chronic Pelvic Pain Syndrome Evaluated by fMRI. *Brain Sci.* 12. doi: 10.3390/brainsci12101344

Geng, J., Yan, R., Shi, J., Chen, Y., Mo, Z., Shao, J., et al. (2019). Altered regional homogeneity in patients with somatic depression: a resting-state fMRI study. *J. Affect. Disord.* 246, 498–505. doi: 10.1016/j.jad.2018.12.066

Goto, M., Abe, O., Aoki, S., Hayashi, N., Miyati, T., Takao, H., et al. (2013). Diffeomorphic anatomical registration through exponentiated lie algebra provides reduced effect of scanner for cortex volumetry with atlas-based method in healthy subjects. *Neuroradiology* 55, 869–875. doi: 10.1007/s00234-013-1193-2

Hartwig, V., Carbonaro, N., Tognetti, A., and Vanello, N. (2017). Systematic review of fMRI compatible devices: design and testing criteria. *Ann. Biomed. Eng.* 45, 1819–1835. doi: 10.1007/s10439-017-1853-1

Houde, F., Martel, M., Coulombe-Lévêque, A., Harvey, M. P., Auclair, V., Mathieu, D., et al. (2020). Perturbing the activity of the superior temporal gyrus during pain encoding prevents the exaggeration of pain memories: a virtual lesion study using single-pulse transcranial magnetic stimulation. *Neurobiol. Learn. Mem.* 169:107174. doi: 10.1016/j.nlm.2020.107174

Huang, J., Li, Y., Xie, H., Yang, S., Jiang, C., Sun, W., et al. (2020). Abnormal intrinsic brain activity and neuroimaging-based fMRI classification in patients with herpes zoster and postherpetic neuralgia. *Front. Neurol.* 11:532110. doi: 10.3389/fneur.2020.532110

James, M. F., Smith, J. M., Boniface, S. J., Huang, C. L., and Leslie, R. A. (2001). Cortical spreading depression and migraine: new insights from imaging? *Trends Neurosci.* 24, 266–271. doi: 10.1016/s0166-2236(00)01793-8

Jones, S. A., Morales, A. M., Holley, A. L., Wilson, A. C., and Nagel, B. J. (2020). Default mode network connectivity is related to pain frequency and intensity in adolescents. *Neuroimage Clin.* 27:102326. doi: 10.1016/j.nicl.2020.102326

Kao, Y. C., Chen, J. Y., Chen, H. H., Liao, K. W., and Huang, S. S. (2022). The association between depression and chronic lower back pain from disc degeneration and herniation of the lumbar spine. *Int. J. Psychiatry Med.* 57, 165–177. doi: 10.1177/00912174211003760

Knight, R. G., Waal-Manning, H. J., and Spears, G. F. (1983). Some norms and reliability data for the state--trait anxiety inventory and the zung self-rating depression scale. *Br. J. Clin. Psychol.* 22, 245–249. doi: 10.1111/j.2044-8260.1983.tb00610.x

Koechlin, H., Coakley, R., Schechter, N., Werner, C., and Kossowsky, J. (2018). The role of emotion regulation in chronic pain: a systematic literature review. *J. Psychosom. Res.* 107, 38–45. doi: 10.1016/j.jpsychores.2018.02.002

Le Borgne, M., Boudoukha, A. H., Petit, A., and Roquelaure, Y. (2017). Chronic low back pain and the transdiagnostic process: how do cognitive and emotional dysregulations contribute to the intensity of risk factors and pain? *Scand J Pain* 17, 309–315. doi: 10.1016/j.sjpain.2017.08.008

Li, H., Song, Q., Zhang, R., Zhou, Y., and Kong, Y. (2021). Enhanced temporal coupling between thalamus and dorsolateral prefrontal cortex mediates chronic low back pain and depression. *Neural Plast.* 2021, 7498714–7498710. doi: 10.1155/2021/7498714

Li, Z., Zhou, J., Lan, L., Cheng, S., Sun, R., Gong, Q., et al. (2020). Concurrent brain structural and functional alterations in patients with migraine without aura: an fMRI study. *J. Headache Pain* 21:141. doi: 10.1186/s10194-020-01203-5

Martin, M. D., Boxell, C. M., and Malone, D. G. (2002). Pathophysiology of lumbar disc degeneration: a review of the literature. *Neurosurg. Focus.* 13, 1–6. doi: 10.3171/foc.2002.13.2.2

Montag, C., Reuter, M., Jurkiewicz, M., Markett, S., and Panksepp, J. (2013). Imaging the structure of the human anxious brain: a review of findings from neuroscientific personality psychology. *Rev. Neurosci.* 24, 167–190. doi: 10.1515/revneuro-2012-0085

Mu, W., Shang, Y., Zhang, C., and Tang, S. (2019). Analysis of the depression and anxiety status and related risk factors in patients with lumbar disc herniation. *Pak J Med Sci* 35, 658–662. doi: 10.12669/pjms.35.3.299

Murphy, K., Bodurka, J., and Bandettini, P. A. (2007). How long to scan? The relationship between fMRI temporal signal to noise ratio and necessary scan duration. *Neuroimage* 34, 565–574. doi: 10.1016/j.neuroimage.2006.09.032

Noble, S., Mejia, A. F., Zalesky, A., and Scheinost, D. (2022). Improving power in functional magnetic resonance imaging by moving beyond cluster-level inference. *Proc. Natl. Acad. Sci. U. S. A.* 119:e2203020119. doi: 10.1073/pnas.2203020119

Pan, Z. M., Li, H. J., Bao, J., Jiang, N., Yuan, Q., Freeberg, S., et al (2018). Altered intrinsic brain activities in patients with acute eye pain using amplitude of low-frequency fluctuation: a resting-state fMRI study. *Neuropsychiatr. Dis. Treat.* 14, 251–257. doi: 10.2147/ndt.S150051

Peng, Q. (2020). *The brain fMRI study of patients with PD and pain induced by contact heat stimulations*. Master thesis. Nanchong: North Sichuan Medical College.

Peng, W., Jia, Z., Huang, X., Lui, S., Kuang, W., Sweeney, J. A., et al. (2019). Data on gray matter alterations in anxious depression. *Data Brief* 25:104322. doi: 10.1016/j.dib.2019.104322

Price, R. B., and Duman, R. (2020). Neuroplasticity in cognitive and psychological mechanisms of depression: an integrative model. *Mol. Psychiatry* 25, 530–543. doi: 10.1038/s41380-019-0615-x

Qing, Z., Dong, Z., Li, S., Zang, Y., and Liu, D. (2015). Global signal regression has complex effects on regional homogeneity of resting state fMRI signal. *Magn. Reson. Imaging* 33, 1306–1313. doi: 10.1016/j.mri.2015.07.011

Serbic, D., and Pincus, T. (2017). The relationship between pain, disability, guilt and acceptance in low back pain: a mediation analysis. *J. Behav. Med.* 40, 651–658. doi: 10.1007/s10865-017-9826-2

Shafshak, T. S., and Elnemr, R. (2021). The visual analogue scale versus numerical rating scale in measuring pain severity and predicting disability in low back pain. *J. Clin. Rheumatol.* 27, 282–285. doi: 10.1097/rhu.0000000000001320

Sheahan, P. J., Nelson-Wong, E. J., and Fischer, S. L. (2015). A review of culturally adapted versions of the oswestry disability index: the adaptation process, construct validity, test-retest reliability and internal consistency. *Disabil. Rehabil.* 37, 2367–2374. doi: 10.3109/09638288.2015.1019647

Sheng, H. Y., and Zhang, Y. Q. (2019). Cognitive and emotional changes caused by chronic pain. *Chinese J. Pain Med.* 25, 885–889. doi: 10.3969/j.issn.1006-9852.2019.12.002

Shirer, W. R., Jiang, H., Price, C. M., Ng, B., and Greicius, M. D. (2015). Optimization of rs-fMRI pre-processing for enhanced signal-noise separation, test-retest reliability, and group discrimination. *Neuroimage* 117, 67–79. doi: 10.1016/j.neuroimage.2015.05.015

Stacheneder, R., Alt, L., Straube, A., and Ruscheweyh, R. (2022). Effects of transcranial direct current stimulation (t-DCS) of the cerebellum on pain perception and endogenous pain modulation: a randomized, monocentric, double-blind, sham-controlled crossover study. *Cerebellum*. doi: 10.1007/s12311-022-01498-x, [Epub ahead of print].

Thong, I. S. K., Jensen, M. P., Miró, J., and Tan, G. (2018). The validity of pain intensity measures: what do the NRS, VAS, VRS, and FPS-R measure? *Scand J Pain* 18, 99–107. doi: 10.1515/sjpain-2018-0012

Thurber, S., Snow, M., and Honts, C. R. (2002). The zung self-rating depression scale: convergent validity and diagnostic discrimination. *Assessment* 9, 401–405. doi: 10.1177/1073191102238471

Tsvetanov, K. A., Henson, R. N. A., and Rowe, J. B. (2021). Separating vascular and neuronal effects of age on fMRI BOLD signals. *Philos. Trans. R. Soc. Lond. Ser. B Biol. Sci.* 376:20190631. doi: 10.1098/rstb.2019.0631

Tu, Y., Jung, M., Gollub, R. L., Napadow, V., Gerber, J., Ortiz, A., et al. (2019). Abnormal medial prefrontal cortex functional connectivity and its association with clinical symptoms in chronic low back pain. *Pain* 160, 1308–1318. doi: 10.1097/j.pain.0000000000001507

Turner, J. A., and Romano, J. M. (1984). Self-report screening measures for depression in chronic pain patients. *J. Clin. Psychol.* 40, 909–913. doi: 10.1002/1097-4679(198407)40:4<909::aid-jclp2270400407>3.0.co;2-j

von Leupoldt, A., Brassen, S., Baumann, H. J., Klose, H., and Büchel, C. (2011). Structural brain changes related to disease duration in patients with asthma. *PLoS One* 6:e23739. doi: 10.1371/journal.pone.0023739

Wang, J. J., Chen, X., Sah, S. K., Zeng, C., Li, Y. M., Li, N., et al. (2016). Amplitude of low-frequency fluctuation (ALFF) and fractional ALFF in migraine patients: a resting-state functional MRI study. *Clin. Radiol.* 71, 558–564. doi: 10.1016/j.crad.2016.03.004

Wang, L., He, T., Liu, J., Tai, J., Wang, B., Zhang, L., et al. (2021). Revealing the immune infiltration landscape and identifying diagnostic biomarkers for lumbar disc herniation. *Front. Immunol.* 12:666355. doi: 10.3389/fimmu.2021.666355

Wang, W., Hou, J., Qian, S., Liu, K., Li, B., Li, M., et al. (2016). Aberrant regional neural fluctuations and functional connectivity in generalized anxiety disorder revealed by resting-state functional magnetic resonance imaging. *Neurosci. Lett.* 624, 78–84. doi: 10.1016/j.neulet.2016.05.005

Wang, X., Wang, R., Li, F., Lin, Q., Zhao, X., and Hu, Z. (2020). Large-scale granger causal brain network based on resting-state fMRI data. *Neuroscience* 425, 169–180. doi: 10.1016/j.neuroscience.2019.11.006

Wang, Y., Yang, Q., Cao, D., Seminowicz, D., Remeniuk, B., Gao, L., et al. (2019). Correlation between nerve atrophy, brain grey matter volume and pain severity in patients with primary trigeminal neuralgia. *Cephalalgia* 39, 515–525. doi: 10.1177/0333102418793643

Wang, L., Ye, H., Li, Z., Lu, C., Ye, J., Liao, M., et al. (2022). Epidemiological trends of low back pain at the global, regional, and national levels. *Eur. Spine J.* 31, 953–962. doi: 10.1007/s00586-022-07133-x

Weizman, L., Dayan, L., Brill, S., Nahman-Averbuch, H., Hendler, T., Jacob, G., et al. (2018). Cannabis analgesia in chronic neuropathic pain is associated with altered brain connectivity. *Neurology* 91, e1285–e1294. doi: 10.1212/wnl.0000000000006293

Wen, Y., Chen, X. M., Jin, X., Ling, D. Y., Chen, S., Huang, Q., et al. (2022). A spinal manipulative therapy altered brain activity in patients with lumbar disc herniation: a resting-state functional magnetic resonance imaging study. *Front. Neurosci.* 16:974792. doi: 10.3389/fnins.2022.974792

Wink, A. M. (2019). Eigenvector centrality dynamics from resting-state fMRI: gender and age differences in healthy subjects. *Front. Neurosci.* 13:648. doi: 10.3389/fnins.2019.00648

Yuan, C., Shi, H., Pan, P., Dai, Z., Zhong, J., Ma, H., et al. (2017). Gray matter abnormalities associated with chronic back pain: a meta-analysis of voxel-based morphometric studies. *Clin. J. Pain* 33, 983–990. doi: 10.1097/ajp.0000000000000489

Zang, Y. F. (2016). DPABI: Data Processing & Analysis for (Resting-State) Brain Imaging. *Neuroinformatics* 14, 339–351. doi: 10.1007/s12021-016-9299-4

Zhang, B., Jung, M., Tu, Y., Gollub, R., Lang, C., Ortiz, A., et al. (2019). Identifying brain regions associated with the neuropathology of chronic low back pain: a resting-state amplitude of low-frequency fluctuation study. *Br. J. Anaesth.* 123, e303–e311. doi: 10.1016/j.bja.2019.02.021

Zhang, S., Wang, W., Wang, G., Li, B., Chai, L., Guo, J., et al. (2020). Aberrant resting-state interhemispheric functional connectivity in patients with postpartum depression. *Behav. Brain Res.* 382:112483. doi: 10.1016/j.bbr.2020.112483

Zhang, S. S., Wu, W., Liu, Z. P., Huang, G. Z., Guo, S. G., and Yang, J. M. (2014). Altered regional homogeneity in experimentally induced low back pain: a resting-state fMRI study. *J. Neuroeng. Rehabil.* 11:115. doi: 10.1186/1743-0003-11-115

Zhang, S. S., Wu, W., Yang, J. M., and Wang, C. H. (2017). Abnormal spontaneous brain activity in acute low-back pain revealed by resting-state functional MRI. *Am. J. Phys. Med. Rehabil.* 96, 253–259. doi: 10.1097/phm.0000000000000597

Zhao, L., Liu, J., Dong, X., Peng, Y., Yuan, K., Wu, F., et al. (2013). Alterations in regional homogeneity assessed by fMRI in patients with migraine without aura stratified by disease duration. *J. Headache Pain* 14:85. doi: 10.1186/1129-2377-14-85

Zhao, L., Manchikanti, L., Kaye, A. D., and Abd-Elsayed, A. (2019). Treatment of discogenic low back pain: current treatment strategies and future options-a literature review. *Curr. Pain Headache Rep.* 23:86. doi: 10.1007/s11916-019-0821-x

Zhou, F., Gu, L., Hong, S., Liu, J., Jiang, J., Huang, M., et al. (2018). Altered low-frequency oscillation amplitude of resting state-fMRI in patients with discogenic low-back and leg pain. *J. Pain Res.* 11, 165–176. doi: 10.2147/jpr.S151562

frontiers | Frontiers in Neuroscience

TYPE Original Research
PUBLISHED 01 August 2023
DOI 10.3389/fnins.2023.1226077

OPEN ACCESS

EDITED BY
Ye Wu,
Nanjing University of Science and Technology, China

REVIEWED BY
Fuli Yan,
Yangzhou University, China
Gian Marco Duma,
Eugenio Medea (IRCCS), Italy

*CORRESPONDENCE
Yan Zhang
✉ fcczhangy61@zzu.edu.cn
Shaoqiang Han
✉ shaoqianghan@163.com
Jingliang Cheng
✉ fccchengjl@zzu.edu.cn

†These authors have contributed equally to this work and share first authorship

RECEIVED 20 May 2023
ACCEPTED 19 July 2023
PUBLISHED 01 August 2023

CITATION
Mao X, Zhang X, Song C, Ma K, Wang K, Wang X, Lian Y, Zhang Y, Han S, Cheng J and Zhang Y (2023) Alterations in static and dynamic regional homogeneity in mesial temporal lobe epilepsy with and without initial precipitating injury.
Front. Neurosci. 17:1226077.
doi: 10.3389/fnins.2023.1226077

Alterations in static and dynamic regional homogeneity in mesial temporal lobe epilepsy with and without initial precipitating injury

Xinyue Mao[1,2,3,4,5,6,7†], Xiaonan Zhang[1,2,3,4,5,6,7†], Chengru Song[1,2,3,4,5,6,7], Keran Ma[1,2,3,4,5,6,7], Kefan Wang[1,2,3,4,5,6,7], Xin Wang[1,2,3,4,5,6,7], Yajun Lian[8], Yong Zhang[1,2,3,4,5,6,7], Shaoqiang Han[1,2,3,4,5,6,7*], Jingliang Cheng[1,2,3,4,5,6,7*] and Yan Zhang[1,2,3,4,5,6,7*]

[1]Department of Magnetic Resonance Imaging, The First Affiliated Hospital of Zhengzhou University, Zhengzhou, China, [2]Key Laboratory for Functional Magnetic Resonance Imaging and Molecular Imaging of Henan Province, Zhengzhou, China, [3]Engineering Technology Research Center for Detection and Application of Brain Function of Henan Province, Zhengzhou, China, [4]Engineering Research Center of Medical Imaging Intelligent Diagnosis and Treatment of Henan Province, Zhengzhou, China, [5]Key Laboratory of Magnetic Resonance and Brain Function of Henan Province, Zhengzhou, China, [6]Key Laboratory of Brain Function and Cognitive Magnetic Resonance Imaging of Zhengzhou, Zhengzhou, China,, [7]Key Laboratory of Imaging Intelligence Research Medicine of Henan Province, Zhengzhou, China, [8]Department of Neurology, The First Affiliated Hospital of Zhengzhou University, Zhengzhou, China

Objectives: Initial precipitating injury (IPI) such as febrile convulsion and intracranial infection will increase the susceptibility to epilepsy. It is still unknown if the functional deficits differ between mesial temporal lobe epilepsy with IPI (mTLE-IPI) and without IPI (mTLE-NO).

Methods: We recruited 25 mTLE-IPI patients, 35 mTLE-NO patients and 33 healthy controls (HC). Static regional homogeneity (sReHo) and dynamic regional homogeneity (dReHo) were then adopted to estimate the alterations of local neuronal activity. One-way analysis of variance was used to analyze the differences between the three groups in sReHo and dReHo. Then the results were utilized as masks for further between-group comparisons. Besides, correlation analyses were carried out to detect the potential relationships between abnormal regional homogeneity indicators and clinical characteristics.

Results: When compared with HC, the bilateral thalamus and the visual cortex in mTLE-IPI patients showed an increase in both sReHo and variability of dReHo. Besides, mTLE-IPI patients exhibited decreased sReHo in the right cerebellum crus1/crus2, inferior parietal lobule and temporal neocortex. mTLE-NO patients showed decreased sReHo and variability of dReHo in the bilateral temporal neocortex compared with HC. Increased sReHo and variability of dReHo were found in the bilateral visual cortex when mTLE-IPI patients was compared with mTLE-NO patients, as well as increased variability of dReHo in the left thalamus and decreased sReHo in the right dorsolateral prefrontal cortex. Additionally, we discovered a negative correlation between the national hospital seizure severity scale testing score and sReHo in the right cerebellum crus1 in mTLE-IPI patients.

Conclusion: According to the aforementioned findings, both mTLE-IPI and mTLE-NO patients had significant anomalies in local neuronal activity, although the functional deficits were much severer in mTLE-IPI patients. The use of sReHo

and dReHo may provide a novel insight into the impact of the presence of IPI on the development of mTLE.

KEYWORDS

mesial temporal lobe epilepsy, initial precipitating injury, resting-state functional MRI, regional homogeneity, dynamic, cognitive impairment

Introduction

Mesial temporal lobe epilepsy (mTLE), characterized by transient aberrant electrical activity originating in the mesial temporal lobe structures (Morgan et al., 2020), is the most common focal drug-resistant epilepsy (Li et al., 2022). The hippocampus is particularly vulnerable to an intracranial infection or febrile convulsion (what we refer to as the initial precipitating injury, or IPI) in childhood (Bien et al., 2007; Polat et al., 2010; Janz et al., 2018), and this vulnerability often leads to hippocampal sclerosis, which is the most common cause of mTLE.

Whether there is IPI may be one of the factors leading to the alterations in brain's structure or function of mTLE patients. It had been reported (Keller et al., 2002) that mTLE patients with a history of childhood febrile convulsions had smaller hippocampal and amygdala volumes in the ipsilateral side of the epileptic foci than those without such a history. Another study (Free et al., 1996) indicated that over half of the subjects with a history of encephalitis or meningitis experienced bilateral hippocampal volume loss. However, all of the current researches focused on alterations in brain structure, leaving the study of brain function in mTLE-IPI patients in the dark. Recently, a notion that there was a separation of cognitive problems and epileptogenesis was proposed (Patterson et al., 2014), which implied that certain kids with a history of febrile convulsions might have memory deficits that preceded the onset of mTLE. So it becomes sense to think that IPI has a high potential for promoting cognitive deterioration.

Resting-state functional magnetic resonance imaging (rs-fMRI) is a powerful tool for measuring the changes of blood oxygen level-dependent (BOLD) signals spontaneously produced by brain (Song and Jiang, 2012). One of the most well-liked rs-fMRI analysis methods, static regional homogeneity (sReHo), is a voxel-based approach that reflects the consistency of neural activity in a given voxel with its adjacent voxels (Zang et al., 2004). Contrary to the functional connection (FC), which depicts the inter-nodal connection, sReHo assesses intra-nodal activity (Hu et al., 2017). An abnormal sReHo indicates poor synchronization of local neural activity. It is well known that the sReHo of numerous brain regions, such as sensorimotor cortex, frontoparietal cortex and DMN, has been demonstrated to be disrupted in mTLE (Zeng et al., 2013; Zhao et al., 2020), which has a close relationship with the cognitive impairment of patients.

Considering the dynamic property of brain activity (Calhoun et al., 2014), recent investigations (Jiang et al., 2021; Liang et al., 2021) had explored the collaboration of brain regions by measuring the time-varying covariance of their neural signals during resting-state, among which dynamic regional homogeneity (dReHo) is a relatively common approach. An rs-fMRI study (Song et al., 2022) reported decreased variability of dReHo in the temporal lobe neocortex ipsilateral to epileptic foci in mTLE. Another study reported (Xue et al., 2022) that patients with major depressive disorder had decreased variability of dReHo in some brain regions associated with emotional and cognitive regulation, including the fusiform gyri, the right temporal pole and hippocampus. These suggest that plenty of diseases are accompanied by impaired regional temporal synchronization of spontaneous brain activity among certain voxels.

Based on the information presented above, regional homogeneity (ReHo) can be used to quantify activity coordination among voxels in a region. Since epilepsy is characterized by abnormal spontaneous brain activity, we predicted that the local neuronal activity of the epileptic foci and the brain regions affected by abnormal discharge transmission is impaired to some extent. From this point of view, the sReHo and dReHo were employed to characterize and compare the differences of neuronal activity among the three subgroups in this study. We hypothesized that (1) mTLE-IPI patients had more extensive alterations of sReHo or dReHo than mTLE-NO patients and (2) sReHo or dReHo in certain brain regions might be associated with some clinical characteristics of mTLE patients.

Materials and methods

Participants

BOLD-fMRI data were gathered in 60 unilateral mTLE cases (27 left- and 33 right-side) in The First Affiliated Hospital of Zhengzhou University between April 2019 and July 2022. At the same time, we recruited 33 age- and sex-matched healthy controls (HC) from the local communities, who also underwent BOLD-fMRI scans.

The diagnosis of mTLE was based on clinical symptom, neurologic examination, electroencephalography (EEG) and MRI findings, and was confirmed by neurologists from the department of neurology, The First Affiliated Hospital of Zhengzhou University. Patients with mTLE who met the following criteria were included: (1) MRI revealed that there were no obvious structural abnormalities other than unilateral hippocampal sclerosis, (2) all right-handed, (3) mini-mental state examination score > 24, and (4) ≥14 years old. Exclusion criteria for patients were as follows: (1) patients with other brain structural abnormalities except for unilateral hippocampal sclerosis, other psychiatric disorders, severe systemic diseases or trauma, (2) left-handed, and (3) had a long history of alcohol or drug abuse. According to whether there was intracranial infection or febrile convulsion in childhood, the patients were divided into two groups: mTLE with IPI (mTLE-IPI, $n = 25$) group and mTLE without IPI (mTLE-NO, $n = 35$) group. The mTLE-IPI group included 13 patients with a history of febrile convulsion and 12 patients with a history of intracranial infection (1 meningitis, 11 encephalitis).

The inclusion criteria for HC were as follows: (1) routine conventional MRI findings were normal, (2) had not taken any psychotropic tablets, and (3) all right-handed. The exclusion criteria: people with any family history of epilepsy or other psychiatric disorders.

Basic demographic data, including gender and age, was collected from all participants. The mTLE patients' seizure-related characteristics, such as epilepsy duration, seizure severity, and the number of concurrent antiseizure medications (ASMs) were noted. Seizure severity was determined by the national hospital seizure severity scale (NHS3) testing score.

This study was approved by the Research Ethics Committee at The First Affiliated Hospital of Zhengzhou University (No.2019-KY-232). According to the Declaration of Helsinki, all participants were fully informed of the purpose of this study and provided written informed consent.

MRI data acquisition

Resting-state fMRI data were acquired using a 3.0 T Magnetom Prisma MRI scanner (Siemens Healthcare, Erlangen, Germany), equipped with a 64-channel head coil. All participants were instructed to lie on their backs with their eyes closed, but to stay awake and to unconsciously relax. In order to reduce noise disturbance and minimize head motion, each participant was provided with a pair of sponge paddings. The scanning parameters were as follows: time of repetition (TR) =1,000 ms, time of echo (TE) = 30 ms, field of view (FOV) = 220 × 220 mm^2, slice thickness = 2.2 mm, slice gap = 0.4 mm, flip angle = 70 °, voxel size = 2.0 × 2.0 × 2.2 mm^3, slice number = 52, volumes = 400.

Resting-state fMRI preprocessing

Data Processing Assistant for Resting-State fMRI Analysis Toolkit (DPARSFA, V5.2) (Yan and Zang, 2010) was used to preprocess the rs-fMRI data. (1) Converting the DICOM images into the NIFTI format, (2) deleting the first 10 time points, (3) slice-timing, (4) realignment (participants with linear shifting distances more than 2.5 mm or rotation angles more than 2.5° were excluded), (5) spatially normalizing the fMRI figures to the Montreal Neurological Institute (MNI) space and resampling to 3 × 3 × 3 mm^3 resolution, (6) detrending, (7) regressing several spurious variances, including 24 head motion parameters (Satterthwaite et al., 2012), cerebrospinal fluid signals, and white matter signals, (8)band-pass temporal filtering between 0.01–0.08 Hz, and (9) framewise displacement (FD) (Power et al., 2012)was calculated for each time point, and participants with mean FD exceeding 0.5 mm were excluded.

sReHo and dReHo analysis

Kendall's coefficient of concordance (KCC) was utilized to calculate the sReHo and dReHo of a voxel's time series and its adjacent voxels (Zang et al., 2004). In our study, the cluster size of KCC was set to be 27, which is adequate for covering all directions in 3D space and to optimize the trade-off between mitigation of partial volume effects and generation of Gaussian random fields (Jiang and Zuo, 2016). However, considering that the size of cluster to be measured might affect KCC value, we validated the results using additional two sorts of cluster size (7 and 19 voxels, respectively). For sReHo, the KCC value of a given voxel with those of its nearest neighbors was calculated through DPARSFA. Then, the sReHo map of each subject was obtained and transformed into standardized z-score. The dReHo analysis was performed using temporal dynamic analysis toolkits (Yan et al., 2017). A method based on sliding window was used to describe the temporal dynamic patterns. It is rather remarkable that the window length is a key parameter. According to prior studies, the minimum window length should exceed $1/f_{min}$, where f_{min} denoted the minimum frequency of time courses (Leonardi and Van De Ville, 2015). Therefore, a window size of 100 TRs (100 s) and a window overlap of 60% (step size by 40 TRs, 40s) were selected (Wen et al., 2021). We also tested the results of other window sizes and overlaps, and the specific information is described in the validation analysis. The standard deviation of the dReHo was calculated to estimate temporal variability. Then, the time variability map of each subject was normalized into a z-score matrix. At last, spatial smoothing with a 6 mm full-width at half-maximum (FWHM) Gaussian kernel was performed for the sReHo and dReHo maps.

Statistical analysis

Demographic and clinical characteristics of participants were analyzed using IBM SPSS22.0 software. The differences in age, gender and mean FD among mTLE-IPI, mTLE-NO and HC were, respectively, analyzed with one-way analysis of variance (ANOVA), Chi-square test and Kruskal–Wallis test ($p < 0.05$). Difference in lateralization between mTLE-IPI and mTLE-NO was analyzed with Chi-square test ($p < 0.05$), while differences in epilepsy duration, NHS3 score and the number of ASMs were analyzed with Mann–Whitney U test, respectively, ($p < 0.05$).

Whole-brain voxel-wise comparisons of sReHo and dReHo among the three groups were employed by one-way ANOVA using SPM12 toolkit, with age, gender and mean FD as covariates. A gaussian random field (GRF) correction was conducted for the F-value map (voxel-wise $p < 0.005$ and cluster-level $p < 0.05$, cluster extent threshold $k > 30$). Then, a new mask (the brain regions where the F value changed significantly) was applied to perform the secondary analyses through two-sample t-test (GRF corrected, $p_{voxel} < 0.005$, $p_{cluster} < 0.05$, $k > 30$) between mTLE-IPI and HC, mTLE-NO and HC, mTLE-IPI and mTLE-NO.

Correlation analysis

To identify whether the sReHo and dReHo abnormalities were associated with clinical characteristics, we conducted Spearman correlation analyses of the sReHo and dReHo values extracted from brain clusters showing significant differences on F map with epilepsy duration, NHS3 score and the number of ASMs, respectively. $p < 0.05$ was set for the statistically significant threshold.

Validation analyses

First, the ReHo's proposer (Zang et al., 2004) claimed that the size of cluster (7, 19, or 27 voxels) to be measured had a considerable effect on KCC; that is, the results may differ depending on this number. Although the generally accepted cluster size is 27 voxels, we also tested additional two sorts of cluster size (7 and 19 voxels, respectively) to investigate how they would affect the outcomes. Second, since the optimal window size and step size of the sliding window method have not yet been identified, different window sizes/step sizes (100/20 TRs and 80/30 TRs) were examined to verify the reproducibility of dReHo results.

Results

Demographic and clinical information

The demographic and clinical information of the three groups are summarized in Table 1. No significant differences were detected in terms of age, gender or mean FD among three groups. For the comparison between mTLE-IPI and mTLE-NO, there were no notable differences between the two groups in lateralization, epilepsy duration, NHS3 score or the number of ASMs.

Group differences in sReHo

The results revealed that mTLE-IPI and mTLE-NO had distinct patterns of sReHo alterations (Figure 1 and Table 2). Compared with HC, mTLE-IPI showed decreased sReHo in the right inferior temporal gyrus (ITG), middle temporal gyrus (MTG), cerebellum crus1/ crus2, inferior parietal lobule (IPL, including angular gyrus and supramarginal gyrus), while increased sReHo in the bilateral thalamus, lingual gyrus (LG), calcarine (CAL) and cuneus. mTLE-NO showed decreased sReHo in the bilateral MTG, left ITG and right superior temporal gyrus (STG). Compared with mTLE-NO, mTLE-IPI manifested decreased sReHo in the right dorsolateral prefrontal cortex (DLPFC), while increased sReHo in the bilateral CAL and right LG (Figure 2).

Group differences in dReHo

The three groups presented significantly different variability of dReHo (Figure 1 and Table 2). Compared with HC, mTLE-IPI showed increased variability of dReHo in the bilateral thalamus, left CAL and cuneus. mTLE-NO, on the other hand, showed decreased variability of dReHo in the bilateral MTG, ITG and right STG. Compared with mTLE-NO, mTLE-IPI manifested increased variability of dReHo in the bilateral CAL, LG, left cuneus and thalamus (Figure 3).

Correlation analysis

As shown in Figure 4, the NHS3 score was negatively correlated with sReHo in right cerebellum crus1 in mTLE-IPI patients ($r = -0.543$, $p = 0.005$). However, there was no discernible correlation between the abnormal variability of dReHo and epilepsy duration, NHS3 score or the number of ASMs.

Validation analyses

Two different cluster sizes (7 and 19 voxels, respectively) were investigated to find out how they might impact the results. The new results were mostly consistent with the results reported above. However, there were slight variances in the outcomes: (1) when 7 and 19 voxels were selected, respectively, to calculate sReHo, the difference in sReHo between mTLE-IPI and mTLE-NO patients in the right cerebellar Crus1/Crus2 vanished, (2) when 7 voxels were selected, the right inferior parietal lobule and right temporal lobe of the mTLE-IPI lost their decreased sReHo as compared to HC, and (3) the right dorsolateral prefrontal cortex's decreased sReHo and the left thalamus's increased variability of dReHo of mTLE-IPI vanished when compared to mTLE-NO. For more information, please consult Supplementary Figures S1–S4. What's more, different window sizes/step sizes (100/20 TRs and 80/30 TRs) were used to validate the variability of dReHo. The new results were basically consistent with the main results. Please see Supplementary Figures S5, S6 for details.

TABLE 1 Demographic and clinical information of participants.

Characteristics	mTLE-IPI	mTLE-NO	HC	Statistic	*p* value
Age (year)	29.92 ± 8.05	29.54 ± 8.76	29.52 ± 8.68	$F = 0.019$	0.981
Gender (male/female)	14/11	14/21	15/18	$\chi^2 = 1.541$	0.469
Mean FD (mm)	0.07 (0.05)	0.05 (0.06)	0.05 (0.05)	$F = 2.038$	0.361
Lateralization (left/right)	10/15	17/18	–	$\chi^2 = 0.433$	0.511
Epilepsy duration (year)	11.00 (18.00)	8.00 (10.00)	–	$Z = -0.661$	0.509
NHS3 score	11.00 (7.00)	10.00 (7.00)	–	$Z = -0.346$	0.729
The number of ASMs	2.00 (1.00)	3.00 (1.00)	–	$Z = -0.703$	0.482

mTLE-IPI, mTLE patients with initial precipitating injury; mTLE-NO, mTLE without IPI; HC, healthy controls; FD, framewise displacement; NHS3, national hospital seizure severity scale; ASMs, antiseizure medications. Values are mean ± standard deviation; others are median (interquartile range).

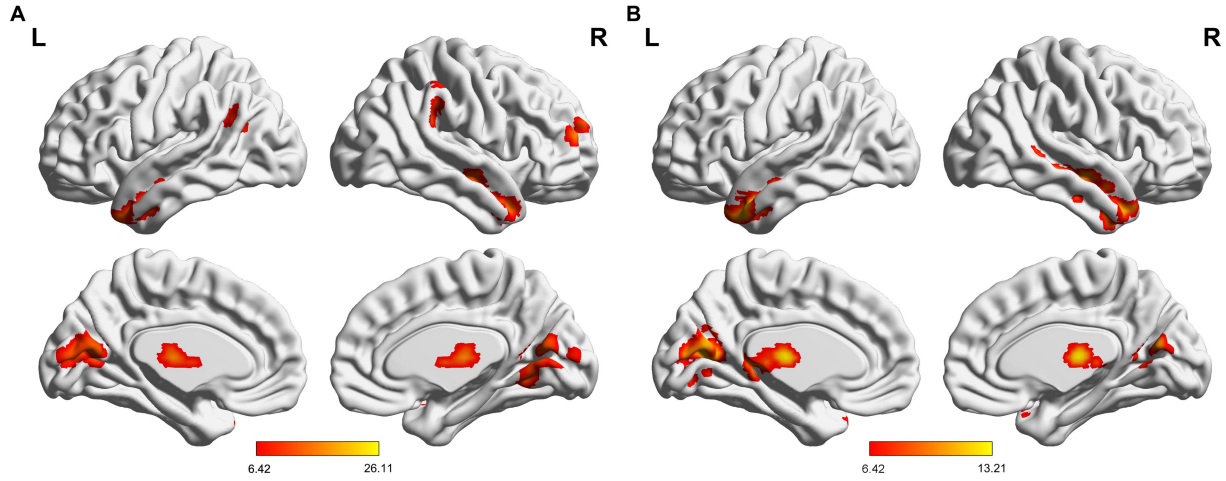

FIGURE 1
(A) Significant alterations of sReHo among three groups; **(B)** Significant alterations of dReHo among three groups. sReHo, static regional homogeneity; dReHo, dynamic regional homogeneity; L, left; R, right.

Discussion

Despite the fact that there have been numerous research on static and dynamic ReHo in the past, we found that the majority of them highlighted the differences between all patients and healthy controls, without detailed grouping of patients, such as with or without IPI, which may lead to inconsistent results. Therefore, we explored the changes in spontaneous neural activity in the three groups from the perspectives of sReHo and dReHo to investigate if IPI had an effect on cognitive impairment in mTLE patients. As results showed, the differences between the three groups were mainly located in the bilateral thalamus, occipital lobe and temporal lobe neocortex, and the activation brain regions of sReHo and dReHo were basically the same, suggesting that the dysfunction of these brain regions was reflected not only in the static state, but also in the dynamic state (Duma et al., 2022, 2023). Besides, mTLE-IPI had decreased sReHo in right cerebellum, IPL and DLPFC compared with HC and mTLE-NO respectively, implying a complementarity between sReHo and dReHo.

The thalamus is a key relay station for communicating information between the cortex and subcortical structures, as well as a crucial extratemporal structure for regulating and propagating TLE epileptogenic discharges (Keller et al., 2014). It functions critically in mental activity, the arousal system of the brain, emotion and movement (Ward, 2013). A significant and expanding body of literature supports the functional and structural impairment of the thalamus in patients with mTLE (Barron et al., 2015; Chen et al., 2015; Gleichgerrcht et al., 2021). In a mouse model of temporal lobe epilepsy (Fei et al., 2022), hippocampal subicular pyramidal neurons were demonstrated to project to the anterior nucleus of the thalamus. As we know, hippocampal neurons are easily damaged by IPI (Janz et al., 2018). Due to the abnormal propagation of hippocampus discharges, we have reason to believe that not only were local neurons in the bilateral thalamus over-activated, but also the stability of neuronal activity was disrupted in mTLE-IPI patients. The abnormal spontaneous brain activity in the thalamus may be associated with attention deficiency, memory impairment and emotion change in mTLE-IPI patients. The dReHo variability of the left thalamus in mTLE-IPI patients was higher than that in mTLE-NO patients, suggesting that mTLE-IPI patients may have severer impairment of thalamic regional brain activity than mTLE-NO patients.

In contrast to HC and mTLE-NO patients, our investigation demonstrated that abnormal sReHo or dReHo took place in the bilateral visual cortex of mTLE-IPI patients. The visual network, which is located in occipital lobe and includes CAL, LG, cuneus and so on, is the key part of the brain for visual information integration and attention processing (Bezdek et al., 2015). A section of the primary visual cortex known as the CAL receives visual information directly from visual stimuli (Wang et al., 2022). LG is involved in the processing of visual memory, especially in the processing of words. Integrating visual information is believed to be a crucial function of the cuneus (Yang et al., 2022). Numerous investigations (Pang et al., 2021; Wills et al., 2021) have revealed that mTLE patients have functionally impaired occipital cortex. In line with these studies, our results reflect that patients with mTLE-IPI may be more likely to have impaired visual networks compared with mTLE-NO and HC. Inflammatory mediators, which can be produced by febrile convulsion as well as intracranial infection, will raise glutamatergic neurons' excitability (Rana and Musto, 2018; Mosili et al., 2020). The high density of glutamate receptors in the occipital cortex may lead the neurons to be in a more excited state and have a long-term influence on the neurons as the disease advances, resulting in unstable local neuronal activity in mTLE-IPI patients. The changed sReHo and dReHo in the bilateral visual cortex support the decline in patients' visual memory, spatial attention and ability to recognize colors and letters (Song et al., 2022). We noted that there were subtle differences in the areas of spontaneous brain activity alterations in the visual cortex. One possible explanation is that the combination of static and dynamic ReHo is more sensitive in reflecting brain abnormalities.

Our findings also suggested that both sReHo and the variability of dReHo in the bilateral MTG, left ITG and right STG in mTLE-NO patients were lower than in HC. Besides, the sReHo in right MTG and ITG was decreased in mTLE-IPI patients. These abnormal ReHo changes could be a result of the temporal neocortex's abnormal neuroplasticity being influenced by frequent abnormal discharges

TABLE 2 Brain regions with changed sReHo and dReHo among the three groups.

Indices	Cluster	Voxels	Brain region	Peak intensity	MNI coordinate
sReHo	1	68	Cerebellum_Crus1 _R	13.230	30, −66, −39
			Cerebellum_Crus2 _R	12.160	33, −67, −40
	2	114	Temporal_Inf_L	16.302	−45, 6, −33
			Temporal_Mid_L	6.981	−51, −4, −25
	3	118	Temporal_Sup_R	17.006	45, −12, −12
			Temporal_Inf_R	11.000	45, 8, −34
			Temporal_Mid_R	9.151	48, 8, −29
	4	326	Calcarine_R	13.083	3, −66, 12
			Calcarine_L	10.160	−2, −67, 14
			Lingual_R	9.773	1, −68, 9
			Lingual_L	6.677	−12, −70, 4
			Cuneus_L	9.644	−10, −72, 22
			Cuneus_R	7.172	6, −75, 20
	5	64	Thalamus_R	21.106	3, −16, 11
			Thalamus_L	6.571	5, −6, 5
	6	72	DLPFC_R	16.239	39, 57, 18
	7	54	Angular_R	9.108	48, −43, 28
			SupraMarginal_R	10.635	57, −39, 27
dReHo	1	233	Temporal_Pole_Mid_R	12.152	42, 9, −36
			Temporal_Mid_R	7.267	47, 4, −28
			Temporal_Inf_R	7.592	45, 1, −33
			Temporal_Sup_R	7.821	45, −15,-9
	2	151	Temporal_Mid_L	12.488	−57, 9, −27
			Temporal_Inf_L	9.127	−46, 4, −34
	3	311	Calcarine_L	13.210	−9, −69, 21
			Calcarine_R	6.314	2, −70, 19
			Cuneus_L	9.356	−9, −73, 27
			Lingual_R	5.661	13, −65, −3
			Lingual_L	5.756	−9, −70, −1
	4	131	Thalamus_L	10.140	−5, −16, 7

GRF corrected, voxel-wise $p < 0.005$, cluster-level $p < 0.05$; sReHo, static regional homogeneity; dReHo, dynamic regional homogeneity; DLPFC, dorsolateral prefrontal cortex; L, left; R, right.

(Jiang et al., 2021). The MTG (Binder et al., 2009) and ITG (Ojemann et al., 2002) play various roles in memory, auditory processing and emotion, while the STG houses a part of the primary and association auditory cortices (Song et al., 2022). Although results varied slightly due to the methodological differences, we could infer that mTLE patients (no matter with or without IPI) may be more prone to have functional deficits in social cognition, auditory processing and emotion management. We have to mention that a task state functional magnetic resonance imaging study (Trimmel et al., 2018) found that the right TIG was activated during picture naming in mTLE patients. Our findings, however, showed a reduction in sReHo in the right temporal neocortex. This inconsistency could be attributed to the fact that the patients in current study did not perform tasks such as picture naming during the scan.

The cerebellum not only plays an important role in the motor dysfunction of mTLE, but also participates in the impairment of cognitive function (Argyropoulos et al., 2020; Hao et al., 2022). The posterior cerebellum, such as crus 1/crus 2, corresponds to the prefrontal cortex (Wang et al., 2021) and IPL (Zhou et al., 2019) structurally and functionally, and participates in advanced cognitive function, especially executive control function. The abnormal sReHo detected in right cerebellum crus1/ crus2 and IPL may imply the disruption of neuronal activity in cerebellum-related neural circuits, supporting the higher-level cognitive and executive dysfunction in mTLE-IPI patients. Additionally, our results indicated that the NHS3 score was negatively correlated with sReHo in right cerebellum crus1 in mTLE-IPI, suggesting that the lower the consistency of local neuronal activity in the right cerebellum crus1, the poorer the patient's condition.

Interestingly, sReHo in the right DLPFC of mTLE-IPI patients was decreased when compared with mTLE-NO patients, whereas there was no significant difference when compared with HC. Therefore,

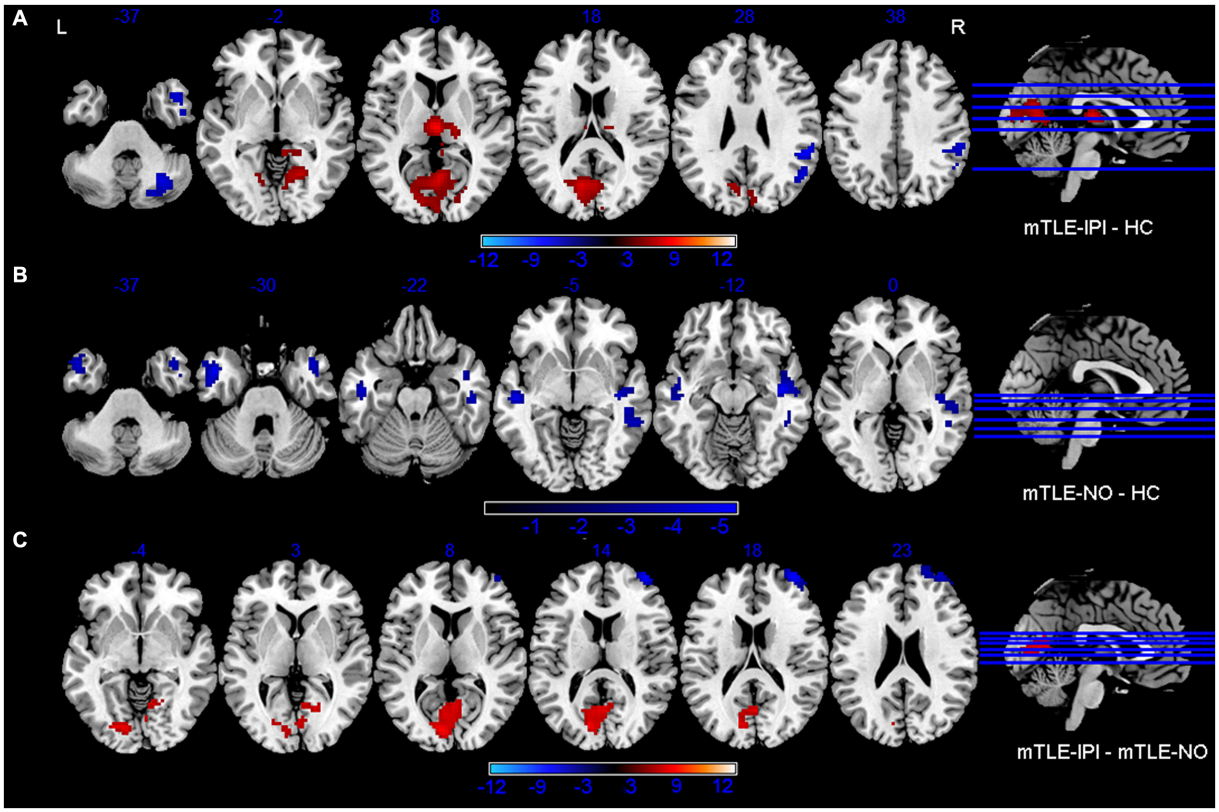

FIGURE 2
Brain regions with significant alterations of sReHo between mTLE-IPI and HC **(A)**, mTLE-NO and HC **(B)**, mTLE-IPI and mTLE-NO **(C)**. GRF corrected; voxel-wise $p < 0.005$, cluster-level $p < 0.05$. Warm colors indicate increased sReHo, while cold colors indicated decreased sReHo. sReHo, static regional homogeneity; mTLE-IPI, mTLE patients with initial precipitating injury; mTLE-NO, mTLE patients without initial precipitating injury; HC, healthy controls; GRF, Gaussian random field theory; L, left; R, right.

we speculated that one of the two groups had a slight increase in sReHo of the right DPLFC, while the other had a tiny decrease. Increases or decreases in sReHo, particularly in the DPLFC, which is widely considered to be a vital cortical region involved in cognitive function (Qin et al., 2020), may cause neuronal activity to deviate from the normal range, which is detrimental to normal cognitive activity.

It is noteworthy that the number of brain regions with significant differences between the three groups changed slightly when we varied the cluster size, and the smaller the cluster size was the fewer distinct brain regions there were. This is consistent with the assertion (Zang et al., 2004) that "larger size of cluster yielded more differences." So, we speculated smaller cluster size probably decreased the detection of spontaneous brain activity and hindered ReHo temporal variability. Recent years, several researchers (Shinn et al., 2023) have advocated using the parcellation method to determine the ReHo value of each parcellated brain region, such that at least one could have a region specific value of homogeneity. It is worth investigating which method can better characterize the constancy of local neural activity.

Limitations

There are several limitations in this study. To mention first, a larger sample size is needed to improve the credibility of our findings. The sample size in this study is relatively small. More individuals should be included in follow-up studies. Secondly, for mTLE-IPI patients, we did not further subdivide them. There may be different patterns of intrinsic brain activities among mTLE patients caused by different IPI. Thus, more detailed grouping is required to deepen the understanding of neuropathological changes of different mTLE-IPI subtypes, which is of profound significance for guiding clinical treatment. Thirdly, the effect of ASMs cannot be ignored. ASMs may confound the results of this study since they can inhibit the epileptogenesis by preventing the excitatory transmission of neurons (Miziak et al., 2020), which may have a certain impact on regional brain activities. Although we compared the number of ASMs between the two groups, it may be far from enough. Finally, the current study is cross-sectional. In order to better explain the mechanism of IPI on mTLE and its ongoing effect, longitudinal research is necessary.

Conclusion

The current study found that there were different patterns of local neuronal activity alterations in mTLE-IPI and mTLE-NO, and the severity of abnormalities in mTLE-IPI patients was greater than that in mTLE-NO patients, especially in the bilateral thalamus and visual cortex. Besides, there were abnormal sReHo in the right temporal neocortex no matter in mTLE-IPI or mTLE-NO patients. Furthermore,

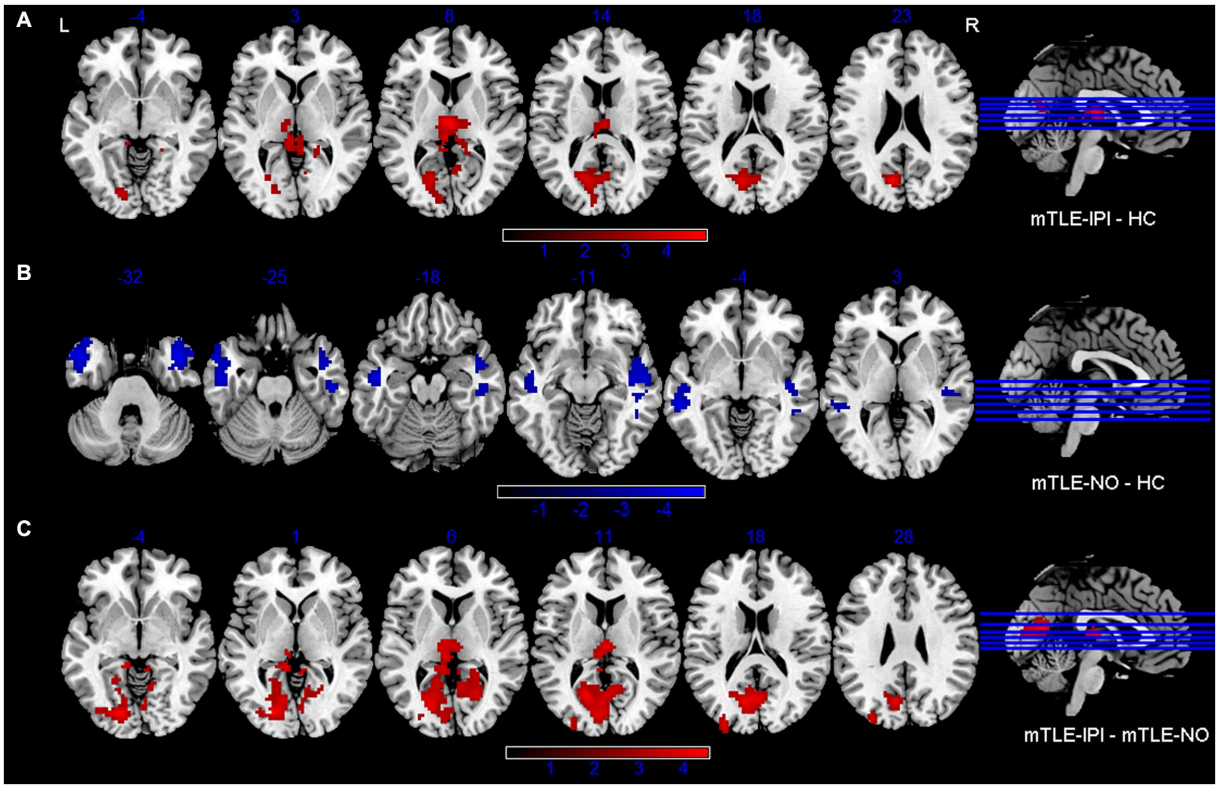

FIGURE 3
Brain regions with significant alterations of variability of dReHo between mTLE-IPI and HC **(A)**, mTLE-NO and HC **(B)**, mTLE-IPI and mTLE-NO **(C)**. GRF corrected; voxel-wise $p < 0.005$, cluster-level $p < 0.05$. Warm colors indicate increased variability of dReHo, while cold colors indicated decreased variability of dReHo. dReHo, dynamic regional homogeneity; mTLE-IPI, mTLE patients with initial precipitating injury; mTLE-NO, mTLE patients without initial precipitating injury; HC, healthy controls; GRF, Gaussian random field theory; L, left; R, right.

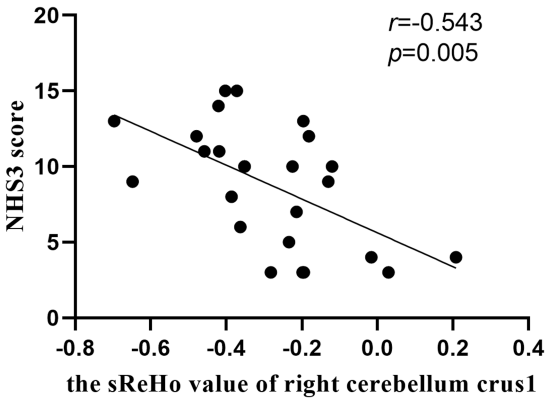

FIGURE 4
The correlation between the sReHo value of right cerebellum crus1 and NHS3 score in patients with mTLE-IPI.

our study also suggested that combining the static and dynamic indicators could build better models of brain function and dysfunction. In a word, these findings can help us comprehend how IPI affects the impaired brain activity of mTLE patients and can assist in carrying out timely intervention for patients with mTLE-IPI in order to control the progress of the disease effectively.

Data availability statement

The raw data supporting the conclusions of this article will be made available by the authors, without undue reservation.

Ethics statement

The studies involving human participants were reviewed and approved by Research Ethical Committee of The First Affiliated Hospital of Zhengzhou University. Written informed consent to participate in this study was provided by the participants' legal guardian/next of kin.

Author contributions

XM wrote the first draft of the manuscript. XM and XZ contributed to design of the study and performed data and statistical analysis. XM, XZ, CS, KM, and KW collected the data. YL provided the clinical diagnosis of the participants. XW and SH provided the methodological advice. XZ, CS, and SH proofread the manuscript. YaZ, YoZ, and JC supervised the conduct of the study. All authors contributed to the article and approved the submitted version.

Conflict of interest

The authors declare that the research was conducted in the absence of any commercial or financial relationships that could be construed as a potential conflict of interest.

Publisher's note

All claims expressed in this article are solely those of the authors and do not necessarily represent those of their affiliated organizations, or those of the publisher, the editors and the reviewers. Any product that may be evaluated in this article, or claim that may be made by its manufacturer, is not guaranteed or endorsed by the publisher.

Supplementary material

The Supplementary material for this article can be found online at: https://www.frontiersin.org/articles/10.3389/fnins.2023.1226077/full#supplementary-material

References

Argyropoulos, G. P. D., van Dun, K., Adamaszek, M., Leggio, M., Manto, M., Masciullo, M., et al. (2020). The cerebellar cognitive affective/Schmahmann syndrome: a task force paper. *Cerebellum* 19, 102–125. doi: 10.1007/s12311-019-01068-8

Barron, D. S., Fox, P. T., Pardoe, H., Lancaster, J., Price, L. R., Blackmon, K., et al. (2015). Thalamic functional connectivity predicts seizure laterality in individual TLE patients: application of a biomarker development strategy. *Neuroimage Clin.* 7, 273–280. doi: 10.1016/j.nicl.2014.08.002

Bezdek, M. A., Gerrig, R. J., Wenzel, W. G., Shin, J., Revill, K. P., and Schumacher, E. H. (2015). Neural evidence that suspense narrows attentional focus. *Neuroscience* 303, 338–345. doi: 10.1016/j.neuroscience.2015.06.055

Bien, C., Urbach, H., Schramm, J., Soeder, B., Becker, A., Voltz, R., et al. (2007). Limbic encephalitis as a precipitating event in adult-onset temporal lobe epilepsy. *Neurology* 69, 1236–1244. doi: 10.1212/01.wnl.0000276946.08412.ef

Binder, J. R., Desai, R. H., Graves, W. W., and Conant, L. L. (2009). Where is the semantic system? A critical review and meta-analysis of 120 functional neuroimaging studies. *Cereb. Cortex* 19, 2767–2796. doi: 10.1093/cercor/bhp055

Calhoun, V. D., Miller, R., Pearlson, G., and Adali, T. (2014). The chronnectome: time-varying connectivity networks as the next frontier in fMRI data discovery. *Neuron* 84, 262–274. doi: 10.1016/j.neuron.2014.10.015

Chen, X. M., Huang, D. H., Chen, Z. R., Ye, W., Lv, Z. X., and Zheng, J. O. (2015). Temporal lobe epilepsy: decreased thalamic resting-state functional connectivity and their relationships with alertness performance. *Epilepsy Behav.* 44, 47–54. doi: 10.1016/j.yebeh.2014.12.013

Duma, G. M., Danieli, A., Mattar, M. G., Baggio, M., Vettorel, A., Bonanni, P., et al. (2022). Resting state network dynamic reconfiguration and neuropsychological functioning in temporal lobe epilepsy: an HD-EEG investigation. *Cortex* 157, 1–13. doi: 10.1016/j.cortex.2022.08.010

Duma, G. M., Danieli, A., Mento, G., Vitale, V., Opipari, R. S., Jirsa, V., et al. (2023). Altered spreading of neuronal avalanches in temporal lobe epilepsy relates to cognitive performance: a resting-state hdEEG study. *Epilepsia* 64, 1278–1288. doi: 10.1111/epi.17551

Fei, F., Wang, X., Xu, C., Shi, J., Gong, Y., Cheng, H., et al. (2022). Discrete subicular circuits control generalization of hippocampal seizures. *Nat. Commun.* 13:5010. doi: 10.1038/s41467-022-32742-x

Free, S., Li, L., Fish, D., Shorvon, S., and Stevens, J. (1996). Bilateral hippocampal volume loss in patients with a history of encephalitis or meningitis. *Epilepsia* 37, 400–405. doi: 10.1111/j.1528-1157.1996.tb00578.x

Gleichgerrcht, E., Kellermann, T. S., Drane, D. L., Keller, S. S., McDonald, C. R., Rorden, C., et al. (2021). Cortical disconnection in temporal lobe epilepsy. *Epilepsy Behav.* 123:108231. doi: 10.1016/j.yebeh.2021.108231

Hao, S., Yang, C., Li, Z., and Ren, J. (2022). Distinguishing patients with temporal lobe epilepsy from normal controls with the directed graph measures of resting-state fMRI. *Seizure* 96, 25–33. doi: 10.1016/j.seizure.2022.01.007

Hu, C.-Y., Gao, X., Long, L., Long, X., Liu, C., Chen, Y., et al. (2017). Altered DMN functional connectivity and regional homogeneity in partial epilepsy patients: a seventy cases study. *Oncotarget* 8:81475. doi: 10.18632/oncotarget.20575

Janz, P., Hauser, P., Heining, K., Nestel, S., Kirsch, M., Egert, U., et al. (2018). Position- and time-dependent arc expression links neuronal activity to synaptic plasticity during Epileptogenesis. *Front. Cell. Neurosci.* 12:244. doi: 10.3389/fncel.2018.00244

Jiang, L., Ma, X., Liu, H., Wang, J., Zhang, J., Zhang, G., et al. (2021). Aberrant dynamics of regional coherence measured by resting-state fMRI in children with benign epilepsy with Centrotemporal spikes (BECTS). *Front. Neurol.* 12:712071. doi: 10.3389/fneur.2021.712071

Jiang, L., and Zuo, X. N. (2016). Regional homogeneity: a multimodal, multiscale neuroimaging marker of the human Connectome. *Neuroscientist* 22, 486–505. doi: 10.1177/1073858415595004

Keller, S. S., O'Muircheartaigh, J., Traynor, C., Towgood, K., Barker, G. J., and Richardson, M. P. (2014). Thalamotemporal impairment in temporal lobe epilepsy: a combined MRI analysis of structure, integrity, and connectivity. *Epilepsia* 55, 306–315. doi: 10.1111/epi.12520

Keller, S. S., Wieshmann, U. C., Mackay, C. E., Denby, C. E., Webb, J., and Roberts, N. (2002). Voxel based morphometry of grey matter abnormalities in patients with medically intractable temporal lobe epilepsy: effects of side of seizure onset and epilepsy duration. *J. Neurol. Neurosurg. Psychiatry* 73, 648–655. doi: 10.1136/jnnp.73.6.648

Leonardi, N., and Van De Ville, D. (2015). On spurious and real fluctuations of dynamic functional connectivity during rest. *NeuroImage* 104, 430–436. doi: 10.1016/j.neuroimage.2014.09.007

Li, R., Deng, C., Wang, X., Zou, T., Biswal, B., Guo, D., et al. (2022). Interictal dynamic network transitions in mesial temporal lobe epilepsy. *Epilepsia* 63, 2242–2255. doi: 10.1111/epi.17325

Liang, X., Pang, X., Zhao, J., Yu, L., Wu, P., Li, X., et al. (2021). Altered static and dynamic functional network connectivity in temporal lobe epilepsy with different disease duration and their relationships with attention. *J. Neurosci. Res.* 99, 2688–2705. doi: 10.1002/jnr.24915

Miziak, B., Konarzewska, A., Ulamek-Koziol, M., Dudra-Jastrzebska, M., Pluta, R., and Czuczwar, S. J. (2020). Anti-epileptogenic effects of antiepileptic drugs. *Int. J. Mol. Sci.* 21:2340. doi: 10.3390/ijms21072340

Morgan, V. L., Chang, C., Englot, D. J., and Rogers, B. P. (2020). Temporal lobe epilepsy alters spatio-temporal dynamics of the hippocampal functional network. *Neuroimage Clin.* 26:102254. doi: 10.1016/j.nicl.2020.102254

Mosili, P., Maikoo, S., Mabandla, M. V., and Qulu, L. (2020). The pathogenesis of fever-induced febrile seizures and its current state. *Neurosci. Insights* 15:2633105520956973. doi: 10.1177/2633105520956973

Ojemann, G. A., Schoenfield-McNeill, J., and Corina, D. P. (2002). Anatomic subdivisions in human temporal cortical neuronal activity related to recent verbal memory. *Nat. Neurosci.* 5, 64–71. doi: 10.1038/nn785

Pang, X., Liang, X., Zhao, J., Wu, P., Li, X., Wei, W., et al. (2021). Abnormal static and dynamic functional connectivity in left and right temporal lobe epilepsy. *Front. Neurosci.* 15:820641. doi: 10.3389/fnins.2021.820641

Patterson, K. P., Baram, T. Z., and Shinnar, S. (2014). Origins of temporal lobe epilepsy: febrile seizures and febrile status epilepticus. *Neurotherapeutics* 11, 242–250. doi: 10.1007/s13311-014-0263-4

Polat, T. B., Cetinkaya, F., ÇALIŞKAN, M., Duran, C., and Karaman, K. (2010). Assessment of hippocampal volumes in infants with a history of bacterial meningitis. *Gazi Med. J.* 21, 34–37.

Power, J. D., Barnes, K. A., Snyder, A. Z., Schlaggar, B. L., and Petersen, S. E. (2012). Spurious but systematic correlations in functional connectivity MRI networks arise from subject motion. *NeuroImage* 59, 2142–2154. doi: 10.1016/j.neuroimage.2011.10.018

Qin, L., Jiang, W., Zheng, J., Zhou, X., Zhang, Z., and Liu, J. (2020). Alterations functional connectivity in temporal lobe epilepsy and their relationships with cognitive function: a longitudinal resting-state fMRI study. *Front. Neurol.* 11:625. doi: 10.3389/fneur.2020.00625

Rana, A., and Musto, A. E. (2018). The role of inflammation in the development of epilepsy. *J. Neuroinflammation* 15:144. doi: 10.1186/s12974-018-1192-7

Satterthwaite, T. D., Wolf, D. H., Loughead, J., Ruparel, K., Elliott, M. A., Hakonarson, H., et al. (2012). Impact of in-scanner head motion on multiple measures of functional connectivity: relevance for studies of neurodevelopment in youth. *NeuroImage* 60, 623–632. doi: 10.1016/j.neuroimage.2011.12.063

Shinn, M., Hu, A., Turner, L., Noble, S., Preller, K. H., Ji, J. L., et al. (2023). Functional brain networks reflect spatial and temporal autocorrelation. *Nat. Neurosci.* 26, 867–878. doi: 10.1038/s41593-023-01299-3

Song, M., and Jiang, T. (2012). A review of functional magnetic resonance imaging for Brainnetome. *Neurosci. Bull.* 28, 389–398. doi: 10.1007/s12264-012-1244-4

Song, C., Zhang, X., Han, S., Ma, K., Wang, K., Mao, X., et al. (2022). More than just statics: static and temporal dynamic changes in intrinsic brain activity in unilateral temporal lobe epilepsy. *Front. Hum. Neurosci.* 16:971062. doi: 10.3389/fnhum.2022.971062

Trimmel, K., van Graan, A. L., Caciagli, L., Haag, A., Koepp, M. J., Thompson, P. J., et al. (2018). Left temporal lobe language network connectivity in temporal lobe epilepsy. *Brain* 141, 2406–2418. doi: 10.1093/brain/awy164

Wang, H., Wang, B., Cen, Z., Wang, J., Zang, Y. F., Yang, D., et al. (2022). Aberrant visual-related networks in familial cortical myoclonic tremor with epilepsy. *Parkinsonism Relat. Disord.* 101, 105–110. doi: 10.1016/j.parkreldis.2022.07.001

Wang, K., Zhang, X., Song, C., Ma, K., Bai, M., Zheng, R., et al. (2021). Decreased intrinsic neural timescales in mesial temporal lobe epilepsy. *Front. Hum. Neurosci.* 15:772365. doi: 10.3389/fnhum.2021.772365

Ward, L. M. (2013). The thalamus: gateway to the mind. *Wiley Interdiscip. Rev. Cogn. Sci.* 4, 609–622. doi: 10.1002/wcs.1256

Wen, M., Yang, Z., Wei, Y., Huang, H., Zheng, R., Wang, W., et al. (2021). More than just statics: temporal dynamic changes of intrinsic brain activity in cigarette smoking. *Addict. Biol.* 26:e13050. doi: 10.1111/adb.13050

Wills, K. E., Gonzalez, H. F. J., Johnson, G. W., Haas, K. F., Morgan, V. L., Narasimhan, S., et al. (2021). People with mesial temporal lobe epilepsy have altered thalamo-occipital brain networks. *Epilepsy Behav.* 115:107645. doi: 10.1016/j.yebeh.2020.107645

Xue, K., Liang, S., Yang, B., Zhu, D., Xie, Y., Qin, W., et al. (2022). Local dynamic spontaneous brain activity changes in first-episode, treatment-naive patients with major depressive disorder and their associated gene expression profiles. *Psychol. Med.* 52, 2052–2061. doi: 10.1017/S0033291720003876

Yan, C.-G., Yang, Z., Colcombe, S. J., Zuo, X.-N., and Milham, M. P. (2017). Concordance among indices of intrinsic brain function: insights from inter-individual variation and temporal dynamics. *Sci. Bull.* 62, 1572–1584. doi: 10.1016/j.scib.2017.09.015

Yan, C.-G., and Zang, Y.-F. (2010). DPARSF: a MATLAB toolbox for "pipeline" data analysis of resting-state fMRI. *Front. Syst. Neurosci.* 4:13. doi: 10.3389/fnsys.2010.00013

Yang, Z., Wen, M., Wei, Y., Huang, H., Zheng, R., Wang, W., et al. (2022). Alternations in dynamic and static functional connectivity density in chronic smokers. *Front. Psych.* 13:843254. doi: 10.3389/fpsyt.2022.843254

Zang, Y., Jiang, T., Lu, Y., He, Y., and Tian, L. (2004). Regional homogeneity approach to fMRI data analysis. *NeuroImage* 22, 394–400. doi: 10.1016/j.neuroimage.2003.12.030

Zeng, H., Pizarro, R., Nair, V. A., La, C., and Prabhakaran, V. (2013). Alterations in regional homogeneity of resting-state brain activity in mesial temporal lobe epilepsy. *Epilepsia* 54, 658–666. doi: 10.1111/epi.12066

Zhao, B., Yang, B., Tan, Z., Hu, W., Sang, L., Zhang, C., et al. (2020). Intrinsic brain activity changes in temporal lobe epilepsy patients revealed by regional homogeneity analysis. *Seizure* 81, 117–122. doi: 10.1016/j.seizure.2020.07.030

Zhou, X., Zhang, Z., Liu, J., Qin, L., Pang, X., and Zheng, J. (2019). Disruption and lateralization of cerebellar-cerebral functional networks in right temporal lobe epilepsy: a resting-state fMRI study. *Epilepsy Behav.* 96, 80–86. doi: 10.1016/j.yebeh.2019.03.020

frontiers | Frontiers in Neuroscience

TYPE Case Report
PUBLISHED 28 September 2023
DOI 10.3389/fnins.2023.1217430

OPEN ACCESS

EDITED BY
Yingying Tang,
Shanghai Jiao Tong University, China

REVIEWED BY
Talyta Grippe,
University of Toronto, Canada
Kotoe Sakihara,
Teikyo University, Japan

*CORRESPONDENCE
Masako Kinoshita
✉ machak@kuhp.kyoto-u.ac.jp

RECEIVED 05 May 2023
ACCEPTED 12 September 2023
PUBLISHED 28 September 2023

CITATION
Takada K, Yamaguchi T, Hyuga Y, Mitsuno Y, Horiguchi S, Kinoshita M and Satow T (2023) Impairment of bimanual in-phase movement during recovery from frontal lobe tumor surgery: a case report.
Front. Neurosci. 17:1217430.
doi: 10.3389/fnins.2023.1217430

Impairment of bimanual in-phase movement during recovery from frontal lobe tumor surgery: a case report

Kozue Takada[1], Takuya Yamaguchi[2], Yuko Hyuga[2], Yuto Mitsuno[3], Satoshi Horiguchi[3], Masako Kinoshita[1]* and Takeshi Satow[3,4]

[1]Department of Neurology, National Hospital Organization Utano National Hospital, Kyoto, Japan, [2]Department of Rehabilitation, Nagahama City Hospital, Nagahama, Shiga, Japan, [3]Department of Neurosurgery, Nagahama City Hospital, Nagahama, Shiga, Japan, [4]Department of Neurosurgery, National Hospital Organization Utano National Hospital, Kyoto, Japan

The mechanisms underlying bimanual coordination have not yet been fully elucidated. Here, we evaluated the clinical features of bimanual movement impairment in a patient following surgery for a frontal lobe tumor. The patient was an 80-year-old man who had undergone subtotal tumor resection for a tumor in the right superior frontal gyrus. Histological examination of the resected specimen led to the diagnosis of malignant lymphoma of the diffuse large B-cell type, and the patient subsequently received high-dose methotrexate-based chemotherapy. Postoperatively, the patient had difficulty with bimanual movement, and on the 5th postoperative day we found that the impairment could not be attributed to weakness. Temporal changes in the characteristics of manual movements were analyzed. Bimanual diadochokinesis (opening/closing of the hands, pronation/supination of the forearms, and sequential finger movements) was more disturbed than unilateral movements; in-phase movements were more severely impaired than anti-phase movements. Bimanual movement performance was better when cued using an auditory metronome. On the 15th postoperative day, movements improved. The present observations show that in addition to the disturbance of anti-phase bimanual movements, resection of the frontal lobe involving the supplementary motor area (SMA) and premotor cortex (PMC) can cause transient impairment of in-phase bimanual diadochokinesis, which can be more severe than the impairment of anti-phase movements. The effect of auditory cueing on bimanual skills may be useful in the diagnosis of anatomical localization of the superior frontal gyrus and functional localization of the SMA and PMC and in rehabilitation of patients with brain tumors, as in the case of degenerative movement disorders.

KEYWORDS

bimanual movement, frontal lobe, primary motor cortex, supplementary motor area, premotor cortex, motor coordination

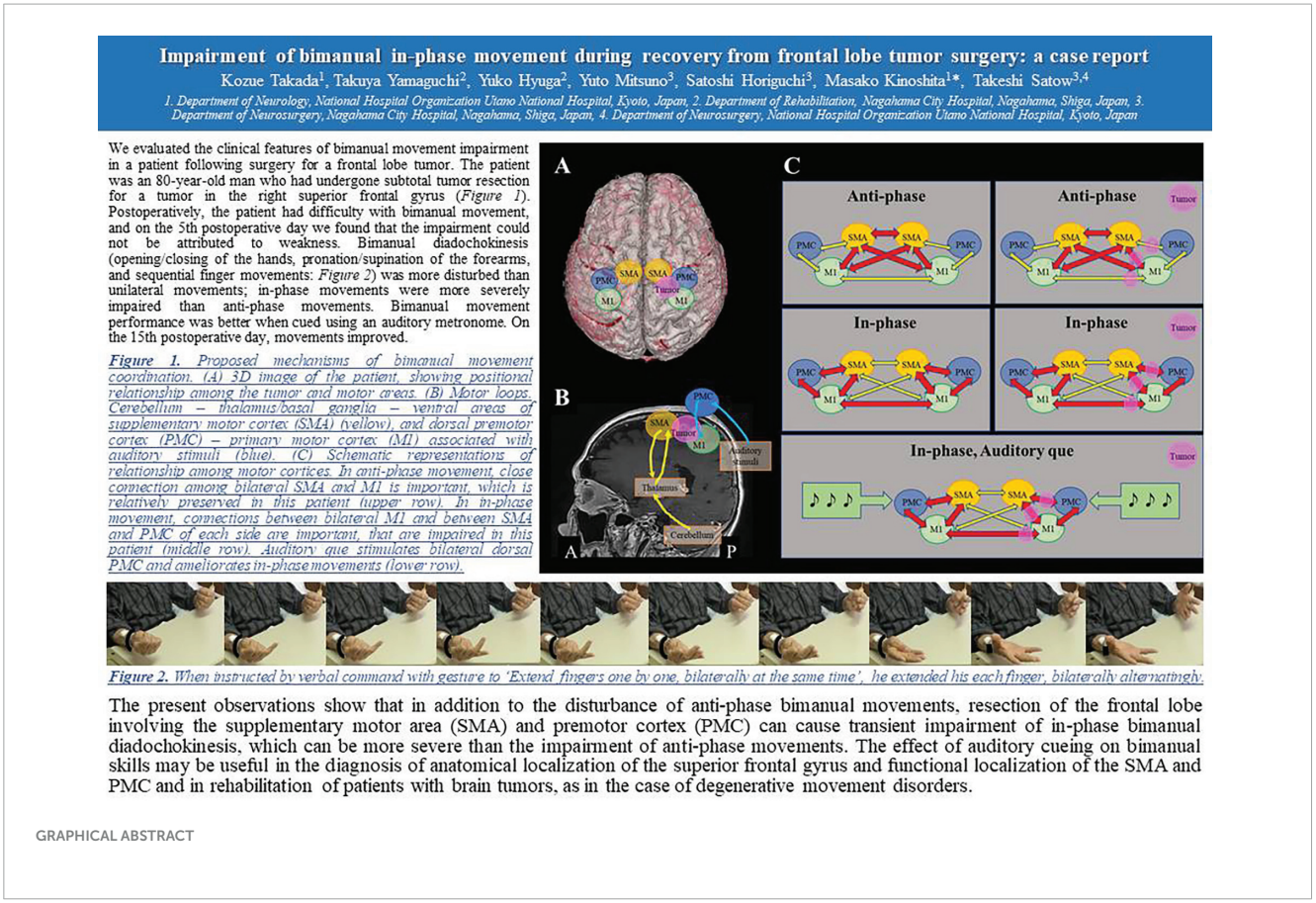

GRAPHICAL ABSTRACT

1. Introduction

Bimanual coordination remains unclear in terms of its underlying mechanisms. In addition to the primary motor cortex, the supplementary motor area (SMA) and premotor cortex (PMC) play significant roles in complex motor control. The SMA and PMC reside in the posterior part of the superior frontal gyrus and in the mesial and lateral portions of Brodmann area 6, respectively. SMA syndrome is characterized by akinesia with preserved muscle strength, which is more severe on the contralateral side of the SMA lesion and usually recovers over several weeks (Laplane et al., 1977). The disturbance of anti-phase bimanual alternating movements is a residual symptom of SMA syndrome (Laplane et al., 1977).

Here, we report the case of a patient with a frontal lobe tumor who showed a rare manifestation of more severe impairment of in-phase than of anti-phase movements after surgery.

2. Case description

An 80-year-old right-handed man underwent subtotal resection of a tumor in the right superior frontal gyrus (**Figures 1A-C**). The tumor was histologically diagnosed as a diffuse large B-cell type malignant lymphoma. and he subsequently received high-dose, methotrexate-based chemotherapy. The tumor did not involve the pre- and postcentral gyri. Diffusion tensor imaging showed that corticospinal tract was intact (**Figures 1D, E**). Thus, the primary sensorimotor cortex was preserved (**Figure 1F**). Postoperatively, the patient had difficulty with bimanual movement. At first, we considered that the difficulty was caused by weakness and akinesia. However, on the 5th postoperative day we found that the impairment could not be attributed to weakness because his motor skills varied depending upon the type of movement. Thus, we precisely evaluated his movement in the recovery process. This study was conducted according to the principles of the Declaration of Helsinki. The Institutional Ethics Review Board waived approval of the study design. Written informed consent was obtained from the patient for publication of the case report and accompanying images.

3. Diagnostic assessment

Temporal changes in the characteristics and performance of manual movements were analyzed by reviewing video recordings (**Supplementary Videos 1–13**).

On the 5th postoperative day, the unilateral left-sided movements were skillful (**Supplementary Videos 1, 3, 5**). In contrast, when the patient was instructed to perform bilateral movements of the hands and arms, such as raising the arms, pronation and supination of the forearms, and opening and closing of the hands, he could not move his left side properly (**Supplementary Videos 2, 4**, and **6**). When an instruction on in-phase sequential finger movement was given by verbal commands with gestures to bend his fingers from the thumb in order and open his fingers bilaterally at the same time, a whole series of

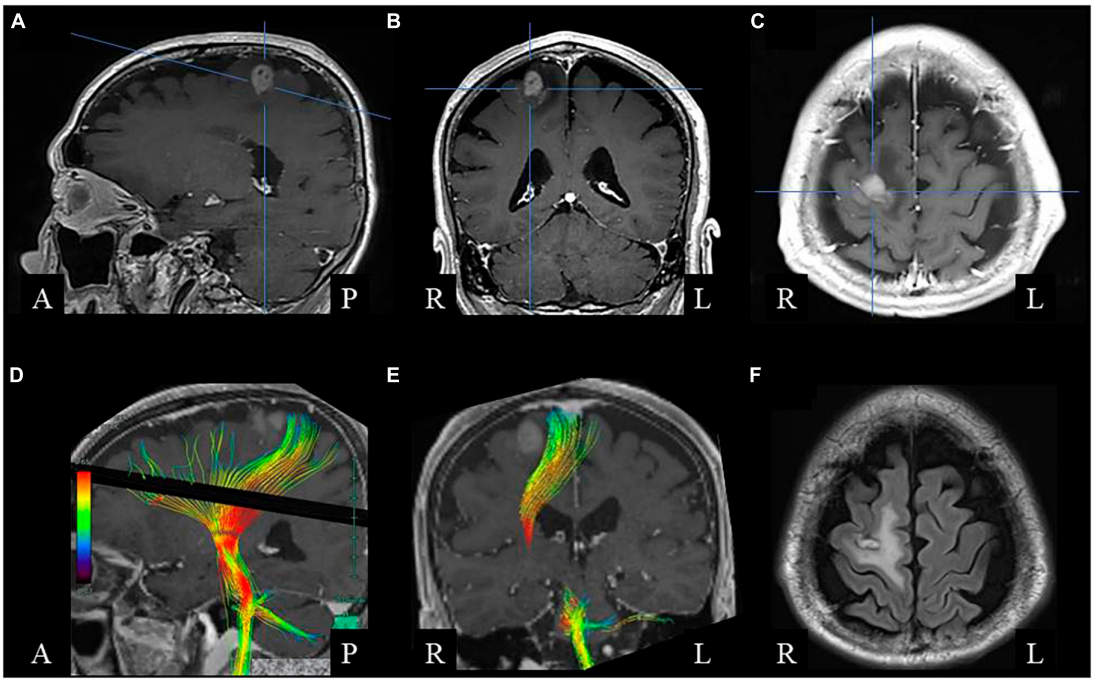

FIGURE 1
Brain magnetic resonance imaging before surgery. Gadolinium-enhanced T1-weighted sagittal **(A)**, coronal **(B)**, and axial **(C)** images show a right frontal lesion with enhancement. **(D,E)** Diffusion tensor image showing the corticospinal tract. **(F)** Postoperative fluid-attenuated inversion recovery axial image, showing small resected area with low-intensity rim surrounded by high-intensity white matter lesion.

movements at once, he bent and extended his fingers, one at a time, alternating bilaterally with a chant to keep time (**Figure 2** and **Supplementary Video 6**). He was aware that he could not move both sides simultaneously and substituted in-phase movements with anti-phase or unilateral movements. The patient often chanted aloud to keep time. Bimanual in-phase closing-opening movement performance improved when cued by the sounds of a metronome at 40 beats per minute (**Supplementary Videos 7, 8**).

As for the other parts of the body, bilateral leg movements showed similar tendency; anti-phase movements were more skillful than in-phase movements (**Supplementary Videos 9, 10**). There was no language impairment.

The next day (the 6th postoperative day), his bimanual movements improved compared to those on the day before; however, every movement was performed by calling out. At the beginning of the bilateral in-phase movement, the left hand was delayed in facing the palm upward and making a fist, but afterward, the opening/closing movements were smooth (**Supplementary Video 11**). As for the anti-phase movements, initial closing of the right hand and opening of the left hand were performed as instructed; however, the patient was unable to perform bilateral opposite movements simultaneously and made fists with both hands. Instead of pronation/supination of both forearms, the patient showed alternating unilateral movement. When instructed to perform sequential movements of the bilateral fingers, he could simultaneously flex the bilateral thumbs and index fingers; however, flexion/extension of the other fingers was performed alternately (**Supplementary Video 12**). Unilateral left-side movements were skillful but the actual movement performed was opposite to his call-out; e.g., he opened his palm while saying "fist."

On the 15th postoperative day, in-phase bimanual movements, namely, closing/opening and sequential finger movements improved (**Supplementary Video 13**).

4. Discussion

To the best of our knowledge, this is the first report to demonstrate disturbance of bimanual in-phase movement after frontal lobe surgery. While functional localization of the SMA and PMC is heterogenous among individuals (Fried et al., 1991; Chung et al., 2005; Genon et al., 2018), the current observation demonstrated that the resected area included the SMA and PMC in the superior frontal gyrus. In addition, the resection interrupted network among bilateral SMA, PMC, and primary motor cortices (**Figure 3**). We found a novel symptom of SMA syndrome, which also indicates an importance of disconnection of motor areas on pathophysiology of SMA syndrome.

In general, anti-phase movements are more complex and require greater activation of the SMA and PMC than in-phase movements (Sadato et al., 1997). There is a phenomenon called phase transition, which is usually observed as a change from anti-phase to in-phase transition during bimanual coordination tasks (Repp, 2005). However, in our patient, in-phase sequential bilateral finger movement was more disturbed than anti-phase movement. Transcranial magnetic stimulation of the primary motor cortex disrupts bimanual in-phase tasks, whereas bimanual anti-phase tasks remain unaffected (Chen et al., 2005). Furthermore, the interhemispheric connectivity between the primary hand motor regions as per functional magnetic resonance imaging decreases

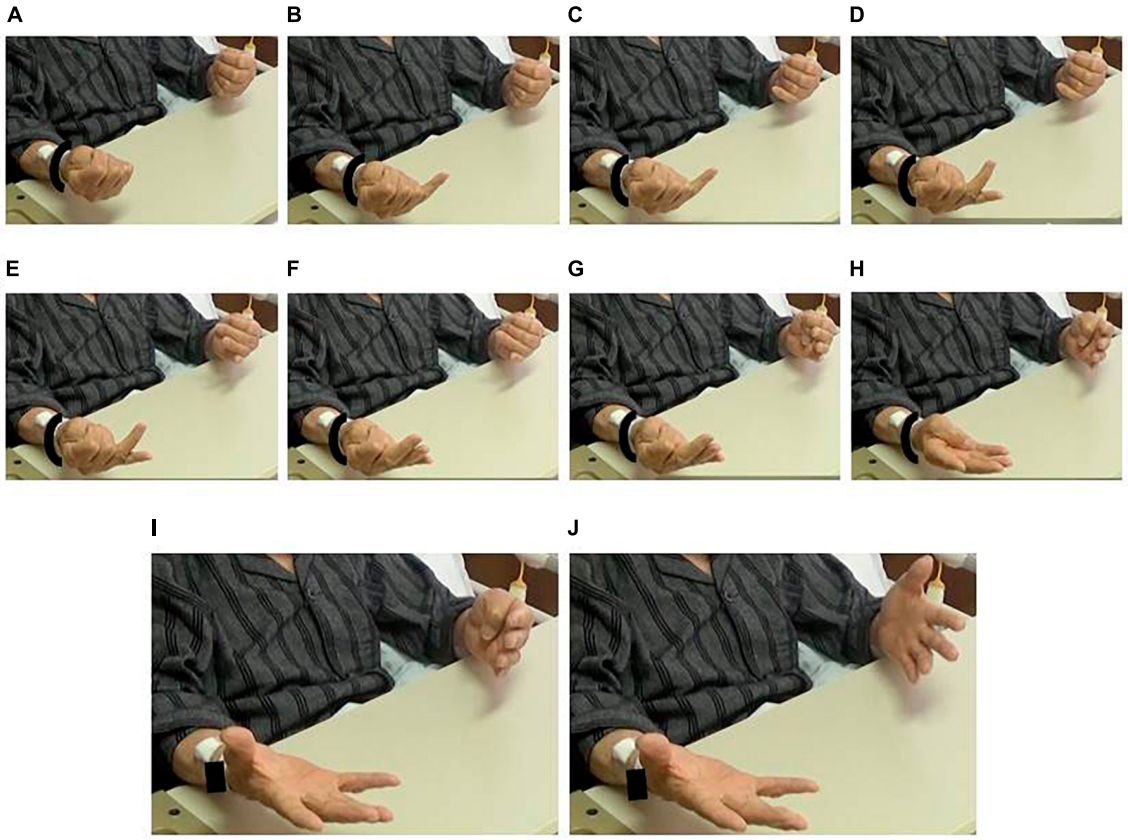

FIGURE 2
Impairment of in-phase movement. Despite an instruction for simultaneous movement, the patient extended his fingers alternatingly. **(A)** Fists. Right-to-left extension of panels **(B,C)** small fingers, **(D,E)** ring fingers, **(F,G)** tall fingers, **(H)** index fingers, and **(I,J)** thumbs. See **Supplementary Video 6**.

during uncoupled bilateral finger movements compared to that during synchronous movements (Meister et al., 2010). Thus, transient dysfunction and disconnection of the bilateral primary motor cortices, in addition to lesions in the SMA and PMC, likely contributed to the current findings.

In humans, the SMA plays a significant role in self-paced, signal-triggered, and sequential finger movements (Mushiake et al., 1991; Tanji, 1996; Tanji and Mushiake, 1996). Lesions in the SMA impede the selection of appropriate movements; however, external sensory cues can ameliorate task impairments in monkeys (Mushiake et al., 1991; Tanji, 1996; Tanji and Mushiake, 1996). The lateral PMC is activated by both externally triggered and self-initiated tasks (Grefkes et al., 2008; Potgieser et al., 2014). Thus, auditory cues and vocalizations helped initiate and execute bimanual movements in our patient probably via residual function of the PMC. External triggers can elicit rapid movements (kinesia paradoxica) (Jankovic, 2008) and have been utilized in rehabilitation mainly of gait disturbance in patients with Parkinson's disease (Arias and Cudeiro, 2008). The effect of auditory cueing on bimanual coordination may be useful for the diagnosis of anatomical localization of the superior frontal gyrus and functional localization of the SMA and PMC of the lesion as well as the resected areas and for rehabilitation of patients with frontal lobe lesions or dysfunction.

Auditory cues were delivered at a tempo of 40 beats per minutes, i.e., interstimulus interval of 1.5 s. The pace is based upon the data that, when interstimulus interval range approximately from 0.6 to 1.8 s, subjects can tap their fingers synchronous to auditory stimuli integrating the timing and movements (Mates et al., 1994; Repp, 2005). There are two distinct motor loops, one is the cerebellum, thalamus/basal ganglia and ventral areas of motor cortex (primary motor cortex, SMA and ventral PMC), and the other is dorsal PMC and primary motor cortex (Middleton and Strick, 2000; **Figure 3**). It is hypothesized that phase correction of bimanual movement according to auditory stimuli in relatively slow pace is associated with the latter loop via dorsal PMC, whereas pace correction, especially rapid movement execution, is associated with ventral motor loop (Repp, 2005).

Impairment of bimanual movement in our patient fulfils operational definitions of apraxia; failure to produce the correct movement in response to a verbal command, and failure to imitate correctly a movement performed by the examiner (Leiguarda and Marsden, 2000). The characteristics of fine finger movement deficits can be categorized as a specific form of limb-kinetic apraxia with preserved muscle strength or perception of various senses. Importance of early diagnosis and treatment intervention of limb-kinetic apraxia using rehabilitation is recently drawing attention in poststroke patients (Jang and Byun, 2022).

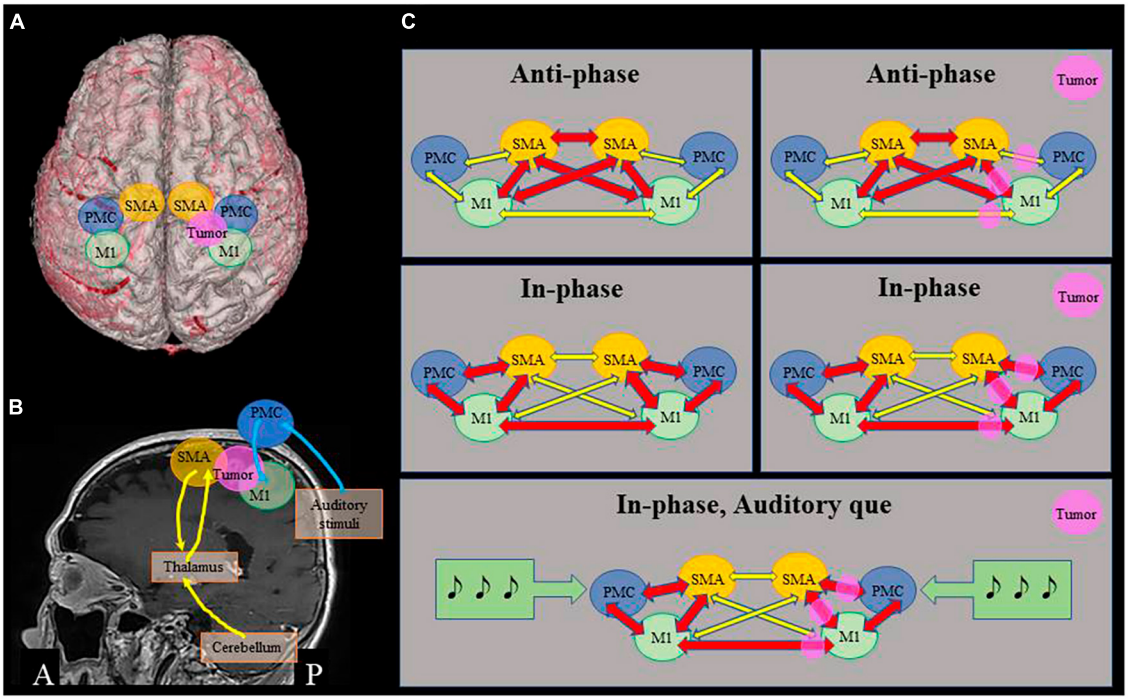

FIGURE 3
Proposed mechanisms of bimanual movement coordination. **(A)** 3D image of the patient, showing positional relationship among the tumor and motor areas. **(B)** Motor loops. Cerebellum – thalamus/basal ganglia – ventral areas of supplementary motor cortex (SMA) (yellow), and dorsal premotor cortex (PMC) – primary motor cortex (M1) associated with auditory stimuli (blue). **(C)** Schematic representations of relationship among motor cortices. In anti-phase movement, close connection among bilateral SMA and M1 is important, which is relatively preserved in this patient (upper row). In in-phase movement, connections between bilateral M1 and between SMA and PMC of each side are important, that are impaired in this patient (middle row). Auditory que stimulates bilateral dorsal PMC and ameliorates in-phase movements (lower row).

Patient perspective

The present observations demonstrate that in addition to the disturbance of anti-phase bimanual movements, resection of the frontal lobe involving the SMA can cause transient impairment of in-phase bimanual diadochokinesis, which can be more severe than the impairment of anti-phase movements. The effect of auditory cueing on bimanual skills may be useful in the diagnosis of anatomical and functional localization of the lesion and in rehabilitation of patients with brain tumors, as in the case of degenerative movement disorders.

Data availability statement

The raw data supporting the conclusions of this article will be made available by the authors, without undue reservation.

Ethics statement

The requirement of ethical approval was waived by the Ethics Committee, Nagahama City Hospital. The studies were conducted in accordance with the local legislation and institutional requirements. Written informed consent was obtained from the individual(s) for the publication of any potentially identifiable images or data included in this article.

Author contributions

KT: conceptualization, investigation, resources, data curation, and writing – original draft. TY and YH: conceptualization, investigation, resources, and data curation. YM: data curation and visualization. SH: investigation, resources, and data curation. MK: conceptualization, writing – review and editing, visualization, supervision, and funding acquisition. TS: investigation, resources, data curation, and supervision. All authors contributed to the article and approved the submitted version.

Funding

MK's neurological research was partially supported by the Japan Society for the Promotion of Science (KAKENHI; JPJSBP 120217720) and the Nakatani Foundation for advancement of measuring technologies in Biomedical Engineering (technology exchange program).

Acknowledgments

We would like to thank Editage (www.editage.com) for English language editing.

Conflict of interest

MK received contracts and honoraria from Eisai Co., Ltd., Daiichi Sankyo Co., Ltd., and UCB Japan Co., Ltd. MK is an associate editor for BMC Neurology and an editorial board member of Clinical Neurophysiology.

The remaining authors declare that this study was conducted in the absence of any commercial or financial relationships that could be construed as potential conflicts of interest.

Publisher's note

Supplementary material

The Supplementary Material for this article can be found online at: https://www.frontiersin.org/articles/10.3389/fnins.2023.1217430/full#supplementary-material

SUPPLEMENTARY VIDEO 1
The 5th postoperative day. Instruction of unilateral left arm elevation was given with gesture, and the movement was smooth.

SUPPLEMENTARY VIDEO 2
The 5th postoperative day. When he was instructed to raise his both arms ('banzai' in Japanese) with gesture, he raised his right arm only.

SUPPLEMENTARY VIDEO 3
The 5th postoperative day. Unilateral left forearm pronation/spination was smooth.

SUPPLEMENTARY VIDEO 4
The 5th postoperative day. Despite instruction of bilateral in-phase forearms pronation/spination but left movement delayed.

SUPPLEMENTARY VIDEO 5
The 5th postoperative day. Sequential movements of unilateral left fingers were smooth.

SUPPLEMENTARY VIDEO 6
The 5th postoperative day. When an instruction on in-phase sequential finger movement was given by verbal commands with gestures to bend his fingers from the thumb in order and open his fingers bilaterally at the same time, a whole series of movements at once, he bent and extended his fingers, one at a time, alternating bilaterally with a chant to keep time. See Figure 2.

SUPPLEMENTARY VIDEO 7
The 5th postoperative day. Bilateral in-phase closing/opening (fist/palm, 'gu/pa' in Japanese) in his own pace was instructed. Left hand delayed at 5th turn and he performed anti-phase movement instead of in-phase movement.

SUPPLEMENTARY VIDEO 8
The 5th postoperative day. The same movement as Supplementary Video 7 with metronome sound que at 40 beats per minute. Opening of 4th turn delayed but he could catch up with the original rhythm.

SUPPLEMENTARY VIDEO 9
The 5th postoperative day. Anti-phase bilateral leg movement was smooth.

SUPPLEMENTARY VIDEO 10
The 5th postoperative day. He was instructed to raise bilateral legs at the same time, but raised his right leg only.

SUPPLEMENTARY VIDEO 11
The 6th postoperative day. Bilateral in-phase closing/opening (fist/palm) in his own pace was instructed. At the beginning of the bilateral in-phase movement, the left hand was delayed in facing the palm upward and making a fist, but afterward, the opening/closing movements were smooth. Every movement was performed by calling out.

SUPPLEMENTARY VIDEO 12
The 6th postoperative day. When instructed to perform sequential movements of the bilateral fingers, he could simultaneously flex the bilateral thumbs and index fingers; however, flexion/extension of the other fingers was performed alternately.

SUPPLEMENTARY VIDEO 13
The 15th postoperative day. In-phase bimanual sequential movements improved.

References

Arias, P., and Cudeiro, J. (2008). Effects of rhythmic sensory stimulation (auditory, visual) on gait in Parkinson's disease patients. *Exp. Brain. Res.* 186, 589–601. doi: 10.1007/s00221-007-1263-y

Chen, J. T., Lin, Y. Y., Shan, D. E., Wu, Z. A., Hallett, M., and Liao, K. K. (2005). Effect of transcranial magnetic stimulation on bimanual movements. *J. Neurophysiol.* 93, 53–63. doi: 10.1152/jn.01063.2003

Chung, G. H., Han, Y. M., Jeong, S. H., and Jack, C. R. Jr. (2005). Functional heterogeneity of the supplementary motor area. *AJNR Am. J. Neuroradiol.* 26, 1819–1823.

Fried, I., Katz, A., McCarthy, G., Sass, K. J., Williamson, P., Spencer, S. S., et al. (1991). Functional organization of human supplementary motor cortex studied by electrical stimulation. *J. Neurosci.* 11, 3656–3666. doi: 10.1523/JNEUROSCI.11-11-03656.1991

Genon, S., Reid, A., Li, H., Fan, L., Müller, V. I., Cieslik, E. C., et al. (2018). The heterogeneity of the left dorsal premotor cortex evidenced by multimodal connectivity-based parcellation and functional characterization. *Neuroimage* 170, 400–411. doi: 10.1016/j.neuroimage.2017.02.034

Grefkes, C., Eickhoff, S. B., Nowak, D. A., Dafotakis, M., and Fink, G. R. (2008). Dynamic intra- and interhemispheric interactions during unilateral and bilateral hand movements assessed with fMRI and DCM. *Neuroimage* 41, 1382–1394. doi: 10.1016/j.neuroimage.2008.03.048

Jang, S. H., and Byun, D. H. (2022). Role of diffusion tensor tractography in diagnosis of limb-kinetic apraxia in stroke patients: A mini-narrative review. *Med. Sci. Monit.* 28:e936417. doi: 10.12659/MSM.936417

Jankovic, J. (2008). Parkinson's disease: Clinical features and diagnosis. *J. Neurol. Neurosurg. Psychiatry* 79, 368–376. doi: 10.1136/jnnp.2007.131045

Laplane, D., Talairach, J., Meininger, V., Bancaud, J., and Orgogozo, J. M. (1977). Clinical consequences of corticectomies involving the supplementary motor area in man. *J. Neurol. Sci.* 34, 301–314. doi: 10.1016/0022-510x(77)90148-4

Leiguarda, R. C., and Marsden, C. D. (2000). Limb apraxias: Higher-order disorders of sensorimotor integration. *Brain* 123, 860–879. doi: 10.1093/brain/123.5.860

Mates, J., Müller, U., Radil, T., and Pöppel, E. (1994). Temporal integration in sensorimotor synchronization. *J. Cogn. Neurosci.* 6, 332–340. doi: 10.1162/jocn.1994.6.4.332

Meister, I. G., Foltys, H., Gallea, C., and Hallett, M. (2010). How the brain handles temporally uncoupled bimanual movements. *Cereb. Cortex* 20, 2996–3004. doi: 10.1093/cercor/bhq048

Middleton, F. A., and Strick, P. L. (2000). Basal ganglia and cerebellar loops: Motor and cognitive circuits. *Brain Res. Brain Res. Rev.* 31, 236–250. doi: 10.1016/s0165-0173(99)00040-5

Mushiake, H., Inase, M., and Tanji, J. (1991). Neuronal activity in the primate premotor, supplementary, and precentral motor cortex during visually guided and internally determined sequential movements. *J. Neurophysiol.* 66, 705–718. doi: 10.1152/jn.1991.66.3.705

Potgieser, A. R., de Jong, B. M., Wagemakers, M., Hoving, E. W., and Groen, R. J. (2014). Insights from the supplementary motor area syndrome in balancing movement initiation and inhibition. *Front. Hum. Neurosci.* 8:960. doi: 10.3389/fnhum.2014.00960

Repp, B. (2005). Sensorimotor synchronization: A review of the tapping literature. *Psychon. Bull. Rev.* 12, 969–992. doi: 10.3758/bf03206433

Sadato, N., Yonekura, Y., Waki, A., Yamada, H., and Ishii, Y. (1997). Role of the supplementary motor area and the right premotor cortex in the coordination of bimanual finger movements. *J. Neurosci.* 17, 9667–9674. doi: 10.1523/JNEUROSCI.17-24-09667.1997

Tanji, J. (1996). New concepts of the supplementary motor area. *Curr. Opin. Neurobiol.* 6, 782–787. doi: 10.1016/s0959-4388(96)80028-6

Tanji, J., and Mushiake, H. (1996). Comparison of neuronal activity in the supplementary motor area and primary motor cortex. *Brain Res. Cogn. Brain. Res.* 3, 143–150. doi: 10.1016/0926-6410(95)00039-9

frontiers | Frontiers in Neuroscience

TYPE Review
PUBLISHED 06 December 2023
DOI 10.3389/fnins.2023.1301778

OPEN ACCESS

EDITED BY
Ye Wu,
Nanjing University of Science and Technology, China

REVIEWED BY
Wenjiao Lyu,
Guangzhou University of Chinese Medicine, China
Ruiwang Huang,
South China Normal University, China

*CORRESPONDENCE
Guang-Bin Cui
✉ cuigbtd@fmmu.edu.cn;
✉ cgbtd@126.com
Lin-Feng Yan
✉ ylf8342@163.com

†These authors have contributed equally to this work

RECEIVED 25 September 2023
ACCEPTED 21 November 2023
PUBLISHED 06 December 2023

CITATION
Xie H, Yu Y, Yang Y, Sun Q, Li Z-Y, Ni M-H, Li S-N, Dai P, Cui Y-Y, Cao X-Y, Jiang N, Du L-J, Gao W, Bi J-J, Yan L-F and Cui G-B (2023) Commonalities and distinctions between the type 2 diabetes mellitus and Alzheimer's disease: a systematic review and multimodal neuroimaging meta-analysis.
Front. Neurosci. 17:1301778.
doi: 10.3389/fnins.2023.1301778

Commonalities and distinctions between the type 2 diabetes mellitus and Alzheimer's disease: a systematic review and multimodal neuroimaging meta-analysis

Hao Xie[1†], Ying Yu[1†], Yang Yang[1†], Qian Sun[1], Ze-Yang Li[1], Min-Hua Ni[1], Si-Ning Li[1,2], Pan Dai[1,2], Yan-Yan Cui[1,3], Xin-Yu Cao[1,4], Nan Jiang[1], Li-Juan Du[1], Wen Gao[5], Jia-Jun Bi[5], Lin-Feng Yan[1*] and Guang-Bin Cui[1*]

[1]Department of Radiology, Functional and Molecular Imaging Key Lab of Shaanxi Province, Tangdu Hospital, Fourth Military Medical University (Air Force Medical University), Xi'an, Shaanxi, China, [2]Faculty of Medical Technology, Xi'an Medical University, Xi'an, Shaanxi, China, [3]Faculty of Medical Technology, Shaanxi University of Chinese Medicine, Xianyang, Shaanxi, China, [4]Faculty of Medical Technology, Medical School of Yan'an University, Yan'an, Shaanxi, China, [5]Student Brigade, Fourth Military Medical University, Xi'an, Shaanxi, China

Background: Alzheimer's disease (AD) and type 2 diabetes mellitus (T2DM) are aging related diseases with high incidence. Because of the correlation of incidence rate and some possible mechanisms of comorbidity, the two diseases have been studied in combination by many researchers, and even some scholars call AD type 3 diabetes. But the relationship between the two is still controversial.

Methods: This study used seed-based d mapping software to conduct a meta-analysis of the whole brain resting state functional magnetic resonance imaging (rs-fMRI) study, exploring the differences in amplitude low-frequency fluctuation (ALFF) and cerebral blood flow (CBF) between patients (AD or T2DM) and healthy controls (HCs), and searching for neuroimaging evidence that can explain the relationship between the two diseases.

Results: The final study included 22 datasets of ALFF and 22 datasets of CBF. The results of T2DM group showed that ALFF increased in both cerebellum and left inferior temporal gyrus regions, but decreased in left middle occipital gyrus, right inferior occipital gyrus, and left anterior central gyrus regions. In the T2DM group, CBF increased in the right supplementary motor area, while decreased in the middle occipital gyrus and inferior parietal gyrus. The results of the AD group showed that the ALFF increased in the right cerebellum, right hippocampus, and right striatum, while decreased in the precuneus gyrus and right superior temporal gyrus. In the AD group, CBF in the anterior precuneus gyrus and inferior parietal gyrus decreased. Multimodal analysis within a disease showed that ALFF and CBF both decreased in the occipital lobe of the T2DM group and in the precuneus and parietal lobe of the AD group. In addition, there was a common decrease of CBF in the right middle occipital gyrus in both groups.

Conclusion: Based on neuroimaging evidence, we believe that T2DM and AD are two diseases with their respective characteristics of central nervous activity and cerebral perfusion. The changes in CBF between the two diseases partially

overlap, which is consistent with their respective clinical characteristics and also indicates a close relationship between them.

Systematic review registration: PROSPERO [CRD42022370014].

KEYWORDS

functional neuroimaging, Alzheimer's disease, type 2 diabetes mellitus, functional magnetic resonance imaging, coordinated-based meta-analysis

1 Introduction

Diabetes is a chronic metabolic disease characterized by hyperglycemia (Zheng et al., 2018), and type 2 diabetes mellitus (T2DM) characterized by insulin dysfunction accounts for the majority (about 95%) (Bruno et al., 2005; Holman et al., 2015). It is estimated that the prevalence rate of diabetes will gradually increase from 6.3% in 2019 to 10.2% in 2030, when the population will reach 578 million, becoming a serious global public health problem (Saeedi et al., 2019). The complications of diabetes include retinopathy, renal failure, heart disease, cerebrovascular disease (Kautzky-Willer et al., 2016; Zheng et al., 2018). In addition, the cognitive impairment caused by diabetes is also increasingly concerned. Research reports that about 25–36% of diabetes patients have cognitive impairment (Geijselaers et al., 2015), and progress to dementia more quickly than healthy people (Exalto et al., 2013; Biessels and Despa, 2018), among which the risk of Alzheimer's disease (AD) increases by about 45–90% (Arvanitakis et al., 2004; Wang et al., 2012).

AD is a chronic neurodegenerative disease with hidden onset (Liu et al., 2019). It is the most common type of dementia, accounting for about 70% (Burns and Iliffe, 2009), and the incidence rate is increasing year by year (Alzheimer's Association, 2021; Scheltens et al., 2021). The pathological feature of AD is hyperphosphorylated TAU protein deposition in the cells, and forms the neurofibrillary tangles when occurring in the nerve cells (Ballard et al., 2011; Scheltens et al., 2021). According to previous studies, T2DM and AD share many common characteristics, including being highly prevalent age-related diseases with a long prodromal period and being chronic complex diseases (Kubis-Kubiak et al., 2019; Diniz Pereira et al., 2021). In addition, T2DM and AD have many pathological mechanisms in common caused by insulin resistance (Janson et al., 2004), such as metabolic syndrome (Więckowska-Gacek et al., 2021), advanced glycation end products (AGEs) (Byun et al., 2017), insulin signal transduction disorder (De Felice et al., 2022), etc. Therefore, some researchers believe that AD is a late complication with the development of T2DM, which can even be called type 3 diabetes (de la Monte et al., 2018; Nguyen et al., 2020). However, another group of scholars believe that the two diseases are different, and T2DM is only a high-risk factor for AD (Moran et al., 2015), which leads to faster disease progress (Chornenkyy et al., 2019). At present, the relationship between T2DM and AD is still unclear, especially the brain damage caused by the two diseases. However, central insulin resistance and signal transduction abnormalities caused by these two diseases are becoming the mainstream (Diehl et al., 2017; Kellar and Craft, 2020).

In clinical studies, researchers tried to use various methods such as electroencephalogram (EEG), positron emission tomography (PET), single photon emission computed tomography (SPECT) and magnetic resonance imaging (MRI) to clarify the process of brain changes in T2DM or AD (Bucerius et al., 2012; Chen and Zhong, 2013; Brundel et al., 2014; Matsuda, 2016; Benwell et al., 2020). The resting-state functional MRI (rs-fMRI) has been increasingly used because of its non-invasive, efficient, high spatial resolution in detecting central nervous system. Amplitude low-frequency fluctuation (ALFF) and cerebral blood flow (CBF) are more widely used indicator derived from fMRI. ALFF is a measure of resting state blood oxygen level dependent (BOLD) signal changes, reflecting local neural activity (Zou et al., 2008), while CBF measured by arterial spin labeling (ASL) technique which can reflect cerebral perfusion (Williams et al., 1992). ALFF and CBF have always been regarded as two independent indicators, but studies have confirmed that CBF was involved in regulating the change of BOLD signal (Kannurpatti et al., 2008; Tak et al., 2014), and they can reflect the intensity of local neural activity in direct and indirect ways (Kim and Lee, 2004; Yu-Feng et al., 2007), respectively. Furthermore, these two indicators can be combined for analysis to represent the neurovascular coupling status of brain regions (Hu et al., 2019; Yu et al., 2019). Therefore, it is necessary to conduct research and analysis on these two indicators.

Since the application of fMRI technology, a lot of scientific achievements have been published on ALFF and CBF alteration in T2DM or AD. However, differences in sample size, demographic information, image acquisition techniques and analysis methods among different studies lead to heterogeneity of results. Meta-analysis has emerged to identify abnormal brain activity from a large number of studies. For example, a published meta-analysis in T2DM patients showed a decrease of ALFF in the parietal lobe, occipital lobe, and cingulate gyrus (Macpherson et al., 2017). The meta-analysis in AD patients showed a general decrease of CBF in whole brain, especially in the posterior cingulate gyrus and temporal parietal lobe (Zhang et al., 2021), while the meta-analysis in T2DM patients showed that CBF decreased in bilateral occipital lobe but increased in right prefrontal lobe and supplementary motor area (Liu et al., 2022). Due to differences of literature inclusion criteria and specific analysis methods, the level of evidence from the combined analysis of the above two indicators might decrease. In summary, it is essential to combine ALFF and CBF for further analysis by using neurovascular coupling coefficient, in order to explore the alteration of brain neural activity in T2DM and AD, and to analyze the similarities and differences of brain damage caused by the two diseases.

The aim of this study is, to perform a voxel-based meta-analysis of ALFF and CBF changes in patients with T2DM and AD, by taking advantage of the large number of whole-brain rs-fMRI studies published in recent years, and to explore whether there are similarities in brain alterations in the two diseases. This is not only helpful to understand the pathophysiology of T2DM and AD more accurately,

but also can provide evidence of brain damages from the perspective of imaging, which is helpful to reveal the pathogenesis and to find the promising biomarkers.

2 Methods

2.1 Protocol and guidance

The meta-analysis was conducted in accordance with the guidelines of the Preferred Reporting Items for Systematic Reviews and Meta-Analyses (PRISMA) and 10 simple rules for neuroimaging meta-analysis (Müller et al., 2018; Page et al., 2021). The protocol of this neuroimaging meta-analysis was registered on PROSPERO (CRD42022370014).[1]

2.2 Search strategy

We used a systematic search strategy to identify published relevant studies in databases including PubMed, Web of Science, from Jan 1, 2007 to Sep 1, 2022. Divided the search process into two parts based on the type of indicator. The first part used keywords ("Diabetes Mellitus, Type 2" OR "Type 2 Diabetes" OR "Diabetes Mellitus, Type II" OR "NIDDM" OR "T2DM" OR "Alzheimer Disease" OR "Alzheimer*" OR "dement*" OR "AD") AND ("amplitude of low frequency fluctuation" OR "ALFF" OR "low frequency fluctuation" OR "LFF" OR "amplitude of low frequency oscillation" OR "LFO"). The second part used keywords ("Diabetes Mellitus, Type 2" OR "Type 2 Diabetes" OR "Diabetes Mellitus, Type II" OR "NIDDM" OR "T2DM" OR "Alzheimer Disease" OR "Alzheimer*" OR "dement*" OR "AD") AND ("Cerebrovascular Circulation" OR "arterial spin labeling" OR "ASL" OR "Cerebral Blood Flow" OR "CBF").

2.3 Study selection

After completing the search, duplicate studies were first excluded. When extracting information in the study by reading the full text, if there was important information that could not be found, such as coordinate values, non-online manuscripts, etc., we contacted the corresponding author by email. After information extraction, studies conforming to the research will be included in the following: (1) an article was published, rather than the abstract, lecture or letters; (2) assessed CBF or ALFF in whole brain analysis; (3) participants were classified into healthy controls (HCs) and T2DM and/or AD groups in cross-sectional and at the baseline of longitudinal studies; (4) the article clearly reported peak coordinates in stereotactic three-dimensional coordinates (MNI or Talairach); (5) be able to extract the t value, z values or *p* values; and (6) subjects were adults (18–75 years old). Exclusion criteria will be: (1) the study participants were individuals diagnosed with dementia other than AD; (2) other neuropsychiatric disorders, macrovascular complications, craniocerebral trauma, and inflammatory lesions of the central nervous system; (3) no HCs; (4) not related to ALFF and CBF; (5) studies with ROI analysis; (6) research on minors; (7) secondary study; and (8) neuroimaging quality score<16 or JBI score<12.

2.4 Quality assessment

We referred to the previous high-quality literature and used the methodological assessment checklist which was specific for neuroimaging meta-analysis to evaluate the quality of the included study (Pan et al., 2017; Supplementary Figure S1; Supplementary Tables S4, S5). In addition, only cross-sectional information was extracted after the study was included, so we introduced the Joanna Briggs Institute (JBI) critical appraisal checklist of the cross-sectional study for secondary assessment (Ma et al., 2020; Supplementary Figure S2; Supplementary Table S6). The quality of the study was first independently evaluated by two reviewers (H.X and ZY.L, Radiologist), and the consistent evaluation results would be adopted. If there were differences in the evaluation results, the third reviewer (LF.Y, Deputy Chief Radiologist and Associate Professor) would evaluate and make final decision.

2.5 Voxel-wise meta-analysis of CBF and ALFF abnormalities

The meta-analyses of ALFF and CBF were performed in the "Gray Matter" templates of the anisotropic effect size-signed differential mapping (AES-SDM) (Radua and Mataix-Cols, 2009; Radua et al., 2012; Radua and Mataix-Cols, 2012; Radua et al., 2014), which has been widely used in the meta-analysis of neuroimaging (Barona et al., 2019; Li et al., 2022). The specific research process has been reported in detail in previous studies (Radua and Mataix-Cols, 2009; Ferreira and Busatto, 2010; Radua et al., 2012), so we summarized the methods as follows: First, extracting the effective coordinates of CBF or ALFF abnormalities (increased or decreased) between T2DM patients or AD patients and HCs in each data set and the size of their brain impacts, and using various heterotypic Gaussian kernels to reconstruct the statistical map on MNI coordinates. Then, the study combined the random effect model considering sample size, intra-study variability and between-study heterogeneity to generate a mean map. Finally, MRICRON[2] software were used to visualize the data.

According to the research of software developers, we have adopted the recommended settings (FWHM = 20 mm, $p = 0.005$, peak height $Z = 1$, and cluster extent ≥20 voxels) in this study (Radua et al., 2012). When extracting data from research, if only z value or *p* value was provided, it can be analyzed by converting it to *t* value through https://www.sdmproject.com/utilities/?show=Statistics. According to the software instruction, the following five standard steps will be followed when processing data: (1) Global analysis, (2) Pre-processing, (3) Mean analysis, (4) Threshold analysis, and (5) Extract peak coordinates and Bias Test.

Next, we compared the covariant brain regions (increased or decreased) of ALFF and CBF in T2DM compared with HCs through

1 https://www.crd.york.ac.uk/prospero/

2 https://www.nitrc.org/projects/bnv/

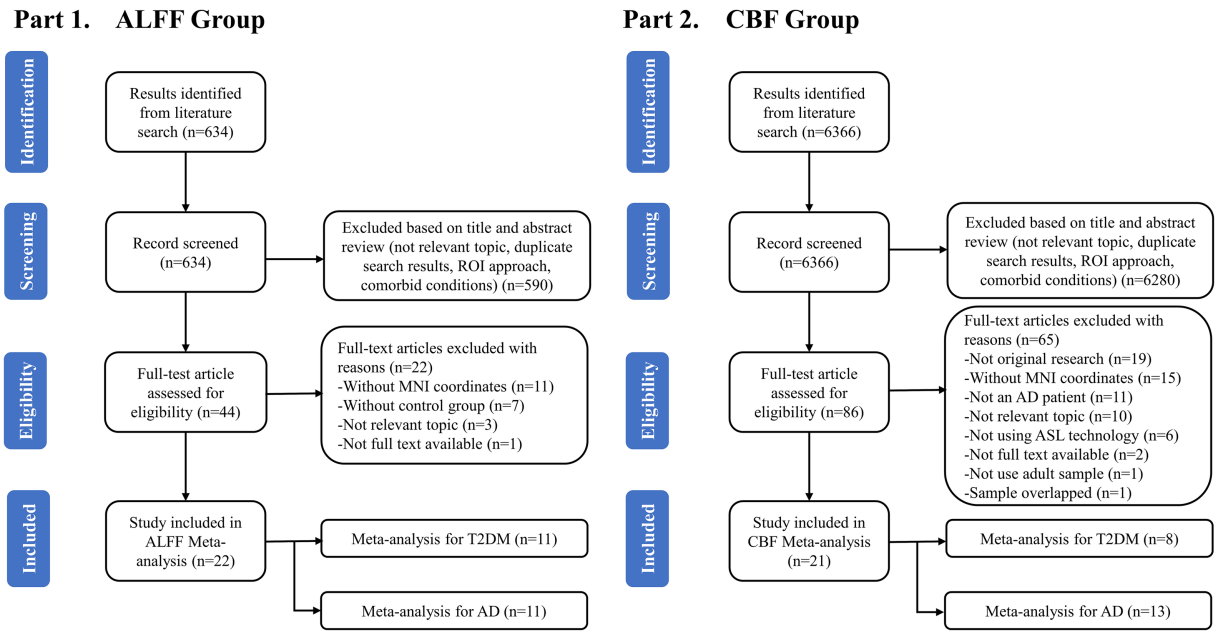

FIGURE 1
Flowchart for identifying studies to be included in the meta-analysis.

quantitative meta-analysis of brain regions with differences among groups obtained from previous analysis, and used standard randomization test to determine statistical significance. The same analysis was performed for AD group. In this process, we took demographic information with statistical differences as covariates. In addition, by combining the result graph of threshold element analysis, we studied the increase/decrease overlap of ALFF between T2DM and AD, and compared the voxel number and z value in the actual interaction area and visualized results. Similarly, we conducted the same analysis on covariant of CBF between T2DM and AD.

2.6 Heterogeneity, sensitivity and publication bias

Extract the MNI peak coordinates with statistical differences, and obtain the standard heterogeneity test I^2. If $I^2 \geq 50\%$, it means significant heterogeneity (Egger et al., 1997). Funnel plots were used to test whether there was publication bias. Asymmetric funnels or $p < 0.05$ were considered to have publication bias (Sterne et al., 2011). These analyses were performed using the SDM-PSI version 6.21.[3] Finally, jackknife sensitivity was used for sensitivity analysis of whole brain voxels. The specific method was to check the stability of results by repeating the same analysis process after excluding one data set each time (Radua et al., 2014). This procedure aimed to analyze the repeatability of the results. If a result was significant different in all or most (>50%) of the study combinations, we believed that the result was highly replicable (Radua and Mataix-Cols, 2009).

3 https://www.sdmproject.com/

2.7 Meta-regression analysis

In the study, the linear regression in AES-SDM was used for meta-regression to explore the impact of demographic information and clinical variables such as years of education, course of disease, and clinical evaluation scale scores on the results. Regression analysis could exclude the regions outside the brain obtained from principal component analysis (Yao et al., 2021).

3 Results

3.1 Included studies

A total of 634 studies were obtained from the first part of the search. After preliminary removing the duplicates and reviewing the titles and abstracts, 44 studies were retained and considered potentially eligible for inclusion. Then, after a detailed reading of the full article text, another 22 studies were excluded. Finally, 22 studies including 22 data sets met the criteria and were included to analyze the ALFF differences between T2DM and AD patients, including 11 studies on AD patients and 11 studies on T2DM patients (Figure 1). A total of 6,366 studies were obtained from the second part of the search. After preliminary removing the duplicates and reviewing the titles and abstracts, 86 studies were retained and considered potentially eligible for inclusion. Then, after a detailed reading of the full article text, another 65 studies were excluded. Finally, 21 studies including 21 data sets met the criteria and were included to analyze the CBF differences between T2DM and AD patients, including 13 studies on AD patients and 8 studies on T2DM patients. A total of 43 studies were included for this meta-analysis (Figure 1).

3.2 Sample characteristics

3.2.1 T2DM

In all of T2DM studies included in ALFF analysis, 302 patients with T2DM (171 males and 131 females, mean age = 56.00 years) and 302 HCs (153 males and 149 females, mean age = 55.36 years) were included (Detailed demographic and clinical information is shown in Table 1, and radiological parameters are shown in Supplementary Tables S2, S3). There was no significant difference in gender ($\chi^2 = 2.157$, $p = 0.14$) and age (standardized mean difference [SMD] = 0.11; 95% confidence interval [CI] = [−0.05, 0.27], $Z = 1.30$, $p = 0.19$) distribution between the two groups. Among all included CBF related studies, 286 T2DM patients (150 males and 136 females) and 280 HCs (131 males and 149 females) were included. No significant difference was observed between patients with T2DM and HCs in gender ($\chi^2 = 1.814$, $p = 0.18$) and age (SMD = 0.91; CI = [−0.34, 2.16], $Z = 1.43$, $p = 0.15$) distribution.

3.2.2 AD

In all of AD studies included in ALFF analysis, 390 patients with AD (160 males and 230 females, mean age = 69.23 years) and 492 HCs (183 males and 309 females, mean age = 68.93 years) were included (Detailed demographic and clinical information is shown in Table 2, and radiological parameters are shown in Supplementary Tables S2, S3). No significant difference were observed between the two groups in gender ($\chi^2 = 1.343$, $p = 0.25$), but there was significant difference in age distribution (SMD = 2.74; CI = [1.56, 3.92], $Z = 4.56$, $p < 0.00001$). Among all included CBF related studies, 310 AD patients (121 males and 189 females) and 335 HCs (142 males and 193 females) were included. No significant difference were observed between AD patients and HCs in gender ($\chi^2 = 0.751$, $p = 0.39$), while there was significant difference in age (SMD = 1.73; CI = [0.90, 2.56], $Z = 4.10$, $p < 0.0001$).

3.3 ALFF meta-analysis

3.3.1 T2DM *vs.* HCs

The brain map derived from meta-analysis showed that compared to HCs, ALFF in the T2DM group increased in the cerebellum (CER) and left inferior temporal gyrus (ITG. L), while decreased in the left middle occipital gyrus (MOG. L), right inferior occipital gyrus (IOG. R), and left precentral gyrus (preCG. L) (Figure 2). These regions existed significant heterogeneity ($I^2 > 50\%$), so random effect model was selected for analysis. Except for preCG.L, there was no publication bias in other brain regions. The research of Zhou et al. (2014) led to publication bias in preCG.L. Jackknife sensitivity analysis showed that the above brain regions were highly repeatable and the results were reliable (Supplementary Table S7).

3.3.2 AD *vs.* HCs

The meta-analysis brain maps showed that compared to HC, ALFF in the AD group increased in CER. R, right striatum, and right hippocampus (HIP. R), while decreased in the precuneus gyrus (PCUN) and right superior temporal gyrus (STG. R) (Figure 2). These regions existed significant heterogeneity ($I^2 > 50\%$), so random effect model was selected for analysis. There was no publication bias in all brain regions. Jackknife sensitivity analysis showed that the above brain regions were highly repeatable and the results were reliable (Supplementary Table S8).

3.3.3 (T2DM *vs.* HCs) and (AD *vs.* HCs) combined analysis

The results of a joint two parts analysis showed that compared to HCs, T2DM and AD did not have brain regions where ALFF increased or decreased simultaneously.

3.4 CBF meta-analysis

3.4.1 T2DM *vs.* HCs

The meta-analysis brain maps showed that compared to HCs, the T2DM group had an increase of CBF in the right supplementary motor area (SMA. R), while a decrease of CBF in the middle occipital gyrus (MOG) and inferior parietal gyri (IPG) (Figure 2). These regions existed significant heterogeneity ($I^2 > 50\%$), so random effect model was selected for analysis. There was no publication bias in all brain regions. Jackknife sensitivity analysis indicated that the most reliable data had been obtained in the above brain regions (Supplementary Table S9).

3.4.2 AD *vs.* HCs

The brain maps showed that in CBF meta-analysis, compared to HC, the AD group's CBF decreased in PCUN and IPG (Figure 2). These regions existed significant heterogeneity ($I^2 > 50\%$), so random effect model was selected for analysis. There was no publication bias in all brain regions. Jackknife sensitivity analysis indicated that the most reliable data had been obtained in the above brain regions (Supplementary Table S10).

3.4.3 (T2DM vs. HCs) and (AD vs. HCs) combined analysis

Compared with HCs, CBF of both T2DM patients and AD patients decreased in the MOG.R (peak MNI coordinate: 44, −74, 26, $Z = -3.059$, 56 voxels) (Figure 3). The subgroup analysis of T2DM and AD in this brain region showed significant heterogeneity ($I^2 > 50\%$), so a random effect model was used for analysis. In subgroup analysis, there was no publication bias in this brain region (Figure 4 and Table 3).

3.5 Multimodal meta-analysis results

For T2DM, there were two brain regions where CBF and ALFF decreased together, respectively in right occipital lobe (peak MNI coordinate: 24, −92, −8, $Z = -2.487$, 53 voxels) and left occipital lobe (peak MNI coordinate: −20, −88, 2, $Z = -2.976$, 564 voxels) (Figure 3). For AD group, there was a brain region where ALFF and CBF decreased together in bilateral precuneus and parietal lobes (peak MNI coordinate: 6, −64, 30, $Z = -9.511$, 1,692 voxels) (Figure 3). The subgroup analysis of ALFF and CBF in these brain regions showed significant heterogeneity ($I^2 > 50\%$), so a random effect model was used for analysis. In subgroup analysis, there were no publication bias in these brain regions (Figure 4 and Table 3).

TABLE 1 Demographic, clinical and cognitive characteristics of T2DM patients and HCs included in the meta-analysis.

Study	Indicator	Subjects (male/female)		Mean age (SD)		Education years (SD)		Duration years (SD)	HbA1c (%) (SD)		MMSE (SD)		MOCA (SD)	
		T2DM	HC	T2DM	HC	T2DM	HC		T2DM	HC	T2DM	HC	T2DM	HC
Xia et al. (Zheng et al., 2018)	ALFF	28 (15/13)	29 (13/16)	58.7 (8.1)	57.7 (7.2)	9.9 (3.7)	11.0 (2.0)	9.8 (5.5)	7.9 (1.7)	5.6 (0.4)	/	/	23.2 (3.1)	24.1 (2.6)
Chen et al. (Bruno et al., 2005)	ALFF	18 (8/10)	18 (7/11)	61.7 (7.6)	62.1 (11.0)	/	/	13.8 (7.9)	7.3 (1.1)	/	26.1 (2.2)	26.6 (2.0)	/	/
Cui et al. (Holman et al., 2015)	ALFF	29 (14/15)	27 (11/16)	58.3 (7.3)	57.8 (5.9)	10.4 (4.0)	10.2 (2.5)	9.3 (3.8)	7.9 (1.7)	5.6 (0.4)	28.3 (1.4)	29.0 (1.1)	23.6 (2.9)	27.3 (1.1)
Wang et al. (Saeedi et al., 2019)	ALFF	26 (17/9)	26 (17/9)	54.7 (10.4)	54.9 (9.8)	11.2 (3.8)	10.7 (3.2)	7[a]	8.3 (1.4)	/	27.8 (2.5)	28.3 (1.3)	24[a]	26.5[a]
Zhou et al. (Kautzky-Willer et al., 2016)	ALFF	14 (6/8)	17 (10/7)	63.5 (6.9)	63.8 (5.8)	10.6 (2.7)	11.7 (3.0)	6.5 (2.1)	7.8 (1.0)	5.4 (0.6)	25.1 (2.0)	28.6 (1.1)	/	/
Wang et al. (Geijselaers et al., 2015)	ALFF	21 (10/11)	16 (7/9)	54.9 (9.9)	54.8 (5.7)	/	/	9.5 (5.0)	8.4 (1.7)	5.6 (0.9)	28.2 (1.1)	29.0 (0.7)	21.7 (0.7)	25.2 (1.9)
Yu et al. (Biessels and Despa, 2018)	ALFF, CBF	33 (28/5)	33 (22/11)	53.5 (8.4)	51.0 (5.3)	12.8 (2.4)	12.9 (3.5)	7.1 (5.2)	8.1 (1.7)	5.6 (0.3)	28.9 (0.9)	28.5 (1.1)	26.5 (2.1)	26.8 (2.0)
Liu et al. (Exalto et al., 2013)	ALFF	37 (24/13)	37 (17/20)	57.6 (7.1)	57.9 (5.7)	11.6 (3.9)	10.9 (2.3)	8.7 (5.5)	7.6 (1.5)	5.7 (0.4)	28.0 (1.5)	28.5 (1.2)	22.5 (2.7)	24.2 (2.7)
Shi et al. (Arvanitakis et al., 2004)	ALFF	31 (16/15)	31 (16/15)	56.0 (4.6)	56.5 (4.3)	/	/	/	/	/	/	/	/	/
Li et al. (Wang et al., 2012)	ALFF	30 (15/15)	30 (15/15)	49.2 (5.5)	45.8 (6.4)	12 (6, 16)[b]	9 (6, 16)[b]	/	8.7 (2.2)	/	/	/	26.5 (26, 29)[b]	28.5 (26, 30)[b]
Qi et al. (Liu et al., 2019)	ALFF	35 (18/17)	38 (18/20)	54.2 (8.7)	53.5 (7.7)	/	/	9.9 (5.1)	7.5 (1.3)	5.6 (0.4)	/	/	/	/
Xia et al. (Burns and Iliffe, 2009)	CBF	38 (17/21)	40 (21/19)	56.0 (6.1)	57.1 (7.6)	9.6 (3.0)	10.3 (1.9)	7.1 (3.5)	7.2 (1.1)	5.6 (0.3)	29.0 (0.9)	29.1 (1.0)	/	/
Jansen et al. (Alzheimer's Association, 2021)	CBF	41 (23/18)	39 (22/17)	61.1 (9.6)	62.6 (6.6)	/	/	9.8 (6.7)	6.7 (0.4)	5.6 (0.4)	28.6 (1.4)	29.4 (0.8)	/	/
Cui et al. (Scheltens et al., 2021)	CBF	40 (21/19)	41 (13/28)	60.5 (6.9)	57.9 (6.5)	10.0 (3.4)	10.3 (2.3)	8.9 (5.0)	7.7 (1.6)	5.6 (0.3)	28.3 (1.0)	28.6 (1.2)	/	/
Dai et al. (Ballard et al., 2011)	CBF	41 (19/22)	32 (16/16)	65.5 (8.3)	67.3 (10.1)	15.4 (3.8)	16.1 (3.0)	9.9 (7.9)	7.3 (1.3)	5.7 (0.3)	28.6 (1.5)	28.9 (1.6)	/	/
Shen et al. (Diniz Pereira et al., 2021)	CBF	36 (17/19)	36 (14/22)	57.6 (6.2)	56.2 (6.8)	9.1 (1.5)	9.8 (2.9)	5.4 (4.9)	/	/	/	/	25.7 (0.9)	26.0 (0.8)
Zhang et al. (Kubis-Kubiak et al., 2019)	CBF	26 (10/16)	26 (11/15)	51.9 (10.7)	48.2 (6.7)	10.3 (3.7)	11.6 (4.5)	9.2 (7.1)	/	/	26.9 (3.9)	27.7 (2.3)	23.5 (5.6)	25.0 (2.9)
Huang et al. (Janson et al., 2004)	CBF	31 (15/16)	33 (12/21)	53.4 (9.1)	51.6 (9.8)	/	/	/	7.3 (1.4)	/	/	/	/	/

Data are presented as mean (SD), or range. T2DM, type 2 diabetes mellitus; HC, healthy control; SD, standard deviation; HbA1c, glycosylated hemoglobin A1c; MMSE, mini-mental state examination; MoCA, montreal cognitive assessment.

[a] Only the mean value of the data is given in the article.

[b] Mean (range).

/means no relevant information was provided in the study.

10.3389/fnins.2023.1301778

TABLE 2 Demographic, clinical and cognitive characteristics of AD patients and HCs included in the meta-analysis.

Study	Indicator	Subjects (male/female)		Mean age (SD)		Education years (SD)		MMSE (SD)		MOCA (SD)		CDR scale	
		AD	HC	AD	HC	AD	HC	AD	HC	AD	HC	AD	HC
Wang et al. (Więckowska-Gacek et al., 2021)	ALFF	16 (8/8)	22 (7/15)	69.6 (7.7)	66.6 (7.7)	10.1 (3.4)	10.0 (3.9)	18.5 (3.2)	28.6 (0.6)	/	/	1.0 (0.0)	0
Xi et al. (Byun et al., 2017)	ALFF	20 (9/11)	20 (10/10)	68.8 (8.7)	64.7 (5.6)	12.1 (4.4)	12.2 (2.5)	20.6 (2.3)	28.2 (1.8)	/	/	1.0 (0.0)	0
Veldsman et al. (De Felice et al., 2022)	ALFF	44 (22/22)	128 (40/88)	78.0 (8.7)	74.6 (6.1)	13.1 (4.8)	13.5 (8.9)	/	/	/	/	/	/
Zheng et al. (de la Monte et al., 2018)	ALFF	14 (6/8)	14 (6/8)	66.9 (8.9)	66.7 (5.8)	8.7 (3.0)	11.8 (4.1)	16.3 (4.9)	28.1 (1.3)	13.3 (4.9)	27.4 (1.9)	(1.0, 2.0)[a]	0
Li et al. (Nguyen et al., 2020)	ALFF	16 (7/9)	69 (23/46)	74.7 (8.5)	74.8 (6.6)	16.4 (2.6)	16.4 (2.4)	20.8 (4.4)	29.1 (1.0)	/	/	1.0 (0.6)	0
Zeng et al. (Moran et al., 2015)	ALFF	14 (9/5)	11 (0/11)	75.5 (4.1)	75.4 (8.2)	15.6 (2.9)	16.1 (6.4)	21.4 (3.7)	29.5 (1.0)	/	/	/	0
Zheng et al. (Chornenkyy et al., 2019)	ALFF, CBF	40 (18/22)	30 (15/15)	65.0 (10.0)	64.0 (8.0)	11.2 (3.2)	12.6 (4.6)	14.0 (6.0)	28.0 (2.0)	14.9 (3.2)	28.6 (0.7)	(0.5, 2.0)[a]	0
Yang et al. (Kellar and Craft, 2020)	ALFF	44 (15/29)	55 (22/33)	71.0 (10.0)	63.4 (8.0)	9.0 (5.9)	11.0 (5.0)	16.5 (6.4)	28.1 (2.1)	12.6 (5.3)	26.1 (3.2)	(1.0, 2.0)[a]	0
Li et al. (Diehl et al., 2017)	ALFF	111 (37/74)	73 (32/41)	68.3 (9.4)	66.3 (9.5)	7.9 (4.4)	8.3 (3.4)	17.2 (5.6)	28.8 (0.3)	13.4 (6.3)	27.2 (1.7)	/	0
Chen et al. (Brundel et al., 2014)	ALFF	31 (12/19)	50 (18/32)	69.9 (11.0)	64.5 (4.4)	8.2 (4.6)	10.5 (2.7)	12.0 (4.5)	27.2 (1.8)	/	/	(1.0, 2.0)[a]	0
Zhan et al. (Chen and Zhong, 2013)	ALFF	40 (17/23)	20 (10/10)	60.5 (7.4)	61.0 (7.3)	9.7 (4.8)	9.9 (4.9)	17.5 (5.5)	27.0 (4.0)	/	/	/	
Asllani et al. (Benwell et al., 2020)	CBF	12 (7/5)	20 (8/12)	70.7 (8.7)	72.4 (6.5)	14.5 (3.8)	15.8 (2.3)	38.7 (11.1)[b]	53.5 (2.8)[b]	/	/	1.0 (0.0)	0
Dai et al. (Bucerius et al., 2012)	CBF	37 (13/24)	41 (14/27)	83.6 (3.5)	82.1 (3.6)	/	/	85.1 (9.4)[c]	95.0 (4.5)[c]	/	/	(1.0, 2.0)[a]	0
Yoshiura et al. (Matsuda, 2016)	CBF	20 (10/10)	23 (11/12)	73.5 (9.6)	72.9 (6.7)	/	/	20.4 (4.3)	29.3 (0.9)	/	/	/	/
Chao et al. (Zou et al., 2008)	CBF	13 (3/10)	35 (5/30)	77.1 (5.0)	76.0 (7.8)	16.7 (2.9)	16.5 (2.8)	27.5 (1.8)	28.5 (1.7)	/	/	(0.5, 1)[a]	0
Dashjamts et al. (Williams et al., 1992)	CBF	23 (9/14)	23 (11/12)	74.6 (8.9)	73.2 (6.9)	/	/	21.1 (4.4)	29.4 (0.9)	/	/	/	/
Alexopoulos et al. (Kannurpatti et al., 2008)	CBF	19 (11/8)	24 (8/16)	72.0 (9.4)	67.1 (6.1)	/	/	/	/	/	/	/	/
Mak et al. (Tak et al., 2014)	CBF	13 (3/10)	15 (1/14)	75.4 (6.8)	70.8 (6.0)	/	/	16.3 (4.6)	28.5 (2.0)	/	/	/	/
Kim et al. (Yu-Feng et al., 2007)	CBF	25 (4/21)	25 (9/16)	70.9 (9.8)	68.4 (5.6)	/	/	17.2 (4.8)	27.3 (2.8)	/	/	(0.5, 2.0)[a]	0
Ding et al. (Kim and Lee, 2004)	CBF	24 (5/19)	21 (8/13)	74.6 (6.7)	69.6 (5.9)	11.6 (4.2)	12.1 (3.4)	16.0 (3.9)	29.4 (1.0)	/	/	2.1 (0.7)	0
Roquet et al. (Hu et al., 2019)	CBF	25 (8/17)	21 (9/12)	73.6 (9.1)	64.8 (8.6)	/	/	19.5 (3.4)	28.9 (1.0)	/	/	/	/
Duan et al. (Yu et al., 2019)	CBF	40 (12/28)	58 (27/31)	84.1 (3.5)	83.4 (3.7)	13.3 (2.9)	14.6 (2.8)	83.6 (10.0)[c]	95.0 (3.9)[c]	/	/	/	/
Soman et al. (Macpherson et al., 2017)	CBF	19 (11/8)	21 (11/10)	66.7 (5.3)	64.6 (5.7)	/	/	/	/	/	/	(0.5, 1.5)[a]	0

Data are presented as mean (SD), or range. AD, Alzheimer's disease; HC, healthy control; SD, standard deviation; MMSE, mini-mental state examination; MoCA, montreal cognitive assessment; CDR, clinical dementia rating.

[a] The study did not give the mean value and variance, only the range.

[b] MMMS, Modified Mini-Mental Status Examination score.

[c] 3MSE, Modified Mini-Mental State Examination score.

/means no relevant information was provided in the study.

10.3389/fnins.2023.1301778

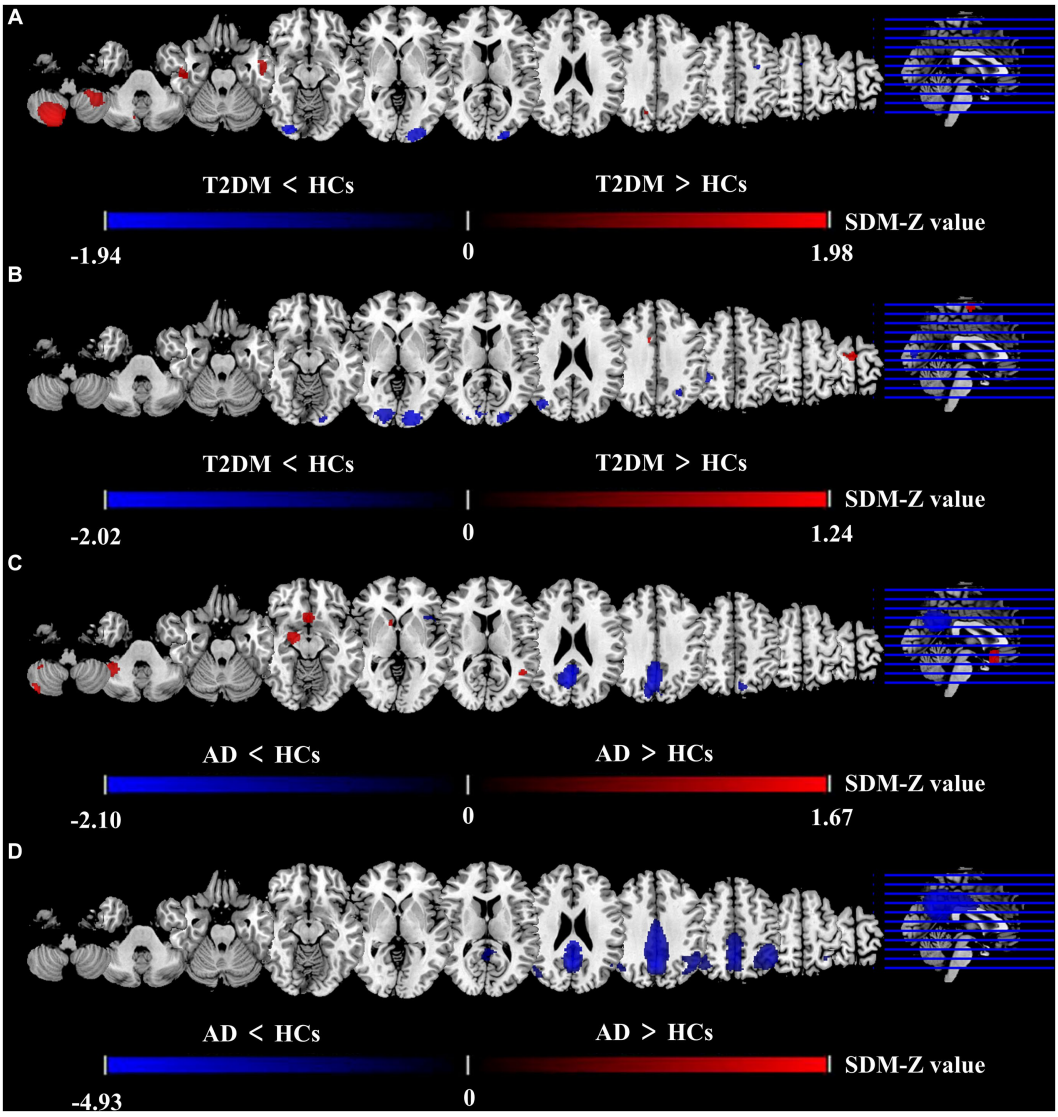

FIGURE 2
Differences between two groups in CBF and ALFF in meta-analysis results. Results of the meta-analysis **(A)** ALFF difference between T2DM and HCs. **(B)** CBF difference between T2DM and HCs. **(C)** ALFF difference between AD and HCs. **(D)** CBF difference between AD and HCs.

3.6 Meta-regression

In the regression analysis, we excluded the abnormal brain regions outside the main results. Meta regression analysis showed that general demographic statistics (age and gender) had no significant impact on the main results in both T2DM and AD patients, even if there was a difference in the age of patients of AD. However, in T2DM patients, lower MMSE scores were associated with lower ALFF in the left frontal lobe (peak MNI coordinate: −30, −4, 56, $Z = 6.432$, 115 voxels) and lower CBF in the right parietal lobe (peak MNI coordinate: 38, −36, 44, $Z = 4.045$, 41 voxels).

4 Discussion

In this paper, we conducted a multimodal voxel based meta-analysis of T2DM and AD, and obtained the following results: (1) In T2DM patients, ALFF in the CER and ITG.L as well as CBF in the SMA.R increased, while ALFF in the MOG.L, IOG.R, and preCG.L as well as CBF in the MOG and IPL decreased. (2) In AD patients, ALFF in the CER.R, right striatum and HIP.R increased, while ALFF in the PCUN and STG.R as well as CBF in the PCUN and IPG decreased. (3) During multimodal analysis of ALFF and CBF, it was found that in T2DM patients, there was a simultaneous decrease of neural activity and blood perfusion in the area of both occipital lobes, while in AD patients, there was a simultaneous decrease of neural activity and blood perfusion in the parietal lobe. Except for decreased CBF in MOG. R in both type of patients, there were no common changes in other brain regions between the two diseases. (4) Regression analysis showed that general demographic information had no impact on the main results of the meta-analysis, while the MMSE scores of T2DM had an impact on ALFF in the left frontal lobe and CBF in the right parietal lobe.

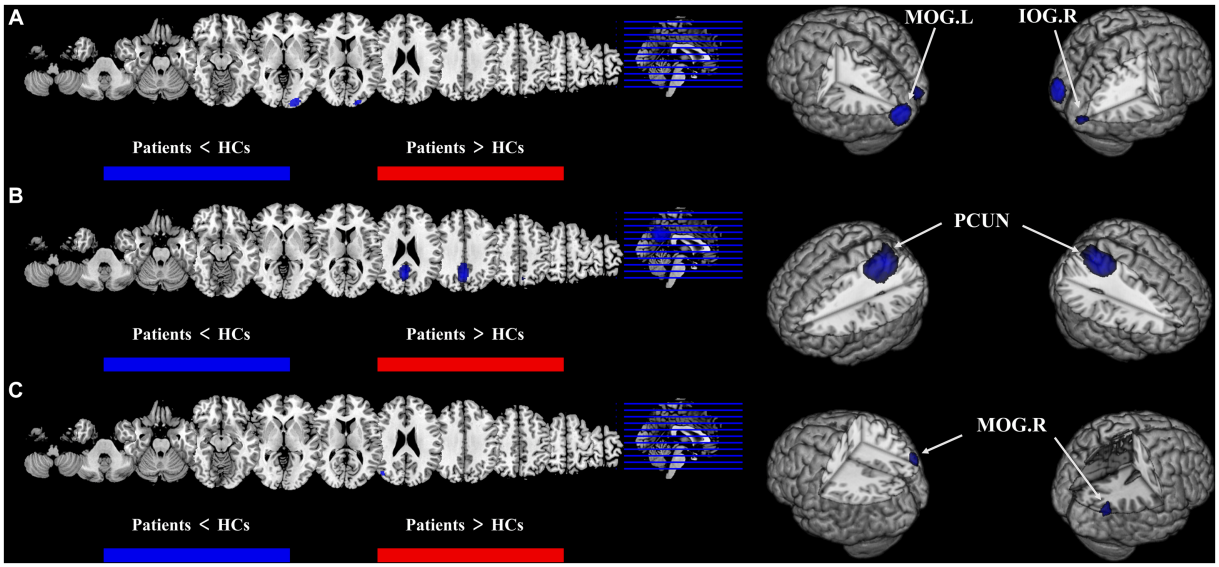

FIGURE 3
Results of multimodal analysis within a disease and joint analysis between diseases. Results of the meta-analysis **(A)** both ALFF and CBF decreased in T2DM. **(B)** Both ALFF and CBF decreased in AD. **(C)** CBF reduction in both T2DM and AD.

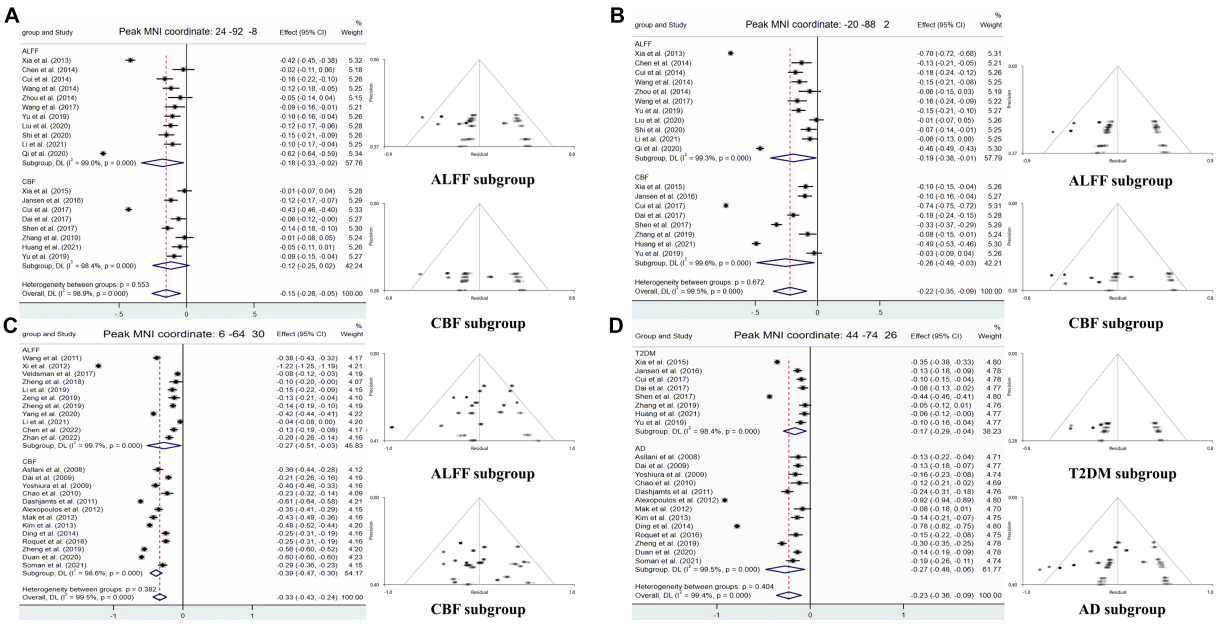

FIGURE 4
Forest and funnel plots of peak MNI coordinates. Peak MNI coordinate regarding **(A,B)** both ALFF and CBF decreased in T2DM and subgroup results. **(C)** Both ALFF and CBF decreased in AD and subgroup results. **(D)** CBF reduction in both T2DM and AD and subgroup results.

The results of this meta-analysis showed that both ALFF and CBF of T2DM in occipital region were significantly reduced. As a key area of the visual cortex, the occipital lobe has decreased blood perfusion and neural activity, which was consistent with the view that visual spatial impairment was one of the main manifestations of T2DM (Cheung et al., 2010; Zeng et al., 2020). The preCG mainly manages the movement of skeletal muscles throughout the body (Li et al., 2015), which is called the motor area. Although the publication bias of this result leads to a decrease in the level of evidence, decreased motor and peripheral sensory abilities in T2DM patients with peripheral neuropathy may be due to a decrease in the neural impulses received by the preCG (Selvarajah et al., 2019), specifically manifested as a decrease in ALFF in T2DM. In addition, the CBF of T2DM reduced in IPG, which played an important role in the integration of human senses and the neural activity of determining the spatial position of objects, as well as in information processing in working

TABLE 3 Results of multimodal analysis within a disease and combined analysis between diseases.

Local maximum region	Peak MNI coordinate (x, y, z)	Peak intensity	SDM Z value	Cluster (NO. of voxels)	Breakdown (No. of voxels)	Egger's test (*p* value)	Heterogeneity (I^2)	Jackknife sensitivity
Both ALFF and CBF decreased in T2DM								
Right occipital lobe	24, −92, −8	−2.4866	−1.560 (ALFF), −1.403 (CBF)	53	Right occipital lobe (53)	0.545 (ALFF) 0.614 (CBF)	99% (ALFF) 98.4% (CBF)	10/11 (ALFF) 8/8 (CBF)
Left occipital lobe	−20, −88, 2	−2.9759	−1.579 (ALFF), −1.544 (CBF)	564	Right middle occipital gyrus (247)	0.887 (ALFF) 0.833 (CBF)	99.3% (ALFF) 99.6% (CBF)	10/11 (ALFF) 8/8 (CBF)
					Right inferior occipital gyrus (74)			
					Right lingual gyrus (50)			
Both ALFF and CBF decreased in AD								
Precuneus and parietal lobe	6, −64, 30	−9.5112	−2.029 (ALFF), −4.686 (CBF)	1,692	Right precuneus (678)	0.339 (ALFF) 0.640 (CBF)	99.7% (ALFF) 98.6% (CBF)	11/11 (ALFF) 13/13 (CBF)
					Left precuneus (504)			
					Left posterior cingulate gyrus (150)			
					Right median cingulate / paracingulate gyri (108)			
					Right posterior cingulate gyrus (103)			
Both T2DM and AD decreased with CBF								
Right occipital lobe	44, −74, 26	−3.0589	−1.551 (T2DM), −1.971 (AD)	56	Right middle occipital gyrus (48)	0.754 (T2DM) 0.745 (AD)	98.4% (T2DM) 99.5% (AD)	8/8 (T2DM) 13/13 (AD)

T2DM, type 2 diabetes mellitus; AD, Alzheimer's disease; ALFF, amplitude of low frequency fluctuation; CBF, cerebral blood flow.

10.3389/fnins.2023.1301778

memory (Koenigs et al., 2009). Working memory is an important process in brain cognition, especially in higher order cognition (Baddeley, 2003), and cognitive impairment in T2DM patients may be related to it. The regression analysis results of T2DM on MMSE also support this viewpoint.

We found that the ALFF of T2DM increased in CER and ITG.L. The cerebellar hemisphere is closely related to motor learning and coordination (Stoodley and Schmahmann, 2009), and the temporal lobe is related to memory, language fluency, language processing and language production, which are important components of cognitive ability (McCrimmon et al., 2012). Many studies have confirmed that T2DM patients would cause cognitive decline (McCrimmon et al., 2012; Biessels and Despa, 2018). Among the 11 T2DM studies we included in the analysis of ALFF, 6/11 were patients with MCI, 3/11 were patients with normal cognition, and 2/11 did not give cognitive assessment results. Therefore, we considered that the enhanced neural activity in these regions may play a role of compensation or supplement in T2DM patients, so that their cognitive performance can be retained or delayed to a certain extent. In addition, the CBF of T2DM increased in the SMA.R, which played an important role in precise control of motion, especially in fine movements such as finger movements (Tanji and Shima, 1994). Sensory and motor dysfunction caused by peripheral neuropathy complications in T2DM patients may be associated with an increase in CBF in this region (Allen et al., 2016).

This study showed that ALFF and CBF of PCUN, parietal lobe and occipital lobe in AD patients existed a consistent decline. The PCUN and parietal lobe are both the main brain regions that constitute the default pattern network (Bathelt and Geurts, 2021; Yeshurun et al., 2021), and are closely related to cognition (Smallwood et al., 2021). As a core brain region that affects visual spatial ability, the occipital lobe region also exhibits a covariate decrease in ALFF and CBF in AD patients, which may be related to perceptual impairments in visual and spatial abilities that are manifested early in AD patients (Mendez et al., 1990; Binetti et al., 1996; Zeng et al., 2020). In addition, studies have confirmed that normal visual ability had a significant impact on the development and persistence of cognitive ability. The parietal lobe and its adjacent occipital lobe are closely related to the temporal spatial structure function and graphic visual attention function (Sakkalou et al., 2021; Zhao et al., 2021). These changes in brain nerve activity and blood flow were closely related to the clinical manifestations of AD patients, such as acquired and persistent mental disorders, memory and cognitive dysfunction, speech and visual spatial skills disorders, and affected their social activities (Burns and Iliffe, 2009; Liu et al., 2019; Scheltens et al., 2021).

The results also showed that the ALFF of the CER.R, HIP.R and right striatum was higher in AD group than that in HCs, indicating that the neural activity in relevant brain regions was enhanced. The cerebellar hemisphere is closely related to motor learning (Stoodley and Schmahmann, 2009), HIP and striatum are important regions in the memory encoding pathway (Pennartz et al., 2011; Chersi and Burgess, 2015), and their anatomical relationship makes them more closely related. HIP and striatum can guide memory and behavior through cooperation or competition, and can regulate when other pathways in the brain are affected (Poldrack and Packard, 2003; Ghiglieri et al., 2011; Squire and Dede, 2015). The above brain regions are mainly related to learning and memory in cognitive activities. Due to the fact that memory impairment is the most significant clinical manifestation of AD patients (Burns and Iliffe, 2009), the above changes can be seen as a compensatory manifestation after memory related brain nerve activity damage.

After analyzing the brain regions with the same changes in T2DM patients and AD patients, the CBF of the two groups decreased uniformly only in the MOG.R region. As a key area of visual cortex, T2DM patients have visual space disorder and the occurrence of diabetes retinopathy also attributes to this change. The change of visual cortex in AD patients as a mediator, which further leaded to the impairment of advanced cognitive function, was also the focus of researchers.

After analyzing the neuroimaging evidence provided by the results of this study, we tend to believe that T2DM and AD are two diseases with their own characteristics of brain activity damage. The main damage area of T2DM was the bilateral occipital lobe, which mainly affects visual spatial function and other functions extended by visual function impairment. However, AD was mainly injured in bilateral PCUN and partial lobes, including posterior cingulate gyrus, PCUN, parietal lobe and part of occipital lobe, resulting in multi-dimensional functional damage in language, memory, learning, vision, etc. Only a small proportion (56 voxels in total) of MOG.R belonged to a part of the visual cortex were found in these two diseases, which was consistent with the clinical characteristics of them, and also suggested that T2DM was a risk factor for AD.

The reason why AD is considered as type 3 diabetes in some studies is briefly discussed tentatively. The main reason is that T2DM and AD have a high epidemiological correlation (Arvanitakis et al., 2004; Wang et al., 2012). However, as a high-risk factor for cerebrovascular diseases, T2DM can increase the risk of cerebral infarction and cerebral hemorrhage, which has achieved clinical consensus (Kannel and McGee, 1979). And as a complication of T2DM, cerebrovascular disease also has a higher incidence rate among T2DM patients (Gregg et al., 2016). Many clinical studies have shown that the occurrence of cerebrovascular events is significantly correlated with cognitive impairment and dementia (Vermeer et al., 2007; Troncoso et al., 2008; Rost et al., 2022). This correlation may help explain the epidemiological correlation between T2DM and AD (Sutherland et al., 2017). Researchers believe that another main reason why AD should be called type 3 diabetes is that T2DM and AD have many common pathophysiological bases, such as central insulin resistance (Janson et al., 2004; De Felice et al., 2022), AGEs and metabolic syndrome (Byun et al., 2017; Więckowska-Gacek et al., 2021). Firstly, lipid metabolism is an important component of metabolic syndrome. There is metabolic syndrome caused by insulin resistance in T2DM (Zheng et al., 2018), and autopsy findings of lipid particles in the brain of AD patients have also led researchers to suspect that lipid metabolism is involved in the pathogenesis of AD (Foley, 2010). In subsequent studies, it was found that sulfatides, an important subtype of sphingolipids, may play an important role in the pathogenesis of AD. Sulfatides are an important part of the myelin sheath and oligodendrocytes (Takahashi and Suzuki, 2012), and their consumption in AD patients is as high as 93% (Han et al., 2002). This change is a specific change of AD, but the pathogenesis of AD is more complex and still under study (Han, 2010; Cheng et al., 2013), and there is no clear evidence to confirm its correlation with abnormal lipid metabolism in diabetes. Secondly, in the past, there have been many studies on hyperglycemia leading to tissue damage through the production of AGEs, altering cell activation functions, and resulting in cognitive impairment (Klein and Waxman, 2003; Brownlee, 2005; Byun et al.,

2017), but most of them are based on basic experiments (Batkulwar et al., 2018; Volpina et al., 2021). The impact of these findings on the human body is uncertain, and more evidence is needed to confirm whether this theory has a comorbidity pathway in T2DM and AD. Finally, there is increasing evidence that insulin resistance, especially central insulin resistance is related to the pathogenesis of AD (Janson et al., 2004; Neth and Craft, 2017; De Felice et al., 2022). Intranasal injection of insulin can alleviate memory deficits in some AD patients (Novak et al., 2014; Craft et al., 2017). However, the mechanism of insulin resistance on cognitive impairment in the brain is still unclear. The above results confirm that T2DM and AD are two closely related diseases, but it is still too early to call AD type 3 diabetes. In comparison, T2DM is a more appropriate high-risk factor for AD, and the relationship between the two diseases still needs further research.

5 Limitations

It should be noted that the following limitations still exist in this study. Firstly, all the literature was cross-sectional and lacked longitudinal tracking of disease progression. Secondly, this study conducted a meta-analysis based on the reported coordinates provided by the article or the corresponding author. Research results that do not provide coordinates are not included, which may cause bias. Thirdly, lack of sufficient data to correct the differences in data processing and the gray matter volume of subjects in the original study (Supplementary Tables S2, S3), which may potentially contribute to the high heterogeneity of our results. Fourthly, because most articles in the AD group did not provide the comorbidity of AD and T2DM, more detailed subgroup analysis cannot be performed. In the future, it is necessary to update the meta-analysis to eliminate the confounding factors of comorbidity and make the level of evidence higher. Fifthly, the population included in the study is mainly concentrated in the East Asian population, resulting in limited universality of the research results. Finally, it was hoped that in future studies, a larger sample of meta-analysis would be conducted, and attention will be paid to longitudinal studies from T2DM to T2DM with AD. Provide more core evidence for the occurrence and mechanism of comorbidity of the two diseases.

6 Conclusion

In summary, after analyzing the evidence provided by neuroimaging, T2DM and AD are two diseases with their own characteristics of brain neural activity and blood flow changes. Even if there is a small common area of reduced blood flow in both diseases, this is consistent with the clinical characteristics of both diseases and suggests a close relationship between the two diseases. This provided an idea for us to study the brain damage and the relationship between these two diseases in the future, and provided new insights for understanding the pathophysiology of brain changes in these two diseases and developing effective early intervention methods.

Author contributions

HX: Data curation, Formal analysis, Investigation, Methodology, Software, Visualization, Writing – original draft, Writing – review & editing. YYu: Funding acquisition, Supervision, Validation, Software, Writing – original draft. YYa: Conceptualization, Methodology, Software, Validation, Writing – original draft. QS: Data curation, Validation, Writing – original draft. Z-YL: Conceptualization, Funding acquisition, Resources, Supervision, Validation, Writing – original draft. M-HN: Methodology, Project administration, Software, Writing – original draft. S-NL: Data curation, Software, Writing – original draft. PD: Data curation, Formal analysis, Writing – original draft. Y-YC: Software, Writing – original draft. X-YC: Software, Writing – original draft. NJ: Data curation, Methodology, Writing – original draft. L-JD: Supervision, Validation, Writing – original draft. WG: Data curation, Writing – original draft. J-JB: Software, Writing – original draft. L-FY: Resources, Software, Visualization, Writing – original draft, Writing – review & editing. G-BC: Conceptualization, Funding acquisition, Resources, Supervision, Validation, Writing – review & editing.

Funding

The author(s) declare financial support was received for the research, authorship, and/or publication of this article. This work was supported by the Key Research and Development Projects of Shaanxi (Grant number 2023-YBSF-331) and "Rapid response" research project of Air Force Military Medical University (Grant number 2023KXKT025).

Acknowledgments

The authors wish to thank the Neurology Department and Endocrinology Department of Tangdu Hospital for providing advice and guidance in support of this study.

Conflict of interest

The authors declare that the research was conducted in the absence of any commercial or financial relationships that could be construed as a potential conflict of interest.

Publisher's note

Supplementary material

The Supplementary material for this article can be found online at: https://www.frontiersin.org/articles/10.3389/fnins.2023.1301778/full#supplementary-material

References

Allen, M. D., Doherty, T. J., Rice, C. L., and Kimpinski, K. (2016). Physiology in medicine: neuromuscular consequences of diabetic neuropathy. *J. Appl. Physiol.* 121, 1–6. doi: 10.1152/japplphysiol.00733.2015

Alzheimer's Association (2021). 2021 Alzheimer's disease facts and figures. *Alzheimers Dement.* 17, 327–406. doi: 10.1002/alz.12328

Arvanitakis, Z., Wilson, R. S., Bienias, J. L., Evans, D. A., and Bennett, D. A. (2004). Diabetes mellitus and risk of Alzheimer disease and decline in cognitive function. *Arch. Neurol.* 61, 661–666. doi: 10.1001/archneur.61.5.661

Baddeley, A. (2003). Working memory: looking back and looking forward. *Nat. Rev. Neurosci.* 4, 829–839. doi: 10.1038/nrn1201

Ballard, C., Gauthier, S., Corbett, A., Brayne, C., Aarsland, D., and Jones, E. (2011). Alzheimer's disease. *Lancet* 377, 1019–1031. doi: 10.1016/S0140-6736(10)61349-9

Barona, M., Brown, M., Clark, C., Frangou, S., White, T., and Micali, N. (2019). White matter alterations in anorexia nervosa: evidence from a voxel-based meta-analysis. *Neurosci. Biobehav. Rev.* 100, 285–295. doi: 10.1016/j.neubiorev.2019.03.002

Bathelt, J., and Geurts, H. M. (2021). Difference in default mode network subsystems in autism across childhood and adolescence. *Autism* 25, 556–565. doi: 10.1177/1362361320969258

Batkulwar, K., Godbole, R., Banarjee, R., Kassaar, O., Williams, R. J., and Kulkarni, M. J. (2018). Advanced glycation end products modulate amyloidogenic APP processing and tau phosphorylation: a mechanistic link between glycation and the development of Alzheimer's disease. *ACS Chem. Neurosci.* 9, 988–1000. doi: 10.1021/acschemneuro.7b00410

Benwell, C. S. Y., Davila-Pérez, P., Fried, P. J., Jones, R. N., Travison, T. G., Santarnecchi, E., et al. (2020). EEG spectral power abnormalities and their relationship with cognitive dysfunction in patients with Alzheimer's disease and type 2 diabetes. *Neurobiol. Aging* 85, 83–95. doi: 10.1016/j.neurobiolaging.2019.10.004

Biessels, G. J., and Despa, F. (2018). Cognitive decline and dementia in diabetes mellitus: mechanisms and clinical implications. *Nat. Rev. Endocrinol.* 14, 591–604. doi: 10.1038/s41574-018-0048-7

Binetti, G., Cappa, S. F., Magni, E., Padovani, A., Bianchetti, A., and Trabucchi, M. (1996). Disorders of visual and spatial perception in the early stage of Alzheimer's disease. *Ann. N. Y. Acad. Sci.* 777, 221–225. doi: 10.1111/j.1749-6632.1996.tb34422.x

Brownlee, M. (2005). The pathobiology of diabetic complications: a unifying mechanism. *Diabetes* 54, 1615–1625. doi: 10.2337/diabetes.54.6.1615

Brundel, M., Kappelle, L. J., and Biessels, G. J. (2014). Brain imaging in type 2 diabetes. *Eur. Neuropsychopharmacol.* 24, 1967–1981. doi: 10.1016/j.euroneuro.2014.01.023

Bruno, G., Runzo, C., Cavallo-Perin, P., Merletti, F., Rivetti, M., Pinach, S., et al. (2005). Incidence of type 1 and type 2 diabetes in adults aged 30-49 years: the population-based registry in the province of Turin, Italy. *Diabetes Care* 28, 2613–2619. doi: 10.2337/diacare.28.11.2613

Bucerius, J., Mani, V., Moncrieff, C., Rudd, J. H. F., Machac, J., Fuster, V., et al. (2012). Impact of noninsulin-dependent type 2 diabetes on carotid wall 18F-fluorodeoxyglucose positron emission tomography uptake. *J. Am. Coll. Cardiol.* 59, 2080–2088. doi: 10.1016/j.jacc.2011.11.069

Burns, A., and Iliffe, S. (2009). Alzheimer's disease. *BMJ* 338:b158. doi: 10.1136/bmj.b158

Byun, K., Yoo, Y., Son, M., Lee, J., Jeong, G. B., Park, Y. M., et al. (2017). Advanced glycation end-products produced systemically and by macrophages: a common contributor to inflammation and degenerative diseases. *Pharmacol. Ther.* 177, 44–55. doi: 10.1016/j.pharmthera.2017.02.030

Chen, Z., and Zhong, C. (2013). Decoding Alzheimer's disease from perturbed cerebral glucose metabolism: implications for diagnostic and therapeutic strategies. *Prog. Neurobiol.* 108, 21–43. doi: 10.1016/j.pneurobio.2013.06.004

Cheng, H., Wang, M., Li, J. L., Cairns, N. J., and Han, X. (2013). Specific changes of sulfatide levels in individuals with pre-clinical Alzheimer's disease: an early event in disease pathogenesis. *J. Neurochem.* 127, 733–738. doi: 10.1111/jnc.12368

Chersi, F., and Burgess, N. (2015). The cognitive architecture of spatial navigation: hippocampal and striatal contributions. *Neuron* 88, 64–77. doi: 10.1016/j.neuron.2015.09.021

Cheung, N., Mitchell, P., and Wong, T. Y. (2010). Diabetic retinopathy. *Lancet* 376, 124–136. doi: 10.1016/S0140-6736(09)62124-3

Chornenkyy, Y., Wang, W. X., Wei, A., and Nelson, P. T. (2019). Alzheimer's disease and type 2 diabetes mellitus are distinct diseases with potential overlapping metabolic dysfunction upstream of observed cognitive decline. *Brain Pathol.* 29, 3–17. doi: 10.1111/bpa.12655

Craft, S., Claxton, A., Baker, L. D., Hanson, A. J., Cholerton, B., Trittschuh, E. H., et al. (2017). Effects of regular and Long-acting insulin on cognition and Alzheimer's disease biomarkers: a pilot clinical trial. *J. Alzheimers Dis.* 57, 1325–1334. doi: 10.3233/JAD-161256

De Felice, F. G., Goncalves, R. A., and Ferreira, S. T. (2022). Impaired insulin signalling and allostatic load in Alzheimer disease. *Nat. Rev. Neurosci.* 23, 215–230. doi: 10.1038/s41583-022-00558-9

de la Monte, S. M., Tong, M., and Wands, J. R. (2018). The 20-year voyage aboard the journal of Alzheimer's disease: docking at 'Type 3 Diabetes', environmental/exposure factors, pathogenic mechanisms, and potential treatments. *J. Alzheimers Dis.* 62, 1381–1390. doi: 10.3233/JAD-170829

Diehl, T., Mullins, R., and Kapogiannis, D. (2017). Insulin resistance in Alzheimer's disease. *Transl. Res.* 183, 26–40. doi: 10.1016/j.trsl.2016.12.005

Diniz Pereira, J., Gomes Fraga, V., Morais Santos, A. L., Carvalho, M. G., Caramelli, P., and Braga Gomes, K. (2021). Alzheimer's disease and type 2 diabetes mellitus: a systematic review of proteomic studies. *J. Neurochem.* 156, 753–776. doi: 10.1111/jnc.15166

Egger, M., Smith, G. D., Schneider, M., and Minder, C. (1997). Bias in meta-analysis detected by a simple, graphical test. *BMJ* 315, 629–634. doi: 10.1136/bmj.315.7109.629

Exalto, L. G., Biessels, G. J., Karter, A. J., Huang, E. S., Katon, W. J., Minkoff, J. R., et al. (2013). Risk score for prediction of 10 year dementia risk in individuals with type 2 diabetes: a cohort study. *Lancet Diabetes Endocrinol.* 1, 183–190. doi: 10.1016/S2213-8587(13)70048-2

Ferreira, L. K., and Busatto, G. F. (2010). Heterogeneity of coordinate-based meta-analyses of neuroimaging data: an example from studies in OCD. *Br. J. Psychiatry* 197, 76–77; author reply 77. doi: 10.1192/bjp.197.1.76a

Foley, P. (2010). Lipids in Alzheimer's disease: a century-old story. *Biochim. Biophys. Acta* 1801, 750–753. doi: 10.1016/j.bbalip.2010.05.004

Geijselaers, S. L. C., Sep, S. J. S., Stehouwer, C. D. A., and Biessels, G. J. (2015). Glucose regulation, cognition, and brain MRI in type 2 diabetes: a systematic review. *Lancet Diabetes Endocrinol.* 3, 75–89. doi: 10.1016/S2213-8587(14)70148-2

Ghiglieri, V., Sgobio, C., Costa, C., Picconi, B., and Calabresi, P. (2011). Striatum-hippocampus balance: from physiological behavior to interneuronal pathology. *Prog. Neurobiol.* 94, 102–114. doi: 10.1016/j.pneurobio.2011.04.005

Gregg, E. W., Sattar, N., and Ali, M. K. (2016). The changing face of diabetes complications. *Lancet Diabetes Endocrinol.* 4, 537–547. doi: 10.1016/S2213-8587(16)30010-9

Han, X. (2010). The pathogenic implication of abnormal interaction between apolipoprotein E isoforms, amyloid-beta peptides, and sulfatides in Alzheimer's disease. *Mol. Neurobiol.* 41, 97–106. doi: 10.1007/s12035-009-8092-x

Han, X., M Holtzman, D., McKeel, D. W. Jr., Kelley, J., and Morris, J. C. (2002). Substantial sulfatide deficiency and ceramide elevation in very early Alzheimer's disease: potential role in disease pathogenesis. *J. Neurochem.* 82, 809–818. doi: 10.1046/j.1471-4159.2002.00997.x

Holman, N., Young, B., and Gadsby, R. (2015). Current prevalence of type 1 and type 2 diabetes in adults and children in the UK. *Diabet. Med.* 32, 1119–1120. doi: 10.1111/dme.12791

Hu, B., Yan, L. F., Sun, Q., Yu, Y., Zhang, J., Dai, Y. J., et al. (2019). Disturbed neurovascular coupling in type 2 diabetes mellitus patients: evidence from a comprehensive fMRI analysis. *Neuroimage Clin.* 22:101802. doi: 10.1016/j.nicl.2019.101802

Janson, J., Laedtke, T., Parisi, J. E., O'Brien, P., Petersen, R. C., and Butler, P. C. (2004). Increased risk of type 2 diabetes in Alzheimer disease. *Diabetes* 53, 474–481. doi: 10.2337/diabetes.53.2.474

Kannel, W. B., and McGee, D. L. (1979). Diabetes and cardiovascular disease. The Framingham study. *JAMA* 241, 2035–2038. doi: 10.1001/jama.1979.03290450033020

Kannurpatti, S. S., Biswal, B. B., Kim, Y. R., and Rosen, B. R. (2008). Spatio-temporal characteristics of low-frequency BOLD signal fluctuations in isoflurane-anesthetized rat brain. *Neuroimage* 40, 1738–1747. doi: 10.1016/j.neuroimage.2007.05.061

Kautzky-Willer, A., Harreiter, J., and Pacini, G. (2016). Sex and gender differences in risk, pathophysiology and complications of type 2 diabetes mellitus. *Endocr. Rev.* 37, 278–316. doi: 10.1210/er.2015-1137

Kellar, D., and Craft, S. (2020). Brain insulin resistance in Alzheimer's disease and related disorders: mechanisms and therapeutic approaches. *Lancet Neurol.* 19, 758–766. doi: 10.1016/S1474-4422(20)30231-3

Kim, S.-G., and Lee, S.-P. (2004). Cortical layer-dependent CBF changes induced by neural activity. *Int. Congr. Ser.* 1265, 201–210. doi: 10.1016/j.ics.2004.04.024

Klein, J. P., and Waxman, S. G. (2003). The brain in diabetes: molecular changes in neurons and their implications for end-organ damage. *Lancet Neurol.* 2, 548–554. doi: 10.1016/S1474-4422(03)00503-9

Koenigs, M., Barbey, A. K., Postle, B. R., and Grafman, J. (2009). Superior parietal cortex is critical for the manipulation of information in working memory. *J. Neurosci.* 29, 14980–14986. doi: 10.1523/JNEUROSCI.3706-09.2009

Kubis-Kubiak, A. M., Rorbach-Dolata, A., and Piwowar, A. (2019). Crucial players in Alzheimer's disease and diabetes mellitus: friends or foes? *Mech. Ageing Dev.* 181, 7–21. doi: 10.1016/j.mad.2019.03.008

Li, N., Chen, T. W., Guo, Z. V., Gerfen, C. R., and Svoboda, K. (2015). A motor cortex circuit for motor planning and movement. *Nature* 519, 51–56. doi: 10.1038/nature14178

Li, L., Zhang, Y., Zhao, Y., Li, Z., Kemp, G. J., Wu, M., et al. (2022). Cortical thickness abnormalities in patients with post-traumatic stress disorder: a vertex-based meta-analysis. *Neurosci. Biobehav. Rev.* 134:104519. doi: 10.1016/j.neubiorev.2021.104519

Liu, P. P., Xie, Y., Meng, X. Y., and Kang, J. S. (2019). History and progress of hypotheses and clinical trials for Alzheimer's disease. *Signal Transduct. Target. Ther.* 4:29. doi: 10.1038/s41392-019-0063-8

Liu, J., Yang, X., Li, Y., Xu, H., Ren, J., and Zhou, P. (2022). Cerebral blood flow alterations in type 2 diabetes mellitus: a systematic review and meta-analysis of arterial spin labeling studies. *Front. Aging Neurosci.* 14:847218. doi: 10.3389/fnagi.2022.847218

Ma, L. L., Wang, Y. Y., Yang, Z. H., Huang, D., Weng, H., and Zeng, X. T. (2020). Methodological quality (risk of bias) assessment tools for primary and secondary medical studies: what are they and which is better? *Mil. Med. Res.* 7:7. doi: 10.1186/s40779-020-00238-8

Macpherson, H., Formica, M., Harris, E., and Daly, R. M. (2017). Brain functional alterations in type 2 diabetes - a systematic review of fMRI studies. *Front. Neuroendocrinol.* 47, 34–46. doi: 10.1016/j.yfrne.2017.07.001

Matsuda, H. (2016). MRI morphometry in Alzheimer's disease. *Ageing Res. Rev.* 30, 17–24. doi: 10.1016/j.arr.2016.01.003

McCrimmon, R. J., Ryan, C. M., and Frier, B. M. (2012). Diabetes and cognitive dysfunction. *Lancet* 379, 2291–2299. doi: 10.1016/S0140-6736(12)60360-2

Mendez, M. F., Tomsak, R. L., and Remler, B. (1990). Disorders of the visual system in Alzheimer's disease. *J. Clin. Neuroophthalmol.* 10, 62–69.

Moran, C., Beare, R., Phan, T. G., Bruce, D. G., Callisaya, M. L., Srikanth, V., et al. (2015). Type 2 diabetes mellitus and biomarkers of neurodegeneration. *Neurology* 85, 1123–1130. doi: 10.1212/WNL.0000000000001982

Müller, V. I., Cieslik, E. C., Laird, A. R., Fox, P. T., Radua, J., Mataix-Cols, D., et al. (2018). Ten simple rules for neuroimaging meta-analysis. *Neurosci. Biobehav. Rev.* 84, 151–161. doi: 10.1016/j.neubiorev.2017.11.012

Neth, B. J., and Craft, S. (2017). Insulin resistance and Alzheimer's disease: bioenergetic linkages. *Front. Aging Neurosci.* 9:345. doi: 10.3389/fnagi.2017.00345

Nguyen, T. T., Ta, Q. T. H., Nguyen, T. K. O., Nguyen, T. T. D., and van Giau, V. (2020). Type 3 diabetes and its role implications in Alzheimer's disease. *Int. J. Mol. Sci.* 21:3165. doi: 10.3390/ijms21093165

Novak, V., Milberg, W., Hao, Y., Munshi, M., Novak, P., Galica, A., et al. (2014). Enhancement of vasoreactivity and cognition by intranasal insulin in type 2 diabetes. *Diabetes Care* 37, 751–759. doi: 10.2337/dc13-1672

Page, M. J., McKenzie, J. E., Bossuyt, P. M., Boutron, I., Hoffmann, T. C., Mulrow, C. D., et al. (2021). The PRISMA 2020 statement: an updated guideline for reporting systematic reviews. *BMJ* 372:n71. doi: 10.1136/bmj.n71

Pan, P., Zhu, L., Yu, T., Shi, H. C., Zhang, B., Qin, R., et al. (2017). Aberrant spontaneous low-frequency brain activity in amnestic mild cognitive impairment: a meta-analysis of resting-state fMRI studies. *Ageing Res. Rev.* 35, 12–21. doi: 10.1016/j.arr.2016.12.001

Pennartz, C. M., Ito, R., Verschure, P. F., Battaglia, F. P., and Robbins, T. W. (2011). The hippocampal-striatal axis in learning, prediction and goal-directed behavior. *Trends Neurosci.* 34, 548–559. doi: 10.1016/j.tins.2011.08.001

Poldrack, R. A., and Packard, M. G. (2003). Competition among multiple memory systems: converging evidence from animal and human brain studies. *Neuropsychologia* 41, 245–251. doi: 10.1016/S0028-3932(02)00157-4

Radua, J., and Mataix-Cols, D. (2009). Voxel-wise meta-analysis of grey matter changes in obsessive-compulsive disorder. *Br. J. Psychiatry* 195, 393–402. doi: 10.1192/bjp.bp.108.055046

Radua, J., and Mataix-Cols, D. (2012). Meta-analytic methods for neuroimaging data explained. *Biol Mood Anxiety Disord.* 2:6. doi: 10.1186/2045-5380-2-6

Radua, J., Mataix-Cols, D., Phillips, M. L., el-Hage, W., Kronhaus, D. M., Cardoner, N., et al. (2012). A new meta-analytic method for neuroimaging studies that combines reported peak coordinates and statistical parametric maps. *Eur. Psychiatry* 27, 605–611. doi: 10.1016/j.eurpsy.2011.04.001

Radua, J., Rubia, K., Canales-Rodríguez, E. J., Pomarol-Clotet, E., Fusar-Poli, P., and Mataix-Cols, D. (2014). Anisotropic kernels for coordinate-based meta-analyses of neuroimaging studies. *Front. Psych.* 5:13. doi: 10.3389/fpsyt.2014.00013

Rost, N. S., Brodtmann, A., Pase, M. P., van Veluw, S. J., Biffi, A., Duering, M., et al. (2022). Post-stroke cognitive impairment and dementia. *Circ. Res.* 130, 1252–1271. doi: 10.1161/CIRCRESAHA.122.319951

Saeedi, P., Petersohn, I., Salpea, P., Malanda, B., Karuranga, S., Unwin, N., et al. (2019). Global and regional diabetes prevalence estimates for 2019 and projections for 2030 and 2045: results from the international diabetes federation diabetes atlas, 9(th) edition. *Diabetes Res. Clin. Pract.* 157:107843. doi: 10.1016/j.diabres.2019.107843

Sakkalou, E., O'Reilly, M. A., Sakki, H., Springall, C., de Haan, M., Salt, A. T., et al. (2021). Mother-infant interactions with infants with congenital visual impairment and associations with longitudinal outcomes in cognition and language. *J. Child Psychol. Psychiatry* 62, 742–750. doi: 10.1111/jcpp.13308

Scheltens, P., de Strooper, B., Kivipelto, M., Holstege, H., Chételat, G., Teunissen, C. E., et al. (2021). Alzheimer's disease. *Lancet* 397, 1577–1590. doi: 10.1016/S0140-6736(20)32205-4

Selvarajah, D., Kar, D., Khunti, K., Davies, M. J., Scott, A. R., Walker, J., et al. (2019). Diabetic peripheral neuropathy: advances in diagnosis and strategies for screening and early intervention. *Lancet Diabetes Endocrinol.* 7, 938–948. doi: 10.1016/S2213-8587(19)30081-6

Smallwood, J., Bernhardt, B. C., Leech, R., Bzdok, D., Jefferies, E., and Margulies, D. S. (2021). The default mode network in cognition: a topographical perspective. *Nat. Rev. Neurosci.* 22, 503–513. doi: 10.1038/s41583-021-00474-4

Squire, L. R., and Dede, A. J. (2015). Conscious and unconscious memory systems. *Cold Spring Harb. Perspect. Biol.* 7:a021667. doi: 10.1101/cshperspect.a021667

Sterne, J. A., Sutton, A. J., Ioannidis, J. P., Terrin, N., Jones, D. R., Lau, J., et al. (2011). Recommendations for examining and interpreting funnel plot asymmetry in meta-analyses of randomised controlled trials. *BMJ* 343:d4002. doi: 10.1136/bmj.d4002

Stoodley, C. J., and Schmahmann, J. D. (2009). Functional topography in the human cerebellum: a meta-analysis of neuroimaging studies. *NeuroImage* 44, 489–501. doi: 10.1016/j.neuroimage.2008.08.039

Sutherland, G. T., Lim, J., Srikanth, V., and Bruce, D. G. (2017). Epidemiological approaches to understanding the link between type 2 diabetes and dementia. *J. Alzheimers Dis.* 59, 393–403. doi: 10.3233/JAD-161194

Tak, S., Wang, D. J., Polimeni, J. R., Yan, L., and Chen, J. J. (2014). Dynamic and static contributions of the cerebrovasculature to the resting-state BOLD signal. *Neuroimage* 84, 672–680. doi: 10.1016/j.neuroimage.2013.09.057

Takahashi, T., and Suzuki, T. (2012). Role of sulfatide in normal and pathological cells and tissues. *J. Lipid Res.* 53, 1437–1450. doi: 10.1194/jlr.R026682

Tanji, J., and Shima, K. (1994). Role for supplementary motor area cells in planning several movements ahead. *Nature* 371, 413–416. doi: 10.1038/371413a0

Troncoso, J. C., Zonderman, A. B., Resnick, S. M., Crain, B., Pletnikova, O., and O'Brien, R. J. (2008). Effect of infarcts on dementia in the Baltimore longitudinal study of aging. *Ann. Neurol.* 64, 168–176. doi: 10.1002/ana.21413

Vermeer, S. E., Longstreth, W. T. Jr., and Koudstaal, P. J. (2007). Silent brain infarcts: a systematic review. *Lancet Neurol.* 6, 611–619. doi: 10.1016/S1474-4422(07)70170-9

Volpina, O. M., Koroev, D. O., Serebryakova, M. V., Volkova, T. D., Kamynina, A. V., and Bobkova, N. V. (2021). Proteolytic degradation patterns of the receptor for advanced glycation end products peptide fragments correlate with their neuroprotective activity in Alzheimer's disease models. *Drug Dev. Res.* 82, 1217–1226. doi: 10.1002/ddr.21836

Wang, K. C., Woung, L. C., Tsai, M. T., Liu, C. C., Su, Y. H., and Li, C. Y. (2012). Risk of Alzheimer's disease in relation to diabetes: a population-based cohort study. *Neuroepidemiology* 38, 237–244. doi: 10.1159/000337428

Więckowska-Gacek, A., Mietelska-Porowska, A., Wydrych, M., and Wojda, U. (2021). Western diet as a trigger of Alzheimer's disease: from metabolic syndrome and systemic inflammation to neuroinflammation and neurodegeneration. *Ageing Res. Rev.* 70:101397. doi: 10.1016/j.arr.2021.101397

Williams, D. S., Detre, J. A., Leigh, J. S., and Koretsky, A. P. (1992). Magnetic resonance imaging of perfusion using spin inversion of arterial water. *Proc. Natl. Acad. Sci. U. S. A.* 89, 212–216. doi: 10.1073/pnas.89.1.212

Yao, L., Yang, C., Zhang, W., Li, S., Li, Q., Chen, L., et al. (2021). A multimodal meta-analysis of regional structural and functional brain alterations in type 2 diabetes. *Front. Neuroendocrinol.* 62:100915. doi: 10.1016/j.yfrne.2021.100915

Yeshurun, Y., Nguyen, M., and Hasson, U. (2021). The default mode network: where the idiosyncratic self meets the shared social world. *Nat. Rev. Neurosci.* 22, 181–192. doi: 10.1038/s41583-020-00420-w

Yu, Y., Yan, L. F., Sun, Q., Hu, B., Zhang, J., Yang, Y., et al. (2019). Neurovascular decoupling in type 2 diabetes mellitus without mild cognitive impairment: potential biomarker for early cognitive impairment. *Neuroimage* 200, 644–658. doi: 10.1016/j.neuroimage.2019.06.058

Yu-Feng, Z., Yong, H., Chao-Zhe, Z., Qing-Jiu, C., Man-Qiu, S., Meng, L., et al. (2007). Altered baseline brain activity in children with ADHD revealed by resting-state functional MRI. *Brain and Development* 29, 83–91. doi: 10.1016/j.braindev.2006.07.002

Zeng, H., Fink, G. R., and Weidner, R. (2020). Visual size processing in early visual cortex follows lateral occipital cortex involvement. *J. Neurosci.* 40, 4410–4417. doi: 10.1523/JNEUROSCI.2437-19.2020

Zhang, H., Wang, Y., Lyu, D., Li, Y., Li, W., Wang, Q., et al. (2021). Cerebral blood flow in mild cognitive impairment and Alzheimer's disease: a systematic review and meta-analysis. *Ageing Res. Rev.* 71:101450. doi: 10.1016/j.arr.2021.101450

Zhao, X., Zhou, Y., Wei, K., Bai, X., Zhang, J., Zhou, M., et al. (2021). Associations of sensory impairment and cognitive function in middle-aged and older Chinese population: the China health and retirement longitudinal study. *J. Glob. Health* 11:08008. doi: 10.7189/jogh.11.08008

Zheng, Y., Ley, S. H., and Hu, F. B. (2018). Global aetiology and epidemiology of type 2 diabetes mellitus and its complications. *Nat. Rev. Endocrinol.* 14, 88–98. doi: 10.1038/nrendo.2017.151

Zhou, X., Zhang, J., Chen, Y., Ma, T., Wang, Y., Wang, J., et al. (2014). Aggravated cognitive and brain functional impairment in mild cognitive impairment patients with type 2 diabetes: a resting-state functional MRI study. *J. Alzheimers Dis.* 41, 925–935. doi: 10.3233/JAD-132354

Zou, Q. H., Zhu, C. Z., Yang, Y., Zuo, X. N., Long, X. Y., Cao, Q. J., et al. (2008). An improved approach to detection of amplitude of low-frequency fluctuation (ALFF) for resting-state fMRI: fractional ALFF. *J. Neurosci. Methods* 172, 137–141. doi: 10.1016/j.jneumeth.2008.04.012

frontiers | Frontiers in Neuroscience

TYPE Original Research
PUBLISHED 07 December 2023
DOI 10.3389/fnins.2023.1301075

OPEN ACCESS

EDITED BY
Yingying Tang,
Shanghai Jiao Tong University, China

REVIEWED BY
Lipeng Ning,
Harvard Medical School, United States
Jiahui Deng,
Peking University Sixth Hospital, China

*CORRESPONDENCE
Chaozhe Zhu
✉ czzhu@bnu.edu.cn

RECEIVED 24 September 2023
ACCEPTED 21 November 2023
PUBLISHED 07 December 2023

CITATION
Chen Y, Jiang Y, Zhang Z, Li Z and Zhu C (2023) Transcranial magnetic stimulation mapping of the motor cortex: comparison of five estimation algorithms.
Front. Neurosci. 17:1301075.
doi: 10.3389/fnins.2023.1301075

Transcranial magnetic stimulation mapping of the motor cortex: comparison of five estimation algorithms

Yuanyuan Chen[1], Yihan Jiang[1,2], Zong Zhang[1], Zheng Li[1,3] and Chaozhe Zhu[1,4,5]*

[1]State Key Laboratory of Cognitive Neuroscience and Learning, Beijing Normal University, Beijing, China, [2]Center for the Cognitive Science of Language, Beijing Language and Culture University, Beijing, China, [3]Center for Cognition and Neuroergonomics, State Key Laboratory of Cognitive Neuroscience and Learning, Beijing Normal University Zhuhai, Zhuhai, China, [4]IDG/McGovern Institute for Brain Research, Beijing Normal University, Beijing, China, [5]Center for Collaboration and Innovation in Brain and Learning Sciences, Beijing Normal University, Beijing, China

Background: There are currently five different kinds of transcranial magnetic stimulation (TMS) motor mapping algorithms available, from ordinary point-based algorithms to advanced field-based algorithms. However, there have been only a limited number of comparison studies conducted, and they have not yet examined all of the currently available algorithms. This deficiency impedes the judicious selection of algorithms for application in both clinical and basic neuroscience, and hinders the potential promotion of a potential superior algorithm. Considering the influence of algorithm complexity, further investigation is needed to examine the differences between fMRI peaks and TMS cortical hotspots that were identified previously.

Methods: Twelve healthy participants underwent TMS motor mapping and a finger-tapping task during fMRI. The motor cortex TMS mapping results were estimated by five algorithms, and fMRI activation results were obtained. For each algorithm, the prediction error was defined as the distance between the measured scalp hotspot and optimized coil position, which was determined by the maximum electric field strength in the estimated motor cortex. Additionally, the study identified the minimum number of stimuli required for stable mapping. Finally, the location difference between the TMS mapping cortical hotspot and the fMRI activation peak was analyzed.

Results: The projection yielded the lowest prediction error (5.27 ± 4.24 mm) among the point-based algorithms and the association algorithm yielded the lowest (6.66 ± 3.48 mm) among field-based estimation algorithms. The projection algorithm required fewer stimuli, possibly resulting from its suitability for the grid-based mapping data collection method. The TMS cortical hotspots from all algorithms consistently deviated from the fMRI activation peak (20.52 ± 8.46 mm for five algorithms).

Conclusion: The association algorithm might be a superior choice for clinical applications and basic neuroscience research, due to its lower prediction error and higher estimation sensitivity in the deep cortical structure, especially for the sulcus. It also has potential applicability in various other TMS domains, including language area mapping and more. Otherwise, our results provide further evidence that TMS motor mapping intrinsically differs from fMRI motor mapping.

KEYWORDS

transcranial magnetic stimulation, TMS motor mapping, estimation algorithm, electric field modeling, functional magnetic resonance imaging

1 Introduction

Transcranial magnetic stimulation (TMS) is a non-invasive focal brain stimulation technique widely used in brain mapping studies (Ilmoniemi et al., 1999; Siebner et al., 2009; Lefaucheur, 2019). When a single supra-threshold TMS pulse is applied to the motor cortex, a motor-evoked potential (MEP) may be recorded from the targeted muscle, such as the first dorsal interosseous muscle (FDI). TMS motor mapping, in which multiple MEPs typically recorded from predetermined stimulation sites on a grid are used to non-invasively probe motor cortex representation, is one of the most important applications of TMS (Wilson et al., 1993; Sondergaard et al., 2021). TMS has several advantages over other noninvasive approaches to motor cortex mapping such as functional magnetic resonance imaging (fMRI). Compared to fMRI, TMS motor mapping is in closer agreement with direct cortical stimulation (DCS) mapping, which is regarded as the current gold standard for delineating the motor cortex (Krieg et al., 2012; Coburger et al., 2013; Mangraviti et al., 2013). Moreover, TMS requires less patient cooperation such as performing motor tasks, which is difficult for patients with paresis or plegia or children with autism or developmental delay (Narayana et al., 2015, 2021; Braden et al., 2022). Such advantages have made TMS motor cortex mapping promising in clinical applications, such as pre-surgical planning (Takahashi et al., 2013; Lefaucheur and Picht, 2016), risk stratification (Rosenstock et al., 2017), motor rehabilitation (Lüdemann-Podubecká and Nowak, 2016) and basic research such as developmental plasticity (Narayana et al., 2015; Grab et al., 2018; Babwani et al., 2021).

Given a set of recorded MEPs as well as the corresponding stimulating sites on the scalp, there are various algorithms, with increasing complexity, for the prediction of the location and spread of the motor cortex. The most traditional and simplest one is called the projection algorithm, which assumes that the effect of a TMS pulse at a scalp site can be reduced to a single point projected onto the cortex (Ruohonen and Karhu, 2010; Julkunen, 2014; Kraus and Gharabaghi, 2015). Simple geometric models cannot characterize the effect of TMS on the cortex well. Therefore, several approaches have been introduced that numerically simulate the electric field induced by TMS, taking into account the coil orientation and the complex geometry of the individual brain (Thielscher et al., 2011; Laakso et al., 2014; Reijonen et al., 2020). Analogous to the projection algorithm, the projection point was substituted by the peak point of the induced electric field on the cortex (called max-EF algorithm here) (Ruohonen and Karhu, 2010; Sollmann et al., 2016; Novikov et al., 2018). But it's still geared to point-based algorithms, rather than field-based algorithms that utilize complete information from the electric field distribution. Opitz et al. hypothesized that when a recorded MEP was large, the induced electric field should be concentrated near the target region and vice versa. Based on this assumption, they used each MEP to weight the corresponding electric field and used the weighted average electric field to estimate the motor cortex (called EF-COG algorithm here) (Opitz et al., 2013). Other studies pointed out that, in the targeted motor cortex, there should be a strong association between the MEP and the corresponding electric field strength. Thus, they evaluated the degree of association in each cortical patch to estimate the motor cortex (called the association algorithm here) (Thielscher and Kammer, 2002; Matthäus et al., 2008; Laakso et al., 2018; Weise et al., 2020; Kataja et al., 2021; Numssen et al., 2021; Weise et al., 2023). Moreover, some algorithms borrowed from the idea of electroencephalography source localization and performed a minimum norm estimation (called MNE algorithm here) to estimate the extent of the motor cortex (Bohning et al., 2001; Pitkänen et al., 2017; Reijonen et al., 2022).

With the emergence of new estimation algorithms for motor mapping, the comparison of different approaches is becoming a growing concern. For example, Seynaeve et al. compared the motor map from the projection, max-EF, and EF-COG algorithm with the DCS mapping result as a standard (Seynaeve et al., 2019). However, it is difficult in practice to obtain DCS data, and the mapping accuracy of DCS mapping is limited by finite discrete sampling (Seynaeve et al., 2019). Fortunately, it has been found that the electric field modeled numerically in the target brain area is a great predictor of the neurophysiological or behavioral response induced by transcranial brain stimulation (Argyelan et al., 2019; Jamil et al., 2020; Fridgeirsson et al., 2021; Mosayebi-Samani et al., 2021). Several studies have been concerned with the potential of optimizing coil position according to the electric field simulation (Weise et al., 2020; Gomez et al., 2021), and Reijonen et al. took the difference between electric-field-based optimized coil position and measured scalp hotspot coil position as the performance index for the MNE algorithm based on realistic and spherical head models (Reijonen et al., 2022). This suggests that the distance between the optimized coil position and measured scalp hotspot coil positions could serve as a viable and practical performance metric for comparing different estimation algorithms.

The number of data points (stimuli) fed into an estimating algorithm is closely related to the stability of the motor map and the acquisition time of mapping data. There is a trade-off between motor map stability and acquisition time. The more stimuli, the greater the stability, but the longer the acquisition time, which leads to practical difficulties (Sinitsyn et al., 2019; Sollmann et al., 2021; Sondergaard et al., 2021). Thus, the minimum number of stimuli required to deliver a stable mapping result is another valuable performance index in the comparison of various estimation algorithms. Pitkänen et al. inferred that the MNE algorithm might need fewer stimuli because of the higher resolution capacity of its mapping, compared with the projection algorithm (Pitkänen et al., 2017). However, no study has investigated the number of stimuli required for currently available algorithms simultaneously, and thus there is no evidence showing which algorithm requires the least number of stimuli.

The results of previous studies have suggested that the cortical hotspot location from TMS mapping based on the projection algorithm was inconsistent with the peak location of fMRI motor task

activation, and the TMS cortical hotspot was always located more anterior (Herwig et al., 2002; Lotze et al., 2003; Diekhoff et al., 2011). This has been ascribed to neurophysiological differences, i.e., neurons activated by TMS and those detected by fMRI differed (Herwig et al., 2002; Wang et al., 2020). However, advanced field-based estimation algorithms have the potential to improve the estimation performance of motor mapping (Seynaeve et al., 2019). Thus, it is important to revisit the incongruency in cortical hotspot locations estimated by TMS and fMRI for advanced algorithms.

Given the above, this study aims to simultaneously compare the aforementioned five estimation algorithms on one set of TMS mapping data. We mainly conducted two experiments to compare them: first, we compared the distance between the measured scalp hotspot and optimized coil position according to the mapping results from all algorithms; second, we probed the relationship between the number of stimuli and estimation stability to determine the minimum number of stimuli required to deliver a stable mapping result for each algorithm. We also investigated whether inconsistencies between TMS and fMRI cortical hotspot locations still exist when considering the induced electric-field distribution in the estimation process.

2 Method

2.1 TMS data acquisition

TMS mapping data were obtained from our previous study (Jiang et al., 2020). Twelve healthy right-handed participants (7 males, 22 ± 2.7 yr) were recruited. None of them had any contraindications to TMS or any history of neurological or psychiatric diseases. All participants provided written informed consent before the experiment. The protocol was approved by the ethics committee of the State Key Laboratory of Cognitive Neuroscience and Learning at Beijing Normal University. TMS motor mapping was conducted using a Magstim rapid2 (Magstim Ltd., Dyfed, United Kingdom) with a D70 Air Film figure-of-eight coil. We designed a 6 × 7 stimulation grid that covered the motor-related area in the left hemisphere, according to the motor-related functional transcranial brain atlas (Jiang et al., 2020). The grid spacing was 3 continuous proportional coordinate (CPC) units, which are normalized scalp coordinates with inter-individual comparability (Xiao et al., 2018), and the group average Euclidean distance of a unit was around 1 cm (see Supplementary Figure S1A). 1 cm^2 stimulation grid is widely adopted (57/75 studies) (Sondergaard et al., 2021), making the comparison results suitable for the majority of scenarios of motor mapping. The coil was placed tangentially to the scalp with the coil handle pointing backward and laterally at 45° away from the midline, which is the optimal orientation to induce MEP (Balslev et al., 2007; Reijonen et al., 2020). The resting motor threshold (RMT) was defined as the lowest intensity eliciting a minimum peak-to-peak amplitude of 50 μV in at least 5 of 10 TMS pulses (Rossini et al., 2015). The stimulation intensity for mapping was set to 120% RMT, resulting in more reliable MEP responses (Ngomo et al., 2012). The best coil position for evoking the largest MEPs in the first dorsal interosseous (FDI) muscle, the resting motor threshold (RMT) was found and recorded.

For reliable measurement of MEP, we delivered 6 TMS pulses per site in the grid with interstimulus intervals of over 5 s (Cavaleri et al., 2017; Nazarova and Asmolova, 2021; Sondergaard et al., 2021). During stimulation, the subjects were asked to maintain complete muscle relaxation. Peak-to-peak amplitudes were recorded from the subjects' FDI muscle in the right upper limb with bipolar surface electrodes using a Brainsight EMG Isolation Unit and Amplifier Pod (Rogue Research Inc., Canada). The measurement of the RMT and input–output (I/O) curve demonstrated that the FDI muscle was more reliable than the abductor pollicis brevies muscle (Malcolm et al., 2006), both of which are commonly used muscles in TMS motor measurement.

2.2 Estimation algorithms for motor mapping

Head modeling and electric field simulation were realized in the SimNIBS v3.2 open-source pipeline (Thielscher et al., 2015) (supplement). The recorded MEPs and stimulation positions (or electric fields) were used to estimate the motor cortex via each algorithm. Since the entire cortical surface consisted of over two hundred thousand triangles leading to a large amount of useless computation, before estimation, an estimation scope was determined by projecting the stimulation grid onto the cortical surface and expanding it by 0.5 cm (see Supplementary Figure S1B).

Figure 1 shows the estimating schemes of five algorithms. Two point-based algorithms initially identify the cortical sites most likely to be influenced at each point within the stimulation grid. Then they undertake the interpolation on the cortical surface using MEP values corresponding to each cortical site, thereby generating a continuous estimated motor map. In the projection algorithm (Figure 1A), the cortical site most likely to be influenced is determined using the Möller–Trumbore intersection algorithm, which identifies the cortical site nearest to the normal of the TMS coil surface (Möller and Trumbore, 1997). In the max-EF algorithm, the cortical site is identified as the location with the highest electric field strength at the 99.9th percentile. The selection of the 99.9th rather than 100th is intended to mitigate the boundary effects of the electric field (Saturnino et al., 2019). To enable interpolation on the 3D cortical surface (Julkunen, 2014), we initiated the process by mapping the pre-identified cortical sites onto the 2D plane parallel to the gyrus (van de Ruit et al., 2015; Jonker et al., 2019). Subsequently, we conducted interpolation of the MEP values through the implementation of a cubic spline algorithm. The interpolated values were then projected from the 2D plane to the 3D cortical surface using the Nearest-neighbor interpolation algorithm.

Opitz et al. referenced the TMS COG position from traditional TMS motor mapping, which calculates a MEP "Center of Gravity," signifying a scalp position where a large MEP is reliably produced (Sondergaard et al., 2021). They introduced the concept of the electric field "Center of Gravity" (Opitz et al., 2013), portrayed as a probability map of the motor cortex. In the EF-COG algorithm (Figure 1B), this concept is realized by conducting a weighted sum of the electric field strength associated with MEPs. The fundamental concept underlying the association algorithm is predicated on the identification of the motor area as the cortical region characterized by a robust correlation between the

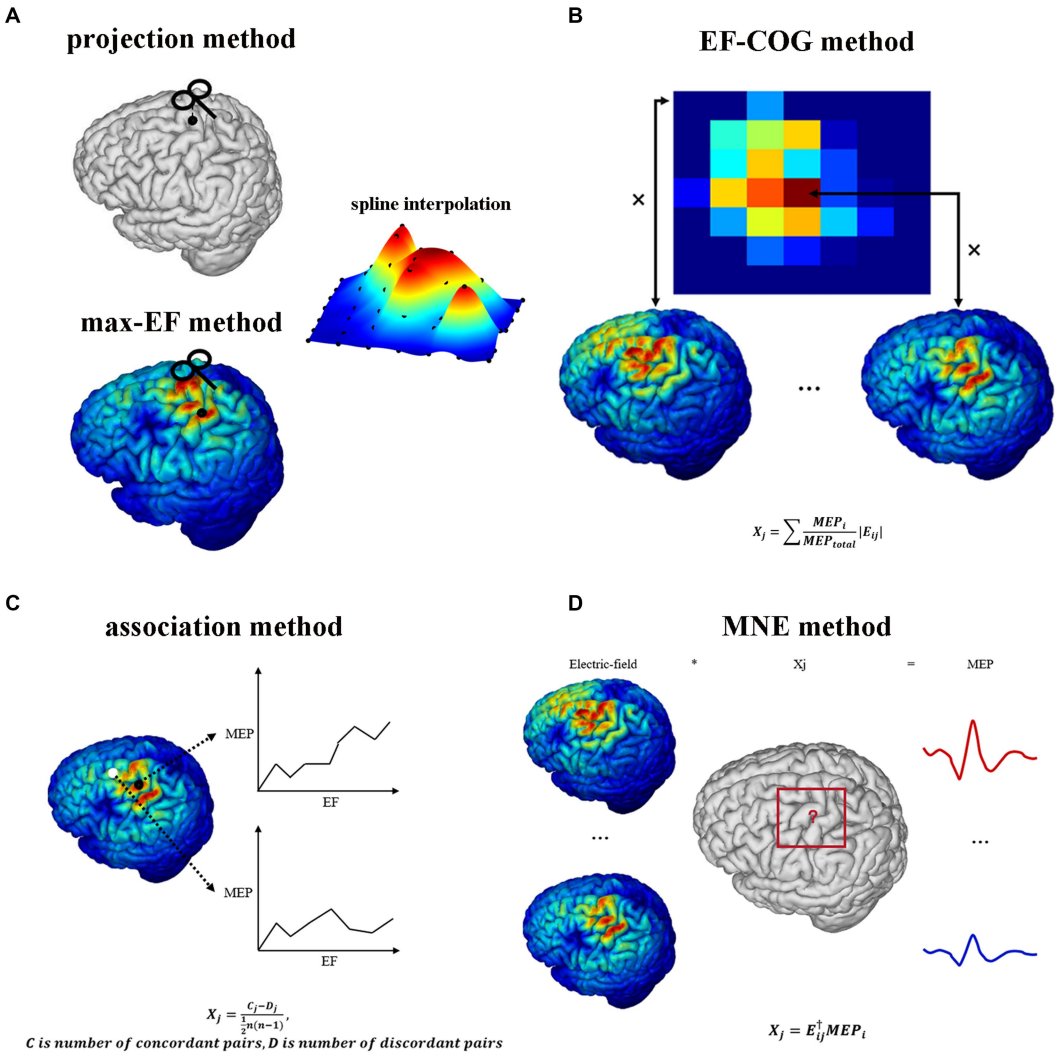

FIGURE 1
TMS motor cortex estimation scheme of five algorithms. It shows each algorithm's logic and mathematical description of part algorithms. **(A)** Projection algorithm and max-EF algorithm. **(B)** EF-COG algorithm. **(C)** Association algorithm. **(D)** MNE algorithm. In the mathematical description, Xj represents the probability that the jth cortical patch belongs to the motor cortex; E_{ij} represents the electric field strength of the jth cortical patch in the ith stimulation; MEP_i represents the MEP value recorded in the ith stimulation; MEP_{total} represents the sum of all recorded MEP.

surrounding electric field strength and the corresponding MEP values. We calculated the Kendall's rank coefficient between the electric field strength and MEPs referred to as Matthäus et al. (2008). The resultant coefficient serves as a representation of the estimated motor map (Figure 1C). The MNE algorithm is rooted in source localization methodologies commonly employed in electroencephalography (Bohning et al., 2001; Pitkänen et al., 2017; Reijonen et al., 2022). It established a computational model to delineate how MEPs are determined by the distributions of electric field strength under each stimulation. In this model, the distribution of electric field strength is the independent variable, the MEP value is the dependent variable, and the unknowns represent the probability of a cortical patch belonging to the motor area. This model is undetermined due to having fewer dependent variables than unknowns. To address this, Wiener regularization is applied to resolve the problem, resulting in an estimated motor map (Pitkänen et al., 2017).

2.3 Similarity of estimation results

The similarities and differences among mapping results from all five estimation algorithms were investigated in several spatial scales: the entire estimated motor map, map maxima (cortical hotspot), and center-of-gravity (COG). The Pearson correlation coefficient (r) was computed as the map level similarity between each pair of algorithms' maps. The Euclidean distance between each pair of cortical hotspots was computed as the cortical hotspot similarity index. The Euclidean distance between each pair of COGs was computed as the COG similarity index. The non-parametric Wilcoxon signed-rank test was used to check that there exists a statistically significant difference between pairs of cortical hotspots or COGs. Account for the folded structure of the cortex, we also adopted the geodesic distance to measure the difference of cortical hotspot location estimated by five algorithms. The geodesic distance of two cortical hotspots was calculated with tvb-gdist 2.1.0.

10.3389/fnins.2023.1301075

2.4 Distance between measured scalp hotspot and optimized coil position

The scalp hotspot is the scalp position where TMS induces maximum MEP response during the motor mapping experiment. The optimized coil position within a mapping algorithm is delineated as the theoretical scalp position capable of inducing the maximum MEP response corresponding to the motor cortex, as estimated by the algorithm. To assess the estimation accuracy of each algorithm, we need to calculate the distance between the optimized coil position and the scalp hotspot position. The shorter distance might mean a more accurate estimation algorithm. The distance is regarded as the prediction error here. Before optimization, we densified the predefined grid to shorten the grid spacing (Figure 2). We fixed the stimulation orientation in the experiment, so we did not consider the influence of orientation when optimization. Then we did an electric field simulation on each densified grid point, and determined the optimized coil position by the maximum electric field strength in the estimated motor cortex. The prediction error data was non-parametric (Shapiro–Wilk normality test), thus differences between algorithms were tested

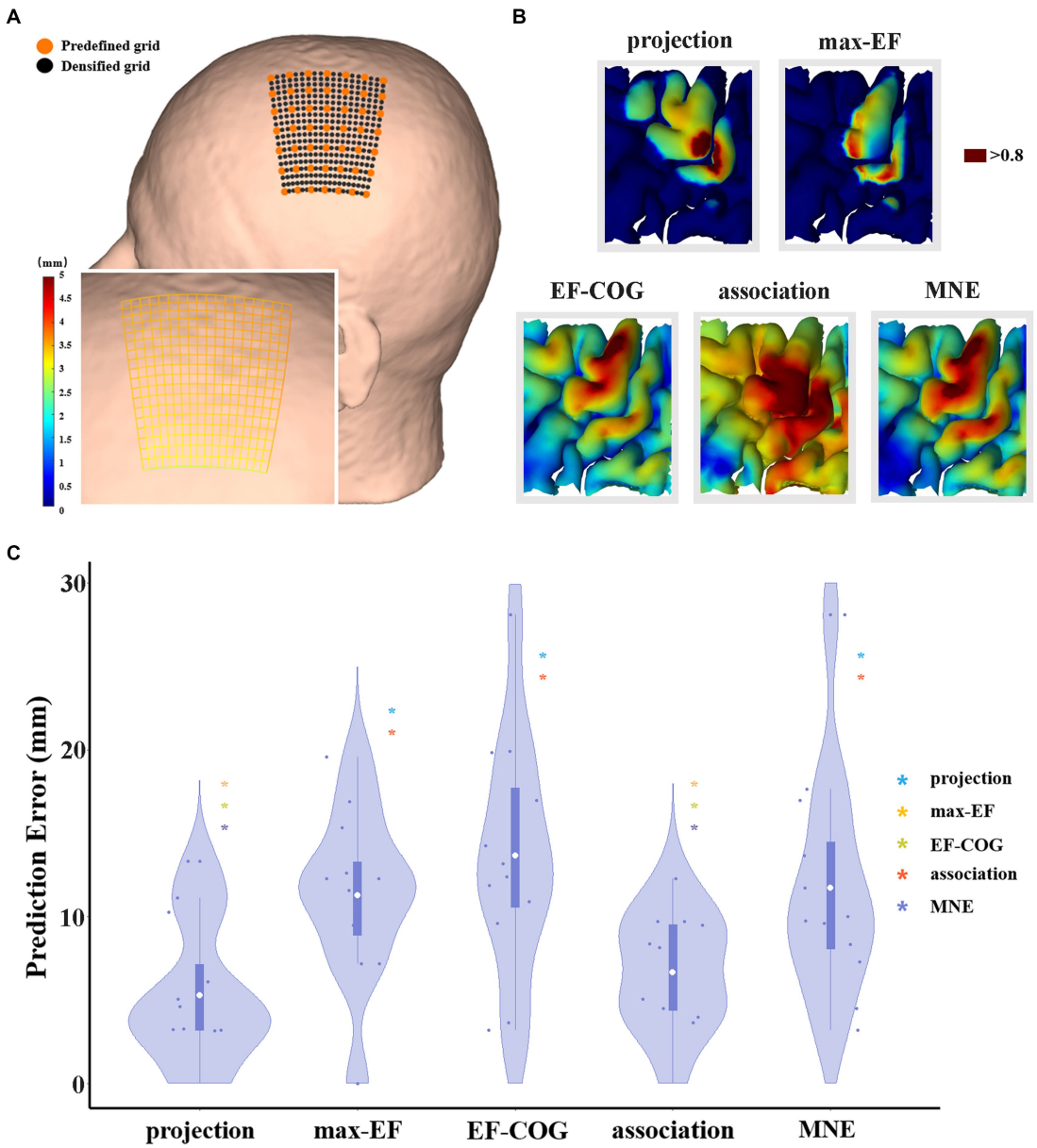

FIGURE 2
The comparison of the prediction error of five algorithms. **(A)** It shows a densified grid exampled on subject 2. The black dot represents the stimulation grid predefined before the experiment, and the orange dot represents the added grid points in the simulation. A zoom-in sub-graph in the left-bottom shows the block distance between any two grid points represented by the gradient color; **(B)** Exampled as subject 4, it shows the distribution of hand area estimated by five algorithms, and the dark red area represents the remaining hand location at the threshold of 0.8; **(C)** Violin plots show the prediction error of five algorithms at the threshold of 0.8. For each algorithm, the prediction error of each subject is represented by the blue dot. The white dot represents the group-average prediction error. Asterisks indicate a significant difference between the prediction error of the algorithm plotted and that of another algorithm (represented by different colors). *$p < 0.05$, **$p < 0.01$, ***$p < 0.001$.

using Kruskal–Wallis's test for independent data. All data met the sphericity assumption, assessed with Mauchly's test. A false-discovery-rate correction was used for multiple comparisons. For all statistical analyses, a p-value of <0.05 was considered significant.

The threshold for outlining the motor cortex is crucial when optimization. However, it is unclear and there is no consensus on how to select the outlining threshold, and whether a uniform threshold should be selected for all algorithms. Thus, we normalized the estimation value to reasonably set the same outlining threshold, and explore the difference in estimation accuracy under various thresholds (0.5–0.9). We selected 0.8 as the recommended threshold because the group average area of the motor cortex estimated by the projection algorithm is close to 270 mm^2 proposed by previous studies (Pitkänen et al., 2017; Nazarova et al., 2021) (see Supplementary Figure S3).

2.5 Relationship between the number of stimuli and estimation stability

To identify the minimum number of stimuli (N_{min}) needed for stable mapping results, we investigated the relationship between a number of stimuli (MEP from 1 stimulus = average MEPs from 6 pulses) and stability for each algorithm. We subsampled the original stimulation data (mean MEPs >50 μV, as standard in TMS) to estimate the motor map for a smaller number of stimuli. For each given number of stimuli, the subsampling process was randomly conducted 1,000 times (Efron, 1979). Stability was defined as the average Pearson correlation coefficient between the 1,000 maps obtained from subsampling (sub-sample map) and the map obtained from the original data (original map).

The N_{min} for each algorithm was defined as the minimum number of stimuli needed to reach a highly stable level when the Person correlation coefficient between maps from sub-sample data and the original data reached 0.9. We conducted statistical analysis in the same method as the comparison of prediction error. In addition, considering correlation analysis might be biased in favor of algorithms that yield a more diffuse map (e.g., the EF-COG algorithm), we also calculated the N_{min} at which the distance between the peak region (top 5% within the search scope) in the sub-sample maps and the original map is reduced to less than 3 mm.

2.6 Comparing the motor mapping of TMS and fMRI

Each subject's fMRI data, based on gradient-echo echo planar imaging (EPI) sequences were also acquired on 332 Siemens Trio 3 T MRI Scanner (32 axial slices; repetition time (TR) = 2000; echo time (TE) = 28 ms; flip angle (FA) = 90°; field of view (FOV) = 102 × 102 mm; 51 × 51 matrix size with a resolution of 2 × 2 mm^2) during a finger tapping task. To mitigate the differences between TMS and fMRI mapping arising from the movement of different muscles, volunteers performed right index finger tapping to activate the FDI muscle at a fixed frequency. In studies comparing the fMRI and TMS, a hand movement task lasting 20–40 s, alternating with rest, was commonly employed, with the majority using 6 blocks (3/5 studies, see Supplementary Table S1). In our study, the task consisted of seven rest blocks of 24 s each, featuring a fixation point, alternating with six task blocks of 24 s each. To ensure the stability of the volunteers, we added a rest block at the beginning of the task.

To acquire images with a higher spatial and temporal resolution, the above fMRI scanning only covered the upper part of the cerebrum containing the motor cortex, from the anterior and posterior commissure to the vertex, so an additional whole EPI volume was acquired for co-registration (96 axial slices; TR/TE/FA = 6000/28 ms/90°; FOV = 102 × 102 mm; 51 × 51 matrix size with a resolution of 2 × 2 mm^2). The analysis of fMRI data is described in the supplement.

The identification of the TMS cortical hotspot has traditionally been defined based on the projection algorithm and can be generalized to other algorithms to find the cortical location with the map maxima. The fMRI activation peak was determined as the point with the highest z-statistic in the estimation scope. The cortical sites were transformed into the Montreal Neurological Institute (MNI) space using the non-linear deformation field, which was obtained by segmenting and spatially normalizing the T1 image using Statistical Parametric Mapping 12. Then, we calculated the Euclidean distance between each algorithm cortical hotspot and the fMRI peak for each subject. We further calculated the divergence in X, Y, and Z coordinates (in the MNI coordinate system) to investigate the directional bias of the TMS cortical hotspot. Similarly, we also investigated the COGs to examine the spatial mismatch between TMS mapping and fMRI activation. The non-parametric Wilcoxon signed-rank test was used to check if there exists a statistically significant difference between each algorithm's results and fMRI activation results.

3 Results

3.1 Estimated motor maps

The results from the five algorithms were normalized and shown for each subject ($N = 12$) in Figure 3. The projection and max-EF algorithms yielded more concentrated motor maps than the others. Interestingly, the estimation sensitivity varies among the five algorithms in the sulcus. Interpolating solely on a 2D plane, the point-based algorithms are incapable of estimating values in the sulcus. Of the field-based algorithms, the association algorithm identified half of the subjects' estimated cortical hotspots in deep structures, while the others were located on the gyrus. In the bottom panel of Figure 3, the estimation results around the omega region (e.g., subject 4) are presented, which serves as the anatomical landmark for the hand area (Yousry et al., 1997). To facilitate a comparison of the estimation results from the five algorithms, we filled in the 0 values in the sulcus of the point-based algorithm's estimation results (Figure 3, top panel). We quantitatively investigated the pattern similarity between the estimated maps and the distance between cortical hotspots or COGs (Figure 4) from the five algorithms. Two pairs of algorithms yielded maps with a strong similarity: EF-COG and MNE ($r = 0.98 \pm 0.02$, mean ± SD); projection and max-EF ($r = 0.75 \pm 0.09$). The grid spacing of the predefined grid is 1CPC (3.36 ± 0.14 mm, Figure 4A). The pairwise correlation was statistically significant in 12 subjects ($p < 0.001$). The cortical hotspot did not significantly differ between EF-COG and MNE algorithms ($p = 0.125$), and the distance was 2.74 ± 6.65 mm (Figure 4B). It showed homogenous results when substituting

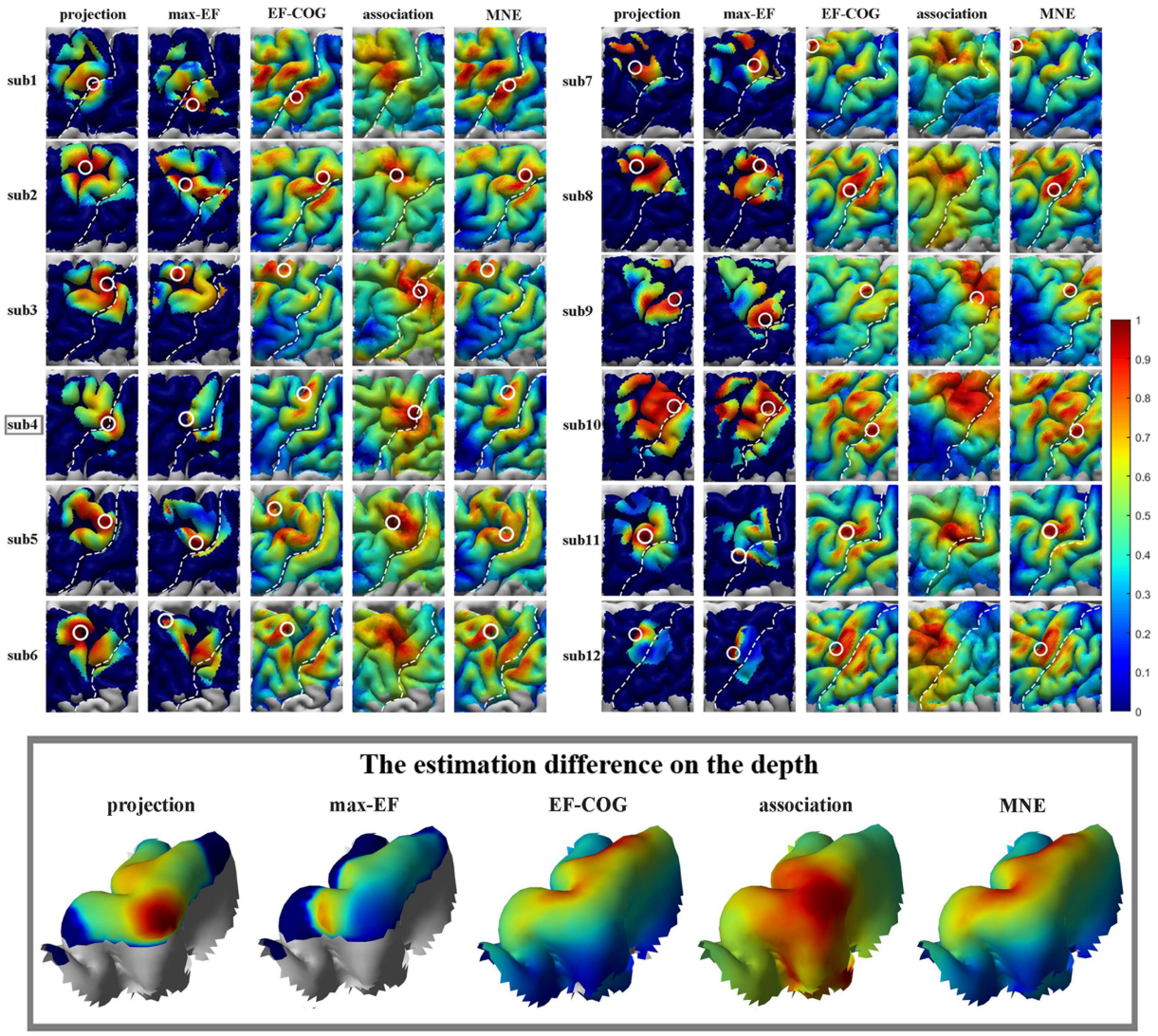

FIGURE 3
Estimated motor maps from five algorithms. The left panel shows motor maps of subjects 1–6, and the right panel shows subjects 7–12. The bottom panel displays the estimation results of five algorithms around the omega region, as illustrated by subject 4. White circles mark the cortical hotspots, and white dotted lines mark the central sulcus. The color bar represents the normalized estimation value, with red indicating a higher probability of inclusion in the motor cortex and blue indicating a lower probability.

cortical hotspots' geodesic distance (see Supplementary Figure S2). The remaining pairwise cortical hotspots differed significantly ($p < 0.001$) with the mean distance all over 12 mm. The shortest distance of COGs was between EF-COG and MNE (0.94 ± 0.74 mm, $p < 0.001$) (Figure 4C).

3.2 Comparison of prediction error

Prediction error was significantly different among the five algorithms (df = 4, $F = 7.269$, $p < 0.001$), and Figure 2C shows pairwise comparison results. At the threshold of 0.8, projection and association algorithms have significantly lower prediction errors than the other three algorithms (projection = 5.27 ± 4.24 mm, association = 6.66 ± 3.48 mm, max-EF = 11.28 ± 5.09 mm, EF-COG = 13.66 ± 6.98 mm, MNE = 11.73 ± 6.75 mm), and the two of them have no significant difference ($p = 0.386$). Supplementary Figure S4 shows the monotonously decreasing prediction error for the projection and association algorithms, but monotonously increasing for the other three algorithms with the increasing of the cutting threshold. In the range of 0.75 to 0.9, the projection and association algorithms keep a significantly lower prediction error than others.

3.3 Comparison of the minimum number of required stimuli

To determine the N_{min} required to produce a stable map, we probed the relationship between the number of stimuli and the estimation stability of each algorithm. Figure 5A shows example curves from one typical subject (subject 4). With the increase in the number of stimuli, the stability of all five algorithms increased

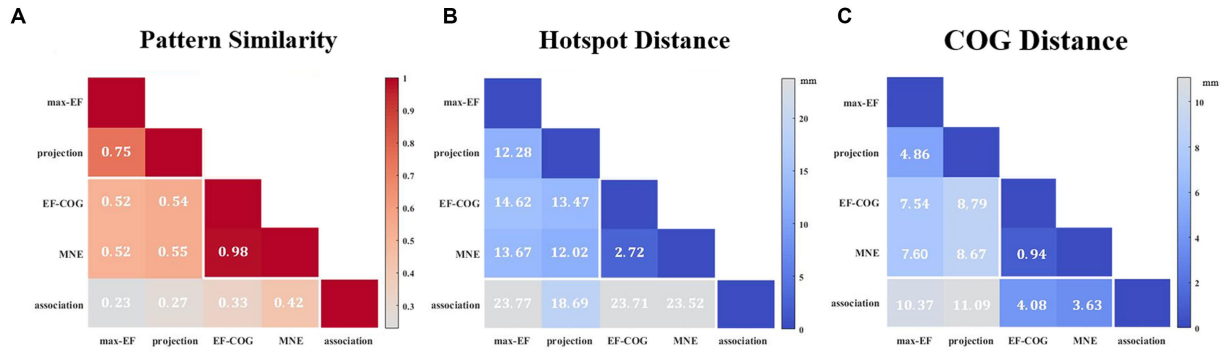

FIGURE 4
Similarity of motor maps from different algorithms. The similarity in terms of **(A)** pattern similarity of the motor map in terms of correlation coefficient r, **(B)** the Euclidean distance between cortical hotspots, and **(C)** the Euclidean distance between COGs. White numbers and shading color indicate the group's average value.

monotonously. The ranking of N_{min} of the five algorithms was: EF-COG < MNE < projection < max-EF = association. EF-COG algorithm required only 3 stimuli to estimate stably (stability = 0.969 ± 0.327), and max-EF and association required 15 stimuli (max-EF stability = 0.901 ± 0.055, association stability = 0.903 ± 0.061). N_{min} was significantly different among the five algorithms (df = 4, $F = 187.362$, $p < 0.001$), and Figure 5B shows pair-wise comparison results. Group-level analysis revealed that the EF-COG algorithm required the least N_{min} (3 ± 0), which was significantly less than each of the other four algorithms ($p < 0.001$). Max-EF and association algorithm required the most N_{min} (max-EF 14.75 ± 1.76; association 14.00 ± 1.81), and no significant difference was found between them ($p = 0.685$). The group average and SD of N_{min} were 6.17 ± 1.11 for MNE, and 11.67 ± 1.50 for projection, which both were significantly different from the other four algorithms. In the investigation of the N_{min} for stable peak region, the EF-COG algorithm still had the smallest N_{min} (see Supplementary Figure S5).

3.4 Comparison of TMS and fMRI motor mapping

Subjects 2 and 12 were not included because they had no significant fMRI activation. The remaining subjects' activation peaks were all located in the central sulcus, but most of the TMS cortical hotspots were located in the precentral gyrus (Figure 6A). The fMRI peak site significantly differed from all cortical hotspot sites estimated by the five algorithms ($distance_{projection}$ = 16.07 ± 8.41 mm, $distance_{max\text{-}EF}$ = 21.13 ± 7.70 mm, $distance_{EF\text{-}COG}$ = 23.59 ± 9.17 mm, $distance_{association}$ = 20.28 ± 7.77 mm, $distance_{MNE}$ = 21.52 ± 9.00 mm, $p = 0.002$) (Figure 6B). In the Y-axis direction, TMS cortical hotspots were located significantly more anterior to the fMRI peak for projection, max-EF, EF-COG, and MNE algorithms (projection $p = 0.02$; max-EF $p = 0.002$; EF-COG $p = 0.004$; MNE $p = 0.004$), but not significantly for association algorithm ($p = 0.492$) (Figure 6C). In the Z-axis direction, TMS cortical hotspots were located significantly more superior to the fMRI peak for projection, EF-COG, and MNE algorithms ($p = 0.027$). In the X-axis direction, no statistically significant differences between the TMS cortical hotspot and fMRI peak were found. Similar results were found for COG (see Supplementary Figure S6).

4 Discussion

4.1 The estimated motor maps of five algorithms

Based on our results (Figure 3), the distribution was more centralized for the projection and max-EF algorithms, which is consistent with previous studies (Pitkänen et al., 2017; Seynaeve et al., 2019). One possible explanation for this is that the projection and max-EF algorithms work based on points and do not consider the spread of neuronal activity induced by TMS, while the other three field-based algorithms work based on the electric field distributions. Notably, approximately half of the subjects' cortical hotspots estimated from the association algorithm were located in the deeper cortex. It is possibly attributed to the association algorithm's higher sensitivity to electric field strength compared to the MNE and EF-COG algorithms. The point-based algorithm is unable to depict the probability distribution of the motor cortex in the sulcus due to the lack of a reliable and physiologically valid interpolation method for the 3D cortex. We adopted a common and demonstrated repeatable 2-D spline interpolation method (Wilson et al., 1993; Borghetti et al., 2008; Julkunen, 2014; Jonker et al., 2019). Although the MNE algorithm had a much higher computational complexity, its results were highly similar to those of the EF-COG algorithm (Figure 4). The reason for this is not clear, but it may be due to the application of Wiener regularization to reduce the effect of MEP variability (Numminen et al., 1995; Pitkänen et al., 2017). Therefore, besides improving the accuracy of the hypothesized forward model, the performance of the MNE algorithm may also be enhanced by selecting an appropriate regularization method.

4.2 Comparison of estimation effectiveness and efficiency among five algorithms

We compared the effectiveness and efficiency of five different estimation algorithms mainly through two experiments. In the first experiment, we evaluated the prediction error of scalp hotspots for each algorithm as a measure of its estimation effectiveness. The projection and association algorithms produced the lowest prediction

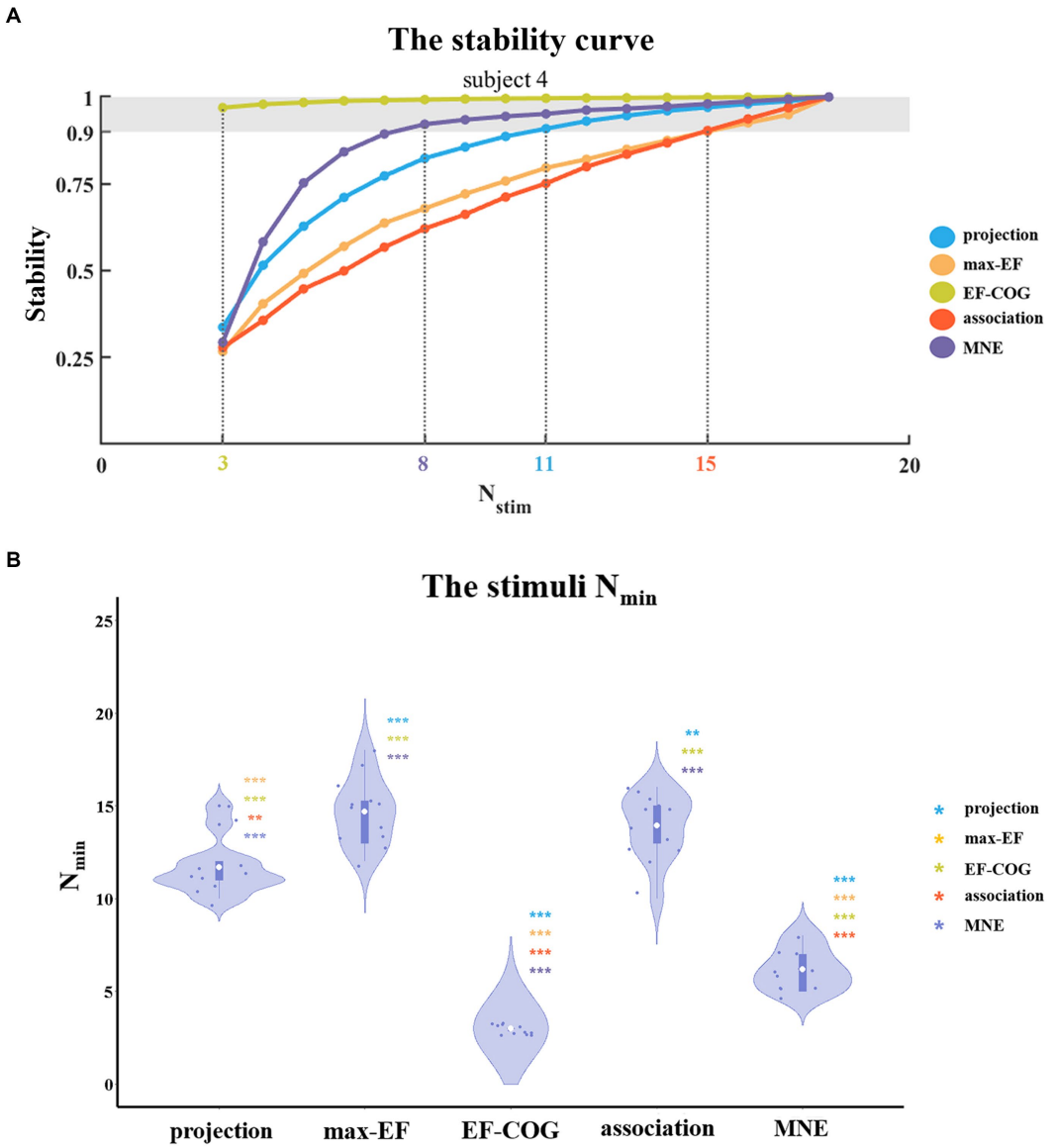

FIGURE 5
The comparison of a minimum number of required stimuli. **(A)** It shows the relationship between the number of stimuli and the stability of five algorithms. Examples are given for subject 4. Color numbers show the N_{min} of the five algorithms, the number of stimuli required for stability > = 0.9 (shade region); and **(B)** Violin plots show the distribution of the N_{min} of the five algorithms. For each algorithm, the N_{min} of each subject is represented by the blue dot. The white dot represents the group-average N_{min} of each algorithm. Asterisks indicate significant differences between the N_{min} of the algorithm plotted and that of another algorithm (represented by different colors). *$p < 0.05$, **$p < 0.01$, ***$p < 0.001$.

(5.27 mm, 6.66 mm) in the point-based and field-based estimation algorithms, respectively. Under the lower outlining threshold, such as 0.5, the prediction error might depend on the search scope range restricted before estimation. It could lead to similar evaluations for all algorithms because the remaining hand area occupies over half of the search scope. With an increasing threshold, the prediction error becomes more dependent on the estimation accuracy rather than the search scope range. Our results indicate that the projection and association algorithms consistently performed better than other algorithms in terms of lower prediction errors over the threshold range of 0.6 to 0.9, with a statistically significant difference observed in the range of 0.75 to 0.9 (see Supplementary Figure S4). The area in the chosen range was regarded as the hotspot extent, which outlines the area where the highest MEPs occur (Reijonen et al., 2020). Considering that prediction error is influenced by errors in scalp hotspot measurement and the selection of the electric field component (Bungert et al., 2017), we have provided two supplements. Firstly, we have interpolated measured MEPs on the densified grid and determined the maximum site to replace the measured scalp hotspot position. This resulted in the projection and association algorithms still performing the best ($p < 0.01$ in the pair-wise comparison). Secondly, when optimizing the coil position, we substituted the electric field strength with components of the field that are normal and tangent to the local cortex orientation, respectively. Both algorithms produced the lowest prediction error when using the tangent component ($p < 0.01$) and produced a

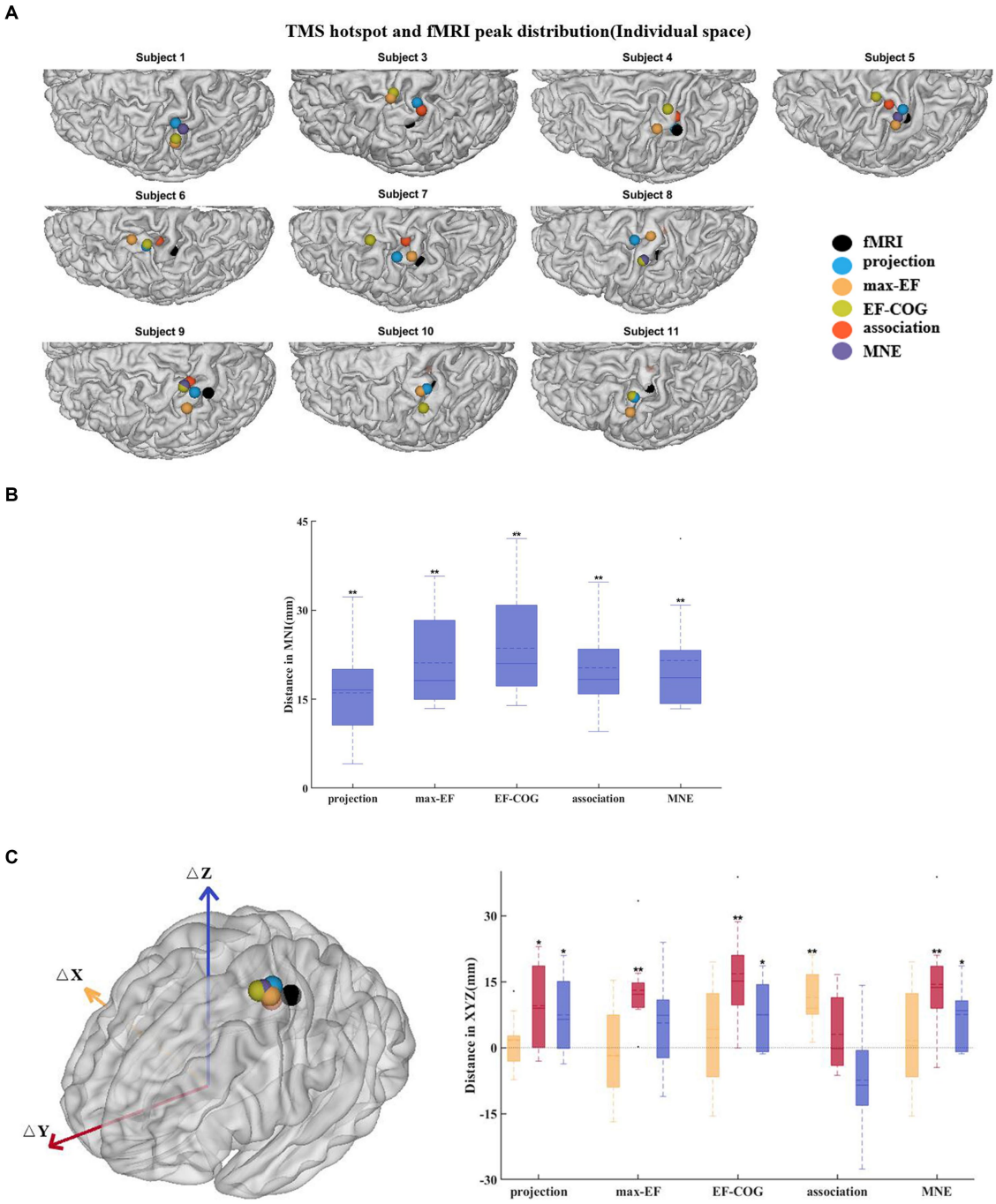

FIGURE 6
Divergence between TMS cortical hotspots and fMRI peaks. **(A)** Cortical hotspots were estimated by five algorithms and fMRI peaks (black spheres) in individual MRI spaces. **(B)** Euclidean distance between the cortical hotspots and fMRI activation peaks. **(C)** The left panel shows group-mean cortical hotspots and fMRI peaks. The right panel shows a divergence between TMS cortical hotspots and fMRI peaks separately in three axes (red, Y-axis; blue, Z-axis; yellow, X-axis). All box plots show median (black solid line), mean (black dashed line), interquartile range (box top and bottom), and 10th and 90th percentiles (error bars). *$p < 0.05$, **$p < 0.01$.

significantly lower prediction error than the EF-COG algorithm when using the normal component ($p < 0.05$). These results reliably suggest that the projection and association algorithms are more effective.

Several studies have shown that both the projection and EF-COG algorithms perform well in motor mapping when taking DCS mapping results as the standard (Coburger et al., 2011, 2013; Opitz et al., 2014; Seynaeve et al., 2019). Seynaeve et al. suggested that the projection and EF-COG algorithms both estimate the motor cortex with high accuracy (85 and 78% respectively) and that the EF-COG algorithm is better at capturing the entire motor cortex representation than the projection algorithm (Seynaeve et al., 2019). In our study, the projection and association algorithms demonstrated lower prediction errors than others. The association algorithm can outline the entire

distribution of the motor cortex without neglecting its deep structures, such as the gyrus lip and sulcus (Figure 3).

Although the projection algorithm is unable to estimate in the sulcus, it still had a similarly better prediction error compared to the association algorithm. This might be related to modeling research suggesting that the primary target of TMS is the crown top and lip regions of cortical gyri (Bungert et al., 2017; Siebner et al., 2022), which can be estimated by the projection algorithm. The part findings of our research are supported by Seynaeve et al., who suggested that the projection algorithm exhibited higher estimation accuracy than the EF-COG algorithm standardized as DCS mapping (Seynaeve et al., 2019). The prediction error of the MNE algorithm in our research is 11.73 mm, whereas it was 7.0 mm in the previous research that used the same method to evaluate the effectiveness of the MNE algorithm (Reijonen et al., 2022). The lower prediction error observed in our research may be attributed to the absence of the I/O curve in the MNE algorithm replication.

We aimed to explore the minimum number of stimuli required for stable mapping with each algorithm in the second experiment of the simulation. In addition to providing a complete depiction of the distribution of the motor cortex in three-dimensional space, the collection of multiple TMS stimuli is utilized to mitigate the effects of MEP variability (Cavaleri et al., 2017; Sinitsyn et al., 2019). In this study, we employed the classic method of collecting TMS data, which involves an even stimulation grid (Sondergaard et al., 2021). It means that the number of stimuli refers to the number of stimulation grid points that contain six TMS pulses. It mitigates the effects of MEP variability by repeatedly sampling MEPs at the same site and obtaining a more stable MEP measurement (Cavaleri et al., 2017; Therrien-Blanchet et al., 2022). With the development of neuronavigation and electric field modeling, several studies have proposed that the collection of a single TMS pulse can be directly used for motor mapping (van de Ruit et al., 2015; Numssen et al., 2021; Sondergaard et al., 2021). It mitigates the effects of MEP variability by capturing more spatial information and obtaining a more stable distribution of the motor cortex. With the TMS data collection method described above, Ruit et al. found that the projection algorithm required at least 80 TMS pulses when using the pseudorandom walk method (van de Ruit et al., 2015), and Numssen et al. found that the association algorithm required at least 180 TMS pulses (Numssen et al., 2021). In our study, we also observed the same phenomenon that the association algorithms may require more TMS stimuli than the projection algorithm (Figure 5B, see Supplementary Figure S5B). Interestingly, we found that the EF-COG algorithm consistently performed best, and the MNE algorithm came next, with estimation results mostly showing similarities (Figure 5, see Supplementary Figure S5). The lower performance of the MNE algorithm might be due to the aggravation of the ill-posed problem by decreasing the number of stimuli (Kabanikhin, 2008). Despite working based on points rather than the distribution of the electric field, the max-EF algorithm required a significantly larger N_{min} than the projection algorithm ($p < 0.001$). The instability of the max-EF algorithm may be the reason for its larger N_{min} requirement, as shown in Supplementary Figure S7. The figure illustrates that even if two stimuli induce MEP with a large discrepancy, their maximum electric field cortical sites are very close to each other.

4.3 Towards application of clinical and basic neuroscience

TMS motor mapping holds promise in various clinical applications, including pre-surgical planning (Takahashi et al., 2013; Lefaucheur and Picht, 2016), risk stratification (Rosenstock et al., 2017), motor rehabilitation (Lüdemann-Podubecká and Nowak, 2016), as well as basic research such as developmental plasticity (Narayana et al., 2015; Grab et al., 2018; Babwani et al., 2021). The fundamental requirement for a superior mapping algorithm is its ability to accurately delineate the location of the motor cortex. Numerous studies have indicated that the caudal band of the hand area resides in the depth of the central sulcus, and the rostral part is located in the more superficial sulcal wall (Geyer et al., 1996, 2000; Siebner et al., 2022). In this context, the association algorithm stands out as it can capture the entire information of the motor cortex, unlike the projection algorithm, which may miss certain portions (Julkunen, 2014). This suggests that the association algorithm could offer more accurate estimation results, potentially enhancing the security of pre-surgical planning for tumor surgery and providing more detailed knowledge of the motor cortex in research. Consequently, we propose that the association algorithm might be a preferable choice for clinical applications and basic neuroscience research.

TMS serves as a non-invasive technology commonly for causal structure–function mapping through its ability to provide supra-threshold stimulation (Siddiqi et al., 2022). While the objectivity and quantifiability of MEP draw more attention to motor mapping, TMS can extend to mapping cognitive functions beyond motor domains. TMS language mapping is equally significant as a procedure before tumor surgery and is typically conducted using the traditional point-based algorithm (Picht et al., 2013; Babajani-Feremi et al., 2016; Lehtinen et al., 2018). In our study, the association algorithm demonstrated lower prediction error and higher estimation sensitivity in the deep cortical structure. This improvement suggests potential enhancement in the accuracy of TMS language mapping and its applicability to more complex functional mapping. Notably, the association algorithm is utilized in the depression treatment to map the efficacy area of TMS, pending further confirmation regarding the selection of the electric field component (Zhang et al., 2022). Therefore, the association algorithm also exhibits great potential in mapping the efficacy area in the TMS treatment for psychiatry.

4.4 Motor mapping divergence between TMS and fMRI

In this study, the group average distance between the location of the cortical hotspot estimated by the projection algorithm and the fMRI activation peak was 16 mm which approached the mean distance reported in previous studies (around 7 to 14 mm) (Herwig et al., 2002; Lotze et al., 2003; Diekhoff et al., 2011). To exclude the possibility that the divergence was caused by the simple projection algorithm itself, we used four other electric-field-based estimation algorithms to re-estimate the cortical hotspot location. The results showed that the divergence in cortical hotspot location (20.52 ± 8.46 mm for five algorithms), as well as in COG (12.21 ± 2.73 mm), remains regardless of the estimation algorithm used (Figure 6, see Supplementary Figure S5). All of the results support the hypothesis

that TMS motor mapping differs from fMRI motor task activation mapping.

To further understand the reasons for this divergence, we analyzed the divergence in terms of distance in the 3 axes in MNI space. The notable finding from this analysis is that divergence mainly occurs in the Y axes. The cortical hotspot estimated by projection, max-EF, EF-COG, and MNE algorithms was found to be always significantly more anterior than the fMRI peak, which is consistent with previous studies (Herwig et al., 2002; Lotze et al., 2003; Diekhoff et al., 2011). One possible explanation is that neurons activated by TMS are different from those detected by fMRI (Herwig et al., 2002; Wang et al., 2020). TMS mapping reveals the causal relationship between finger movement and activation of neurons, whereas fMRI mapping simply shows a correlation between the two. Thus the TMS mapping finds neurons that directly cause finger movement and they are mainly in the primary motor cortex (PMC) in the precentral gyrus (Säisänen et al., 2010; Holmes et al., 2019). fMRI mapping detects activation of neurons that are related to voluntary finger movement not only in PMC in the precentral gyrus but also in other regions, such as the somatosensory cortex in the postcentral gyrus (Mima et al., 1999; Ehrsson et al., 2003; Akhlaghi et al., 2012). Another possible explanation is that the brain shift might also result in slightly anterior TMS cortical hotspots. The brain shift results from different conditions during the sMRI when the subject is lying and the TMS session when the subject is sitting. However, we cannot confirm the existence of divergence along the Y-axis yet, as the cortical hotspots estimated by association were not significantly more anterior than the fMRI activation peak ($p = 0.492$). The discrepancy with the association algorithm could be due to its higher estimation accuracy or the insufficient number of participants in our study.

In conclusion, both previous and our own suggest that the deviation between the TMS mapping cortical hotspot and the fMRI activation peak may arise from differences in the neurons activated by TMS compared to those detected by fMRI. Wang et al. also noted that this deviation was linked to distinct brain circuits in non-voluntary and voluntary finger movements (Wang et al., 2020). This deviation suggests the necessity of choosing an appropriate mapping technology based on research objectives. For instance, in the treatment of movement disorder, selecting the fMRI activation peak as the TMS target might be preferable. Considering the deviation between TMS and fMRI mapping, as well as the similarity between TMS and DCS mapping (Coburger et al., 2013; Mangraviti et al., 2013), fMRI mapping could be significantly supplemented by pre-surgical planning to avoid excising the area responsible for voluntary rather than non-voluntary movement.

4.5 Limitations and future work

There are several limitations to this study, which will guide our future work. Several enhanced association algorithms have been proposed (Weise et al., 2020; Kataja et al., 2021; Numssen et al., 2021; Weise et al., 2023), with the latest protocol and code for one of them publicly available (Weise et al., 2023). This protocol incorporates additional parameters of the mapping procedure, including I/O curves and coil orientations. This underscores the superiority of algorithms utilizing the electric field modeling, given that the projection algorithm cannot capture the influence of orientations, despite orientation being a crucial parameter in TMS. In our study, we examined five estimation algorithms using a classical motor mapping procedure without regard to the coil orientation. While this facilitated the result of comparisons suitable for the majority of motor mapping scenarios, further investigations employing new motor mapping procedures are needed to demonstrate the superiority of the association algorithm. It was observed that the association algorithm exhibited lower mapping efficiency than the projection algorithm and converged slowly in the second experiment. Further investigation is warranted in the new procedure because the association algorithm might require a more diverse set of TMS pulses to achieve a more reliable mapping.

Although more and more studies strive to demonstrate the physiological significance of the numerical electric field (Argyelan et al., 2019; Jamil et al., 2020; Fridgeirsson et al., 2021; Mosayebi-Samani et al., 2021), the prediction error might not be determined solely by the estimation accuracy of the mapping algorithm. Therefore, in our future work, using the DCS mapping result as the gold standard (Coburger et al., 2011, 2013; Opitz et al., 2014; Seynaeve et al., 2019) is needed for validating the higher estimation accuracy of the association algorithm. Besides the number of stimuli, the reliability of each estimation algorithm is also affected by the combination of stimulation site and orientation. Therefore, future research should explore the optimization of stimulation patterns to enhance the performance of the estimation.

5 Conclusion

In this study, we used the same set of experimental data to compare five TMS motor mapping estimation algorithms mainly in two experiments. In the first experiment, we found that the projection algorithm performed best among the point-based algorithms, while the association algorithms performed best among the field algorithms. However, the projection algorithm might miss part of the hand area because it cannot estimate it accurately in the sulcus, and even might not be in the gyrus lip. In the second experiment, we observed that the projection algorithm required fewer stimuli compared to the association algorithms when collecting TMS mapping data using the typical grid-based method. Generally, we suggest that the association algorithm may be a preferable choice for clinical applications and basic neuroscience research, even across various TMS mapping domains, including language area mapping and mapping the areas effective in depression treatment, among others. Finally, we found that even when using advanced estimation algorithms, the location of all cortical hotspots estimated by the five algorithms still deviated from the activation peak obtained from fMRI, without showing a consistent orientation preference.

Data availability statement

The data analyzed in this study is subject to the following licenses/restrictions: The datasets generated or analyzed during the current study are not publicly available due to the privacy of volunteers but are available from the corresponding author on reasonable request.

Requests to access these datasets should be directed to YC 764190303@qq.com.

Ethics statement

The studies involving humans were approved by the Ethics Committee of the State Key Laboratory of Cognitive Neuroscience and Learning at Beijing Normal University. The studies were conducted in accordance with the local legislation and institutional requirements. The participants provided their written informed consent to participate in this study.

Author contributions

YC: Conceptualization, Formal analysis, Investigation, Methodology, Validation, Visualization, Writing – original draft, Writing – review & editing. YJ: Data curation, Methodology, Resources, Writing – review & editing. ZZ: Conceptualization, Supervision, Writing – review & editing. ZL: Supervision, Writing – review & editing. CZ: Conceptualization, Funding acquisition, Investigation, Supervision, Writing – review & editing.

Funding

The author(s) declare financial support was received for the research, authorship, and/or publication of this article. This work was supported by the National Natural Science Foundation of China (grant no. 82071999 and 61431002).

Conflict of interest

The authors declare that the research was conducted in the absence of any commercial or financial relationships that could be construed as a potential conflict of interest.

The handling editor YT declared a past co-authorship with the author CZ.

Publisher's note

All claims expressed in this article are solely those of the authors and do not necessarily represent those of their affiliated organizations, or those of the publisher, the editors and the reviewers. Any product that may be evaluated in this article, or claim that may be made by its manufacturer, is not guaranteed or endorsed by the publisher.

Supplementary material

The Supplementary material for this article can be found online at: https://www.frontiersin.org/articles/10.3389/fnins.2023.1301075/full#supplementary-material

References

Akhlaghi, H., Corben, L., Georgiou-Karistianis, N., Bradshaw, J., Delatycki, M. B., Storey, E., et al. (2012). A functional MRI study of motor dysfunction in Friedreich's ataxia. *Brain Res.* 1471, 138–154. doi: 10.1016/j.brainres.2012.06.035

Argyelan, M., Oltedal, L., Deng, Z. D., Wade, B., Bikson, M., Joanlanne, A., et al. (2019). Electric field causes volumetric changes in the human brain. *elife* 8:e49115. doi: 10.7554/eLife.49115

Babajani-Feremi, A., Narayana, S., Rezaie, R., Choudhri, A. F., Fulton, S. P., Boop, F. A., et al. (2016). Language mapping using high gamma electrocorticography, fMRI, and TMS versus electrocortical stimulation. *Clin. Neurophysiol.* 127, 1822–1836. doi: 10.1016/j.clinph.2015.11.017

Babwani, A., Giuffre, A., Carlson, H., Zewdie, E., and Kirton, A. (2021). The role of overlap and distribution of robotic TMS motor maps in children's hand function. *Brain Stimul.* 14:1679. doi: 10.1016/j.brs.2021.10.289

Balslev, D., Braet, W., McAllister, C., and Miall, R. C. (2007). Inter-individual variability in optimal current direction for transcranial magnetic stimulation of the motor cortex. *J. Neurosci. Methods* 162, 309–313. doi: 10.1016/j.jneumeth.2007.01.021

Bohning, D. E., He, L., George, M. S., and Epstein, C. M. (2001). Deconvolution of transcranial magnetic stimulation (TMS) maps. *J. Neural Transm. (Vienna)* 108, 35–52. doi: 10.1007/s007020170095

Borghetti, D., Sartucci, F., Petacchi, E., Guzzetta, A., Piras, M. F., Murri, L., et al. (2008). Transcranial magnetic stimulation mapping: a model based on spline interpolation. *Brain Res. Bull.* 77, 143–148. doi: 10.1016/j.brainresbull.2008.06.001

Braden, A. A., Weatherspoon, S. E., Boardman, T., Williard, T., Adkins, A., Gibbs, S. K., et al. (2022). Image-guided TMS is safe in a predominately pediatric clinical population. *Clin. Neurophysiol.* 137, 193–206. doi: 10.1016/j.clinph.2022.01.133

Bungert, A., Antunes, A., Espenhahn, S., and Thielscher, A. (2017). Where does TMS stimulate the motor cortex? Combining electrophysiological measurements and realistic field estimates to reveal the affected cortex position. *Cereb. Cortex* 27, 5083–5094. doi: 10.1093/cercor/bhw292

Cavaleri, R., Schabrun, S. M., and Chipchase, L. S. (2017). The number of stimuli required to reliably assess corticomotor excitability and primary motor cortical representations using transcranial magnetic stimulation (TMS): a systematic review and meta-analysis. *Syst. Rev.* 6:48. doi: 10.1186/s13643-017-0440-8

Coburger, J., Musahl, C., Henkes, H., Horvath-Rizea, D., Bittl, M., Weissbach, C., et al. (2013). Comparison of navigated transcranial magnetic stimulation and functional magnetic resonance imaging for preoperative mapping in rolandic tumor surgery. *Neurosurg. Rev.* 36, 65–76. doi: 10.1007/s10143-012-0413-2

Coburger, J., Musahl, C., Weissbach, C., and Bittl, M. (2011). Navigated transcranial magnetic stimulation-guided resection of a left parietal tumor: case report. *Minim. Invasive Neurosurg.* 54, 38–40. doi: 10.1055/s-0031-1273732

Diekhoff, S., Uludağ, K., Sparing, R., Tittgemeyer, M., Cavuşoğlu, M., von Cramon, D. Y., et al. (2011). Functional localization in the human brain: gradient-Echo, spin-Echo, and arterial spin-labeling fMRI compared with neuronavigated TMS. *Hum. Brain Mapp.* 32, 341–357. doi: 10.1002/hbm.21024

Efron, B. (1979). Bootstrap methods: another look at the jackknife. *Ann. Stat.* 7, 1–26. doi: 10.1214/aos/1176344552

Ehrsson, H. H., Geyer, S., and Naito, E. (2003). Imagery of voluntary movement of fingers, toes, and tongue activates corresponding body-part-specific motor representations. *J. Neurophysiol.* 90, 3304–3316. doi: 10.1152/jn.01113.2002

Fridgeirsson, E. A., Deng, Z. D., Denys, D., van Waarde, J. A., and van Wingen, G. A. (2021). Electric field strength induced by electroconvulsive therapy is associated with clinical outcome. *Neuroimage Clin.* 30:102581. doi: 10.1016/j.nicl.2021.102581

Geyer, S., Ledberg, A., Schleicher, A., Kinomura, S., Schormann, T., Bürgel, U., et al. (1996). Two different areas within the primary motor cortex of man. *Nature* 382, 805–807. doi: 10.1038/382805a0

Geyer, S., Matelli, M., Luppino, G., and Zilles, K. (2000). Functional neuroanatomy of the primate isocortical motor system. *Anat. Embryol. (Berl)* 202, 443–474. doi: 10.1007/s004290000127

Gomez, L. J., Dannhauer, M., and Peterchev, A. V. (2021). Fast computational optimization of TMS coil placement for individualized electric field targeting. *NeuroImage* 228:117696. doi: 10.1016/j.neuroimage.2020.117696

Grab, J. G., Zewdie, E., Carlson, H. L., Kuo, H. C., Ciechanski, P., Hodge, J., et al. (2018). Robotic TMS mapping of the motor cortex in the developing brain. *J. Neurosci. Methods* 309, 41–54. doi: 10.1016/j.jneumeth.2018.08.007

Herwig, U., Kölbel, K., Wunderlich, A. P., Thielscher, A., von Tiesenhausen, C., Spitzer, M., et al. (2002). Spatial congruence of neuronavigated transcranial magnetic stimulation and functional neuroimaging. *Clin. Neurophysiol.* 113, 462–468. doi: 10.1016/s1388-2457(02)00026-3

Holmes, N. P., Tamè, L., Beeching, P., Medford, M., Rakova, M., Stuart, A., et al. (2019). Locating primary somatosensory cortex in human brain stimulation studies: experimental evidence. *J. Neurophysiol.* 121, 336–344. doi: 10.1152/jn.00641.2018

Ilmoniemi, R. J., Ruohonen, J., and Karhu, J. (1999). Transcranial magnetic stimulation--a new tool for functional imaging of the brain. *Crit. Rev. Biomed. Eng.* 27, 241–284.

Jamil, A., Batsikadze, G., Kuo, H. I., Meesen, R. L. J., Dechent, P., Paulus, W., et al. (2020). Current intensity- and polarity-specific online and aftereffects of transcranial direct current stimulation: an fMRI study. *Hum. Brain Mapp.* 41, 1644–1666. doi: 10.1002/hbm.24901

Jiang, Y., Li, Z., Zhao, Y., Xiao, X., Zhang, W., Sun, P., et al. (2020). Targeting brain functions from the scalp: transcranial brain atlas based on large-scale fMRI data synthesis. *NeuroImage* 210:116550. doi: 10.1016/j.neuroimage.2020.116550

Jonker, Z. D., van der Vliet, R., Hauwert, C. M., Gaiser, C., Tulen, J. H. M., van der Geest, J. N., et al. (2019). TMS motor mapping: comparing the absolute reliability of digital reconstruction methods to the golden standard. *Brain Stimul.* 12, 309–313. doi: 10.1016/j.brs.2018.11.005

Julkunen, P. (2014). Methods for estimating cortical motor representation size and location in navigated transcranial magnetic stimulation. *J. Neurosci. Methods* 232, 125–133. doi: 10.1016/j.jneumeth.2014.05.020

Kabanikhin, S. I. (2008). Definitions and examples of inverse and ill-posed problems. *Journal of Inverse and Ill-posed Problems* 16, 317–357. doi: 10.1515/JIIP.2008.019

Kataja, J., Soldati, M., Matilainen, N., and Laakso, I. (2021). A probabilistic transcranial magnetic stimulation localization method. *J. Neural Eng.* 18:0460f3. doi: 10.1088/1741-2552/ac1f2b

Kraus, D., and Gharabaghi, A. (2015). Projecting navigated TMS sites on the Gyral anatomy decreases inter-subject variability of cortical motor maps. *Brain Stimul.* 8, 831–837. doi: 10.1016/j.brs.2015.03.006

Krieg, S. M., Shiban, E., Buchmann, N., Gempt, J., Foerschler, A., Meyer, B., et al. (2012). Utility of presurgical navigated transcranial magnetic brain stimulation for the resection of tumors in eloquent motor areas. *J. Neurosurg.* 116, 994–1001. doi: 10.3171/2011.12.JNS111524

Laakso, I., Hirata, A., and Ugawa, Y. (2014). Effects of coil orientation on the electric field induced by TMS over the hand motor area. *Phys. Med. Biol.* 59, 203–218. doi: 10.1088/0031-9155/59/1/203

Laakso, I., Murakami, T., Hirata, A., and Ugawa, Y. (2018). Where and what TMS activates: experiments and modeling. *Brain Stimul.* 11, 166–174. doi: 10.1016/j.brs.2017.09.011

Lefaucheur, J. P. (2019). Transcranial magnetic stimulation. *Handb. Clin. Neurol.* 160, 559–580. doi: 10.1016/B978-0-444-64032-1.00037-0

Lefaucheur, J. P., and Picht, T. (2016). The value of preoperative functional cortical mapping using navigated TMS. *Neurophysiol. Clin.* 46, 125–133. doi: 10.1016/j.neucli.2016.05.001

Lehtinen, H., Mäkelä, J. P., Mäkelä, T., Lioumis, P., Metsähonkala, L., Hokkanen, L., et al. (2018). Language mapping with navigated transcranial magnetic stimulation in pediatric and adult patients undergoing epilepsy surgery: comparison with extraoperative direct cortical stimulation. *Epilepsia Open* 3, 224–235. doi: 10.1002/epi4.12110

Lotze, M., Kaethner, R. J., Erb, M., Cohen, L. G., Grodd, W., and Topka, H. (2003). Comparison of representational maps using functional magnetic resonance imaging and transcranial magnetic stimulation. *Clin. Neurophysiol.* 114, 306–312. doi: 10.1016/s1388-2457(02)00380-2

Lüdemann-Podubecká, J., and Nowak, D. A. (2016). Mapping cortical hand motor representation using TMS: a method to assess brain plasticity and a surrogate marker for recovery of function after stroke? *Neurosci. Biobehav. Rev.* 69, 239–251. doi: 10.1016/j.neubiorev.2016.07.006

Malcolm, M. P., Triggs, W. J., Light, K. E., Shechtman, O., Khandekar, G., and Gonzalez Rothi, L. J. (2006). Reliability of motor cortex transcranial magnetic stimulation in four muscle representations. *Clin. Neurophysiol.* 117, 1037–1046. doi: 10.1016/j.clinph.2006.02.005

Mangraviti, A., Casali, C., Cordella, R., Legnani, F. G., Mattei, L., Prada, F., et al. (2013). Practical assessment of preoperative functional mapping techniques: navigated transcranial magnetic stimulation and functional magnetic resonance imaging. *Neurol. Sci.* 34, 1551–1557. doi: 10.1007/s10072-012-1283-7

Matthäus, L., Trillenberg, P., Fadini, T., Finke, M., and Schweikard, A. (2008). Brain mapping with transcranial magnetic stimulation using a refined correlation ratio and Kendall's tau. *Stat. Med.* 27, 5252–5270. doi: 10.1002/sim.3353

Mima, T., Sadato, N., Yazawa, S., Hanakawa, T., Fukuyama, H., Yonekura, Y., et al. (1999). Brain structures related to active and passive finger movements in man. *Brain* 122, 1989–1997. doi: 10.1093/brain/122.10.1989

Möller, T., and Trumbore, B. (1997). Fast, minimum storage ray-triangle intersection. *J. Graphics Tools* 2, 21–28. doi: 10.1080/10867651.1997.10487468

Mosayebi-Samani, M., Jamil, A., Salvador, R., Ruffini, G., Haueisen, J., and Nitsche, M. A. (2021). The impact of individual electrical fields and anatomical factors on the neurophysiological outcomes of tDCS: a TMS-MEP and MRI study. *Brain Stimul.* 14, 316–326. doi: 10.1016/j.brs.2021.01.016

Narayana, S., Gibbs, S. K., Fulton, S. P., McGregor, A. L., Mudigoudar, B., Weatherspoon, S. E., et al. (2021). Clinical utility of transcranial magnetic stimulation (TMS) in the Presurgical evaluation of motor, speech, and language functions in young children with refractory epilepsy or brain tumor: preliminary evidence. *Front. Neurol.* 12:650830. doi: 10.3389/fneur.2021.650830

Narayana, S., Rezaie, R., McAfee, S. S., Choudhri, A. F., Babajani-Feremi, A., Fulton, S., et al. (2015). Assessing motor function in young children with transcranial magnetic stimulation. *Pediatr. Neurol.* 52, 94–103. doi: 10.1016/j.pediatrneurol.2014.08.031

Nazarova, M., and Asmolova, A. (2021). Towards more reliable TMS studies – how fast can we probe cortical excitability? *Clin. Neurophysiol. Pract.* 7, 21–22. doi: 10.1016/j.cnp.2021.11.004

Nazarova, M., Novikov, P., Ivanina, E., Kozlova, K., Dobrynina, L., and Nikulin, V. V. (2021). Mapping of multiple muscles with transcranial magnetic stimulation: absolute and relative test-retest reliability. *Hum. Brain Mapp.* 42, 2508–2528. doi: 10.1002/hbm.25383

Ngomo, S., Leonard, G., Moffet, H., and Mercier, C. (2012). Comparison of transcranial magnetic stimulation measures obtained at rest and under active conditions and their reliability. *J. Neurosci. Methods* 205, 65–71. doi: 10.1016/j.jneumeth.2011.12.012

Novikov, P. A., Nazarova, M. A., and Nikulin, V. V. (2018). TMSmap – software for quantitative analysis of TMS mapping results. *Front. Hum. Neurosci.* 12:239. doi: 10.3389/fnhum.2018.00239

Numminen, J., Ahlfors, S., Ilmoniemi, R., Montonen, J., and Nenonen, J. (1995). Transformation of multichannel magnetocardiographic signals to standard grid form. *I.E.E.E. Trans. Biomed. Eng.* 42, 72–78. doi: 10.1109/10.362916

Numssen, O., Zier, A. L., Thielscher, A., Hartwigsen, G., Knösche, T. R., and Weise, K. (2021). Efficient high-resolution TMS mapping of the human motor cortex by nonlinear regression. *NeuroImage* 245:118654. doi: 10.1016/j.neuroimage.2021.118654

Opitz, A., Legon, W., Rowlands, A., Bickel, W. K., Paulus, W., and Tyler, W. J. (2013). Physiological observations validate finite element models for estimating subject-specific electric field distributions induced by transcranial magnetic stimulation of the human motor cortex. *NeuroImage* 81, 253–264. doi: 10.1016/j.neuroimage.2013.04.067

Opitz, A., Zafar, N., Bockermann, V., Rohde, V., and Paulus, W. (2014). Validating computationally predicted TMS stimulation areas using direct electrical stimulation in patients with brain tumors near precentral regions. *Neuroimage Clin.* 4, 500–507. doi: 10.1016/j.nicl.2014.03.004

Picht, T., Krieg, S. M., Sollmann, N., Rösler, J., Niraula, B., Neuvonen, T., et al. (2013). A comparison of language mapping by preoperative navigated transcranial magnetic stimulation and direct cortical stimulation during awake surgery. *Neurosurgery* 72, 808–819. doi: 10.1227/NEU.0b013e3182889e01

Pitkänen, M., Kallioniemi, E., Julkunen, P., Nazarova, M., Nieminen, J. O., and Ilmoniemi, R. J. (2017). Minimum-norm estimation of motor representations in navigated TMS mappings. *Brain Topogr.* 30, 711–722. doi: 10.1007/s10548-017-0577-8

Reijonen, J., Pitkänen, M., Kallioniemi, E., Mohammadi, A., Ilmoniemi, R. J., and Julkunen, P. (2020). Spatial extent of cortical motor hotspot in navigated transcranial magnetic stimulation. *J. Neurosci. Methods* 346:108893. doi: 10.1016/j.jneumeth.2020.108893

Reijonen, J., Saisanen, L., Pitkanen, M., Julkunen, M., Ilmoniemi, R. J., Nieminen, P., et al. (2022). Minimum-norm estimation of TMS-activated motor cortical sites in realistic head and brain geometry. *IEEE Trans. Neural Syst. Rehabil. Eng.* 30, 441–454. doi: 10.1109/TNSRE.2022.3151678

Rosenstock, T., Giampiccolo, D., Schneider, H., Runge, S. J., Bährend, I., Vajkoczy, P., et al. (2017). Specific DTI seeding and diffusivity-analysis improve the quality and prognostic value of TMS-based deterministic DTI of the pyramidal tract. *Neuroimage Clin.* 16, 276–285. doi: 10.1016/j.nicl.2017.08.010

Rossini, P. M., Burke, D., Chen, R., Cohen, L. G., Daskalakis, Z., Di Iorio, R., et al. (2015). Non-invasive electrical and magnetic stimulation of the brain, spinal cord, roots and peripheral nerves: basic principles and procedures for routine clinical and research application. An updated report from an I.F.C.N. Committee. *Clin. Neurophysiol.* 126, 1071–1107. doi: 10.1016/j.clinph.2015.02.001

Ruohonen, J., and Karhu, J. (2010). Navigated transcranial magnetic stimulation. *Neurophysiol. Clin.* 40, 7–17. doi: 10.1016/j.neucli.2010.01.006

Säisänen, L., Könönen, M., Julkunen, P., Määttä, S., Vanninen, R., Immonen, A., et al. (2010). Non-invasive preoperative localization of primary motor cortex in epilepsy surgery by navigated transcranial magnetic stimulation. *Epilepsy Res.* 92, 134–144. doi: 10.1016/j.eplepsyres.2010.08.013

Saturnino, G. B., Puonti, O., Nielsen, J. D., Antonenko, D., Madsen, K. H., and Thielscher, A. (2019). SimNIBS 2.1: a comprehensive pipeline for individualized electric field modelling for transcranial brain stimulation. eds. Makarov, S., Horner, M. and Noetscher, G. Brain and Human Body Modeling: Springer, Cham. 3–26.

Seynaeve, L., Haeck, T., Gramer, M., Maes, F., De Vleeschouwer, S., and Van Paesschen, W. (2019). Optimized preoperative motor cortex mapping in brain tumors

using advanced processing of transcranial magnetic stimulation data. *Neuroimage Clin.* 21:101657. doi: 10.1016/j.nicl.2019.101657

Siddiqi, S. H., Kording, K. P., Parvizi, J., and Fox, M. D. (2022). Causal mapping of human brain function. *Nat. Rev. Neurosci.* 23, 361–375. doi: 10.1038/s41583-022-00583-8

Siebner, H. R., Bergmann, T. O., Bestmann, S., Massimini, M., Johansen-Berg, H., Mochizuki, H., et al. (2009). Consensus paper: combining transcranial stimulation with neuroimaging. *Brain Stimul.* 2, 58–80. doi: 10.1016/j.brs.2008.11.002

Siebner, H. R., Funke, K., Aberra, A. S., Antal, A., Bestmann, S., Chen, R., et al. (2022). Transcranial magnetic stimulation of the brain: what is stimulated? – a consensus and critical position paper. *Clin. Neurophysiol.* 140, 59–97. doi: 10.1016/j.clinph.2022.04.022

Sinitsyn, D. O., Chernyavskiy, A. Y., Poydasheva, A. G., Bakulin, I. S., Suponeva, N. A., and Piradov, M. A. (2019). Optimization of the navigated TMS mapping algorithm for accurate estimation of cortical muscle representation characteristics. *Brain Sci.* 9:88. doi: 10.3390/brainsci9040088

Sollmann, N., Goblirsch-Kolb, M. F., Ille, S., Butenschoen, V. M., Boeckh-Behrens, T., Meyer, B., et al. (2016). Comparison between electric-field-navigated and line-navigated TMS for cortical motor mapping in patients with brain tumors. *Acta Neurochir.* 158, 2277–2289. doi: 10.1007/s00701-016-2970-6

Sollmann, N., Krieg, S. M., Säisänen, L., and Julkunen, P. (2021). Mapping of motor function with Neuronavigated transcranial magnetic stimulation: a review on clinical application in brain tumors and methods for ensuring feasible accuracy. *Brain Sci.* 11:897. doi: 10.3390/brainsci11070897

Sondergaard, R. E., Martino, D., Kiss, Z. H. T., and Condliffe, E. G. (2021). TMS motor mapping methodology and reliability: a structured review. *Front. Neurosci.* 15:709368. doi: 10.3389/fnins.2021.709368

Takahashi, S., Vajkoczy, P., and Picht, T. (2013). Navigated transcranial magnetic stimulation for mapping the motor cortex in patients with rolandic brain tumors. *Neurosurg. Focus.* 34:E3. doi: 10.3171/2013.1.FOCUS133

Therrien-Blanchet, J. M., Ferland, M. C., Rousseau, M. A., Badri, M., Boucher, E., Merabtine, A., et al. (2022). Stability and test-retest reliability of neuronavigated TMS measures of corticospinal and intracortical excitability. *Brain Res.* 1794:148057. doi: 10.1016/j.brainres.2022.148057

Thielscher, A., Antunes, A., and Saturnino, G. B. (2015). Field modeling for transcranial magnetic stimulation: a useful tool to understand the physiological effects of TMS? *Annu. Int. Conf. IEEE Eng. Med. Biol. Soc.* 2015, 222–225. doi: 10.1109/EMBC.2015.7318340

Thielscher, A., and Kammer, T. (2002). Linking physics with physiology in TMS: a sphere field model to determine the cortical stimulation site in TMS. *NeuroImage* 17, 1117–1130. doi: 10.1006/nimg.2002.1282

Thielscher, A., Opitz, A., and Windhoff, M. (2011). Impact of the gyral geometry on the electric field induced by transcranial magnetic stimulation. *NeuroImage* 54, 234–243. doi: 10.1016/j.neuroimage.2010.07.061

van de Ruit, M., Perenboom, M. J., and Grey, M. J. (2015). TMS brain mapping in less than two minutes. *Brain Stimul.* 8, 231–239. doi: 10.1016/j.brs.2014.10.020

Wang, J., Meng, H. J., Ji, G. J., Jing, Y., Wang, H. X., Deng, X. P., et al. (2020). TMS hotspot: different locations and networks. *Brain Topogr.* 33, 123–134. doi: 10.1007/s10548-019-00741-9

Weise, K., Numssen, O., Kalloch, B., Zier, A. L., Thielscher, A., Haueisen, J., et al. (2023). Precise motor mapping with transcranial magnetic stimulation. *Nat. Protoc.* 18, 293–318. doi: 10.1038/s41596-022-00776-6

Weise, K., Numssen, O., Thielscher, A., Hartwigsen, G., and Knösche, T. R. (2020). A novel approach to localize cortical TMS effects. *NeuroImage* 209:116486. doi: 10.1016/j.neuroimage.2019.116486

Wilson, S. A., Thickbroom, G. W., and Mastaglia, F. L. (1993). Transcranial magnetic stimulation mapping of the motor cortex in normal subjects. The representation of two intrinsic hand muscles. *J. Neurol. Sci.* 118, 134–144. doi: 10.1016/0022-510x(93)90102-5

Xiao, X., Yu, X., Zhang, Z., Zhao, Y., Jiang, Y., Li, Z., et al. (2018). Transcranial brain atlas. *Sci. Adv.* 4:eaar6904. doi: 10.1126/sciadv.aar6904

Yousry, T. A., Schmid, U. D., Alkadhi, H., Schmidt, D., Peraud, A., Buettner, A., et al. (1997). Localization of the motor hand area to a knob on the precentral gyrus. A new landmark. *Brain* 120, 141–157. doi: 10.1093/brain/120.1.141

Zhang, B. B. B., Stöhrmann, P., Godbersen, G. M., Unterholzner, J., Kasper, S., Kranz, G. S., et al. (2022). Normal component of TMS-induced electric field is correlated with depressive symptom relief in treatment-resistant depression. *Brain Stimul.* 15, 1318–1320. doi: 10.1016/j.brs.2022.09.006

10.3389/fnins.2023.1301075

Glossary

TMS	Transcranial magnetic stimulation
MEP	Motor-evoked potential
FDI	First dorsal interosseous muscle
fMRI	functional magnetic resonance imaging
DCS	Direct cortical stimulation
CPC	Continuous proportional coordinate
RMT	Resting motor threshold
I/O curve	Input–output curve
COG	Center-of-gravity
MNE	Minimum norm estimation
N_{min}	the minimum number of stimuli needed for stable mapping results
TR	Repetition time
TE	Echo time
FA	Flip angle
FOV	Field of view
EPI	Echo planar imaging
MNI	Montreal Neurological Institute space

Frontiers in Neuroscience

Provides a holistic understanding of brain function from genes to behavior

Part of the most cited neuroscience journal series which explores the brain - from the new eras of causation and anatomical neurosciences to neuroeconomics and neuroenergetics.

Discover the latest Research Topics

See more →

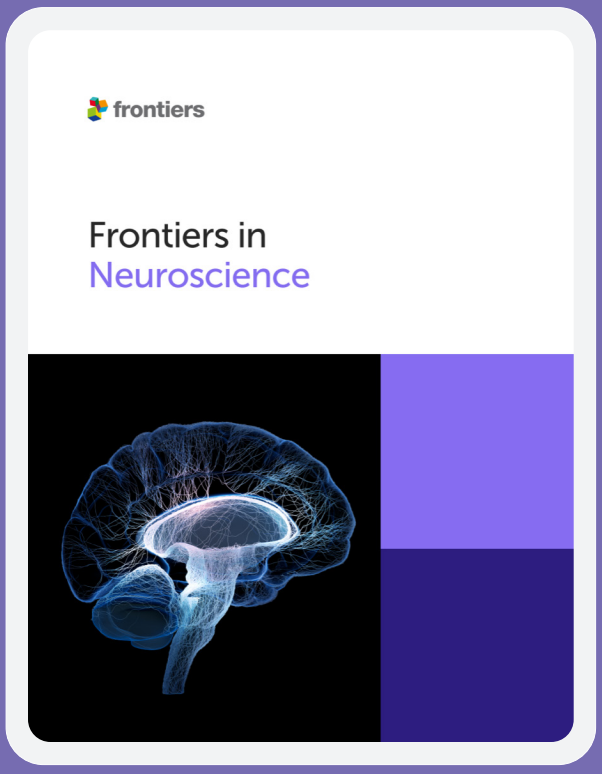

Frontiers

Avenue du Tribunal-Fédéral 34
1005 Lausanne, Switzerland
frontiersin.org

Contact us

+41 (0)21 510 17 00
frontiersin.org/about/contact